

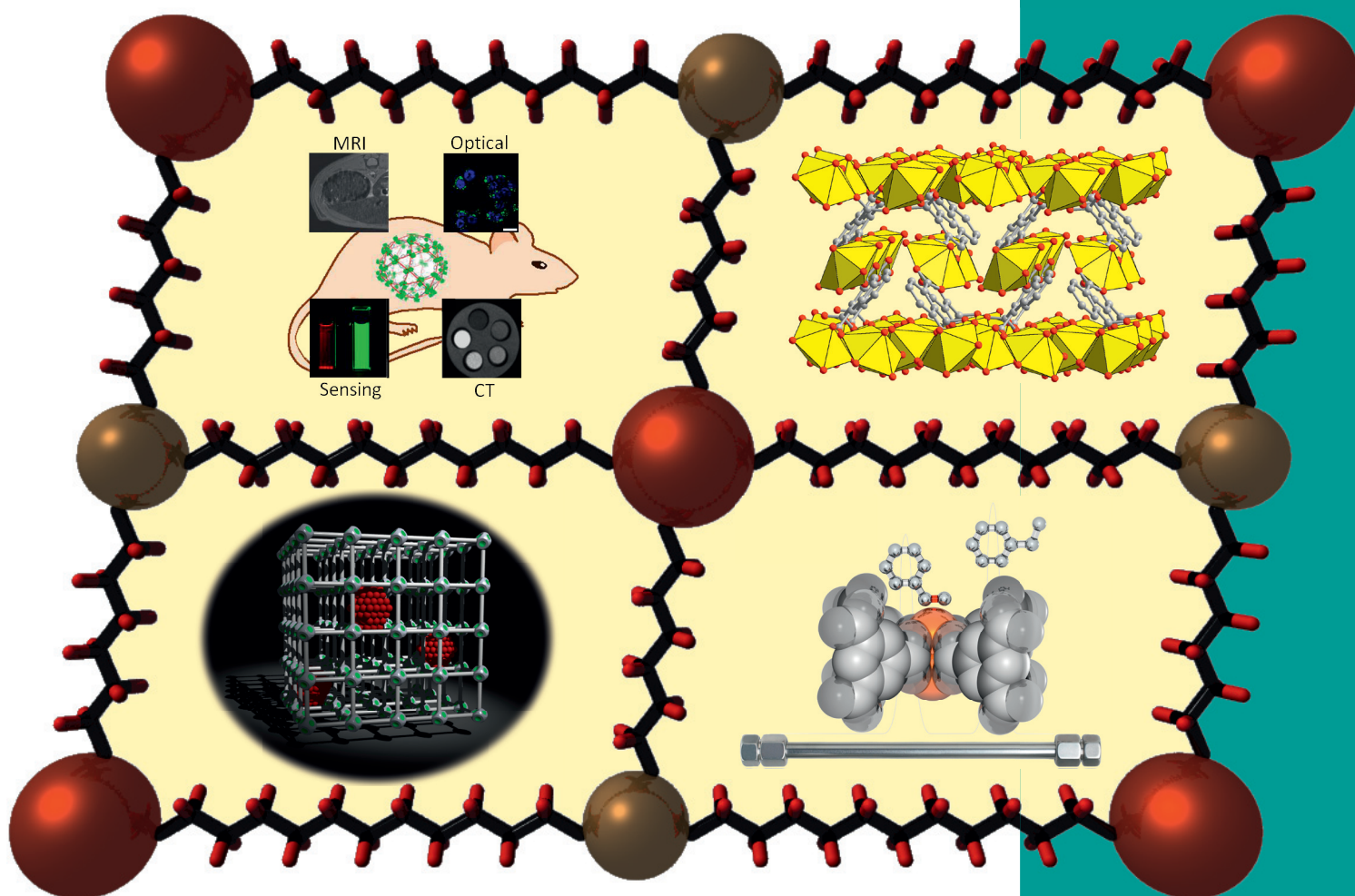


EurJIC

European Journal of
Inorganic Chemistry

24/2010
3rd August Issue

Cluster Issue:
Targeted Fabrication of MOFs
for Hybrid Functionality



Contributions to the Cover Picture by

Roland A. Fischer *et al.*; Wenbin Lin *et al.*; Dirk E. De Vos *et al.*; Jie-Sheng Chen *et al.*

Microreviews

Roland A. Fischer *et al.*

Loading MOFs with Metal Nanoparticles for Hybrid Functions

Rie Makiura and Hiroshi Kitagawa

Porous Porphyrin Nanoarchitectures on Surfaces

Wenbin Lin *et al.*

Nanoscale Metal–Organic Frameworks: MRI Contrast Agents and Beyond

 WILEY-VCH

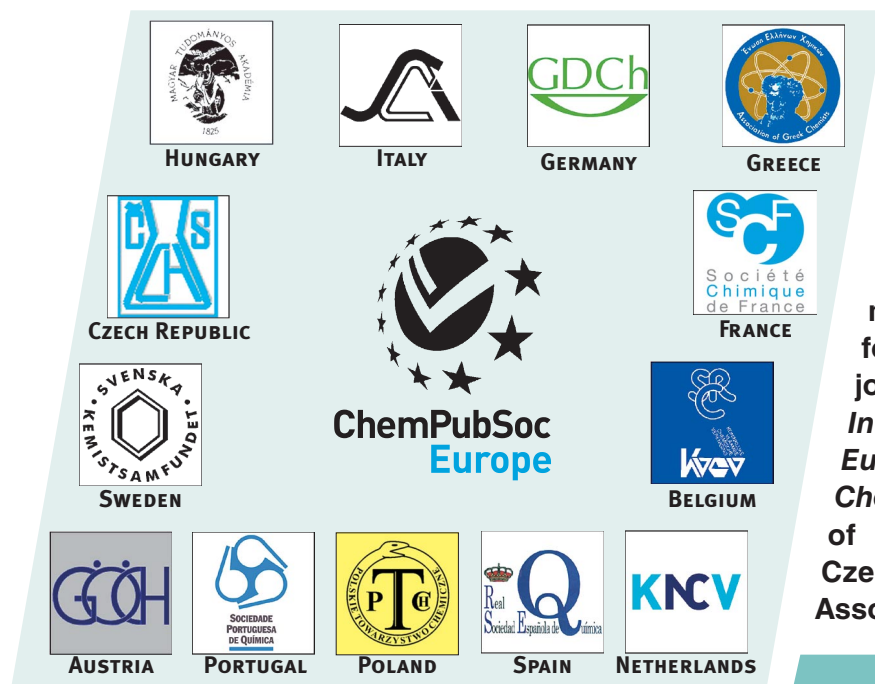
www.eurjic.org

A Journal of



ChemPubSoc
Europe

CONTENTS

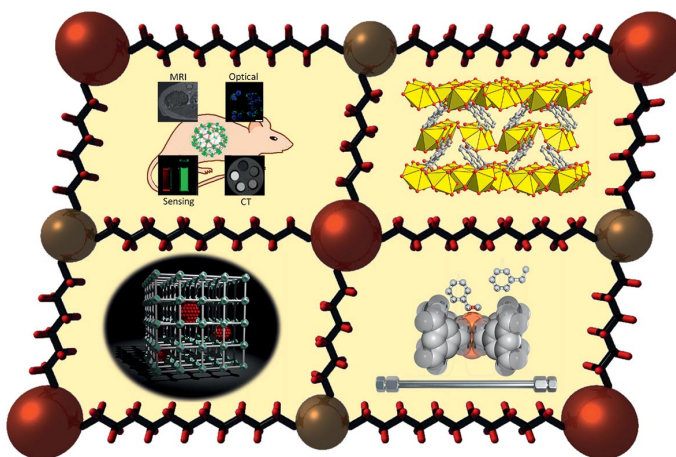


EurJIC is co-owned by 11 societies of ChemPubSoc Europe, a union of European chemical societies for the purpose of publishing high-quality science. All owners merged their national journals to form two leading chemistry journals, the *European Journal of Inorganic Chemistry* and the *European Journal of Organic Chemistry*. Three further members of ChemPubSoc Europe (Austria, Czech Republic and Sweden) are Associates of the two journals.

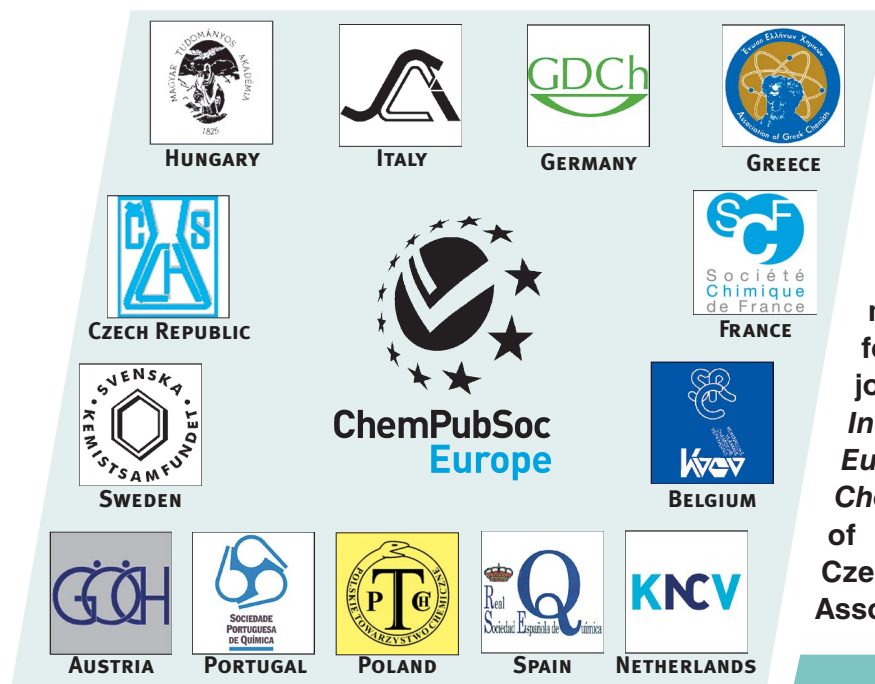
Other ChemPubSoc Europe journals are *Chemistry – A European Journal*, *ChemBioChem*, *ChemPhysChem*, *ChemMedChem*, *ChemSusChem* and *ChemCatChem*.

COVER PICTURE

The cover picture shows a schematic design of a porous metal–organic framework as the background. Embedded in the MOF are illustrations representing some of the thought-provoking contributions that make up this Cluster Issue entitled “Targeted Fabrication of MOFs for Hybrid Functionality”. With a focus towards application, this issue serves to showcase the research at the forefront of the field. The top left-hand graphic symbolises the use of nanoscale MOFs as MRI contrast agents (W. Lin et al.; p. 3725ff), while the bottom left depicts the use of MOFs as supports for metal nanoparticles in catalysis (R. A. Fischer et al.; p. 3701ff). The structure–property relationship of uranyl–organic frameworks (top right-hand corner), important in photovoltaics, is highlighted by J.-S. Chen et al. (p. 3780ff), and the synthesis of MOF composites for use as a stationary phase in HPLC (bottom right-hand corner) is discussed by D. E. DeVos et al. (p. 3735ff). A sincere thanks to the authors for their excellent contributions to the cover. We thank Heulwen Price for designing the background.



CONTENTS

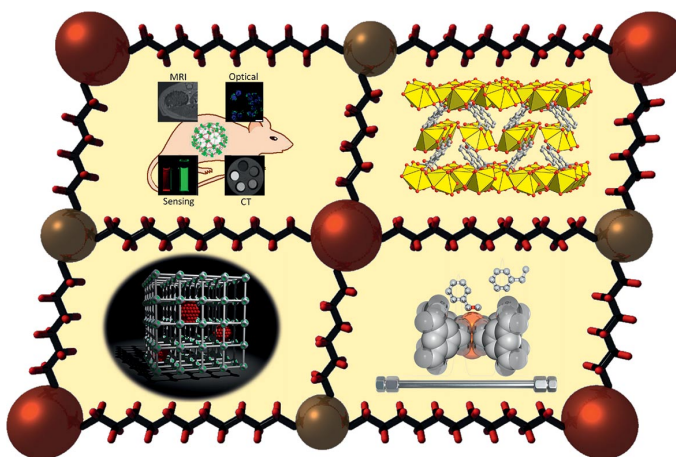


EurJIC is co-owned by 11 societies of ChemPubSoc Europe, a union of European chemical societies for the purpose of publishing high-quality science. All owners merged their national journals to form two leading chemistry journals, the *European Journal of Inorganic Chemistry* and the *European Journal of Organic Chemistry*. Three further members of ChemPubSoc Europe (Austria, Czech Republic and Sweden) are Associates of the two journals.

Other ChemPubSoc Europe journals are *Chemistry – A European Journal*, *ChemBioChem*, *ChemPhysChem*, *ChemMedChem*, *ChemSusChem* and *ChemCatChem*.

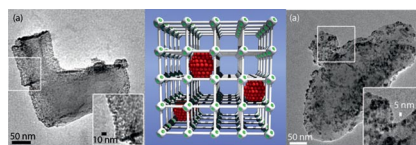
COVER PICTURE

The cover picture shows a schematic design of a porous metal–organic framework as the background. Embedded in the MOF are illustrations representing some of the thought-provoking contributions that make up this Cluster Issue entitled “Targeted Fabrication of MOFs for Hybrid Functionality”. With a focus towards application, this issue serves to showcase the research at the forefront of the field. The top left-hand graphic symbolises the use of nanoscale MOFs as MRI contrast agents (W. Lin et al.; p. 3725ff), while the bottom left depicts the use of MOFs as supports for metal nanoparticles in catalysis (R. A. Fischer et al.; p. 3701ff). The structure–property relationship of uranyl–organic frameworks (top right-hand corner), important in photovoltaics, is highlighted by J.-S. Chen et al. (p. 3780ff), and the synthesis of MOF composites for use as a stationary phase in HPLC (bottom right-hand corner) is discussed by D. E. DeVos et al. (p. 3735ff). A sincere thanks to the authors for their excellent contributions to the cover. We thank Heulwen Price for designing the background.



MICROREVIEWS

Metal–organic frameworks (MOFs) can be used for the stabilization of metal nanoparticles with adjustable size. This makes MOFs a promising new class of templates for hosting nanoparticles. “Metal@MOF” systems are interesting for several applications including heterogeneous catalysis and gas storage. This review compiles the main aspects and problems associated with these novel nanocomposite systems.



MOFs as Metal Nanoparticle Hosts

M. Meilikhov, K. Yusenkov, D. Esken, S. Turner, G. Van Tendeloo, R. A. Fischer* 3701–3714

Metals@MOFs – Loading MOFs with Metal Nanoparticles for Hybrid Functions

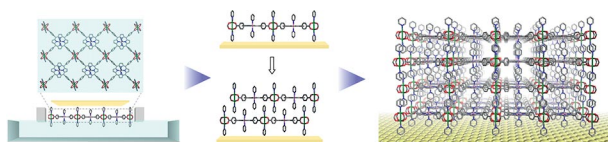
Keywords: Metal–organic frameworks / Nanoparticles / Heterogeneous catalysis / Electron tomography / Hydrogen storage

Porphyrin MOF Nanofilms

R. Makiura,* H. Kitagawa* ... 3715–3724

Porous Porphyrin Nanoarchitectures on Surfaces

Keywords: Metal–organic frameworks / Coordination polymers / Porphyrinoids / Nanostructures / Thin films



Bottom-up fabrication protocols are highly suitable to be extended to the formation of quasi-infinite nanostructures on surfaces. The perfectly crystalline, preferentially oriented MOF surface nanoarchitecture

NAFS-1, comprising metalloporphyrin units, was grown by a combined Langmuir–Blodgett and layer-by-layer (LB–LbL) methodology.

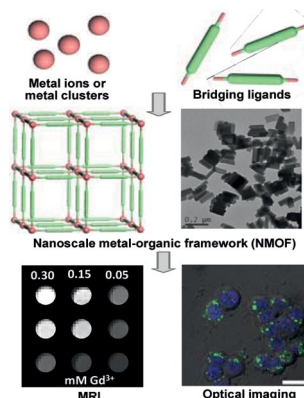
MRI Agents

J. Della Rocca, W. Lin* 3725–3734

Nanoscale Metal–Organic Frameworks: Magnetic Resonance Imaging Contrast Agents and Beyond

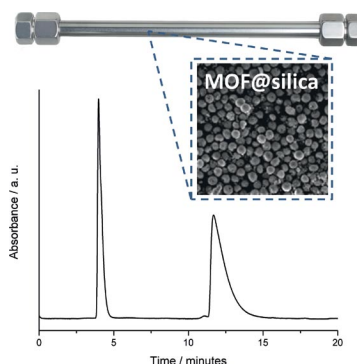
Keywords: Metal–organic frameworks / Nanoparticles / Imaging agents / Magnetic resonance imaging / Nanomedicine

This microreview covers the development of nanoscale metal–organic frameworks (NMOFs) as magnetic resonance imaging contrast agents. NMOFs not only provide large amounts of paramagnetic metal ions but are superior to clinically used contrast agents on a per-metal basis. NMOFs show promise as contrast agents for other imaging modalities and in chemical and biological sensing applications.



SHORT COMMUNICATIONS

Silica modified with a metal–organic framework (MOF) is presented as an HPLC stationary phase. This composite material combines the good column packing properties of the monodisperse silica spheres and separation ability of the MOF material.



Silica–MOF Composites for HPLC

R. Ameloot, A. Liekens, L. Alaerts, M. Maes, A. Galarneau, B. Coq, G. Desmet, B. F. Sels, J. F. M. Denayer, D. E. De Vos* 3735–3738

Silica–MOF Composites as a Stationary Phase in Liquid Chromatography

Keywords: Metal–organic frameworks / Liquid chromatography / Crystal engineering / Solvent effects

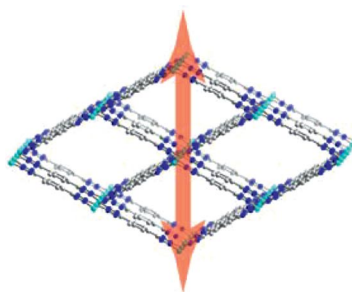
Flexible Copper(II) MOFs

K. Sumida, M. L. Foo, S. Horike,
J. R. Long* 3739–3744



Synthesis and Structural Flexibility of a Series of Copper(II) Azolate-Based Metal–Organic Frameworks

Keywords: Metal–organic frameworks / Porous materials / N ligands / Copper



The reaction of $\text{CuCl}_2 \cdot 2\text{H}_2\text{O}$ with three novel ligands, 2-methyl-1,4-benzeneditetrazolate (MeBDT^{2-}), 4,4'-biphenylditetrazolate (BPD^{2-}), and 2,3,5,6-tetrafluoro-1,4-benzeneditetrazolate (TFBD^{2-}), affords three metal–organic frameworks with a common network topology but a significantly different flexibility, highlighting the significant impact the ligand component can have on the dynamic properties of the material.

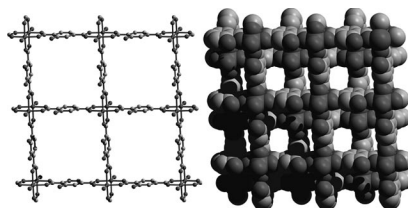
FULL PAPERS

MOFs for Gas Sorption

Z. Chen, S. Xiang, H. D. Arman,
P. Li, S. Tidrow, D. Zhao,*
B. Chen* 3745–3749

A Microporous Metal–Organic Framework with Immobilized –OH Functional Groups within the Pore Surfaces for Selective Gas Sorption

Keywords: Copper / Microporous materials / Structure elucidation / Immobilization / Adsorption



A new 2D microporous metal–organic framework, $\text{Cu}(\text{BDC}-\text{OH})(\text{H}_2\text{O}) \cdot 0.5\text{DEF}$ with functional OH groups on the pore surfaces was solvothermally synthesized and structurally characterized, and realized for the selective separation of $\text{C}_2\text{H}_2/\text{CH}_4$ and CO_2/CH_4 with a selectivity of 6.7 and 9.3, respectively, at 296 K.

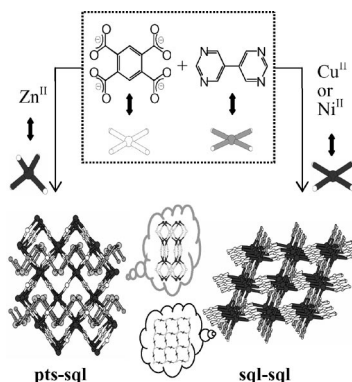
Crystal Engineering

T.-W. Tseng,* T.-T. Luo, C.-C. Tsai,
J.-Y. Wu, H.-L. Tsai,
K.-L. Lu 3750–3755



Crystal Engineering of Three Net-to-Net Intersecting Metal–Organic Frameworks from Two Comparable Organic Linking Squares

Keywords: Crystal engineering / Metal–organic frameworks / Self-assembly / Topochemistry



The engineering of three mixed-ligand metal–organic frameworks with **sql–sql** and **pts–sql** intersecting topologies from two distinct square-planar-type organic scaffolds, benzene-1,2,4,5-tetracarboxylate and 5,5'-bipyrimidine, under mild conditions is reported.

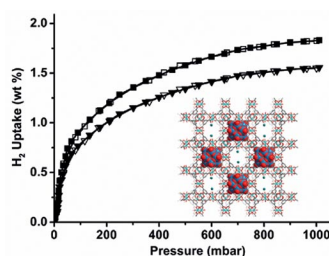
Hydrogen Adsorption

F. Ma, S. Liu,* D. Liang, G. Ren,
C. Zhang, F. Wei, Z. Su 3756–3761



Hydrogen Adsorption in Polyoxometalate Hybrid Compounds Based on Porous Metal–Organic Frameworks

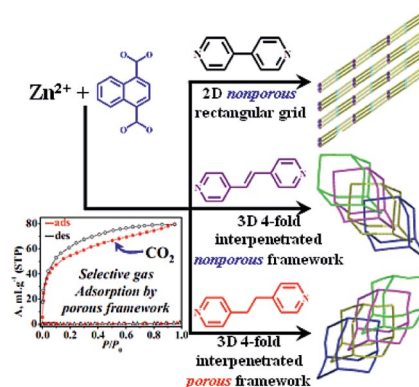
Keywords: Metal–organic frameworks / Polyoxometalates / Adsorption / Microporous materials / Ion exchange



Two polyoxometalate hybrid compounds based on porous metal–organic frameworks (PMOFs/POMs) have been prepared by lithium ion exchange. With the introduction of POMs and lithium ions, the compounds not only display strong H_2 adsorption behavior, but also exhibit some differences in H_2 binding energy.

Interpenetrating Frameworks

A 2D rectangular grid and 3D fourfold interpenetrated diamondoid frameworks have been fabricated by changing the organic pillar modules. The structural regularity, flexibility, and ligand polarity control the overall functionalities.



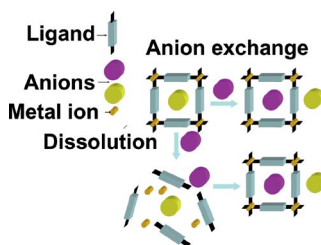
P. Kanoo, T. K. Maji* 3762–3769

Construction of a 2D Rectangular Grid and 3D Diamondoid Interpenetrated Frameworks and Their Functionalities by Changing the Second Spacers

Keywords: Zinc / Metal–organic frameworks / Crystal engineering / Diamondoid / Interpenetration / Adsorption

Selective Anion Separation

In situ crystallization of Cd^{II} coordination compounds derived from bis(pyridyl)urea/amide ligands under a highly competitive environment containing a mixture of anions, such as SO₄^{2−}, NO₃[−], ClO₄[−], AcO[−], Cl[−] and Br[−], proved to be viable for the selective separation of sulfate anions.



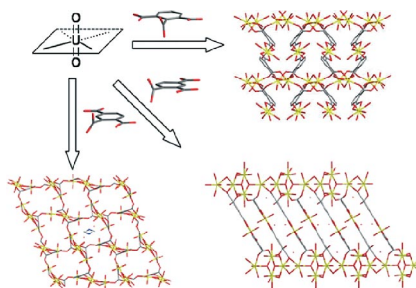
S. Banerjee, N. N. Adarsh, P. Dastidar* 3770–3779

Selective Separation of the Sulfate Anion by In Situ Crystallization of Cd^{II} Coordination Compounds Derived from Bis(pyridyl) Ligands Equipped with a Urea/Amide Hydrogen-Bonding Backbone

Keywords: Coordination polymers / Anion separation / Hydrogen bonds / Crystal engineering / Cadmium / Amides

Uranyl–Organic Frameworks

Owing to their planar coordination, uranyl–organic assemblies prefer to form chains or layers rather than three-dimensional frameworks. By employing 1,2,3- and 1,2,4-benzenetricarboxylate acids as ligands, new 3D frameworks with adsorption and photovoltaic properties are possible, as the planar tendency of the conformation of these uranyl assemblies is overcome.



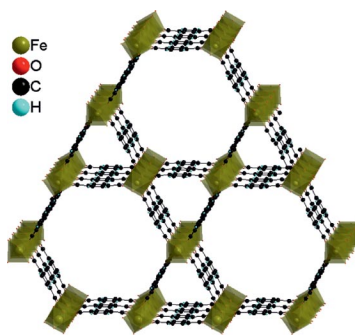
Z.-L. Liao, G.-D. Li, X. Wei, Y. Yu, J.-S. Chen* 3780–3788

Construction of Three-Dimensional Uranyl–Organic Frameworks with Benzenetricarboxylate Ligands

Keywords: Uranium / Metal–organic frameworks / Microporous materials / Photovoltaics

A Porous MIL-68 MOF

A new porous Fe^{III}-based MOF presenting the MIL-68 topology was prepared. Its structure and properties were studied by means of X-ray diffraction, thermogravimetric analysis, nitrogen sorption, Mössbauer spectrometry, and electrochemical lithium insertion.




A. Fateeva, P. Horcajada, T. Devic,* C. Serre,* J. Marrot, J.-M. Grenèche, M. Morcrette, J.-M. Tarascon, G. Maurin, G. Férey 3789–3794

Synthesis, Structure, Characterization, and Redox Properties of the Porous MIL-68(Fe) Solid

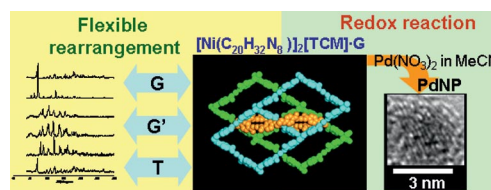
Keywords: Metal–organic frameworks / Iron / Microporous materials / Redox activity / Polymorphism

Redox-Active Coordination Polymer

H. R. Moon, M. P. Suh* 3795–3803

 Flexible and Redox-Active Coordination Polymer: Control of the Network Structure by Pendant Arms of a Macrocyclic Complex

Keywords: Coordination polymers / Flexible networks / Macrocycles / Palladium / Nickel




A doubly catenated rhombic grid is assembled from a Ni^{II} macrocyclic complex with pyridyl pendant arms. It exhibits flexible behavior upon desorption/resorption and exchange of guest molecules as well as

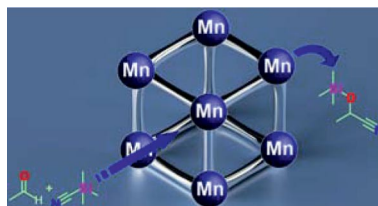
temperature change. It produces small Pd nanoparticles on immersion in a Pd(NO₃)₂ solution at room temperature in the absence of extra reducing or capping agents.

Mn-Based MOF Catalysts

T. Ladrak, S. Smulders,
O. Roubeau,* S. J. Teat, P. Gamez,*
J. Reedijk 3804–3812

 Manganese-Based Metal–Organic Frameworks as Heterogeneous Catalysts for the Cyanosilylation of Acetaldehyde


Keywords: Metal–organic networks / Heterogeneous catalysis / Manganese / Lewis acids / Trigonal prisms



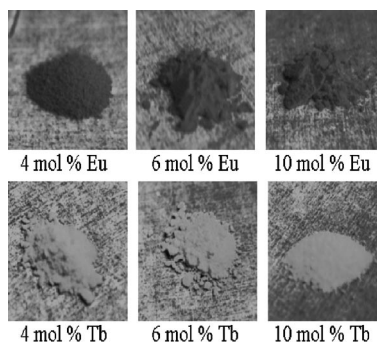
Four porous Mn-based metal–organic frameworks (MOFs) were used as efficient catalysts for the cyanosilylation of acetaldehyde. These structurally related, heterogeneous MOF catalysts can be re-used without loss of activity.

Rare-Earth MOFs

D. Sarma, M. Prabu, S. Biju,
M. L. P. Reddy,*
S. Natarajan* 3813–3822

 Synthesis, Structure and Optical Studies of a Family of Three-Dimensional Rare-Earth Aminoisophthalates [M(μ₂-OH)(C₈H₅NO₄)] (M = Y³⁺, La³⁺, Pr³⁺, Nd³⁺, Sm³⁺, Eu³⁺, Gd³⁺, Dy³⁺, and Er³⁺)


Keywords: Rare earths / Metal-organic frameworks / Luminescence / Doping



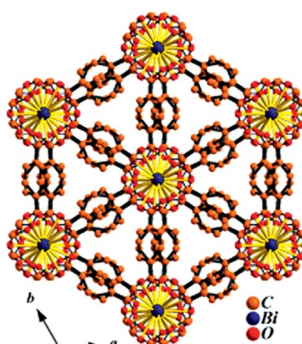
Three-dimensional rare-earth isophthalates [M(μ₂-OH)(C₈H₅NO₄)] have been isolated by hydrothermal methods and the structures, determined by single-crystal methods, exhibit a (5,5) net with the amino group of the isophthalate anion participating in bonding with the lanthanide center. The Eu³⁺ and Tb³⁺ doped samples exhibit characteristic metal-centered emission.

Photoluminescent Bi MOFs

A. Thirumurugan,
A. K. Cheetham* 3823–3828

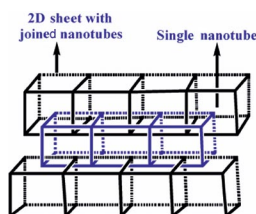
 Anionic Metal–Organic Frameworks of Bismuth Benzenedicarboxylates: Synthesis, Structure and Ligand-Sensitized Photoluminescence

Keywords: Metal–organic frameworks / Bismuth / Luminescence / Lanthanides / Network topology



Four hybrid organic–inorganic bismuth benzenedicarboxylate frameworks with two- and three-dimensional structures have been synthesized, and their structural and optical properties were investigated.

A highly crystalline-stable coordination polymer $\{[Zn_2(cpa)_2(bpy)] \cdot 3H_2O\}_n$ (**1**) has been synthesized solvothermally which has interesting entangled nanotubular structure. Solid state crystal-to-crystal sliding is observed by dehydration and guest-exchange. The polymer is showing guest dependent photoluminescence properties.



Entangled Coordination Polymers

A. Aijaz, P. Lama,
P. K. Bharadwaj* 3829–3834

A Dynamically Entangled Coordination Polymer: Synthesis, Structure, Luminescence, Single-Crystal-to-Single-Crystal Reversible Guest Inclusion and Structural Transformation

Keywords: Coordination polymers / Dynamic frameworks / Inclusion compounds / SC-SC transformation / Photoluminescence / Zinc

Four supramolecular isomeric MOFs based on *N,N,N',N'*-benzidinetetracarboxylate were synthesized. Conformational effects of the ligand were observed in DUT-10(Zn) and DUT-11, having an *lvt* and *pts* net, respectively, whereas DUT-10(Cu) and DUT-12, with the same linker conformation, have *lvt* and *ssb* net topologies, respectively. DUT-10(Zn) shows solvent-induced change in fluorescence and selective gas adsorption properties.

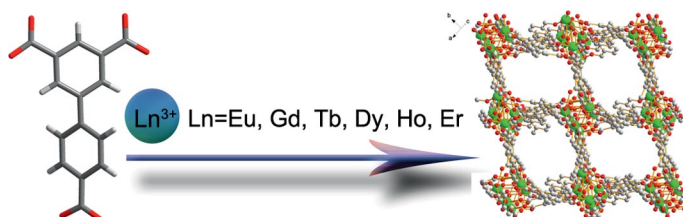


R. Grünker, I. Senkovska, R. Biedermann,
N. Klein, A. Klausch, I. A. Baburin,
U. Mueller, S. Kaskel* 3835–3841

Topological Diversity, Adsorption and Fluorescence Properties of MOFs Based on a Tetracarboxylate Ligand

Keywords: Metal–organic frameworks / Carboxylate ligands / Physisorption / Gas separation / Topology

Luminescent Lanthanide MOFs



A series of isostructural lanthanide metal–organic frameworks based on biphenyl-3,4',5-tricarboxylate (BPT) were hydrothermally synthesized and structurally characterized. Complexes **1** and **3** are highly

emissive at room temperature with quantum yields of 14% and 60.9%, respectively. It is interesting that guest molecules in these complexes enhance rather than quench the luminescence of Ln^{III} ions.

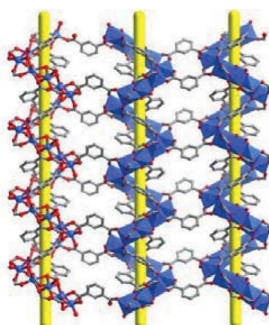
Z.-J. Lin, B. Xu, T.-F. Liu, M.-N. Cao,
J. Lü, R. Cao* 3842–3849

A Series of Lanthanide Metal–Organic Frameworks Based on Biphenyl-3,4',5-tricarboxylate: Syntheses, Structures, Luminescence and Magnetic Properties

Keywords: Metal–organic frameworks / Luminescence / Magnetic properties / Lanthanides / Carboxylate ligands

Molecular Magnets

Through changing the solvent from methanol to *i*PrOH, a Co_6 -cluster-based 3D porous framework and a Co^{II}_4 -helical- Δ -chain-based porous framework were synthesized with bridging ipa^{2-} ligands. Both of them show spin-canting behavior for the antiferromagnetic triangular geometry and weak long-range ordering for the existence of guest molecules.



X.-N. Cheng,* W. Xue,
X.-M. Chen* 3850–3855

Synthesis, Structures, and Magnetic Properties of Two Cobalt(II) Isophthalate Coordination Polymers

Keywords: Cobalt / Carboxylate ligands / Magnetic properties / Cluster compounds / Chain structures

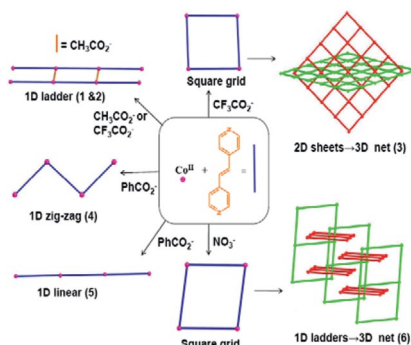
Anion Effects

A. M. P. Peedikakkal,
Y.-M. Song, R.-G. Xiong, S. Gao,
J. J. Vittal* 3856–3865



Cobalt(II) Coordination Polymers Containing *trans*-1,2-Bis(4-pyridyl)ethene and Their Magnetic Properties

Keywords: Cobalt / Metal–organic frameworks / Bridging ligands / Magnetic properties / Anions



Six coordination polymers were synthesized from the Co^{II} ion and bpe [bpe = 1,2-bis(4-pyridyl)ethene] ligand in the presence of the CH₃CO₂[−], CF₃CO₂[−], C₆H₅CO₂[−] and NO₃[−] anions. The topology of the coordination polymers were varied by using different anions and reaction conditions. Two interpenetrated diagonal (4,4) and (4,3) nets exhibit interesting magnetic properties.

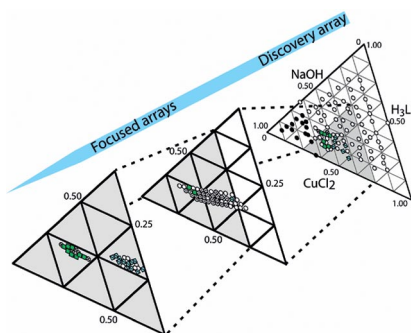
High-Throughput Methods

P. Maniam, C. Näther,
N. Stock* 3866–3874



Systematic Hydrothermal Investigation of Metal Phosphonatobenzenesulfonates by High-Throughput Methods

Keywords: Organic-inorganic hybrid compounds / High-throughput screening / Hydrothermal synthesis / Metal phosphonatosulfonates



A high-throughput study using the rigid 4-phosphonosulfonic acid was conducted. Metal screening using divalent ions followed by discovery and focused arrays employing Cu²⁺ and Pb²⁺ salts led to five new organic-inorganic hybrid compounds. The formation fields could be established and the compounds were characterized in detail for their thermal, magnetic and IR spectroscopic properties.

* Author to whom correspondence should be addressed.



Supporting information on the WWW (see article for access details).

If not otherwise indicated in the article, papers in issue 23 were published online on August 3, 2010

Quo vadis MOFs?



Karen Hindson
Editor EurJIC

When I see the number of papers published on MOFs and coordination polymers, it is difficult to grasp that this is a young field that began to take off only in the last decade of the 20th century. Arising from supramolecular chemistry, host–guest chemistry and crystal engineering, the field intrigued researchers who had a vision of designing sturdy framework structures instead of seeing what their synthesis provided. The analogy to zeolites fired hopes for

MOFs – an intriguing field

porous materials, but initially, interpenetrating structures filled the pores or the removal of guest molecules led to the collapse of the frameworks.

The huge potential for variation of the metal nodes and organic ligands led to a flurry of activity in which structure was the focus. The possibilities were limited only by the imagination. As a few examples, flexible and inflexible ligands were employed, oxidation states were tuned in situ during the synthesis, mixed-metal and mixed-ligand systems were created, and other building blocks such as polyoxometalates or porphyrinoid units were built into the structures. Lately the structures have been tweaked by postsynthetic modification. The vision proved hard to achieve. Even now a premeditated design of a particular structure is elusive. Nevertheless, the properties of the frameworks can be tailored to particular applications. After the first wave of research on an empirical basis, the focus has moved to practical uses of the networks.

Properties tailored for application

Although the prediction of a structure through crystal engineering remains a challenge, the tuning of properties for applications is bringing an excellent harvest of results.

Of the manuscripts that EurJIC receives, 10–15% alone are in the broad field of organic–inorganic hybrid networks. As a result, this topic is ideal for a special issue in this journal, and we readily agreed to the suggestion of Advisory Board Member and Guest Editor Srinivasan Natarajan, of the Indian Institute of Science in Bangalore, that EurJIC should publish a Cluster Issue on Metal–Organic Frameworks. In the light of the latest developments towards applications, we were immediately enthusiastic about the topic of this issue proposed by Guest Editor and EurJIC Board Member Susumu Kitagawa: Targeted Fabrication of MOFs for Hybrid Functionality. It, therefore, gives me great pleasure to present you with this cluster issue that concentrates on the synthesis of

MOFs to design functionality into the structures and the exploration of their uses. The field is huge, and to keep it within the limits of a single issue, the choice of authors had to be highly selective. It could not be comprehensive, but a window selected by the Guest Editors to provide you with a wide view of quality papers with a bearing on targeted fabrication. Many of the groups working in the field, but not represented as author, have nevertheless made their mark in the peer review. We thank our authors and peer reviewers alike for their important contributions to a successful Cluster Issue.

The issue brings you three fine Microreviews on the immobilization of nanoparticles in MOFs and applications in catalysis (Roland Fischer et al., Dortmund), on the preparation of thin films of MOFs (Hiroshi Kitagawa and Rie Makiura, Kyoto) and on the use of MOFs in MRI and other imaging techniques (Wenbin Lin and Joseph Della Rocca, Chapel Hill). You can read about an entirely different aspect – a synthesis method that allows the use of MOFs in liquid chromatography – in the Short Communication by Dirk De Vos's group in Leuven. Adsorption in the frameworks, the redox properties, luminescence and magnetism all have their place, as does catalysis. The dynamic behavior on adsorption of guests and the control of structure might catch your interest or perhaps an adaptation of a high-throughput synthesis workflow to metal–organic frameworks.

This cluster issue could not have been so efficiently produced without the close cooperation of our Guest Editors, Susumu Kitagawa and Srinivasan Natarajan. They have put together a focused issue with a selection of leading international experts to showcase the research on the cutting edge of this field. I would like to thank them most sincerely for their ideas and advice on all aspects of the content. Their input is very much appreciated. At the beginning of our collaboration, a lot of the administrative work was handled by Satoshi Horike, Kyoto University. Preeti Vashi and I are grateful for his services and insightful ideas.

Let me no longer keep you, the reader, from this gallery of papers on metal–organic frameworks. We hope you will find many papers either to stimulate ideas for your own research or simply to satisfy your interest in the subject.

Karen J. Hindson

Targeted Fabrication of MOFs for Hybrid Functionality



Susumu Kitagawa
Guest Editor
Kyoto University
Kyoto, Japan



Srinivasan Natarajan
Guest Editor
Indian Institute of Science
Bangalore, India

Metal–organic frameworks (or porous coordination polymers), known popularly as MOFs (or PCPs), are a class of compounds that combine the functionalities of organic chemistry and the coordination preferences of inorganic chemistry. MOFs exhibit considerable variety and diversity in their structures and are also stable even at 300°C. When we look back at coordination chemistry in the 1950s, a clathrate solid compound having a layered structure existed, which is now known

Designer solids

novelty of MOFs lies in the fact that the concept of a framework is introduced into molecule-based chemistry, and the design of the building block is well related to that of the framework. Moreover, the structures are directly correlated to the functionalities, which leads to designer solids with specific

MOFs at the forefront of Inorganic Materials Chemistry

The various developments that have been taking place in this area prompted us to propose and dedicate a cluster issue to this class of compounds, with the aim of showcasing the importance of MOFs. This cluster issue contains 22 peer-reviewed scientific articles. The emerging developments on the use of nanoscale MOFs and nanomaterials within the chan-

as a Hoffmann compound. At the same time, a three-dimensional coordination framework had already been synthesized and its crystal structure had been determined. The area is maturing rapidly and is at the forefront of research in Inorganic Materials Chemistry.

nels of MOFs are extensively discussed in the form of Microreviews. The immense opportunities that this class of compounds presents are highlighted in these reviews. The efficacy of MOF composites in selective separation is also covered in this issue.

This issue showcases the importance of MOFs

Numerous important aspects of the synthesis, structure, and properties of MOFs are covered. MOFs based on main group elements, f elements, and the ever dominant transition metals, and their properties have been discussed in great detail. The high-throughput synthesis, structural interpenetration, magnetism, luminescence, and catalysis of MOFs, amongst other topics, have also been reported in the individual research articles.

This issue comprises contributions from many active researchers from around the globe in the field of MOFs, which makes it special and truly universal. The cover picture, in fact, highlights not only this aspect very well, with representative contributions from around the world, but also the versatility of MOFs. Contributions to the composite cover artwork were provided by Wenbin Lin et al., Jie-Sheng Chen et al., Roland Fischer et al., and Dirk De Vos et al.

Truly universal coverage

We take this opportunity to thank all the authors and reviewers for helping us to bring this excellent issue on MOFs to the chemistry community.



On these pages, we feature a selection of the excellent work that has recently been published in our sister journals. If you are reading these pages on a

computer, click on any of the items to read the full article. Otherwise please see the DOIs for easy online access through Wiley InterScience.



Conformational Analysis

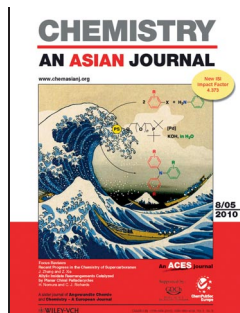
M. Benaglia, F. Cozzi,* M. Mancinelli, A. Mazzanti*

The Intramolecular Interaction of Thiophene and Furan with Aromatic and Fluoroaromatic Systems in Some [3.3]Meta(heterocyclo)paracyclophanes: A Combined Computational and NMR Spectroscopic Study

A dive into an electron sea! Four thiophene- and furan-containing [3.3]meta(heterocyclo)paracyclophanes were designed and synthesized to study the intramolecular interaction between standard heteroaromatic rings and tetra-H- or tetra-F-substituted benzenes. The furan-derived adducts were shown by calculations and NMR spectroscopy to adopt a perpendicular edge-to-face disposition of the rings with the oxygen atom pointing toward the benzene platform (see figure).



Chem. Eur. J.
DOI: 10.1002/chem.201000783

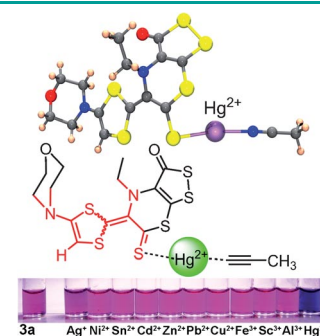


Chromogenic Probes

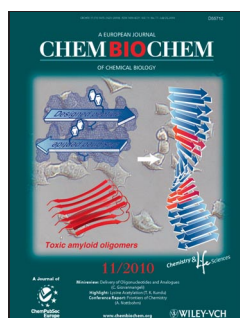
P. Fuertes, D. Moreno, J. V. Cuevas, M. García-Valverde, T. Torroba*

A Selective Chromogenic Probe for Mercury(II) and Cyanide in Aqueous Buffered Solution from a Cycloaddition Reaction of an Ynamine to Polycyclic Dithiolethiones

Mercury rising! A new polysulfur-nitrogen heterocycle is described as a new selective chromogenic probe for the naked-eye detection of mercury(II), by a dramatic change of color from purple to blue-violet in a HEPES-buffered water/acetonitrile 1:1 mixture, with sub-micromolar sensitivity. The chemical probe also changes from purple to red in the presence of cyanide.



Chem. Asian J.
DOI: 10.1002/asia.201000063

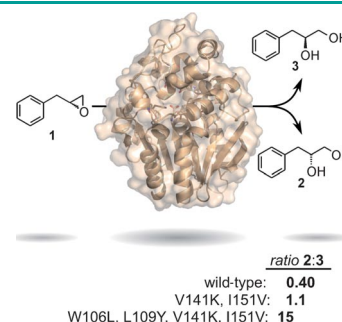


Enzyme Catalysis

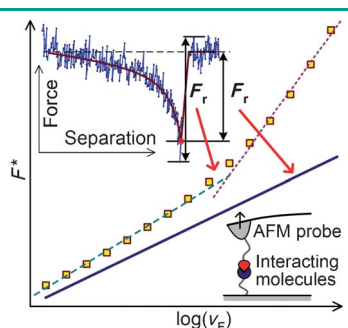
A. Gurell, M. Widersten*

Modification of Substrate Specificity Resulting in an Epoxide Hydrolase with Shifted Enantiopreference for (2,3-Epoxypropyl)benzene

Mutagenesis of the active-site residues of the epoxide hydrolase StEH1 led to enzyme variants with modified enantiopreference for (2,3-epoxypropyl)benzene. The wild-type enzyme favors the *S* enantiomer, whereas a quadruple mutant displays a 15:1 preference for the *R* enantiomer, due to crippled catalytic efficiency in the hydrolysis of the *S* enantiomer, but retained activity with the *R* enantiomer.



ChemBioChem
DOI: 10.1002/cbic.201000185



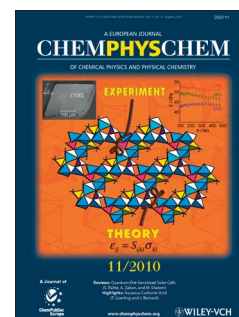
ChemPhysChem
DOI: 10.1002/cphc.201000251

Force Spectroscopy

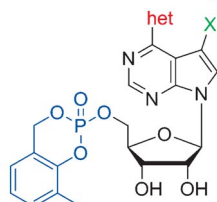
N. Li, S. Guo, B. B. Akhremitchev*

Apparent Dependence of Rupture Force on Loading Rate in Single-Molecule Force Spectroscopy

Mighty noise: Non-linear dependence of the most probable rupture force on the logarithm of the loading rate might appear if the contributions from noise are included in extracted rupture forces (see figure).



het = furyl, thienyl etc. X = H or F



cytostatic activity ($\text{GI}_{50} = 9 \text{ nm} - 5 \mu\text{M}$)
inhibition of human adenosine kinase
($\text{IC}_{50} = 0.08 - 5 \mu\text{M}$)

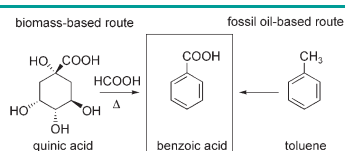
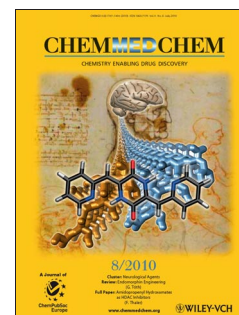
ChemMedChem
DOI: 10.1002/cmdc.201000192

Prodrugs

P. Spáčilová, P. Nauš, R. Pohl, I. Votruba, J. Snášel, H. Záborská, I. Pichová, R. Ameral, G. Birkuš, T. Cihlář, M. Hocek*

CycloSal-phosphate Pronucleotides of Cytostatic 6-(Het)aryl-7-deazapurine Ribonucleosides: Synthesis, Cytostatic Activity, and Inhibition of Adenosine Kinases

Inhibiting ADK: CycloSal-phosphate prodrugs of nucleoside cytostatics (6-hetaryl-7-deazapurine ribonucleosides) were prepared. The pronucleotides display nanomolar cytostatic activities similar to those of the parent nucleosides. In addition, they exhibit pronounced inhibitory effects toward human adenosine kinase.



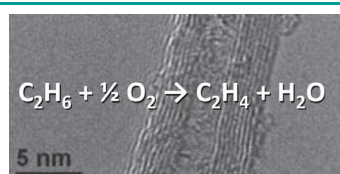
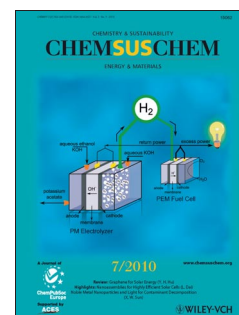
ChemSusChem
DOI: 10.1002/cssc.201000111

Renewable Resources

E. Arceo, J. A. Ellman,* R. G. Bergman*

A Direct, Biomass-Based Synthesis of Benzoic Acid: Formic Acid-Mediated Deoxygenation of the Glucose-Derived Materials Quinic Acid and Shikimic Acid

Shikimic Gimmick: An alternative biomass-based route to benzoic acid from the renewable starting materials quinic acid and shikimic acid is described. Benzoic acid is obtained selectively using a highly efficient, one-step formic acid-mediated deoxygenation method.



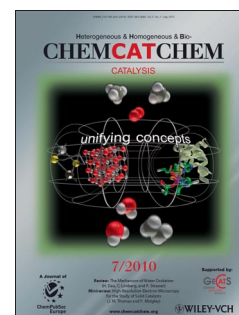
ChemCatChem
DOI: 10.1002/cctc.201000035

Carbon Nanotubes

B. Frank, M. Morassutto, R. Schomäcker, R. Schlögl, D. S. Su*

Oxidative Dehydrogenation of Ethane over Multiwalled Carbon Nanotubes

At eye level: The high C–H bond strength of ethane challenges the stability of metal-free carbon nanotubes (CNTs) as a catalyst for oxidative dehydrogenation (ODH). However, surface modification of the CNTs with B_2O_3 or P_2O_5 leads to drastically enhanced oxidation resistance of the catalysts during ODH and increases alkene selectivity due to the suppression of electrophilic oxygen intermediates on the carbon surface.



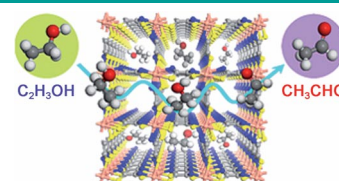


MOF Electrocatalysts

L. Yang, S. Kinoshita, T. Yamada, S. Kanda, H. Kitagawa,*
M. Tokunaga, T. Ishimoto, T. Ogura, R. Nagumo, A. Miyamoto,
M. Koyama

A Metal–Organic Framework as an Electrocatalyst for Ethanol Oxidation

No need for nobles: The copper-based metal–organic framework material *N,N'*-bis(2-hydroxyethyl)dithiooxamidatocopper(II) (see picture, Cu pink, N blue, S yellow, O red, C gray, H white) is an active catalyst for ethanol electrooxidation. The performance of this noble-metal-free material is comparable to those of some reported Pt-based catalysts.



Angew. Chem. Int. Ed.
DOI: 10.1002/anie.201000863

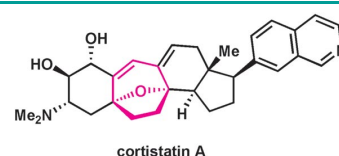


Natural Products

A. R. Hardin Narayan, E. M. Simmons, R. Sarpong*

Synthetic Strategies Directed Towards the Cortistatin Family of Natural Products

The cortistatin family of natural products have captured the attention both of synthetic chemists and of workers interested in understanding and exploiting their potent anti-angiogenic activity. Many synthetic strategies have been devised to build the rearranged steroidal cortistatin core, which has in turn enabled studies probing the origins and mechanism of these compounds' biological activity.



cortistatin A
Eur. J. Org. Chem.
DOI: 10.1002/ejoc.201000247

New Journal

Heterogeneous, Homogeneous and BioCatalysis

www.chemcatchem.org

FREE ONLINE ACCESS

In 2010 for all users from institutions that have registered

Ask your librarian to register for complimentary online access TODAY

www.interscience.wiley.com/newjournals

Founding Societies:

GDCh
GESELLSCHAFT
DEUTSCHER CHEMIKER

WILEY-VCH

Metals@MOFs – Loading MOFs with Metal Nanoparticles for Hybrid Functions

Mikhail Meilikhov,^[a] Kirill Yusenkov,^[a] Daniel Esken,^[a] Stuart Turner,^[b]
Gustaaf Van Tendeloo,^[b] and Roland A. Fischer*^[a]

Keywords: Metal–organic frameworks / Nanoparticles / Heterogeneous catalysis / Electron tomography / Hydrogen storage

Metal–organic frameworks (MOFs) as well as porous coordination polymers (PCPs) are porous, organic–inorganic hybrid solids with zeolite-like structures and properties. Due to their extraordinarily high surface area and well defined pore structure MOFs can be used for the stabilization of metal nanoparticles with adjustable size. The embedded metal nanoparticles are still accessible for other reagents due to the high porosity of the MOF systems. This fact makes “metal@MOF” systems especially interesting for heterogeneous catalysis, gas storage and chemical sensing. This review compiles the cases of metal nanoparticles supported by or embedded into MOFs reported so far and the main aspects and

problems associated with these novel nanocomposite systems. The determination of the dispersion and the location of the particles at the MOF support, the control of the loading degree and its effect on the catalytic activity of the system are discussed as well as the partial degradation of the MOF structure upon particle formation. Examples of the introduction of stabilizing groups into the MOF network that direct the loading and can influence the size and shape of the embedded particles are still rare and point into the possible direction of future investigations. Finally, the formation of bi-metallic nanoparticles, which are stabilized and supported by a MOF network, will also be reviewed.

1. Introduction

The template-directed synthesis route is a very common way of producing various types of nanoparticles. The size and shape of the nanoparticles can be well defined by the right template. However, many templates do not provide a three-dimensionally ordered, crystalline support or make the included nanoparticles inaccessible for any further use. Recently, metal–organic frameworks (MOFs) or porous coordination polymers (PCPs) have been shown to be suitable for embedding and supporting functional nanoparticles similar to microporous zeolites or mesoporous siliceous materials and related matrices. The combination of the long-range order of a solid-state template material with the tuneable dimensionality and chemical tailoring of the inner surface of the channels and cavities makes MOFs a promising new class of templates for hosting nanoparticles. It has been shown that the embedding of functional nanoparticles inside the cavities of MOFs is relevant for a number of applications, including heterogeneous catalysis. During the last five years, a number of examples for incorporation of a range of metals like Cu, Ru, Pd, Au, Ag and Pt into MOF cavities have been reported. In particular, Hermes et al.^[1] introduced solvent-free gas-phase loading of MOFs by volatile organo-

metallic precursors. The following decomposition of the precursors and the formation of metal particles can be achieved thermally or photochemically under a reactive or inert gas atmosphere depending on the metal. Other loading methods that have been applied include liquid and incipient wetness impregnation, solid grinding and microwave-assisted methods (Table 1). All the different systems and preparative procedures have a number of common aspects and in particular share the issues of nonselective deposition at the outer surface of the MOF support versus loading the cavities inside the bulk phase, control of the size distribution and the formation of particles of a size exceeding the MOF cavities, framework degradation during nanoparticle formation, control of the particle size distribution, and so on. In fact, achieving a high loading of MOFs with cavity-size-matched metal particles and a homogeneous dispersion throughout the bulk of the MOF matrix is a nontrivial target both for the synthesis and characterization of the obtained microstructure and for ruling out any artefacts. This review will comprehensively discuss these issues on the basis of a selection of examples taken from the literature and will also give reference to some applications of the obtained materials in catalysis and hydrogen gas storage.

2. Overview of Existing “Metal@MOF” Systems

The number of different MOFs used as a supporting host matrix for metal nanoparticles is rather small as compared

[a] Anorganische Chemie II – Organometallics and Materials, Ruhr-Universität Bochum, 44780 Bochum, Germany
Fax: +49-234-321-4174
E-mail: roland.fischer@rub.de

[b] EMAT, University of Antwerp, Groenenborgerlaan 171, 2020 Antwerp, Belgium

to the vast number of known MOF structures. Early reports on the incorporation of nanosized metals, that is, Pd, Ru, Cu and Au, used MOF-5 $\{\text{MOF-5} = [\text{Zn}_4\text{O}(\text{bdc})_3]_n$; bdc = 1,4-terephthalate $\}$ as the template.^[2] A range of different methods of particle inclusion have been employed, and these methods will be described and discussed in detail separately. In particular, the fabrication of “Pd@MOF” systems has caught the attention of many research groups. Supporting Pd particles at MOFs was demonstrated by the following case studies: MOF-5,^[1,3,4] MOF-177^[5] $\{\text{MOF-177}^{[6]} = [\text{Zn}_4\text{O}(\text{btb})_2]_n$; btb = benzene-1,3,5-tribenzoate $\}$,

MIL-101(Cr)^[7,8] $\{\text{MIL-101(Cr)}^{[9]} = [\text{Cr}_3\text{L}_3(\text{bdc})_2]_n$ with $\text{L} = \text{H}_2\text{O}, \text{O}^{2-}, \text{F}^-$ $\}$, MIL-100(Al)^[10] $\{\text{MIL-100(Al)} = [\text{Al}_3\text{L}_3(\text{btc})_2]_n$ with $\text{L} = \text{H}_2\text{O}, \text{O}^{2-}, \text{F}^-$; btc = 1,3,5-benzenetricarboxylate $\}$, $\{\text{Zn}_3(\text{ntb})(\text{EtOH})_2\cdot 4\text{EtOH}\}^{[11]}$ (ntb = 4,4',4''-nitriлотrisbenzoate) and $\{[\text{Ni}(\text{cyclam})]_2(\text{mtb})\}_n\cdot 8\text{H}_2\text{O}\cdot 4\text{DMF}^{[12]}$ (cyclam = 1,4,8,11-tetraazacyclotetradecane; mtb = methanetetra benzoate; DMF = dimethylformamide). The catalytic activity of nanosized Pd is certainly the main reason for the investigations of new systems for nanoparticle stabilization without loss of the accessible surface area for catalytic processes. Supporting gold par-



Mikhail Meilikhov, born 1982 in Novosibirsk, Russia, obtained his Bachelor of Science in 2005 at the Ruhr-Universität Bochum and received his Master of Science in 2007. He is currently working on his doctoral thesis under the supervision of Roland A. Fischer on the topic “Investigations of MOF Chemistry as Bulk and Surface Material”. His work is supported by the Research Centre 558 “Metal–Support Interactions in Heterogeneous Catalysis” of the German Research Foundation and specific targeted research project “SURMOF” of the European Union (6th FP). His research interests include reduction chemistry and post-synthetic functionalization of MOFs, surface chemistry and fabrication of metal nanoparticles supported by metal–organic frameworks.



Kirill Yusenko studied chemistry at the Novosibirsk State University in Russia and received his Ph. D. in 2005 at the Nikolaev Institute of Inorganic Chemistry in Novosibirsk, Russia, in the area of coordination chemistry of platinum metals. After one year as a postdoctoral researcher at the Hohenheim University in Stuttgart, Germany, he started working as a postdoctoral researcher at the Ruhr-Universität Bochum. His scientific interests are focused on the chemistry of platinum metals and nanomaterials based on metallic particles and MOFs.



Daniel Esken studied chemistry at the Ruhr-Universität Bochum, received his Bachelor of Science in 2005 and obtained his Master's degree in 2007. He currently works on his doctoral thesis at the Chair of Inorganic Chemistry II under the supervision of Roland A. Fischer on the topic “Embedding of Metal, Metal Oxide and Metal Nitride Nanoparticles inside Porous Coordination Polymers”, within the frame of the Priority Program 1362 “Metal–Organic Frameworks” of the German Research Foundation (DFG). His work is also supported by the Research Centre 558 “Metal–Support Interactions in Heterogeneous Catalysis” and the Ruhr-Universität Research School.



Stuart Turner studied chemical engineering at the Karel de Grote University College and received his Master's degree in 2005. He recently obtained his Ph. D. in physics at the EMAT laboratory of the University of Antwerp under the supervision of Gustaaf Van Tendeloo with his doctoral thesis entitled “Transmission Electron Microscopy Characterization of 0-D Nanomaterials”. His research interests are focused on the characterization of nanoparticle-loaded porous materials as well as other nanoparticulate materials by (scanning) transmission electron microscopy, electron energy-loss spectroscopy and electron tomography.



Gustaaf Van Tendeloo received his Ph. D. in physics in 1974 at the University of Antwerp on ordering phenomena in alloys. He had several research periods abroad (UC Berkeley, UoI Champaign-Urbana, Université de Caen). He is a co-author of over 600 papers and his h-index is 54. Presently he is the head of the EMAT research group and the NANO Centre of Excellence of the University of Antwerp. His current interest is in advanced electron microscopy and nanostructured materials. In 2009 he received an ERC advanced grant.



Roland A. Fischer studied chemistry at the Technische Universität München (TUM) and received his Dr. rer. nat. in 1989 under the guidance of Wolfgang A. Herrmann. After a postdoc with Herb Kaesz at UCLA, he returned to TUM in 1990, obtained his Habilitation in 1995 and was appointed Assoc. Prof. at the Ruprecht-Karls Universität, Heidelberg, in 1996. He moved to Ruhr-Universität Bochum in 1998 for a chair in Inorganic Chemistry. Currently he is Dean of the Ruhr-Universität Research School. His research interests focus on bonds between group 13 elements and transition metals and their clusters, precursor chemistry for inorganic materials, chemical vapour deposition (CVD), thin films, nanoparticles, colloids and host–guest chemistry of porous coordination polymers (MOFs).

Table 1. Overview of existing “Metal@MOF” systems.^[a]

Metal@MOF cavity sizes (nm)	M (wt.-%)	Metal particle size (nm)	Preparation method	Comments	Ref.
Ag@MOF-508 1.5 × 1.5	29	20 (TEM, ET), 1–2 (EPR)	Impregnation, AgNO ₃ , EtOH	–	[18]
Ag@[Cu ₃ (btc) ₂] 1.5 × 1.5, 1.1 × 1.1	8	20 (TEM, ET), 1–2 (EPR)	Impregnation, AgNO ₃ , EtOH	–	[18, 19]
Ag@MIL-68(In) 1.1 × 1.1	31	20 (TEM, ET), 1–2 (EPR)	Impregnation, AgNO ₃ , EtOH	–	[18]
Ag@[Ni(C ₁₀ H ₂₆ N ₆) ₃ (bpdc) ₃] 9.7 × 9.7	0.15	3 (TEM, EPR)	Impregnation, AgNO ₃ , EtOH	Autoreduction properties of MOF	[20]
Ag@[Ni(cyclam)] ₂ (bptc) 1.0 × 1.1	0.15	4 (TEM, HRTEM, XPS, EPR)	Impregnation, AgNO ₃ , EtOH	Autoreduction properties of MOF	[21]
Ag@MOF-5 1.5 × 1.5	15.3	not reported	Impregnation, AgNO ₃ , MeCN	Catalytic activity in epoxidation of propylene	[36]
Au@MOF-5 1.5 × 1.5	48	5–20 (TEM)	Gas-phase infiltration, [(CH ₃) ₂ Au(PMe ₃) ₂]	CO oxidation test: negative	[1]
Au@MOF-5 1.5 × 1.5	up to 1	3.3 ± 2.3 (TEM, HAADF-STEM)	Solid grinding, [(CH ₃) ₂ Au(acac)]	Catalytic activity in alcohol oxidation	[13]
Au@CPL-1 0.4 × 0.6	up to 1	not reported	Solid grinding, [(CH ₃) ₂ Au(acac)]	Catalytic activity in alcohol oxidation	[13]
Au@CPL-2 0.6 × 0.8	up to 1	2.4 ± 1.0 (TEM, HAADF-STEM)	Solid grinding, [(CH ₃) ₂ Au(acac)]	Catalytic activity in alcohol oxidation	[13]
Au@MIL-53(Al) 0.85 × 0.85	up to 1	1.5 ± 0.7 (TEM, HAADF-STEM)	Solid grinding, [(CH ₃) ₂ Au(acac)]	Catalytic activity in alcohol oxidation	[13]
Au@[Cu ₃ (btc) ₂] _n 1.5 × 1.5, 1.1 × 1.1	up to 1	not reported	Solid grinding, [(CH ₃) ₂ Au(acac)]	Catalytic activity in alcohol oxidation	[13]
Au@[Ni(cyclam)] ₂ (bptc) 1.0 × 1.1	0.15	3.7 ± 0.4 (TEM, HRTEM, XPS, EPR)	Impregnation, NaAuCl ₄ ·2H ₂ O	Autoreduction properties of MOF	[21]
Au@ZIF-8 1.16 (diameter)	up to 30	1–5 (HRTEM, HAADF-STEM, ET, PXRD)	Gas-phase infiltration, [(CO)AuCl]	Catalytic activity in alcohol oxidation	[22]
Au@ZIF-8 1.16 (diameter)	up to 5	3.4 ± 1.4 (TEM)	Solid grinding, [(CH ₃) ₂ Au(acac)]	Catalytic activity in CO oxidation	[14]
Au@ZIF-90 1.16 (diameter)	up to 30	1–2 (HRTEM, HAADF-STEM, ET, PXRD)	Gas-phase infiltration, [(CO)AuCl]	Post synthetic aldehyde oxidation	[22]
Cu@MOF-5 1.5 × 1.5	13.8	3–4 (TEM, PXRD)	Gas-phase infiltration, [(η ⁵ -C ₅ H ₅)Cu(PMe ₃) ₂]	Catalytic activity in MeOH synthesis	[1]
Cu/ZnO@MOF-5 1.5 × 1.5	up to 8	1–3 (TEM; PXRD)	Gas-phase infiltration, [(η ⁵ -C ₅ H ₅)Cu(PMe ₃) ₂]	Catalytic activity in MeOH synthesis	[39]
Cu@MOF-177 1.4 (pore aperture)	10.6	2–3 (TEM, PXRD, UV/Vis)	Gas-phase infiltration, [(η ⁵ -C ₅ H ₅)Cu(PMe ₃) ₂]	–	[5]
Cu@MIL-101(Cr) 3.4, 2.9 (pore diameters)	up to 5	2–6 (TEM)	Impregnation, Cu(NO ₃) ₂ , H ₂ O	Catalytic activity in CO oxidation	[23]
Ni@MesMOF-1 4.7, 3.9 (pore diameters)	up to 35	1.4–1.9 (calculated)	Gas-phase infiltration, [Ni(η ⁵ -C ₅ H ₅) ₂]	Catalytic activity in styrene or nitrobenzene reduction	[45]
Pd@MOF-5 1.5 × 1.5	up to 35	2.4 ± 0.2 (TEM, XRD, ET)	Gas-phase infiltration, [Pd(η ⁵ -C ₅ H ₅)(η ³ -C ₃ H ₃) ₂]	Stability towards hydrogen tested	[3]
Pd@MOF-5 1.5 × 1.5	1	not reported	Impregnation, [Pd(acac) ₂]	Catalytic activity in cyclooctene hydrogenation	[4]
Pd@MOF-5 1.5 × 1.5	1.6	not reported	Impregnation, [Pd(acac) ₂], DEF	Catalytic activity in H ₂ O ₂ formation	[37]
Pd@MOF-5(bdc/bdc-NH ₂) 1.5 × 1.5	10	not reported	Impregnation, [Pd(OAc) ₂], DMF	Catalytic activity in CO oxidation	[40]
Pd@MOF-5 1.5 × 1.5	up to 0.64	not reported	Coprecipitation, Pd(NO ₃) ₂ ·2H ₂ O, H ₂ O	Catalytic activity in ethyl cinnamate hydrogenation	[41]
Pd@MOF-5/SAM 1.5 × 1.5	–	not reported	Gas-phase infiltration, [Pd(η ⁵ -C ₅ H ₅)(η ³ -C ₃ H ₃) ₂]	Pd in MOF layers on substrate surfaces	[42]
Pd@MOF-177 1.4 (pore aperture)	32.5	> 3 (TEM), 2.6 (PXRD)	Gas-phase infiltration, [Pd(η ⁵ -C ₅ H ₅)(η ³ -C ₃ H ₃) ₂]	–	[5]
Pd@MIL-101(Cr) 3.4, 2.9 (pore diameters)	1	2–4 (TEM)	Impregnation, [PdCl ₄] ²⁻ /[PdCl ₆] ²⁻	Catalytic activity in Heck reaction	[7]
Pd@MIL-101(Cr) 3.4, 2.9 (pore diameters)	1	1.9 ± 0.7 (TEM)	Impregnation, Pd(NO ₃) ₂ ·2H ₂ O, DMF	Catalytic activity in Ullmann and Suzuki–Miyaura coupling	[44]
Pd@MIL-101(Cr) 3.4, 2.9 (pore diameters)	up to 5	2–6 (TEM, HRTEM)	Impregnation, Pd(NO ₃) ₂ ·2H ₂ O, H ₂ O	Catalytic activity in CO oxidation	[23]
Pd/Cu@MIL-101(Cr) 3.4, 2.9 (pore diameters)	1/2	1–6 (TEM)	Impregnation, Pd(NO ₃) ₂ ; Cu(NO ₃) ₂	Catalytic activity in CO oxidation	[23]
Pd@MIL-101(Cr) 3.4, 2.9 (pore diameters)	up to 2.79	2.5 ± 0.5 (TEM)	Impregnation, Pd(NO ₃) ₂ ·2H ₂ O, DMF	Catalytic activity in IMBK synthesis	[8]
Pd@MIL-100(Al)	10	1.8 ± 0.4 (TEM, HAADF-STEM)	Impregnation,	Hydrogen adsorption	[10]

Table 1. (Continued)

Metal@MOF cavity sizes (nm)	M (wt.-%)	Metal particle size (nm)	Preparation method	Comments	Ref.
3.4, 0.87 (pore diameters)		2.5 ± 0.2 (XRD, in situ PXRD)	[H ₂ PdCl ₄], H ₂ O		
Pd@[Ni(cyclam)] ₂ (mtb)]	0.1	2.0 ± 0.6 (TEM, HRTEM, XPS, EPR)	Impregnation, Pd(NO ₃) ₂ ·2H ₂ O, MeCN	–	[12]
1.34 × 1.34					
Pd@[Zn ₃ (ntb) ₂ (EtOH) ₂ ·4EtOH]	up to 3	3.0 ± 0.4 (TEM, HRTEM, XPS, EPR)	Impregnation, Pd(NO ₃) ₂ ·2H ₂ O, MeCN	Hydrogen adsorption	[11]
0.77 (diameter)					
Pt@MOF-177	up to 43	2–3 (TEM), PXRD	Gas-phase infiltration, [Me ₃ PtCp']	Catalytic activity in alcohol oxidation	[24]
1.4 (pore aperture)					
Ru@MOF-5	up to 30	1.5–1.7 (HRTEM, HAADF-STEM, ET)	Gas-phase infiltration, [Ru(cod)(cot)]	Catalytic activity in alcohol oxidation	[25]
1.5 × 1.5					
Ru/Pt@MOF-5	9.8/17	4–6 (TEM)	Gas-phase infiltration, [Ru(cod)(cot)]/[Pt(cod)Me ₂]	–	[26]
1.5 × 1.5					

[a] Abbreviations: *MOF systems*: MOF-5 = [Zn₄O(bdc)₃]_n; MOF-177 = [Zn₄O(btb)₂]_n; MOF-508 = [Zn(bdc)(bipy)]_n; MIL-53(Al) = [Al(OH)(bdc)]_n; MIL-68(In) = [In(OH)(bdc)]_n; MIL-100(Al) = [Al₃L₃(btc)₂]_n with L = H₂O, O²⁻, F⁻; MIL-101(Cr) = [Cr₃L₃(bdc)₃]_n; CPL-1 = [Cu₂(pzdc)₂(pyz)]_n; CPL-2 = [Cu₂(pzdc)₂(bipy)]_n; ZIF-8 = [Zn(MeIM)₂]_n; ZIF-90 = [Zn(ICA)₂]_n; *Linker and functional groups*: bdc = 1,4-terephthalate; bdc-NH₂ = 2-amino-1,4-terephthalate; bipy = 4,4'-bipyridine; btb = benzene-1,3,5-tribenzoate; btc = 1,3,5-benzene-tricarboxylate; pzdc = pyrazine-2,3-dicarboxylate; pyz = pyrazine; bpdc = 4,4'-biphenyldicarboxylate; bpdc = 1,1'-biphenyl-2,2',6,6'-tetracarboxylate; cyclam = 1,4,8,11-tetraazacyclotetradecane; MeIM = 2-methylimidazole; ICA = imidazolate-2-carboxyaldehyde; mtb = methanetetra benzoate; ntb = 4,4',4''-nitrotrisenzoate; Cp' = methylcyclopentadienyl; cod = 1,5-cyclooctadiene; cot = 1,3,5-cyclooctatriene; acac = acetylacetonate; SAM = self-assembled monolayer; MIBK = methyl isobutyl ketone; DEF = *N,N*-diethylformamide; DMF = *N,N*-dimethylformamide. *Characterization methods*: TEM = transmission electron microscopy. HRTEM = high-resolution transmission electron microscopy; HAADF-STEM = high-angle annular dark-field scanning transmission electron microscopy; XRD = X-ray diffraction; XPS = X-ray photoelectron spectrum; ET = electron tomography; EPR = electron paramagnetic resonance.

icles of 1–2 nm size by MOFs was achieved^[13,14] by using systems of different pore structures {1D channels: CPL-1^[15] (CPL-1 = [Cu₂(pzdc)₂(pyz)]_n; pzdc = pyrazine-2,3-dicarboxylate; pyz = pyrazine), CPL-2^[15] (CPL-2 = [Cu₂(pzdc)₂(bipy)]_n; bipy = 4,4'-bipyridine) and MIL-53(Al)^[16] [MIL-53(Al) = [Al(OH)(bdc)]_n]; 3D pores: [Cu₃(btc)₂]^[17] and MOF-5}. These systems have shown reasonable catalytic activity for several reactions and seem to be promising candidates for industrial applications. The formation of very small Ag₃ clusters supported by different MOFs and the problems associated with microstructure characterization by TEM arising from the instability of these as-synthesized composites under the conditions of imaging with an electron beam were demonstrated and discussed.^[18] Table 1 summarizes all reported cases named “metals@MOFs” and their possible applications. Taking together all available data, the reported systems can be grouped into three classes. Class A contains the cases in which the metal nanoparticles were deposited *preferentially* at the outer surface of a MOF crystal or close to it and exhibit a particle size substantially larger than the accessible pore dimensions. These systems should rather be addressed as “metals/MOFs”. Particles distributed throughout the volume of the MOF crystal but still exhibiting a broad size distribution with a particle size characteristically larger than the dimensions of the pores are assigned to class B. Particles distributed throughout the MOF crystal and exhibiting an average particle size matching the pore dimensions are regarded as class C (Figure 1). Both classes B and C may be called “metals@MOFs” or “metals□MOFs”.

The formation of metal nanoparticles may be accompanied by a partial or even full degradation of the MOF as shown in Figure 1. It is assumed that initially many small nuclei are formed, which rapidly agglomerate

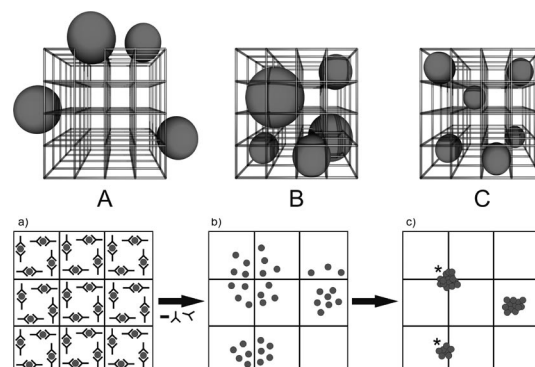


Figure 1. Top: The limiting cases A, B and C of metal nanoparticles supported by MOFs addressed as metals/MOFs (A) and as metals@MOFs (B, C). Bottom: The concept of particle formation inside MOF cavities: (a) The MOF matrix is loaded with a metal precursor. The balls represent the metal centre, and Y-shaped sticks represent the organic ligands or counterions. (b) After the decomposition of the precursor the agglomeration process starts. (c) Stars indicate the partial degradation of the framework and the formed metal nanoparticles. Note that processes like (b) and (c) may also take place during thermal annealing and/or TEM imaging of the as-synthesized sample.

in the case of a very weakly interacting (stabilizing) framework until a certain point is reached where no other feed particles are available in the direct environment of the formed bigger nanoparticles. This explains the observed inhomogeneity of the loading when MOF systems with 3D pore structure and large windows between the pores are used. The diffusion of preformed small nanoparticles inside MOFs can be decreased by using frameworks with directed porosity where the single pores are not connected to each other.

3. Preparation of Metal@MOF Materials

3.1. Solvent-Free Gas-Phase Loading

Volatile metalorganic compounds known as precursors for metalorganic chemical vapour deposition (MOCVD) applications were incorporated into the pores or channels of MOFs by a sublimation process.^[1] This solvent-free method avoids some of the deficiencies of liquid-phase impregnation of MOFs with guest molecules that are typically dissolved in organic solvents. The absence of any solvent molecules during the gas-phase incorporation process allows particularly high loading levels of up to 30–40 wt.-% in a single loading step, which is remarkable with regard to the data compared in Table 1. The drawback of such high loading degrees is the agglomeration of nanoparticles and partial or even full degradation of the MOF in case of highly reactive particles (e.g. Pd). For use in catalysis, however, high loadings are not required, 1–5 wt.-% of active metal are sufficient. On the other hand, the quantitative loading of every cavity of a given MOF with size-matching particles is difficult and has not yet been achieved (or even attempted). The first study on the solvent-free method of introduction of metal nanoparticles into a MOF matrix was performed by using the highly porous MOF-5 framework with a 3D pore structure.^[2] The cubic MOF-5 framework consists of $[\text{Zn}_4\text{O}]$ tetrahedrons bridged by bidentate terephthalate linkers. For the preparation of Cu, Au and Pd nanoparticles inside MOF-5, $[(\eta^5\text{-C}_5\text{H}_5)\text{Cu}(\text{PMe}_3)]$, $[(\text{CH}_3)\text{-Au}(\text{PMe}_3)]$ and $[(\eta^5\text{-C}_5\text{H}_5)\text{Pd}(\eta^3\text{-C}_3\text{H}_5)]$ were used as volatile metal sources, respectively.^[1] To be loaded with these precursors, the activated MOF-5 material was exposed to the vapour of the precursor in static vacuum. Guest molecules penetrated into the MOF volume within 5–10 minutes. However, to achieve a homogeneous and saturated loading with the precursors, much longer time may be needed to reach adsorption equilibrium. The obtained materials were characterized by IR spectroscopy, inductively coupled plasma atomic emission spectroscopy (ICP-AES), PXRD and solid-state NMR spectroscopy. PXRD is a powerful technique for the control of particle incorporation by a detailed analysis of the changes in the relative intensities of the low-index diffraction peaks, which are more or less sensitive to the cavity filling. In principle, gas-phase loading provides inclusion compounds, which are structurally interesting. However, there are still few cases of successful determination of the ordered adsorbate structure of organometallic species hosted within a MOF either by PXRD or single-crystal XRD. In the case of the more or less stoichiometric inclusion compounds “[precursor]_n@MOFs”, $[(\eta^5\text{-C}_5\text{H}_5)\text{Cu}(\text{PMe}_3)]_n\text{@MOF-5}$,^[1] $[(\text{CH}_3)\text{Au}(\text{PMe}_3)]_n\text{@MOF-5}$ ^[1] and $[(\eta^5\text{-C}_5\text{H}_5)\text{Pd}(\eta^3\text{-C}_3\text{H}_5)]_4\text{@MOF-5}$,^[3] the guest molecules have a low symmetry, and ordering of the molecules inside the cubic pores of MOF-5 is hindered. Therefore, comparison of PXRD patterns before and after adsorption shows that the MOF-5 topology, space group and cell parameters do not reveal any changes but only some more or less significant variations in the relative intensities of the

diffraction peaks. The absence of extra diffraction peaks shows that the materials still have a high cubic symmetry (space group $Fm\bar{3}m$) like the initial MOF-5, whereas the guest molecules are completely disordered. An ordered adsorbate structure is favoured for highly symmetric molecules like $[(\eta^5\text{-C}_5\text{H}_5)_2\text{Fe}]$ or for host frameworks with small pores and a low symmetry. For example, the ordered structures for $[(\eta^5\text{-C}_5\text{H}_5)_2\text{Fe}]_7\text{@MOF-5}$ and $[(\eta^5\text{-C}_5\text{H}_5)_2\text{Fe}]_{0.5}\text{@[Al(OH)(bdc)]}$ have previously been solved by using single crystal XRD^[32] and PXRD,^[30] respectively, and are shown in Figure 2. Elemental analysis provides information about the number of guest molecules inside the pores and the corresponding amount of the resulting metallic nanoparticles.

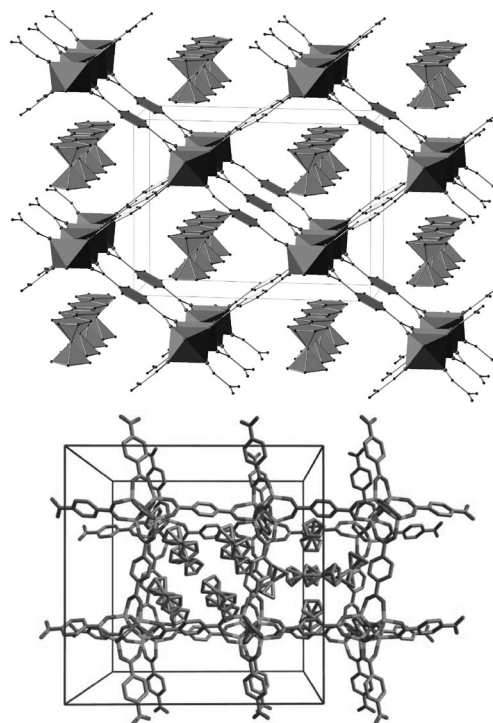


Figure 2. Top: Crystal structure of the inclusion compound $[(\eta^5\text{-C}_5\text{H}_5)_2\text{Fe}]@[Al(OH)(bdc)]_n$ as a projection close to the a axis. Bottom: Crystal structure of $[(\eta^5\text{-C}_5\text{H}_5)_2\text{Fe}]_7\text{@MOF-5}$.

Depending on the molecular volume of the precursors and the conditions of the adsorption process, typically 30–45% of the available cavity space is occupied. In special cases, up to 80% of the pores can be filled with precursors. This corresponds to a typical range of 1–10 precursor molecules per formula unit of the MOF. This precursor loading controls the final loading with metal after conversion of the precursor and particle growth.

The formation of Ru nanoparticles inside MOF-5 is another well investigated example for the capability of the solvent-free gas-phase loading technique.^[25] Similarly, Ru@MOF-5 is a thoroughly investigated system with emphasis on the interaction of the metal particle with the MOF. The highly reactive all-hydrocarbon compound $[Ru(\text{cod})(\text{cot})]$ (cod = 1,5-cyclooctadiene, cot = 1,3,5-cyclooctatriene) was applied as a volatile precursor; however, its volatility is lower than that of the Cu, Au and Pd species described

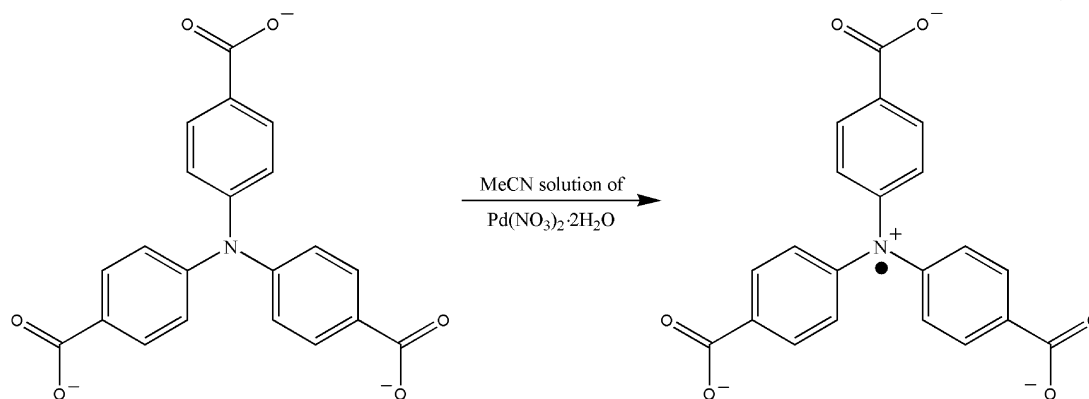
above. The loading was performed in static vacuum at 30 °C over six days in order to achieve saturation and both the microcrystalline powder and single crystals were used for the loading studies. The material obtained was investigated by IR, UV/Vis and solid-state NMR spectroscopy, as well as by TEM^[27] and PXRD. According to the elemental analysis data, the maximal loading rate was 3.5 molecules of [Ru(cod)(cot)] per formula unit of the host framework. Thus, four and three guest molecules should occupy the A and B type cavity of the host framework, respectively.^[2] The formation of Pt, Pd, Cu nanoparticles inside the pores of MOF-177 was achieved by the same method.^[5,24] The precursors [Me₃PtCp⁺], [Pd(η^5 -C₅H₅)(η^3 -C₃H₅)] and [(η^5 -C₅H₅)Cu(CN*t*Bu)], respectively, were used. The solvent-free gas-phase method also allows the fabrication of gold particles inside the pores of MOFs. For example, ZIF-8 and ZIF-90 were loaded with cavity-size-matching particles.^[22] The narrow pore apertures of both ZIFs (3.5 Å diameter) require a very small Au precursor to be able to pass, which was the linear molecule [(CO)AuCl]. In order to obtain metal nanoparticles inside MOF hosts, the incorporated precursors are decomposed under conditions that (should) rule out the decomposition of the MOF. The decomposition of the precursor can be achieved by a thermal or chemical treatment or by UV irradiation of the sample and a reactive gas atmosphere. The limitation of the thermal approach is the stability of the MOF itself. UV irradiation can be applied only for systems with light-sensitive precursors. After the precursor is decomposed, the organic ligands are removed from the reaction vessel in dynamic vacuum. Thermal treatment is often supported by the application of a reducing hydrogen atmosphere, as in the cases of Pd@MOF-5, Ru@MOF-5 or Au@MOF-5. In the case of Ru@MOF-5, [Ru(cod)(cot)] is an extremely reactive compound, which gives Ru nanoparticles at ambient conditions under H₂ treatment. However, [Ru(cod)(cot)] molecules incorporated into the MOF-5 cavities did not directly form metallic particles. On the basis of the analysis of the solid-state NMR spectroscopic data, it was concluded that stable [(cod)Ru⁰] fragments coordinated to the aromatic linkers were formed at room temperature at the first stage. In the next step, a mixture of [(cod)Ru⁰] and Ru was formed, and a quantitative formation of the pure Ru occurred after heating up to 150 °C for 48 hours. The resulting material consisted of a stable MOF-5 host framework and Ru nanoparticles. The presented examples show that the availability and the choice of the right precursor is the main limiting step for the solvent-free gas-phase loading method. The maximum metal loading is limited by the amount of precursor molecules that can be stored in the cavities or channels of the MOF. Also, the dimensions of the organometallic precursor should obviously not exceed the pore size, otherwise the selective incorporation or formation of the particles inside the cavities throughout the bulk of the MOF is not possible and preferential particle formation at the outer surface may occur (case A in Figure 1). For example, this situation is likely to be true for the use of [(CH₃)₂Au(acac)] for Au deposition in/on ZIF-8.^[14] The commercial availability

of such volatile and often air- and moisture-sensitive precursors is a second limiting step. However, the precise control of the loading degree over a wide range by using these precursors makes this method a particularly suitable approach for fundamental studies of metal nanoparticle incorporation into MOFs.

3.2. Solution Impregnation

The most obvious possibility for the introduction of metal nanoparticles into MOFs is the use of an aqueous solution of simple metal salts for liquid impregnation. The technique was applied for the fabrication of Ag, Au, Pd, Cu particles in different MOF structures. Once the salts are incorporated in or supported by the MOF material, the methods for the particle formation differ from the gas-phase precursor methods already discussed above. The reduction of the metal salt necessitates the introduction or co-adsorption of an external chemical reducing agent like hydrazine^[23] or NaBH₄.^[7] The reduction with hydrazine was supported by microwave irradiation, resulting in the formation of Pd and Cu particles that were supported by MIL-101(Cr).^[23] Interestingly, the incorporated metal salt can also be reduced by a redox-active MOF itself (autoreduction). The formation of Pd nanoparticles inside the {[Zn₃(ntb)(EtOH)₂]·4EtOH}_{*n*} (ntb = 4,4',4''-nitrilotrisbenzoate) framework in the absence of extra reducing agents and capping agents has been reported.^[11] The redox reaction between the organic linker of {[Zn₃(ntb)(EtOH)₂]·4EtOH}_{*n*} (ntb = 4,4',4''-nitrilotrisbenzoate) and the palladium salt Pd(NO₃)₂·2H₂O results in the formation of nanoparticles with a size of 3 nm and a maximum loading of 3 wt.-% (Scheme 1). The possibility of fabrication of Pd nanoparticles by the autoreduction of the MOF was also shown in the case of fourfold interpenetrating 3D diamondoid framework {[Ni(cyclam)]₂(mtb)}_{*n*}·8H₂O·4DMF (cyclam = 1,4,8,11-tetraazacyclotetradecane; mtb⁴⁻ = methanetetra benzoate, DMF = dimethylformamide) by the same group.^[12] The incorporation of Pd(NO₃)₂·2H₂O salt into the 1D channels (pore window: 2.05 × 2.05 Å; inside size of the pore cavity: 13.36 × 13.36 Å) of the nickel-containing framework results in the formation of palladium nanoparticles with a size of 2 nm. The Ni^{II} azamacrocyclic complex mtb, coordinating anionic ligands at the axial sites, can be oxidized to Ni^{III} by using suitable oxidizing agents. Therefore, the formed coordination polymer with Ni^{II} macrocyclic species is redox-active and reacts with Pd metal ions. The formation of gold, silver and palladium metal nanoparticles supported by MOFs with Ni macrocycles by using Ag^I, Au^{III} and Pd^{II} salts as oxidizing agents were among the earliest reports on metals@MOFs.^[20]

An important concept to direct the precursor loading and the subsequent decomposition to achieve composites B or even C (Figure 1) was demonstrated by the amine-grafting of unsaturated coordination sites of MIL-101(Cr).^[7] A stabilization and shaping effect on the incorporated metal components was observed. The encapsulation procedure



Scheme 1. Redox reaction of ntb linker with $\text{Pd}(\text{NO}_3)_2$ salt. Adopted with permission from ref.^[11]

comprised the neutralization of the surface amine groups with HCl, ionic reactions of the positively charged surface ammonium groups with anionic noble metal salts like $[\text{PdCl}_4]^{2-}$, $[\text{PtCl}_6]^{2-}$ and $[\text{AuCl}_4]^-$ by anionic exchange of the chloride anions and the final gentle reduction of metal salts with NaBH_4 at low temperature.

Using anchoring groups like amines for the metal precursor species, which may also interact with the formed metal nanoparticles like surfactants, and mimicking the situation in nanoparticle colloids may be a route to linking crystalline MOF materials as hosts with the existing knowledge on metal colloid chemistry. For example, post-synthetic functionalization of the organic linkers by click-chemistry may be used to introduce anchoring groups.^[28] Functional groups attached to the linkers may be quite useful, as demonstrated by the aldehyde group of imidazolate-2-carboxyaldehyde (ICA) in ZIF-90, which acts as an anchor for gold species and influences the shape and size of the particles, when ZIF-90 is compared to the nonfunctionalized, and thus less interactive, ZIF-8. Interestingly, the catalytic and selective in situ oxidation of the ICA linkers with methanol in close proximity to the Au nanoparticles embedded inside ZIF-90 leads to sterically more demanding ester groups at the linkers and therefore to nearly fully encapsulated gold nanoparticles inside the ZIF cavities.^[22] It is noteworthy that the metallation of $[(\text{Zn}_4\text{O})_3(\text{bdc-NH}_2)_3(\text{btc})_4]$ (bdc = 1,4-terephthalic acid) is related to this metal/linker chemistry. After the formation of the framework, the aminoterephthalic acid linker reacted with 2-pyridinecarboxaldehyde to form the covalently bound iminopyridine chelate derivative, which was treated with $[\text{PdCl}_2(\text{CH}_2\text{CN})_2]$ to give a metal-complexed MOF.^[29] Nevertheless, the introduction of dangling functional groups inside the MOF with the ability to stabilize precursor species as well as metal particles will have a limitation due to the accessible pore size.

3.3. Incipient Wetness Impregnation

The introduction of precursors for metal nanoparticles into a MOF by use of nonaqueous techniques has been demonstrated.^[4] In principle, this method is quite similar to solution impregnation; however, the amount of solution is

reduced to the minimum. The introduction of palladium particles into MOF-5 was performed by using a solution of $[\text{Pd}(\text{acac})_2]$ in CHCl_3 and subsequent thermal hydrogenolysis of the formed intermediate material. The obtained loading degree was about 1 wt.-% of Pd in MOF-5. Later, the method of solution impregnation was applied for the introduction of different amounts of Pd and the results were compared with the solvent-free loading method.^[3] It was possible to obtain loading degrees up to 15.4 wt.-% without observed degradation of the MOF-5 framework. The incipient wetness method is generally limited by the solubility of the selected precursor in suitable solvents. In aiming at higher metal loadings, removing (desorption) the solvent in the case of the incipient wetness method may cause problems in terms of segregation of the precursor molecules to the outer surface of the MOF crystallites, which is favoured by capillary forces. Quite interestingly, it was found that the MOF-5 matrix totally collapsed during a second loading cycle, irrespective of the precursor and the method, solvent-free gas-phase or incipient wetness. This effect is probably typical for highly catalytically active metal nanoparticles such as Pd. During a second loading step of the preformed Pd@MOF materials, the existing Pd particles will preferentially grow, which may destroy the MOF.^[3]

3.4. Solid Grinding

The deposition of metal nanoparticles into MOFs can also be achieved by solid grinding of a volatile precursor together with activated MOF material. This method was especially developed for supporting nanosized gold clusters on different MOF materials (MOF-5, $[\text{Cu}_3(\text{btc})_2]$, $[\text{Al}(\text{OH})(\text{bdc})]$, ZIF-8, CPL-1 and CPL-2).^[13] The volatile $[(\text{CH}_3)_2\text{Au}(\text{acac})]$ complex was used as the gold source. After the grinding process, the resulting materials were treated in a stream of 10% H_2 in N_2 at 120 °C and 1 atm for two hours to obtain gold nanoparticles supported by the MOF. Essentially, the solid-grinding method is similar to the solvent-free gas-phase loading method, because the chosen precursors are volatile and may be absorbed from the gas phase inside the MOF during the grinding process. The ob-

served particle size below 2 nm [in case of Au nanoparticles supported by MIL-53(Al)] shows that the method is a simple and effective way of producing nanosized metal particles without solvent and washing procedures after deposition. The obtained systems exhibited noticeably high activity for several catalytic reactions (e.g. aerobic oxidation of alcohols) and surprisingly high selectivity depending on the used MOF support material.^[13]

4. Structural Characterization

The structural characterization of the “metal@MOF” systems is a challenging, nontrivial topic. Note that in the literature, the exact distinction between the limiting cases A, B and C is sometimes not explicitly made, which may cause some confusion. The most essential issues regarding the characterization of “metal@MOF” materials are presented in the following paragraphs.

(1) The localization of the particles: The fabricated system should be assigned to one of the limiting cases A, B or C of “metal nanoparticles supported by MOF” systems (Figure 1). Therefore, data on the particle size and particle size distribution are important. Different TEM techniques like bright-field TEM (BF-TEM), high-angle annular dark field scanning TEM (HAADF-STEM) and electron tomography should be combined with PXRD and other techniques such as UV/Vis surface plasmon resonance, ESR, and so on. The precise characterization of the localization of the particles throughout the specimen can, however, only be achieved by a tomographic method, typically electron tomography. Routine TEM imaging without angle-dependent measurements, that is, the rotation of the sample, provide only two-dimensional maps of a three-dimensional structural environment. This is not enough for the precise estimation of the particle location.

(2) Characterization of possible interactions between the metal particles and the MOF: for example, the preformed Ru nanoparticles form complexes with the terephthalic acid linker of the MOF-5. For the investigation of such effects, again PXRD is important, but in addition UHV FTIR analyses including adsorption studies with probe molecules (e.g. CO) and magic angle spinning (MAS) solid-state NMR spectroscopy should be performed. The investigation of hydride mobility on the surface of the embedded metal nanoparticles was performed by low-temperature ²H MAS solid-state NMR spectroscopy, for example. The investigations of the host–guest chemistry of the organometallic precursors incorporated into the MOF can also give insight in the possible reactions between the MOF and metal species.^[30,31] Therefore, the elucidation of the crystal structure of the adsorbate compound by single-crystal or powder XRD can be useful.

(3) The loading amount of the MOF material with the metal species and the characterization of the remaining porosity after metal loading are important. The loading degree is important for the physical and chemical properties of the “metal@MOF” system. For catalysis, even low load-

ing degrees can provide interesting properties. For chemical sensors based on surface enhanced Raman scattering (SERS), a higher loading may be relevant. To control the morphology and activity of the incorporated metallic nanoparticles, detailed investigation of the loading process, properties and structure of adsorbate systems such as “precursor@MOF” and “metal@MOF” should be performed.

(4) Finally, one should try to rule out any artefacts created by the characterization processes themselves. MOFs are particularly sensitive to electron beam imaging, quite in contrast to zeolites and other purely inorganic porous matrices and templates. Collapse of the whole framework and/or chemical degradation may occur under the high electron doses in TEM analysis and must be taken into account. For example, imaging of [Cu₃btc₂] must be done with great care; otherwise, the formation of Cu and Cu_xO particles takes place and can be observed.^[38] Agglomeration of as-synthesized particles may also take place during routine TEM imaging.^[18] Last but not least, the materials should be thoroughly checked before and after application in catalysis test reactions in order to compare their microstructures.^[39]

4.1. Ru@MOF and Pd@MOF

According to the aspects discussed above, the characterization of Ru@MOF-5 was performed with the help of IR, UV/Vis and solid-state NMR spectroscopy, as well as TEM^[27] and PXRD. Up to now, this nanocomposite is among the few most thoroughly investigated “metal@MOF” systems. According to the elemental analysis data, the maximal loading rate is 3.5 molecules of [Ru(cod)-(cot)] per formula unit of the host framework. Thus, four and three guest molecules should occupy the large and small cavities of the host framework, respectively. The guest molecules in the [Ru(cod)(cot)]@MOF-5 material seem to be highly disordered, only tetragonal distortion of the host framework is present. PXRD data cannot be indexed in the *Fm* $\bar{3}$ *m* space group with the cell parameter *a* = 25.8849(2) Å known for MOF-5. The patterns can only be indexed in the primitive space group with four axes as the highest symmetry element (*P4/mmm* space group or lower) with the following cell parameters: *a* = 25.6716(3) Å, *c* = 25.4741(5) Å. All attempts to solve the crystal structure by using single-crystal XRD and PXRD data still did not give satisfactory results. Similarly, solid-state NMR spectroscopic data also showed a high disordering of the guests. Compared to “Pd@MOF-5”, “Ru@MOF-5” shows a more inhomogeneous distribution of the metallic particles throughout the bulk of the matrix volume. According to the electron tomographic reconstruction, the majority of the nanoparticles are localized more closely to the surface of the MOF crystals with a maximal penetration depth of 20 nm. The different mobility of the guest molecules, [(η⁵-C₅H₅)Pd(η³-C₃H₅)] and [Ru(cod)(cot)], or the self-catalyzed nature of the decomposition reaction of the [Ru(cod)(cot)] molecule could be a reasonable origin of the differences between the morphologies of the Pd@MOF-5 and Ru@MOF-5 com-

posites. The nanocomposite material obtained is highly air-sensitive and immediately forms RuO_x species. In oxidized form, RuO_x @MOF-5 has been tested in the catalytic oxidation of benzyl alcohol to benzaldehyde. The conversion observed was not higher than 25% after 48 hours, due to the low stability of the host framework under the reaction conditions. To understand the catalytic nature of Ru particles incorporated into a MOF, CO adsorption and hydride mobility have been studied by IR and solid-state NMR spectroscopy, respectively, at different temperatures in the range 23–200 K. The Ru@MOF-5 system (Langmuir surface area: $860 \text{ m}^2 \text{ g}^{-1}$) reversibly adsorbs CO molecules due to the formation of relatively strong complexes detectable in IR spectra at ambient conditions. Additionally, solid-state NMR spectroscopic data showed a high D/H exchange at the terephthalate linkers. Therefore, results obtained are quite optimistic and urge the search for more stable host frameworks with the aim to prepare highly catalytically active “metal@MOF” systems with a higher thermal and moisture stability.

The formation of Pd nanoparticles inside MIL-100(Al) has recently been reported. The in situ powder X-ray diffraction under a hydrogen atmosphere was applied to study the hydrogen adsorption properties of the palladium nanoparticles formed.^[10] The XRD patterns of the sample under vacuum and a hydrogen pressure of up to 0.5 kPa do not change significantly (Figure 3). Further increase in the pressure up to 4.5 kPa induces a constant shift of the diffraction peaks toward lower 2θ angles, demonstrating an expansion of the lattice parameters due to hydrogen insertion at the interstitial sites of Pd. Since the α and β phases of palladium hydride are coexistent, a clear identification of the pressure value for which the β phase starts to form is rather difficult. The formation of the β palladium hydride phase is complete at 4.5 kPa, and the exposure to higher pressure induces no significant changes in the XRD patterns.

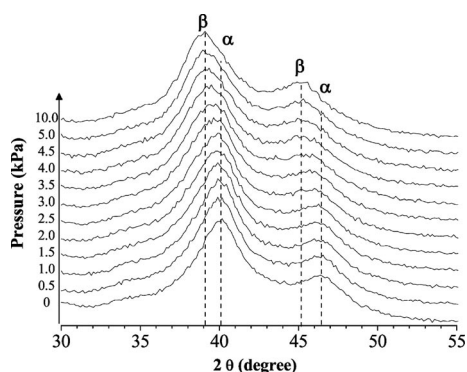


Figure 3. In situ powder XRD of the “Pd@MIL-100(Al)” system during hydrogen adsorption at room temperature. The α and β phases of palladium hydride are shown to monitor the phase transition. Reproduced with permission from ref.^[10]

The characterization of the spin state of prepared systems of metal nanoparticles supported by MOFs can be achieved by EPR and XPS techniques.^[18,11,12,20,21] The EPR spectrum of Pd nanoparticles supported by a four-

fold interpenetrating 3D diamondoid framework $[\{\text{Ni}(\text{cyclam})\}_2(\text{mtb})\}_n \cdot 8\text{H}_2\text{O} \cdot 4\text{DMF}$ shows anisotropic signals at $g_{\perp} = 2.175$ and $g_{\parallel} = 2.016$, which are indicative of the tetragonally distorted Ni^{III} species, and a peak at $g = 1.992$ for Pd^0 particles. However, not all of the introduced Pd^{II} salt was reduced to Pd^0 . This fact is shown by the coexistence of Pd^{II} , Pd^0 and Ni^{III} species in the solid by XPS and EDS. The absence of Ni^{II} and the appearance of Pd^{II} species indicate that all Ni centres in the framework are oxidized by the palladium salt and that there is still more unreacted Pd salt, which is also incorporated into the MOF or is adsorbed on the outer surface of the MOF crystals.

The surface accessibility of metal nanoparticles supported by a MOF matrix can be probed by CO adsorption/desorption. In the case of “Ru@MOF-5”, CO adsorption was followed by Fourier transform infrared spectroscopy (FTIR).^[25] After an exposure of the sample to an atmosphere of 1 bar CO for 30 min, two additional bands at 2000 and 1890 cm^{-1} were observed. These were assigned to CO molecules in different bonding modes to the Ru metal nanoparticles (linear bonding to the metal surface and bonding in a bridging position to adjacent metal atoms). The “Ru@MOF-5” system exhibits CO adsorption behaviour similar to that of Ru colloids supported by organic ligands such as PVP. In summary, the FTIR monitoring of the CO adsorption provides an elegant method for the investigation of the accessible particle surface. The investigations of the adsorption behaviour of “metal@MOF” systems can provide information about the location of the metal nanoparticles as well. Changes in specific surface area, micropore and total volumes of “Pd@MIL-100(Al)” relative to the MIL-100(Al) phase indicate that Pd nanoparticles in this system are located within the MIL-100(Al) matrix.^[10] The decrease in the calculated surface area combined with the retained crystallinity of the framework can only be achieved by Pd nanoaggregates located inside the cavities of the host material. The formed nanoparticles can block the access of N_2 to the framework pores and therefore decrease the observed N_2 uptake, which results in a low calculated surface area. Density measurements with the He pycnometer method delivered further proof for the existence of Pd nanoparticles within the cavities. The observed discrepancy between the calculated and measured density values could only be explained by a decrease in the accessible porous volume probed by He pycnometry, which is directly linked to the presence of Pd nanoparticles within the pores.

Due to the small particle size and low loading of metal nanoparticles incorporated into MOFs, TEM is often the only possible method for particle size determination. However, the particle size derived from the TEM images should be interpreted with care, because of the possible generation of artefacts in routine measurements.^[18] Since MOFs are very flexible materials, decomposition might occur under high-dose TEM irradiation. So, all information obtained by using electron microscopy must be carefully interpreted, as MOF materials are easy to damage under an intense elec-

tron beam. Nevertheless, it was shown that HRTEM can directly image the metal particles within the framework without structural changes to the particles themselves (although the framework host is degraded under HRTEM conditions).^[27] HRTEM imaging is hindered in some cases by sample charging, which was primarily observed in samples with particles smaller than 2 nm. This effect disappears if larger particles or surface agglomerates are present. It is thought that larger particles can conduct the charge away from the sample, whereas when only small particles are present, the charge accumulates and perturbs the images. Chemical information can be given by HAADF-STEM (Z-contrast) imaging; the image contrast in this technique is proportional to atomic number Z^n ($n \approx 1.7$), making “heavy” metallic nanoparticles/clusters easy visible, even when embedded in porous networks. However, HAADF-STEM images need to be taken at very short exposure times, as prolonged probe scanning on the samples can cause beam damage, carbon contamination and unwanted growth of nanoparticles due to agglomeration processes. Electron tomography provides spatial information, that is, the uniform or random distribution of the particles throughout the MOF matrix. With the introduction of this technique, determination of the exact position and distribution of particles within a framework is possible. It has been shown that MOF-5 crystals remain largely intact under low-intensity electron beams (BF-TEM at the lowest possible magnification and low beam intensity), even during prolonged experiments like a tomographic acquisition. However, a limited amount of degradation of the MOF-5 crystals under the beam is unavoidable.

The TEM investigation of the “Pd@MOF-5” (Figure 4) and “Ru@MOF-5” (Figure 5) systems showed that the loading of the particles is not always uniform throughout a single sample. In both samples, MOF-5 crystals densely packed with metal particles were observed as well as other

MOF-5 crystals with nearly no particles inside the MOF-5 matrix. As mentioned above, differences in particle loading between samples were also observed: while small nanoparticles were spread evenly throughout the MOF-5 framework host in the majority of Pd@MOF-5 crystals, the particles were present closer to or at the surface in most cases of Ru@MOF-5. In both samples, the nanoparticles mainly exhibited sizes ranging from 1 to 3 nm. Particles larger than approximately 5 nm were not found inside MOF-5 crystals but always at the crystal surface.

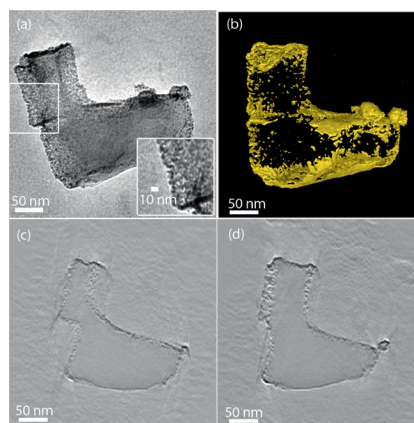


Figure 5. “Ru@MOF-5” not fully loaded: (a) Bright-field TEM image of a Ru-loaded MOF-5; the inset shows that particles from 1 to 5 nm in diameter are present; the matrix appears to be densely packed. (b) Tomographically reconstructed Ru particles (matrix not imaged); some overlapping of the particles is present due to diffraction contrast. (c and d) Slices through the tomographically reconstructed volume; the metallic particles are not embedded inside the MOF-5 matrix. All particles are located at the surface of the matrix or close to the surface (up to approximately 20 nm deep). Reproduced with permission from ref.^[27]

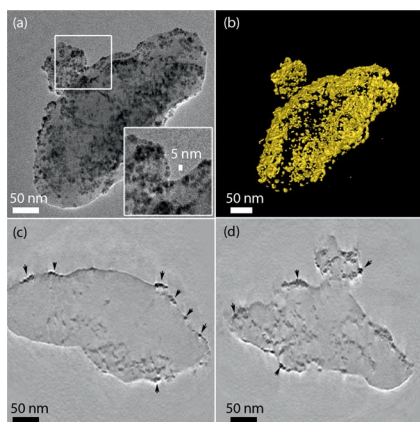


Figure 4. “Pd@MOF-5” fully loaded: (a) Bright-field TEM image of a Pd-loaded MOF-5; the inset shows that particles from 1 to 5 nm in diameter are present. (b) Tomographically reconstructed Pd particles. (c and d) Slices through the tomographically reconstructed volume; the metallic particles are embedded inside the MOF-5 matrix. The particles that are at the surface of the crystal are larger or have formed agglomerates. Reproduced with permission from ref.^[27]

4.2. Cu@MOF, Ag@MOF and Au@MOF

Another valuable technique for the determination of the oxidation state of the metal nanoparticles is UV/Vis spectroscopy. In case of Cu@MOF-177, the UV/Vis spectrum exhibits the Cu⁰ plasmon resonance at 580 nm.^[5] The spectrum of Ag⁰ nanoparticles with a particle size of 3 nm supported by [$\text{Ni}(\text{C}_{10}\text{H}_{26}\text{N}_6)_3(\text{bpdc})_3$] $\cdot 2\text{C}_5\text{H}_5\text{N} \cdot 6\text{H}_2\text{O}$ (bpdc = 4,4'-biphenyldicarboxylate) (1D channels with an effective pore size of 7.3 Å) exhibits two maxima at 378 and 449 nm.^[20] The absence of the plasmon resonance peak at around 520 nm assigned to Au particles larger than 2 nm provides an additional hint for the size of the Au nanoparticles supported by MIL-53(Al). In the latter case, the data should be backed up by TEM images and electron tomography because of the low loading degree of 1 wt.-% Au.^[13,22] In the case of silver nanoparticles supported by $[\text{Cu}_3(\text{btc})_2]$, the EPR data give insight into the formation of Ag₃ clusters as the primary species present in the as-synthesized samples, which were not observable by other techniques because of the small size and degradation of the sample under TEM beam radiation (Figure 6).

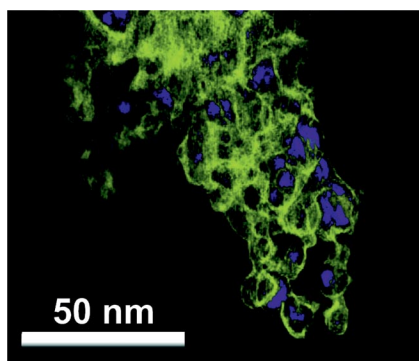


Figure 6. Three-dimensional tomographic reconstruction of Ag@MOF-508. Ag particles are dark blue, the framework is light yellow. The Ag particles are intermixed throughout the framework and are not segregated at the surface. Reproduced with permission from ref.^[18]

4.3. Bimetallics@MOFs

The formation of bimetallic nanoparticles was realized by the co-hydrogenolysis of two metal precursors under hydrogen pressure. The adjustment of a defined metal(1)/metal(2) molar ratio inside the MOF cavities was highly challenging. However, the simultaneous gas-phase loading of MOF-5 material with [Ru(cod)(cot)] and [Pt(cod)Me₂] resulted in a molar ratio of 1:1 measured by AAS and elemental analysis.^[26] Alloyed Ru/Pt nanoparticles were obtained by a subsequent hydrogenolysis of the precursors with coincidental partial hydrogenation of the bdc linkers. However, it was shown that some parts of the nanocrystallites of the composite material were enriched with Ru. The formation of bimetallic nanoparticles can be assisted by microwave irradiation in the presence of hydrazine. However, the problem of the precise characterization of the Cu/Pd phase supported by MIL-101(Cr) has not been solved yet.^[23] In summary, the results clearly show that the formation of bimetallic nanoparticles supported by a MOF matrix is a very challenging field, which requires a precise control of the molar ratio of both metal precursors and similar kinetic and chemical behaviour of the precursors during the hydrogenolysis process.

5. Applications

5.1. Catalytic Properties of “Metal@MOF”

5.1.1. Au@MOFs

The investigation of the catalytic properties of nanosized metal particles supported or embedded into a MOF matrix was the main focus of several reported studies. As discussed above, MOF matrices are able to stabilize colloidal metals. Haruta et al. reported on the formation of colloidal gold with a cluster size smaller than 2 nm, which showed high catalytic activity for aerobic oxidation of alcohols at room temperature.^[13] The Au particle size of 2 nm was found to be a critical point, at which the particles dramatically

change their catalytic and physicochemical properties. After the formation of gold clusters supported by different MOF systems like MIL-53(Al) (Figure 7), CPL-1, CPL-2 and MOF-5, the observed compounds were tested for their catalytic activity in the aerobic oxidation of benzyl alcohol in methanol solution. Two characteristic aspects could be pointed out: (1) The selection of the MOF matrix significantly affected catalytic activity and product selectivity. (2) Compared to those of known materials such as Au supported by active carbon or SiO₂, the catalytic activity of “Au@MOF” systems under base-free conditions was higher. It is thought to be the case that the observed difference in product selectivity depends on the degree of surface acidity of the MOF materials.

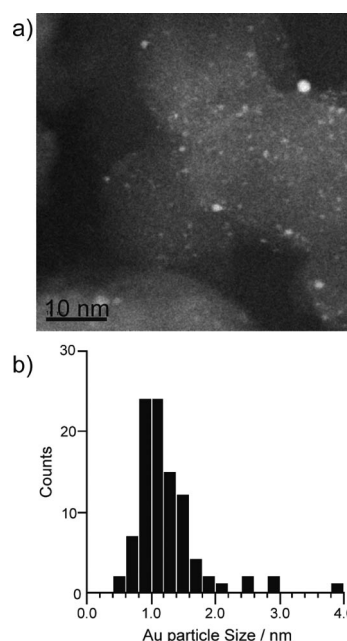


Figure 7. (a) HAADF-STEM image and (b) size distribution of 1 wt.-% Au@[Al(OH)(bdc)]_n. Reproduced with permission from ref.^[13]

Recently, it has been shown that “Au@ZIF-90” systems undergo an in situ oxidation of imidazolate-2-carboxyaldehyde groups of the ZIF-90 matrix with methanol under aerobic conditions, which leads to the formation of new composite material: Au@ZIF-90(ox) with imidazolate-2-methylcarboxylate (IMC) as a linker.^[22] Not all, but a substantial fraction of the aldehyde functions were converted into the corresponding esters. This can be expected, as not all but only a fraction of the cavities are filled or affected by the loading with Au nanoparticles. The catalytic and selective in situ oxidation of the ICA linkers in close proximity to the Au nanoparticles inside ZIF-90 leads to sterically more demanding ester groups at the linkers, which causes a downsizing of the pore aperture, and therefore this also leads to nearly fully encapsulated gold nanoparticles inside the ZIF cavities.

5.1.2. Cu@MOF-5 and Cu/ZnO@MOF-5

Nanoparticles of Cu 1–3 nm in size supported by a MOF-5 matrix exhibit catalytic activity for methanol production from synthesis gas ($70 \mu\text{mol}_{\text{MeOH}} \text{g}_{\text{cat}}^{-1} \text{h}^{-1}$).^[1] This activity of Cu@MOF-5 is surprising, as the promotion of copper by zinc or ZnO is normally essential for catalytic activity. Apparently, the complicated metal–support interaction of Cu–O–Zn can be provided by the MOF-5 framework. The initial catalytic activity of $220 \mu\text{mol}_{\text{MeOH}} \text{g}_{\text{cat}}^{-1} \text{h}^{-1}$ of Cu/ZnO@MOF-5 for methanol production after 1 h on stream at 220 °C is remarkably high.^[39] However, the deactivation of the catalyst occurs gradually over a period of 20 h, stabilizing at a level of $12 \mu\text{mol}_{\text{MeOH}} \text{g}_{\text{cat}}^{-1} \text{h}^{-1}$. The TEM image of the Cu/ZnO@MOF-5 material after the catalytic test revealed sintering of the Cu particles. Taking into account the rather low Cu loading degree (1–8 wt.-%) of Cu/ZnO@MOF-5, the measured productivities are still remarkable.

5.1.3. Pd@MOFs

The catalytic activity of Pd nanoparticles supported by MIL-101(Cr) was studied for different reactions. Férey et al. tested the catalytic activity of Pd particles supported by amine-grafted MIL-101(Cr) for the Heck reaction (coupling reaction of acrylic acid with iodobenzene).^[7] It was found that the observed activity of the material was comparable with that of a commercial catalyst like Pd supported by active carbon. The observed drawback was the long induction time of 0.5–1 h, probably due to the slow diffusion of reactants to accessible metal surfaces in the pores. Pd supported by MIL-101(Cr) was also tested for CO oxidation and one-step synthesis of methyl isobutyl ketone.^[8] In the latter case, it was found out that the loading degree is important for the catalytic activity of the “Pd@MIL-101(Cr)”. The material with a low loading degree (0.11 wt.-%) can easily be recovered and shows no loss of efficiency for five additional cycles. PXRD analysis after the five catalysis cycles shows no loss in the crystallinity of the material. The observed selectivity and conversion are comparable with those of known catalyst systems like Pd supported by a Zn/Cr mixed oxide.

The catalysis of the oxidation of CO by a “metal@MOF” system was reported for “Au@ZIF-8”^[14] and “Pd@MIL-101”.^[23] In the case of Au particles (size of 3.4 ± 1.4 nm before the reaction and 3.1 ± 0.9 nm after the catalysis cycle) supported by ZIF-8, it was found out that the CO oxidation activity improves with increasing Au loading degree. The catalytic activity appeared from the second run and became reproducible after the 3rd or 4th run. No agglomeration of the particles or loss of ZIF-8 crystallinity was observed after the performed catalysis. However, in the case of the “Pd@MIL-101(Cr)” system the highest catalytic activity was observed for the material with 2.9 wt.-% Pd (Figure 8). Increasing the loading degree of Pd resulted in a decrease of the catalytic activity. It was also found out that the catalytic activity did not decrease significantly by removal of Pd nanoparticles from the surface of MOF crystals. It was suggested that most of the activity

comes from Pd particles incorporated into the pore system of MIL-101(Cr). This fact is in agreement with the previous discussion about the high accessible surface area of particles incorporated into the MOF matrix and well distributed throughout the whole MOF crystal.

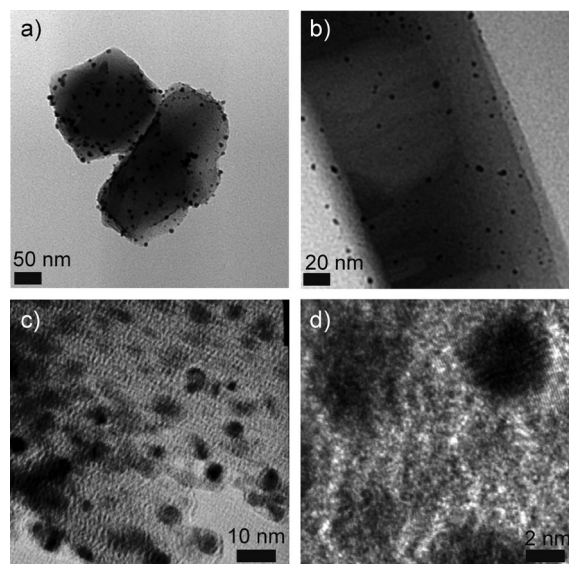


Figure 8. TEM images of “Pd@MIL-101(Cr)” prepared by microwave heating in the presence of hydrazine. (a) 2.9 wt.-% Pd; (b) 0.3 wt.-% Pd; (c) and (d) HRTEM images of “Pd@MIL-101(Cr)”. Reproduced with permission from ref.^[23]

However, the reported examples of catalytic activity imply the thermal and chemical stability of the MOF under the conditions of the catalytic reaction. Therefore, the choice of the supporting system should strongly depend on the stability and robustness of the MOF. MOFs with high thermal stability, like ZIF-8, MIL-53(Al) or MIL-101(Cr), are preferred. Their stability towards air and moisture makes them even more attractive. The reported investigation of the possible catalytic activity of the “Ru@MOF-5” system for alcohol oxidation have shown a breakdown of the MOF-5 matrix after the catalytic cycle. The material has lost most of its porosity as well. Recently, the detailed description of catalytic applications of “Metal@MOF” systems was reported by Corma et al.^[43]

5.2. Hydrogen Storage

5.2.1. Pd@MOFs at Pt@MOFs

The exceptional properties of MOFs have induced many studies on hydrogen storage.^[33] Until now, the reported uptake of MOFs at room temperature is lower than 1 wt.-% and is close to the values for other porous materials.^[34] Strategies to improve the uptake performance are, among others, the optimization of the pore size and the introduction of exposed metal sites. Another strategy is to use the so-called “spillover” effect (catalytic formation of monatomic hydrogen) by the introduction of nanosized metal catalysts into the pores of the MOF matrix. The migration

of formed monatomic hydrogen onto the MOF matrix can increase the storage capacity of MOF materials. However, the mechanism of “spillover” is poorly understood. The hydrogen sorption properties of systems such as “Pd@MOF-5”^[4] and “Pd@[Zn₃(ntb)₂(EtOH)₂·4EtOH]”^[11] were investigated in this context.

Recently, the hydrogen adsorption properties of “Pd@MIL-100(Al)” was investigated. It was found out that the hydrogen storage capacity (1.3 wt.-% at 4 MPa) at low temperatures is lower than values reported for MOF materials without metal nanoparticles incorporated inside the matrix. This can be explained by the reduced surface area of the loaded material [MIL-100(Al): 1200 m² g⁻¹; Pd@MIL-100(Al): 380 m² g⁻¹]. Interestingly, the situation changes significantly at room temperature. The amount of adsorbed hydrogen is almost doubled (0.35 wt.-%) relative to the unloaded material. The isotherm shows a steep increase at low pressures, which can be attributed to the formation of palladium hydride (Figure 9). It is known from the literature that bulk Pd absorbs hydrogen at room temperature and forms a β palladium hydride phase at low pressures. This process might also take place in the Pd@MIL-100(Al) system. As shown above, the formation of palladium hydride phases was proven by in situ PXRD. In summary, this work gives the first hints for the possible appearance of some kind of “spillover” effect and the subsequent diffusion of the monatomic hydrogen in the pores of the MOF host. However, the data should be interpreted very carefully, because of the lack of knowledge on the mechanism of the “spillover” effect.

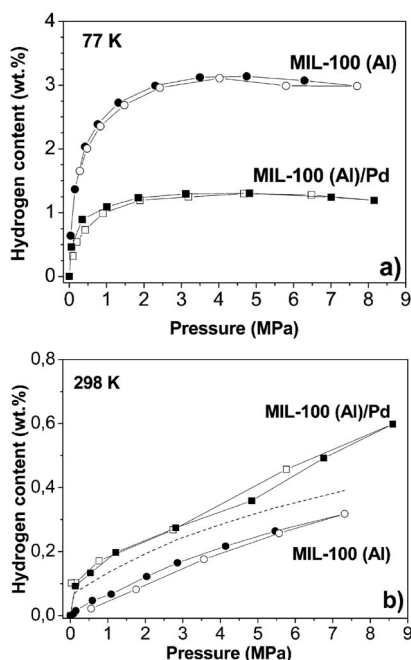


Figure 9. (a) Hydrogen uptake at 77 K by MIL-100(Al) (circles) and “Pd@MIL-100(Al)” (squares). (b) Hydrogen uptake at 298 K by MIL-100(Al) (circles) and “Pd@MIL-100(Al)” (squares). Reproduced with permission from ref.^[10]

Investigations of the hydrogen adsorption properties of Pt@MOF-177 have shown an uptake of 2.5 wt.-% of H₂ in the first adsorption cycle (room temperature and 144 bar H₂ pressure).^[24] However, in the second cycle, the storage capacity drops down to 0.5 wt.-%, which is close to the room-temperature uptake of pure MOF-177. It was also observed that the hydrogen uptake is not completely reversible in the first adsorption cycle, but it becomes completely reversible in the second cycle after the drop in hydrogen uptake. The observed loss in uptake can be attributed to the formation of platinum hydrides that are not desorbed at room temperature.

6. Conclusions

Each of the presented methods for the formation of metal particles supported by MOF materials has its own benefits as well as drawbacks. A rising number of publications demonstrate the potential of “metal@MOF” systems for catalytic applications. Other possible areas besides the investigation of the “metal nanoparticle” formation mechanism should also be taken into account, for example combining the selectivity of molecule penetration and adsorption of MOFs with SERS effects and using embedded metal nanoparticles for chemical sensing.^[35] Nevertheless, the formation of nanoparticles inside MOF cavities is still not really well understood. The observed local degradation of the networks during particle formation can be avoided by the introduction of better stabilization factors like functional organic linkers. The improvement of the characterization methods for such complex systems should be in the main focus of future work. The presented method of electron tomography is the first step on the way to the precise determination of the location of particles within a framework. As shown above, the fabrication of bimetallic nanoparticles is a very challenging field. The control of the metal ratio within these particles and the improvement of the fabrication conditions should also be investigated in the future.

Acknowledgments

The authors thank the German Research foundation for funding projects on “metals@MOFs” within the frame of the Research Centre in heterogeneous Catalysis (SFB 558). K. Y. is grateful to the Research Department Interfacial Systems Chemistry at Ruhr-Universität Bochum; M. M. and D. E. thank the Ruhr University Research School and the Graduate College of SFB 558 for supporting their Ph. D. thesis. The authors acknowledge support from the European Union under the Framework 6 program by a contract from an Integrated Infrastructure Initiative (Reference 026019 ESTEEM).

- [1] S. Hermes, M.-K. Schröter, R. Schmid, L. Khodeir, M. Muhler, A. Tissler, R. W. Fischer, R. A. Fischer, *Angew. Chem. Int. Ed.* **2005**, *44*, 6237–6241.
- [2] H. Li, M. Eddaoudi, M. O’Keeffe, M. Yaghi, *Nature* **1999**, *402*, 276–279.
- [3] D. Esken, X. Zhang, O. I. Lebedev, F. Schröder, R. A. Fischer, *J. Mater. Chem.* **2009**, *19*, 1314–1319.

- [4] M. Sabo, A. Henschel, H. Fröde, E. Klemm, S. Kaskel, *J. Mater. Chem.* **2007**, *17*, 3827–3832.
- [5] M. Müller, O. I. Lebedev, R. A. Fischer, *J. Mater. Chem.* **2008**, *18*, 5274–5281.
- [6] H. Furukawa, M. A. Miller, O. M. Yaghi, *J. Mater. Chem.* **2007**, *17*, 3197–3204.
- [7] Y. K. Hwang, D.-Y. Hong, J.-S. Chang, S. H. Jung, Y.-K. Seo, J. Kim, A. Vimont, M. Daturi, C. Serre, G. Férey, *Angew. Chem. Int. Ed.* **2008**, *47*, 4144–4148.
- [8] Y. Pan, B. Yuan, Y. Li, D. He, *Chem. Commun.* **2010**, *46*, 2280–2282.
- [9] G. Férey, C. Mellot-Draznicks, C. Serre, F. Millange, J. Dutour, S. Surblé, I. Margiolaki, *Science* **2005**, *309*, 2040–2042.
- [10] C. Zlotea, R. Campesi, F. Cuevas, E. Leroy, P. Dibandjo, C. Volkringer, T. Loiseau, F. Férey, M. Latroche, *J. Am. Chem. Soc.* **2010**, *132*, 2991–2997.
- [11] Y. E. Cheon, M. P. Suh, *Angew. Chem. Int. Ed.* **2009**, *48*, 2899–2903.
- [12] Y. E. Cheon, M. P. Suh, *Chem. Eur. J.* **2008**, *14*, 3961–3967.
- [13] a) T. Ishida, M. Nagaoka, T. Akita, M. Haruta, *Chem. Eur. J.* **2008**, *14*, 8456–8460; b) T. Ishida, N. Kawakita, T. Akita, M. Haruta, *Gold Bull.* **2009**, *42*, 267–274.
- [14] H.-L. Jiang, B. Liu, T. Akita, M. Haruta, H. Sakurai, Q. Xu, *J. Am. Chem. Soc.* **2009**, *131*, 11302–11303.
- [15] M. Kondo, T. Okubo, A. Asami, S.-I. Noro, T. Yoshitomi, S. Kitagawa, T. Ishii, H. Matsuzaka, K. Seki, *Angew. Chem. Int. Ed.* **1999**, *38*, 140–143.
- [16] T. Loiseau, C. Serre, C. Huguenard, G. Fink, F. Taulelle, M. Henry, T. Betaille, G. Férey, *Chem. Eur. J.* **2004**, *10*, 1373–1382.
- [17] S. S.-Y. Chui, S. M.-F. Lo, J. P. H. Charmant, A. G. Orpen, I. D. Williams, *Science* **1999**, *283*, 1148–1150.
- [18] R. J. T. Houk, B. W. Jacobs, F. E. Gabaly, N. N. Chang, A. A. Talin, D. D. Graham, S. D. House, I. M. Robertson, M. D. Allendorf, *Nano Lett.* **2009**, *9*, 3413–3418.
- [19] M. D. Allendorf, R. J. T. Houk, L. Andruszkiewicz, A. A. Talin, J. Pikarsky, A. Choudhury, K. A. Gall, P. J. Hesketh, *J. Am. Chem. Soc.* **2008**, *130*, 14404–14405.
- [20] H. R. Moon, J. H. Kim, M. P. Suh, *Angew. Chem. Int. Ed.* **2005**, *44*, 1261–1265.
- [21] M. P. Suh, H. R. Moon, E. Y. Lee, S. Y. Jang, *J. Am. Chem. Soc.* **2006**, *128*, 4710–4718.
- [22] D. Esken, Dissertation, Ruhr University of Bochum, **2010/2011**.
- [23] M. S. Al-Shall, V. Abdelsayed, A. E. R. S. Khder, H. M. A. Hassan, H. M. El-Kaderi, T. E. Reich, *J. Mater. Chem.* **2009**, *19*, 7625–7631.
- [24] S. Proch, J. Herrmannsdörfer, R. Kempe, C. Kern, A. Jess, L. Seyfarth, J. Senker, *Chem. Eur. J.* **2008**, *14*, 8204–8212.
- [25] F. Schröder, D. Esken, M. Cokoja, M. W. E. van den Berg, O. I. Lebedev, G. Van Tendeloo, B. Walaszek, G. Buntkovsky, H.-H. Limbach, B. Chaudret, R. A. Fischer, *J. Am. Chem. Soc.* **2008**, *130*, 6119–6130.
- [26] F. Schröder, S. Henke, X. Zhang, R. A. Fischer, *Eur. J. Inorg. Chem.* **2009**, 3131–3140.
- [27] S. Turner, O. I. Lebedev, F. Schröder, D. Esken, R. A. Fischer, G. Van Tendeloo, *Chem. Mater.* **2008**, *20*, 5622–5627.
- [28] a) Z. Wang, S. M. Cohen, *Chem. Soc. Rev.* **2009**, *38*, 1315–1329; b) M. Meilikhov, K. Yushenko, R. A. Fischer, *J. Am. Chem. Soc.* **2009**, *131*, 9644–9645.
- [29] C. J. Doonan, W. Morris, H. Furukawa, O. M. Yaghi, *J. Am. Chem. Soc.* **2009**, *131*, 9492–9493.
- [30] M. Meilikhov, K. Yushenko, R. A. Fischer, *Dalton Trans.* **2009**, 600–602.
- [31] M. Meilikhov, K. Yushenko, A. Torrisi, B. Jee, A. Pöpl, C. Mellot-Draznicks, R. A. Fischer, *Angew. Chem. Int. Ed.*, DOI: 10.1002/anie.200907126.
- [32] H. Kim, H. Chun, G. Kim, H. Lee, K. Kim, *Chem. Commun.* **2006**, 2759–2761.
- [33] L. J. Murray, M. Dincă, J. R. Long, *Chem. Soc. Rev.* **2009**, *38*, 1294–1314.
- [34] a) B. Panella, M. Hirscher, *Carbon* **2005**, *43*, 2209–2214; b) S. H. Jung, J. S. Lee, J. W. Yoon, D. P. Kim, J. S. Chang, *Int. J. Hydrogen Energy* **2007**, *32*, 4233–4237.
- [35] a) D. Zacher, A. Shekhah, C. Wöll, R. A. Fischer, *Chem. Soc. Rev.* **2009**, *38*, 1418–1429; b) K. Yushenko, M. Meilikhov, D. Zacher, F. Wieland, C. Sternemann, X. Stammer, T. Ladnorg, C. Wöll, R. A. Fischer, *Cryst. Eng. Commun.* **2010**, DOI: 10.1039/b92721g.
- [36] U. Müller, L. Lobree, M. Hesse, O. M. Yaghi, M. Eddaoudi, *WO 03/101975*, **2003**.
- [37] U. Müller, O. Metelkina, H. Junicke, T. Butz, O. M. Yaghi, *US 2004/081611*, **2004**.
- [38] X. Zhang, Dissertation, Ruhr University of Bochum, **2010**.
- [39] M. Müller, S. Hermes, K. Kähler, M. W. E. van den Berg, M. Muhler, R. A. Fischer, *Chem. Mater.* **2008**, *20*, 4576–4587.
- [40] W. Kleist, M. Maciejewski, A. Baiker, *Thermochim. Acta* **2010**, *499*, 71–78.
- [41] S. Opelt, S. Türk, E. Dietzsch, A. Henschel, S. Kaskel, E. Klemm, *Catal. Commun.* **2008**, *9*, 1286–1290.
- [42] S. Hermes, D. Zacher, A. Baunemann, C. Wöll, R. A. Fischer, *Chem. Mater.* **2007**, *19*, 2168–2173.
- [43] A. Corma, H. García, F. X. Llabrés i Xamena, *Chem. Rev.* **2010**, DOI: 10.1021/cr9003924.
- [44] B. Yuan, Y. Pan, Y. Li, B. Yin, H. Jiang, *Angew. Chem. Int. Ed.* **2010**, *49*, 4054–4058.
- [45] Y. K. Park, S. B. Choi, H. J. Nam, D.-Y. Jung, H. C. Ahn, K. Choi, H. Furukawa, J. Kim, *Chem. Commun.* **2010**, *46*, 3086–3088.

Received: April 28, 2010
Published Online: July 9, 2010

Porous Porphyrin Nanoarchitectures on Surfaces

Rie Makiura*^[a,b] and Hiroshi Kitagawa*^[b,c]

Keywords: Metal–organic frameworks / Coordination polymers / Porphyrinoids / Nanostructures / Thin films

Controlling the size and the growth direction of porous hybrid objects – metal–organic frameworks (MOFs) or porous coordination polymers (PCPs) – at the nanoscale is a critical issue for enabling their use in a number of potential applications that have arisen from the current remarkable activity in studying such porous materials. This microreview describes the recent progress in the design, growth, and characteriza-

tion of multidimensional nanoarchitectures by employing porphyrin-based components. The versatility of the sequential bottom-up fabrication process, which uses multitopic molecular building units assembled by appropriately chosen linkers, is suitable to be extended to the formation of a rich variety of nanostructures endowed with pores on surfaces.

1. Introduction

The recent explosion of interest in new metal–organic frameworks (MOFs), porous coordination polymers (PCPs), or related porous hybrid solids arising from the virtually unlimited structural possibilities involving combina-

tions of inorganic and organic building components has implications for general fundamental crystal growth techniques and for a number of potential applications ranging from materials science to the life sciences.^[1–9]

In many cases of targeted synthesis of polycrystalline or single-crystalline bulk MOFs by using solvothermal reactions, the desired structures, possessing well-defined pores, were generated by following rational molecular design routes, a strategic choice of a combination of molecular components based on a knowledge of coordination chemistry, and exploration of the reaction conditions. On the other hand, controlling the size of porous objects at the nanoscale and aligning such objects on/with various substances in certain desired ways (e.g. sequentially layered on top of each other, patterned on surfaces) has remained as a challenge that needs to be addressed, especially when we consider that

- [a] Nanoscience and Nanotechnology Research Center, Osaka Prefecture University, Gakuencho 1-2, Sakai, Osaka 599-8570, Japan
Fax: +81-72-254-9851
E-mail: r-makiura@21c.osakafu-u.ac.jp
[b] Japan Science and Technology Agency – Core Research for Evolutional Science and Technology (JST-CREST) Sanbancho 5, Chiyoda-ku, Tokyo 102-0075, Japan
[c] Division of Chemistry, Graduate School of Science, Kyoto University, Kitashirakawa-Oiwakecho, Sakyo-ku, Kyoto 606-8502, Japan
Fax: +81-75-753-4035
E-mail: kitagawa@kuchem.kyoto-u.ac.jp



Rie Makiura graduated from the University of Tsukuba in 2002 (M.Sc., Chemistry). Following an extended spell as a Researcher at the Frontier Device Research Center of SEIKO EPSON Cooperation in Nagano (2002–2007), where she worked on the development of organic electronic (OLED, TFT) devices and thin film all-solid batteries, she returned to academia as an Assistant Professor at the Department of Chemistry, Kyushu University (2007–2010). She was awarded her Ph.D. degree from Kyushu University in 2010. In April 2010, she was appointed as a tenure-track Lecturer at the Nanoscience and Nanotechnology Research Center, Osaka Prefecture University. Her research focus is currently on the rational design and construction of functional surface interface nanostructures.



Hiroshi Kitagawa, born in December 1961 in Osaka, obtained his Ph.D. at Kyoto University in 1991 and, after working as Research Associate at IMS (Okazaki) and JAIST (Kanazawa), he was appointed Associate Professor at the University of Tsukuba in 2000. He became Professor of Chemistry at Kyushu University in 2003 and Adjunct Professor in 2009 and was appointed to Kyoto University as Professor in the same year. He is Adjunct Professor at iCeMS, Kyoto University, and Visiting Professor at Inamori Frontier Research Center, Kyushu University. He was Associate Editor in Chemistry Letters. He is Principal Investigator (Research Director, 2006–2012) for Core Research for Evolutional Science & Technology (CREST) at the Japan Science & Technology Agency (JST). He was also a Researcher (2000–2004) for Precursory Research for Embryonic Science & Technology (PRESTO) at JST. He serves as one of the first generation of Program Officers for the Special Coordination Funds for Promoting Science & Technology at JST and Science Officer at MEXT. Professor Kitagawa has published about 170 papers on research dealing with multifunctionalities and properties of coordination complexes and nanomaterials.

such thin-film architectures are necessary for any applications of these porous materials in nanotechnological devices. In addition, understanding the roles played by the nanoscale size and by the interfacial conditions in integrated systems in defining the properties of such porous solids can lead to optimization of their potential functionalities.

In studying porous materials starting from the aspect of topological design, our first concern is to avoid the tendency of molecules to closely aggregate in order to stabilize their intermolecular assembly [as, for example, observed in self-assembled monolayers (SAMs),^[10] which are representative cases of self-aggregated surface modifications]. Instead, our target strategy is to devise soft chemical routes to align the molecular entities on surfaces in a way that each component adopts ideal topological proximity and separation distances that can lead to the creation of cavities and the development of porosity.

In this microreview, we discuss the recent progress in the design, growth, and characterization of surface nanoarchitectures composed of molecular solids, especially porphyrins. Indeed, porphyrins and metalloporphyrin derivatives have generated significant research activity from the viewpoint of topological design of two-dimensional (2D) and three-dimensional (3D) extended porous networks by solution-based fabrication techniques as well as because of their varied and rich chemical/physical properties.^[11–19] We start our discussion by considering some reports on 2D porphyrin-based structures formed directly on solid surfaces and whose stability is driven by a variety of bonding interactions between the molecules. We then move to studies on the formation of monolayers on liquid surfaces or on liquid/liquid interfaces by applying the Langmuir–Blodgett (LB) method. We also consider some notable studies of MOF thin films fabricated on solid surfaces by applying layer-by-layer (LbL) growth techniques (also discussed in ref.^[14]), leading to our own recent report of the growth by an unconventional preparative route of a combined Langmuir–Blodgett and layer-by-layer methodology (LB–LbL) of the first perfectly crystalline, preferentially oriented MOF surface nanoarchitecture comprising metalloporphyrin units.^[19]

1.1. Two-Dimensional Porphyrin Networks

Porphyrins are excellent candidates to employ in the construction of 2D supramolecular architectures. They are very stable π -conjugated macrocyclic ligands, characterized by an approximate 2D square-planar geometry. Metalloporphyrins are formed when a metal ion occupies the cavity at the center of porphyrin molecules. There is a rich variety of available (metallo)porphyrin derivatives incorporating different center-coordinated metals (or void) and various functional group substituents in the periphery of the molecule, such as alkyl chains, pyridyl derivatives, or carboxylate ions, thereby allowing fine control of the linkage motif.^[11–19] (Metallo)porphyrins with suitably chosen active coordina-

tion sites can be linked by metal linkers, which leads to the formation of extended 2D arrays.

Drain et al. reported oligomeric assemblies of porphyrin arrays with various sizes and shapes ranging from one-dimensional (1D) tapes to 2D sheets, by utilizing metal-coordinated linkage of individual monomer units.^[20–22] Specifically, a tessellated porphyrin nonamer with a size of 25 nm² can be successfully obtained by solvothermal synthesis from suitably designed porphyrin molecular precursors and appropriate linker units.^[20]

In order to go beyond oligomers and construct larger sizes of 2D architectures, assembling on substrate surfaces is necessary so that the long-range planar shape can be retained. Planar molecules with extended π -electron systems such as (metallo)porphyrins preferentially lie in many cases on the substrate surface. Both ultra-high vacuum (UHV) and solution fabrication processes have led to spontaneous assembly and retention of the flat-lying manner of the molecules on the substrate. Furthermore, efforts have focused on controlling the manner of surface assembly by introducing and tuning various types of bonding interactions, such as hydrogen bonds, covalent bonds, and van der Waals interactions between the porphyrin molecules. Such surface-assembled structures of various porphyrin molecules have been authenticated by scanning tunneling microscopy (STM) techniques.^[23–41]

However, here we note that, although the supramolecular chemistry developed in solvothermal reaction processes has resulted in the successful creation of a variety of desired supramolecular structures in the bulk (crystals), these methods and knowledge cannot be directly transferred to achieve large-scale molecular assembly on surfaces. The chemical condition and identity of the surface and of the substrate lattice structure have to be carefully considered together with the modification of the molecular components themselves, because the intermolecular interactions and the interactions between molecule and substrate surface now become strongly competitive. For example, in early work on surface structures using porphyrin molecules, Jung et al. reported that the self-assembly patterns of tetrakis(3,5-di-*tert*-butylphenyl) porphyrin copper (CuTBPP) formed under UHV conditions strongly depended on the chemical identity (Cu, Au, Ag) of the substrate.^[23,24] In addition, the stability of the surface supramolecular structures obtained was driven either by dipole–dipole interactions or by intermolecular hydrogen bonding in TBPP molecules peripherally substituted by CN- or COOH- groups.^[25–27] Recently, the first surface molecular assembly induced by strong covalent bonding was also reported by Grill et al.^[28] The topologies of the resulting nanostructures [dimers, 1D chains, 2D sheets] were precisely engineered by controlling the chemical structure of the building blocks.

There are also many reports on surface assemblies of porphyrins at ambient conditions,^[31–41] that is, the molecular components are prepared in solution and are deposited dropwise on the substrate surfaces (or by immersion of the substrate into the solution) with/without subsequent drying. Such surface assemblies fabricated by solution-based

processes are more realistic candidates for use in device applications, because they retain their structure under ambient conditions. Surface assemblies of octaethylporphyrin nickel (NiOEP) with a large domain size were obtained by simple immersion of a freshly cleaved highly ordered pyrolytic graphite (HOPG) substrate into a benzene or chloroform solution of NiOEP at room temperature.^[31,32] In this case, it was proposed that the dominant intermolecular interaction was one of van der Waals cohesive attraction, which led to the close-packed arrangement of the NiOEP molecular units. Formation of hydrogen-bonded, network-driven assemblies on HOPG or Au(111) substrates was also reported for peripherally functionalized porphyrins with carboxyphenyl groups, such as 5,10,15,20-tetrakis(4-carboxyphenyl)-21*H*,23*H*-porphyrin (TCPP) or its cobalt-substituted derivative in the central molecular void (CoTCPP).^[33–35] These self-assembled networks have a square packing order with a large unit cell size (2.3–2.5 nm), and typically contain some trapped species inside the intermolecular voids. The molecular design and fabrication protocols of such 2D networks, which incorporate large empty space, are useful starting points for the construction of porous 3D architectures on substrate surfaces that we focus on. Furthermore, to the best of our knowledge, there have been no reports to date on porphyrin-based 2D networks linked by coordination bonds, which directly formed on solid substrate surfaces under ambient conditions.

1.2. Method for Preparing Langmuir–Blodgett Films

Substrates do not necessarily have to be solid, and the liquid phase can also be employed as an excellent substrate for the initial formation of 2D networks, which can be subsequently deposited and stacked onto solid substrates. The Langmuir–Blodgett (LB) method is one of the superior techniques for the fabrication of well-ordered monolayers on liquid substrate surfaces.^[10,42–45] The LB technique was originally applied for the formation of films of alkyl chain compounds consisting of hydrophilic and hydrophobic parts. Water-insoluble substances prepared as a solution (i.e. dissolved in a highly volatile solvent) can be easily spread on the water surface to form an insoluble monolayer at the air/water interface. Compressing the surface laterally causes the molecules swimming on the water surface to assemble themselves.

The LB method has been widely applied to various functional materials ranging from molecular systems including porphyrins to inorganic metal oxides.^[46–59] Qian et al. employed a metal salt aqueous solution as a subphase and porphyrin molecules as the spreading substance.^[54–59] The combination of functionalized porphyrin molecules such as 5,10,15,20-tetrakis(4-pyridyl)-21*H*,23*H*-porphyrin (H₂TPyP) and its metal ion derivatives (MTPyP, M = Zn^{II}, Mn^{III}, TiO) with palladium salts was expected to lead to the formation of metal-mediated porphyrin arrays.^[54–57] The specific combination of molecular building blocks was

anticipated to mimic the conditions that led to the formation of the square packing structure of the supramolecularly assembled nonamers, reported by Drain et al.,^[20–22] as mentioned in the previous section. However, no structural results providing evidence for such a packing order were reported.

The same group also used H₂TPyP molecules with different assembly-mediating metal ions (Cd²⁺, PtCl₆^{2–}/PtCl₄^{2–}, Ag⁺, and Hg²⁺).^[58–59] It should be noted that, in this case, the metal ion aqueous solution was added onto the H₂TPyP chloroform solution. In this procedure, the order of the layers is inverted relative to that in the general LB fabrication method. The aqueous metal ion solution (low volatility) on top of the chloroform molecular building block solution (high volatility) prevents the chloroform solution from volatilizing, thereby resulting in the preservation of the liquid–liquid interface for a long time so that the interfacial reaction continues to proceed. This experimental procedure favors a continuous reaction to produce nanocrystals at the interface instead of monolayer formation. The resulting crystals can be transferred to solid substrates by the LB technique. The shapes of the nanocrystals (wires, plates) as observed by SEM or TEM vary with the identity of the metal ion linker and its coordination linking motif. Although powder XRD measurements of the nanocrystalline materials yielded diffraction patterns containing sharp reflections, the structural details remained unknown.

In addition, we stress that porphyrins are excellent candidates as building components not only for 2D structures but also for three-dimensionally linked frameworks including MOFs.^[15–17,60–71]

1.3. Layer-by-Layer Film Growth

LbL deposition is a representative technique for film growth, and the notation LbL has usually been employed to describe the alternating adsorption of electrostatically charged polymers or colloids. Nowadays, LbL is widely used to describe various stepwise bottom-up protocols of film growth.^[17–19] The basis of the LbL growth technique is that the components of the reaction (adsorption) are simply combined in a sequential manner. Usually, two solutions consisting of different components are prepared and a substrate is immersed in the solutions in an alternating fashion. Unreacted or weakly physisorbed components are removed between successive deposition steps by rinsing with an appropriate solvent.

Focusing on the reaction between metal ions and organic molecules based on coordination chemistry, such LbL protocols have been widely used to grow supramolecular networks on surfaces.^[72–75] However, it has only recently been utilized in the fabrication of thin films of MOFs or crystalline coordination polymers.^[18,76–81] Shekhah et al. first reported a step-by-step route of the synthesis of crystalline MOFs that was driven by the desire to understand the MOF formation process in a rational way rather than to attempt to fabricate MOF thin films.^[76,77] [Cu₃BTC₂–

(H₂O)_n] (HKUST-1) was chosen for this study. The surface plasmon resonance (SPR) technique was employed to monitor the deposition of the molecular species on the Au surface with submonolayer resolution at each procedure. XRD patterns in both out-of-plane and in-plane orientations were observed, providing evidence that the step-by-step grown MOF on the surface was crystalline and had the same structure as that reported for the bulk HKUST-1.

The same research group also later demonstrated that the formation of the interpenetrated framework, which greatly reduces the available void space in MOF architectures, can be suppressed by using the LbL technique (or as alternatively termed, step-by-step liquid-phase epitaxy).^[79] Although further structural data, especially the in-plane XRD profile of this surface MOF, are absolutely essential to properly characterize its three-dimensionally connected structure, it is apparent that the step-by-step LbL approach shows tremendous promise to potentially create new classes of MOFs that cannot be accessed by conventional solvothermal synthetic routes.

We also note that there are many reports on layered films containing porphyrin molecules fabricated by the LbL technique. Such films have been examined as components of various functional devices such as sensors and photovoltaics and in modifications of electrodes. However, application of the LbL growth technique had not been demonstrated in (metallo)porphyrin-based MOF film fabrication previously.

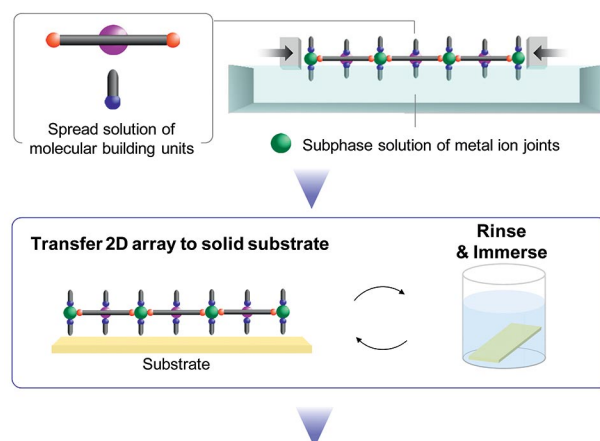
2. Fabrication of a Highly Ordered Porphyrin MOF Nanofilm by the LB–LbL Technique

The assembly of thin MOF films whose size and growth direction are completely controlled has proven an extremely challenging task. As mentioned above, there have been experimental reports that showed promising results in obtaining partially ordered systems or with some ordering preference. Nevertheless, the structural details, especially in the film orientation parallel to the substrate surface, have remained completely unknown. Therefore, our recent focus has been (a) to develop a rational construction protocol of MOF nanofilms by controlling the molecular arrangement of appropriate building blocks on surfaces at the nanoscale, especially in the direction parallel to the substrate, and (b) to find experimental ways to actually probe in detail the ordered structures of such nanoscale thin films. Indeed we have been successful in achieving both our targets and have recently reported the facile bottom-up fabrication of a perfectly crystalline, preferentially oriented MOF nanofilm on a solid surface, namely “nanofilm of metal–organic frameworks on surfaces no. 1” (NAFS-1), consisting of metalloporphyrin building units, and the ordered structure was demonstrated by surface synchrotron X-ray crystallography.^[19]

The fabrication strategy we developed was based on the principle of first attempting to prepare well-ordered 2D arrays of the desired building blocks on liquid surfaces by utilizing the LB method. In this way, we were able to re-

move any influence of the solid substrate on the in-plane molecular arrangement. Such influence can be of paramount (and often detrimental) importance when conventional epitaxial growth techniques on solid surfaces are undertaken. Having fabricated ordered monolayers in the air–water interface, these can then be deposited on appropriate substrates and sequentially stacked by following an LbL growth protocol (Figure 1).

2D array formation on liquid surface by LB method



LbL film growth by sequential stacking protocol

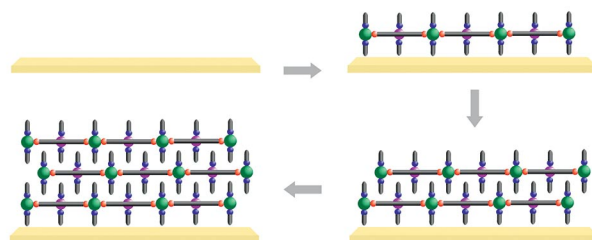


Figure 1. Schematic illustration of the representative steps involved in the combined LB–LbL (Langmuir–Blodgett/layer-by-layer) film fabrication technique.

In addition to the fact that we have already mentioned, namely that (metallo)porphyrin molecules can act as excellent components to be incorporated in the construction of both 2D arrays and 3D networks (including MOF architectures), (metallo)porphyrins are also highly suitable to be integrated in LB growth procedures because most of them are insoluble in water. We selected as proof-of-concept components in our attempted formation of 2D arrays the metalloporphyrin [5,10,15,20-tetrakis(4-carboxyphenyl)-porphyrinato]cobalt(II) (CoTCPP) together with a source of copper(II) ions to act as secondary building units and pyridine (py) as a coordination-saturating ligand to form CoTCPP–py–Cu (Figure 2). The fabrication protocol was initiated by spreading a solution of CoTCPP and py onto an aqueous solution of CuCl₂·2H₂O at room temperature. In order to follow the formation of the ordered arrays on the surface, the surface pressure (π) was monitored during pressing by moving the barriers of the LB trough, and the molecular areas in the array were evaluated (Figure 3). The same spread solution of CoTCPP and py was also applied onto

a pure water subphase for comparison. In the case of the copper chloride solution subphase, the larger molecular area observed for the CoTCPP-py-Cu monolayer is consistent with the linking of copper to the tetratopic CoTCPP molecules and indicates that they lie flat on the solution surface (i.e. the porphyrin 2D plane is parallel to the surface) (Figure 4, left). On the other hand, when a pure water subphase is used, the smaller molecular area measured implies that the CoTCPP molecules either stand vertically at some angle to the solution surface (Figure 4, top right) or remain in the horizontal orientation but pack more closely (Figure 4, bottom right).

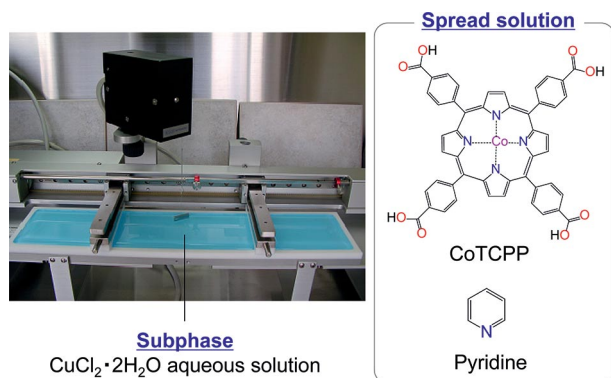


Figure 2. The Langmuir–Blodgett (LB) film fabrication system and selected molecular building components utilized in the present work.

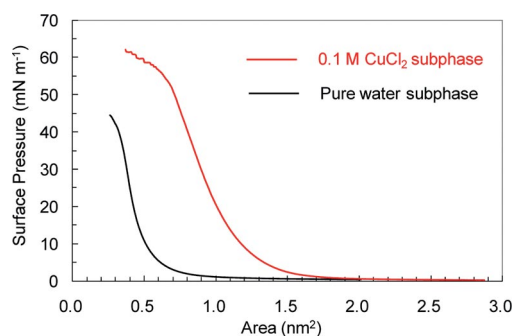
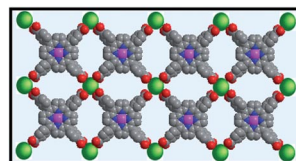


Figure 3. Surface-pressure–area (π – a) isotherms for CoTCPP-py monolayers on two different subphases (copper chloride aqueous solution vs. pure water).

The arrays were then transferred from the liquid subphase to a quartz substrate and ultraviolet/visible (UV/Vis) absorption spectroscopic measurements were undertaken. Absorption spectra for CoTCPP-py solutions in chloroform/methanol in the presence and absence of CuCl₂ were also recorded to follow the reaction of CoTCPP with copper ions in solution, as shown in Figure 5. The Soret band shift for the CoTCPP-py solution with CuCl₂ indicates that a change in the electronic state of CoTCPP was induced by the coordination between Cu²⁺ ions and the carboxylate units of CoTCPP. The comparable Soret band shift for CoTCPP-py-Cu arrays formed on CuCl₂ solution surface and deposited on the quartz substrate suggests that the CoTCPP-py molecular units successfully reacted with Cu²⁺

Subphase : CuCl₂ aqueous solution



Subphase : pure water

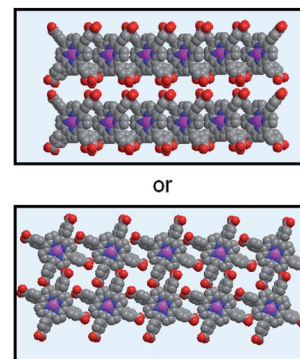


Figure 4. Proposed molecular arrangements of CoTCPP-py monolayers in two different subphases as deduced by consideration of the molecular areas derived by the π – a isotherm measurements. C atoms are shown in gray, N in blue, O in red, Co²⁺ ions in pink and Cu²⁺ in green.

ions, leading to the formation of copper-mediated CoTCPP-py-Cu 2D arrays. In addition, the increased absorbance observed for the array formed on pure water (Figure 5) implies that more CoTCPP molecules exist in the same area of the film than in the array fabricated on CuCl₂ aqueous solution. This supports the proposed CoTCPP arrangements derived from the π – a isotherm measurements.

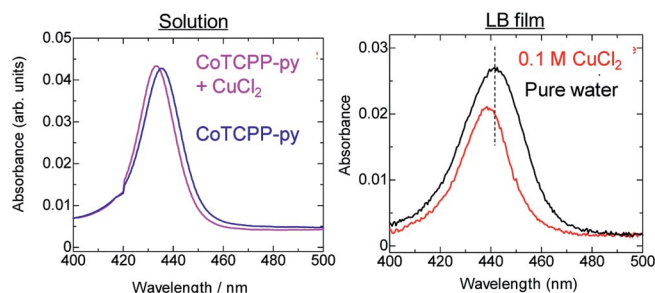


Figure 5. UV/Vis absorption spectra. Left: CoTCPP-py solution in the presence (violet trace) or absence (blue trace) of CuCl₂. Right: CoTCPP-py monolayers fabricated on CuCl₂ aqueous solution and on pure water subphase.

The 2D array of CoTCPP-py-Cu formed on the liquid surface at a surface pressure of 5 mN m^{−1} was transferred to the solid substrate by the horizontal dipping method (the substrate surface is parallel to the subphase surface) at room temperature. The substrate with the CoTCPP-py-Cu sheet was then rinsed with flowing distilled water, immersed in distilled water for 3 min, and finally dried by blowing nitrogen. To stack further layers, CoTCPP-py-Cu monolayers on the subphase were repeatedly transferred onto the substrate. The number of layers deposited is controlled by the number of cycles of sheet deposition and rinsing/solvent immersion/drying. The successive LbL growth procedure of NAFS-1 was monitored by UV/Vis spectroscopy.^[19] The linear increase in absorbance of the CoTCPP Soret band indicates that roughly the same amount of CoTCPP is deposited in each step of the layer stacking protocol (Figure 6).

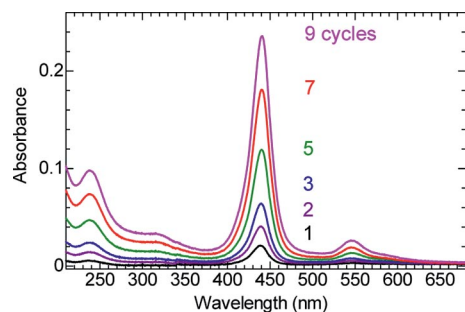


Figure 6. UV/Vis absorption spectra of NAFS-1 films on a quartz substrate after successive cycles of sheet deposition as labeled. Reproduced from ref.[19]

3. Characterization of the NAFS-1 Film by XPS and IR Spectroscopy

A 20-layer NAFS-1 nanofilm grown on a Si(100) substrate was characterized by X-ray photoelectron spectroscopy (XPS) and infrared (IR) spectroscopy. XPS measurements were performed at room temperature with a monochromatized Al- K_{α} X-ray source of 1486.6 eV. XPS spectra of a CoTCPP-py LB film fabricated on pure water subphase (20 layers) and of the CoTCPP (bulk powder) and $\text{CuCl}_2 \cdot 2\text{H}_2\text{O}$ (bulk powder) starting materials were also collected for comparison (Figure 7). Qualitative analysis of the wide-range spectrum confirms the successful introduction of copper ions into the NAFS-1 architecture [Figure 7(a)]. The absence of the signal of Cl in NAFS-1 implies that the carboxylic acid groups of CoTCPP were deprotonated and coordinated to copper ions, resulting in a balanced charge for the system without the presence of any chloride ions. The satellite structure observed in selected energy regions corresponding to Co3p and Cu3p [Figure 7(b) and (c)] provides unambiguous evidence that both the cobalt and copper oxidation states in NAFS-1 are +2.

The IR spectrum of NAFS-1 is shown in Figure 8 together with spectra of the CoTCPP-py LB film fabricated on pure water subphase (20 layers), as well as those of the reference compounds CoTCPP (bulk powder), copper benzoate (bulk powder), and benzoic acid (bulk powder) for comparison. Copper benzoate is a representative compound whose structure has a dinuclear paddle-wheel unit. When the dinuclear paddle-wheel structure is formed, the COO stretching mode from the carboxylate ion (COO^-) becomes IR-active and appears around 1400 cm^{-1} . On the other hand, benzoic acid shows strong absorption around 1700 cm^{-1} , which is attributed to the C=O stretching mode of the carboxyl group (COOH). A strong absorption band around 1400 cm^{-1} observed in NAFS-1 provides strong evidence for the formation of the dinuclear paddle-wheel structure in the film.

4. Structural Analysis

4.1. Synchrotron X-ray Diffraction (XRD) Measurements

XRD is a representative technique to study crystalline order, and synchrotron X-ray radiation provides an intense

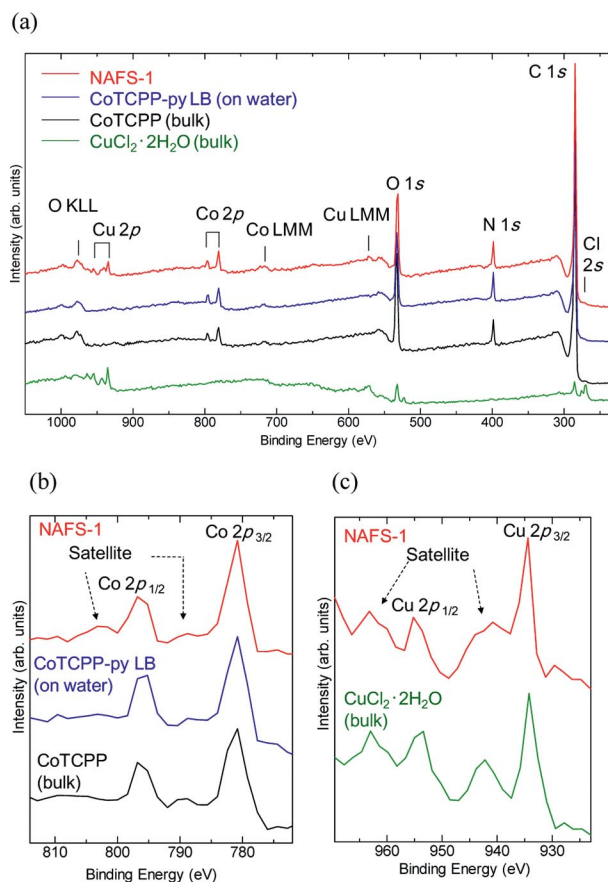


Figure 7. XPS spectra of NAFS-1 and reference materials. (a) Wide-range scans and qualitative analysis. (b) Co3p spectra. (c) Cu3p spectra.

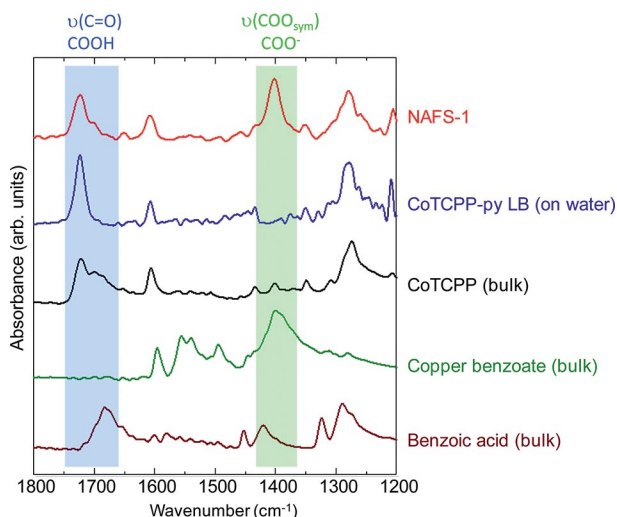


Figure 8. IR spectrum of the NAFS-1 film together with those of key reference materials.

beam appropriate to obtain good quality data even for thin films of nanosize thickness. In the present experiments, XRD measurements were performed at room temperature in two scattering geometries: the out-of-plane mode, which is sensitive to the lattice parameter in the film growth direc-

tion, and the in-plane (grazing incidence) mode, which is sensitive to the lattice dimensions parallel to the substrate surface, which provided crucial information about the preferential orientation of NAFS-1 nanofilms grown on Si(100) substrates. Flatness of the substrate surface strongly affects the crystallinity of the grown film, while at the same time it is of critical importance for the XRD measurements, especially in the in-plane scattering geometry. Therefore, we employed single crystals of silicon [(100) surface plane] as substrates for XRD measurements; their surface was polished to obtain a macroflatness of less than 0.01° and a microroughness (r.m.s.) of less than 5 \AA .

4.2. Out-of-Plane XRD Measurements

The XRD profile measured in out-of-plane scans by using a θ - 2θ scattering geometry shows three diffraction peaks, which can be indexed as (001), (002), and (003), as shown in Figure 9(a). This immediately reveals that NAFS-1 has a highly ordered growth perpendicular to the film growth direction.^[19] The value of the interlayer spacing was estimated as $0.938(3) \text{ nm}$ from the Bragg reflections (Figure 10). The total thickness of NAFS-1 is expected to be approximately 19 nm from the obtained interlayer distance and the number of the stacking layers ($0.938 \text{ nm} \times 20 \text{ layers} \approx 19 \text{ nm}$). This value is coincident with the crystalline domain size (20 nm) calculated from the full width at half maximum (FWHM) of the observed peaks by using Scherrer's equation. Rocking curve (θ -scan) measurements carried out at the (001) peak position provided further information on the manner of layer stacking. The observation of a single peak with a FWHM of approximately 0.3° implies that each sheet is tidily stacked almost parallel to each other with an average tilting angle of approximately 0.3° only.

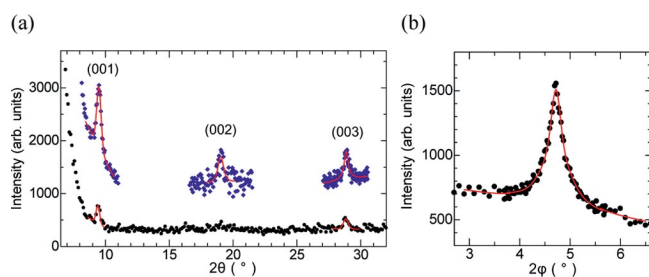


Figure 9. Out-of-plane synchrotron XRD profiles of NAFS-1. (a) θ - 2θ scattering geometry. (b) Rocking curve for the (001) reflection. Reproduced from ref.^[19]

4.3. In-plane XRD Measurements

The grazing incidence XRD (GIXRD) measurements were carried out at an incident angle of $\alpha = 0.1^\circ$. Diffraction from NAFS-1 was detected in the in-plane direction with a detection angle of 0.1° to the surface. Observation of a

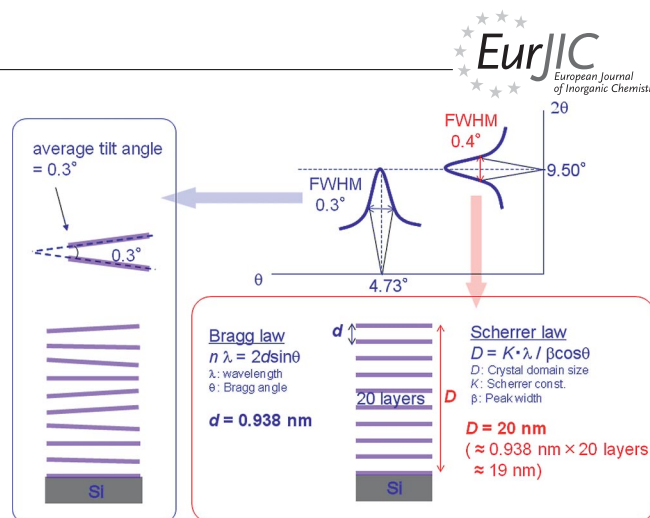


Figure 10. Derivation of the interlayer spacing and of the film thickness from out-of-plane synchrotron XRD measurements.

number of distinct sharp diffraction peaks implies that NAFS-1 has a highly ordered nature in the parallel direction to the substrate surface (Figure 11). A very important point is that all Bragg reflections obtained in the grazing incidence (in-plane) scattering geometry can be indexed as ($hk0$), namely, (110), (200), (320), (400), (330), (440), and (550)/(710) by using a pseudo-2D tetragonal unit cell with basal plane dimensions, $a = b = 1.6460(3) \text{ nm}$. Moreover, none of the observed reflections is found at the same Bragg angle as any of the peaks recorded in the out-of-plane geometry that have all been indexed as (00l). This shows that the combination of the LbL protocol coupled with the LB method in a modular fashion is a superb, highly controllable nanofilm fabrication technique, which can lead to perfect thin film growth of suitably chosen precursor building blocks in preferentially oriented fashion.

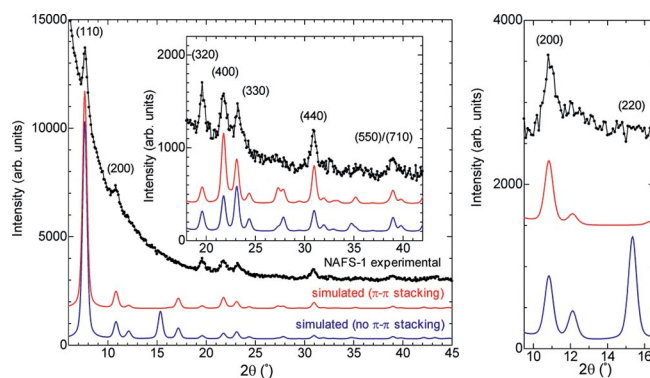


Figure 11. Measured in-plane XRD profile of NAFS-1 shown together with simulated XRD patterns for two different structural models. Right: selected 2θ region of the profile highlighting the differences in the simulated patterns. Reproduced from ref.^[19]

4.4. Construction of a Structural Model of the Nanofilm

The observation of Bragg reflections in both out-of-plane and in-plane scattering geometries has provided un-

ambiguous evidence that NAFS-1 is endowed with periodically ordered structures along the directions both parallel and perpendicular to the substrates. Very importantly, the XRD profiles allowed the development of a robust structural model for the fabricated NAFS-1 nanofilm.

Choi et al. reported the synthesis of three pillared homologous series of MOF crystalline materials (porphyrin paddle-wheel frameworks, or PPF) by employing as building blocks metallocporphyrins, which are able to provide an additional linking site at the metal center for bidentate organic pillar molecules to bind.^[68–69] Stacking sequences were controlled by utilizing different metal-centered porphyrins, MTCPP ($M = \text{Co}^{3+}$, Zn^{2+} , Pd^{2+}), in which the coordination number of the metal site is varied from six (octahedral geometry, Co^{3+}) to five (square-pyramidal geometry, Zn^{2+}) and to four (square-planar geometry, Pd^{2+}), while a 2D “checkerboard” in-plane linkage pattern remains the same for all analogues.^[68]

An in-plane structural motif of NAFS-1 comprising CoTCPP units linked by binuclear $\text{Cu}_2(\text{COO})_4$ paddle wheels (Figure 12) and resulting in a similar checkerboard pattern to that encountered in the bulk PPF series leads to a simulated in-plane XRD profile, which is in good agreement with that observed experimentally (Figure 11). The lattice size (1.65 nm), which is comparable to those of the PPF systems (1.66–1.67 nm),^[68] as well as the results of XPS and IR spectroscopic measurements (Figures 7 and 8) support a NAFS-1 structural model in which binuclear paddle-wheel units are present and provide the necessary linker motifs to develop the 2D order of the film. Further detailed structural analysis was driven by the motivation to address another important question: “Why is the interlayer spacing of 0.94 nm – extracted from the structural analysis of the out-of-plane XRD profile – considerably smaller than the estimated layer thickness of approximately 1.24 nm, if stacking of the layers is driven exclusively by physical adsorption?” (Figure 13). As a result, careful fine modification of the details of the in-plane structural model to include the structural and electronic roles played by the ligating pyridine molecules provided further structural insight even about the manner of layer stacking perpendicular to the film growth direction.

Therefore, we undertook an exhaustive number of simulations of the in-plane XRD patterns by considering a plethora of interlayer stacking models in which the pyridine molecules, bound to both the Co^{II} ion at the center of the porphyrin ring and the $\text{Cu}_2(\text{COO})_4$ paddle-wheel units, were explicitly considered. Excellent agreement between model calculations and experiment was obtained for a well-defined interdigitated layer stacking motif in NAFS-1 driven by π – π interactions between neighboring pyridine molecules coordinating axially to the paddle wheels (Figure 13). Such pyridine-driven stereoelectronic control of successive layer docking in the NAFS-1 nanofilm not only accounts well for the observed lattice metrics in both in-plane and out-of-plane directions but is also instrumental in defining the perfect highly ordered manner in which the film grows.^[19]

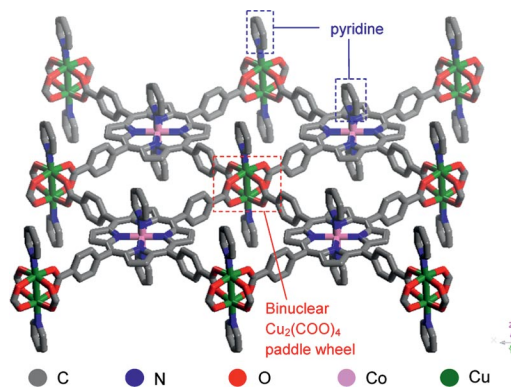


Figure 12. The in-plane structural model for NAFS-1 consisting of a 2D “checkerboard” motif of CoTCPP units linked by binuclear $\text{Cu}_2(\text{COO})_4$ paddle wheels.

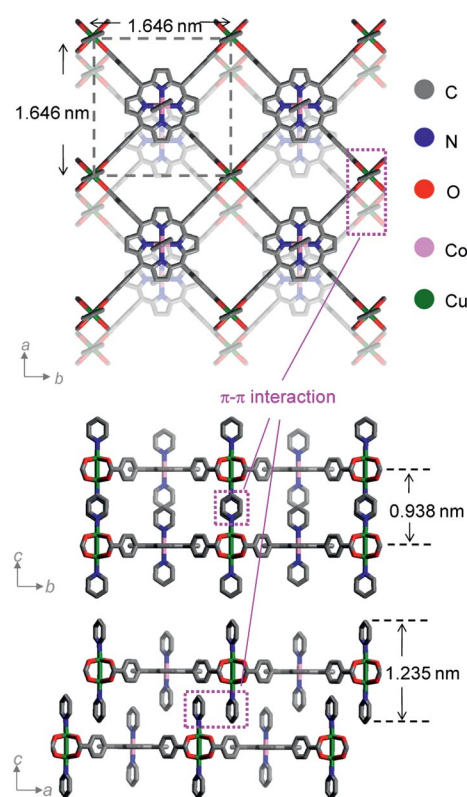


Figure 13. Schematic diagrams of the proposed crystalline structure for NAFS-1 shown in different projections along the three unit cell axes. Reproduced from ref.^[19]

5. Conclusions and Perspective

We have discussed in this microreview several approaches to employing (metallo)porphyrin-based components to build multidimensional nanoarchitectures. The versatility of the bottom-up fabrication process, which uses multitopic molecular building units assembled by appropriately chosen linkers has been extensively utilized in supramolecular chemistry and in crystal engineering, mainly by employing solvothermal synthetic routes. Bottom-up fabrication protocols are highly suitable to be extended to the formation

of quasi-infinite nanostructures on surfaces. The linkage motif of such nanostructures, which also create intermolecular voids (for 2D networks) or cavities (for 3D frameworks), can be strategically modified by the design of building molecules with various linkage sites and the choice of their combinations and stoichiometry. Regarding control of the size and growth direction of nano-objects, the LbL protocol is highly appropriate for molecular assemblage on surfaces and can ideally provide any desired film thickness at the molecular scale with simultaneous complete preferential orientation. This can be contrasted with the outcome of solvothermal synthetic routes, in which submicrometer control of the crystalline size can be exercised by changes in concentration and/or growth times. As structural design has been the main focus of current attempts towards fabrication of surface assemblies, the future direction will surely be targeted towards various physical properties and functionalities, including structural dynamics associated with the frameworks and the responses of their cavities to external stimuli that may differ from comparable well-studied bulk porous systems.

On the other hand, utilizing the chemical/physical properties of well-designed nanoarchitectures is still at a developing stage. Porphyrins can play an important role not only from the aspect of supramolecular design, but also because of their rich variety of electrochemical and optical properties, which derive from the superior thermal/oxidative stability of their available derivatives. For example, the axial metal sites of porphyrins, which are commonly used for binding guest molecules or act as active sites for catalytic reactions, can be sterically and electronically exposed to the pore, in contrast to the metal sites in most MOFs that are three-dimensionally blocked by organic ligands that prevent the guest molecules from accessing the metals easily. Actually, Hupp et al. have recently reported on the catalytic reactions of such a metal-exposed metalloporphyrin-based bulk MOF, ZnPO-MOF.^[70,71] The acyl-transfer reaction between *N*-acetylimidazole and 3-pyridylcarbinol was performed in ZnPO-MOF, and an approximately 2400-fold rate enhancement was observed relative to the uncatalyzed (in the absence of ZnPO-MOF) reaction conditions.

From the methodological viewpoint, in order to directly observe the surface nanoarchitecture of 2D monolayers formed on solid surfaces, the STM technique can be directly employed in combination with the use of conductive substrates – these will be also useful in exploring physical properties related to electron transfer or chemical reactions. On the other hand, when the assemblies consist of multilayers having thicknesses of several tens of nanometers or more, XRD crystallography becomes a powerful tool to observe the ordered structures. However, for a few layers of molecular surface assemblies, which form at ambient conditions or by solution processes including the LB–LbL protocol that we discussed here, no promising technique has been developed as yet. While the deposition process can be followed very precisely by SPR, UV/Vis spectroscopy, and other spectroscopic techniques, these basically give information only about the successful fabrication of the multilayers. As

there are many reports of structural studies on a few atomic layers of inorganic compounds (metals, oxides, semiconductors) deposited or epitaxially grown on cleaned surfaces under UHV conditions, further work is needed to develop comparable methods for molecule-based systems. Finally, an intriguing possibility is presented by surface-exposed nanofilms consisting only of a few layers of porous framework units: these may show unique adsorption and reactivity properties that may considerably differ from or are not encountered in the larger scale of both multilayer and bulk structures.

Acknowledgments

We acknowledge financial support by the Japan Science and Technology Agency (JST) under the Core Research for Evolutional Science and Technology (CREST) project, the New Energy and Industrial Technology Development Organization (NEDO), and the Japan Society for the Promotion of Science (JSPS) under Grants-in-Aid for Scientific Research (No. 20350030), Challenging Exploratory Research (No. 20655030), Scientific Research on Innovative Areas (No. 22108524), and Young Scientists (B) (No. 22750056). We thank Super Photon ring-8 GeV (SPring-8) for access to the synchrotron X-ray facilities.

- [1] J. R. Long, O. M. Yaghi, *Chem. Soc. Rev.* **2009**, 38, 1213–1214 (and references cited therein).
- [2] G. Férey, *Chem. Soc. Rev.* **2008**, 37, 191–214.
- [3] S. Kitagawa, R. Matsuda, *Coord. Chem. Rev.* **2007**, 251, 2490–2509.
- [4] Q. Li, W. Zhang, O. S. Miljanic, C.-H. Sue, Y.-L. Zhao, L. Liu, C. B. Knobler, J. F. Stoddart, O. M. Yaghi, *Science* **2009**, 325, 855–859.
- [5] C. G. Bezzi, M. Helliwell, J. E. Warren, D. R. Allan, N. B. McKeown, *Science* **2010**, 327, 1627–1630.
- [6] T. Yamada, H. Kitagawa, *J. Am. Chem. Soc.* **2009**, 131, 6312–6313.
- [7] T. Yamada, M. Sadakiyo, H. Kitagawa, *J. Am. Chem. Soc.* **2009**, 131, 3144–3145.
- [8] M. Sadakiyo, T. Yamada, H. Kitagawa, *J. Am. Chem. Soc.* **2009**, 131, 9906–9907.
- [9] H. Okawa, A. Shigematsu, M. Sadakiyo, T. Miyagawa, K. Yoneda, M. Ohba, H. Kitagawa, *J. Am. Chem. Soc.* **2009**, 131, 13516–13522.
- [10] M. Kind, C. Wöll, *Prog. Surf. Sci.* **2009**, 84, 230–278.
- [11] K. M. Smith, *Porphyrins and Metalloporphyrins*, Elsevier, Amsterdam, **1972**.
- [12] R. A. Sheldon, *Metalloporphyrins in Catalytic Oxidations*, Marcel Dekker, New York, **1994**.
- [13] K. Kadish, K. M. Smith, R. Guiard (Eds.), *The Porphyrin Handbook*, Academic Press, New York, **1999–2003**, vols. 1–20.
- [14] S. J. Lee, J. T. Hupp, *Coord. Chem. Rev.* **2006**, 250, 1710–1723.
- [15] K. S. Suslick, P. Bhyrappa, J.-H. Chou, M. E. Kosal, S. Nakagaki, D. W. Smithenry, S. R. Wilson, *Acc. Chem. Res.* **2005**, 38, 283–291.
- [16] I. Goldberg, *Cryst. Eng. Commun.* **2008**, 10, 637–645.
- [17] C. M. Drain, A. Varotto, I. Radivojevic, *Chem. Rev.* **2009**, 109, 1630–1658.
- [18] D. Zacher, O. Shekhah, C. Wöll, R. A. Fischer, *Chem. Soc. Rev.* **2009**, 38, 1418–1429.
- [19] R. Makiura, S. Motoyama, Y. Umemura, H. Yamanaka, O. Sakata, H. Kitagawa, *Nat. Mater.* **2010**, 9, 565–571.
- [20] C. M. Drain, F. Nifiaty, A. Vasenko, J. D. Batteas, *Angew. Chem. Int. Ed.* **1998**, 37, 2344–2347.

- [21] T. N. Milic, N. Chi, D. G. Yablon, G. W. Flynn, J. D. Batteas, C. M. Drain, *Angew. Chem. Int. Ed.* **2002**, *41*, 2117–2119.
- [22] T. Milic, J. C. Garino, J. D. Batteas, G. Smeureanu, C. M. Drain, *Langmuir* **2004**, *20*, 3974–3983.
- [23] T. A. Jung, R. R. Schlittler, J. K. Gimzewski, H. Tang, C. Joachim, *Science* **1996**, *271*, 181–184.
- [24] T. A. Jung, R. R. Schlittler, J. K. Gimzewski, *Nature* **1997**, *386*, 696–698.
- [25] T. Yokoyama, S. Yokoyama, T. Kamikado, Y. Okuno, S. Mashiko, *Nature* **2001**, *413*, 619–621.
- [26] T. Yokoyama, T. Kamikado, S. Yokoyama, S. Mashiko, *J. Chem. Phys.* **2004**, *121*, 11993–11997.
- [27] J. P. Hill, Y. Wakayama, M. Akada, K. Ariga, *J. Phys. Chem. C* **2007**, *111*, 16174–16180.
- [28] L. Grill, M. Dyer, L. Lafferentz, M. Persson, M. V. Peters, S. Hecht, *Nat. Nanotechnol.* **2007**, *2*, 687–691.
- [29] O. Shoji, H. Tanaka, T. Kawai, Y. Kobuke, *J. Am. Chem. Soc.* **2005**, *127*, 8598–8599.
- [30] J. P. Hill, Y. Wakayama, W. Schmitt, T. Tsuruoka, T. Nakaniishi, M. L. Zandler, A. L. McCarty, F. D'Souza, L. R. Milgrom, K. Ariga, *Chem. Commun.* **2006**, 2320–2322.
- [31] D. E. Barlow, L. Scudiero, K. W. Hipps, *Langmuir* **2004**, *20*, 4413–4421.
- [32] A. Ogunrinde, K. W. Hipps, L. Scudiero, *Langmuir* **2006**, *22*, 5697–5701.
- [33] S. Yoshimoto, N. Yokoo, T. Fukuda, N. Kobayashi, K. Itaya, *Chem. Commun.* **2006**, 500–502.
- [34] S. Yoshimoto, T. Sawaguchi, *J. Am. Chem. Soc.* **2008**, *130*, 15944–15949.
- [35] Q. Yuan, Y. Xing, E. Borguet, *J. Am. Chem. Soc.* **2010**, *132*, 5054–5060.
- [36] S. Yoshimoto, K. Itaya, *J. Porphyrins Phthalocyanines* **2007**, *11*, 313–333.
- [37] M. Kunitake, U. Akiba, N. Batina, K. Itaya, *Langmuir* **1997**, *13*, 1607–1615.
- [38] K. Suto, S. Yoshimoto, K. Itaya, *Langmuir* **2006**, *22*, 10766–10776.
- [39] N. Katsonis, J. Vicario, T. Kudernac, J. Visser, M. M. Pollard, B. L. Feringa, *J. Am. Chem. Soc.* **2006**, *128*, 15537–15541.
- [40] J. Otsuki, E. Nagamine, T. Kondo, K. Iwasaki, M. Asakawa, K. Miyake, *J. Am. Chem. Soc.* **2005**, *127*, 10400–10405.
- [41] J. Otsuki, S. Kawaguchi, T. Yamakawa, M. Asakawa, K. Miyake, *Langmuir* **2006**, *22*, 5708–5715.
- [42] G. Roberts (Ed.), *Langmuir–Blodgett Films*, Plenum Press, New York, **1990**.
- [43] I. Langmuir, *J. Am. Chem. Soc.* **1917**, *39*, 1848–1906.
- [44] K. B. Blodgett, *J. Am. Chem. Soc.* **1935**, *57*, 1007–1022.
- [45] V. Vogel, C. Wöll, *J. Chem. Phys.* **1986**, *84*, 5200–5204.
- [46] K. Töllner, R. P. Biro, M. Lahav, D. Milstein, *Science* **1997**, *278*, 2100–2102.
- [47] D. Y. Takamoto, E. Aydil, J. A. Zasadzinski, A. T. Ivanova, D. K. Schwartz, T. Yang, P. S. Cremer, *Science* **2001**, *293*, 1292–1295.
- [48] Y. Umemura, E. Shinohara, A. Koura, T. Nishioka, T. Sasaki, *Langmuir* **2006**, *22*, 3870–3877.
- [49] Y. Umemura, E. Shinohara, *Chem. Commun.* **2004**, 1110–1111.
- [50] Y. Umemura, A. Yamagishi, R. Schoonheydt, A. Persoons, F. DeSchryver, *J. Am. Chem. Soc.* **2002**, *124*, 992–997.
- [51] S. M. O'Flaherty, L. Wiegart, O. Konovalov, B. Struth, *Langmuir* **2005**, *21*, 11161–11166.
- [52] S. M. O'Flaherty, L. Wiegart, B. Struth, *J. Phys. Chem. B* **2006**, *110*, 19375–19379.
- [53] L. F. Chi, M. Anders, H. Fuchs, R. R. Johnston, H. Ringsdorf, *Science* **1993**, *259*, 213–216.
- [54] D.-J. Qian, C. Nakamura, J. Miyake, *Thin Solid Films* **2001**, *397*, 266–275.
- [55] D.-J. Qian, C. Nakamura, J. Miyake, *Langmuir* **2000**, *16*, 9615–9619.
- [56] C.-F. Zhang, M. Chen, C. Nakamura, J. Miyake, D.-J. Qian, *Langmuir* **2008**, *24*, 13490–13495.
- [57] D.-J. Qian, C. Nakamura, J. Miyake, *Chem. Commun.* **2001**, 2312–2313.
- [58] B. Liu, D.-J. Qian, M. Chen, T. Wakayama, C. Nakamura, J. Miyake, *Chem. Commun.* **2006**, 3175–3177.
- [59] B. Liu, D.-J. Qian, H.-X. Huang, T. Wakayama, S. Hara, W. Huang, C. Nakamura, J. Miyake, *Langmuir* **2005**, *21*, 5079–5084.
- [60] T. Ohmura, A. Usuki, K. Fukumori, T. Ohta, M. Ito, K. Tatsu-umi, *Inorg. Chem.* **2006**, *45*, 7988–7990.
- [61] L. Carlucci, G. Ciani, D. M. Proserpio, F. Porta, *Angew. Chem. Int. Ed.* **2003**, *42*, 317–322.
- [62] Y. D. Posner, S. Dahal, I. Goldberg, *Angew. Chem. Int. Ed.* **2000**, *39*, 1288–1292.
- [63] I. Goldberg, *Chem. Commun.* **2005**, 1243–1254.
- [64] D. W. Smithenry, S. R. Wilson, K. S. Suslick, *Inorg. Chem.* **2003**, *42*, 7719–7721.
- [65] M. E. Kosal, J. H. Chou, S. R. Wilson, K. S. Suslick, *Nat. Mater.* **2002**, *1*, 118–121.
- [66] T. Sato, W. Mori, C. N. Kato, T. Ohmura, T. Sato, K. Yokoyama, S. Takamizawa, S. Naito, *Chem. Lett.* **2003**, *32*, 854–855.
- [67] B. F. Abrahams, B. F. Hoskins, D. M. Michail, R. Robson, *Nature* **1994**, *369*, 727–729.
- [68] E. Y. Choi, P. M. Barron, R. W. Novotny, H.-T. Son, C. Hu, W. Choe, *Inorg. Chem.* **2009**, *48*, 426–428.
- [69] H. Chung, P. M. Barron, R. W. Novotny, H.-T. Son, C. Hu, W. Choe, *Cryst. Growth Des.* **2009**, *9*, 3327–3332.
- [70] A. M. Shultz, O. K. Farha, J. T. Hupp, S. T. Nguyen, *J. Am. Chem. Soc.* **2009**, *131*, 4204–4205.
- [71] J. Y. Lee, O. K. Farha, J. Roberts, K. A. Scheidt, S. T. Nguyen, J. T. Hupp, *Chem. Soc. Rev.* **2009**, *38*, 1450–1459.
- [72] H. C. Yang, K. Aoki, H. G. Hong, D. D. Sackett, M. F. Arendt, S. L. Yau, C. M. Bell, T. E. Mallouk, *J. Am. Chem. Soc.* **1993**, *115*, 11855–11862.
- [73] M. Altman, A. D. Shukla, T. Zubkov, G. Evmenenko, P. Dutta, M. E. van der Boom, *J. Am. Chem. Soc.* **2006**, *128*, 7374–7382.
- [74] M. Haga, K. Kobayashi, K. Terada, *Coord. Chem. Rev.* **2007**, *251*, 2688–2701.
- [75] H. Nishihara, K. Kanaizuka, Y. Nishimori, Y. Yamanoi, *Coord. Chem. Rev.* **2007**, *251*, 2674–2687.
- [76] O. Shekhah, H. Wang, S. Kowarik, F. Schreiber, M. Paulus, M. Tolan, C. Sternemann, F. Evers, D. Zacher, R. A. Fischer, C. Wöll, *J. Am. Chem. Soc.* **2007**, *129*, 15118–15119.
- [77] O. Shekhah, H. Wang, T. Strunskus, P. Cyganik, D. Zacher, R. Fischer, C. Wöll, *Langmuir* **2007**, *23*, 7440.
- [78] C. Munuera, O. Shekhah, H. Wang, C. Wöll, C. Ocal, *Phys. Chem. Chem. Phys.* **2008**, *10*, 7257.
- [79] O. Shekhah, H. Wang, M. Paradinas, C. Ocal, B. Schüpbach, A. Terfort, D. Zacher, R. A. Fischer, C. Wöll, *Nat. Mater.* **2009**, *8*, 481–484.
- [80] O. Shekhah, H. Wang, D. Zacher, R. A. Fischer, C. Wöll, *Angew. Chem. Int. Ed.* **2009**, *48*, 5038–5041.
- [81] K. Kanaizuka, R. Haruki, O. Sakata, M. Yoshimoto, Y. Akita, H. Kitagawa, *J. Am. Chem. Soc.* **2008**, *130*, 15778–15779.

Received: July 5, 2010

Published Online: July 26, 2010

Nanoscale Metal–Organic Frameworks: Magnetic Resonance Imaging Contrast Agents and Beyond

Joseph Della Rocca^[a] and Wenbin Lin^{*[a]}

Keywords: Metal–organic frameworks / Nanoparticles / Imaging agents / Magnetic resonance imaging / Nanomedicine

Magnetic resonance imaging (MRI) is an imaging technique based on the detection of nuclear spin reorientations in a magnetic field. MRI provides high spatial resolution and soft-tissue contrast in anatomical images, and a large penetration depth; however, it is relatively insensitive and typically relies on large doses of administered contrast agents to give adequate contrast between normal and diseased tissues. This review covers the development of nanoscale metal–organic frameworks (NMOFs) as novel MRI contrast agents. NMOFs

not only provide an effective vehicle for delivering large amounts of paramagnetic metal centers but also exhibit enhanced per-metal-based relaxivity relative to clinically used small-molecule contrast agents. The in vitro and in vivo effectiveness of these agents has also been demonstrated. The potential of NMOFs as contrast agents for other imaging modalities, such as optical imaging (OI) and X-ray computed tomography (CT), and as chemical and biological sensors is also discussed.

Introduction

Magnetic resonance imaging (MRI) is a noninvasive imaging technique based on the detection of nuclear spin reorientations in a magnetic field.^[1,2] Because the difference in spin state populations is very small, MRI is insensitive and is generally used for the detection of highly abundant water protons. The longitudinal relaxation time (T_1) and the transverse relaxation time (T_2) of the proton spins, along with their densities, determine the MRI signal intensity. Protons having a more rapid longitudinal relaxation time will relax back to their equilibrium state faster, yielding higher net electromagnetic signals and brighter MRI images. T_2 -weighted MRI signals are generated on the basis of the rate of transverse relaxation ($1/T_2$). A faster trans-

verse relaxation leads to rapid dephasing of individual spins, resulting in reduced signal intensity. MRI provides high spatial resolution, high soft-tissue contrast, and large penetration depth. However, due to the low sensitivity of MRI, contrast agents are often administered in large doses to enhance image contrast in target tissues. Approximately 35% of all clinical MRI scans are performed with the aid of imaging contrast agents.^[3] Most of the currently used MRI contrast agents are small-molecule Gd chelates, which act as T_1 -weighted contrast agents providing increased signal intensity.^[4,5] The efficiency of a contrast agent in modifying the relaxation rate is expressed by the longitudinal (r_1) or transverse relaxivity value (r_2), which is defined as the slope of a plot of $1/T_1$ or $1/T_2$ vs. the concentration. Gd chelates typically have only modest r_1 values ($4\text{--}5\text{ mM}^{-1}\text{ s}^{-1}$), thus requiring large doses for effective contrast. Superparamagnetic iron oxides (SPIOs) are clinically used as T_2 -weighted MRI contrast agents, leading to negative image enhancement.^[6–8]

[a] Department of Chemistry, University of North Carolina at Chapel Hill, Caudill and Kenan Laboratories, CB#3290, Chapel Hill, North Carolina 27599, USA
Fax: +1-919-962-2388
E-mail: wlin@unc.edu



Joseph Della Rocca was born in New Haven, CT, USA in 1984. He received a BA in chemistry from Middlebury College in 2007. He is currently pursuing a doctorate in chemistry at the University of North Carolina at Chapel Hill under the supervision of Professor Wenbin Lin. His current research is focused on the development of hybrid nanoparticles for biomedical applications.



Wenbin Lin obtained his BS degree from the University of Science and Technology of China (Hefei) in 1988. He received a PhD degree in 1994 from the University of Illinois at Urbana-Champaign. After a NSF postdoctoral fellowship at Northwestern University, he became an assistant professor of chemistry at Brandeis University in 1997. He moved to the University of North Carolina at Chapel Hill in 2001 and was promoted to associate and full professor of chemistry in 2003 and 2007, respectively. His research focuses on designing hybrid materials for applications in chemical, energy, and life sciences.

Because of the need for high concentrations of paramagnetic species for MRI contrast, it remains a great challenge to develop T_1 -weighted contrast agents that can provide adequate image contrast at lower effective doses. Nanomaterials offer one possible solution. Nanoparticulate imaging agents exhibit several advantages, including tunable size, high agent loading, tailorable surface properties, controllable or stimuli-responsive release kinetics, improved pharmacokinetics, and biocompatibility.^[9–11] Nanoparticles can be specifically targeted to certain regions of the body (e.g., tumor regions) by conjugation with targeting ligands to enhance their accumulation in the intended parenchymal sites. Nanomaterials possess additional desirable characteristics for MR contrast enhancement, such as decreased tumbling rates, which lead to increased relaxivities. Whereas SPIO is the only clinically approved MRI contrast agent, a large number of nanoparticle platforms for chemotherapeutic delivery have received clinical approval or are in clinical trials.^[12–14]

Metal–organic frameworks (MOFs), also known as coordination polymers, are hybrid materials constructed from metal connecting points and organic bridging ligands (Figure 1).^[15–20] MOFs are typically synthesized under mild conditions by self-assembly of metal ions (or metal clusters) and bridging ligands. These materials are particularly known for their large porosity with tunable pore sizes, shapes and functionalities. MOFs can be constructed from a limitless number of bridging ligands and metal ions, which allows the properties of the material to be tailored for a particular application. As a result, MOFs are well studied for applications such as gas storage,^[21–24] nonlinear optics,^[25] sensing,^[26,27] catalysis,^[28–31] magnetism,^[32–34] and drug delivery.^[35] MOFs possess many desirable characteristics for biological applications, including high agent loadings through several methods (direct incorporation into the framework or post-synthetic modification), intrinsic biodegradability from labile metal–ligand bonds, high porosity for loading/release of entrapped agents, and versatile functionalization methodologies. More recently, these materials have been scaled down to the nanoregime to form nanoscale metal–organic frameworks (NMOFs), which are potentially more suitable for biological applications via systemic administration.^[36–38] A related topic on potential applications of NMOFs as a drug delivery vehicle was recently reviewed.^[35]

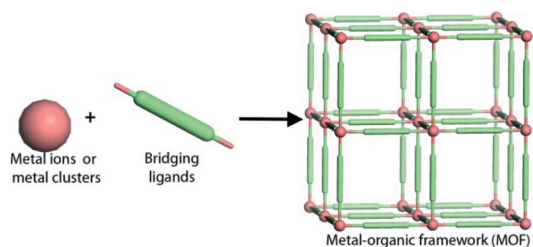


Figure 1. Generalized schematic for synthesis of a MOF. All solvent molecules are omitted and only a few repeating units are shown for clarity.

This review will discuss the development of NMOFs as novel MRI contrast agents. The synthesis, characterization, and contrast-enhancement properties of NMOFs will be covered. Preliminary applications of NMOFs in other imaging modalities will also be discussed.

NMOFs as MRI Contrast Agents

The potential of NMOFs as MRI contrast agents was first demonstrated by Lin and co-workers in their development of Gd carboxylate materials.^[39] Crystalline Gd-(BDC)_{1.5}(H₂O)₂ nanorods (BDC = 1,4-benzenedicarboxylate) were prepared by a reverse microemulsion method. The particle morphology of these systems was found to be dependent on the w value (water-to-surfactant molar ratio) of the microemulsion. Nanorods synthesized at $w = 5$ (**1**) were 100–125 nm in length and 40 nm in diameter; however, nanorods synthesized at $w = 10$ were 1–2 μm in length and 100 nm in diameter (Figure 2a). Powder X-ray diffraction (PXRD) measurements of **1** showed that the material was crystalline and matched a known lanthanide BDC phase. Additionally, nanoplates of Gd(BTC)(H₂O)₃ (**2**) (BTC = benzene-1,2,4-tricarboxylate) were synthesized at $w = 15$ (Figure 2b). These nanoplates were 100 nm in diameter and 35 nm thick. The presence of large amounts of Gd³⁺ ions at or near the NMOF surface prompted the researchers to test them as potential MRI contrast agents. Relaxivity measurements of **1** and **2** showed unprecedentedly high r_1 values (Figure 2c). They acted as T_2 -weighted contrast agents as well, when a different pulse sequence was employed (Table 1). The r_1 relaxivity values showed an inverse dependence on the nanoparticle size, which can be attributed to the reduced surface areas for larger particles and hence the reduced accessibility of the Gd centers to bulk water. NMOFs **1** and **2** exhibited much higher r_1 relaxivity values than OmniScan, a clinically used small-molecule contrast agent. Additionally, luminescent versions of the nanorods were synthesized by adding a small amount of

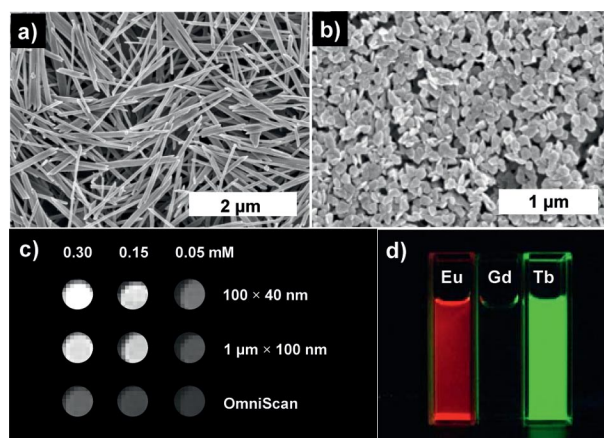


Figure 2. (a) SEM micrograph of **1** synthesized at $w = 10$. (b) SEM micrograph of **2** synthesized at $w = 15$. (c) T_1 -weighted MR phantoms of **1** in water with 0.1% xanthan gum at 3 T. (d) Luminescence images of ethanol suspensions of **1** doped with Eu³⁺ or Tb³⁺. Reproduced with permission from ref.^[39]

Eu³⁺ or Tb³⁺ ions to the synthesis microemulsion, leading to Eu- or Tb-doped NMOFs, which luminesce in different spectral regions (Figure 2d). Doped **1** or **2** could thus be used as potential multimodal contrast agents.

Table 1. Relaxivity values of Gd–carboxylate NMOFs on a per mM Gd basis.

NMOF (dimensions)	Field strength	r_1 (mm ^{−1} s ^{−1})	r_2 (mm ^{−1} s ^{−1})
1 (100 × 40 nm) ^[39]	3 T	35.8	55.6
1 (400 × 70 nm) ^[39]	3 T	26.9	49.1
1 (1000 × 100 nm) ^[39]	3 T	20.1	45.7
2 (100 × 35 nm) ^[39]	3 T	13.0	29.4
3 (25 × 50 × 100 nm) ^[40]	9.4 T	1.5	122.6
Omniscan ^[39]	3 T	4.1	NA

For many metal–ligand combinations, the NMOFs synthesized by using the reverse microemulsion method tend to have poorly defined morphologies and a wide particle size distribution. NMOF synthesis at higher temperatures can have altered nucleation and crystal growth kinetics and thus lead to the formation of uniform nanomaterials. Lin and co-workers demonstrated a surfactant-mediated hydrothermal method for the synthesis of Gd₂(BHC)(H₂O)₆ (BHC = benzenehexacarboxylate) (**3**) nanoparticles.^[40] Numerous attempts to make **3** by microemulsion synthesis were unsuccessful, but the particles were successfully formed by heating a microemulsion of [NMeH₃]₆[BHC] and GdCl₃ in a Parr reactor at 120 °C. SEM and TEM images showed that **3** adopted a block-shaped morphology with dimensions of approximately 25 × 50 × 100 nm (Figure 3a). The PXRD pattern of **3** matches that of a known lanthanum bulk phase [La₂(BHC)(H₂O)₆] (Figure 3b). Interestingly, NMOFs of different particle compositions and morphologies were obtained by simply changing the pH values during the particle synthesis. The nanoparticles obtained from the reaction of GdCl₃ and BHC at 60 °C with microwave irradiation were found to have the formula of [Gd₂(BHC)(H₂O)₈](H₂O)₂ (**4**) and a PXRD pattern different from that of **3**. SEM and TEM studies of **4** showed that the nanoparticles are rods of 100–300 nm in diameter and several microns in length (Figure 3c). Increasing the reaction temperature of the microwave to 120 °C led to crystalline octahedral nanoparticles (**4'**) that are of the same phase as **4**. The difference between **3** and **4** (or **4'**) lies in the different metal–ligand coordination modes. In **3**, the Gd is nine-coordinate, and each metal center is bound to two bridging and two chelating carboxylates from four different BHC ligands. Water molecules occupy the three remaining coordination sites. In **4** and **4'**, each Gd ion is coordinated to two chelating carboxylates and one monodentate carboxylate from three different BHC molecules, water occupying the remaining four coordination sites (Figure 3d). The obtained phase was pH-dependent and showed no dependence on reaction temperature (Figure 3). Nanoparticles of **3** were evaluated as potential MRI contrast agents at 9.4 T (Table 1). These nanoparticles had only modest longitudinal relaxivity (r_1) and very high transverse relaxivity (r_2) values, indicating that they may act as potential T_2 -

weighted contrast agents. Luminescent analogues of **3** were also made by adding 5 mol-% of either Eu³⁺ or Tb³⁺ during the synthesis. The resulting nanoparticles were of the same size and morphology as **3** and displayed intense luminescence under UV excitation.

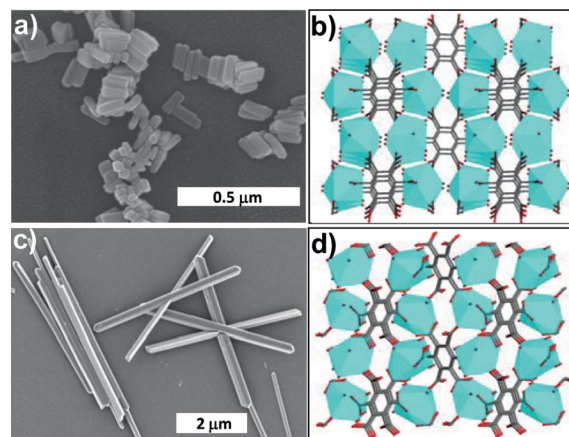


Figure 3. (a) SEM micrograph of **3**. (b) Stick/polyhedra model of the crystal structure of **3**. (c) SEM micrograph of **4** obtained at 60 °C under microwave heating. (d) Stick/polyhedra model of the crystal structure of **4**. Reproduced with permission from ref.^[40]

The NMOFs described above were all demonstrated to readily break down under aqueous conditions, a serious limitation for in vivo application. The free Gd³⁺ ions are very toxic and are known to be the culprit of nephrogenic systemic fibrosis in renal impaired patients who have been administered certain small-molecule Gd chelates. Lin and co-workers developed a method to encapsulate **1** within a thin shell of amorphous silica.^[41] A silica shell offers several advantages including enhanced water dispersibility, biocompatibility, and ease of functionalization with a variety of silyl-derived molecules. Nanoparticles of **1** were first coated with a monolayer of polyvinylpyrrolidone, isolated to form **1**@PVP (Figure 4b) and then coated with a silica shell by using tetraethylorthosilicate (TEOS) as a silica source in basic ethanol (Figure 4e). The silica shell thickness could be varied by both the reaction time and the amount of the silica precursor, TEOS, added to the reaction (Figure 4). PXRD studies demonstrated that the crystalline structure of **1** was maintained in both **1**@PVP and **1**@silica. Subsequent NMOF dissolution studies showed that the silica coating significantly decreased the release of Gd³⁺, but did not completely prevent it (Figure 4f). The silica shell could then be functionalized with a variety of silyl-derived molecules. Lin and co-workers extended this silica coating and functionalization strategy to several other NMOFs used for imaging and drug delivery applications.^[42–44]

Boyes and co-workers developed an alternative method to coat **1** by using a biocompatible polymer.^[45] First, they synthesized a copolymer of poly(*N*-isopropylacrylamide)-*co*-poly(*N*-acryloxysuccinimide)-*co*-poly(fluorescein *O*-methacrylate)(PNIPAM-*co*-PNAOS-*co*-PFMA) (**A**) by RAFT polymerization. This polymer has both optical imaging capabilities (fluorescein) and can further conjugate ad-

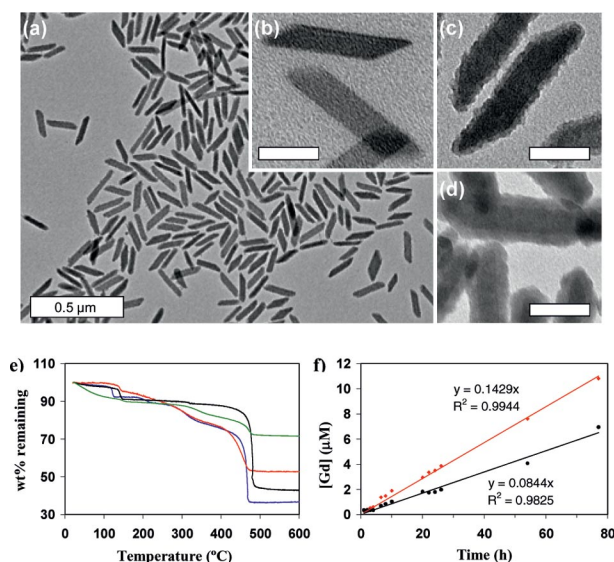


Figure 4. (a and c) TEM images of **1**@silica (2–3 nm). (b) TEM image of **1**@PVP. (d) TEM image of **1**@silica (8–9 nm). (e) TGA curves of **1** (black), **1**@PVP (blue), **1**@silica (2–3 nm) (red), and **1**@silica (8–9 nm) (green). (f) Dissolution studies of **1** (red) and **1**@silica (8–9 nm) (black) in water at pH = 4 and 37 °C. TEM scale bars are 50 nm unless noted. Reproduced with permission from ref.^[41]

ditional agents via the succinimide groups. The succinimide was used to graft a chemotherapeutic (methotrexate) (MTX-A) and a targeting peptide (GRGDS) (GRGDS-MTX-A). The synthesized polymer contained a thiol end group, which was used to modify **1** through the binding of the thiol group to vacant metal coordination sites. Compound **1** contained approximately 25,000 polymer chains/particle. Subsequent studies demonstrated that the polymer coating retarded the release of Gd^{3+} ions relative to the unmodified particles. Polymer-coated **1** was then evaluated as MRI contrast agent at 1.5 T (Table 2). The polymer modification tripled the effectiveness of the contrast agent compared to **1**. Polymer-modified **1** with and without GRGDS targeting were evaluated as optical contrast agents against canine FITZ-HSA cells. Only the targeted nanoparticles showed fluorescence by confocal microscopy, as the untargeted nanoparticles were washed away during sample preparation. Cell viability assays with methotrexate-loaded **1** showed cytotoxicity comparable to the free drug against FITZ-HSA cells. Boyes and co-workers undertook a systematic study on how polymer modification could tune the relaxivity of the resulting conjugate.^[46] A variety of different hydrophilic polymers [PHPMA (B), PNIPAM (C), PDMAEA (D), PPEGMEA (E), and PAA (F)] and one hydrophobic polymer, (PS)(G), were synthesized by RAFT polymerization at different molecular weights. These were then conjugated to **1** through thiol end groups, and the relaxivity was measured at 1.5 T (Table 2). The hydrophilic polymers led to an increase in the r_1 relaxivity of the nanoparticles relative to the unmodified nanoparticle and caused relatively decreased r_2 values. The authors attributed this to increased water retention by the polymer, which allows for

faster exchange with the Gd centers within **1**. The highly hydrophobic polystyrene-modified **1** showed very poor longitudinal relaxivity but high transverse relaxivity, which the authors attribute to decreased water retention by the hydrophobic polymer, and all contrast is due to the water within the framework structure $[\text{Gd}(\text{BDC})_{1.5}(\text{H}_2\text{O})_2]$.

Table 2. Relaxivity values of polymer-modified NMOFs on a per Gd basis at 1.5 T.

NMOF ^[a]	r_1 ($\text{mM}^{-1} \text{s}^{-1}$)	r_2 ($\text{mM}^{-1} \text{s}^{-1}$)
Magnevist ^[45]	13.4	21.4
Multihance ^[45]	19.4	30.4
1 ^[45]	9.86	17.9
A- 1 ^[45]	33.4	47.2
MTX-A- 1	38.5	53.9
GRGDS-MTX-A- 1 ^[45]	14.4	25.3
B(5327)- 1 ^[46]	17.8	25.8
B(10281)- 1 ^[46]	32.9	44.8
B(19370)- 1 ^[46]	105.4	129.6
C(5690)- 1 ^[46]	20.27	29.73
C(8606)- 1 ^[46]	46.99	64.10
C(17846)- 1 ^[46]	62.51	79.9
D(15120)- 1 ^[46]	37.20	54.2
E(19542)- 1 ^[46]	59.93	81.5
F(1088)- 1 ^[46]	21.3	31.8
G (4802)- 1 ^[46]	1.17	14.16
G(8972)- 1 ^[46]	1.2	25.75
G(15245)- 1 ^[46]	3.91	123.4

[a] All particles synthesized in ref.^[45] are 25×125 nm. All particles synthesized in ref.^[46] are 55×125 nm. A = poly(*N*-isopropylacrylamide)-*co*-poly(*N*-acryloxysuccinimide)-*co*-poly(fluorescein *O*-methacrylate)(PNIPAM-*co*-PNAOS-*co*-PFMA), B = PHPMA-poly[*N*-(2-hydroxypropyl)methacrylamide], C = PNIPAM-poly(*N*-isopropylacrylamide), D = PDMAEA-poly[2-(dimethylamino)ethyl acrylate], E = PPEGMEA-poly{[(poly)ethylene glycol] methyl ether acrylate}, F = PAA-poly(acrylic acid), G = PS-polystyrene. The molecular weight of the homopolymers is in parentheses.

Kimizuka and co-workers developed an NMOF system of lanthanides and nucleotides, which has been demonstrated as a potent MRI contrast agent.^[47,48] Mixing equimolar amounts of GdCl_3 and a nucleobase in HEPES buffer produced amorphous nanoparticles ranging in size from 30 to 180 nm, depending on the identity of the nucleobase. The Gd^{3+} ion was coordinated to both the nucleobase and the phosphate group present in the nucleotide (Figure 5). 5'AMP/Gd (**5**) and 5'GMP(**6**) were evaluated as MRI contrast agents at 0.3 T (Table 3). Both **5** and **6** were demonstrated to possess higher longitudinal relaxivity than Magnevist. Additionally, there was a size dependence on relaxivity, the smaller **6** giving larger relaxivity. This was attributed to a greater proportion of Gd^{3+} ions near the surface of the nanoparticle, as water exchange to the interior of the nanoparticles is limited. This size-dependent relaxivity behavior is consistent with that observed by Lin and co-workers earlier with **1**.^[39]

Larionova and co-workers reported a Gd cyanometalate coordination polymer within a chitosan matrix as an MRI contrast agent.^[49] Nanocomposite beads of $\text{Gd}^{3+}/\text{Fe}(\text{CN})_6/\text{chitosan}$ (**7**) were synthesized by treating porous chitosan beads with methanol solutions of Gd^{3+} and $[\text{N}(\text{C}_4\text{H}_9)_4]_3^-$

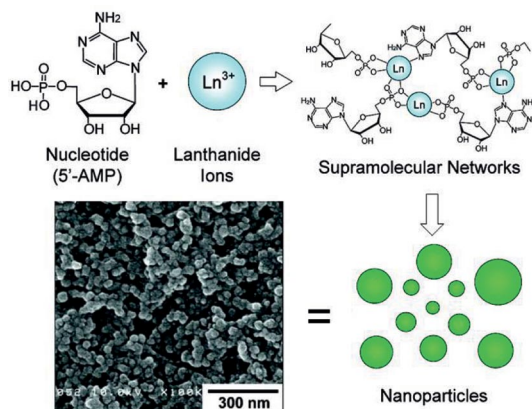


Figure 5. Formation of lanthanide–nucleotide NMOFs and SEM micrograph of **5**. Reproduced with permission from ref.^[47]

Table 3. Relaxivity values of synthesized NMOFs.

NMOF (dimensions)	Field strength	r_1 (mm ^{−1} s ^{−1})	r_2 (mm ^{−1} s ^{−1})
5 (41 nm) ^[47]	0.3 T	12	NR
6 (30 nm) ^[47]	0.3 T	13.4	NR
Magnevist ^[47]	0.3 T	5.4	NR
8 (60 × 400–1000 nm) ^[50]	11.7 T	1.08	121.7
9 (50–100 nm × 1 μm) ^[43]	3 T	5.5	80
10' (50–300 nm) ^[43]	3 T	7.8	70.8
10' (50–300 nm) ^[43]	9.4 T	4.6	141.2
10'@silica (50–300 nm) ^[43]	9.4 T	4.0	112.8

[Fe(CN)₆], which formed discrete NMOF–chitosan core shell nanoparticles after solubilization of the chitosan beads. The ¹H relaxometric characterization of the nanoparticles was performed, and the results were compared with those of commercially used Omniscan and Gd-DTPA. The relaxivity of **7** was sixfold higher than that of the small-molecule Gd chelates. This was attributed to increases in the molecular rotation time and increased water exchange rates in comparison to Omniscan and Gd-DTPA. Geraldes and co-workers developed a Ln(H₂CMP)(H₂O) MOF material as a potential MRI contrast agent [CMP = (carboxymethyl)iminobis(methylphosphonic acid)].^[50] The formed materials were thin plates (60 nm thick) with lengths and widths varying from 400 to 1 μm, and the particle size and morphology varied slightly with different Ln ions. Gd(H₂CMP)(H₂O) (**8**) particles were evaluated at 11.75 T as *T*₁- and *T*₂-weighted contrast agents (Table 3). These nanoparticles gave very low *r*₁ relaxivity and high *r*₂ relaxivity, indicating that these particles may act as *T*₂-weighted contrast agents. The authors proposed that the low *r*₁ values were due to either slow water exchange from the bound water and bulk water or the very slow diffusion of water through the framework.

While the NMOFs discussed above show great promise as MRI contrast agents, they face significant hurdles in a clinical setting. NMOFs, upon aqueous decomposition, can potentially release free Gd³⁺ ions, which are highly toxic. Free Gd³⁺ ions leached from clinically used Gd chelates can

cause nephrogenic systemic fibrosis, which predominately affects the skin, but may involve other organs, such as the liver, lungs, and heart, in patients.^[51,52] NMOFs with other formulations are needed in order to overcome the problem with Gd-based NMOFs. Manganese ions are also known to act as potent MRI contrast agents and have shown promising results in rodent models. Simple MnCl₂ shows effective *T*₁ contrast and is less toxic than free Gd³⁺, so it may be more suitable for MRI contrast agent development.^[5,53]

Mn-based NMOFs were synthesized by Lin and co-workers by treating MnCl₂ with either BDC or trimesic acid (1,3,5-benzenetricarboxylic acid, BTC).^[43] Nanorods of Mn(BDC)(H₂O)₂ (**9**) were synthesized in a reverse micro-emulsion, yielding particles with diameters of 50–100 nm and lengths from 750 nm to several microns. They were also able to produce nanoparticles of Mn₃(BTC)₂(H₂O)₆ (**10**) in a reverse microemulsion. The resulting nanoparticles **10** adopted a spiral rod morphology 50–100 nm in diameter and 1–2 μm in length. Microwave heating was also attempted to adjust the morphologies of the resulting materials. Nanoparticles **9** retained the same phase and morphology. However, microwave heating of MnCl₂ and BTC produced nanoparticles **10'**, which had the same crystalline phase as **10**, but showed a lower aspect ratio. Nanoparticles **10'** had a blocklike morphology with lengths ranging from 50 to 300 nm in all three dimensions. The relaxivity values of **9** and **10'** were determined at 3 T and 9.4 T (Table 3). The *r*₁ values displayed by **9** and **10'** were very modest, and the nanoparticles would not be expected to act as efficient *T*₁-contrast agents, but may act as a way to deliver large doses of Mn²⁺ ions, which are efficient *T*₁-weighted contrast agents upon binding to biological macromolecules (e.g., proteins) in vivo. Nanoparticles **10'** were coated with a thin shell of amorphous silica and functionalized with a silyl-derived fluorophore and targeting peptide, cRGD. The cRGD peptide targets many angiogenic cancers by binding to integrins. These particles were then evaluated as optical and MR contrast agents in vitro against a human colon cancer line. MR imaging showed selective uptake of targeted nanoparticles, and much greater image contrast was observed with the targeted nanoparticle (Figure 6A). This observation was supported by ICP-MS analysis of the cell pellets for Mn content. Confocal microscopy images also demonstrated the enhanced in vitro uptake of the targeted nanoparticles, demonstrating a possible multimodal nanoparticle for cancer imaging (Figure 6B–D).

Superparamagnetic iron oxide nanoparticles are clinically used MRI contrast agents. Two recent reports provide a potential strategy for creating nanocomposites of iron oxide and NMOFs. Sweigart and colleagues developed a method to incorporate Fe₃O₄ nanoparticles within a coordination polymer.^[54] In this work, Fe₃O₄ nanoparticles capped with oleic acid/oleylamine undergo ligand exchange with [(η⁵-semiquinone)Mn(CO)₃](SQMTC). The resulting surface-modified iron oxide nanoparticles were then used to generate crystalline coordination polymers. The resulting composite of iron oxide and NMOF retained the super-

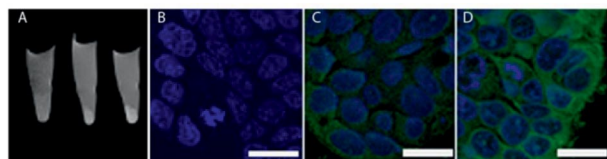


Figure 6. (A) MR phantoms of HT-29 cells taken with (left) no particle, (center) **11'**, and (right) cRGDFK-targeted **10'** at 9.4 T showing effective T_1 -weighted image enhancement. Confocal microscopy images showing HT-29 cells incubated with no particle (B), **10'** (C), or cRGDFK-targeted **10'** (D). Green fluorescence is from the rhodamine fluorophore used to functionalize **10'**, and blue fluorescence is from the DRAQ5 nuclear stain. The scale bars represent 20 μm . Reproduced with permission from ref.^[43]

paramagnetic properties of SPIO. An alternative method to encapsulate iron oxide nanoparticles within MOF microspheres was presented by Maspoch and co-workers. Zinc-based NMOF microparticles were created by mixing zinc ions and 1,4-bis(imidazol-1-ylmethyl)benzene (bix), followed by rapid precipitation to create particles **11**, which were spherical and ranged in size from 100 to 1500 nm.^[55] Iron oxide@**11** particles were created by adding 10 nm iron oxide particles during the synthesis, which became entrapped within the resulting 600 nm nanoparticle. Magnetization studies showed that the iron oxide nanoparticles retained their magnetic properties after encapsulation. Fluorescent dyes and quantum dots were also encapsulated within **11** by the same methodology. Although nanocomposites of iron oxide and NMOFs have potential implications in MR imaging, these authors did not characterize their magnetic relaxivities, so the utility of these composites as MRI contrast agents has not been established.

Horcajada and co-workers developed an iron carboxylate NMOF system for T_2 -weighted MRI imaging and drug delivery.^[56] Several highly porous iron(III) carboxylate NMOFs were synthesized with sizes ranging from 50 to 350 nm by using different synthesis conditions. These nanoparticles corresponded to known bulk-phase materials of MIL-89 (**12**), MIL-88A (**13**), MIL-100 (**14**), MIL101-NH₂ (**15**), MIL-88Bt (**16**), and MIL-53 (**17**). These NMOFs could be modified with biocompatible polymers such as PEG, chitosan, or dextran. The in vivo toxicity of **13**, **14**, and **16** was studied in Wistar rats. No significant toxic effects for any of the NMOFs were observed at all tested doses. The NMOFs were evaluated as T_2 -weighted contrast agents. Mössbauer spectroscopy proved that the NMOFs themselves acted as contrast agents, and the relaxivity data of **13**, PEG-**13**, **14**, and PEG-**14** were obtained at 9.4 T (Table 4). No r_1 values were reported, but the nanoparticles showed very high r_2 relaxivity and behaved similarly to iron oxides. In vivo studies on Wistar rats showed T_2 -weighted enhancement of the liver and spleen after injection of **13** (Figure 7). The images of these organs returned to normal after three months, indicating the accumulation and then clearance of **13**. These materials were also used to successfully encapsulate several different chemotherapeutics with very high loadings.

Table 4. Relaxivity values of iron carboxylate NMOFs on a per Fe basis.

NMOF (dimensions)	Field strength	r_2 ($\text{mM}^{-1} \text{s}^{-1}$)
13 (150 nm) ^[56]	9.4 T	56
Peg- 13 (150 nm) ^[56]	9.4 T	95
14 (200 nm) ^[56]	9.4 T	73
Peg- 14 (200 nm) ^[56]	9.4 T	92

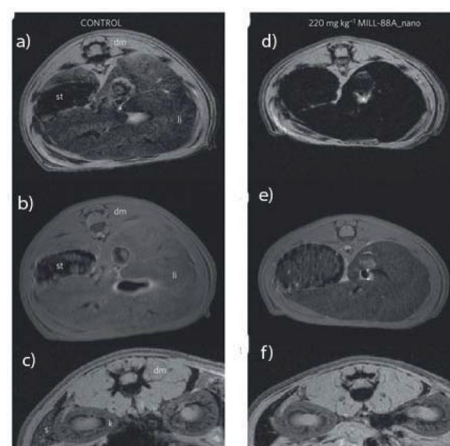


Figure 7. MR images of Wistar rats injected with no particle (a–c) or 220 mg kg^{-1} **13** (d–f). The images were acquired with either gradient echo (a, c, d, f) or spin echo sequences (b, e). The images show either liver (a, b, d, e) or spleen (c, f) regions 30 min after injection. [dm = dorsal muscle, k = kidney, li = liver, s = spleen, st = stomach]. Reproduced with permission from ref.^[56]

NMOFs as Potential Contrast Agents for Other Imaging Modalities

Fluorescence and phosphorescence imaging have been widely used in biological applications. Visible light in the 400–600 nm range is typically used to excite fluorophores within tissue, which fluoresce at longer wavelengths.^[1,57,58] This technique is ubiquitous for in vitro and ex vivo analysis, but has severe limitations for in vivo applications due to poor tissue penetration depth. Tissue penetration can be increased by using photons in the near infrared region of the spectrum (650–900 nm), where absorption by water and biomolecules is low. MOFs have also been developed for use as optical contrast agents. Many MOFs display inherent fluorescent properties but cannot be used for biological imaging, because of the macroscopic sizes of the materials.^[36,59–63] However, there have been recent reports of the use of NMOFs as delivery vehicles for optical contrast agents.

Lin and co-workers developed an iron carboxylate NMOF system, which was post-synthetically modified to contain a Bodipy-based fluorophore or a chemotherapeutic.^[44] Iron(III) NMOFs of the formula $\text{Fe}_3(\mu_3\text{-O})\text{Cl}(\text{H}_2\text{O})_2\text{-}(\text{BDC})_3$ (**18**) were synthesized by microwave heating equimolar solutions of FeCl_3 and BDC in DMF. Scanning electron microscopy of **18** showed octahedral particles of 200 nm, which matched the previously reported MIL101 phase by PXRD. These particles could be modified to in-

corporate varying amounts of 2-aminoBDC (up to 17.4 mol-%). The amino-functionalized particles **19** were further grafted with an optical imaging agent, 3,3-difluoro-8-bromomethyl-4-bora-3a,4a-diaza-s-indacene (Br-Bodipy) in 5.6–11.6 wt.-% fluorophore loadings (Figure 8). The resulting framework, Bodipy-**19**, was not fluorescent because of quenching by the iron centers within the framework, but it showed strong fluorescence upon its release from the framework. Bodipy-**19** particles were coated with a thin layer of silica and targeted, by using silyl-derived cRGDFK, to angiogenic cancers. Preliminary in vitro assays demonstrated that such a NMOF–dye conjugate can be an efficient platform for developing optical contrast agents. Confocal microscopy studies showed strong Bodipy fluorescence after incubation with silica-coated Bodipy-**19**. Furthermore, targeting with the cRGDFK peptide increased the cellular localization of Bodipy-**19** (Figure 8b). A cisplatin prodrug, *c,c,t*-Pt(NH₃)₂Cl₂(OEt)(O₂CCH₂CH₂CO₂H) was also conjugated to **19** and showed comparable cytotoxicity to cisplatin against colon cancer cells, demonstrating the versatility of **19** to deliver a variety of biologically and biomedically relevant cargo.

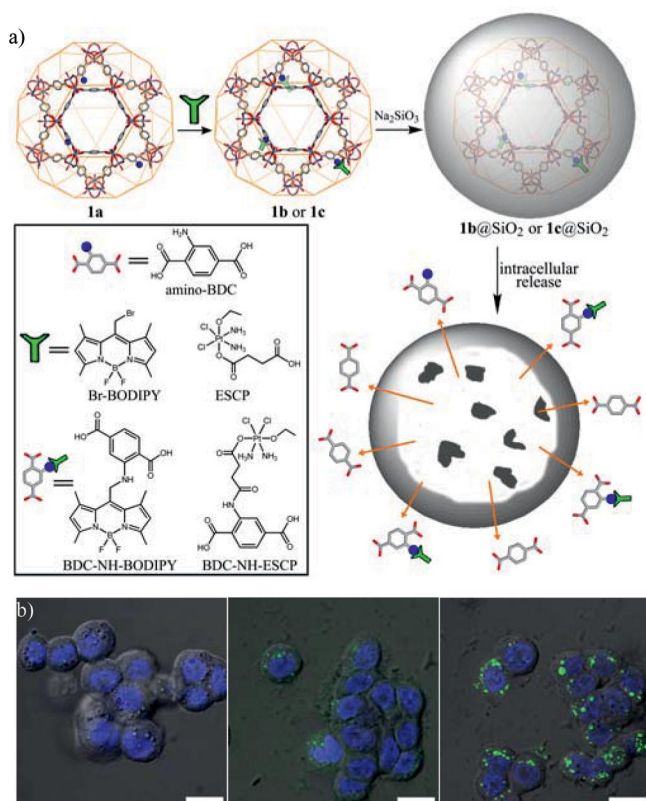


Figure 8. (a) Generalized scheme showing the post-synthetic modification of **19** with a fluorophore or chemotherapeutic, subsequent silica coating, and its intracellular release. (b) Overlayed DIC and confocal fluorescence images of the DRAQ5 channel (blue, nuclear stain) and the BDC-NH-BODIPY channel (green) of HT-29 cells incubated with no particles (left), 0.19 mg mL^{−1} of **1b**@silica particles (equivalent to 17 μM BODIPY) (center), and 0.38 mg mL^{−1} of **1b**@silica particles (equivalent to 34 μM BODIPY) (right). The bars represent 25 μm. Reproduced with permission from ref.^[44]

The intrinsic phosphorescence of the Eu and Tb ions can potentially be explored for optical imaging applications, as discussed earlier for Eu- and Tb-doped NMOFs **1** and **3**. There are several examples of lanthanide–nucleotide NMOFs, which are inherently fluorescent or encapsulate fluorophores.^[47,48,64] Kimizuka and co-workers adapted their synthesis of **5** and **6** to a range of nucleotide–lanthanide combinations.^[47] One of these, 5′GMP/Tb (**20**), possessed intense green luminescence. Analogous nanoparticles with other nucleotides did not show luminescence because of poor Tb–nucleobase interactions. This was attributed to energy transfer from the guanine base to the coordinated Tb³⁺ ions within the interior of the nanoparticle. Analogous nanoparticles **21** were created by reacting Tb³⁺ ions with dimeric guanine nucleotides, but they were not luminescent.

Water-soluble anionic dyes were incorporated into nucleotide–lanthanide frameworks.^[47,48] The dye was added during the synthesis of the NMOF and coordinated to the metal ions in the framework (Figure 9a). Cationic dyes could not be incorporated within the framework by this method. Encapsulation of the dye within the NMOF increased the fluorescence relative to the free dye alone. The anionic dye perylene-3,4,9,10-tetracarboxylic acid was doped into **5** to create fluorescent nanoparticles (Perylene-**5**), and the localization of the particles was monitored in vitro and in vivo. Confocal microscopy showed the uptake of Perylene-**5** into the lysosomes of HeLa cells, while the free dye alone was not internalized (Figure 9b). The biodistribution of Perylene-**5** was studied in vivo in a murine model. Perylene-**5** was rapidly accumulated in the liver by both fluorescence and ICP-MS analysis and remained in the liver for up to 48 hours post-injection (Figure 9c). No fluorescence was detected in the kidneys, lungs, or spleen. The nucleotide–lanthanide NMOFs were also used to successfully entrap smaller Au nanoparticles (3–10 nm) and proteins.

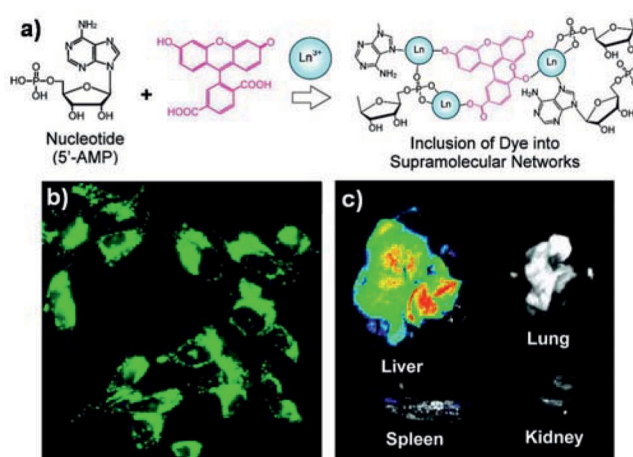


Figure 9. (a) Generalized schematic for incorporation of anionic dyes within lanthanide–nucleotide frameworks. (b) Confocal microscopy image of HeLa cells incubated with Perylene-**5**. (c) Ex vivo fluorescent images of organs from mice injected with Perylene-**5**. Reproduced with permission from ref.^[47]

Li and co-workers developed polyoxometalate–peptide hybrid spheres for the encapsulation of guest molecules.^[65] Keggin-type polyoxometalates (POMs) of phosphotungstic acid were treated with cationic dipeptides to form colloidal spheres **22** of approximately 150 nm in diameter. Structural studies of **22** demonstrated that the peptide and polyoxometalate were strongly bound together, the peptides linking together individual POMs through multiple noncovalent interactions. Compound **22** was highly responsive to changes in pH, maintaining its structure under acidic conditions, but rapidly disassembled under neutral or basic conditions. A number of fluorescent dyes were incorporated within the spheres. The charge of the entrapped dye made little difference in the encapsulation efficiency, unlike the observation for **5**. Additionally, hydrophilic macromolecules (dextran) and hydrophobic drugs were also embedded within **22**. Hydrophilic gold nanoparticles were also encapsulated within **22** to form a core/shell hybrid structure with a single gold nanoparticle within each shell.

Rosi and co-workers developed NIR-luminescent MOFs for potential adaptation for biological imaging.^[66,67] Many lanthanide metals can emit in the NIR region; however, they must be in close proximity to a chromophore, because of the weak absorptivity of the metal center. A crystalline MOF of the formula $[\text{Yb}_2(\text{PVDC})_3(\text{H}_2\text{O})_2](\text{DMF})_6(\text{H}_2\text{O})_{8.5}$ (**23**) was created by using Yb^{3+} centers and 4,4'-[(2,5-dimethoxy-1,4-phenylene)di-2,1-ethenediyl]bis(benzoic acid) (PVDC) bridging ligands. The MOF is composed of infinite Yb carboxylate chains of alternating octa- and hexacoordinate Yb^{3+} , bridged by carboxylates of three different PVDC linkers. The crystallinity of **23** was maintained under a variety of conditions. The UV/Vis and fluorescence spectrum of **23** demonstrates strong absorbance at 340 and 415 nm and fluorescence at 980 nm, indicating that the PVDC ligand sensitizes Yb^{3+} by the antenna effect. A second PVDC- Yb^{3+} MOF of the formula $[\text{Yb}_2(\text{PVDC})_3](\text{DMF})_{12}(\text{H}_2\text{O})_{10}$ (**24**) was created. The connectivity of **24** is different from that of **23**: **24** is composed of alternating octa- and hexacoordinate metal centers. The metals are bridged by two carboxylates in a di-monodentate fashion and a third carboxylate that chelates the octacoordinate Yb^{3+} center and coordinates to the hexacoordinate center, resulting in a chain of corner-sharing Yb^{3+} ions. Luminescence of **24** showed absorption band maxima at 370 and 500 nm. The redshifted absorption of **24** was proposed to be due to close π – π stacking. The quantum yield of **24** was higher than that of **23**, because of coordinated water molecules in **23**, which quench emission. Rosi and co-workers also created NIR-luminescent MOFs containing Yb^{3+} , Er^{3+} , and PVDC, which could show luminescence at two different wavelengths.^[67] The intensity of the photoluminescence of these MOFs could be tailored by varying the Yb/Er ratio. These MOFs are bulk-phase materials and are impracticable for biological applications, but could potentially be scaled down to form nanoparticle contrast agents.

Computed tomography (CT) imaging is a powerful imaging technique, which is based on X-ray attenuation by a specimen, and can provide 3D images with excellent spatial

resolution.^[1,68,69] Contrast agents for CT are elements such as iodine, barium, and bismuth, which possess a high Z number. Currently the only clinically approved CT contrast agents are iodinated aromatic molecules and barium sulfate. CT contrast agents need to be administered in very large doses (tens of grams) to provide adequate contrast, so a nanoparticle-based contrast agent may provide superior image enhancement. Lin and co-workers have recently developed an iodinated nanoscale coordination polymer as a potential CT contrast agent.^[70] Five new bulk MOFs were synthesized by combining 2,3,5,6-tetraiodo-1,4-benzenedicarboxylic acid (I_4 -BDC) with Cu^{2+} or Zn^{2+} connecting points. Single-crystal X-ray diffraction studies revealed 1D polymeric structures for all five MOFs. More importantly, NMOFs containing either Cu^{2+} (**25**) or Zn^{2+} (**26**) were synthesized (Figure 10). Platelike nanoparticles of **25** were synthesized within a reverse microemulsion and have a diameter of 300 nm and a thickness of 50 nm. PXRD and TGA studies matched **25** with one of the generated bulk phases. The morphology of **25** could also be tuned by changing the microemulsion conditions to generate rodlike particles of 1.5 μm in length and 200 nm in width. Zn^{2+} -containing **26** was generated by a rapid precipitation method. Crystalline rods of 10–30 μm were initially generated, but smaller particles **26'** could be obtained by concentrating the precursor solutions. Compound **26'** had a truncated cube morphology with a diameter of 200–600 nm and was partially crystalline. CT phantom studies were performed on dispersions of **25** and **26'**. Both nanoparticles showed attenuation factors slightly higher than iodixanol, which was due to the contribution from the metal centers to X-ray attenuation.

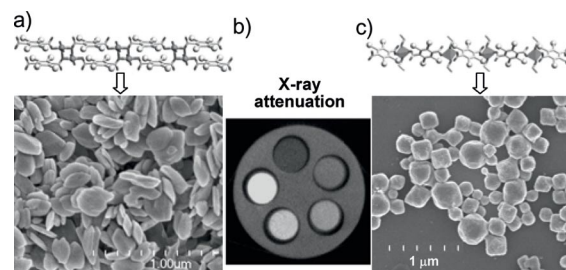


Figure 10. (a) X-ray crystal structure (top) and SEM image (bottom) of **25**. (b) CT phantom image of **25**. (c) X-ray crystal structure (top) and SEM image (bottom) of **26'**. Reproduced with permission from ref.^[70]

MOFs Used for Sensory Applications

Luminescence properties of NMOFs can also be explored for biological and chemical sensing. In an ideal scenario, the luminescence of the material would remain off until the analyte is introduced, turning on the sensor. Such materials would allow for the monitoring of cellular processes, the location/presence of certain analytes, or the specific identification of diseased tissue.

Lin and co-workers adapted Eu-doped **1** for the detection of dipicolinic acid (DPA), a major component of bacte-

rial spores.^[41] The doped material was coated with a thin shell of amorphous silica by sol–gel polymerization. The silica shell was functionalized with a silyl-derived Tb-EDTA monoamide derivative (Figure 11a). Tb³⁺ ions and complexes are known to act as sensors for anthrax and other bacterial spores by complexing to DPA, which constitutes up to 15 wt.-% of the spore dry weight. Upon excitation of Eu-doped 1@silica, only Eu-based luminescence was detected, as the grafted Tb complex is nonemissive. Upon addition of DPA, Tb-based luminescence was detected from the formation of an emissive Tb-EDTA-DPA complex. This luminescence varies linearly with the amount of DPA added until it levels off because of the saturation of the Tb-EDTA sites (Figure 11b). The Eu³⁺ luminescence does not interfere with Tb³⁺ luminescence and can act as an internal standard. Eu-doped 1@silica was estimated to have a limit of detection of 48 nM. This sensor is also able to selectively detect DPA in the presence of other biologically relevant molecules such as amino acids (Figure 11).

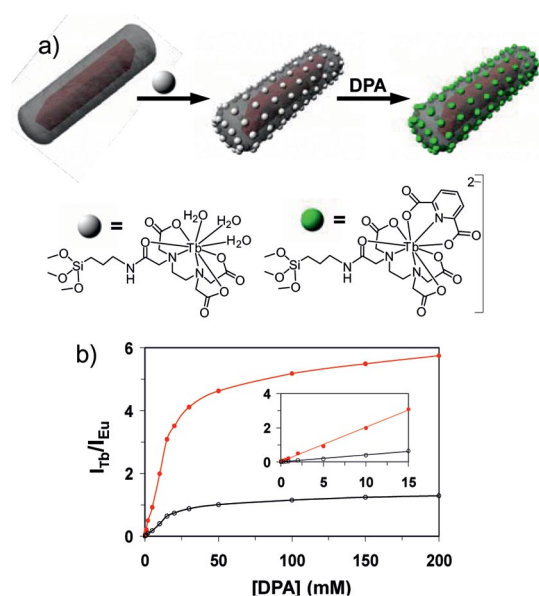


Figure 11. (a) Generalized scheme showing the functionalization of Eu-doped 1@silica with silyl-derived Tb-EDTA monoamide derivative and subsequent sensing of DPA. (b) Graph of dependence of the ratio of Tb/Eu emission intensities as a function of DPA concentration (red = 544 nm/592 nm, black = 544 nm/615 nm). The inset shows the linear relationship at low [DPA]. Reproduced with permission from ref.^[41]

Nucleotide–lanthanide NMOFs were also demonstrated to have switchable luminescence.^[71] Spherical NMOFs **27** formed between 5'AMP and Tb were nonemissive due to low coordination between the adenine nucleobase and Tb³⁺, allowing water molecules to enter the metal coordination sphere to quench the luminescence. However, if 2-hydroxypicolinic acid is added during the synthesis of **27**, a green luminescent NMOF is obtained. This luminescent MOF arises from the coordination of 2-hydroxypicolinic acid to Tb³⁺ ions and the formation of a luminescent complex. Additionally, if 2-hydroxypicolinic acid is added to preformed **27**, a luminescent material is formed from the

coordination of 2-hydroxypicolinic acid to Tb³⁺ ions within **27**. Spectral analysis suggests that the NMOF retains its structure with the addition of the acid and a free complex of Tb and hydroxypicolinic acid is not formed.

Rocha and co-workers developed a MOF as a pH sensor.^[72] MOF **28**, composed of Eu³⁺ ions and 1,10-phenanthroline-2,9-dicarboxylic acid, was created. Analysis of this material showed that the formula of **28** was [Eu₃(C₁₄H₆N₂O₄)₄(OH)(H₂O)₄]·2H₂O. This MOF adopts a layered structure with two different sheets containing Eu³⁺ ions in different coordination environments, which gives two distinct luminescence bands. One of the sheets was anionic, the other cationic. Preliminary results showed that the material could be used as a pH sensor from pH 5 to 7.5. Below pH 5, the carboxylic acids in the material become protonated, and the framework structure changes. Above pH 7.5, the metal hydroxide is formed. However, between pH 5 and 7.5, the material is stable, and there is a linear, reversible response between photoluminescence and pH. No calibration of the sensor is required, because only one of the Eu³⁺ luminescence bands will respond to pH and the other remains constant, acting as an internal standard.

Conclusions

Nanoscale metal–organic frameworks have been developed as potential MRI contrast agents. NMOF contrast agents generally have superior relaxivity to small-molecule contrast agents. Additionally, these agents can be stabilized and functionalized to optimize their performance under biological conditions. The in vitro and in vivo utility of these agents have also been demonstrated. NMOFs have also been shown to act as effective contrast agents for optical and CT imaging, and for sensors. However, much more work needs to be performed to demonstrate the effectiveness of NMOFs for clinical translation.

Acknowledgments

We thank National Science Foundation and National Institute of Health for providing financial support and are indebted to the invaluable contributions from former and present members of the Lin group working on the NMOF project, particularly Dr. William J. Rieter, Dr. Kathryn M. L. Taylor-Pashow, and Ms. Kathryn E. deKrafft.

- [1] K. Brindle, *Nat. Rev. Canc.* **2008**, *8*, 94–107.
- [2] R. H. Hashemi, W. G. Bradley Jr., *MRI The Basics*, Williams and Wilkins, Baltimore, **1997**.
- [3] S. Aime, S. G. Crich, E. Gianolio, G. B. Giovenzana, L. Tei, E. Terreno, *Coord. Chem. Rev.* **2006**, *250*, 1562–1579.
- [4] P. Caravan, J. J. Ellison, T. J. McMurry, R. B. Lauffer, *Chem. Rev.* **1999**, *99*, 2293–2352.
- [5] L. Thunus, R. Lejeune, *Coord. Chem. Rev.* **1999**, *184*, 125–155.
- [6] S. Laurent, S. Boutry, I. Mahieu, L. Vander Elst, R. N. Muller, *Curr. Med. Chem.* **2009**, *16*, 4712–4727.
- [7] S. Laurent, D. Forge, M. Port, A. Roch, L. Vander Elst, R. N. Muller, *Chem. Rev.* **2008**, *108*, 2064–2110.
- [8] W. B. Lin, T. Hyeon, G. M. Lanza, M. Q. Zhang, T. J. Meade, *MRS Bull.* **2009**, *34*, 441–448.

- [9] M. Ferrari, *Nat. Rev. Cancer* **2005**, *5*, 161–171.
- [10] F. Alexis, E. Pridgen, L. K. Molnar, O. C. Farokhzad, *Mol. Pharm.* **2008**, *5*, 505–515.
- [11] S. D. Li, L. Huang, *Mol. Pharm.* **2008**, *5*, 496–504.
- [12] K. Cho, X. Wang, S. Nie, Z. Chen, D. M. Shin, *Clin. Cancer Res.* **2008**, *14*, 1310–1316.
- [13] V. P. Torchilin, *Nat. Rev. Drug Disc.* **2005**, *4*, 145–160.
- [14] D. Peer, J. M. Karp, S. Hong, O. C. Farokhzad, R. Margalit, R. Langer, *Nat. Nanotechnol.* **2007**, *2*, 751–760.
- [15] D. Bradshaw, J. E. Warren, M. J. Rosseinsky, *Science* **2007**, *315*, 977–980.
- [16] G. Ferey, C. Mellot-Draznieks, C. Serre, F. Millange, *Acc. Chem. Res.* **2005**, *38*, 217–225.
- [17] R. J. Hill, D. L. Long, N. R. Champness, P. Hubberstey, M. Schroder, *Acc. Chem. Res.* **2005**, *38*, 335–348.
- [18] S. Kitagawa, R. Kitaura, S. I. Noro, *Angew. Chem. Int. Ed.* **2004**, *43*, 2334–2375.
- [19] B. Moulton, M. J. Zaworotko, *Chem. Rev.* **2001**, *101*, 1629–1658.
- [20] O. M. Yaghi, M. O’Keeffe, N. W. Ockwig, H. K. Chae, M. Eddaoudi, J. Kim, *Nature* **2003**, *423*, 705–714.
- [21] B. Chen, X. Zhao, A. Putkham, K. Hong, E. B. Lobkovsky, E. J. Hurtado, A. J. Fletcher, K. M. Thomas, *J. Am. Chem. Soc.* **2008**, *130*, 6411–6423.
- [22] B. Kesanli, Y. Cui, M. R. Smith, E. W. Bittner, B. C. Bockrath, W. Lin, *Angew. Chem. Int. Ed.* **2005**, *44*, 72–75.
- [23] L. Ma, D. J. Mihalcik, W. Lin, *J. Am. Chem. Soc.* **2009**, *131*, 4610–4612.
- [24] N. L. Rosi, J. Eckert, M. Eddaoudi, D. T. Vodak, J. Kim, M. O’Keeffe, O. M. Yaghi, *Science* **2003**, *300*, 1127–1129.
- [25] O. R. Evans, W. Lin, *Acc. Chem. Res.* **2002**, *35*, 511–522.
- [26] B. L. Chen, L. B. Wang, F. Zapata, G. D. Qian, E. B. Lobkovsky, *J. Am. Chem. Soc.* **2008**, *130*, 6718.
- [27] Z. Xie, L. Ma, K. E. Dekrafft, A. Jin, W. Lin, *J. Am. Chem. Soc.* **2010**, *132*, 922–923.
- [28] D. N. Dybtsev, A. L. Nuzhdin, H. Chun, K. P. Bryliakov, E. P. Talsi, V. P. Fedin, K. Kim, *Angew. Chem. Int. Ed.* **2006**, *45*, 916–920.
- [29] L. Ma, C. Abney, W. Lin, *Chem. Soc. Rev.* **2009**, *38*, 1248–1256.
- [30] C. Wu, A. Hu, L. Zhang, W. Lin, *J. Am. Chem. Soc.* **2005**, *127*, 8940–8941.
- [31] C. Wu, W. Lin, *Angew. Chem. Int. Ed.* **2007**, *46*, 1075–1078.
- [32] R. J. Kuppler, D. J. Timmons, Q. R. Fang, J. R. Li, T. A. Makal, M. D. Young, D. Q. Yuan, D. Zhao, W. J. Zhuang, H. C. Zhou, *Coord. Chem. Rev.* **2009**, *253*, 3042–3066.
- [33] D. Maspoch, D. Ruiz-Molina, J. Veciana, *Chem. Soc. Rev.* **2007**, *36*, 770–818.
- [34] D. Maspoch, D. Ruiz-Molina, J. Veciana, *J. Mater. Chem.* **2004**, *14*, 2713–2723.
- [35] R. C. Huxford, J. Della Rocca, W. Lin, *Curr. Opin. Chem. Biol.* **2010**, *14*, 262–268.
- [36] L. Catala, F. Volatron, D. Brinzei, T. Mallah, *Inorg. Chem.* **2009**, *48*, 3360–3370.
- [37] W. Lin, W. J. Rieter, K. M. L. Taylor, *Angew. Chem. Int. Ed.* **2009**, *48*, 650–658.
- [38] A. M. Spokoyny, D. Kim, A. Sumrein, C. A. Mirkin, *Chem. Soc. Rev.* **2009**, *38*, 1218–1227.
- [39] W. J. Rieter, K. M. L. Taylor, H. An, W. Lin, W. Lin, *J. Am. Chem. Soc.* **2006**, *128*, 9024–9025.
- [40] K. M. L. Taylor, A. Jin, W. Lin, *Angew. Chem. Int. Ed.* **2008**, *47*, 7722–7725.
- [41] W. J. Rieter, K. M. L. Taylor, W. B. Lin, *J. Am. Chem. Soc.* **2007**, *129*, 9852–9853.
- [42] W. J. Rieter, K. M. Pott, K. M. L. Taylor, W. Lin, *J. Am. Chem. Soc.* **2008**, *130*, 11584–11585.
- [43] K. M. L. Taylor, W. J. Rieter, W. Lin, *J. Am. Chem. Soc.* **2008**, *130*, 14358–14359.
- [44] K. M. L. Taylor-Pashow, J. Della Rocca, Z. Xie, S. Tran, W. Lin, *J. Am. Chem. Soc.* **2009**, *131*, 14261–14263.
- [45] M. D. Rowe, D. H. Thamm, S. L. Kraft, S. G. Boyes, *Biomacromolecules* **2009**, *10*, 983–993.
- [46] M. D. Rowe, C. C. Chang, D. H. Thamm, S. L. Kraft, J. F. Harmon, A. P. Vogt, B. S. Sumerlin, S. G. Boyes, *Langmuir* **2009**, *25*, 9487–9499.
- [47] R. Nishiyabu, N. Hashimoto, T. Cho, K. Watanabe, T. Yasunaga, A. Endo, K. Kaneko, T. Niidome, M. Murata, C. Adachi, Y. Katayama, M. Hashizume, N. Kimizuka, *J. Am. Chem. Soc.* **2009**, *131*, 2151–2158.
- [48] R. Nishiyabu, C. Aime, R. Gondo, T. Noguchi, N. Kimizuka, *Angew. Chem. Int. Ed.* **2009**, *48*, 9465–9468.
- [49] Y. Guari, J. Larionova, M. Corti, A. Lascialfari, M. Marinone, G. Poletti, K. Molvinger, C. Guerin, *Dalton Trans.* **2008**, 3658–3660.
- [50] G. A. Pereira, J. A. Peters, F. A. Almeida Paz, J. Rocha, C. F. G. C. Geraldies, *Inorg. Chem.* **2010**, *49*, 2969–2974.
- [51] H. Ersoy, F. J. Rybicki, *J. Magn. Reson. Imag.* **2007**, *26*, 1190–1197.
- [52] S. P. Lin, J. J. Brown, *J. Magn. Reson. Imag.* **2007**, *25*, 884–899.
- [53] J. H. Lee, A. P. Koretsky, *Curr. Pharm. Biotechnol.* **2004**, *5*, 529–537.
- [54] S. B. Kim, C. Cai, S. Sun, D. A. Sweigart, *Angew. Chem. Int. Ed.* **2009**, *48*, 2907–2910.
- [55] I. Imaz, J. Hernando, D. Ruiz-Molina, D. Maspoch, *Angew. Chem. Int. Ed.* **2009**, *48*, 2325–2329.
- [56] P. Horcajada, T. Chalati, C. Serre, B. Gillet, C. Sebrie, T. Baati, J. F. Eubank, D. Heurtaux, P. Clayette, C. Kreuz, J. S. Chang, Y. K. Hwang, V. Marsaud, P. N. Bories, L. Cynober, S. Gil, G. Ferey, P. Couvreur, R. Gref, *Nat. Mater.* **2010**, *9*, 172–178.
- [57] N. Kosaka, M. Ogawa, P. L. Choyke, H. Kobayashi, *Fut. Oncol.* **2009**, *5*, 1501–1511.
- [58] K. Licha in *Contrast Agents II: Optical, Ultrasound, X-ray and Radiopharmaceutical Imaging*, Vol. 222, *Topics in Current Chemistry* (Ed.: W. Krause), Springer, Berlin, **2002**, pp. 1–29.
- [59] M. D. Allendorf, C. A. Bauer, R. K. Bhakta, R. J. T. Houk, *Chem. Soc. Rev.* **2009**, *38*, 1330–1352.
- [60] C. L. Cahill, D. T. de Lilla, M. Frisch, *CrystEngComm* **2007**, *9*, 15–26.
- [61] C. Janiak, *Dalton Trans.* **2003**, 2781–2804.
- [62] D. Maspoch, D. Ruiz-Molina, J. Veciana, *Chem. Soc. Rev.* **2007**, *36*, 770–818.
- [63] M. P. Suh, Y. E. Cheon, E. Y. Lee, *Coord. Chem. Rev.* **2008**, *252*, 1007–1026.
- [64] C. Aime, R. Nishiyabu, R. Gondo, K. Kaneko, N. Kimizuka, *Chem. Commun.* **2008**, 6534–6536.
- [65] X. H. Yan, P. L. Zhu, J. B. Fei, J. B. Li, *Adv. Mater.* **1999**, *11*, 1283–1287.
- [66] K. A. White, D. A. Chengelis, M. Zeller, S. J. Geib, J. Szakos, S. Petoud, N. L. Rosi, *Chem. Commun.* **2009**, 4506–4508.
- [67] K. A. White, D. A. Chengelis, K. A. Gogick, J. Stehman, N. L. Rosi, S. Petoud, *J. Am. Chem. Soc.* **2009**, *131*, 18069–19071.
- [68] W. A. Kalender, *Phys. Med. Biol.* **2006**, *51*, R29–R43.
- [69] S. Yu, A. D. Watson, *Chem. Rev.* **1999**, *99*, 2353–2378.
- [70] K. E. Dekrafft, Z. G. Xie, G. H. Cao, S. Tran, L. Q. Ma, O. Z. Zhou, W. B. Lin, *Angew. Chem. Int. Ed.* **2009**, *48*, 9901–9904.
- [71] C. Aime, R. Nishiyabu, R. Gondo, N. Kimizuka, *Chem. Eur. J.* **2010**, *16*, 3604–3607.
- [72] B. V. Harbuzaru, A. Corma, F. Rey, J. L. Jorda, D. Ananias, L. D. Carlos, J. Rocha, *Angew. Chem. Int. Ed.* **2009**, *48*, 6476–6479.

Received: May 4, 2010
Published Online: July 7, 2010

Silica–MOF Composites as a Stationary Phase in Liquid Chromatography

Rob Ameloot,^[a] Anuschka Liekens,^[b] Luc Alaerts,^[a] Michael Maes,^[a] Anne Galarneau,^[c] Bernard Coq,^[c] Gert Desmet,^[b] Bert F. Sels,^[a] Joeri F. M. Denayer,^[b] and Dirk E. De Vos^{*[a]}

Keywords: Metal-organic frameworks / Liquid chromatography / Crystal engineering / Solvent effects

Metal-organic framework materials (MOFs) are a class of microporous and crystalline materials with great potential for adsorption-based separations. Harnessing the separation ability of these materials in high-performance liquid chromatography (HPLC) requires the use of small and uniform particles in order to achieve good column packing. The well-known MOF material $[\text{Cu}_3(\text{BTC})_2]$ is, however, typically synthesized as a polydisperse mixture due to its nucleation

and growth mechanism. It is demonstrated how a new synthesis method for $[\text{Cu}_3(\text{BTC})_2]$ enables the formation of the MOF inside the pores of silica beads often used in chromatography, leading to monodisperse silica–MOF composite spheres with a uniform particle size of 3 μm . When employed as an HPLC stationary phase, this material combines the good column packing properties of the silica and separation ability of the MOF material.

Introduction

Metal-organic frameworks (MOFs) are a novel class of microporous and crystalline materials. The crystal lattice of these compounds is constructed by coordination bonds between nodes of metal ions and multidentate organic ligands.^[1] Because of the wide range of metal ions and ligands that can be combined as MOF building blocks, most efforts have been focused on the synthesis of a vast variety of crystal structures. However, research interest in this domain is mainly driven by the potential applications related to the unique combination of properties of MOF materials. Characteristics such as a very high internal surface area and accessible void space, an intrinsically high metal content, possible open coordination sites at the structural metal ions, etc. make MOFs promising catalysts and adsorbents.^[2]

An application field receiving particular interest is separation technology. In this domain, zeolite materials, which can be considered as the inorganic counterparts of MOFs, currently play a key role in commercial adsorptive separations.^[3–5] In these processes, a mixture is fed into an adsorbent bed through which the components of the mixture migrate at different rates. At the bed outlet, the fastest migrating component is collected in pure form until other compo-

nents start to appear, after which the bed is typically regenerated and the process repeated. MOF materials have already demonstrated great potential in such breakthrough-type separations, both in the liquid and in the gas phase. Reported separation mechanisms include interaction with coordinatively unsaturated metal sites,^[6] cage effects,^[7] interaction with organic functional groups,^[8] adsorbate stacking effects,^[9] diffusivity differences,^[10] etc.

On the other hand, analytical chromatographic separations, involving pulse injection of a mixture to be separated into quantifiable peaks, are typically performed on silica stationary phases in pure or modified form. In liquid phase chromatography, considerable effort has been devoted to the modification of stationary phases with immobilized transition metal ions, in order to exploit coordinative interactions in the separation of analytes containing heteroatoms or π -electron systems. Transition metal ions are immobilized either by direct interaction with the stationary phase^[11–13] or by complexation with ligands bonded to the stationary phase.^[14–19] This type of chromatography, often referred to as “ligand exchange chromatography”, has been successfully demonstrated in the separation of compounds such as amines,^[13–17] sulfur compounds,^[19] phenols,^[18] or polycyclic aromatics.^[11,12]

$[\text{Cu}_3(\text{BTC})_2]$ is a well-known MOF built up by Cu^{2+} ions connected by 1,3,5-benzenetricarboxylate (BTC) ligands.^[20] As the Cu^{2+} sites in this structure are coordinatively unsaturated, this material has been proposed as a chromatographic stationary phase based on the interaction with π -electron systems.^[21] However, since the crystallization of $[\text{Cu}_3(\text{BTC})_2]$ from a synthesis mixture proceeds by continuous formation of nuclei followed by fast crystal growth, the resulting crystallites vary greatly in size.^[22,23] Use of such a polydisperse mixture as an HPLC stationary phase

[a] Center for Surface Chemistry and Catalysis, Katholieke Universiteit Leuven, Kasteelpark Arenberg 23, 3001 Leuven, Belgium
Fax: +32-16-321-998
E-mail: Dirk.DeVos@biw.kuleuven.be

[b] Department of Chemical Engineering, Vrije Universiteit Brussel, Pleinlaan 2, 1050 Brussel, Belgium

[c] Institut Charles Gerhardt Montpellier, UMR 5253 CNRS/UM2/ENSCM/UM1, ENSCM,

8 rue de l'Ecole Normale, 34296 Montpellier, France
Supporting information for this article is available on the WWW under <http://dx.doi.org/10.1002/ejic.201000494>.

inevitably leads to undesirable peak shapes and high column backpressure.

Here, we present how the synthesis of $[\text{Cu}_3(\text{BTC})_2]$ directly inside the pores of the monodisperse silica spheres typically used as an HPLC stationary phase allows for combining the good column packing properties of the silica and the separation ability of the MOF material.

Results and Discussion

Whereas $[\text{Cu}_3(\text{BTC})_2]$ is classically synthesized under solvothermal conditions,^[20] we recently introduced a novel method based on a clear precursor solution in which nucleation can be induced by solvent evaporation.^[24] This method allows for more flexible ways of processing this MOF material. $[\text{Cu}_3(\text{BTC})_2]$ was deposited inside the mesopores of Nucleosil 100-3 by impregnation with a clear solution, consisting of the metal salt and ligand in dimethyl sulfoxide (DMSO), and subsequent solvent evaporation. Afterwards, residual DMSO and reagents were removed by stirring the powder in boiling ethanol. Following separation by filtration and drying at 393 K, the modified silica powder demonstrated a color change from light blue to purple, characteristic for $[\text{Cu}_3(\text{BTC})_2]$.^[25]

Whereas the powder XRD pattern is dominated by the amorphous silica matrix (very broad signal at $2\theta \approx 20^\circ$), the presence of $[\text{Cu}_3(\text{BTC})_2]$ is confirmed by its characteristic peaks (Figure 1A). The MOF loading of the modified silica was determined by thermal gravimetric analysis (TGA) at 14 wt.-%. Nitrogen physisorption confirms the deposition of $[\text{Cu}_3(\text{BTC})_2]$ inside the Nucleosil material by a simultaneous decrease in mesopore volume of the silica (from 1.097 to 1.028 mL/g_{silica}) and a slight increase in the microporosity of the modified sample compared to the bare Nucleosil material (Figure 1B). Electron micrographs show that the original spherical morphology of the Nucleosil material remains unaffected (Figure 2A). Notably, the few $[\text{Cu}_3(\text{BTC})_2]$ crystallites occasionally observed on the surface of the silica spheres (Figure 2B) are unlikely to account for the measured MOF loading.

The silica–MOF composite material was slurry-packed into a stainless steel column (length 150 mm, inner diameter 4.6 mm) by using methanol as the packing solvent at a pressure of 400 bar. The same procedure was repeated for the reference materials, being bare Nucleosil and pure $[\text{Cu}_3(\text{BTC})_2]$. After packing, columns were flushed successively with 2-propanol and heptane as preparation for normal-phase HPLC experiments. No leaching of Cu^{2+} was observed during conditioning of the column, as confirmed by atomic absorption spectrometry (AAS). The separation of ethylbenzene and styrene was chosen as a test case since this separation has been demonstrated on pure $[\text{Cu}_3(\text{BTC})_2]$ under similar conditions.^[21]

Indeed, when a mixture of these analytes was passed through the pure $[\text{Cu}_3(\text{BTC})_2]$ column in heptane at a flow rate of 1 mL/min, ethylbenzene and styrene could be resolved with retention times of 8 and 17 min, respectively.

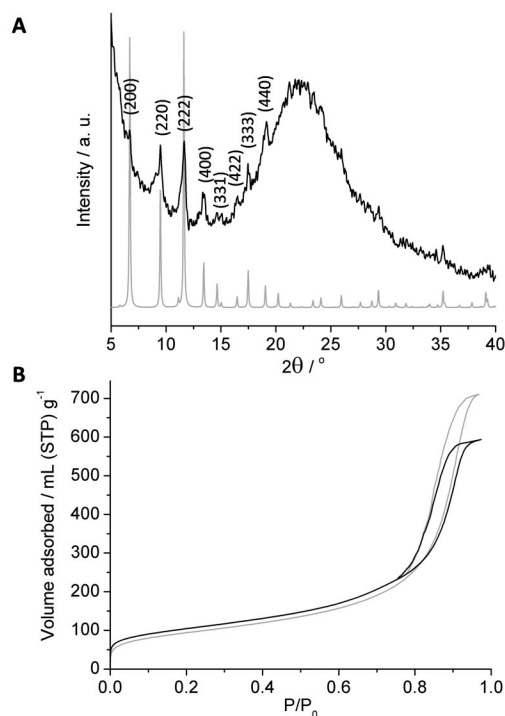


Figure 1. Characterization of the silica material modified with $[\text{Cu}_3(\text{BTC})_2]$. (A) Powder XRD pattern of the composite material (black curve) and simulated pattern of $[\text{Cu}_3(\text{BTC})_2]$ (grey curve); diffraction peaks attributed to $[\text{Cu}_3(\text{BTC})_2]$ are marked with their corresponding hkl indices. (B) Nitrogen sorption isotherms at 77 K of unmodified silica (grey curve) and silica–MOF composite (black curve).

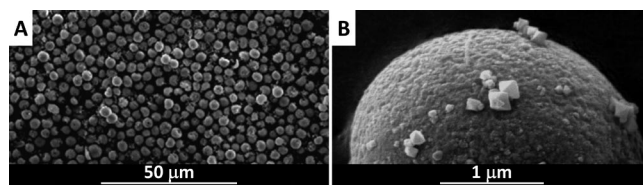


Figure 2. Electron micrographs of the silica material modified with $[\text{Cu}_3(\text{BTC})_2]$. (A) Overview showing the uniform size of the microspheres. (B) Detail of a silica microsphere showing the occasionally occurring extra-particle $[\text{Cu}_3(\text{BTC})_2]$ crystallites.

However, as could be expected from the broad size distribution of $[\text{Cu}_3(\text{BTC})_2]$ particles (0.5–4 μm), column backpressure was high (200 bar) and peaks were broad (Figure 3A). On the other hand, columns filled with uniform bare Nucleosil spheres demonstrated a much lower backpressure of 52 bar at a heptane flow rate of 1 mL/min. Whereas single-compound injections on this latter column resulted in sharp peaks, a mixture of ethylbenzene and styrene could not be separated (Figure 3B). This lack of resolution under these conditions lies within expectations, as the separation mechanism on $[\text{Cu}_3(\text{BTC})_2]$ is suggested to be interaction with free transition metal sites, which are absent on bare Nucleosil. Nevertheless, the silica–MOF composite material was found to separate mixtures of ethylbenzene and styrene effectively under the same conditions, with retention times of 4 and 12 min, respectively (Figure 3C). In addition, col-

umn backpressure was low at 47 bar, and peaks were narrow. This result illustrates the combined effect of the good packing properties of the monodisperse silica spheres and the separation ability of the MOF material based on free Cu^{2+} sites.

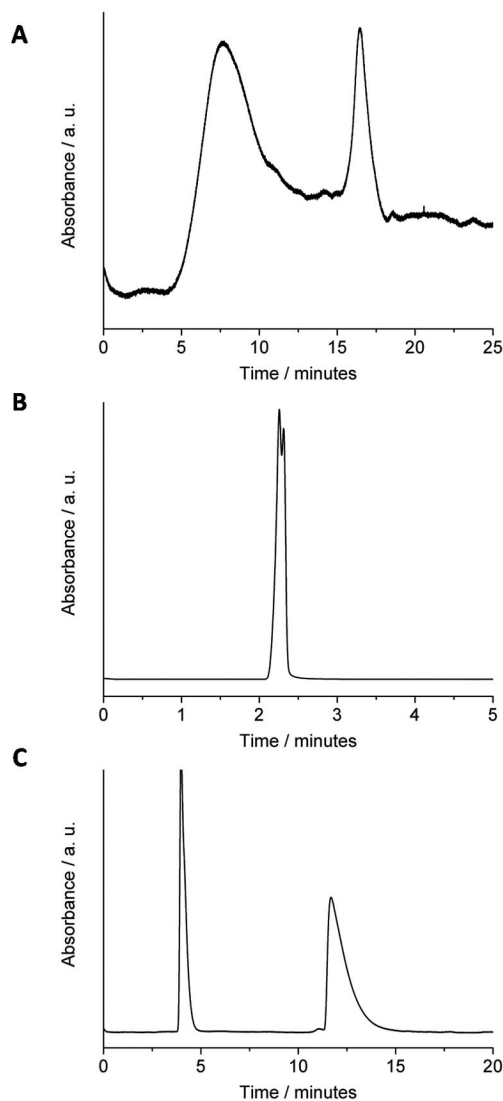


Figure 3. HPLC experiments. (A) Injection of a mixture of ethylbenzene and styrene on a pure $[\text{Cu}_3(\text{BTC})_2]$ column. (B) Injection of the same mixture on an unmodified silica column. (C) Injection of the same mixture on a silica column modified with $[\text{Cu}_3(\text{BTC})_2]$.

Chromatographic data for the separation of ethylbenzene and styrene on the silica–MOF material are summarized in Table 1. Note that the resolution for this separation is 7.9, which is significantly higher than 1.5, a value typically considered as indicative of baseline separation.^[26] Whereas some parameters, such as the effect of endcapping, remain to be explored in the preparation of the silica–MOF material, it is clear that the advantageous combination of properties in this composite is promising for chromatographic applications. For instance, when extending the analyte scope to the separation of *p*-ethyltoluene and *p*-methyl-

styrene (Figure S1), the resolution amounts to 14. Just like in a recent report on employing MOFs in wall-coated gas chromatography columns, achieving this chromatographic performance relies on the correct method to deposit $[\text{Cu}_3(\text{BTC})_2]$ inside the silica support.^[27]

Table 1. Chromatographic data for the silica column modified with $[\text{Cu}_3(\text{BTC})_2]$.

Parameter	Value
Retention time ethylbenzene	4.1 min
Retention time styrene	12.3 min
Resolution (R_s)	7.9
Retention factor ethylbenzene ^[a]	0.89
Retention factor styrene ^[a]	4.63
Separation factor (α) ^[a]	5.2

[a] For calculations, the retention time of an unretained peak was estimated as the retention time of ethylbenzene on the bare Nucleosil column.

Conclusions

We demonstrated how a new synthesis method for the MOF $[\text{Cu}_3(\text{BTC})_2]$ enables the formation of a silica–MOF composite. When employed as an HPLC stationary phase, this material combines the good column packing properties of the silica and separation ability of the $[\text{Cu}_3(\text{BTC})_2]$ material.

Experimental Section

Preparation of Materials: $[\text{Cu}_3(\text{BTC})_2]$ precursor solution was prepared by dissolving $\text{Cu}(\text{NO}_3)_2 \cdot 3\text{H}_2\text{O}$ (1.22 g, 5 mmol) and BTC (0.58 g, 2.76 mmol) in DMSO (5 g). Nucleosil 100-3 was used as received from Macherey–Nagel with following properties as indicated by the manufacturer: a particle size of 3 μm , a pore volume of 1.1 mL/g and a pore-size distribution ranging from 50 to 150 Å. For impregnation, 1 mL of precursor solution was used per gram of Nucleosil. Afterwards, the impregnated powder was spread out as a thin layer, and the solvent was evaporated at 373 K for several hours. During evaporation, the powder was shaken regularly to ensure even drying. Afterwards, the powder was stirred in boiling ethanol for 1 h, separated by filtration and dried at 393 K. Reference $[\text{Cu}_3(\text{BTC})_2]$ material was prepared electrochemically by using the procedure described in ref.^[6]

Characterization: Nitrogen physisorption at 77 K was carried out with a Micromeritics Tristar 3000 apparatus after dehydration of the samples at 393 K under N_2 flow. SEM micrographs were recorded with a Philips XL-30 FEG after coating with Au. MOF content of the modified samples was determined at 14.07 wt.-% by TGA (TA Instruments TGA Q500) by relating the observed loss to the decomposition of $[\text{Cu}_3(\text{BTC})_2]$ to CuO under O_2 . Powder XRD patterns were recorded with a STOE STADI P Combi instrument in Debye–Scherrer geometry ($\text{Cu-K}\alpha_1$) by using an IP-position-sensitive detector ($2\theta = 0\text{--}60^\circ$; $\Delta 2\theta = 0.03$) operating in capillary mode.

HPLC Column Preparation and Experiments: A 10 wt.-% slurry of the stationary phase was prepared in methanol by short bursts of sonication. By using a slurry packer and methanol as the packing solvent, stainless steel columns (length 150 mm, inner diameter 4.6 mm) were packed and allowed to settle at 400 bar for 30 min.

Afterwards, the columns were flushed successively with methanol, 2-propanol and heptane. The column effluent was collected during flushing and the absence of Cu²⁺ was confirmed by AAS. HPLC experiments were performed with an Agilent Technologies 1100 series apparatus in heptane at a flow rate of 1 mL/min. Solutions of analytes were injected (1 µL injection volume), and UV absorption at 254 nm was monitored.

Supporting Information (see footnote on the first page of this article): HPLC measurement of the injection of a *p*-ethyltoluene/*p*-methylstyrene mixture on a column filled with silica–MOF composite.

Acknowledgments

The authors are grateful to the Belgian Federal Government for support in the IAP project 6/27 Functional Supramolecular Systems, to K. U. Leuven for the Methusalem CASAS grant, to FWO Vlaanderen for funding project G.0453.09. R. A. and L. A. are grateful for support from FWO Vlaanderen for a graduate and a postdoctoral fellowship, respectively. This work was also supported by 7PCRD EU funds from the Marie-Curie initial Training Network NANO-HOST (grant agreement ITN 215193-2). The authors thank Prof. S. Eeltink for help with the preparation of HPLC columns.

- [1] A. K. Cheetham, G. Ferey, T. Loiseau, *Angew. Chem. Int. Ed.* **1999**, *38*, 3268; A. K. Cheetham, C. N. R. Rao, R. K. Feller, *Chem. Commun.* **2006**, 4780.
- [2] R. J. Kuppler, D. J. Timmons, Q. R. Fang, J. R. Li, T. A. Makal, M. D. Young, D. Q. Yuan, D. Zhao, W. J. Zhuang, H. C. Zhou, *Coord. Chem. Rev.* **2009**, *253*, 3042.
- [3] R. Hulme, R. Rosensweig, D. Ruthven, *Ind. Eng. Chem. Res.* **1991**, *30*, 752.
- [4] J. Kaerger, D. Ruthven in *Handbook of Porous Solids* (Eds.: F. Schüth, K. Sing, J. Weitkamp), Wiley-VCH, Weinheim, **2002**, pp. 2089–2173.
- [5] D. Ruthven, *Principles of Adsorption and Adsorption Processes*, Wiley, New York, **1984**, pp. 332, 401–405.
- [6] U. Mueller, M. Schubert, F. Teich, H. Puetter, K. Schierle-Arndt, J. Pastre, *J. Mater. Chem.* **2006**, *16*, 626.
- [7] M. Maes, L. Alaerts, F. Vermoortele, R. Ameloot, S. Couck, V. Finsy, J. F. M. Denayer, D. E. De Vos, *J. Am. Chem. Soc.* **2010**, *132*, 2284.
- [8] S. Couck, J. F. M. Denayer, G. V. Baron, T. Remy, J. Gascon, F. Kapteijn, *J. Am. Chem. Soc.* **2009**, *131*, 6326.
- [9] L. Alaerts, C. E. A. Kirschhock, M. Maes, M. A. van der Veen, V. Finsy, A. Depla, J. A. Martens, G. V. Baron, P. A. Jacobs, J. F. M. Denayer, D. E. De Vos, *Angew. Chem. Int. Ed.* **2007**, *46*, 4293.
- [10] K. H. Li, D. H. Olson, J. Seidel, T. J. Emge, H. W. Gong, H. P. Zeng, J. Li, *J. Am. Chem. Soc.* **2009**, *131*, 10368.
- [11] D. Thomas, S. M. Crain, P. G. Sim, F. M. Benoit, *J. Chromatogr. A* **1995**, *695*, 1.
- [12] P. G. Sim, H. Perreault, F. M. Benoit, L. Ramaley, S. M. Crain, G. K. McCully, D. Thomas, R. K. Boyd, *Polycyclic Aromat. Compd.* **1996**, *8*, 105.
- [13] D. K. Singh, A. Darbari, *Chromatographia* **1987**, *23*, 93.
- [14] F. K. Chow, E. Grushka, *Anal. Chem.* **1977**, *49*, 1756.
- [15] C. R. Silva, I. Jardim, C. Airoidi, *J. Sep. Sci.* **2001**, *24*, 197.
- [16] H. Takayanagi, H. Tokuda, H. Uehira, K. Fujimura, T. Ando, *J. Chromatogr.* **1986**, *356*, 15.
- [17] U. Pyell, G. Stork, *Fresenius J. Anal. Chem.* **1992**, *343*, 576.
- [18] S. Srijaranai, W. Siriangkhawut, C. Ruksakulpiwat, R. L. Deming, *Anal. Lett.* **2004**, *37*, 2577.
- [19] H. Takayanagi, O. Hatano, K. Fujimura, T. Ando, *Anal. Chem.* **1985**, *57*, 1840.
- [20] S. S. Y. Chui, S. M. F. Lo, J. P. H. Charmant, A. G. Orpen, I. D. Williams, *Science* **1999**, *283*, 1148.
- [21] R. Ahmad, A. G. Wong-Foy, A. J. Matzger, *Langmuir* **2009**, *25*, 11977.
- [22] D. Zacher, J. N. Liu, K. Huber, R. A. Fischer, *Chem. Commun.* **2009**, 1031.
- [23] F. Millange, M. I. Medina, N. Guillou, G. Ferey, K. M. Golden, R. I. Walton, *Angew. Chem. Int. Ed.* **2010**, *49*, 763.
- [24] R. Ameloot, E. Gobechiya, H. Uji-i, J. A. Martens, J. Hofkens, L. Alaerts, B. F. Sels, D. E. De Vos, *Adv. Mater.*, DOI: 10.1002/adma.200903867.
- [25] C. Prestipino, L. Regli, J. G. Vitillo, F. Bonino, A. Damin, C. Lamberti, A. Zecchina, P. L. Solari, K. O. Kongshaug, S. Bordiga, *Chem. Mater.* **2006**, *18*, 1337.
- [26] M. W. Dong, *Modern HPLC for Practicing Scientists*, Wiley & Sons, Hoboken, NJ, **2006**, pp. 23–24.
- [27] Z. Gu, X. Yan, *Angew. Chem. Int. Ed.*, DOI: 10.1002/anie.200906560.

Received: May 3, 2010
Published Online: June 16, 2010

Synthesis and Structural Flexibility of a Series of Copper(II) Azolate-Based Metal–Organic Frameworks

Kenji Sumida,^[a] Maw Lin Foo,^[a] Satoshi Horike,^[a] and Jeffrey R. Long^{*[a]}

Keywords: Metal–organic frameworks / Porous materials / N ligands / Copper

The reaction of $\text{CuCl}_2 \cdot 2\text{H}_2\text{O}$ with three novel ditopic ligands, 2-methyl-1,4-benzenedinitrazolate (MeBDT^{2-}), 4,4'-biphenyldinitrazolate (BPDT^{2-}), and 2,3,5,6-tetrafluoro-1,4-benzenedinitrazolate (TFBDTri^{2-}), affords the metal–organic frameworks $\text{Cu}(\text{MeBDT})(\text{dmf})$ (**1**), $\text{Cu}(\text{BPDT})(\text{dmf})$ (**2**), and $\text{Cu}(\text{TFBDTri})(\text{dmf})$ (**3**), respectively. These materials feature a common network topology in which octahedral Cu^{2+} ions are bridged by azolate ligands and dmf molecules to form one-dimensional chains. The individual chains are connected by the organic bridging units to form diamond-shaped channels, in which the solvent molecules project into the pores.

The bridging dmf molecules in **1** are readily displaced by other coordinating solvent molecules, which leads to a change in the pore dimensions according to the steric bulk of the solvent. Interestingly, attempts to exchange the analogous solvent molecules in the expanded framework **2** induced no change in the pore size, revealing the rigidity of the framework. Meanwhile, **3** exhibits modest flexibility and an improved thermal stability consistent with its chemical functionality. The marked difference in flexibility highlights the considerable impact the organic linker can have on the dynamic framework properties.

Introduction

Metal–organic frameworks have attracted much recent investigation because of their high permanent porosity, convenient modular synthesis, and chemical tunability.^[1] The ability to judiciously select the metal ion and organic linker suggests that if the appropriate components are combined, frameworks that are tailor-made for specific applications, such as gas storage^[2] and separation,^[3] may be prepared. However, significant improvements in the understanding of structure–property relationships within this class of material are still needed in order to fulfill their great potential. Indeed, despite the large number of frameworks studied for their gas sorption behavior, flexibility, and chemical stability, it still remains difficult to predict how changes to the framework constituents or network structure might affect the observed properties. Thus, improvements in this regard would greatly aid in materials design, and from a practical point of view, dramatically reduce the number of compounds that need to be studied for the discovery of high-performance materials.

The systematic investigation of the adsorptive and dynamic properties of materials exhibiting a common network topology may allow the effect of subtle changes to the framework, such as the metal node or the functionality or length of the organic bridging unit, to be elucidated. For

example, the IRMOF series of frameworks, which feature a cubic network of tetrahedral $[\text{Zn}_4\text{O}]^{6+}$ clusters bridged by dicarboxylate linkers, demonstrates that a common network type can be adopted despite the use of a diverse range of ligands.^[1a,4] Meanwhile, in the $\text{M}_2(\text{DOBDC})$ ($\text{M} = \text{Mg}, \text{Mn}, \text{Co}, \text{Ni}, \text{Zn}$; $\text{DOBDC}^{4-} = 2,5\text{-dioxido-1,4-benzenedicarboxylate}$) and the $\text{M}_3[(\text{M}_4\text{Cl})_3(\text{BTT})_8]_2$ ($\text{M} = \text{Mn}, \text{Fe}, \text{Cu}$; $\text{BTT}^{3-} = 1,3,5\text{-benzenetristetrazolate}$) frameworks, the same network connectivity is facilitated by a variety of metals.^[5,6] These materials are of significant interest due to the presence of unsaturated coordination sites on the pore surface, and depending on the metal employed, the frameworks can exhibit enhanced affinities or selectivities for certain gas molecules, which is crucial for the development of high-performance materials for hydrogen storage and carbon dioxide capture.

In addition to variations in the composition of the materials, metal–organic frameworks exhibiting reversible structural flexibility have also received significant attention due to their structural dynamics and unusual response to the adsorption of guest molecules.^[7] These materials frequently exhibit stepwise or hysteretic adsorption phenomena owing to transitions in the framework structure, which can be of benefit for gas storage and separation applications. For instance, in the separation of gases of very similar kinetic diameters, such as O_2 and N_2 , a potentially viable approach might be to modulate the gate-opening pressure by tuning the internal pore surface of the material. Thus, the two strategies mentioned above, namely modification of the metal or ligand component of the framework, are potential avenues for the preparation of optimized materials.

[a] Department of Chemistry, University of California, Berkeley
Berkeley, CA 94720-1460, USA
E-mail: jrlong@berkeley.edu

Supporting information for this article is available on the WWW under <http://dx.doi.org/10.1002/ejic.201000490> or from the author.

Recently, we have reported two copper-based frameworks: $\text{Cu}(\text{BDT})(\text{dmf})$ ($\text{BDT}^{2-} = 1,4\text{-benzeneditrazolate}$) and $\text{Cu}(\text{BDTri})(\text{L})$ ($\text{L} = \text{dmf, def}$; $\text{BDTri}^{2-} = 1,4\text{-benzeneditrazolate}$).^[8,9] Despite the use of different azolate functional groups, the frameworks are isostructural to each other, and in the case of the triazolate-based materials, the same network topology is adopted despite a different bridging solvent molecule being present in the structure. Interestingly, these materials exhibit reversible changes in the pore dimensions depending on the quantity of guest solvent in the pores. In the case of the evacuated frameworks, a state in which the pore apertures are closed, a high selectivity of O_2 over N_2 is observed due to a kinetic sieving effect based on the slightly smaller kinetic diameter of O_2 (3.46 Å) relative to N_2 (3.64 Å).^[10] Here, we extend this library of metal-organic frameworks based on copper(II) azolate derived from three new organic linkers depicted in Figure 1: 2-methyl-1,4-benzeneditrazolate (MeBDT^{2-}), 4,4'-biphenylditrazolate (BPDT^{2-}), and 2,3,5,6-tetrafluoro-1,4-benzeneditrazolate (TFBDTri^{2-}). The ligands have been synthesized for their different functionalities and lengths, which are anticipated to allow access to unique dynamic properties within the resulting frameworks. Indeed, while the resulting frameworks exhibit the same network topology, they possess significantly different flexibility and chemical stability profiles with respect to exchange of the bridging ligand, demonstrating the exquisite dependence of the framework properties on the organic linker.

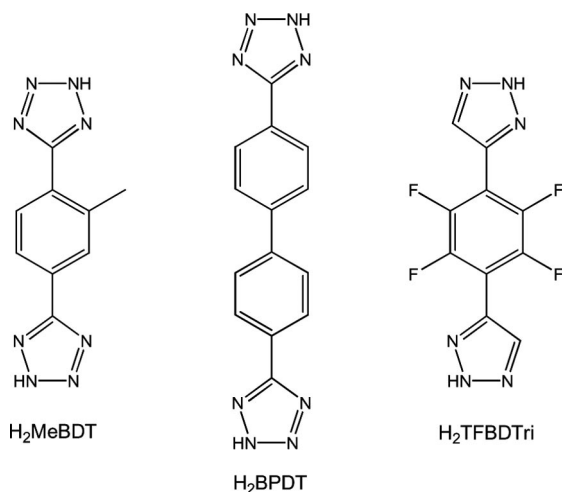


Figure 1. Protonated forms of the organic bridging units employed in the present work: 2-methyl-1,4-benzeneditrazolate (MeBDT^{2-}), 4,4'-biphenylditrazolate (BPDT^{2-}), and 2,3,5,6-tetrafluoro-1,4-benzeneditrazolate (TFBDTri^{2-}).

Results and Discussion

The combination of $\text{CuCl}_2 \cdot 2\text{H}_2\text{O}$ and H_2MeBDT in an acidified mixture of dmf and methanol at room temperature yielded blue-green, block-shaped single crystals of the solvated form of $\text{Cu}(\text{MeBDT})(\text{dmf})$ (**1-AS**). X-ray diffraction analysis of the crystals revealed an orthorhombic network

crystallizing in the space group *Imma* (Figure 2), which is isostructural to both $\text{Cu}(\text{BDT})(\text{dmf})$ ^[8] and $\text{Cu}(\text{BDTri})(\text{L})$ ($\text{L} = \text{dmf, def}$).^[9] The network consists of octahedral Cu^{2+} ions, in which the four equatorial coordination sites are coordinated by nitrogen atoms of four different tetrazolate groups, while the axial sites are occupied by bridging dmf molecules resulting in one-dimensional chains in the [010] direction. The individual chains are linked by the MeBDT^{2-} ligands, creating diamond-shaped one-dimensional channels that run parallel to the Cu^{2+} chains. Note that the methyl substituent on the bridging ligand was crystallographically disordered over the four possible sites on the benzene ring. Thermogravimetric analysis of a sample of **1-AS** following immersion in dichloromethane revealed that, following the initial evaporation of dichloromethane up to approximately 50 °C, the material maintains its structure until approximately 200 °C, above which the bound dmf molecules are lost, resulting in decomposition of the framework. The thermal stability is indeed comparable to that of other tetrazolate-based frameworks reported recently.^[6,8]

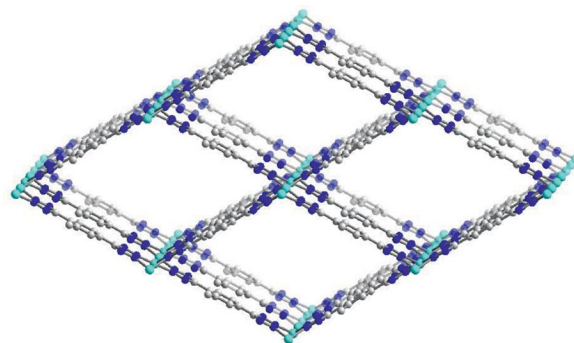


Figure 2. A portion of the crystal structure of as-synthesized $\text{Cu}(\text{MeBDT})(\text{dmf})$ (**1-AS**) as viewed down the [010] direction. Turquoise, gray, and blue spheres represent Cu, C, and N atoms, respectively. Hydrogen atoms and bridging dmf molecules have been omitted for clarity.

Surprisingly, the single-crystallinity of the as-synthesized material was lost after evacuation of the pores by immersing the crystals in dichloromethane and evaporating the solvent within the pores under a slow flow of dinitrogen. This is presumably due to the mechanical stress generated by the significant changes in the dimensions of the channels within the framework. Indeed, comparison of the powder X-ray diffraction pattern of **1-AS** (Figure 3a) with that of the desolvated material (**1-dmf**, Figure 3b) revealed a significant shift in several of the predominant reflections, most notably the (101) reflection. Furthermore, full indexing of the powder pattern was possible to a significantly smaller unit cell within the same space group, *Imma*, wherein the cell parameter *c* was significantly contracted relative to the solvated structure, indicating partial collapse of the one-dimensional channels upon removal of the non-coordinated solvent molecules. Infrared spectroscopy confirmed that the bridging dmf molecules, and hence the original network connectivity, had been retained in **1-dmf**. Moreover, after solvation of

the pores of **1**-dmf by soaking in neat dmf, a powder X-ray diffraction pattern matching that of **1**-AS was obtained, indicating the opening of the pore aperture.

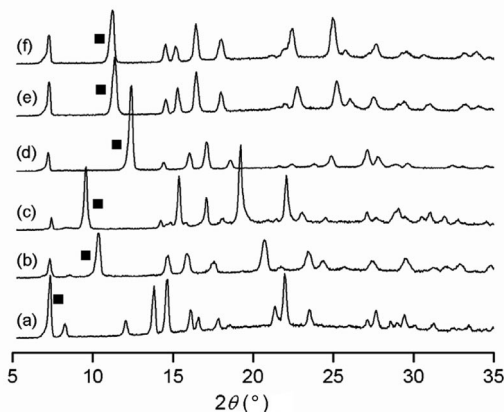


Figure 3. Powder X-ray diffraction patterns for (a) as-synthesized Cu(MeBDT)(dmf) (**1**-AS), (b) evacuated Cu(MeBDT)(dmf) (**1**-dmf), (c) Cu(MeBDT)(def) (**1**-def), (d) Cu(MeBDT)(MeOH) (**1**-MeOH), (e) Cu(MeBDT)(EtOH) (**1**-EtOH), (f) Cu(MeBDT)(dmso) (**1**-dmso). The filled square symbol indicates the (101) reflection, which readily evolves upon solvent exchange.

The ability of the bridging solvent to be modified in the Cu(BDTri)(L) (L = dmf, def) system prompted our efforts to probe the extent to which this is possible for **1**. In our hands, while the framework could not be prepared directly within other solvents, we found that the as-synthesized material **1**-AS could be immersed in def to generate Cu(MeBDT)(def) (**1**-def), in which the bridging dmf solvent molecules were fully displaced by def. Furthermore, indexing of the powder X-ray pattern of the dried form of **1**-def (Figure 3c) was possible within the space group *Imma* by using a unit cell larger than that observed for **1**-dmf, which is consistent with the slightly greater steric bulk of def relative to dmf.

The generality of the substitution of the bridging solvent was tested by submerging samples of **1**-AS within a number of common organic solvents. Indeed, dmf could be displaced by a broad range of other coordinating solvents, such as methanol, ethanol, and dmso, to generate Cu(MeBDT)(MeOH) (**1**-MeOH), Cu(MeBDT)(EtOH) (**1**-EtOH), and Cu(MeBDT)(dmso) (**1**-dmso), respectively. Immersion of single crystals of **1**-AS within these coordinating solvents resulted in rapid cracking of the crystals, which is consistent with the significant mechanical stress imparted

by the changes in the dimensions of the one-dimensional channels. However, the powder X-ray diffraction patterns (Figure 3d–f) could be fully indexed within the space group *Imma* in all cases, affording the unit cell parameters tabulated in Table 1. Comparison of the unit cell volumes reveals that the pore dimensions follow that of the steric bulk of the coordinated solvent, suggesting the possibility for tuning the porosity and the surface chemistry by use of the appropriate solvent molecule. Notably, the use of solvent molecules larger than the size of the pores, such as 1-butanol and benzyl alcohol, resulted in no displacement of the bridging solvent, as evidenced by the unchanged powder X-ray pattern after drying the sample.

The reaction of CuCl₂·2H₂O and H₂BPDT in an acidified dmf and EtOH mixture at room temperature yielded blue, block-shaped crystals of the solvated form of Cu(BPDT)(dmf) (**2**-AS). Indexing of the powder X-ray diffraction within the space group *Imma* revealed that the framework is indeed an expanded version of **1**. The unit cell parameter *a* [31.559(4) Å] is significantly larger than the corresponding value observed in **1**-AS [22.709(5) Å], which is consistent with the use of a longer organic linker and the formation of wider channels. Interestingly, in contrast to **1**, samples of **2** that were washed with dichloromethane and air-dried retained the same powder X-ray diffraction pattern (Figure S1), indicating structural rigidity upon evacuation of the pores of the framework. The flexibility of **2** and its solvent exchange properties were further assessed by submerging crystals of **2** within the same organic solvents as those successfully incorporated into **1**. Surprisingly, under all conditions, the framework structure remained rigid, and no changes to the powder X-ray diffraction pattern were detected.

The solvothermal reaction of CuCl₂·2H₂O and the fluorinated ligand H₂TFBDTri at 80 °C in dmf over four days resulted in the precipitation of Cu(TFBDTri)(dmf) (**3**-AS) as a blue-purple powder. Analysis of the powder X-ray diffraction pattern revealed that the material is indeed isostructural to **1**. Note that, in the case of perfluorinated ligands bearing carboxylate functionalities, materials that are isostructural to their non-fluorinated counterparts have not yet been reported.^[11] As expected from the higher coordination strength of the ligand, thermogravimetric analysis revealed a modest increase in the thermal stability of the framework over **1** and **2** (Figures S4–S6), which may be attributed to the higher thermal stability of the triazole functionality^[12] and/or aryl carbon–fluorine bonds.^[13] A similar

Table 1. Unit cell parameters of as-synthesized and solvent-exchanged forms of **1**–**3** as determined from indexing^[a] of the powder X-ray diffraction patterns.

	1 -AS	1 -dmf	1 -def	1 -MeOH	1 -EtOH	1 -dmso	2	3 -dmf	3 -def	3 -dmso
<i>a</i> (Å)	22.72	24.66	24.39	25.10	24.88	25.01	31.23	24.54	24.55	24.64
<i>b</i> (Å)	7.234	7.090	7.124	7.270	7.195	7.137	6.667	6.970	6.980	6.960
<i>c</i> (Å)	14.95	9.290	10.21	7.561	8.338	8.480	12.98	9.390	9.948	8.618
<i>V</i> (Å ³)	2349.0	1624.3	1773.0	1379.5	1494.0	1513.6	2702.6	1606.1	1705.0	1478.3

[a] Space group: *Imma*.

soaking of **3**-AS within def and dmsO generated the corresponding frameworks Cu(TFBDTri)(def) (**3**-def) and Cu(TFBDTri)(dmsO) (**3**-dmsO), respectively. As was observed for **1**, the powder X-ray diffraction patterns (Figures S2a–c) indicated the flexibility of the framework, and the resulting unit cell volumes correlate with the steric bulk of the solvent employed. Surprisingly, when samples of **3**-AS were submerged in water or methanol, significant broadening of the reflections in the powder pattern was observed, indicating a decrease in the crystallinity of the sample.

The significant difference in the framework flexibility between compounds **1**, **2**, and **3** is quite unexpected, because of the structural similarities and network connectivity of the materials. While the exact mechanism giving rise to the solvent substitution is currently unknown, one origin for the different behavior may lie in the strength of the binding of the bridging solvent molecules as a result of electronic effects and steric demands imposed by the various bridging ligands. Similar effects have been reported recently by Férey and co-workers for derivatives of the MIL-53(Fe) structure type,^[14] which exhibited linker-dependent flexibility upon immersion in a variety of organic solvents. Ongoing studies will be directed towards gaining a more detailed understanding of the mechanism of solvent substitution and effects on the resulting gas sorption properties.

Conclusions

The foregoing results demonstrate broad applicability of the Cu(BDT)(dmf) structure type, allowing for the generation of three isostructural materials from a variety of organic linkers. The flexibility within this series of framework is strongly influenced by the specific organic bridging unit that is employed, wherein **1** is readily flexible upon the incorporation of guest solvent molecules into the pores, while the **2** remains rigid under all conditions attempted in this study. Flexibility could also be demonstrated for **3**, in which def and dmsO could be exchanged for dmf. Studies directed towards elucidating the reasons for such a significant difference in the flexibility between these frameworks are currently underway. Furthermore, efforts to achieve a more detailed understanding of the chemical properties of the channels, such as polarity-dependent guest solubility, and the adsorptive properties of the frameworks, are also ongoing. We envisage that this structure type can be adopted by an even broader range of ligand functionalities, which should lead to an increased understanding of the structure–property relationships within this class of metal–organic framework.

Experimental Section

General: All ligand syntheses were performed under a nitrogen atmosphere by using standard Schlenk techniques. Azidomethyl pivalate^[15] and 1,4-diethynyl-2,3,5,6-tetrafluorobenzene^[16] were prepared as previously reported. All glassware was dried in an oven

set to a temperature of 150 °C for 24 h prior to use. Toluene was dried with activated 4 Å molecular sieves, passed through a column of activated alumina, and degassed with nitrogen. Methanol was dried with calcium hydride and then distilled. All other syntheses and manipulations were carried out in air. All reagents were obtained from commercial vendors and used without further purification.

1,4-Ditetrazol-5-yl-2-methylbenzene (H₂MeBDT): Toluene (20 mL) was added to a 100 mL round-bottom flask containing 2-methyl-terephthalonitrile (0.34 g, 2.4 mmol), sodium azide (0.95 g, 15 mmol), and triethylamine hydrochloride (2.0 g, 15 mmol). The reaction mixture was heated at reflux for three days, after which time a pale-brown solid was observed on the walls of the reaction vessel. The reaction mixture was dissolved in NaOH (30 mL, 1 M) and vigorously stirred for 30 min, then the aqueous phase was collected by phase separation. This fraction was treated with HCl (30 mL, 1 M) until the pH of the solution was ca. 1, and the resulting white solid was collected by filtration and dried overnight at 120 °C. The dried product was finely ground to yield a pale-yellow powder (0.43 g, 79%). IR (neat): $\tilde{\nu}$ = 3137 (m), 3065 (m), 3007 (m br), 2927 (m br), 2827 (m br), 2707 (s br), 2625 (s br), 2495 (s br), 1807 (m br), 1580 (s), 1496 (m), 1454 (m), 1435 (m), 1390 (s), 1350 (w), 1282 (w), 1238 (s), 1153 (m), 1109 (m), 1086 (m), 1030 (m), 986 (s), 920 (s), 887 (s), 835 (s), 741 (s), 705 (w br) cm⁻¹. ¹H NMR ([D₆]dmsO): δ = 17.10 (br. s, 2 H, -NH), 8.14 (s, 1 H, H_{Ph}), 8.07 (d, J = 8 Hz, 1 H, H_{Ph}), 7.96 (d, J = 8 Hz, 1 H, H_{Ph}), 2.61 (s, 3 H, -CH₃) ppm.

4,4'-Ditetrazol-5-yl-biphenyl (H₂BPDT): Toluene (20 mL) was added to a 100 mL round-bottom flask containing 4,4'-biphenyldicarbonitrile (0.50 g, 2.4 mmol), sodium azide (0.95 g, 15 mmol) and triethylamine hydrochloride (2.0 g, 15 mmol). A workup procedure analogous to H₂MeBDT was followed, yielding the pure product as an off-white powder (0.61 g, 87%). C₁₄H₁₀N₈ (290.28): C 57.93, H 3.47, N 38.60; found C 57.75, H 3.49, N 38.30. IR (neat): $\tilde{\nu}$ = 3130 (m br), 3064 (m br), 3005 (m br), 2853 (s br), 2731 (s br), 2645 (s br), 1612 (s), 1556 (m), 1486 (s), 1423 (s), 1158 (m), 1055 (m), 1034 (m), 987 (m), 847 (w), 823 (s), 741 (s), 698 (w) cm⁻¹. ¹H NMR ([D₆]dmsO): δ = 17.01 (br. s, 2 H, -NH), 8.21 (d, J = 8 Hz, 4 H, H_{Ph}), 8.04 (d, J = 8 Hz, 4 H, H_{Ph}) ppm. MS (FAB): m/z (%) = 289 (37) [M – H]⁺.

4,4'-(Perfluoro-1,4-phenylene)bis(1*H*-1,2,3-triazole-4,1-diyl)bis-(methylene)bis(2,2-dimethylpropanoate) (FBTriMP): Water (3 mL) and *tert*-butyl alcohol (6 mL) were added to a 50 mL round-bottom flask containing 4-diethynyl-2,3,5,6-tetrafluorobenzene (0.17 g, 0.83 mmol) and azidomethyl pivalate (0.29 g, 1.8 mmol). Sodium L-ascorbate (17 mg, 0.042 mmol) and CuSO₄ solution (42 μ L, 0.083 mmol, 1 M) were added under vigorous stirring. The reaction mixture was heated to 60 °C for 16 h, after which time an orange solid was observed. Ice water (10 mL) was added, followed by NH₃ solution (3 mL, 10%). The resultant suspension was stirred for 2 h, and the product was isolated by filtration, washing with water, and drying under vacuum to yield a pale orange powder (0.35 g, 82%). C₂₂H₂₄F₄N₆O₄ (512.46): C 51.56, H 4.72, N 16.40; found C 51.29, H 4.62, N 16.10. IR (neat): $\tilde{\nu}$ = 3093 (w), 2983 (w), 1743 (s), 1490 (s), 1435 (m), 1389 (m), 1355 (w), 1275 (m), 1232 (m), 1116 (vs), 1058 (m), 1035 (s), 999 (m), 972 (s), 915 (m), 873 (w), 826 (m), 790 (m), 763 (m), 725 (w), 674 (w), 631 (w), 584 (w), 532 (w) cm⁻¹. ¹H NMR ([D₆]dmsO): δ = 8.82 (s, 2 H, -CH), 6.46 (s, 4 H, -CH₂), 1.15 [s, 18 H, -C(CH₃)₃] ppm. ¹⁹F NMR ([D₆]dmsO): δ = -140 ppm.

2,3,5,6-Tetrafluoro-1,4-benzeneditriazolate (H₂TFBDTri): Methanol (5 mL) and water (5 mL) were added to FBTriMP (0.55 g, 1.1 mmol) in a 50 mL glass round-bottom flask and vigorously

stirred for 5 h. Water (40 mL) was added, and the mixture was extracted with ether (4 × 20 mL). The aqueous layer was then acidified with an excess of HCl (1 M) to obtain an off-white precipitate. The product was filtered, copiously washed with water, ether, and dichloromethane, and dried under vacuum to afford an off-white powder (0.21 g, 70%). The product can be further purified if necessary from residual copper catalyst by dissolution in aqueous ethylenediamine (15%) followed by precipitation with HCl (1 M) and washing with water, ether, and dichloromethane. IR (neat): $\tilde{\nu}$ = 3098 (br. w), 2883 (br. m), 2784 (br. m), 2661 (br. m), 1474 (s), 1445 (m), 1404 (w), 1348 (w), 1245 (m), 1234 (m), 1203 (m), 1157 (m), 1147 (m), 1081 (m), 1018 (w), 976 (vs), 907 (m), 854 (m), 825 (m), 781 (m), 727 (w), 673 (w), 619 (w) cm^{-1} . ^1H NMR ($[\text{D}_6]\text{dmsO}$): δ = 15.73 (br. s, 2 H, -NH), 8.41 (br. s, 2 H, -CH) ppm. ^{13}C NMR ($[\text{D}_6]\text{dmsO}$): δ = 144 (d, $^1J_{\text{C,F}}$ = 254 Hz, -CF), 134 (s, -C_{Ar}), 125 (br. s, -CH), 110 (s, C_{Tri}) ppm. ^{19}F NMR ($[\text{D}_6]\text{dmsO}$): -135 ppm. MS (HR-ESI): m/z = 284.0438 (100.00%; $^{12}\text{C}_{10}\text{H}_4\text{N}_6\text{F}_4$), 285.0462 (12.16%; $^{12}\text{C}_9^{13}\text{CH}_4\text{N}_6\text{F}_4$).

Cu(MeBDT)(dmf) (1, Cu–MeBDT): H_2MeBDT (9.0 mg, 0.04 mmol) and $\text{CuCl}_2 \cdot 2\text{H}_2\text{O}$ (6.8 mg, 0.04 mmol) were added to a 4 mL scintillation vial. A 1:1 (v/v) mixture of dmf and ethanol (2 mL), and concentrated HCl (20 μL) were added to the solids, and the vial was placed on a hotplate set at 120 °C following tight sealing with a Teflon-lined cap. A blue-purple microcrystalline powder was collected after two days to afford 5.0 mg of product (37%). IR (neat): $\tilde{\nu}$ = 3305 (m, br), 3154 (w), 2977 (w), 1652 (s), 1568 (w), 1475 (w), 1438 (m), 1395 (m), 1364 (w), 1265 (w), 1213 (m), 1156 (m), 1119 (m), 1090 (m), 986 (s), 849 (m), 823 (s) cm^{-1} . Crystals appropriate for single-crystal X-ray diffraction analysis were prepared as follows: A solution of H_2MeBDT (9.0 mg, 0.042 mmol) in dmf (1 mL) was added to a solution of $\text{CuCl}_2 \cdot 2\text{H}_2\text{O}$ (6.8 mg, 0.040 mmol) in methanol (1 mL) in a 4 mL scintillation vial. Concentrated HCl (20 μL , 12 M) was added to the reaction mixture to yield a green solution, which was kept at room temperature for five days. The resulting pale blue rod-shaped crystals were stored in the mother liquor.

Cu(BPDT)(dmf) (2, Cu–BPDT): H_2BPDT (12 mg, 0.041 mmol) and $\text{CuCl}_2 \cdot 2\text{H}_2\text{O}$ (6.8 mg, 0.040 mmol) were added to a 4 mL glass scintillation vial. A 1:1 (v/v) mixture of dmf and methanol (2 mL), and concentrated HCl (20 μL) were added to the solids, and the vial was placed on a hotplate set at 90 °C following tight sealing with a Teflon-lined cap. A blue-purple microcrystalline powder was collected after two days to afford 6.0 mg (37%) of product. IR (neat): $\tilde{\nu}$ = 3317 (m br), 3074 (w), 2915 (w), 2539 (m br), 1673 (s), 1590 (s), 1545 (s), 1424 (m), 1369 (m), 1246 (s), 1126 (m), 1024 (s) cm^{-1} .

Cu(TFBDTri)(dmf) (3, Cu–TFBDTri): $\text{H}_2\text{TFBDTri}$ (8.5 mg, 0.029 mmol) and $\text{CuCl}_2 \cdot 2\text{H}_2\text{O}$ (51 mg, 0.30 mmol) were added to a 4 mL glass scintillation vial. Then, dmf (3 mL) acidified with three drops of HNO_3 (0.2 M) was added to the solids, and the vial was placed on a hotplate set at 80 °C following tight sealing with a Teflon-lined cap. A blue-purple microcrystalline powder was collected after four days by filtration, washing with dmf, and evacuation under vacuum to afford 4 mg of product. This solid is isostructural to the CuBDTri(dmf) C phase,^[9] and its unit cell can be indexed with the same space group, *Imma*, with lattice parameters a = 24.53(2) Å, b = 6.959(7) Å, c = 9.393(7) Å. IR (neat): $\tilde{\nu}$ = 1643 (s), 1488 (s), 1384 (m), 1370 (sh), 1337 (w), 1245 (w), 1223 (w), 1106 (m), 1060 (w), 1021 (w), 974 (vs), 849 (m), 789 (s), 696 (w), 665 (w), 637 (w), 482 (m) cm^{-1} .

Crystal Data for 1-AS: $\text{C}_{13}\text{H}_4\text{CuN}_8\text{O}$, M = 351.79, orthorhombic, *Imma*, a = 22.709(5) Å, b = 7.1180(14) Å, c = 12.828(3) Å, V = 2073.6(8) Å³, T = 100(2) K, λ = 0.71073 Å, Z = 4, ρ = 1.127 g/cm³,

2554 data measured, 470 unique data, R_{int} = 0.0470, $R1$ = 0.0809, $wR2$ = 0.2241 for 470 contributing reflections [$I \geq 2\sigma(I)$], GOF = 0.902. A description of the refinement procedure can be found in the Supporting Information. CCDC-778563 contains the supplementary data for this paper. These data can be obtained free of charge from The Cambridge Crystallographic Data Centre via www.ccdc.cam.ac.uk/data_request/cif.

Other Physical Measurements: Powder X-ray diffraction data was collected by using $\text{Cu-K}\alpha$ radiation (λ = 1.5406 Å) with a Siemens D5000 diffractometer. Indexing of the diffraction patterns for 1–3 was performed within the Bruker EVA software. Single-crystal X-ray diffraction data were collected with a Siemens SMART 1000 diffractometer, and structures were subsequently solved using the SHELXTL 5.0^[17] software package following absorption corrections applied by SADABS.^[18] ^1H NMR spectra were recorded at ambient temperature with Bruker AV-300, AVQ-400, AVB-400, and AV-600 spectrometers, and all chemical shifts are given in relation to residual solvent peaks. Thermogravimetric analyses were carried out with a TA Instruments TGA 2950 instrument at a temperature ramping rate of 4 °C/min under a flow of nitrogen gas. Infrared spectra were collected by using a Nicolet Avatar 360 FTIR spectrometer equipped with an attenuated total reflectance accessory (ATR). Carbon, hydrogen, and nitrogen analyses were performed by the Microanalytical Laboratory at the University of California, Berkeley.

Supporting Information (see footnote on the first page of this article): Powder X-ray diffraction patterns, TGA profiles, and details of the structure refinement procedure.

Acknowledgments

This work was supported by the Center for Gas Separations Relevant to Clean Energy Technologies, an Energy Frontier Research Center funded by the U.S. Department of Energy, Office of Science, Office of Basic Energy Sciences under award number DE-SC0001015, and the Korea Research Foundation Grant funded by the Korean Government (MEST) (KRF-2009-220-C00021). We thank Fulbright New Zealand for partial support of K. S., and Dr. A. G. DiPasquale for helpful discussions.

- [1] a) M. Eddaoudi, J. Kim, N. Rosi, D. Vodak, J. Wachter, M. O’Keeffe, O. M. Yaghi, *Science* **2002**, 295, 469–472; b) R. Matsuda, R. Kitaura, S. Kitagawa, Y. Kubota, R. V. Belosludov, T. C. Kobayashi, H. Sakamoto, T. Chiba, M. Takata, Y. Kawazoe, *Nature* **2005**, 436, 238–241; c) G. Férey, *Chem. Soc. Rev.* **2008**, 37, 191–214; d) R. E. Morris, P. S. Wheatley, *Angew. Chem. Int. Ed.* **2008**, 47, 4966–4981; e) G. Férey, *Dalton Trans.* **2009**, 4400–4415.
- [2] a) A. R. Millward, O. M. Yaghi, *J. Am. Chem. Soc.* **2005**, 127, 17998–17999; b) H. Furukawa, M. A. Miller, O. M. Yaghi, *J. Mater. Chem.* **2007**, 17, 3197–3204; c) S. Ma, D. Sun, J. M. Simmons, C. D. Collier, D. Yuan, H.-C. Zhou, *J. Am. Chem. Soc.* **2008**, 130, 1012–1016; d) P. L. Llewellyn, S. Bourrelly, C. Serre, A. Vimont, M. Daturi, L. Hamon, G. De Weireld, J.-S. Chang, D.-Y. Hong, Y. K. Hwang, S. H. Jhung, G. Férey, *Langmuir* **2008**, 24, 7245–7250; e) L. J. Murray, M. Dincă, J. R. Long, *Chem. Soc. Rev.* **2009**, 38, 1294–1314; f) K. Sumida, M. R. Hill, S. Horike, A. Dailly, J. R. Long, *J. Am. Chem. Soc.* **2009**, 131, 15120–15121.
- [3] a) A. Demessence, D. M. D’Alessandro, M. L. Foo, J. R. Long, *J. Am. Chem. Soc.* **2009**, 131, 8784–8786; b) A. Ö. Yazaydin, R. Q. Snurr, T.-H. Park, K. Koh, J. Liu, M. D. LeVan, A. I. Benin, P. Jakubczak, M. Lanuza, D. B. Galloway, J. J. Low, R. R. Willis, *J. Am. Chem. Soc.* **2009**, 131, 18198–18199; c) D.

- Britt, H. Furukawa, B. Wang, T. G. Glover, O. M. Yaghi, *Proc. Natl. Acad. Sci. USA* **2009**, *106*, 20637–20640.
- [4] a) J. L. C. Rowsell, O. M. Yaghi, *J. Am. Chem. Soc.* **2006**, *128*, 1304–1315; b) S. Pawsey, I. Moudrakovski, J. Ripmeester, L.-Q. Wang, G. J. Exarhos, J. L. C. Rowsell, O. M. Yaghi, *J. Phys. Chem. C* **2007**, *111*, 6060–6067; c) S. S. Kaye, A. Dailly, O. M. Yaghi, J. R. Long, *J. Am. Chem. Soc.* **2007**, *129*, 14176–14177; d) K. K. Tanabe, Z. Wang, S. M. Cohen, *J. Am. Chem. Soc.* **2008**, *130*, 8508–8517.
- [5] a) P. D. C. Dietzel, Y. Morita, R. Blom, H. Fjellvag, *Angew. Chem. Int. Ed.* **2005**, *44*, 6354–6358; b) N. L. Rosi, J. Kim, M. Eddaoudi, B. Chen, M. O’Keeffe, O. M. Yaghi, *J. Am. Chem. Soc.* **2005**, *127*, 1504–1518; c) P. D. C. Dietzel, B. Panella, M. Hirscher, R. Blom, H. Fjellvag, *Chem. Commun.* **2006**, 959–961; d) S. R. Caskey, A. G. Wong-Foy, A. J. Matzger, *J. Am. Chem. Soc.* **2008**, *130*, 10870–10871; e) P. D. C. Dietzel, R. Blom, H. Fjellvag, *Eur. J. Inorg. Chem.* **2008**, 3624–3632; f) W. Zhou, H. Wu, T. Yildirim, *J. Am. Chem. Soc.* **2008**, *130*, 15268–15269.
- [6] a) M. Dincă, A. Dailly, Y. Liu, C. M. Brown, D. A. Neumann, J. R. Long, *J. Am. Chem. Soc.* **2006**, *128*, 16876–16883; b) M. Dincă, W. S. Han, Y. Liu, A. Dailly, C. M. Brown, J. R. Long, *Angew. Chem. Int. Ed.* **2007**, *46*, 1419–1422; c) K. Sumida, S. Horike, S. S. Kaye, Z. R. Herm, W. L. Queen, C. M. Brown, F. Grandjean, G. J. Long, A. Dailly, J. R. Long, *Chem. Sci.*, DOI: 10.1039/c0sc00179a.
- [7] a) E. J. Cussen, J. B. Claridge, M. J. Rosseinsky, C. J. Kepert, *J. Am. Chem. Soc.* **2002**, *124*, 9574–9581; b) S. Kitagawa, R. Kitaura, S.-I. Noro, *Angew. Chem. Int. Ed.* **2004**, *43*, 2334–2375; c) T. K. Maji, G. Mostafa, R. Matsuda, S. Kitagawa, *J. Am. Chem. Soc.* **2005**, *127*, 17152–17153; d) P. L. Llewellyn, S. Bourrelly, C. Serre, Y. Filinchuk, G. Férey, *Angew. Chem. Int. Ed.* **2006**, *45*, 7751–7754; e) A. Kondo, H. Noguchi, L. Carlucci, D. M. Proserpio, G. Ciani, H. Kajiro, T. Ohba, H. Kanoh, K. Kaneko, *J. Am. Chem. Soc.* **2007**, *129*, 12362–12363; f) C. Serre, C. Mellot-Draznieks, S. Surblé, N. Audebrand, Y. Filinchuk, G. Férey, *Science* **2007**, *315*, 1828–1831; g) H. J. Choi, M. Dincă, J. R. Long, *J. Am. Chem. Soc.* **2008**, *130*, 7848–7850; h) S. Horike, S. Shimomura, S. Kitagawa, *Nat. Chem.* **2009**, *1*, 695–704.
- [8] M. Dincă, A. F. Yu, J. R. Long, *J. Am. Chem. Soc.* **2006**, *128*, 8904–8913.
- [9] A. Demessence, J. R. Long, *Chem. Eur. J.* **2010**, *16*, 5902–5908.
- [10] D. W. Breck, *Zeolite Molecular Sieves*, Wiley, New York, **1984**.
- [11] Z. Hulvey, E. H. L. Falcao, J. Eckert, A. K. Cheetham, *J. Mater. Chem.* **2009**, *19*, 4307–4309.
- [12] Y. Akutsu, M. Tamura, *J. Energy Mater.* **1993**, *11*, 205–217.
- [13] R. D. Chambers, *Fluorine in Organic Chemistry*, Blackwell Publishing, Oxford, **2004**.
- [14] T. Devic, P. Horcajada, C. Serre, F. Salles, G. Maurin, B. Moulin, D. Heurtaux, G. Clet, A. Vimont, J.-M. Grenèche, B. Le Ouay, F. Moreau, E. Magnier, Y. Filinchuk, J. Marrot, J.-C. Lavalley, M. Daturi, G. Férey, *J. Am. Chem. Soc.* **2010**, *132*, 1127–1136.
- [15] J. C. Loren, A. Krasinski, V. V. Fokin, K. B. Sharpless, *Synlett* **2005**, *18*, 2847–2850.
- [16] T. X. Neenan, G. M. Whitesides, *J. Org. Chem.* **1988**, *53*, 2489–2496.
- [17] G. M. Sheldrick, *SHELXTL*, version 5.0, Bruker Analytical X-ray Systems, Madison, WI, **1994**.
- [18] G. M. Sheldrick, *SADABS*, version 2.03, Bruker Analytical X-ray Systems, Madison, WI, **2000**.

Received: May 1, 2010

Published Online: July 5, 2010

A Microporous Metal–Organic Framework with Immobilized –OH Functional Groups within the Pore Surfaces for Selective Gas Sorption

Zhenxia Chen,^[a,b] Shengchang Xiang,^[b] Hadi D. Arman,^[b] Peng Li,^[b] Steven Tidrow,^[c] Dongyuan Zhao,^{*[a]} and Banglin Chen^{*[b]}

Keywords: Copper / Microporous materials / Structure elucidation / Immobilization / Adsorption

A new two-dimensional microporous metal–organic framework $\text{Cu}(\text{BDC-OH})(\text{H}_2\text{O}) \cdot 0.5\text{DEF}$ [abbreviation: **Cu(BDC-OH)**; $\text{H}_2\text{BDC-OH}$ = 2-hydroxybenzene-1,4-dicarboxylic acid; DEF = diethylformamide] with functional OH groups on the pore surfaces was solvothermally synthesized and structur-

ally characterized. The activated **Cu(BDC-OH)** exhibits a moderate Langmuir surface of $584 \text{ m}^2 \text{ g}^{-1}$, a pore volume of $0.214 \text{ cm}^3 \text{ g}^{-1}$, and $\text{C}_2\text{H}_2/\text{CH}_4$ and CO_2/CH_4 selectivity of 6.7 and 9.3, respectively, at 296 K, thereby highlighting the promise for its application in gas separation.

Introduction

The past decades have witnessed the rapid development of metal–organic frameworks (MOFs) as a new type of porous material that exhibits great potential for applications in gas storage, gas separation, and catalysis.^[1–8] The richness of metal ions/clusters and organic linkers of diverse geometry and bridging length has enabled us to construct a variety of porous MOFs of different pore structures and porosities.^[9–15] In terms of porous MOFs for selective gas separation, extensive efforts have been made to tune the micropores and thus make use of the pore-size-exclusive effect to target a series of porous MOFs for their selective gas sorption and separation.^[15–34] To immobilize functional groups such as NH_2 and so on within the porous surfaces of some prototypical MOFs so as to ultimately direct their different interactions with the gas substrate, another very promising strategy has recently emerged to enhance gas-separation selectivity.^[35] Herein we report a new microporous MOF, $\text{Cu}(\text{BDC-OH})(\text{H}_2\text{O}) \cdot 0.5\text{DEF}$ [**Cu(BDC-OH)**; $\text{H}_2\text{BDC-OH}$ = 2-hydroxybenzene-1,4-dicarboxylic acid; DEF = diethylformamide], with immobilized OH groups on the pore surfaces for its selective gas sorption of $\text{C}_2\text{H}_2/\text{CH}_4$ and CO_2/CH_4 at room temperature.

Results and Discussion

Single-crystal X-ray diffraction analysis reveals that **Cu(BDC-OH)** crystallizes in the tetragonal space group

$P4/nmm$. **Cu(BDC-OH)** consists of the well-known copper paddle-wheel secondary building unit (SBU),^[36–51] which is bridged by BDC-OH to form 2D microporous layers with the terminal water molecules occupying the fifth position (Figure 1). The framework of **Cu(BDC-OH)** is basically the same as that of the well-known MOF-2 (Figure 2, a),^[40] however, the overall packing is quite different due to the existence of the hydroxy group on BDC-OH. The hydroxy groups of BDC-OH remain uncoordinated and exposed, stretching into the pore space between the 2D layers, and hydrogen bonded to an adjacent coordinated water mole-

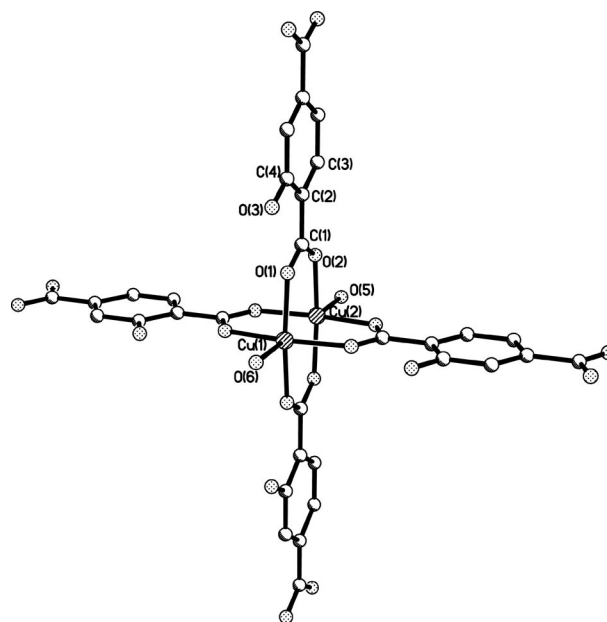


Figure 1. Crystal structure of **Cu(BDC-OH)** indicating the local coordination geometry and the paddle-wheel SBU (hydrogen atoms are omitted for the clarity).

[a] Department of Chemistry, Fudan University, Shanghai 200433, P. R. China
E-mail: dyzhao@fudan.edu.cn

[b] Department of Chemistry, University of Texas at San Antonio, TX 78249-0698, USA
E-mail: banglin.chen@utsa.edu

[c] Department of Physics and Geology, University of Texas-Pan American, TX 78539, USA

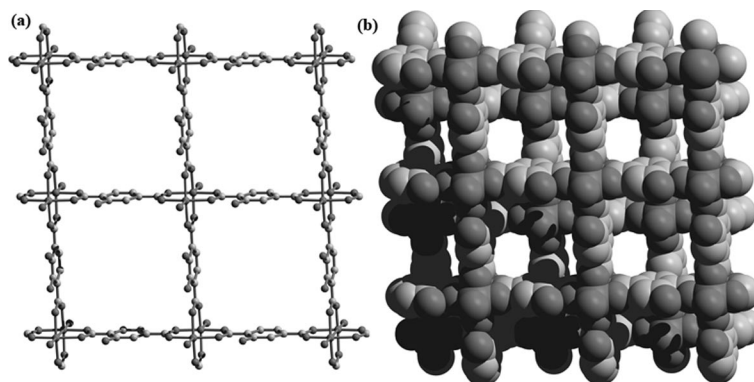


Figure 2. Crystal structure of **Cu(BDC-OH)** indicating (a) one layer viewing along the *c* axis, and (b) pack viewing along the *c* axis represented by space-filling spheres.

cule with an O–H···O distance of 2.50 Å. Because pores within the 2D sheets are partially occupied by the OH groups, the resulting 1D channels along the *c* axis of a size of about 3.0 Å (the pore size is measured with the consideration of van der Waals radius; Figure 2, b) are smaller than that of 5 Å in MOF-2. **Cu(BDC-OH)** has a total solvent-accessible volume of 58.1%, as calculated using the SQUEEZE module of the PLATON routine.

Thermogravimetric analysis (TGA) indicates that **Cu(BDC-OH)** loses the free solvent molecules and the coordinated water molecules up to 200 °C (calcd. weight loss: 22.0%; ext. weight loss: 22.2%), and the desolvated framework is stable at 200 °C (Figures S2 and S3 in the Supporting Information).

The permanent porosity of activated **Cu(BDC-OH)** was confirmed by both gas (N_2 and H_2) and vapor (methanol) adsorption isotherms. A freshly as-synthesized sample was activated under high vacuum at 150 °C overnight before gas adsorption studies. The N_2 adsorption isotherm of the activated **Cu(BDC-OH)** at 77 K shows typical type-I adsorption behavior with the saturated N_2 adsorption amount of about $140 \text{ cm}^3 \text{ g}^{-1}$ at STP, common features of microporous materials (Figure 3, a). The Langmuir and Brunauer–Emmett–Teller (BET) surface areas of the activated **Cu(BDC-OH)** deduced from the N_2 adsorption were 584 and $397 \text{ m}^2 \text{ g}^{-1}$, respectively, and the micropore volume was $0.214 \text{ cm}^3 \text{ g}^{-1}$. The surface areas and pore volume of **Cu(BDC-OH)** are comparable to those of **Cu(BDC)** by Seki^[37] and Carson,^[39] but are more than twice as high as those of **Zn(BDC)** ($270 \text{ m}^2 \text{ g}^{-1}$ and $0.093 \text{ cm}^3 \text{ g}^{-1}$, respectively), partly because the copper paddle-wheel SBUs $\text{Cu}_2(\text{COO})_4$ are more favorable to stabilization of the pore structures than the zinc ones $\text{Zn}_2(\text{COO})_4$, which have been commonly observed in other paddle-wheel-containing MOFs.^[50] The activated **Cu(BDC-OH)** takes up $138 \text{ cm}^3 \text{ g}^{-1}$ (1.12 wt.-%) of H_2 at 77 K and 1 atm. The large amounts of hydroxy groups in **Cu(BDC-OH)** encouraged us to examine the vapor adsorption property for methanol. As expected, it exhibited a type-I adsorption isotherm, thus indicating the excellent accommodation for methanol. The maximum amount of methanol uptake is 12.3 wt.-% at

298 K and 160 mbar, which is equivalent to the adsorption of about one MeOH molecule per formula unit (Figure 3, b).

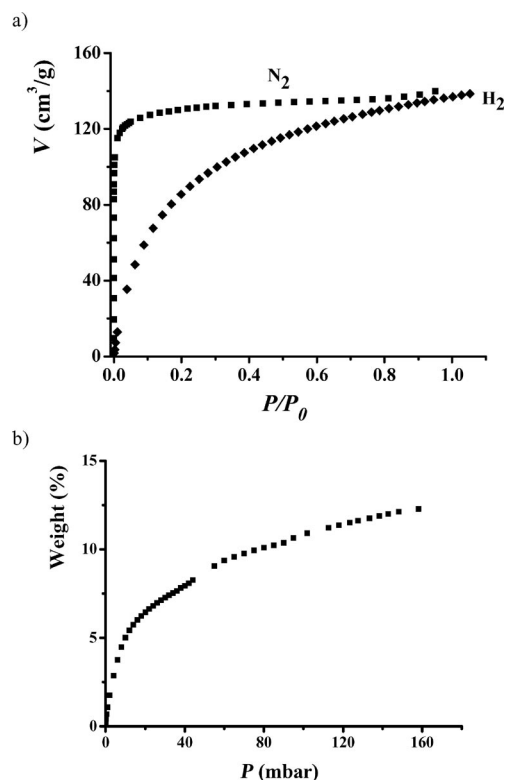


Figure 3. (a) The N_2 and H_2 adsorption isotherms at 77 K, and (b) the methanol sorption isotherm at 298 K for evacuated **Cu(BDC-OH)**.

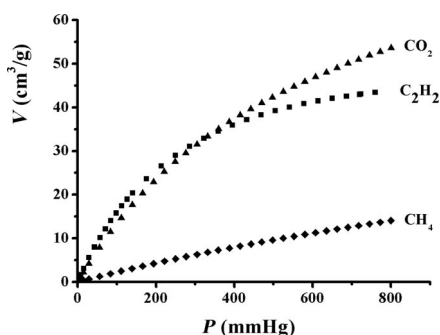
The small micropores and moderate pore volume enabled us to examine the potential application of **Cu(BDC-OH)** for $\text{C}_2\text{H}_2/\text{CH}_4$ and CO_2/CH_4 separation. As shown in Figure 4, **Cu(BDC-OH)** takes up moderate amounts of acetylene ($43 \text{ cm}^3 \text{ g}^{-1}$) and carbon dioxide ($52 \text{ cm}^3 \text{ g}^{-1}$), which are much higher than that of methane ($13 \text{ cm}^3 \text{ g}^{-1}$) at 296 K and 1 atm. The virial graphs for gas adsorption on **Cu(BDC-**

Table 1. Virial graph analyses data for **Cu(BDC-OH)** and its CO₂/CH₄ and C₂H₂/CH₄ separation selectivities.

Adsorbate	<i>T</i> [K]	<i>K_H</i> [mol g ^{−1} Pa ^{−1}]	<i>A</i> ₀ [ln(mol g ^{−1} Pa ^{−1})]	<i>A</i> ₁ [g mol ^{−1}]	<i>R</i> ²	<i>S_{ij}</i> ^[a]	<i>Q</i> _{st} [kJ mol ^{−1}]
CH ₄	273	1.96 × 10 ^{−6}	−13.142 ± 0.005	−366.965 ± 6.592	0.9917		18.5
	296	1.04 × 10 ^{−6}	−13.773 ± 0.001	−457.347 ± 3.110	0.9988		
CO ₂	273	1.69 × 10 ^{−5}	−10.990 ± 0.006	−250.057 ± 7.176	0.9959	8.61	26.2
	296	6.94 × 10 ^{−6}	−11.879 ± 0.003	−256.281 ± 4.974	0.9977	6.65	
C ₂ H ₂	273	1.69 × 10 ^{−5}	−10.990 ± 0.006	−250.057 ± 7.176	0.9959	8.61	25.7
	296	9.66 × 10 ^{−6}	−11.547 ± 0.003	−431.594 ± 7.412	0.9985	9.26	

[a] The Henry's Law selectivity for gas component *i* over CH₄ at the speculated temperature is calculated based on the equation $S_{ij} = K_H(i)/K_H(\text{CH}_4)$.

OH) at 273 and 296 K are shown in Figure S3 of the Supporting Information, and the virial parameters are given in Table 1. The isosteric enthalpies of adsorption ($Q_{\text{st},n=0}$) at zero surface coverage were calculated from the A_0 virial parameters for adsorption data at 273 and 296 K. The values for CH₄, CO₂, and C₂H₂ were 18.5, 26.2, and 25.7 kJ mol^{−1}, respectively. These values are systematically higher than those found in MIL-53 with larger pores.^[35,51] Apparently, the narrow pores within **Cu(BDC-OH)** enforce their stronger interactions with the gas molecules.^[8] The Henry's Law selectivities for CO₂ and C₂H₂ over CH₄, calculated based on the equation $S_{ij} = K_H(i)/K_H(\text{CH}_4)$, are 6.7 and 9.3, respectively, at 296 K, which are moderately high. The CO₂/CH₄ selectivity of 6.7 in **Cu(BDC-OH)** is higher than the one of about 3 in a well-examined microporous MOF-508 for CO₂/CH₄ separation,^[16] thereby highlighting the promising potential of **Cu(BDC-OH)** for this industrially important gas separation. Such enhanced selectivities are attributed to both the size-exclusive molecular sieving effect and their different interactions with the host porous material.

Figure 4. The gas sorption isotherms for evacuated **Cu(BDC-OH)** at 296 K.

Conclusion

In this study, we have successfully synthesized one new microporous metal–organic framework, **Cu(BDC-OH)**, with immobilized –OH functional groups on the pore surfaces. The moderate pore volume and narrow pore sizes would indicate that **Cu(BDC-OH)** is a very promising material for CO₂/CH₄ and C₂H₂/CH₄ separation, which has been experimentally realized by gas adsorption studies.

Experimental Section

Materials and Measurements: All reagents and solvents were used as received from commercial suppliers without further purification. Thermogravimetric analyses (TGA) were performed with a Mettler Toledo TGA/SDTA851 analyzer in air with a heating rate of 5 K min^{−1}, from 30–800 °C. X-ray powder diffraction (XRD) patterns were measured with a Bruker D4 powder diffractometer at 40 kV, 40 mA for Cu-*K_α* radiation ($\lambda = 1.5418 \text{ \AA}$), with a scan speed of 0.2 s per step and a step size of 0.02° (2 θ). The elemental analyses were performed with Perkin–Elmer 240 CHN Analyzers. Surface-area measurements and gas adsorptions were obtained with a Micromeritics ASAP 2020 instrument. A freshly prepared sample of **Cu(BDC-OH)** (66.5 mg) was activated at 423 K under high vacuum for 12 h until the outgas rate was <5 $\mu\text{mHg min}^{-1}$ prior to measurements. The sorption isotherms for methanol were recorded with an automatic gravimetric adsorption apparatus (IGA-003 series, Hiden Isochema Ltd.) at 298 K.

Synthesis of Cu(BDC-OH): Equimolar quantities of Cu(NO₃)₂·2.5H₂O (0.2734 g, 1.2 mmol) and H₂BDC-OH (0.1855 g, 1.0 mmol) were dissolved in mixed solvents of DEF (8 mL) and EtOH (3 mL) in a screw-capped vial. The vial was capped and placed in an oven at 65 °C for 24 h. The green column single crystals were washed with EtOH several times to give **Cu(BDC-OH)**, Cu(BDC-OH)(H₂O)·0.5DEF (0.253 g, yield 81.1%); calcd. C 40.40, H 3.71, N 2.24; found C 40.00, H 3.63, N 2.15.

Single-Crystal X-ray Structure Determination: Intensity data for the reported MOF were collected at 98 K with a Rigaku Saturn724 diffractometer equipped with graphite-monochromated Mo-*K_α* radiation ($\lambda = 0.71073 \text{ \AA}$) using a ω -scan technique. The structure was solved by direct methods and subsequent difference Fourier syntheses, and refined with the SHELXTL software package.^[52,53] The H atoms on the ligand were placed in idealized positions and refined using a riding model. The H atoms of the coordinated H₂O molecules could not be located but are included in the formula. The solvent of DEF also could not be located; we employed PLATON/SQUEEZE to calculate the diffraction contribution of the solvent molecules and thereby produced a set of solvent-free diffraction intensities.^[54]

CCDC-768340 [for solvent-free **Cu(BDC-OH)**] contains the supplementary crystallographic data for this paper. These data can be obtained free of charge from The Cambridge Crystallographic Data Centre via www.ccdc.cam.ac.uk/data_request/cif. The detailed crystallographic data are shown in Tables 2 and 3.

Virial Graph Analyses: Isotherm data were analyzed using the virial equation [Equation (1)]:

$$\ln(n/P) = A_0 + A_1 \cdot n + A_2 \cdot n^2 + \dots \quad (1)$$

Table 2. Crystal data and structure refinement for **Cu(BDC-OH)**.

Empirical formula	C ₈ H ₆ CuO ₆
Formula weight	261.67
Temperature [K]	120(2)
Wavelength [Å]	0.71073
Crystal system	tetragonal
Space group	<i>P4/nmm</i>
Unit cell [Å]	<i>a</i> = <i>b</i> = 10.867(2), <i>c</i> = 16.175(3)
Volume [Å ³]	1910.1(6)
<i>Z</i>	4
Calculated density [Mg m ⁻³]	0.910
Absorption coefficient [mm ⁻¹]	1.146
<i>F</i> (000)	524
Crystal size [mm]	0.20 × 0.10 × 0.10
θ range for data collection [°]	2.26 to 25.09
Limiting indices	−11 ≤ <i>h</i> ≤ 12, −12 ≤ <i>k</i> ≤ 12, −19 ≤ <i>l</i> ≤ 19
Reflections collected / unique	7987 / 1016 [<i>R</i> (int) = 0.0859]
Completeness to θ = 25.09 (%)	98.8
Absorption correction	semiempirical from equivalents
Max. / min. transmission	0.8940 / 0.8033
Refinement method	Full-matrix least-squares on <i>F</i> ²
Data/restraints / parameters	1016/18/61
Goodness-of-fit on <i>F</i> ²	1.064
Final <i>R</i> indices [<i>I</i> > 2 σ (<i>I</i>)]	<i>R</i> 1 = 0.0937, <i>wR</i> 2 = 0.2606
<i>R</i> indices (all data)	<i>R</i> 1 = 0.0975, <i>wR</i> 2 = 0.2669
Largest diff. peak and hole	1.271 and −0.799 e Å ⁻³

Table 3. Selected bond lengths [Å] and angles [°] for **Cu(BDC-OH)**.^[a]

Cu(1)–O(1)	1.977(6)	C(1)–C(2)	1.496(13)
Cu(1)–O(6)	2.161(12)	C(2)–C(4)	1.392(11)
Cu(1)–Cu(2)	2.637(3)	C(2)–C(3)	1.421(14)
Cu(2)–O(2)	1.951(6)	C(3)–O(4)	1.37(3)
Cu(2)–O(5)	2.183(18)	C(3)–C(3)#4	1.38(2)
C(1)–O(1)	1.256(9)	C(4)–O(3)	1.26(2)
C(1)–O(2)	1.265(10)	C(4)–C(4)#4	1.398(18)
O(1)#1–Cu(1)–O(1) #2	89.38(3)	O(1)–C(1)–C(2)	116.6(7)
O(1)#2–Cu(1)–O(1) #3	168.1(3)	O(2)–C(1)–C(2)	118.1(7)
O(1)#2–Cu(1)–O(1)	89.38(3)	C(4)–C(2)–C(3)	119.4(10)
O(1)#1–Cu(1)–O(6)	95.96(15)	C(4)–C(2)–C(1)	120.7(8)
O(1)#1–Cu(1)–Cu(2)	84.04(15)	C(3)–C(2)–C(1)	120.0(8)
O(6)–Cu(1)–Cu(2)	180.0	O(4)–C(3)–C(3)#4	111.7(15)
O(2)#1–Cu(2)–O(2)	168.6(4)	O(4)–C(3)–C(2)	128.1(17)
O(2)#1–Cu(2)–O(2)	89.43(4)	C(3)#4–C(3)–C(2)	120.2(6)
O(2)#3–Cu(2)–O(2) #2	168.6(4)	O(3)–C(4)–C(2)	122.1(16)
O(2)#1–Cu(2)–O(5)	95.7(2)	O(3)–C(4)–C(4)#4	117.4(13)
O(2)#1–Cu(2)–Cu(1)	84.3(2)	C(2)–C(4)–C(4)#4	120.5(5)
O(5)–Cu(2)–Cu(1)	180.000(1)	C(1)–O(1)–Cu(1)	122.8(5)
O(1)–C(1)–O(2)	125.3(8)	C(1)–O(2)–Cu(2)	123.6(6)

[a] Symmetry transformations used to generate equivalent atoms: #1: $-x + \frac{1}{2}, y, z$; #2: $-y + \frac{1}{2}, -x + \frac{1}{2}, z$; #3: $-y + \frac{1}{2}, x, z$; #4: $-x - \frac{1}{2}, y, z$.

in which *P* is pressure, *n* is amount adsorbed, and *A*₀, *A*₁, and so on are virial coefficients. *A*₀ is related to adsorbate–adsorbent interactions, whereas *A*₁ describes adsorbate–adsorbate interactions. The virial graphs for gas adsorption on **1** at 273 and 296 K are shown in Figure S4 in the Supporting Information, and the virial parameters are given in Table 1.

Acknowledgments

This work was supported by the American National Science Foundation (NSF) (Award CHE 0718281) (to B. C.). Z. C. and D. Z. thank for the financial support from the National Natural Science Foundation of China. B. C. and S. T. thank for the financial support from the Department of Defense (DOD) (ARO contract, W911NF-08-1-0353).

- [1] M. Eddaoudi, D. B. Moler, H. Li, B. Chen, T. M. Reineke, M. O'Keeffe, O. M. Yaghi, *Acc. Chem. Res.* **2001**, *34*, 319.
- [2] S. Kitagawa, R. Kitaura, S. Noro, *Angew. Chem. Int. Ed.* **2004**, *43*, 2334.
- [3] C. N. R. Rao, S. Natarajan, R. Vaidhyanathan, *Angew. Chem. Int. Ed.* **2004**, *43*, 1466.
- [4] D. Bradshaw, J. B. Claridge, E. J. Cussen, T. J. Prior, M. J. Rosseinsky, *Acc. Chem. Res.* **2005**, *38*, 273.
- [5] G. Férey, *Chem. Soc. Rev.* **2008**, *37*, 191.
- [6] L. Ma, C. Abney, W. Lin, *Chem. Soc. Rev.* **2009**, *38*, 1248.
- [7] M. P. Suh, Y. E. Cheon, E. Y. Lee, *Coord. Chem. Rev.* **2008**, *252*, 1007.
- [8] K. M. Thomas, *Dalton Trans.* **2009**, 1487.
- [9] T. Wu, X. Bu, R. Liu, Z. Lin, J. Zhang, P. Feng, *Chem. Eur. J.* **2008**, *14*, 7771; J. Zhang, T. Wu, C. Zhou, S. Chen, P. Feng, X. Bu, *Angew. Chem. Int. Ed.* **2009**, *48*, 2542.
- [10] S. L. Qiu, G. S. Zhu, *Coord. Chem. Rev.* **2009**, *253*, 2891.
- [11] M. Eddaoudi, H. Li, O. M. Yaghi, *J. Am. Chem. Soc.* **2000**, *122*, 1391.
- [12] M. O'Keeffe, M. Eddaoudi, H. Li, T. Reineke, O. M. Yaghi, *J. Solid State Chem.* **2000**, *152*, 3.
- [13] L. Pan, K. M. Adams, H. E. Hernandez, X. Wang, C. Zheng, Y. Hattori, K. Kaneko, *J. Am. Chem. Soc.* **2003**, *125*, 3062.
- [14] J. J. Perry IV, J. A. Perman, M. J. Zaworotko, *Chem. Soc. Rev.* **2009**, *38*, 1400.
- [15] X. Lin, I. Telepeni, A. J. Blake, A. Dailly, C. M. Brown, J. M. Simmons, M. Zoppi, G. S. Walker, K. M. Thomas, T. J. Mays, P. Hubberstey, N. R. Champness, M. Schröder, *J. Am. Chem. Soc.* **2009**, *131*, 2159.
- [16] L. Bastin, P. S. Barcia, E. J. J. Hurtado, A. C. Silva, A. E. Rodrigues, B. Chen, *J. Phys. Chem. C* **2008**, *112*, 1575.
- [17] B. Wang, A. P. Côté, H. Furukawa, M. O'Keeffe, O. M. Yaghi, *Nature* **2008**, *453*, 207.
- [18] S. Ma, D. Sun, X. S. Wang, H. C. Zhou, *Angew. Chem. Int. Ed.* **2007**, *46*, 2458; S. Ma, X. S. Wang, C. D. Collier, E. S. Manis, H. C. Zhou, *Inorg. Chem.* **2007**, *46*, 8499; S. Ma, D. Sun, D. Yuan, X. S. Wang, H. C. Zhou, *J. Am. Chem. Soc.* **2009**, *131*, 6445; S. Ma, D. Yuan, X. S. Wang, H. C. Zhou, *Inorg. Chem.* **2009**, *48*, 2072; S. Ma, X. S. Wang, D. Yuan, H. C. Zhou, *Angew. Chem. Int. Ed.* **2008**, *47*, 4130; J. R. Li, R. J. Kuppler, H. C. Zhou, *Chem. Soc. Rev.* **2009**, *38*, 1477.
- [19] Y. E. Cheon, M. P. Suh, *Chem. Commun.* **2009**, 2296.
- [20] B. Chen, C. Liang, J. Yang, D. S. Contreras, Y. L. Clancy, E. B. Lobkovsky, O. M. Yaghi, S. Dai, *Angew. Chem. Int. Ed.* **2006**, *45*, 1390; B. Chen, S. Ma, F. Zapata, F. R. Fronczek, E. B. Lobkovsky, H. C. Zhou, *Inorg. Chem.* **2007**, *46*, 1233; B. Chen, S. Ma, E. J. Hurtado, E. B. Lobkovsky, H. C. Zhou, *Inorg. Chem.* **2007**, *46*, 8490; B. Chen, S. Ma, E. J. Hurtado, E. B. Lobkovsky, C. Liang, H. Zhu, S. Dai, *Inorg. Chem.* **2007**, *46*, 8705; P. S. Barcia, F. Zapata, J. A. C. Silva, A. E. Rodrigues, B. Chen, *J. Phys. Chem. B* **2007**, *111*, 6101; B. Chen, X. Zhao, A. Putkham, K. Hong, E. B. Lobkovsky, E. J. Hurtado, A. J. Fletcher, K. M. Thomas, *J. Am. Chem. Soc.* **2008**, *130*, 6411; M. Xue, S. Q. Ma, Z. Jin, R. M. Schaffino, G.-S. Zhu, E. B. Lobkovsky, S.-L. Qiu, B. Chen, *Inorg. Chem.* **2008**, *47*, 6825; M. Xue, Z.-J. Zhang, S.-C. Xiang, Z. Jin, C. Liang, G.-S. Zhu, S.-L. Qiu, B. Chen, *J. Mater. Chem.* **2010**, *20*, 3984.
- [21] L. Pan, B. Parker, X. Huang, D. H. Olson, J. Lee, J. Li, *J. Am. Chem. Soc.* **2006**, *128*, 4180; L. Pan, D. H. Olson, L. R. Ciemolonski, R. Heddy, J. Li, *Angew. Chem. Int. Ed.* **2006**, *45*, 616.

- [22] D. N. Dybtsev, H. Chun, S. H. Yoon, D. Kim, K. Kim, *J. Am. Chem. Soc.* **2004**, *126*, 32; H. Kim, D. G. Samsonenko, M. Yoon, J. W. Yoon, Y. K. Hwang, J. S. Chang, K. Kim, *Chem. Commun.* **2008**, 4697; D. G. Samsonenko, H. Kim, Y. Sun, G.-H. Kim, H.-S. Lee, K. Kim, *Chem. Asian J.* **2007**, *2*, 484.
- [23] R. Kitaura, K. Seki, G. Akiyama, S. Kitagawa, *Angew. Chem. Int. Ed.* **2003**, *42*, 428.
- [24] R. Matsuda, R. Kitaura, S. Kitagawa, Y. Kubota, R. V. Belosludov, T. C. Kobayashi, H. Sakamoto, T. Chiba, M. Takata, Y. Kawazoe, Y. Mita, *Nature* **2005**, *436*, 238.
- [25] D. Tanaka, M. Higuchi, S. Horike, R. Matsuda, Y. Kinoshita, N. Yanai, S. Kitagawa, *Chem. Asian J.* **2008**, *3*, 1343.
- [26] J.-P. Zhang, X.-M. Chen, *J. Am. Chem. Soc.* **2009**, *131*, 5516; A. X. Zhu, J. B. Lin, J.-P. Zhang, X.-M. Chen, *Inorg. Chem.* **2009**, *48*, 3882.
- [27] Z. X. Chen, X. C. Xiang, D. Y. Zhao, B. Chen, *Cryst. Growth Des.* **2009**, *9*, 5293.
- [28] M. Dinca, J. R. Long, *J. Am. Chem. Soc.* **2005**, *127*, 9376.
- [29] S. Bourrelly, P. L. Llewellyn, C. Serre, F. Millange, T. Loiseau, G. Férey, *J. Am. Chem. Soc.* **2005**, *127*, 13519.
- [30] J. A. R. Navarro, E. Barea, J. M. Salas, N. Masciocchi, S. Galli, A. Sironi, C. O. Ania, J. B. Parra, *Inorg. Chem.* **2006**, *45*, 2397.
- [31] Y. S. Bae, O. K. Farha, A. M. Spokoyny, C. A. Mirkin, J. T. Hupp, R. Q. Snurr, *Chem. Commun.* **2008**, 4135; Y. S. Bae, O. K. Farha, J. T. Hupp, R. Q. Snurr, *J. Mater. Chem.* **2009**, *19*, 2131.
- [32] S. M. Humphrey, J. S. Chang, S. H. Jung, J. W. Yoon, P. T. Wood, *Angew. Chem. Int. Ed.* **2007**, *46*, 272.
- [33] J. R. Li, Y. Tao, Q. Yu, X. H. Bu, H. Sakamoto, S. Kitagawa, *Chem. Eur. J.* **2008**, *14*, 2771.
- [34] R. Banerjee, H. Furukawa, D. Britt, C. Knobler, M. O'Keeffe, O. M. Yaghi, *J. Am. Chem. Soc.* **2009**, *131*, 3875.
- [35] S. Couck, J. F. M. Denayer, G. V. Baron, T. Rémy, J. Gascon, F. Kapteijn, *J. Am. Chem. Soc.* **2009**, *131*, 6326.
- [36] W. Mori, S. Takamizawa, *J. Solid State Chem.* **2000**, *152*, 120.
- [37] K. Seki, S. Takamizawa, W. Mori, *Chem. Lett.* **2001**, *30*, 122.
- [38] R. Kitaura, F. Iwahori, R. Matsuda, S. Kitagawa, Y. Kubota, M. Takata, T. C. Kobayashi, *Inorg. Chem.* **2004**, *43*, 6522.
- [39] C. G. Carson, K. Hardcastle, J. Schwartz, X. Liu, C. Hoffmann, R. A. Gerhardt, R. Tannenbaum, *Eur. J. Inorg. Chem.* **2009**, 2338.
- [40] H. Li, C. E. Davis, T. L. Groy, D. G. Kelley, O. M. Yaghi, *J. Am. Chem. Soc.* **1998**, *120*, 2186.
- [41] S. S. Y. Chui, S. M. F. Lo, J. P. H. Charmant, A. G. Orpen, L. D. Williams, *Science* **1999**, *283*, 1148.
- [42] M. Eddaoudi, J. Kim, J. B. Wachter, H. K. Chae, M. O'Keeffe, O. M. Yaghi, *J. Am. Chem. Soc.* **2001**, *123*, 4368; J. Kim, B. Chen, T. M. Reineke, H. Li, M. Eddaoudi, D. B. Moler, M. O'Keeffe, O. M. Yaghi, *J. Am. Chem. Soc.* **2001**, *123*, 8293; M. Eddaoudi, J. Kim, M. O'Keeffe, O. M. Yaghi, *J. Am. Chem. Soc.* **2002**, *124*, 376–377; M. Eddaoudi, J. Kim, D. Vodak, A. Sudik, J. Wachter, M. O'Keeffe, O. M. Yaghi, *Proc. Natl. Acad. Sci. USA* **2002**, *99*, 4900.
- [43] B. Rather, M. J. Zaworotko, *Chem. Commun.* **2003**, 830.
- [44] L. Feng, Z. X. Chen, T. B. Liao, P. Li, Y. Jia, X. F. Liu, Y. T. Yang, Y. M. Zhou, *Cryst. Growth Des.* **2009**, *9*, 1505.
- [45] A. Pichon, C. M. Fierro, M. Nieuwenhuyzen, S. L. James, *Cry-stEngComm* **2007**, *9*, 449.
- [46] Z. Q. Wang, V. C. Kravtsov, R. B. Walsh, M. J. Zaworotko, *Cryst. Growth Des.* **2007**, *7*, 1154.
- [47] H. Kumagai, M. Akita-Tanaka, K. Inoue, K. Takahashi, H. Kobayashi, S. Vilminot, M. Kurmoo, *Inorg. Chem.* **2007**, *46*, 5949.
- [48] S. Horike, S. Hasegawa, D. Tanaka, M. Higuchi, S. Kitagawa, *Chem. Commun.* **2008**, 4436.
- [49] P. Kanoo, R. Matsuda, M. Higuchi, S. Kitagawa, T. K. Maji, *Chem. Mater.* **2009**, *21*, 5860.
- [50] Y.-G. Lee, H. R. Moon, Y. E. Cheon, M. P. Suh, *Angew. Chem. Int. Ed.* **2008**, *47*, 7741.
- [51] S.-C. Xiang, W. Zhou, J. M. Gallegos, Y. Liu, B. Chen, *J. Am. Chem. Soc.* **2009**, *131*, 12415.
- [52] G. M. Sheldrick, *SADABS, Program for Empirical Absorption Correction of Area Detector Data*, University of Göttingen, Göttingen, Germany, **1996**.
- [53] G. M. Sheldrick, *SHELXS 97, Program for Crystal Structure Refinement*, University of Göttingen, Göttingen, Germany, **1997**.
- [54] A. L. Spek, *PLATON, A Multipurpose Crystallographic Tool*, Utrecht University, The Netherlands, **2006**.

Received: March 29, 2010
Published Online: June 14, 2010

Crystal Engineering of Three Net-to-Net Intersecting Metal–Organic Frameworks from Two Comparable Organic Linking Squares

Tien-Wen Tseng,^{*,[a]} Tzuoo-Tsair Luo,^[b] Cheng-Chuan Tsai,^[a,b] Jing-Yun Wu,^[b] Hui-Lien Tsai,^[c] and Kuang-Lieh Lu^[b]

Keywords: Crystal engineering / Metal-organic frameworks / Self-assembly / Topochemistry

The syntheses and structures of three mixed-ligand metal–organic frameworks (MOFs), $\{[M_2(\text{btec})(\text{bpym})(\text{H}_2\text{O})_4] \cdot 4\text{H}_2\text{O}\}_n$ [$M = \text{Cu}$ (**1**), Ni (**2**)] and $[\text{Zn}_4(\text{btec})_2(\text{bpym})(\text{H}_2\text{O})_6]_n$ (**3**) (btec = benzene-1,2,4,5-tetracarboxylate, bpym = 5,5'-bipyrimidine) are described. MOFs **1** and **2** feature 3D grid-type frameworks with a **cds**-type topology, which are comprised of two mutually intersecting $M(\text{btec})$ -based and $M(\text{bpym})$ -based 4^4 -**sql** layers. MOF **3** consists of an anionic 3D (4,4)-connected **pts** network that is intersected by cationic hydrogen-bonded 4^4 -**sql** layers, $[(\text{H}_2\text{O})_3\text{Zn}(\mu\text{-anti-}\eta^2\text{-bpym})\text{-Zn}(\text{H}_2\text{O})_3]^{4+}$, thereby giving rise to a 3D network. The struc-

tural diversities between the two types of MOF architectures can be attributed to the coordination geometry preference of the metal ions (square planar for Cu^{II} and Ni^{II} and tetrahedral for Zn^{II}). In addition, temperature-controlled X-ray powder diffraction studies reveal that MOF **1** possesses reversible desorption/sorption properties upon the removal/uptake of water molecules. The magnetic behavior of **1** was investigated in the 2–300 K range. The data indicate the presence of weak antiferromagnetic interactions between the two Cu^{II} metal centers that are bridged by a pyrimidine ring.

Introduction

Logical methodologies for the assembly of metal–organic frameworks (MOFs) from selected molecular precursors with defined shape and connectivity have led to significant advances in materials science.^[1] Thanks to effective design and synthesis strategies, MOF materials not only have useful properties for applications that range from gas storage to drug delivery, but they also show many intriguing topological structures.^[2,3] Conceptually, nothing is impossible in the realm of MOF materials, just as a notable dictum goes, “The limits are in our imagination.”^[1c] Also inspired by nature, the greater the chemical versatility, the more complicated the framework.^[4] Thus, to produce interesting MOF materials, more creative approaches to their preparation are critical and urgent.^[5] The extent of those creative approaches and how achievable their results currently remain a challenge and will require considerable imagination.^[4,6]

Herein we employ a useful net-to-net intersecting strategy^[3a] for the assembly of three new MOFs from anionic benzene-1,2,4,5-tetracarboxylate (btec), neutral 5,5'-bipyrimidine (bpym) ligands, and divalent transition-metal ions (Cu^{II} , Ni^{II} , and Zn^{II}) under mild self-assembly reaction conditions. Both of the btec and bpym ligands, in spite of their simplicity, are versatile organic scaffolds and are suitable for use as variable linkers.^[7–9] In particular, because btec is comparable to bpym in size, their combination will result in the formation of new MOF structures. As shown in Scheme 1, $\{[M_2(\text{btec})(\text{bpym})(\text{H}_2\text{O})_4] \cdot 4\text{H}_2\text{O}\}_n$ [$M = \text{Cu}$ (**1**), Ni (**2**)] belongs to a 4^4 -**sql**-to- 4^4 -**sql** intersecting network, in which all of the building blocks serve as four-connected square-planar moieties, thereby giving rise to a neutral 3D network with a $6^5.8$ -**cds**-type topology.^[10,11] The known **cds**-type MOFs are currently mainly constructed from flexible linear ligands, and their networks tend to be highly distorted.^[12] To the best of our knowledge, such a **cds**-type network that consists of three distinct square nodes is rare.^[11–14] $[\text{Zn}_4(\text{btec})_2(\text{bpym})(\text{H}_2\text{O})_6]_n$ (**3**) is a novel case and similar to our earlier reported structure, $[\text{Zn}_4(\text{btec})_2(\text{H}_2\text{O})_6]_n$, which comprises a 3D (4,4)-connected **pts** network.^[7] Interestingly, MOF **3** features the cationic hydrogen-bonded 4^4 -**sql** layer, $[(\text{H}_2\text{O})_3\text{Zn}(\mu\text{-anti-}\eta^2\text{-bpym})\text{-Zn}(\text{H}_2\text{O})_3]^{4+}$, which is connected to the prototypical **pts** net by means of a unique 3D-to-2D subnet-intersecting system. The diversities between the two types of MOF structures can be attributed to the preference of the coordination geometries of the metal ions. Although the btec and bpym ligands have individually been applied in the MOF systems,^[7–9] since their inception, the use of these two comparably sized building blocks has not yet been fully explored. Surprisingly, the results of the present studies reveal that

[a] Department of Chemical Engineering, National Taipei University of Technology, Taipei 106, Taiwan
Fax: +886-2-2776-2383
E-mail: fl0403@ntut.edu.tw

[b] Institute of Chemistry, Academia Sinica, Taipei 115, Taiwan

[c] Department of Chemistry, National Cheng Kung University, Tainan 701, Taiwan

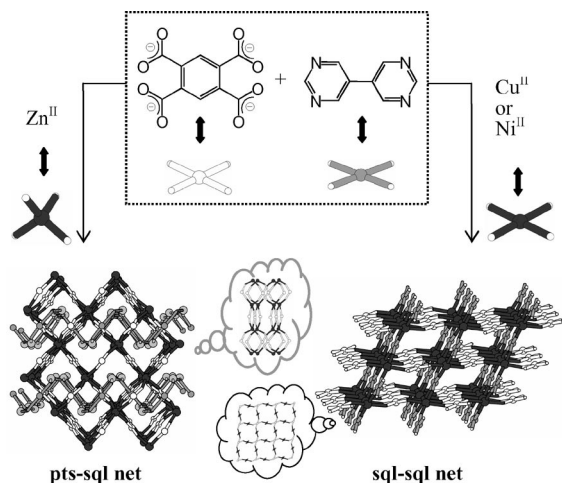
Supporting information for this article is available on the WWW under <http://dx.doi.org/10.1002/ejic.201000291>.

their combination results in a strong tendency to form a 3D network with a net-to-net intersecting system, which is a very suitable method for the realization of new and intriguing MOF structures.^[3]

Results and Discussion

Synthesis

Compound **1** was synthesized in high yield (78%) by reaction of copper chloride, K_4btec , and bpym in a water/THF/MeOH diffusion system at room temperature (Scheme 1). The reasons for combining btec, bpym, and Cu^{II} together are fourfold: (1) the anionic btec ligand is comparable to the ancillary neutral bpym moiety in both shape and size; (2) both the ligands are able to be coordinated in similar distorted square-planar geometries; (3) a neutral framework can be constructed from multiple aromatic components; (4) all of the moieties tend to act as square building units, thereby leading to the target default nets, such as 4^4 -**sql**, $6^4.8^2$ -**nbo**, and $6^5.8$ -**cds** nets.^[3a,11] Blue-green crystals of $\{[Ni_2(btec)(bpym)(H_2O)_4] \cdot 4H_2O\}_n$ (**2**) and pale-yellow crystals of $[Zn_4(btec)_2(bpym)(H_2O)_6]_n$ (**3**) were also easily synthesized under similar reaction conditions using the same molar ratios of reactants, except that $NiCl_2 \cdot 2H_2O$ or $ZnCl_2$ were used instead.



Scheme 1. Schematic representation of the assembly of compounds **1–3** shows the characteristic 3D frameworks with the distinct net-to-net intersecting system.

Structural Analysis

Single-crystal X-ray diffraction analyses revealed that compounds **1** and **2** are isomorphous and crystallized in the monoclinic space group $C2/c$. Therefore, only the structure of **1** is discussed in detail. The asymmetric unit of **1** consists of one copper(II) center, one-half of the btec ligand, one-half of the bpym ligand, and two coordinated water molecules; the others are disordered water molecules. The Cu^{II} center is bound to two oxygen atoms from two different

btec ligands, two nitrogen atoms from the two bpym ligands, and two water oxygen atoms in a slightly distorted octahedral *trans,trans,trans*- $CuN_2O_2Ow_2$ coordination geometry (Figure 1). The Cu^{II} center can be considered a four-connected square-planar node. The btec ligand coordinates to four Cu^{II} centers by means of a 1,2,4,5-coordination mode and serves as a four-connecting node with a slightly distorted square-planar geometry. Moreover, the bpym ligand also connects to four Cu^{II} centers and adopts a four-connecting node in a more perfect square-planar mode (Figure 1).

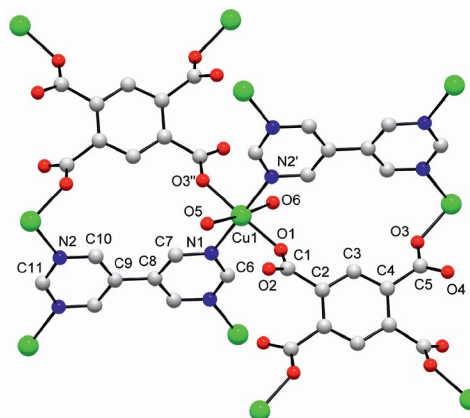


Figure 1. Coordination environments of the Cu^{II} center and the btec and bpym ligands. Hydrogen atoms are omitted for clarity (Cu: green, C: gray, O: red, N: blue).

Analysis using the TOPOS software package shows that the network of **1** has a $6^5.8$ -**cds** topology that is similar to the structure of $CdSO_4$.^[10] To better appreciate and obtain greater insight into this intriguing MOF, rather than analyzing the overall networks through the connectivity of the individual nodes, a new strategy based on the consideration of the structures as combinations of intersected 2D sheets or subnet tectons has recently been proposed by Hill et al.^[3i] Using the subnet tecton approach, the structure of **1** can be appropriately depicted. As shown in Figure 2, if only the connections of the Cu^{II} centers and the btec ligands are considered, a 2D $Cu_2(btec)$ -based sheet appears in the *bc* plane; similarly, a 2D $Cu_2(bpym)$ -based sheet is apparent in the *ab* plane. Both the $Cu_2(btec)$ - and $Cu_2(bpym)$ -based sheets adopt a gridlike 4^4 -**sql** topology by utilizing the organic ligands as four-connected nodes and the Cu^{II} centers as linear linkers.

Unlike the four-connected **nbo** and eight-connected **bcu** nets that are a dual pair, the **cds** net is self-dual. It would be expected that the **cds**-type MOFs easily tend to be interpenetrated.^[11b] It is noteworthy that compound **1** is not only noninterpenetrated but also shows a distinct 1D channel. This result may be attributed to the suitable combination of the two square organic scaffolds.

This framework can also be regarded as a structure that is constructed from two distinct 4^4 -nets, which are mutually pillared to each other, thus giving rise to a porous and ordered material.^[3h] Unlike the body-centered cubic and α -polonium frameworks, the centers of each parallel 4^4 -net in

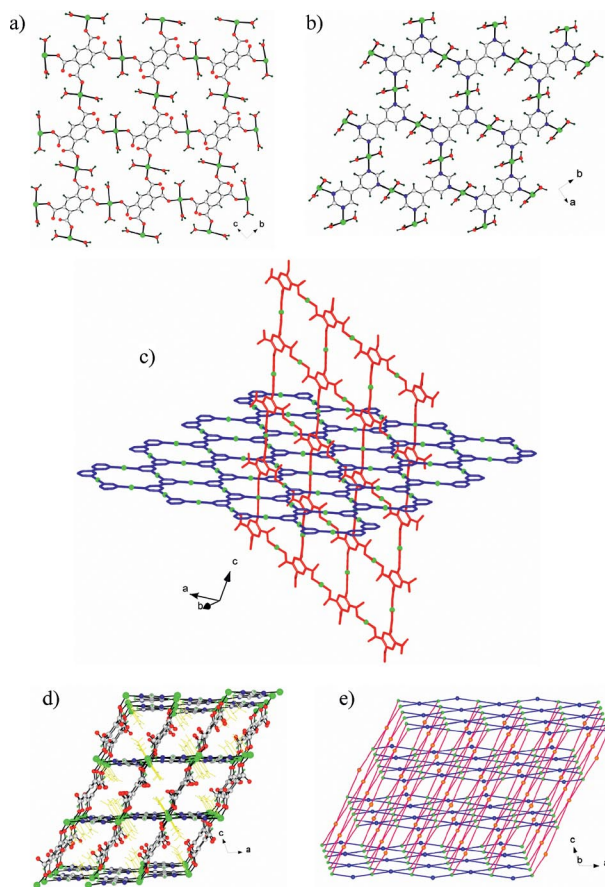


Figure 2. The distinct motifs in **1**: (a) the $\text{Cu}_2(\text{btec})$ -based 4^4-sql grids; (b) the $\text{Cu}_2(\text{bpym})$ -based 4^4-sql grids; (c) the sq1-sq1 intersecting system; (d) view of the available channel along the b axis; (e) the simplified cds net.

1 provide no links to the centers of adjacent nets.^[14] On the other hand, the two distinct gridlike 2D sheets intersect with a cross angle of 107.26° , which is the same as the β angle of the unit cell, through the interconnections of the Cu^{II} centers (Figure 2d).

Compound **3** possesses an entirely different three-dimensional polymeric architecture compared with that of compounds **1** and **2**. The asymmetric unit of **3** consists of crystallographically distinct Zn^{II} centers, one btec ligand, one-half of the bpym ligand, and three coordinated water molecules. As shown in Figure 3, the tetrahedrally coordinated Zn^{II} center has a ZnO_4 core with $\text{Zn-O}_{\text{COO}^-}$ bond lengths of $1.958(10)$ – $2.46(2)$ Å. The octahedrally coordinated Zn^{II} center shows a $\text{fac-ZnNO}_2(\text{OH}_2)_3$ core: one N_{bpym} [Zn-N , $2.171(13)$ Å], two O_{COO^-} atoms [Zn-O , $2.075(10)$ – $2.109(10)$ Å] from two btec ligands, as well as three water molecules [Zn-O , $2.069(11)$ – $2.153(11)$ Å]. The btec ligands exist in two types of μ_6 bridging modes: one involves paired monodentate and paired bidentate carboxylate groups in *para* positions, respectively (Scheme 2, mode B), whereas the other has one pair of *ortho*-positioned monodentate and one pair of *ortho*-positioned bidentate carboxylate groups (Scheme 2, mode C). The btec ligands, both modes B and C, serve as elongated square-planar nodes to connect to the

$\text{Zn}(\text{O}_2\text{C})_4$ tetrahedral nodes, thereby giving rise to an anionic (4,4)-connected MOF, $[\text{Zn}_2(\text{btec}^{\text{B}})(\text{btec}^{\text{C}})]^{4-}$ (or $[\text{Zn}_2(\text{btec})_2]^{4-}$), a topologically $6^4.8^2\text{-pts}$ -type network (Figure 3b).^[11] When viewed along the crystallographic b axis, rhombic windows with a Zn-to-Zn cross section of 9.72×10.89 Å² are apparent.

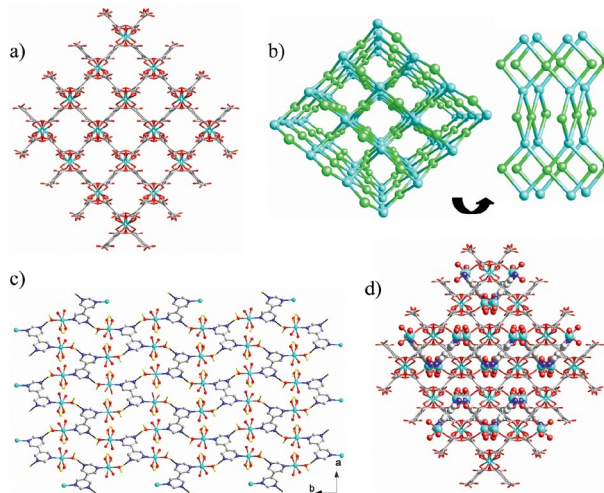
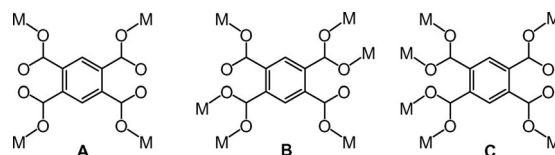
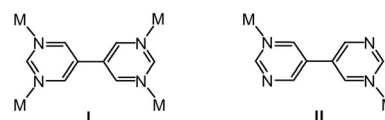


Figure 3. (a) View of the (4,4)-connected net of $[\text{Zn}_2(\text{btec})_2]^{4-}$ in **3**. (b) Simplified representations of the (4,4)-connected network of $[\text{Zn}_2(\text{btec})_2]^{4-}$ in **3** showing the pts net topology. (c) The hydrogen-bonded sheet of $[(\text{H}_2\text{O})_3\text{Zn}(\mu\text{-anti-}\eta^2\text{-bpym})\text{Zn}(\text{H}_2\text{O})_3]^{4+}$ in the ab plane. (d) The whole structure of **3** in wires/sticks representation; the dinuclear $[(\text{H}_2\text{O})_3\text{Zn}(\mu\text{-anti-}\eta^2\text{-bpym})\text{Zn}(\text{H}_2\text{O})_3]^{4+}$ moieties are shown in ball-and-stick models (Zn: cyan, O: red, N: blue, C: gray, H: yellow).



Scheme 2. Coordination modes of the btec ligand in **1** and **2** (A) as well as in **3** (B and C).

The bpym ligand is $\mu\text{-anti-}\eta^2$ -bidentate to bridge two $\text{fac-Zn}(\text{H}_2\text{O})_3$ cores (Scheme 3, mode II), thereby leading to a dinuclear $[(\text{H}_2\text{O})_3\text{Zn}(\mu\text{-anti-}\eta^2\text{-bpym})\text{Zn}(\text{H}_2\text{O})_3]^{4+}$ moiety, which extends to a cationic undulating supramolecular 2D sheet with a (4,4)-topology in the ab plane through hydrogen-bonded interactions between the coordinated water molecules and the pyrimidyl groups [$\text{O}\cdots\text{N}$ $2.749(19)$ Å] (Figure 3c). Through directed Zn–carboxylate donating bonds [Zn-O $2.075(10)$ – $2.109(10)$ Å], the cationic sheets intersect with the anionic (4,4)-connected pts net,



Scheme 3. Coordination modes of the bpym ligand in **1** and **2** (I) as well as in **3** (II).

which is stabilized by water⋯carboxylate interactions [O⋯O 2.721(14)–2.999(16) Å], thereby resulting in a three-dimensional network (Figure 3d).

The structure of compound **3** is similar to those of MOFs, $\{A_2[Zn(btec)] \cdot 8H_2O\}_n$ ($A = K, NH_4$) and $\{K_2[Co(btec)] \cdot 7H_2O\}_n$,^[7] prepared using $[(H_2O)_3Zn(\mu\text{-anti-}\eta^2\text{-bpym})Zn(H_2O)_3]^{4+}$ moieties instead of K^+ or NH_4^+ ions as counteranions. All of them exhibited a topological (4,4)-connected **pts** network that combined both tetrahedral (metal ions) and distorted square-planar (btec ligands) connectors.

Thermal Stability and Removal of Guests

A thermogravimetric analysis (TGA) of **1** shows that guest water molecules are readily eliminated from the network (calcd. 21.0%; found 20.1%) when the temperature is increased from room temperature to about 70 °C, and a wide plateau then appears up to a temperature of about 250 °C, beyond which the compound decomposes. A powder X-ray diffraction (PXRD) study shows that the simulated peaks of **1** are in good agreement with those of the as-synthesized sample. When the temperature was maintained at 110 °C, even 200 °C, the PXRD patterns of the totally dehydrated crystalline samples are different from the original patterns. Moreover, when the dehydrated crystals were exposed to moist air, the original PXRD pattern of **1** was recovered. This indicates that the framework of **1** is bistable and can undergo a reversible crystal-to-crystal structural transformation upon the removal/uptake of water molecules (Figure 4).^[3c,15] This phenomenon can be attributed to the unique **cds**-type framework that can be tuned slightly by changing the sheet-to-sheet intersecting angles.

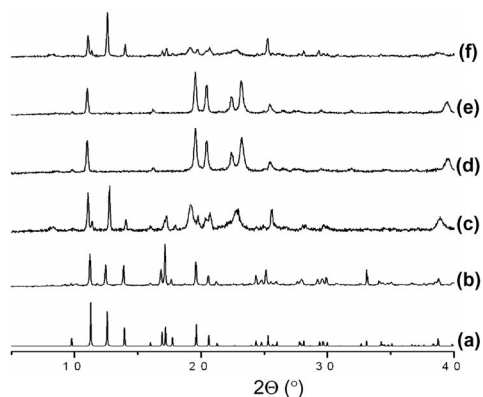


Figure 4. Powder X-ray diffraction patterns of **1**: (a) simulated; (b) as-synthesized at room temperature, (c) 45 °C, (d) 110 °C, and (e) 200 °C; (f) the dehydrated sample (e) after exposure to the moist air for 24 h.

Magnetic Studies

The magnetic susceptibility of **1** was determined as a function of temperature in the range 2–300 K. The plot of χ_M^{-1} versus T has a negative intercept, for which data be-

tween 130 K < T < 300 K were considered to fit (Figure 5). This permitted us to obtain the value for the Weiss constant, $\theta = -36.435$ K. The slope of the curve corresponds to a Curie constant of $C = 0.3069$ emu mol⁻¹ K, from which a magnetic moment of 1.47 μ_B per copper atom was calculated after the subtraction of the Pascal diamagnetic contribution is 3.71×10^{-4} emu mol⁻¹. The magnetic moment of **1** at room temperature for **1** is less than the spin-only value and suggests the presence of antiferromagnetic exchange. In this compound, μ_{eff} remains practically constant in the temperature range of 130–300 K and then falls rapidly with a further decrease in temperature (Figure 5), thereby showing paramagnetic behavior in the first zone and weak antiferromagnetic interactions at lower temperatures. As the temperature is lowered, χ increases until a maximum is reached at approximately 4.5 K, thereby indicating the existence of antiferromagnetic interactions between the Cu^{II} centers.

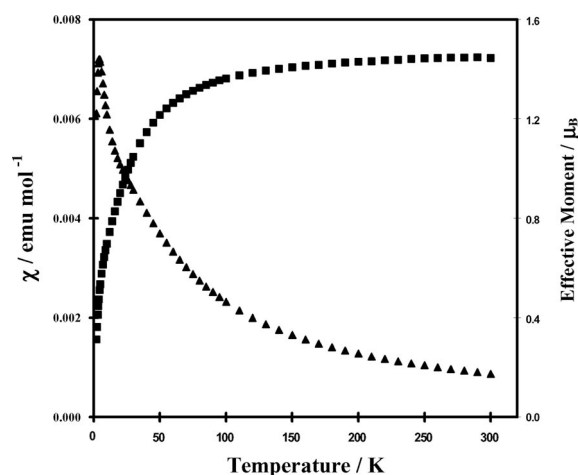


Figure 5. Inverse of molar susceptibility (▲) and effective magnetic moment (■) per copper(II) ion versus temperature curves for **1**.

In the crystal packing, the tetranuclear moieties $[Cu_4(\text{bpym})_{4/4}]$ are interconnected, and contain two dinuclear $[Cu_2(\text{pym})]$ units bridged by two bpym ligands, and, in each dinuclear moiety, two copper(II) centers are bridged by the pyrimidine ring. As a result, in the case of **1**, two different coupling constants must be taken into account. However, these two values cannot be determined separately by a fitting procedure.^[15] Consequently, the tetranuclear moieties can be described magnetically as dimeric. The observed data for **1** were therefore fitted to the modified Bleaney–Bowers equation (see Figure S1 in the Supporting Information), which is used for copper dimers.^[17] The good quality of the fits to the dimer equation showed that the tetranuclear moieties can be considered as being composed of two weakly associated pairs of dimers. The fit for the data resulted in a J value of (-13.3 ± 0.2) cm⁻¹, which is indicative of weak antiferromagnetic coupling between the metal centers in **1**. The small $-J$ value observed for **1** is as pre-

dicted, given the absence of a Cu–Cu bond or a direct single-atom bridge between the Cu^{II} metal centers.^[18] In **1**, the only connection between the Cu^{II} metal centers is through a five-atom π -conjugated bridge.

Conclusion

In conclusion, we successfully exploited an effective net-to-net intersecting methodology to prepare three novel metal–organic frameworks from two distinct square-planar building units under mild conditions. Using the subnet tectonic approach, these 3D MOFs can be appropriately described as 4⁴-sql-to-4⁴-sql and 6⁴.8²-nbo-to-4⁴-sql net-to-net intersecting networks, respectively. In addition, as a result of the specific intersected network, compound **1** shows a crystal-to-crystal structural transformation upon the removal/uptake of water molecules. Magnetic measurements of **1** indicated the presence of weak antiferromagnetic interactions between two adjacent Cu^{II} centers bridged by the pyrimidine ring.

Experimental Section

General Remarks: All reagents were purchased commercially and were used as received without further purification. 5,5'-Bipyrimidine (bpym) was prepared according to literature methods.^[9c] TGA was performed under nitrogen with a Perkin–Elmer TGA-7 TG analyzer. Elemental analyses were conducted with a Perkin–Elmer 2400 CHN elemental analyzer. X-ray powder diffraction (XRPD) data were recorded with a Siemens D-5000 diffractometer at 40 kV, 30 mA for Cu- K_{α} ($\lambda = 1.5406$ Å), with a step size of 0.02° in θ and a scan speed of 1 s per step size. Variable-temperature dc magnetic susceptibility data were collected for polycrystalline samples of **1** in an applied field of 1.0 T, and in the temperature range 2.0–300.0 K, which were measured with a SQUID magnetometer (Quantum Design, MPMS-7). The samples were embedded in eicosane wax to prevent any torquing of the polycrystalline in the magnetic field. Diamagnetic corrections were made with Pascal's constants for all constituent atoms, and the magnetic moments were calculated using the equation $\mu_{\text{eff}} = 2.828 (\chi T)^{1/2}$.

Synthesis of $\{[\text{Cu}_2(\text{btcc})(\text{bpym})(\text{H}_2\text{O})_4] \cdot 4\text{H}_2\text{O}\}_n$ (1**):** A solution of $\text{CuCl}_2 \cdot 6\text{H}_2\text{O}$ (0.40 mmol) in MeOH (5 mL) was carefully layered on top of a bilayer solution composed of a solution of tetrapotassium benzene-1,2,4,5-tetracarboxylate (K_4btcc , 0.10 mmol) and 5,5'-bipyrimidine (bpym, 0.10 mmol) in water (5 mL) on the bottom and a buffer solvent of THF on the top. It was then allowed to stand at room temperature for a week, whereupon blue prismatic crystals of **1** were formed in 78% yield (53.0 mg, based on btcc). $\text{C}_{18}\text{H}_{24}\text{Cu}_2\text{N}_4\text{O}_{16}$ (679.49): calcd. C 31.82, H 3.56, N 8.25; found C 31.60, H 3.85, N 7.93.

Synthesis of $\{[\text{Ni}_2(\text{btcc})(\text{bpym})(\text{H}_2\text{O})_4] \cdot 4\text{H}_2\text{O}\}_n$ (2**):** In a tube at ambient temperature, a solution of $\text{NiCl}_2 \cdot 2\text{H}_2\text{O}$ (0.40 mmol) in MeOH (5 mL) was carefully layered on top of a bilayer solution comprised of an aqueous solution (5 mL) that contained tetrapotassium benzene-1,2,4,5-tetracarboxylate (0.10 mmol) and 5,5'-bipyrimidine (0.10 mmol) on the bottom and a buffer solvent of THF on the top. Blue-green crystals of **2**·7H₂O were produced within a 7-day period; yield 32% (21.4 mg, based on btcc).

Synthesis of $[\text{Zn}_4(\text{btcc})_2(\text{bpym})(\text{H}_2\text{O})_6]_n$ (3**):** In a tube at ambient temperature, a solution of ZnCl_2 (0.40 mmol) in MeOH (5 mL) was

carefully layered on top of a bilayer solution comprised of an aqueous solution (5 mL) that contained tetrapotassium benzene-1,2,4,5-tetracarboxylate (0.10 mmol) and 5,5'-bipyrimidine (0.10 mmol) on the bottom and a buffer solvent of THF on the top. Pale-yellow crystals of **3** were produced within a 7-day period; yield 68% (35.0 mg, based on btcc).

X-ray Crystallographic Studies: A suitable single crystal ($0.28 \times 0.25 \times 0.20$ mm³) of **1** was mounted on the tip of a glass fiber and placed onto the goniometer head for indexing and intensity data collection with a Nonius Kappa CCD diffractometer with graphite-monochromated Mo- K_{α} radiation ($\lambda = 0.71073$ Å). Absorption correction was applied by SADABS. The structure was solved by direct methods and refined against F^2 by the full-matrix least-squares technique, using the WINGX,^[19] PLATON,^[20] and SHELX^[21] software packages. All non-hydrogen atoms were refined with anisotropic displacement parameters. The hydrogen atoms of the aromatic rings were calculated and refined as riding models. The hydrogen atoms of the coordinated water molecule and the assigned guest water molecules were located from difference Fourier maps. Compounds **2** and **3** were also characterized by single-crystal X-ray diffraction analysis and their crystallographic details are also given in Table 1. Anisotropic thermal factors were assigned to non-hydrogen atoms, except the crystallographically disordered carboxylate group (C14, C14', O7, O7', O8, and O8') in **3**.

Table 1. Crystal data collection and structure refinement for **1**–**3**.

	1	2	3
Formula	$\text{C}_{18}\text{H}_{24}\text{Cu}_2\text{N}_4\text{O}_{16}$	$\text{C}_{18}\text{H}_{24}\text{Ni}_2\text{N}_4\text{O}_{16}$	$\text{C}_{28}\text{H}_{22}\text{N}_4\text{O}_{22}\text{Zn}_4$
M_r	679.49	669.88	1027.98
Crystal system	monoclinic	monoclinic	orthorhombic
Space group	$C2/c$	$C2/c$	$Pbcn$
a [Å]	11.5882(3)	11.742(2)	9.7230(19)
b [Å]	15.6757(4)	16.066(3)	16.423(3)
c [Å]	14.7695(5)	14.376(3)	21.784(4)
α [°]	90	90	90
β [°]	107.262(1)	104.25(3)	90
γ [°]	90	90	90
V [Å ³]	2562.1(1)	2628.6(9)	3478.5(12)
Z	4	4	4
T [K]	293(2)	293(2)	293(2)
λ [Å]	0.71073	0.71073	0.71073
$D_{\text{calcd.}}$ [g cm ^{−3}]	1.762	1.706	1.963
μ [mm ^{−1}]	1.746	1.531	2.825
$F(000)$	1384	1368	2056
GOF	1.028	1.107	1.184
$R_1^{\text{[a]}}$ [$I > 2\sigma(I)$]	0.0477	0.0695	0.1066
$wR_2^{\text{[b]}}$ [$I > 2\sigma(I)$]	0.1283	0.1666	0.2892
$R_1^{\text{[a]}}$ (all data)	0.0546	0.1488	0.1302
$wR_2^{\text{[b]}}$ (all data)	0.1342	0.2050	0.3142

$$[\text{a}] R_1 = \sum ||F_o| - |F_c|| / \sum |F_o|. [\text{b}] wR_2 = \{ \sum [w(F_o^2 - F_c^2)^2] / \sum [w(F_o^2)^2] \}^{1/2}.$$

CCDC-741018 (for **1**), -769225 (for **2**), and -769226 (for **3**) contain the supplementary crystallographic data for this paper. These data can be obtained free of charge from The Cambridge Crystallographic Data Centre via www.ccdc.cam.ac.uk/data_request/cif.

Supporting Information (see also the footnote on the first page of this article): The molar magnetic susceptibility data for **1** were fitted to a modified Bleaney–Bowers equation (see Figure S1).

Acknowledgments

We are grateful to the National Taipei University of Technology, the Academia Sinica, and the National Science Council of Taiwan for financial support of this research.

- [1] a) M. J. Zaworotko, *Nature* **2008**, *451*, 410–411; b) A. K. Cheetham, C. N. R. Rao, *Science* **2007**, *318*, 58–59; c) G. Férey, *Chem. Soc. Rev.* **2008**, *37*, 191–214.
- [2] a) R. Banerjee, H. Furukawa, D. Britt, C. Knobler, M. O’Keeffe, O. M. Yaghi, *J. Am. Chem. Soc.* **2009**, *131*, 3875–3877; b) J. P. Zhang, X. M. Chen, *J. Am. Chem. Soc.* **2009**, *131*, 5516–5521; c) Y. F. Zeng, X. Hu, F. C. Liu, X. H. Bu, *Chem. Soc. Rev.* **2009**, *38*, 469–480; d) B. K. Olmsted, S. Ferlay, P. Dechambenoit, M. W. Hosseini, M. D. Ward, *Cryst. Growth Des.* **2009**, *9*, 2841–2847.
- [3] a) O. M. Yaghi, M. O’Keeffe, N. W. Ockwig, H. K. Chae, M. Eddaoudi, J. Kim, *Nature* **2003**, *423*, 705–714; b) G. R. Desiraju, *Angew. Chem. Int. Ed.* **2007**, *46*, 8342–8356; c) D. Bradshaw, J. B. Claridge, E. J. Cussen, T. J. Prior, M. J. Rosseinsky, *Acc. Chem. Res.* **2005**, *38*, 273–282; d) C. N. R. Rao, S. Natarajan, R. Vaidhyanathan, *Angew. Chem. Int. Ed.* **2004**, *43*, 1466–1496; e) S. Kitagawa, R. Kitaura, S. Noro, *Angew. Chem. Int. Ed.* **2004**, *43*, 2334–2375; f) D. Tanaka, S. Kitagawa, *Chem. Mater.* **2008**, *20*, 922–931; g) M. W. Hosseini, *Acc. Chem. Res.* **2005**, *38*, 313–323; h) M. Tsapatsis, S. Maheshwari, *Angew. Chem. Int. Ed.* **2008**, *47*, 4262–4263; i) R. J. Hill, D. L. Long, N. R. Champness, P. Hubberstey, M. Schröder, *Acc. Chem. Res.* **2005**, *38*, 337–350.
- [4] a) Editorial, *Nat. Mater.* **2009**, *8*, 161–161; b) H. Furukawa, J. Kim, N. W. Ockwig, M. O’Keeffe, O. M. Yaghi, *J. Am. Chem. Soc.* **2008**, *130*, 11650–11661.
- [5] M. Jansen, J. C. Schön, *Angew. Chem. Int. Ed.* **2006**, *45*, 3406–3412.
- [6] a) X. Q. Zhao, B. Zhao, W. Shi, P. Cheng, D. Z. Liao, S. P. Yan, *Dalton Trans.* **2009**, 2281–2283; b) L. Hou, J. P. Zhang, X. M. Chen, *Cryst. Growth Des.* **2009**, *9*, 2415–2419; c) P. Dechambenoit, S. Ferlay, N. Kyritsakas, M. W. Hosseini, *J. Am. Chem. Soc.* **2008**, *130*, 17106–17113.
- [7] a) J. Y. Wu, M. T. Ding, Y. S. Wen, Y. H. Liu, K. L. Lu, *Chem. Eur. J.* **2009**, *15*, 3604–3614; b) J. Y. Wu, S. L. Yang, T. T. Luo, Y. H. Liu, Y. W. Cheng, Y. F. Chen, Y. S. Wen, L. G. Lin, K. L. Lu, *Chem. Eur. J.* **2008**, *14*, 7136–7139, and references therein.
- [8] a) I. Georgiev, E. Bosch, C. L. Barnes, M. Draganjac, *Cryst. Growth Des.* **2004**, *4*, 235–239; b) C. L. Barnes, E. Bosch, *Cryst. Growth Des.* **2005**, *5*, 1049–1053.
- [9] a) J. Y. Wu, H. Y. Hsu, C. C. Chan, Y. S. Wen, C. T. Tsai, K. L. Lu, *Cryst. Growth Des.* **2009**, *9*, 258–262; b) J. M. Matheny, E. Bosch, C. L. Barnes, *Cryst. Growth Des.* **2007**, *7*, 984–988; c) T. T. Luo, Y. H. Liu, C. C. Chan, S. M. Huang, B. C. Chang, Y. L. Lu, G. H. Lee, S. M. Peng, J. C. Wang, K. L. Lu, *Inorg. Chem.* **2007**, *46*, 10044–10046, and references therein.
- [10] To identify unique nets and topologies, O’Keeffe and co-workers proposed a three-letter code as code-name for nets (similar to zeolites names); a) O. D. Friedrichs, M. O’Keeffe, O. M. Yaghi, *Acta Crystallogr., Sect. A* **2003**, *59*, 22–27; b) M. O’Keeffe, M. A. Peskov, S. J. Ramsden, O. M. Yaghi, *Acc. Chem. Res.* **2008**, *41*, 1782–1789. Or visit the Reticular Chemistry Structure Resource (RCSR) website of M. O’Keeffe at <http://rcsr.anu.edu.au/>. The topology analysis was performed using the freely available software TOPOS (<http://www.topos.ssu.samara.ru/>); c) V. A. Blatov, *IUCr CompComm NewsL.* **2006**, *7*, 4–38.
- [11] a) M. Eddaoudi, J. Kim, D. T. Vodak, A. C. Sudik, J. Wachter, M. O’Keeffe, O. M. Yaghi, *Proc. Natl. Acad. Sci. USA* **2002**, *99*, 4900–4904; b) O. D. Friedrichs, M. O’Keeffe, O. M. Yaghi, *Solid State Sci.* **2003**, *5*, 73–78.
- [12] For example: a) J. Yang, J. F. Ma, Y. Y. Liu, S. R. Batten, *CrystEngComm* **2009**, *11*, 151–159; b) E. M. Lyons, M. A. Braverman, R. M. Supkowski, R. L. LaDuca, *Inorg. Chem. Commun.* **2008**, *11*, 855–858; c) A. J. Blake, N. R. Brooks, N. R. Champness, J. W. Cunningham, P. Hubberstey, M. Schröder, *CrystEngComm* **2000**, *2*, 41–45; d) L. Carlucci, G. Ciani, D. M. Proserpio, *Chem. Commun.* **2004**, 380–381; e) S. A. Barnett, A. J. Blake, N. R. Champness, C. Wilson, *Chem. Commun.* **2002**, 1640–1641.
- [13] For example: a) D. L. Long, A. J. Blake, N. R. Champness, M. Schröder, *Chem. Commun.* **2000**, 1369–1370; b) V. Niel, A. L. Thompson, M. C. Munoz, A. Galet, A. E. Goeta, J. A. Real, *Angew. Chem. Int. Ed.* **2003**, *42*, 3760–3763; c) B. R. Bhogala, P. K. Thallapally, A. Nangia, *Cryst. Growth Des.* **2004**, *4*, 215–218.
- [14] a) D. R. Turner, J. Strachan-Hatton, S. R. Batten, *CrystEngComm* **2008**, *10*, 34–38; b) B. Ding, Y. Y. Liu, Y. Q. Huang, W. Shi, P. Cheng, D. Z. Liao, S. P. Yan, *Cryst. Growth Des.* **2009**, *9*, 593–601; c) N. Zheng, J. Zhang, X. Bu, P. Feng, *Cryst. Growth Des.* **2007**, *7*, 2576–2581; d) B. Moulton, H. Abourahma, M. W. Bradner, J. Lu, G. J. McManus, M. J. Zaworotko, *Chem. Commun.* **2003**, 1342–1343.
- [15] a) A. K. Cheetham, C. N. R. Rao, R. K. Feller, *Chem. Commun.* **2006**, 4780–4795; b) S. Kitagawa, K. Uemura, *Chem. Soc. Rev.* **2005**, *34*, 109–119; c) M. Kawano, M. Fujita, *Coord. Chem. Rev.* **2007**, *251*, 2592–2605.
- [16] a) Y. Elerman, E. Kavlakoglu, A. Elmali, *Z. Naturforsch., Teil A* **2002**, *57*, 919–924; b) E. Kavlakoglu, A. Elmali, Y. Elerman, I. Svoboda, *Polyhedron* **2002**, *21*, 1539–1549.
- [17] a) B. Bleaney, K. Bowers, *Proc. R. Soc. London, Ser. A* **1952**, *214*, 451–465; b) B. Bleaney, K. Bowers, *Phil. Mag.* **1952**, *43*, 372–374.
- [18] a) J. M. Veauthier, E. Tomat, V. M. Lynch, J. L. Sessler, U. Mirsaidov, J. T. Markert, *Inorg. Chem.* **2005**, *44*, 6736–6743; b) S. Brooker, J. D. Ewing, T. K. Ronson, C. J. Harding, J. Nelson, D. J. Speed, *Inorg. Chem.* **2003**, *42*, 2764–2773.
- [19] L. J. Farrugia, *J. Appl. Crystallogr.* **1999**, *32*, 837–838.
- [20] A. L. Spek, *J. Appl. Crystallogr.* **2003**, *36*, 7–13.
- [21] G. M. Sheldrick, *Acta Crystallogr., Sect. A* **2008**, *64*, 112–122.

Received: March 15, 2010
Published Online: July 16, 2010

Hydrogen Adsorption in Polyoxometalate Hybrid Compounds Based on Porous Metal-Organic Frameworks

Fengji Ma,^[a] Shuxia Liu,^{*[a]} Dadong Liang,^[a] Guojian Ren,^[a] Chundane Zhang,^[a]
Feng Wei,^[a] and Zhongmin Su^[a]

Keywords: Metal-organic frameworks / Polyoxometalates / Adsorption / Microporous materials / Ion exchange

Two polyoxometalate hybrid compounds based on porous metal-organic frameworks (PMOFs/POMs) have been prepared by lithium ion exchange and their crystal structures, stabilities and gas adsorption properties have been characterized. Both compounds consist of neutral $\text{Cu}_3(\text{BTC})_2$ (BTC = 1,3,5-benzenetricarboxylate) metal-organic frameworks (MOFs) as hosts and Keggin polyoxometalates (POMs)

anions and lithium ions as guests with the MOFs maintaining their permanent porosity. H_2 adsorption studies demonstrated that the guests play a key role in increasing the H_2 adsorption capacity of the frameworks. With the introduction of POMs and lithium ions, the compounds not only display strong hydrogen adsorption behavior, but also exhibit some differences in H_2 binding energy.

Introduction

Metal-organic frameworks (MOFs) represent a new class of crystalline materials consisting of multiple metal ions linked together by polyfunctional organic ligands, resulting in highly microporous networks.^[1] The unique advantage of these emerging materials lies in the possibility of their highly specific functionalization for particular applications, such as catalysis,^[2] magnetism,^[3] separation,^[4] and gas adsorption.^[5] They not only offer higher surface areas and the potential for enhanced activity, but also provide shape/size selectivity, which is important for the incorporation of functional groups to increase the number of applications.^[6] Recently, we developed an approach for the synthesis of promising crystalline materials that involves the encapsulation of polyoxometalates (POMs), which are the polyoxoanions of early-transition metals,^[7] in the nanosized spaces of porous metal-organic frameworks (PMOFs). A series of polyoxometalate hybrid compounds based on porous metal-organic frameworks (PMOFs/POMs) have been prepared and studied for their use in catalysis.^[8] In these compounds, Keggin polyanions were alternately arranged as noncoordinating guests in the cubo-octahedral cages of a $\text{Cu}_3(\text{BTC})_2$ ^[9] (HKUST-1; BTC = 1,3,5-benzenetricarboxylate) MOF host matrix which maintained its permanent porosity.

On the other hand, owing to their exceptionally high surface areas and tailored pore dimensions, MOFs are ideal materials for H_2 storage based on physisorption. It is noteworthy that some MOFs have arguably reached or even surpassed the U.S. Department of Energy (DOE) 2010 H_2 storage target.^[10] However, because of their typically weak interactions with H_2 , these materials function best only at low temperature and high pressure. Clearly, significant innovations are necessary to build viable hydrogen-storage systems at near-ambient temperatures and the greatest challenge for physisorptive materials is increasing the strength of the H_2 binding interaction.

The H_2 adsorption enthalpy obtained from isotherms is an important measure of the H_2 binding energy within MOFs. More and more strategies are being employed to increase the H_2 adsorption enthalpy further to accomplish the target for H_2 storage. For instance, incorporating coordinatively unsaturated metal sites into the frameworks is particularly attractive because multiple metal- H_2 binding sites become available for producing higher H_2 affinity.^[11,12] In addition, a recent development in the field of H_2 adsorption in MOFs is the use of Li.^[13] This is considered to be an effective strategy for enhancing H_2 adsorption through guest ion-exchange, but only exposed Li^+ can increase the H_2 adsorption enthalpy. Nevertheless reports of H_2 adsorption capacity enhanced by anion guests are still rare. Herein, we present two new PMOFs/POMs, $\text{Li}_2[\text{Cu}_{12}(\text{BTC})_8 \cdot 12\text{H}_2\text{O}][\text{HPW}_{12}\text{O}_{40}] \cdot 27\text{H}_2\text{O}$ (NENU-29) and $\text{Li}_2[\text{Cu}_{12}(\text{BTC})_8 \cdot 12\text{H}_2\text{O}][\text{H}_2\text{SiMo}_{12}\text{O}_{40}] \cdot 25\text{H}_2\text{O}$ (NENU-30). In these two compounds, the POMs act as anion guests within the $\text{Cu}_3(\text{BTC})_2$ hosts. In addition to thermal gravimetric analysis (TGA), infrared spectroscopy (IR), single-crystal X-ray diffraction and powder X-ray diffraction (PXRD), gas

[a] Key Laboratory of Polyoxometalates Science of the Ministry of Education, College of Chemistry, Northeast Normal University, Changchun City, Jilin 130024, P. R. China
Fax: +86-431-85099328
E-mail: liusx@nenu.edu.cn

Supporting information for this article is available on the WWW under <http://dx.doi.org/10.1002/ejic.201000331>.

adsorption measurements have also been conducted to investigate the H_2 adsorption behavior of these two compounds.

Results and Discussion

Synthesis and Crystal Structures

Compounds **NENU-29** and **NENU-30** were prepared by immersing the crystals of as-synthesized **NENU-3** $\{(C_4H_{12}N)_2[Cu_{12}(BTC)_8 \cdot 12H_2O][HPW_{12}O_{40}] \cdot 25H_2O\}$ and **NENU-4** $\{(C_4H_{12}N)_2[Cu_{12}(BTC)_8 \cdot 12H_2O][H_2SiMo_{12}O_{40}] \cdot 28H_2O\}$,^[8] respectively, in saturated solutions of $LiNO_3$ for a week, the $LiNO_3$ solution being refreshed everyday. In addition, if **NENU-3** and **NENU-4** were evacuated under a dynamic vacuum at 150 °C for 12 h, **NENU-3a** $\{H_2[Cu_{12}(BTC)_8][HPW_{12}O_{40}]\}$ and **NENU-4a** $\{H_2[Cu_{12}(BTC)_8][H_2SiMo_{12}O_{40}]\}$, respectively, were obtained, the $C_4H_{12}N^+$ guests having been eliminated. These compounds were then immersed in saturated solutions of $LiNO_3$ for 24 h to give **NENU-29** and **NENU-30**.

Single-crystal X-ray diffraction analysis revealed that the two PMOFs/POMs are isomorphic and consist of the $Cu_3(BTC)_2$ host framework and different Keggin-type POMs as guests. As shown in Figure 1, two kinds of pores contain the POM anions and Li^+ . A view along the c axis of the cubic cell reveals two approx. 1-nm-sized channels (ca. 13 and 10 Å). The total accessible volumes in **NENU-29** and **NENU-30** after removal of the water molecules are 17.8 and 19.5%, as determined by using PLATON.^[14] These values are smaller than those of **NENU-3** (29.8%) and **NENU-4** (25.2%).^[8]

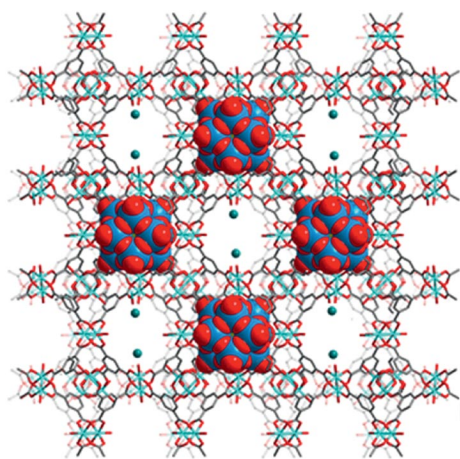


Figure 1. A view of the PMOFs/POMs along the c axis. All hydrogen and solvent water molecules have been omitted for clarity. Red, cyan, blue, grey and dark cyan represent O, Cu, W or Mo, C and Li, respectively.

Thermal Stabilities and Structural Integrities

Thermal gravimetric analysis (TGA; Figures S2 and S3) indicated weight loss of 11.82% (calcd. 11.67%) for **NENU-**

29 and 13.61% (calcd. 13.52%) for **NENU-30** at 150 °C, which corresponds to the loss of all the water molecules. The solids were thermally stable up to 300 °C. The PXRD patterns of the two compounds were coincident with the simulated patterns derived from the single-crystal X-ray data (Figures S4 and S5), which implies that the structures of the bulk samples are the same as those of the single crystals. The PXRD patterns also clearly confirm that the structures remained intact after Li^+ exchange. The elimination of $(CH_3)_4N^+$ from **NENU-3** and **NENU-4** was indicated by the disappearance of the C–H vibrating peak from the IR spectra (Figures S6 and S7). In addition, elemental analysis showed that nitrogen was not present in either **NENU-29** or **NENU-30**. All of these results reveal that complete ion exchange occurred without the loss of structural integrity.

Adsorption Studies

N_2 adsorption studies were conducted at 77 K to evaluate the permanent porosity of **NENU-29** and **NENU-30**. The samples were heated at 150 °C under vacuum for 12 h to give the desolvated $Li_2[Cu_{12}(BTC)_8][HPW_{12}O_{40}]$ (**NENU-29a**) and $Li_2[Cu_{12}(BTC)_8][H_2SiMo_{12}O_{40}]$ (**NENU-30a**). Both N_2 isotherms show typical Type-I adsorption behavior, which confirms the retention of microporous structures.^[15] N_2 uptakes of 169 and 180 cm^3 (STP) g^{-1} (Figure 2) were observed, which correspond to 7.5 and 8.0 $mmol g^{-1}$. These values are higher than those for **NENU-3a** or **NENU-4a** [ca. 140 cm^3 (STP) g^{-1}],^[8] which indicates that the adsorption capacity increases by more than 20% on Li^+ exchange. The Brunauer–Emmett–Teller (BET) surface areas for **NENU-29a** and **NENU-30a** were estimated to be 466 and 487 $m^2 g^{-1}$ and the pore volumes were estimated to be 0.336 and 0.341 $cm^3 g^{-1}$, respectively (Table 1).

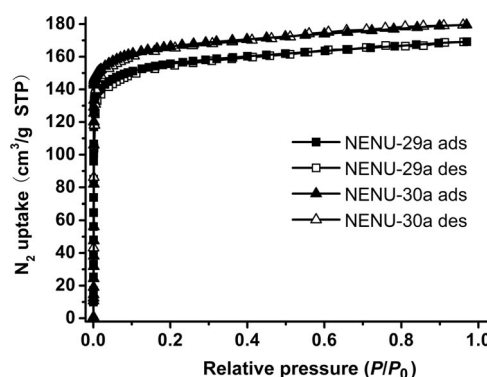


Figure 2. N_2 adsorption isotherms of **NENU-29a** and **NENU-30a** at 77 K.

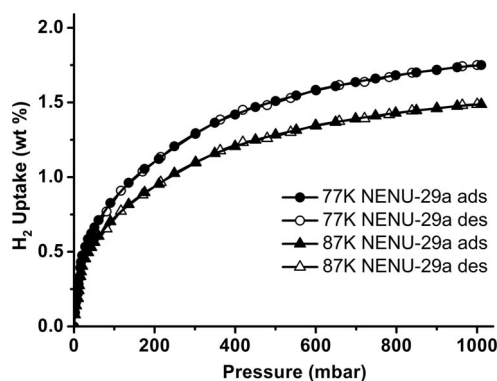
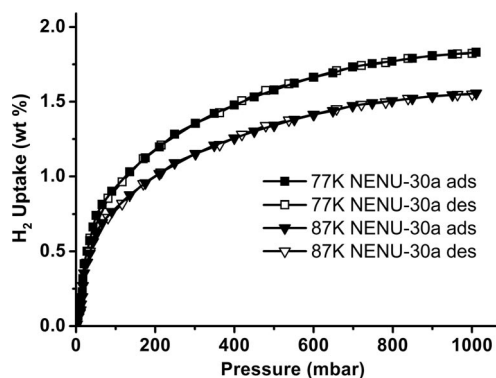
H_2 adsorption measurements were also undertaken to evaluate H_2 storage performance. As shown in Figure 3, **NENU-29a** can store up to 1.75 wt.-% at 77 K and 1 atm. This value is comparable to those of reported porous MOFs with much larger surface areas and higher even than some famous MOFs. For instance, MOF-5 and MOF-177 display H_2 uptakes of 1.32 and 1.23 wt.-%, respectively, with BET

Table 1. N₂ and H₂ adsorption properties of NENU-29a, NENU-30a, and some other reported MOFs.

	S _A ^{BET} ^[a] [m ² g ⁻¹]	Pore volume [cm ³ g ⁻¹]	H ₂ uptake [wt.-%] (77 K, 1 atm)	ρ_{H_2} ^[b] [g cm ⁻³]	H ₂ uptake (298 K) <i>P</i> [bar] Uptake [wt.-%]	ΔH_{ads} ^[c] [kJ mol ⁻¹]	Ref.
NENU-29a	466	0.336	1.75	0.052	20 0.31	7.42	this work
NENU-30a	487	0.341	1.83	0.054	20 0.40	7.94	this work
NENU-3a	405	0.314	1.59	0.050	– –	7.28	this work, ^[8]
NENU-4a	422	0.319	1.67	0.051	– –	7.79	this work, ^[8]
Cu ₃ (BTC) ₂	1507	0.75	2.48	0.033	65 0.35	6.8	[17a,22]
MOF-5	3362	1.18	1.32	0.011	60 0.45	5.2	[16,17b]
MOF-177	4526	1.69	1.23	0.007	100 0.62	4.4	[10c,16]

[a] Obtained from the N₂ isotherms at 77 K. [b] Based on the pore volume and the H₂ uptake at 77 K and 1 atm. [c] Obtained from the H₂ isotherms at 77 and 87 K and 1 atm.

surface areas of 3362 and 4526 m² g⁻¹.^[16] Although Cu₃(BTC)₂ exhibits a H₂ uptake of 2.48 wt.-%, its pore volume is 0.75 cm³ g⁻¹,^[17a] which is twice that of NENU-29a. NENU-30a has a higher H₂ uptake than NENU-29a with a value of 1.83 wt.-% (Figure 4). Notably, the densities for adsorbed H₂ in NENU-29a and NENU-30a are 0.052 and 0.054 g cm⁻³, respectively. These values are clearly higher than that of Cu₃(BTC)₂ (0.033 g cm⁻³) (Table 1) and high compared with the porous MOFs reported to date.^[13a,18]

Figure 3. H₂ adsorption isotherms of NENU-29a at 77 and 87 K and 1 atm.Figure 4. H₂ adsorption isotherms of NENU-30a at 77 and 87 K and 1 atm.

A remarkable aspect of both NENU-29 and NENU-30 is that the POMs and Li⁺ act as guests in the host framework. The enhancement of H₂ uptake that they exhibit is likely due to specific interactions between the H₂ molecules and

the guests. Compared with NENU-3a (1.59 wt.-%) and NENU-4a (1.67 wt.-%; Figures S8 and S9), which contain no Li⁺, the H₂ adsorption capacity (77 K, 1 atm) of NENU-29a and NENU-30a is greater by around 10% upon Li⁺ exchange. It is noteworthy that NENU-29a and NENU-30a, which contain Li⁺ and have smaller volumes, adsorb a greater amount of H₂. This suggests that Li⁺ could lead to an increase in the H₂ adsorption capacity. At the same time, a comparison of the data indicates that PMOFs/POMs adsorb a greater amount of H₂ per unit volume than the parent MOFs (Table 1). In other words, the presence of POMs is beneficial to the enhancement of H₂ uptake. In the limited space, the intimate contact between H₂ molecules and the O atoms of the POMs may also allow the increase of H₂ uptake. The strong interaction between O and H may enhance H₂ binding by the formation of H–O bonds. In addition, compounds containing different POM guests exhibit some differences in H₂ adsorption capacity. It is well known that H₃PW₁₂O₄₀ is the strongest Brønsted acid in the Keggin series and that the O atoms on its surface have weaker constraints on protons than H₄SiMo₁₂O₄₀.^[19,20] Thus, NENU-3a and NENU-29a, in which PW₁₂O₄₀³⁻ act as the guests, exhibit weaker binding interactions with H₂ than NENU-4a and NENU-30a, in which SiMo₁₂O₄₀⁴⁻ are the anion guests, resulting in a lower enhancement of H₂ uptake.

To further investigate the influence of the guests on H₂ adsorption, we estimated the H₂ adsorption enthalpies. Thus, a second set of H₂ isotherms were measured at 87 K and the enthalpies of H₂ adsorption were calculated by using the modified Clausius–Clapeyron equation.^[21] Moderate H₂ adsorption enthalpies of 7.42 and 7.94 kJ mol⁻¹ were estimated for NENU-29a and NENU-30a, respectively, at low coverage, which decreased with increasing H₂ loading (Figures S10 and S11). Although these values are lower than for some reported MOFs,^[12a,13b,17a] they are both higher than those determined for Cu₃(BTC)₂ (6.8 kJ mol⁻¹),^[17a] MOF-5 (5.2 kJ mol⁻¹),^[17b] and MOF-177 (4.4 kJ mol⁻¹).^[10c] By comparing the data for NENU-3a (7.28 kJ mol⁻¹) and NENU-4a (7.79 kJ mol⁻¹; Figures S12 and S13), we find that POMs play a more important role than Li⁺ in the enhancement of the H₂ adsorption enthalpies. The H₂ adsorption enthalpies were found to be in the order: NENU-30a > NENU-4a > NENU-29a > NENU-3a. This is, in part, probably because Li⁺ ions are surrounded

by other atoms and are inaccessible to H_2 molecules, whereas the terminal and bridging O atoms in the POMs can interact easily with H_2 molecules. These results led us to believe that the increased H_2 binding affinity can mainly be attributed to the presence of POMs. In addition, different POMs produce different degrees of enhancement owing to their different strengths of the interactions with H_2 . We further corroborated this conclusion by measuring H_2 adsorption at 20 bar and 298 K (Figure 5). **NENU-29a** adsorbs 0.31 wt.-% of H_2 and **NENU-30a** adsorbs 0.40 wt.-% of H_2 at 298 K and 20 bar, which is more than that of $\text{Cu}_3(\text{BTC})_2$ (0.35 wt.-%) at 298 K and 65 bar.^[22] The results of H_2 adsorption at room temperature indicate that POMs as guests within MOF hosts can indeed enhance H_2 adsorption capacity and binding affinity.

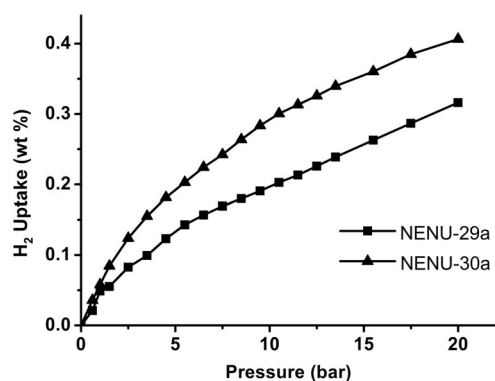


Figure 5. H_2 adsorption isotherms of **NENU-29a** and **NENU-30a** at 298 K and 20 bar.

Conclusions

We have presented herein two PMOFs/POMs that were obtained by Li^+ ion exchange. H_2 adsorption studies demonstrated that the guests play an important role in increasing the H_2 adsorption capacity of the MOFs. Despite their higher weight, POMs cannot be ignored for their contribution to the increase in the H_2 adsorption capacity and binding enthalpy of the MOFs, which is mainly a result of the oxygen-rich nature of the POMs. The mechanistic details of the interactions between H_2 molecules and the O atoms of the POMs are currently poorly understood. However, the results presented herein provide a feasible approach for increasing H_2 adsorption. Furthermore, these polyoxometalate hybrid compounds based on porous metal-organic frameworks display great potential as porous materials. On account of their particular nature, POM guests could provide an appropriate and controllable interaction with adsorbed molecules. By virtue of the porosity of the MOFs and the numerous properties of POMs, for example, as catalysts, this kind of material may find applications in other areas. Our future efforts will focus on the design and synthesis of stable MOFs with multifunctional guests for other applications, such as in vapor adsorption and gas-phase catalysis.

Experimental Section

Materials and Methods: All chemicals were obtained commercially and used without additional purification. Elemental analyses (C, H, and N) were performed with a Perkin–Elmer 2400 CHN elemental analyzer and analysis for Li was carried out with a PLASMA-SPEC(I) ICP atomic emission spectrometer. IR spectra were recorded in the range 400–4000 cm^{-1} with an Alpha Centaur FT/IR spectrophotometer using KBr pellets. Thermal gravimetric analyses (TGA) were performed with a Perkin–Elmer TGA7 instrument in a flow of N_2 with a heating rate of 10 $^\circ\text{C min}^{-1}$. Powder X-ray diffraction (PXRD) measurements were performed with a Rigaku D/MAX-3 instrument with Cu-K_α radiation in the 2θ range of 3–60 $^\circ$ at 293 K.

Gas Adsorption: Gas adsorption measurements were performed with a Hiden Isochema Intelligent Gravimetric Analyser (IGA-100B). The sample (ca. 100 mg) was out-gassed to a constant weight at 423 K under a high vacuum ($<10^{-6}$ mbar) prior to measurement of the isotherms. High purity gases (N_2 , 99.999%; H_2 , 99.9995%) were used for the gas adsorption measurements performed at 77, 87, and 298 K. The temperatures were maintained with liquid nitrogen, liquid argon, and a constant-temperature water bath, respectively. All data were rigorously corrected for the buoyancy of the system, samples and adsorbates.

Synthesis of the PMOFs/POMs

$\text{Li}_2[\text{Cu}_{12}(\text{BTC})_8 \cdot 12\text{H}_2\text{O}][\text{HPW}_{12}\text{O}_{40}] \cdot 27\text{H}_2\text{O}$ (**NENU-29**)

Method 1: Crystals of as-synthesized **NENU-3** $\{(\text{C}_4\text{H}_{12}\text{N})_2[\text{Cu}_{12}(\text{BTC})_8 \cdot 12\text{H}_2\text{O}][\text{HPW}_{12}\text{O}_{40}] \cdot 25\text{H}_2\text{O}\}^{[8]}$ (2.0 g) were immersed in a saturated solution of LiNO_3 (100 mL) for a week with the LiNO_3 solution being refreshed everyday. The completely Li^+ -exchanged crystals of **NENU-29** (≈ 2.0 g) were obtained and washed with distilled water three times.

Method 2: As-synthesized crystals of **NENU-3** (2.0 g) were evacuated under a dynamic vacuum ($\approx 10^{-6}$ mbar) at 150 $^\circ\text{C}$ for 12 h, to give **NENU-3a** $\{\text{H}_2[\text{Cu}_{12}(\text{BTC})_8][\text{HPW}_{12}\text{O}_{40}]\}$. These were immersed in a saturated solution of LiNO_3 (100 mL) for 24 h, during which time the LiNO_3 solution was refreshed once. The completely Li^+ -exchanged crystals of **NENU-29** (ca. 2.0 g) were isolated and washed with distilled water three times. Both of the methods described above resulted in exactly the same product **NENU-29**. Yield 1.96 g (98%). IR (KBr): $\tilde{\nu} = 1888$ (w), 1656 (vs), 1591 (w), 1456 (m), 1373 (vs), 1115 (w), 1078 (s), 976 (s), 903 (m), 821 (m), 799 (w), 762 (m), 728 (m), 599 (w), 495 (w) cm^{-1} . $\text{C}_{72}\text{H}_{128}\text{Cu}_{12}\text{Li}_2\text{O}_{127}\text{PW}_{12}$ (6039.20): calcd. C 14.32, H 2.12, N 0.00; found C 14.23, H 2.19, N 0.00.

$\text{Li}_2[\text{Cu}_{12}(\text{BTC})_8 \cdot 12\text{H}_2\text{O}][\text{H}_2\text{SiMo}_{12}\text{O}_{40}] \cdot 25\text{H}_2\text{O}$ (NENU-30**):** Compound **NENU-30** was prepared following the procedure described for compound **NENU-29**, but **NENU-4** $\{(\text{C}_4\text{H}_{12}\text{N})_2[\text{Cu}_{12}(\text{BTC})_8 \cdot 12\text{H}_2\text{O}][\text{H}_2\text{SiMo}_{12}\text{O}_{40}] \cdot 28\text{H}_2\text{O}\}$ was used instead of **NENU-3**. Yield 1.92 g (96%). IR: $\tilde{\nu} = 1896$ (w), 1653 (vs), 1593 (w), 1457 (m), 1373 (vs), 1114 (w), 1064 (s), 956 (s), 905 (m), 813 (m), 800 (w), 756 (m), 726 (m), 599 (w), 498 (w) cm^{-1} . $\text{C}_{72}\text{H}_{124}\text{Cu}_{12}\text{Li}_2\text{Mo}_{12}\text{O}_{125}\text{Si}$ (4945.48): calcd. C 17.48, H 2.52, N 0.00; found C 17.62, H 2.41, N 0.00.

We also tried to prepare **NENU-29** and **NENU-30** following the procedure used to synthesize **NENU-3** and **NENU-4** by changing $(\text{CH}_3)_4\text{NOH}$ to LiOH under the same hydrothermal conditions. Unfortunately, the yields were so low that we failed to obtain suitable crystals for single-crystal X-ray diffraction.

X-Ray Crystallography: Single-crystal diffractometry was conducted on a Bruker Smart Apex CCD diffractometer with Mo-K_α

monochromated radiation ($\lambda = 0.71073 \text{ \AA}$) at room temperature. The linear absorption coefficients, scattering factors for the atoms, and anomalous dispersion corrections were taken from the International Tables for X-ray Crystallography.^[23] Empirical absorption corrections were applied. The structures were solved by using the direct method and refined by the full-matrix least-squares method on F^2 using SHELXS-97.^[24] Anisotropic thermal parameters were used to refine all non-hydrogen atoms. The hydrogen atoms attached to carbon positions were placed in geometrically calculated positions. The crystallization water molecules were estimated by thermogravimetry, and only partial oxygen atoms of water molecules were analyzed in the X-ray structure determination. The most important crystallographic data are summarized in Table 2.

Table 2. Crystal data and structure refinement for NENU-29 and NENU-30.

	NENU-29	NENU-30
Formula	C ₁₄₄ H ₄₈ Cu ₂₄ Li ₄ O ₂₄₈ P ₂ W ₂₄	C ₇₂ H ₂₄ O ₁₁₆ Cu ₁₂ Li ₂ SiMo ₁₂
Formula mass [g mol ⁻¹]	11785.68	4700.90
Crystal system	cubic	cubic
Space group	<i>Fm</i> $\bar{3}$ <i>m</i>	<i>Fm</i> $\bar{3}$ <i>m</i>
<i>a</i> [Å]	26.3929(13)	26.3765(11)
<i>V</i> [Å ³]	18384.9(16)	18350.7(13)
<i>Z</i>	2	4
<i>D</i> _c [Mg m ⁻³]	2.129	1.702
μ [mm ⁻¹]	8.935	2.247
<i>F</i> (000)	10832	9024
Refins. collected	28109	22728
Indep. reflections	1197	877
GOF on F^2	1.101	1.118
<i>R</i> _{int}	0.0505	0.0535
<i>R</i> ₁ [$I > 2\sigma(I)$] ^[a]	0.0347	0.0437
<i>wR</i> ₂ (all data) ^[b]	0.1108	0.1192

[a] $R_1 = \sum ||F_o| - |F_c|| / \sum |F_o|$. [b] $wR_2 = \{\sum [w(F_o^2 - F_c^2)^2] / \sum [w(F_o^2)^2]\}^{1/2}$.

CCDC-761127 (for NENU-29) and -761126 (for NENU-30) contain the supplementary crystallographic data for this paper. These data can be obtained free of charge from The Cambridge Crystallographic Data Centre via www.ccdc.cam.ac.uk/data_request/cif.

Supporting Information (see also the footnote on the first page of this article): IR spectra, TG curves, and PXRD data of the samples and details of the estimation of H₂ adsorption enthalpy.

Acknowledgments

This work was supported by the National Nature Science Foundation of China (grant numbers 20871027 and 20973035) and the Ministry of Education of China (Program for New Century Excellent Talents in University, NCET-07-0169 and Program for Changjiang Scholars and Innovative Research Team in University).

- [1] a) O. M. Yaghi, H. Li, C. Davis, D. Richardson, T. L. Groy, *Acc. Chem. Res.* **1998**, *31*, 474–484; b) G. Férey, C. Mellot-Draznieks, C. Serre, F. Millange, *Acc. Chem. Res.* **2005**, *38*, 217–225; c) O. R. Evans, W. Lin, *Acc. Chem. Res.* **2002**, *35*, 511–522; d) B. Moulton, M. J. Zaworotko, *Chem. Rev.* **2001**, *101*, 1629–1658.
- [2] a) J. S. Seo, D. Whang, H. Lee, S. I. Jun, J. Oh, J. Young, K. Kim, *Nature* **2000**, *404*, 982–986; b) R. Zou, H. Sakurai, Q. Xu, *Angew. Chem. Int. Ed.* **2006**, *45*, 2542–2546.
- [3] a) G. J. Halder, C. J. Kepert, B. Moubaraki, K. S. Murray, J. D. Cashion, *Science* **2002**, *298*, 1762–1765; b) C. Janiak, *Dalton*

- Trans.* **2003**, 2781–2784; c) Y. Z. Zheng, M. L. Tong, W. X. Zhang, X. M. Chen, *Angew. Chem. Int. Ed.* **2006**, *45*, 6310–6314.
- [4] a) R. Matsuda, R. Kitaura, S. Kitagawa, Y. Kubota, R. V. Belosludov, T. C. Kobayashi, H. Sakamoto, T. Chiba, M. Takata, Y. Kawazoe, Y. Mita, *Nature* **2005**, *436*, 238–241; b) S. Ma, D. Sun, X. S. Wang, H. C. Zhou, *Angew. Chem. Int. Ed.* **2007**, *46*, 2458–2462; c) P. L. Llewellyn, S. Bourrelly, C. Serre, Y. Filinchuk, G. Férey, *Angew. Chem. Int. Ed.* **2006**, *45*, 7751–7754.
- [5] a) K. J. Eddaoudi, N. Rosi, D. Vodak, J. Wachter, M. O'Keeffe, O. M. Yaghi, *Science* **2002**, *295*, 469–472; b) A. R. Millward, O. M. Yaghi, *J. Am. Chem. Soc.* **2005**, *127*, 17998–17999; c) R. Li, Y. Tao, Q. Yu, X. H. Bu, H. Sakamoto, S. Kitagawa, *Chem. Eur. J.* **2008**, *14*, 2771–2776; d) C. Y. Gao, S. X. Liu, L. H. Xie, C. Y. Sun, J. F. Cao, Y. H. Ren, D. Feng, Z. M. Su, *Crysc. EngComm* **2009**, *11*, 177–182.
- [6] a) P. Horcajada, C. Serre, M. Vallet-Regi, M. Sebban, F. Tauler, G. Férey, *Angew. Chem. Int. Ed.* **2006**, *45*, 5974–5978; b) Q. R. Fang, G. S. Zhu, Z. Jin, Y. Y. Ji, J. W. Ye, M. Xue, H. Yang, Y. Wang, S. L. Qiu, *Angew. Chem. Int. Ed.* **2007**, *46*, 6638–6642; c) M. H. Alkordi, Y. Liu, R. W. Larsen, J. F. Eubank, M. Eddaoudi, *J. Am. Chem. Soc.* **2008**, *130*, 12639–12641.
- [7] a) M. T. Pope, A. Muller, *Angew. Chem. Int. Ed. Engl.* **1991**, *30*, 34–48; b) C. L. Hill, *Chem. Rev.* **1998**, *98*, 1–2; c) M. T. Pope, A. Müller (Eds.), in: *Polyoxometalate Chemistry from Topology via Self-Assembly to Applications*, Kluwer Academic Publishers, The Netherlands, **2001**.
- [8] C. Y. Sun, S. X. Liu, D. D. Liang, K. Z. Shao, Y. H. Ren, Z. M. Su, *J. Am. Chem. Soc.* **2009**, *131*, 1883–1888.
- [9] S. S. Y. Chui, S. M. F. Lo, J. P. H. Charmant, A. GuyOrpen, I. D. Williams, *Science* **1999**, *283*, 1148–1150.
- [10] a) S. Ma, J. Eckert, P. M. Forster, J. W. Yoon, Y. K. Hwang, J. S. Chang, C. D. Collier, J. B. Parise, H. C. Zhou, *J. Am. Chem. Soc.* **2008**, *130*, 15896–15902; b) M. Latroche, S. Surble, C. Serre, C. Mellot-Draznieks, P. L. Llewellyn, J. H. Lee, J. S. Chang, S. H. Jung, G. Férey, *Angew. Chem. Int. Ed.* **2006**, *45*, 8227–8231; c) H. Furukawa, M. A. Miller, O. M. Yaghi, *J. Mater. Chem.* **2007**, *17*, 3197–3204.
- [11] a) B. L. Chen, X. Zhao, A. Putkham, K. Hong, E. B. Lobkovsky, E. J. Hurtado, A. J. Fletcher, K. M. Thomas, *J. Am. Chem. Soc.* **2008**, *130*, 6411–6423; b) W. Zhou, H. Wu, T. Yildirim, *J. Am. Chem. Soc.* **2008**, *130*, 15268–15269; c) G. L. Law, K. L. Wong, Y. Y. Yang, Q. Y. Yi, G. Jia, W. T. Wong, P. A. Tanner, *Inorg. Chem.* **2007**, *46*, 9754–9759; d) G. Férey, C. Mellot-Draznieks, C. Serre, F. Millange, J. Dutour, S. Surble, I. Margiolaki, *Science* **2005**, *309*, 2040–2042.
- [12] a) M. Dincă, J. R. Long, *Angew. Chem. Int. Ed.* **2008**, *47*, 6766–6779; b) M. Dincă, W. S. Han, Y. Liu, A. Dailly, C. M. Brown, J. R. Long, *Angew. Chem. Int. Ed.* **2007**, *46*, 1419–1422; c) M. Dincă, J. R. Long, *J. Am. Chem. Soc.* **2007**, *129*, 11172–11176; d) M. Dincă, A. Dailly, Y. Liu, C. M. Brown, D. A. Neumann, J. R. Long, *J. Am. Chem. Soc.* **2006**, *128*, 16876–16883; e) M. Dincă, A. F. Yu, J. R. Long, *J. Am. Chem. Soc.* **2006**, *128*, 8904–8913.
- [13] a) S. H. Yang, X. Lin, K. M. Thomas, P. Hubberstey, N. R. Champness, M. Schröder, *Chem. Commun.* **2008**, 6108–6110; b) S. H. Yang, X. Lin, A. J. Blake, G. S. Walker, P. Hubberstey, N. R. Champness, M. Schröder, *Nat. Chem.* **2009**, *1*, 487–493.
- [14] A. L. Spek, *J. Appl. Crystallogr.* **2003**, *36*, 7–13.
- [15] F. Rouquerol, J. Rouquerol, K. Sing in *Adsorption by powders and porous solids*, Academic Press, London, **1999**.
- [16] J. L. C. Rowsell, A. R. Millward, K. S. Park, O. M. Yaghi, *J. Am. Chem. Soc.* **2004**, *126*, 5666–5667.
- [17] a) J. L. C. Rowsell, O. M. Yaghi, *J. Am. Chem. Soc.* **2006**, *128*, 1304–1315; b) S. S. Kaye, J. R. Long, *J. Am. Chem. Soc.* **2005**, *127*, 6506–6507.
- [18] a) L. Pan, B. Parker, X. Y. Huang, D. H. Olson, J. Y. Lee, J. Li, *J. Am. Chem. Soc.* **2006**, *128*, 4180–4181; b) M. Xue, S. Q. Ma, Z. Jin, R. M. Schaffino, G. S. Zhu, E. B. Lobkovsky, S. L. Qiu, B. L. Chen, *Inorg. Chem.* **2008**, *47*, 6825–6828.

- [19] I. V. Kozhevnikov, *Russ. Chem. Rev.* **1987**, 56, 811–825.
- [20] X. Lopez, J. M. Maestre, C. Bo, J. M. Poblet, *J. Am. Chem. Soc.* **2001**, 123, 9571–9576.
- [21] F. Daniels, J. W. Williams, P. Bender, R. A. Alberty, C. D. Cornwell in *Experimental Physical Chemistry*, McGraw-Hill, New York, **1962**.
- [22] B. Panella, M. Hirscher, H. Pütter, U. Müller, *Adv. Funct. Mater.* **2006**, 16, 520–524.
- [23] N. F. M. Henry, K. Lonsdale (Eds.), *International Tables for X-ray Crystallography*, Kynoch Press, Birmingham, **1952**.
- [24] G. M. Sheldrick, *SHELXS-97: Programs for Crystal Structure Solution*, University of Göttingen, Göttingen, Germany, **1997**.

Received: March 26, 2010

Published Online: June 16, 2010

Construction of a 2D Rectangular Grid and 3D Diamondoid Interpenetrated Frameworks and Their Functionalities by Changing the Second Spacers

Prakash Kanoo^[a] and Tapas Kumar Maji^{*[a]}

Keywords: Zinc / Metal–organic frameworks / Crystal engineering / Diamondoid / Interpenetration / Adsorption

Three new metal–organic Zn^{II} frameworks, {[Zn(bipy)(1,4-ndc)(H₂O)₂·2H₂O} (**1**), {[Zn(bpe)(1,4-ndc)]₂·2DMF} (**2**), {[Zn(bpee)(1,4-ndc)]₂·2DMF} (**3**) [bipy = 4,4'-bipyridyl, 1,4-ndc = 1,4-naphthalenedicarboxylate, bpe = 1,2-bis(4-pyridyl)ethane, bpee = 1,2-bis(4-pyridyl)ethylene], have been synthesized by using mixed-ligand systems under solvothermal conditions and characterized structurally by single-crystal X-ray diffraction. Compound **1** has a 2D structure with 4⁴-sqI net topology, whereas **2** and **3** have a 3D diamondoid structure with interesting fourfold interpenetrated topology. Topological analyses of the diamondoid nets in compounds **2** and **3** reveal a 4-connected net with 6⁶ topology. Thermogravimetric

experiments suggest that the solvent-free compounds **1**–**3** are stable up to 370, 330, and 280 °C, respectively. The grids of **1** stack in –ABCD– fashion without any regular channel structure. Desolvated compound **2** (**2'**) selectively adsorbs CO₂ over N₂, and such discrimination is regulated by the restricted window dimension of the channels. Solvent vapor (H₂O, MeOH, and EtOH) adsorption studies with **2'** suggest a hydrophobic nature of the pore surface. Gas and vapor adsorption studies with **3'** reveal no uptake, which can be correlated to a smaller pore size relative to the kinetic diameter of the respective adsorbates.

Introduction

Metal–organic frameworks (MOFs) or porous coordination polymers (PCPs) are solid-state materials that are constructed through the linking of organic ligands with metals. The last two decades have witnessed enormous growth in the field of MOFs and many interesting properties and applications have been unveiled.^[1] MOFs have found wide applications that include gas storage,^[2] separation,^[3] catalysis,^[4] ion exchange,^[5] sensing,^[6] and drug delivery.^[7] Because of the enormous possibilities of combining metals with ligands, it is feasible to design a range of MOF structures using a single metal node while only changing the organic linkers. Moreover, the linker backbone can be tuned by modifying functional groups, which offers an additional opportunity to change the chemical environment of the pore surface.^[6d,8] A literature survey of MOFs shows that structures that contain only carboxylate ligands are fairly rigid, as found in the MOFs of Yaghi et al.;^[9] however, the introduction of pyridyl linkers in addition to carboxylates imparts flexibility to the structure, as seen in Kitagawa and co-workers' PCPs.^[10] This kind of structural flexibility leads toward many interesting functionalities, such as guest-induced asymmetry and fitting,^[11] selective sorption and switching,^[12] guest-dependent magnetic modulation,^[13] and

so on. The structural flexibility in mixed-ligand systems that have both carboxylate and pyridyl linkers has been well studied and their dynamic behavior has also been explored in depth.^[10] It has been observed that the use of long organic linkers in the construction of MOFs often leads to interpenetration in the structure.^[14] The origin of the interpenetration can be attributed to the presence of large free voids in a single framework, and recently it has been demonstrated that interpenetration does not prevent the possibility of obtaining open porous frameworks;^[15] however, the factors that control the resulting degree of interpenetration remain largely unknown.^[16] Diamondoid frameworks are very important from a topological point of view and have attracted a great deal of attention not only for the robust structural motifs in the construction of different solids but also for its potential application in nonlinear optical properties (NLO).^[17] 3D diamondoid frameworks that contain tetrahedral building units are common,^[18] and recently Proserpio et al. have shown that 64% of the interpenetrated frameworks bear a diamondoid topology.^[18b,18i] The metal ions that have a tetrahedral geometry, such as Cu^I, Ag^I, Zn^{II}, Cu^{II}, and Cd^{II}, have the propensity to form diamondoid frameworks with various degrees of interpenetration including 2–5-fold, 7–9-fold, and even 11-fold degeneracy.^[19] For example, recently an unusual 12-fold interpenetrated **dia** net with a longer *N,N'*-bis(4-pyridyl)-adipoamide ligand as a linker has been reported by Hsu et al.^[18g]

In this article, we report the design and synthesis of three new MOFs, {[Zn(bipy)(1,4-ndc)(H₂O)₂·2H₂O} (**1**), {[Zn-

[a] Molecular Materials Laboratory, Chemistry and Physics of Materials Unit, Jawaharlal Nehru Centre for Advanced Scientific Research, Jakkur Bangalore 560064, India
Fax: +91-80-2208 2766
E-mail: tmaji@jncasr.ac.in

Supporting information for this article is available on the WWW under <http://dx.doi.org/10.1002/ejic.201000362>.

(bpe)(1,4-ndc) $_2$ ·2DMF} (**2**), and {[Zn(bpee)(1,4-ndc)]·2DMF} (**3**) [bipy = 4,4'-bipyridyl, 1,4-ndc = 1,4-naphthalenedicarboxylate, bpe = 1,2-bis(4-pyridyl)ethane, bpee = 1,2-bis(4-pyridyl)ethylene] by changing the pillar modules in the Zn-1,4-ndc system under solvothermal conditions. Compound **1** has been constructed from bipy and 1,4-ndc and possesses a 2D network with 4⁴ topology. Compounds **2** and **3** have been constructed from bpe/bpee and 1,4-ndc, and both possess a fourfold interpenetrated 3D diamondoid net topology. Topological analyses of both the nets of **2** and **3** reveal a 4-connected net with 6⁶ topology. Compound **1** does not contain any regular channel, whereas **2** shows highly selective CO₂ adsorption properties over N₂ and a strongly hydrophobic pore surface decorated by 1,4-ndc backbones.

Results and Discussion

Crystal Structure Description of 1

Compound **1** crystallizes in the monoclinic system with space group *P2₁/c*. The asymmetric unit of **1** comprises one Zn^{II} atom, one 1,4-ndc ligand, one bipy linker, two coordinated water molecules, and two guest water molecules. The geometry around Zn^{II} is a slightly distorted octahedral with the ZnO₄N₂ chromophore, and the coordinations are furnished by two carboxylate oxygen atoms (O1, O1a), two pyridyl nitrogen atoms (N1, N2), and two water molecules (O5, O5a; Figure 1, a). Zn1–O and Zn1–N bond lengths are in the range of 2.090(4)–2.093(4) Å and 2.184(6)–2.252(6) Å, respectively. The observed *cisoid* [88.69(10)–91.31(10)°] and *transoid* [177.39(14)–180.00(2)°] angles suggest a slight distortion from ideal octahedral geometry.

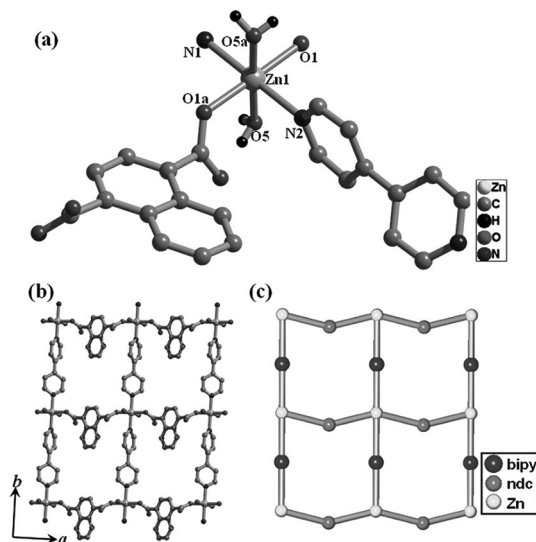


Figure 1. The crystal structure of **1** {[Zn(bipy)(1,4-ndc)(H₂O)₂]·2H₂O}: (a) Coordination environment around Zn^{II} in a ball-and-stick model; hydrogen atoms of 1,4-ndc and bipy are omitted for clarity. Symmetry codes: a = 2 – x, y, 1.5 – z. (b) View of the 2D square grid constructed by Zn^{II}, 1,4-ndc, and bipy linkers (H atoms are not shown). (c) Simplified view of the 4⁴-sql topology in **1**.

Structural analysis reveals that **1** has a 2D structure with 4⁴-sql topology (see parts b and c of Figure 1), and the grids can best be described as constructed from 1D [Zn(bipy)-(H₂O)₂] chains that are linked hand-to-hand by the 1,4-ndc ligand in the (40–4) plane. When the structure is viewed along the [010] direction it reveals an –ABCD– type of packing in which the stacking progresses along the [10–1] direction (Figure S4 in the Supporting Information). The neighboring grids “talk” to each other through the hydrogen-bonding interaction of water molecules and carboxylate oxygen atoms to generate a 3D supramolecular structure. The dimension of the rectangular grid is about (3.7 × 6.7) Å², which reduces drastically because of –AB– stacking and converts the structure into a nonporous condensed phase (Figure S5). Zn···Zn separation along Zn···bipy···Zn and Zn···1,4-ndc···Zn is 11.53 and 11.32 Å², respectively.

Crystal Structure Description of 2

Compound **2** crystallizes in the orthorhombic space group *P222₁*, and X-ray structural determination reveals a fourfold interpenetrated 3D structure made up of Zn^{II}, 1,4-ndc, and bpe linkers. Geometrically, there are two different Zn^{II} sites in **2** and they are octahedral (Figure 2, a). Octahedral coordination to Zn1 is furnished by O1a, O2a, O1b, and O2b oxygen atoms from two chelated carboxylate groups of two different 1,4-ndc and two N atoms, N1c and N1d, of pyridyl groups from two different bpe linkers. Similarly, coordination around Zn2 is provided by four oxygen atoms (O3a, O4a, O3e, O4e) from two chelated carboxylate groups, and two pyridyl nitrogen atoms (N2a, N2e). Zn–O

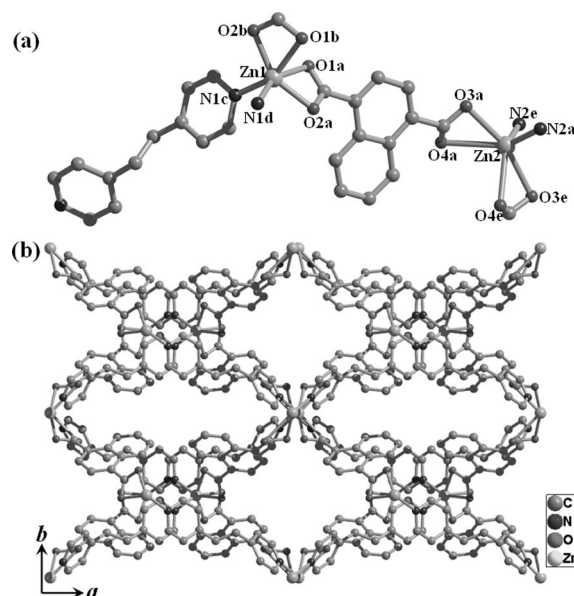


Figure 2. Crystal structure of **2** {[Zn(bpe)(1,4-ndc)]·2DMF}: (a) Coordination environment around Zn^{II} atoms. Symmetry codes, a: 2 – x, 2 – y, 0.5 + z; b: 2 – x, –1 + y, 0.5 – z; c: 1 – x, 1 – y, 0.5 + z; d: 1 – x, y, 0.5 – z; e: 2 – x, y, 1.5 – z. (b) View of the 3D framework constructed by Zn^{II}, 1,4-ndc, and bpe linkers (hydrogen atoms and DMF molecules are not shown for clarity).

and Zn–N bond lengths are in the range of 2.066(7)–2.650(3) and 2.052(9)–2.063(10) Å, respectively. The nodes Zn1 and Zn2 are connected with each other in three directions by 1,4-ndc and bpe linkers to generate a 3D diamondoid framework (Figure 2, a and b). If one assumes carboxylate coordinations to Zn nodes as monodentate, the octahedral geometry can be approximated to a tetrahedral, and the assumption supports the occurrence of a diamondoid net in **2**. In fact, topological analysis with TOPOS^[18h,27] software suggests that each Zn^{II} atom acts as a 4-connecting node (Figure 3, a and b), and the overall structure has **dia** net topology. The diamondoid net houses large cavities (Figure 3, c) that assist further nucleation in

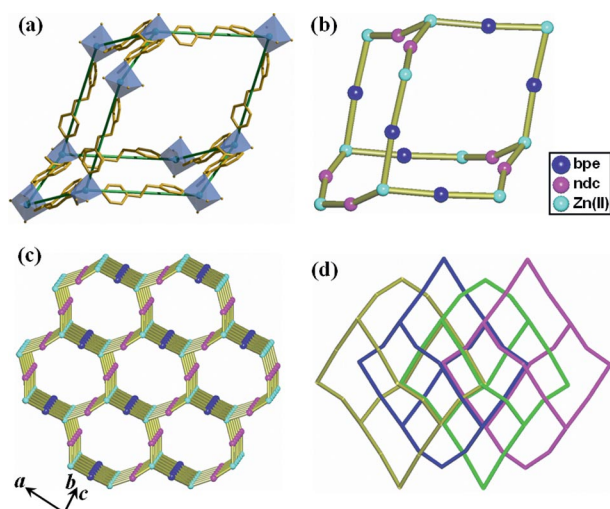


Figure 3. (a, b) A single **dia** unit cage of **2**. (c) View of a single 3D net showing large cavities. (d) Topological representation of the fourfold interpenetrating net in **2** (four different nets are shown in four different colors).

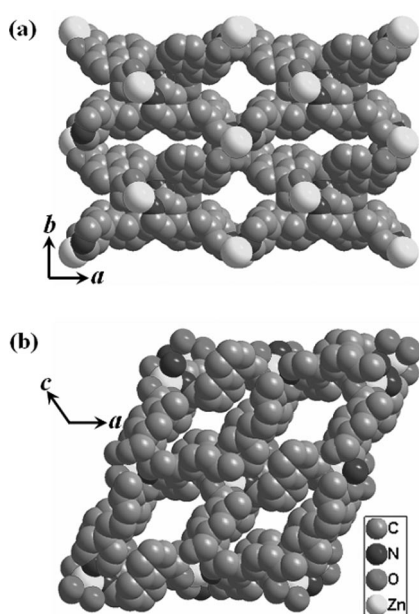


Figure 4. Space-fill model showing the pore structure in (a) **2** and (b) **3** (hydrogen atoms are not shown for clarity).

vacant spaces and allow the formation of new 3D nets in those regions. The cavities are large enough to generate a complex fourfold interpenetrated 3D structure (Figure 3, d). Interpenetration analysis with TOPOS suggests the presence of a rare case of Class IIIa interpenetration^[18i] in which both translating and nontranslating symmetry operations relate the 4 **dia** nets. The Zn^{II}–Zn separation along Zn^{II}–1,4-ndc–Zn and Zn^{II}–bpe–Zn are 10.86 and 13.35 Å, respectively. The fourfold interpenetrated framework houses small rectangular channels of dimensions (3.3 × 3.2) Å² along the *c* direction (Figure 4, a). Calculation using PLATON^[24] suggests that the framework possesses 618 Å³ (25% per unit cell volume) void volume after removal of guest DMF molecules.

Crystal Structure Description of **3**

Compound **3** crystallizes in the monoclinic system with space group *P*2₁; X-ray structure determination reveals, similar to **2**, a fourfold interpenetrated 3D framework composed of Zn^{II}, 1,4-ndc, and bpee linkers. The basic structural feature of **3** is similar to **2**; however, unlike **2**, there are two different Zn^{II} nodes: Zn1 is tetrahedral and Zn2 is octahedral. Tetrahedral coordination to Zn1 is provided by two carboxylate oxygen atoms (O1a, O8a) and two pyridyl nitrogen atoms (N2c, N2d) from two different 1,4-ndc and two bpee linkers, respectively (Figure 5, a). Zn2 is octahedrally surrounded by O3b, O4b, O5b, and O6b oxygen atoms from two different chelated carboxylate groups of

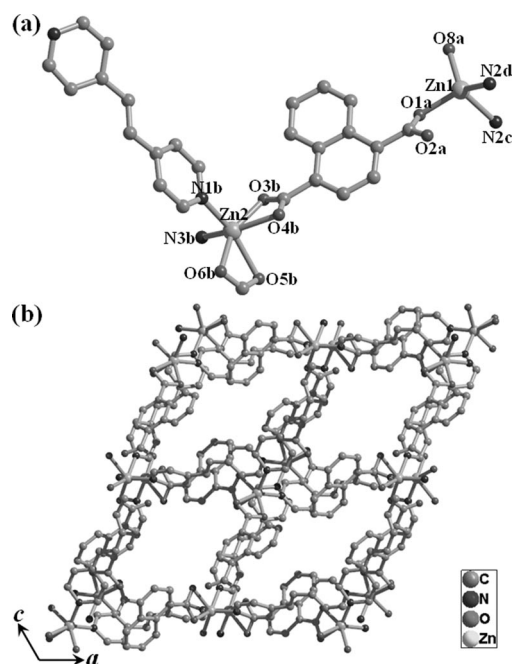


Figure 5. Crystal structure of **3** {[Zn(bpee)(1,4-ndc)]₂·2DMF}: (a) Coordination environment around Zn^{II} atoms. Symmetry codes, a: 1 - x, 0.5 + y, 2 - z; b: 1 - x, -0.5 + y, 1 - z; c: -x, -0.5 + y, 1 - z; d: -x, 0.5 + y, -z. (b) View of the 3D framework constructed by Zn^{II}, 1,4-ndc, and bpee linkers (hydrogen atoms and DMF molecules are not shown for clarity).

1,4-ndc, and N1b and N3b nitrogen atoms from two different bpee linkers (Figure 5, a). The Zn–O and Zn–N bond lengths are in the range of 1.934(10)–2.250(8) and 2.046(9)–2.139(11) Å, respectively. Similar to **1**, topological analysis with TOPOS^[18h,27] software suggests that each Zn^{II} atom acts as a 4-connecting node (Figure 6, a and b), and the overall structure has **dia** net topology. Similar to **2**, a four-fold interpenetrated net results because of the presence of large cavities in a single net (Figure 6, c and d). Interpenetration analysis with TOPOS suggests the presence of Class IIIa interpenetration as found in **2**. The average Zn···Zn separation along Zn···1,4-ndc···Zn and Zn···bpee···Zn is 10.92 and 13.54 Å, respectively. Similar to **2**, a 3D structure is constructed by linking Zn^{II} nodes by 1,4-ndc and bpee linkers that house small rectangular channels of dimensions (2.8 × 2.6) Å² along the *b* direction (Figure 4, b). Calculation using PLATON^[24] suggests that the framework possesses 758 Å³ (29% per unit cell volume) void volume after removal of guest DMF molecules.

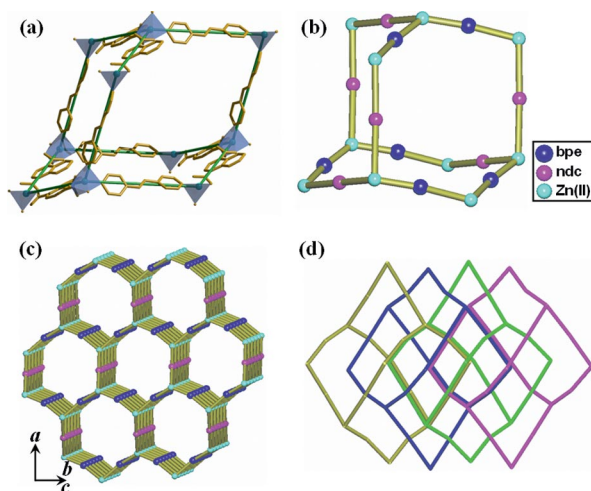


Figure 6. (a, b) A single **dia** unit cage of **3**. (c) View of a single 3D net showing large cavities. (d) Topological representation of the fourfold interpenetrating net in **3** (four different nets are shown in four different colors).

Thermal and Powder X-ray Diffraction (PXRD) Study

Compound **1** loses its single crystallinity at room temp. because of the release of guest water molecules. This observation is in line with the thermogravimetric analysis (TGA) curve of **1** that shows only a single-step weight loss (found 8.2%, calcd. 7.6%) at high temperature (130–195 °C) due to the loss of two coordinated water molecules (Figure 7, a). The dehydrated compound is stable up to 370 °C and then decomposes into an unidentified product. Compound **2** loses two guest DMF molecules in one step (found 14.0%, calcd. 13.6%, temperature range about 130–180 °C). The desolvated compound, **2'**, is thermally stable up to 250 °C and then decomposes in two overlapping steps (Figure 7, b). Similar to compound **1**, compound **3** also loses its single crystallinity at room temp. due to release of one guest DMF

molecule. This can be confirmed from the TGA curve that shows only one-step weight loss (found 7.4%, calcd. 8.5%) in the temperature range 100–180 °C, which corresponds to the release of a second guest DMF molecule. The guest-free compound, **3'**, is stable up to 280 °C (Figure 7, c). The phase purity of the bulk samples for compounds **1–3** was confirmed by very good correspondence of the observed PXRD patterns with the simulated patterns (see Figures S6–S8 in the Supporting Information). The PXRD patterns of desolvated compounds **2'** and **3'** show significant changes in peak positions compared to the as-synthesized frameworks, thereby suggesting structural transformation upon removal of solvent molecules rather than collapse of the framework (Figures S7 and S8). However, when **2'** is exposed to DMF vapor for 2 d, the original structure regenerates as confirmed by PXRD experiments (Figure S7).

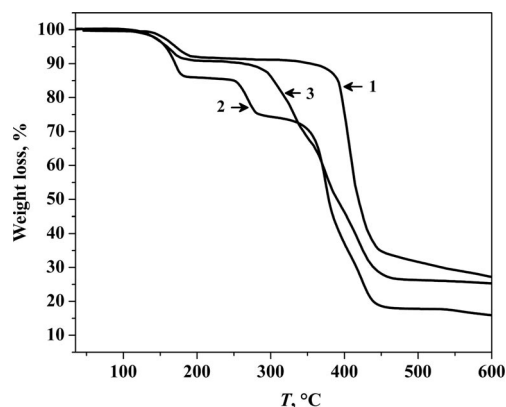


Figure 7. TGA curves of compounds **1–3** in the temperature range 35–600 °C under a nitrogen atmosphere (heating rate 5 °C min^{−1}).

Adsorption Study

To study porous properties, adsorption studies with gases such as CO₂ and N₂ were carried out with the desolvated compounds **2'** and **3'**. The N₂ (kinetic diameter 3.6 Å) adsorption study of **2'** at 77 K revealed no uptake (Figure 8, b), which is evident because of the larger kinetic diameter of the adsorbate relative to the window dimension of the channels. Interestingly, the CO₂ (kinetic diameter 3.3 Å) adsorption profile measured at 195 K with **2'** shows a typical type-I profile, which suggests the microporous nature of the framework. The profile reveals rapid uptake at low pressure that gradually increases at high *P/P*₀, and the adsorption ends with final uptake volume of 79.6 mL g^{−1} (Figure 8, a). The inclusion of CO₂ is justified because the channel dimension of **2'** is close to the kinetic diameter of CO₂. The CO₂ isotherm was analyzed with the Langmuir equation and suggests a surface area of 418 m² g^{−1}; the corresponding BET surface area is 237 m² g^{−1}. A high value of enthalpy of adsorption, 32.9 kJ mol^{−1} [calculated by the Dubinin Radushkevich (DR) equation^[28]], suggests the strong interaction of CO₂ molecules with **2'**. This type of selective gas adsorption is a unique property of metal–organic frame-

work compounds in which the window dimension of the channel plays a crucial role and is well documented in the literature.^[2b,29] Compound **3'** has a smaller channel dimension than the kinetic diameter of N₂ and CO₂ and hence does not show any uptake (Figure S9 in the Supporting Information). To understand the interaction of different solvent molecules with the host frameworks, adsorption studies with different solvent vapors, namely, H₂O, MeOH, and EtOH, were carried out with desolvated compounds **2'** and **3'**. Similar to the CO₂ profile, type-I isotherms were obtained in MeOH (kinetic diameter 4 Å) and EtOH (kinetic diameter 4.3 Å) adsorption experiments with compound **2'** (Figure 9). A significant amount of MeOH, 83 mL g⁻¹, which corresponds to 1.6 molecules per formula unit, was occluded into the pore surfaces of **2'**. The EtOH adsorption profile reveals an uptake of 61 mL g⁻¹, which corresponds to 1.2 molecules of the adsorbate per formula unit of **2'**. The adsorbate–adsorbent affinity, defined by parameter βE_0 calculated by the DR equation,^[28] suggests values of 10.9 and 7.2 kJ mol⁻¹ for MeOH and EtOH, respectively. The high values of βE_0 indicate strong interaction between the host framework and adsorbate molecules. Surprisingly, the H₂O adsorption (kinetic diameter, 2.68 Å) profile of **2'** shows different behavior when compared to MeOH and EtOH isotherms and reveals small uptake at low pressure and then a gradual increase of uptake at higher pressure (Figure 9, a). This observation can be correlated with the presence of a hydrophobic pore surface regulated by 1,4-ndc ligands, which do not allow the adsorbate molecules to diffuse through the channel. The gradual uptake at higher pressure (when the vapor pressure of H₂O is high) is attributed to the presence of strong adsorbate–adsorbate interaction in addition to the adsorbate–adsorbent interaction, which probably leads to the cluster formation in the pore^[30] and eventually higher uptake. The solvent vapor adsorption study of **2'** suggests that the framework has a stronger affinity towards molecules that are less polar than H₂O and carry hydrophobic groups such as –CH₃, –C₂H₅. The weak affinity of **2'** towards H₂O is also supported by a smaller βE_0 value (4.80 kJ mol⁻¹) when compared with MeOH and

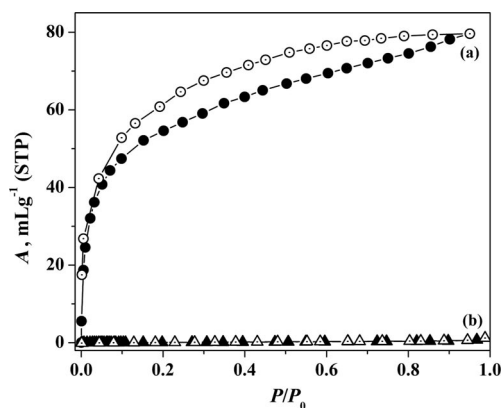


Figure 8. Gas adsorption isotherms of **2'**: (a) CO₂ at 195 K and (b) N₂ at 77 K (P_0 is the saturated vapor pressure of the corresponding adsorbates at the measurement temperature).

EtOH. MeOH and EtOH vapor adsorption studies with **3'** reveal no uptake, which can be correlated to smaller pore size relative to the kinetic diameter of the respective adsorbate molecules (Figure S10 in the Supporting Information); however, the H₂O adsorption profile shows low uptake at high-pressure regions, which can be attributed to the hydrophobic pore surface that leads to cluster formation in the pore, as in **2'**.

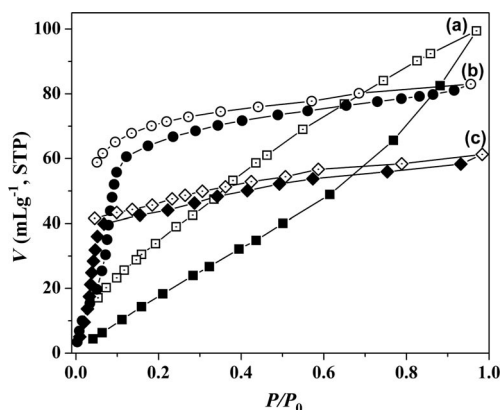


Figure 9. Vapor adsorption isotherms for **2'**: (a) H₂O at 298 K; (b) MeOH at 293 K; and (c) EtOH at 298 K (P_0 is the saturated vapor pressure of the adsorbates at the corresponding temperature).

Conclusion

We have fabricated three new MOFs of Zn^{II} using a mixed-ligand system and characterized them structurally with single-crystal X-ray diffraction measurements. Structural analyses show that **1** has a 2D rectangular-grid-type network, whereas **2** and **3** possess an interesting 3D fourfold interpenetrated diamondoid structure. The structural versatility and regularity was controlled by changing the pillar module from 4,4'-bipyridyl to 1,2-bis(4-pyridyl)ethylene. The selectivity and different affinity of the frameworks towards different adsorbates are correlated by the window dimension and polarity of the pore surface. Compound **2** selectively adsorbs CO₂ over N₂ and hence can find potential application in separating a mixture of CO₂/N₂. Compound **2** also shows strong affinity towards solvent molecules such as MeOH and EtOH.

Experimental Section

Materials: All the reagents and solvents employed were commercially available and used as supplied without further purification. Zn(NO₃)₂·6H₂O, 1,4-naphthalenedicarboxylic acid, 4,4'-bipyridine, 1,2-bis(4-pyridyl)ethane, and 1,2-bis(4-pyridyl)ethylene were obtained from the Aldrich Chemical Company.

Physical Measurements: The elemental analyses were carried out with a Flash 2000 Elemental Analyzer. IR spectra of the compounds were recorded with a Bruker IFS 66v/S spectrophotometer using KBr pellets in the region of 4000–400 cm⁻¹. TGA was carried out with a Mettler Toledo TGA850 instrument in the temperature range of 35–600 °C under a nitrogen atmosphere (flow rate of

50 mL min⁻¹) at a heating rate of 5 °C min⁻¹. PXRD patterns of the samples in different states were recorded with a Bruker D8 Discover instrument using Cu-K α radiation.

Adsorption Measurements: N₂ and CO₂ adsorption studies with the dehydrated samples of **2** and **3**, prepared at 423 K under high vacuum for 12 h, were carried out with a Quantachrome Quadrasorb SI analyzer at 77 and 195 K, respectively. The adsorption isotherms of different solvents (such as H₂O and EtOH at 298 K, and MeOH at 293 K) were measured in the vapor state with a BELSORP-aqua-3 volumetric adsorption instrument from BEL, Japan. The adsorbent sample (100–150 mg), which had been pre-treated at 423 K for **2** and **3**, respectively, was placed in the sample chamber (ca. 12 mL) maintained at $T \pm 0.03$ K with a vacuum level of 10⁻¹ Pa for about 12 h prior to measurement of the isotherms. The adsorbate was charged into the sample tube, and then the change of the pressure was monitored and the degree of adsorption was determined by the decrease in pressure at the equilibrium state. All operations were computer-controlled and automatic.

{[Zn(bipy)(1,4-ndc)(H₂O)₂·2H₂O]} (1): Compound **1** was synthesized under solvothermal conditions at 120 °C. 1,4-ndc (0.108 g, 0.5 mmol) and bipy (0.078 g, 0.5 mmol) were dissolved in DMF/H₂O (6 mL, 5:1) and stirred for 30 min. Zn(NO₃)₂·6H₂O (0.149 g, 0.5 mmol) was added to the above ligand solution and stirred for another 30 min. Subsequently, the reaction mixture was transferred into a Teflon bomb, placed in a steel autoclave, and heated at 120 °C. After 3 d, a white crystalline solid was isolated. The solid was filtered and washed several times with DMF; yield 78% relative to Zn^{II}. C₂₂H₂₂N₂O₈Zn (507.80): calcd. C 52.03, H 4.37, N 5.52; found C 51.63, H 4.04, N 5.16. IR (KBr): $\tilde{\nu}$ = 3444 ν (O–H), 1600 $\nu_{\text{as}}(\text{OCO})$, 1357 $\nu_{\text{s}}(\text{OCO})$ cm⁻¹.

{[Zn(bpe)(1,4-ndc)]₂·2DMF} (2): Compound **2** was synthesized under solvothermal conditions at 150 °C. 1,4-ndc (0.108 g, 0.5 mmol) and bpe (0.092 g, 0.5 mmol) were dissolved in DMF (6 mL) and stirred for 30 min. Zn(NO₃)₂·6H₂O (0.149 g, 0.5 mmol) was added to the above ligand solution and stirred for another 30 min. The mixture was then transferred into a Teflon bomb, which was subsequently placed in a steel autoclave and heated at 150 °C. After 3 d, a light yellow crystalline solid was isolated. The solid was filtered and washed several times with DMF; yield 89% relative to Zn^{II}. C₅₄H₅₀N₆O₁₀Zn₂ (1073.78): calcd. C 60.40, H 4.69, N 7.83; found C 59.92, H 4.83, N 7.58. IR (KBr): $\tilde{\nu}$ = 1571 $\nu_{\text{as}}(\text{OCO})$, 1352 $\nu_{\text{s}}(\text{OCO})$ cm⁻¹.

{[Zn(bpee)(1,4-ndc)]₂·2DMF} (3): Compound **3** was synthesized under solvothermal conditions at 150 °C by adopting a similar reaction procedure to that of **2**, only changing the linker to bpee instead of bpe; yield 83% relative to Zn^{II}. C₅₄H₄₆N₆O₁₀Zn₂ (1069.75): calcd. C 60.63, H 4.33, N 7.86; found C 59.82, H 4.65, N 7.47. IR (KBr): $\tilde{\nu}$ = 1611 $\nu(\text{C}=\text{C})$, 1576 $\nu_{\text{as}}(\text{OCO})$, 1361 $\nu_{\text{s}}(\text{OCO})$ cm⁻¹.

Single-Crystal X-ray Diffraction: Suitable single crystals of compounds **1–3** were mounted on a thin glass fiber with commercially available super glue. X-ray single-crystal structural data were collected with a Bruker Smart CCD diffractometer equipped with a normal focus and a 2.4 kW sealed-tube X-ray source with graphite-monochromated Mo-K α radiation (λ = 0.71073 Å) operating at 50 kV and 30 mA. For all the compounds, data were collected at 100 K. The SAINT^[20] program was used for the integration of diffraction profiles, and absorption correction was made with the SADABS^[21] program. All the structures were solved by SIR 92^[22] and refined by full-matrix least-squares methods using SHELXL97.^[23] For all the compounds the non-hydrogen atoms were refined anisotropically. The hydrogen atoms were fixed by HFIX and placed in ideal positions. Potential solvent accessible area or void space was

calculated using PLATON 99^[24] multipurpose crystallographic software. All crystallographic data and structure refinement parameters of the compounds are summarized in Table 1. Selected bond lengths and angles of **1–3** are given in Tables S1–S3, respectively. All calculations were carried out with SHELXL 97,^[23] PLATON 99,^[24] SHELXS 97,^[25] and the WinGX system, version 1.70.01.^[26]

Table 1. Crystal data and structure refinement parameters for **1–3**.

	1	2	3
Empirical formula	C ₂₂ H ₂₂ N ₂ O ₈ Zn	C ₅₄ H ₅₀ N ₆ O ₁₀ Zn ₂	C ₅₄ H ₄₆ N ₆ O ₁₀ Zn ₂
M_r	507.77	1073.8	1069.76
Crystal system	monoclinic	orthorhombic	monoclinic
Space group	$P2_1/c$	$P22_21$	$P2_1$
a [Å]	9.8849(2)	16.3611(10)	19.0493(10)
b [Å]	11.5339(3)	10.8518(7)	14.4336(10)
c [Å]	9.8248(2)	13.9023(8)	10.9838(6)
β [°]	109.8970(10)	–	122.294(3)
V [Å ³]	1053.27(4)	2468.3(3)	2552.9(2)
Z	2	2	2
T [K]	294	100	100
λ (Mo-K α)	0.7107	0.7107	0.7107
ρ_{calcd} [g cm ⁻³]	1.589	1.512	1.384
μ [mm ⁻¹]	1.220	1.044	1.003
θ_{max} [°]	26.5	19.6	30.3
Total data	13815	13550	30342
Unique data	2182	2203	12103
R_{int}	0.038	0.041	0.083
Data [$I > 2\sigma(I)$]	2036	2045	7098
R^{a}	0.0418	0.0678	0.0998
R_w^{b}	0.1194	0.1835	0.3008
GOF	1.12	1.04	1.02

[a] $R = \Sigma||F_o| - |F_c||/\Sigma|F_o|$. [b] $R_w = [\Sigma\{w(F_o^2 - F_c^2)^2\}/\Sigma\{w(F_o^2)^2\}]^{1/2}$.

CCDC-771424 (for **1**), -771425 (for **2**), and -771426 (for **3**) contain the supplementary crystallographic data for this paper. These data can be obtained free of charge from The Cambridge Crystallographic Data Centre via www.ccdc.cam.ac.uk/data_request/cif.

Supporting Information (see also the footnote on the first page of this article): IR spectra of compounds **1–3** (Figures S1–S3), PXRD figures of **1–3** (Figures S4–S6), gas adsorption profiles of **3** (Figure S7), and bond length and bond angle tables for **1–3** (Tables S1–S3).

Acknowledgments

T. K. M. gratefully acknowledges the financial support from the Department of Science and Technology, Government of India (Fast Track Proposal). P. K. is grateful to the Council of Scientific and Industrial Research, India for an SRF fellowship.

- a) G. Férey, *Chem. Soc. Rev.* **2008**, 37, 191; b) T. K. Maji, S. Kitagawa, *Pure Appl. Chem.* **2007**, 79, 2155; c) J. L. C. Rowsell, O. M. Yaghi, *Angew. Chem. Int. Ed.* **2005**, 44, 4670; d) S. Kitagawa, R. Kitaura, S. Noro, *Angew. Chem. Int. Ed.* **2004**, 43, 2334; e) C. N. R. Rao, S. Natarajan, R. Vaidhyanathan, *Angew. Chem. Int. Ed.* **2004**, 43, 1466; f) C. Janiak, *Dalton Trans.* **2003**, 2781.
- a) M. Dincă, A. F. Yu, J. R. Long, *J. Am. Chem. Soc.* **2006**, 128, 8904; b) D. N. Dybtsev, H. Chun, S. H. Yoon, D. Kim, K. Kim, *J. Am. Chem. Soc.* **2004**, 126, 32; c) L. Pan, B. Parker, X. Huang, D. H. Olson, J. Y. Lee, J. Li, *J. Am. Chem. Soc.* **2006**, 128, 4180; d) S. Ma, D. Sun, J. M. Simmons, C. D. Collier, D. Yuan, H.-C. Zhou, *J. Am. Chem. Soc.* **2008**, 130, 1012.

- [3] a) R.-G. Xiong, X.-Z. You, B. F. Abrahams, Z. Xue, C.-M. Che, *Angew. Chem. Int. Ed.* **2001**, *40*, 4422; b) L. Pan, D. H. Olson, L. R. Ciemnolonski, R. Heddy, J. Li, *Angew. Chem. Int. Ed.* **2006**, *45*, 616; c) B. Chen, C. Liang, J. Yang, D. S. Contreas, Y. L. Clancy, E. B. Lobkovsky, O. M. Yaghi, S. Dai, *Angew. Chem. Int. Ed.* **2006**, *45*, 1390; d) S. Mohapatra, K. Hembram, U. Waghmare, T. K. Maji, *Chem. Mater.* **2009**, *21*, 5406.
- [4] a) S. Horike, M. Dincă, K. Tamaki, J. R. Long, *J. Am. Chem. Soc.* **2008**, *130*, 5854; b) C. D. Wu, A. Hu, L. Zhang, W. B. Lin, *J. Am. Chem. Soc.* **2005**, *127*, 8940; c) D. N. Dybtsev, A. L. Nuzhdin, H. Chun, K. P. Bryliakov, E. P. Talsi, V. P. Fedin, K. Kim, *Angew. Chem. Int. Ed.* **2006**, *45*, 916; d) J. S. Seo, D. Whang, H. Lee, S. I. Jun, J. Oh, Y. J. Jeon, K. Kim, *Nature* **2000**, *404*, 982.
- [5] a) M. Plabst, L. B. McCusker, T. Bein, *J. Am. Chem. Soc.* **2009**, *131*, 18112; b) A. N. Părvulescu, G. Marin, K. Suwinska, V. C. Kravtsov, M. Andruh, V. Părvulescu, V. I. Părvulescu, *J. Mater. Chem.* **2005**, *15*, 4234; c) B.-C. Tzeng, T.-H. Chiu, B.-S. Chen, G.-H. Lee, *Chem. Eur. J.* **2008**, *14*, 5237.
- [6] a) B. L. Chen, L. B. Wang, F. Zapata, G. D. Qian, E. B. Lobkovsky, *J. Am. Chem. Soc.* **2008**, *130*, 6718; b) Z. G. Xie, L. Q. Ma, K. E. Dekrafft, A. Jin, W. B. Lin, *J. Am. Chem. Soc.* **2010**, *132*, 922; c) L. G. Qiu, Z. Q. Li, Y. Wu, W. Wang, T. Xu, X. Jiang, *Chem. Commun.* **2008**, 3642; d) B. L. Chen, L. B. Wang, Y. Q. Xiao, F. R. Fronczek, M. Xue, Y. J. Cui, G. D. Qian, *Angew. Chem. Int. Ed.* **2009**, *48*, 500.
- [7] a) P. Horcajada, C. Serre, G. Maurin, N. A. Ramsahye, F. Balas, M. Vallet-Regi, M. Sebban, F. Taulelle, G. Férey, *J. Am. Chem. Soc.* **2008**, *130*, 6774; b) P. Horcajada, C. Serre, M. Vallet-Regi, M. Sebban, F. Taulelle, G. Férey, *Angew. Chem. Int. Ed.* **2006**, *45*, 5974.
- [8] a) Y. F. Song, L. Cronin, *Angew. Chem. Int. Ed.* **2008**, *47*, 4635; b) K. K. Tanabe, S. M. Cohen, *Angew. Chem. Int. Ed.* **2009**, *48*, 7424; c) W. J. Rieter, K. M. L. Taylor, W. B. Lin, *J. Am. Chem. Soc.* **2007**, *129*, 9852.
- [9] a) M. Eddaoudi, H. L. Li, O. M. Yaghi, *J. Am. Chem. Soc.* **2000**, *122*, 1391; b) M. Eddaoudi, J. Kim, N. Rosi, D. Vodak, J. Wachter, M. O'Keeffe, O. M. Yaghi, *Science* **2002**, *295*, 469.
- [10] a) R. Matsuda, R. Kitaura, S. Kitagawa, Y. Kubota, T. C. Kobayashi, S. Horike, M. Takata, *J. Am. Chem. Soc.* **2004**, *126*, 14063; b) W. Kaneko, M. Ohba, S. Kitagawa, *J. Am. Chem. Soc.* **2007**, *129*, 13706; c) S. K. Ghosh, W. Kaneko, D. Kiriya, M. Ohba, S. Kitagawa, *Angew. Chem. Int. Ed.* **2008**, *47*, 8843; d) D. Tanaka, K. Nakagawa, M. Higuchi, S. Horike, Y. Kubota, L. C. Kobayashi, M. Takata, S. Kitagawa, *Angew. Chem. Int. Ed.* **2008**, *47*, 3914; e) K. L. Gurunatha, T. K. Maji, *Inorg. Chem.* **2009**, *48*, 10886.
- [11] a) H. Cui, B. Zhou, L. S. Long, Y. Okano, H. Kobayashi, A. Kobayashi, *Angew. Chem. Int. Ed.* **2008**, *47*, 3376; b) T. K. Maji, G. Mostafa, R. Matsuda, S. Kitagawa, *J. Am. Chem. Soc.* **2005**, *127*, 17152; c) J. A. R. Navarro, E. Barea, A. R.-Dieguez, J. M. Salas, C. O. Ania, J. B. Parra, N. Masciocchi, S. Galli, A. Sironi, *J. Am. Chem. Soc.* **2008**, *130*, 3978.
- [12] a) L. Alaerts, C. E. A. Kirschhock, M. Maes, M. A. van der Veen, V. Finsy, A. Depla, J. A. Martens, G. V. Baron, P. A. Jacobs, J. E. M. Denayer, D. E. De Vos, *Angew. Chem. Int. Ed.* **2007**, *46*, 4293; b) Y. E. Cheon, J. Park, M. P. Suh, *Chem. Commun.* **2009**, 5436; c) H. S. Choi, M. P. Suh, *Angew. Chem. Int. Ed.* **2009**, *48*, 6865; d) T. Haneda, M. Kawano, T. Kojima, M. Fujita, *Angew. Chem. Int. Ed.* **2007**, *46*, 6643; e) A. V. Nosov, D. V. Soldatov, J. A. Ripmeester, *J. Am. Chem. Soc.* **2001**, *123*, 3563; f) P. Kanoo, K. L. Gurunatha, T. K. Maji, *J. Mater. Chem.* **2010**, *20*, 1322.
- [13] a) P. D. Southon, L. Liu, E. A. Fellows, D. J. Price, G. J. Halder, K. W. Chapman, B. Moubarak, K. S. Murray, J. F. Letard, C. J. Kepert, *J. Am. Chem. Soc.* **2009**, *131*, 10998; b) M. Nihei, L. Q. Han, H. Oshio, *J. Am. Chem. Soc.* **2007**, *129*, 5312; c) V. Niel, A. L. Thompson, M. C. Munoz, A. Galet, A. S. E. Goeta, J. A. Real, *Angew. Chem. Int. Ed.* **2003**, *42*, 3760; d) W. Kaneko, M. Mito, S. Kitagawa, M. Ohba, *Chem. Eur. J.* **2008**, *14*, 3481.
- [14] a) R. G. Xiong, J. L. Zuo, X. Z. You, B. F. Abrahams, Z. P. Bai, C. M. Che, H. K. Fun, *Chem. Commun.* **2000**, 2061; b) C. J. Kepert, M. J. Rosseinsky, *Chem. Commun.* **1998**, 31; c) S. Q. Ma, D. F. Sun, M. Ambrogio, J. A. Fillinger, S. Parkin, H.-C. Zhou, *J. Am. Chem. Soc.* **2007**, *129*, 1858; d) D. Sun, S. Ma, Y. Ke, D. J. Collins, H.-C. Zhou, *J. Am. Chem. Soc.* **2006**, *128*, 3896; e) H.-Y. Wang, S. Gao, L.-H. Huo, S. W. Ng, J.-G. Zhao, *Cryst. Growth Des.* **2008**, *8*, 665; f) M. R. Montney, R. M. Supkowski, R. L. LaDuca, *CrystEngComm* **2008**, *10*, 111; g) L. Zhang, Y.-L. Yao, Y.-X. Che, J.-M. Zheng, *Cryst. Growth Des.* **2010**, *10*, 528; h) P. Kanoo, R. Matsuda, M. Higuchi, S. Kitagawa, T. K. Maji, *Chem. Mater.* **2009**, *21*, 5860; i) S. Y. Vyasamudri, T. K. Maji, *Chem. Phys. Lett.* **2009**, *473*, 312.
- [15] a) T. M. Reineke, M. Eddaoudi, D. M. Moler, M. O'Keeffe, O. M. Yaghi, *J. Am. Chem. Soc.* **2000**, *122*, 4843; b) M. Kondo, M. Shimamura, S.-I. Noro, S. Minakoshi, A. Asami, K. Seki, S. Kitagawa, *Chem. Mater.* **2000**, *12*, 1288; c) L. Carlucci, G. Ciani, P. Macchi, D. M. Proserpio, S. Rizzato, *Chem. Eur. J.* **1999**, *5*, 237; d) L. Carlucci, G. Ciani, D. M. Proserpio, S. Rizzato, *Chem. Eur. J.* **2002**, *8*, 1519.
- [16] a) S. R. Batten, R. Robson, *Angew. Chem. Int. Ed.* **1998**, *37*, 1460; b) S. R. Batten, *CrystEngComm* **2001**, *3*, 67; c) O. D. Friedrichs, M. O'Keeffe, O. M. Yaghi, *Solid State Sci.* **2003**, *5*, 73.
- [17] a) O. Ermer, A. Eling, *Angew. Chem. Int. Ed. Engl.* **1988**, *27*, 829; b) O. Ermer, *J. Am. Chem. Soc.* **1988**, *110*, 3747.
- [18] a) X. L. Wang, C. Qin, E. B. Wang, Z. M. Su, *Chem. Commun.* **2007**, 4245; b) J. M. Taylor, A. H. Mahmoudkhani, G. K. H. Shimizu, *Angew. Chem. Int. Ed.* **2007**, *46*, 795; c) K.-W. Kim, M. G. Kanatzidis, *J. Am. Chem. Soc.* **1992**, *114*, 4878; d) A. J. Blake, N. R. Champness, P. Hubberstey, W.-S. Li, M. A. Withersby, M. Schröder, *Coord. Chem. Rev.* **1999**, *183*, 117; e) S. R. Batten, *CrystEngComm* **2001**, *18*, 1; f) B. F. Hoskins, R. Robson, *J. Am. Chem. Soc.* **1990**, *112*, 1546; g) Y. F. Hsu, C. H. Lin, J. D. Chen, J. C. Wang, *Cryst. Growth Des.* **2008**, *8*, 1094; h) V. A. Blatov, L. Carlucci, G. Ciani, D. M. Proserpio, *CrystEngComm* **2004**, *6*, 377; i) I. A. Baburin, V. A. Blatov, L. Carlucci, G. Ciani, D. M. Proserpio, *J. Solid State Chem.* **2005**, *178*, 2452.
- [19] a) M. Du, X.-H. Bu, Y. M. Guo, H. Liu, S. R. Batten, J. Ribas, T. C. W. Mak, *Inorg. Chem.* **2002**, *41*, 4904; b) A. J. Blake, N. R. Champness, A. N. Khllobystov, D. A. Lemenovskii, W.-S. Li, M. Schröder, *Chem. Commun.* **1997**, 1339; c) L. Carlucci, G. Ciani, M. Moret, D. M. Proserpio, S. Rizzato, *Chem. Mater.* **2002**, *14*, 12; d) I. Ino, J. C. Zhong, M. Munakata, T. Kuroda-Sowa, M. Maekawa, Y. Suenaga, Y. Kitamori, *Inorg. Chem.* **2000**, *39*, 4273; e) K. A. Hirsch, D. Venkataraman, S. R. Wilson, J. S. Moore, S. Lee, *J. Chem. Soc., Chem. Commun.* **1995**, 2199; f) D. S. Reddy, T. Dewa, K. Endo, Y. Aoyama, *Angew. Chem. Int. Ed.* **2000**, *39*, 4266.
- [20] SAINT+, 6.02 ed., Bruker AXS, Madison, WI, **1999**.
- [21] G. M. Sheldrick, *SADABS, Empirical Absorption Correction Program*, University of Göttingen, Göttingen, Germany, **1997**.
- [22] A. Altomare, G. Cascarano, C. Giacovazzo, A. Gualaradi, *J. Appl. Crystallogr.* **1993**, *26*, 343.
- [23] G. M. Sheldrick, *SHELXL 97*, Program for the Solution of Crystal Structure, University of Göttingen, Germany, **1997**.
- [24] A. L. Spek, *J. Appl. Crystallogr.* **2003**, *36*, 7.
- [25] G. M. Sheldrick, *SHELXS 97*, Program for the Solution of Crystal Structure, University of Göttingen, Germany, **1997**.
- [26] WinGX, A Windows Program for Crystal Structure Analysis: L. J. Farrugia, *J. Appl. Crystallogr.* **1999**, *32*, 837.
- [27] a) V. A. Blatov, A. P. Shevchenko, V. N. Serezhkin, *J. Appl. Crystallogr.* **2000**, *33*, 1193.
- [28] M. M. Dubinin, *Chem. Rev.* **1960**, *60*, 235.
- [29] a) L. Pan, K. M. Adams, H. E. Hernandez, X. Wang, C. Zheng, Y. Hattori, K. Kaneko, *J. Am. Chem. Soc.* **2003**, *125*, 3062; b) A. Comotti, S. Bracco, P. Sozzani, S. Horike, R. Mat-

- suda, J. Chen, M. Takata, Y. Kubota, S. Kitagawa, *J. Am. Chem. Soc.* **2008**, *130*, 13664.
- [30] a) E. Bekyarova, Y. Hanzawa, K. Kaneko, J. Silvestre-Albero, A. Sepulveda-Escribano, F. Rodriguez-Reinoso, D. Kasuya, M. Yudasaka, S. Iijima, *Chem. Phys. Lett.* **2002**, *366*, 463; b) K. Kaneko, Y. Hanzawa, T. Iiyama, T. Kanda, T. Suzuki, *Adsorption* **1999**, *5*, 7; c) D. Li, K. Kaneko, *Chem. Phys. Lett.* **2001**, *335*, 50.

Received: April 1, 2010
Published Online: July 21, 2010

Selective Separation of the Sulfate Anion by In Situ Crystallization of Cd^{II} Coordination Compounds Derived from Bis(pyridyl) Ligands Equipped with a Urea/Amide Hydrogen-Bonding Backbone

Subhabrata Banerjee,^[a] N. N. Adarsh,^[a] and Parthasarathi Dastidar^{*[a]}

Keywords: Coordination polymers / Anion separation / Hydrogen bonds / Crystal engineering / Cadmium / Amides

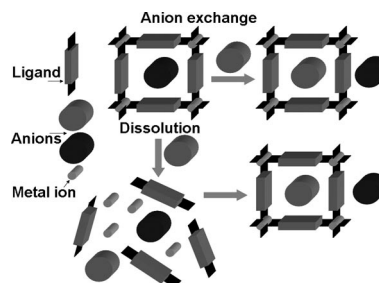
Five new coordination compounds, namely $[\{\text{Cd}(\mu\text{-L1})(\mu\text{-SO}_4)(\text{H}_2\text{O})_2\}\cdot\text{MeOH}]_\infty$ (**1**), $[\{\text{Cd}(\mu\text{-L2})_2(\text{SO}_4)(\text{H}_2\text{O})\}\cdot 3.5\text{H}_2\text{O}]_\infty$ (**2**), $[\{\text{Cd}(\mu\text{-L3})(\text{SO}_4)(\text{H}_2\text{O})_3\}\cdot\text{MeOH}]_\infty$ (**3**), $[\{\text{Cd}(\text{L4})_4(\text{H}_2\text{O})_2\}\cdot\text{SO}_4\cdot 8\text{H}_2\text{O}]$ (**4**) and $[\{\text{Cd}(\mu\text{-L5})(\mu_3\text{-SO}_4)(\text{H}_2\text{O})\}\cdot 2\text{H}_2\text{O}]_\infty$ (**5**), [**L1** = *N*-(3-picolyl)-*N'*-(3-pyridyl)urea, **L2** = *N*-(4-picolyl)-*N'*-(3-pyridyl)urea, **L3** = *N,N'*-di-3-pyridylurea, **L4** = *N,N'*-di-4-pyridylurea and **L5** = *N,N'*-di-3-pyridylnicotinamide] have been synthesized and characterized by single-crystal X-ray diffraction. It is revealed that the positional isomers **L1,L2** and **L3,L4** play a crucial role in determining the resultant supramolecular structures of **1–4**. Various supramolecular architectures, that is, a 3D coordination polymer (**1**), a 1D looped-chain coordination polymer (**2**), a 1D zigzag coordination polymer (**3**), a discrete coordination complex (**4**) and a 2D

corrugated sheet (**5**), were observed. In situ crystallization of compound **2** under competitive crystallization conditions in the presence of competing anions such as SO_4^{2-} , NO_3^- , ClO_4^- , AcO^- , Cl^- and Br^- resulted in the isolation of **2**, which indicates the selective separation of SO_4^{2-} from an aqueous mixture of other competing anions, as revealed by FTIR spectroscopy, X-ray powder diffraction and elemental analysis. The X-ray structure of **2** indicates that both intermolecular hydrogen bonding and metal–ligand coordination of SO_4^{2-} play an important role in the selective separation of SO_4^{2-} . A similar competitive crystallization also resulted in selective SO_4^{2-} separation in the form of compound **5**, as determined by FTIR spectroscopy and elemental analysis.

Introduction

One of the most prolific research activities in materials science is focussed on coordination network compounds [metal–organic frameworks (MOFs) and coordination polymers (CPs)] because of their various potential applications.^[1] Their ease of synthesis combined with the opportunity of isolating highly pure crystalline products that are amenable to detailed single-crystal X-ray structural characterization and the ability to readily modify the organic ligands to achieve need-based tuning of the final supramolecular structures make this class of functional materials more attractive. Among the various applications that this class of materials offers, anion-binding/recognition/separation has attracted attention because it is highly relevant in the clean-up of the environment.^[2] The ability of MOFs to exchange anions was first reported nearly two decades ago.^[3] Since then efforts have been made to develop coordination networks that are capable of exchanging and/or separating anions from a complex mixture.^[4] However, designing such

organic–inorganic hybrid systems requires a deeper understanding of the mechanism of anion exchange/separation. The widely accepted view supports a solid-state exchange mechanism because of the insoluble nature of coordination network compounds in most common solvents and the similarity between the initial and final network structures. However, this apparent single-crystal-to-single-crystal anion-exchange mechanism is counter-argued, and it has been proven beyond doubt that at least in certain one-dimensional coordination polymers anion exchange in water is solvent-mediated and involves dissolution and competitive crystallization (Scheme 1).^[5]



Scheme 1. Schematic representation of selective anion separation.

[a] Department of Organic Chemistry, Indian Association for the Cultivation of Science (IACS), 2A & 2B Raja S. C. Mullick Road, Jadavpur, Kolkata 700032, India
Fax: +91-33-2473-2805
E-mail: parthod123@rediffmail.com
ocpd@iacs.res.in

Supporting information for this article is available on the WWW under <http://dx.doi.org/10.1002/ejic.201000359>.

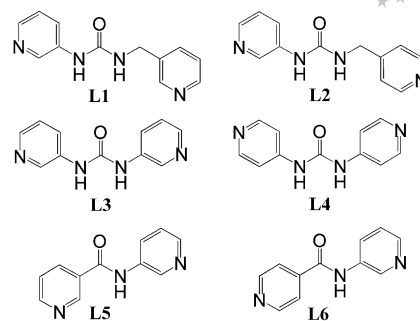
Inspired by the second alternative mechanism involving dissolution and competitive crystallization, Custelcean and co-workers^[4,6] demonstrated that the crystallization process in a coordination network synthesis itself can be exploited as a separation tool. In this process, the coordination compound is competitively crystallized from a complex mixture of anions, which results in the selective inclusion of certain anions depending on their size, shape and specific interactions within the network structures. This process has a clear advantage over traditional anion exchange as it can avoid the common problem of slow solid-state ion-exchange kinetics.

As a part of our ongoing research into the use of various hydrogen-bonded functionalized bidentate ligands for generating intriguing metal–organic compounds,^[7] we recently focussed our attention on developing metal–organic compounds capable of binding and separating important anions from a complex mixture of anions.^[8] The separation of SO_4^{2-} from an aqueous solution containing another oxo anion like NO_3^- is important in the cleaning of radioactive waste tanks.^[2] Separating SO_4^{2-} from an aqueous solution containing other competing anions is difficult, because the ease of extracting anions from an aqueous solution to an organic layer follows the so-called Hofmeister series: $\text{ClO}_4^- > \text{I}^- > \text{SCN}^- > \text{NO}_3^- > \text{Br}^- > \text{Cl}^- \gg \text{SO}_4^{2-} > \text{CO}_3^{2-} > \text{PO}_4^{3-}$.^[9] However, in situ competitive crystallization of coordination compounds from a complex mixture of competing anions has proved a viable approach to separating anions, overcoming the Hofmeister bias, as demonstrated by Custelcean and co-workers^[4,6] and our group.^[8,10] In this process, a phase change from liquid to solid occurs as the targeted anion is crystallized as part of the coordination compound, which is unlike the process of separation to which the Hofmeister series applies.

Because the environment around the anion may vary considerably in such materials and (the environment around the anion) may have a direct influence on the binding and selectivity of anions, it is important to recognize structural features that might affect the anion selectivity. Both urea and amide moieties can interact with oxo anions through multiple hydrogen bonds; urea, in particular, is a more attractive hydrogen-bonding group due to its affinity towards oxo anions through highly complementary hydrogen-bonding interactions.^[7b,11]

Very recently we demonstrated that a Borromean weave coordination polymer^[12] sustained by urea⋯sulfate hydrogen bonding is able to separate the important SO_4^{2-} anion from a complex mixture of anions (SO_4^{2-} , NO_3^- , ClO_4^- and CF_3COO^-).^[10]

In this report we present the synthesis and single-crystal structures of five coordination compounds **1–5** derived from **L1–L5** and CdSO_4 (Scheme 2). In each case, selective separation of SO_4^{2-} was attempted from an aqueous solution containing competing anions, namely SO_4^{2-} , NO_3^- , ClO_4^- , AcO^- , Cl^- and Br^- , and only in the cases of **2** and **5** could the SO_4^{2-} anion be separated selectively. Single-crystal structures of these coordination compounds are discussed in the context of SO_4^{2-} anion separation.



Scheme 2. Urea compounds **L1–L6**.

Results and Discussion

We decided to work with six bis(pyridyl) ligands equipped with a hydrogen-bonding backbone (urea/amide). With amide and urea both being highly polar as well as being a good hydrogen-bonding donor and acceptor, it is expected that these moieties will interact favourably with the anions. To induce structural variation into the resulting coordination compounds, we deliberately selected pairwise (**L1,L2**, **L3,L4** and **L5,L6**) positional isomers (Scheme 2). We decided to study the coordination compounds derived from these ligands and CdSO_4 , mainly because SO_4^{2-} is a good hydrogen-bond acceptor especially towards the urea moiety, and a borderline base may help in the selective separation of anions through hydrogen-bonding interactions and coordination to a soft acid metal centre like Cd^{II} . When treated with CdSO_4 in $\text{MeOH}/\text{EtOH}/\text{H}_2\text{O}$ at room temperature in a metal/ligand ratio of 1:2, five coordination compounds **1–5** derived from **L1–L5**, respectively, were isolated and characterized by single-crystal X-ray diffraction (Table 1). The reaction of CdSO_4 with **L6** also resulted in a crystalline material, which, unfortunately, could not be characterized by single-crystal X-ray diffraction.

Crystal Structures of **1–5**

Single-crystal X-ray diffraction studies revealed that the coordination compounds **1** and **2** derived from the positional isomers **L1** and **L2**, respectively, are drastically different. Whereas **1** belongs to the non-centrosymmetric orthorhombic space group $P2_12_12_1$, compound **2** crystallized in the centrosymmetric triclinic space group $P\bar{1}$ (Table 1). The ligands in both structures show a highly non-planar conformation mainly due to the presence of a tetrahedral CH_2 moiety; the dihedral angles in **1** and **2** involving the pyridylurea plane and the pyridyl moiety of the picolyl group are found to be 70.5(1) and 75.3(1)–84.3(1)°, respectively. The bis(pyridyl)urea ligand **L1** in **1** displays an *anti*-ligating topology, whereas **L2** in **2** shows a *syn* ligating topology (Figure 1a,b). The Cd^{II} centres in both structures adopt a slightly distorted octahedral geometry (Table 2). Whereas the equatorial positions of Cd^{II} in **1** are occupied by three water molecules and one O atom from SO_4^{2-} , the axial positions are occupied by the pyridyl N atoms of the ligand. The SO_4^{2-} counter-anion in this structure acts as a

Table 1. Crystal data for **1–5**.

	1	2	3	4	5
CCDC-	771625	771622	771624	771623	771621
Empirical formula	C ₁₃ H ₂₀ CdN ₄ O ₈ S	C ₂₄ H ₂₈ CdN ₈ O ₈ S	C ₁₂ H ₂₀ CdN ₄ O ₉ S	C ₄₄ H ₆₀ CdN ₁₆ O ₁₈ S	C ₁₁ H ₁₅ CdN ₃ O ₈ S
Formula mass	504.79	701.00	508.78	1245.54	461.72
Crystal size [mm]	0.22 × 0.18 × 0.12	0.38 × 0.24 × 0.08	0.28 × 0.18 × 0.12	0.26 × 0.14 × 0.10	0.28 × 0.22 × 0.12
Crystal system	orthorhombic	triclinic	monoclinic	monoclinic	monoclinic
Space group	<i>P</i> 2 ₁ 2 ₁ 2 ₁	<i>P</i> $\bar{1}$	<i>P</i> 2 ₁ / <i>n</i>	<i>C</i> 2/ <i>c</i>	<i>P</i> 2 ₁ / <i>n</i>
<i>a</i> [Å]	8.5328(5)	8.9312(9)	7.844(5)	23.357(3)	11.8205(17)
<i>b</i> [Å]	8.9113(5)	12.6841(13)	11.054(7)	15.7856(17)	6.9347(10)
<i>c</i> [Å]	23.9587(14)	13.7130(13)	21.656(14)	18.448(2)	18.765(3)
α [°]	90	87.699(2)	90	90	90
β [°]	90	81.445(2)	94.310(9)	125.268(5)	90.962(3)
γ [°]	90	82.031(2)	90	90	90
Volume [Å ³]	1821.78(18)	1521.0(3)	1872(2)	5553.5(11)	1538.0(4)
<i>Z</i>	4	2	4	4	4
<i>F</i> (000)	1016	712	1024	2576	920
μ (Mo- <i>K</i> α) [mm ⁻¹]	1.364	0.844	1.332	0.515	1.604
Temperature [K]	298(2)	298(2)	298(2)	298(2)	298(2)
<i>R</i> _{int}	0.0455	0.0215	0.0471	0.0564	0.0506
<i>h</i> , <i>k</i> , <i>l</i> range	−9/10, −10/10, −28/28	−10/10, −15/15, −16/16	−9/9, −13/13, −25/25	−17/20, −13/13, −15/10	−14/14, −8/8, −22/22
$\theta_{\min/\max}$ [°]	1.70/25.00	1.5/25.00	1.89/25.00	1.67/18.00 ^[a]	2.02/25.00
Reflections collected/ unique/observed					
[<i>I</i> > 2σ(<i>I</i>)]	17321/3207/3055	14480/5358/4863	17389/3294/2675	8983/1896/1466	13139/2710/2387
Data/restraints/parameters	3207/0/246	5358/0/387	3294/0/246	1896/0/363	2710/6/241
Goodness of fit on <i>F</i> ²	1.008	1.042	1.104	0.988	1.028
Final <i>R</i> indices	<i>R</i> ₁ = 0.0255	<i>R</i> ₁ = 0.0244	<i>R</i> ₁ = 0.0362	<i>R</i> ₁ = 0.0436	<i>R</i> ₁ = 0.0316
[<i>I</i> > 2σ(<i>I</i>)]	<i>wR</i> ₂ = 0.0670	<i>wR</i> ₂ = 0.0633	<i>wR</i> ₂ = 0.0990	<i>wR</i> ₂ = 0.1215	<i>wR</i> ₂ = 0.0858
<i>R</i> indices	<i>R</i> ₁ = 0.0273	<i>R</i> ₁ = 0.0274	<i>R</i> ₁ = 0.0466	<i>R</i> ₁ = 0.0583	<i>R</i> ₁ = 0.0368
(all data)	<i>wR</i> ₂ = 0.0680	<i>wR</i> ₂ = 0.0646	<i>wR</i> ₂ = 0.1067	<i>wR</i> ₂ = 0.1331	<i>wR</i> ₂ = 0.0888

[a] The crystal of **4** did not diffract beyond 18° due to its poor quality.

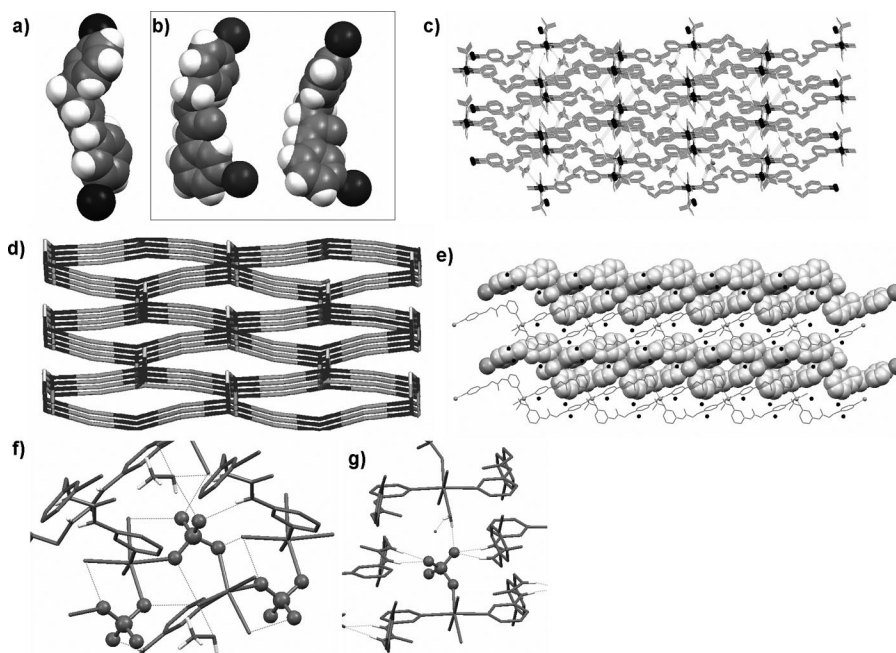


Figure 1. Crystal structures of **1** and **2**. (a) Non-planar “anti” conformation of **L1** in **1**. (b) Non-planar “syn” conformation of **L2** in **2**. (c) 3D coordination polymeric network in **1** displaying the inclusion of MeOH through various hydrogen-bonding interactions. (d) Topological diagram (TOPOS)^[19] of the 3D network in **1**. (e) 1D looped-chain coordination polymer in **2** displaying the offset packing. Various hydrogen-bonding interactions involving the SO₄^{2−} counter-anion in (f) **1** and (g) **2**.

Table 2. Selected bond lengths and angles for the coordination geometries of **1–5**.

Bond length [Å]		Bond angle [°]		Bond length [Å]		Bond angle [°]	
1				2			
Cd(1)–O(19)	2.284(3)	O(19)–Cd(1)–N(1)	90.68(11)	Cd(1)–O(35)	2.3113(16)	O(35)–Cd(1)–N(15)	88.17(6)
Cd(1)–N(1)	2.300(3)	N(1)–Cd(1)–O(23)	90.70(12)	Cd(1)–O(39)	2.3394(19)	O(39)–Cd(1)–N(15)	94.27(7)
Cd(1)–O(23)	2.304(3)	O(19)–Cd(1)–N(14)	91.85(12)	Cd(1)–N(15)	2.3457(19)	O(35)–Cd(1)–N(1)	95.03(6)
Cd(1)–N(14)	2.305(3)	O(23)–Cd(1)–N(14)	86.29(13)	Cd(1)–N(1)	2.3480(19)	O(39)–Cd(1)–N(1)	93.55(7)
Cd(1)–O(18)	2.318(3)	O(19)–Cd(1)–O(18)	80.85(9)	Cd(1)–N(18)	2.3609(18)	N(15)–Cd(1)–N(1)	88.72(7)
Cd(1)–O(22)	2.371(3)	N(1)–Cd(1)–O(18)	90.97(12)	Cd(1)–N(32)	2.3636(19)	O(35)–Cd(1)–N(18)	87.64(6)
		N(14)–Cd(1)–O(18)	92.48(13)			O(39)–Cd(1)–N(18)	83.89(7)
		O(19)–Cd(1)–O(22)	84.05(10)			N(15)–Cd(1)–N(18)	88.90(7)
		N(1)–Cd(1)–O(22)	92.84(14)			O(35)–Cd(1)–N(32)	92.13(6)
		O(23)–Cd(1)–O(22)	86.23(12)			O(39)–Cd(1)–N(32)	85.86(7)
		N(14)–Cd(1)–O(22)	84.36(14)			N(1)–Cd(1)–N(32)	88.38(7)
						N(18)–Cd(1)–N(32)	93.99(7)
3				4			
Cd(1)–O(21)	2.292(3)	O(21)–Cd(1)–O(22)	86.72(12)	Cd(1)–O(33)	2.337(5)	O(33)–Cd(1)–N(1)	95.0(2)
Cd(1)–O(22)	2.303(3)	O(22)–Cd(1)–O(23)	99.97(12)	Cd(1)–N(1)	2.340(7)	O(33)–Cd(1)–N(1)	85.0(2)
Cd(1)–O(23)	2.304(3)	O(21)–Cd(1)–O(17)	86.92(12)	Cd(1)–N(17)	2.372(7)	O(33)–Cd(1)–N(17)	90.0(3)
Cd(1)–O(17)	2.305(3)	O(23)–Cd(1)–O(17)	86.61(11)			N(1)–Cd(1)–N(17)	85.3(3)
Cd(1)–N(13)	2.310(4)	O(21)–Cd(1)–N(13)	92.57(13)			N(1)–Cd(1)–N(17)	94.7(3)
Cd(1)–N(1)	2.327(4)	O(22)–Cd(1)–N(13)	87.35(12)	5			
		O(23)–Cd(1)–N(13)	93.51(13)	Cd(1)–O(17)	2.288(3)	O(17)–Cd(1)–O(16)	90.23(10)
		O(17)–Cd(1)–N(13)	90.41(12)	Cd(1)–O(16)	2.294(3)	O(16)–Cd(1)–N(1)	96.80(11)
		O(21)–Cd(1)–N(1)	87.67(13)	Cd(1)–N(1)	2.320(3)	O(17)–Cd(1)–N(12)	78.64(10)
		O(22)–Cd(1)–N(1)	86.83(13)	Cd(1)–N(12)	2.337(3)	O(16)–Cd(1)–N(12)	90.19(11)
		O(23)–Cd(1)–N(1)	86.94(13)	Cd(1)–O(18)	2.346(3)	O(16)–Cd(1)–O(18)	91.80(9)
		O(17)–Cd(1)–N(1)	95.44(13)	Cd(1)–O(20)	2.398(3)	N(1)–Cd(1)–O(18)	87.51(9)
						N(12)–Cd(1)–O(18)	91.35(9)
						O(17)–Cd(1)–O(20)	94.24(10)
						N(1)–Cd(1)–O(20)	85.92(11)
						N(12)–Cd(1)–O(20)	87.03(10)

bridging ligand. Both the *anti*-ligating topology of **L1** and the counter-anion's role as a bridging ligand seem to be responsible for the formation of a 3D coordination polymer in which the metal/ligand ratio is 1:1 (Figure 1c). On the other hand, the equatorial positions of the metal centre in **2** are occupied by the pyridyl N atoms, and the apical positions are coordinated by one water and an O atom from the SO_4^{2-} counter-anion, which remains unidentate. In this case, the *syn*-ligating topology of **L2** and the SO_4^{2-} anion's role as unidentate ligand seem to have prompted the formation of a 1D looped-chain architecture in which the metal/ligand ratio is 1:2 (Figure 1d). The non-coordinating O atoms of the SO_4^{2-} anion in **1** are hydrogen-bonded to one of the N atoms of the urea moiety of the ligand, lattice-occluded MeOH and metal-bound water molecules, whereas the coordinated O atoms of the anion are involved in hydrogen-bonding interactions with the metal-bound water molecules (Figure 1e, Table 3). Note that with the exception of the interaction with the guest MeOH, which is located within the interstitial space generated within this 3D coordination polymer, the other hydrogen-bonding interactions involving the anion are intramolecular in nature. On the other hand, the SO_4^{2-} anion in **2** is located within the interstitial space generated by the offset parallel packing of the 1D looped chains (Figure 1d) and is involved in intermolecular hydrogen-bonding interactions (Figure 1f) with two urea moieties from two neighbouring 1D looped

chains, one metal-bound water molecule from another neighbouring looped chain, one fully occupied lattice-included water molecule and 1.5 disordered water molecules, as indicated by SQUEEZE calculations^[13] and thermogravimetric analysis (TGA) data (see the Exp. Sect. and Figure S7).

Unlike **L1** and **L2**, which have not been explored in the context of metal–organic compounds or otherwise, **L3** and **L4**, which are also positional isomers, have previously been explored to a great extent by our group^[7b,14] and also by Custelcean^[6a–6c] and Nangia^[15] and their co-workers. Although the ligating topology of **L3** is dependent on conformation, it is understandable that the topology of **L4** is independent of its conformation owing to the fact that the pyridyl N atoms are located at the symmetric 4-position of the aromatic ring. Therefore, **L4** always displays a linear ligating topology, whereas **L3** may show either a *syn*- or *anti*-ligating topology. Thus, the coordination compounds **3** and **4** derived from the two ligands **L3** and **L4**, respectively, turn out to be completely different; whereas compound **3** is found to crystallize in the centrosymmetric monoclinic space group $P2_1/n$, compound **4** displays the centrosymmetric monoclinic space group $C2/c$ (Table 1). Ligand **L3** is found to be reasonably planar with dihedral angles involving the terminal pyridyl rings and the urea moiety of 4.3(2)–13.0(2)° and displays an *anti*-ligating topology (Figure 2a) leading to the formation of a zigzag coordination polymer

Table 3. Hydrogen-bonding parameters in **1**–**5**.^[a]

D–H...A	D–H [Å]	H...A [Å]	D...A [Å]	D–H...A [°]	Symmetry operation for A
1					
N(7)–H(7)···O(20)	0.86	2.16	2.968(5)	155.6	$-x + 1, y - \frac{1}{2}, -z + \frac{1}{2}$
N(10)–H(10)···O(24)	0.86	2.22	3.004(6)	152.1	$-x, y - \frac{1}{2}, -z + \frac{1}{2}$
O(24)–H(24)···O(20)	0.82	1.96	2.716(5)	153.5	$x - 1, y, z$
O(21)···O(22)			2.829(4)		$1 - x, -\frac{1}{2} + y, \frac{1}{2} - z$
O(22)···O(21)			2.708(4)		$-1 + x, y, z$
O(23)···O(24)			2.698(5)		x, y, z
O(23)···O(19)			2.992(4)		x, y, z
O(23)···O(18)			2.821(4)		$1 - x, -\frac{1}{2} + y, \frac{1}{2} - z$
2					
N(7)–H(7)···O(36)	0.86	2.00	2.835(3)	163.3	$-x, -y + 1, -z + 2$
N(10)–H(10)···O(38)	0.86	2.38	3.200(3)	159.2	$-x, -y + 1, -z + 2$
N(24)–H(24)···O(37)	0.86	2.10	2.897(2)	154.2	$-x, -y, -z + 1$
N(27)–H(27)···O(37)	0.86	2.18	2.968(3)	152.0	$-x, -y, -z + 1$
N(27)–H(27)···O(35)	0.86	2.62	3.309(3)	138.2	$-x, -y, -z + 1$
O(39)–H(39A)···O(40)	0.87(4)	1.86(4)	2.697(3)	162(3)	$-x + 1, -y + 1, -z + 1$
O(39)–H(39B)···O(37)	0.78(3)	1.95(3)	2.734(3)	174(3)	$x + 1, y, z$
O(9)···O(40)			2.694(3)		$1 - x, 1 - y, 1 - z$
O(36)···O(40)			2.794(3)		$-x, 1 - y, 1 - z$
O(39)···O(40)			2.697(3)		$1 - x, 1 - y, 1 - z$
3					
N(7)–H(7)···O(20)	0.86	2.13	2.964(5)	163.6	$-x + \frac{3}{2}, y - \frac{1}{2}, -z + \frac{3}{2}$
N(10)–H(10)···O(19)	0.86	2.02	2.865(6)	168.5	$-x + \frac{3}{2}, y - \frac{1}{2}, -z + \frac{3}{2}$
O(24)–H(24)···O(9)	0.82	1.96	2.772(6)	172.4	$x + \frac{1}{2}, -y + \frac{3}{2}, z + \frac{1}{2}$
O(17)···O(21)			2.689(5)		$\frac{3}{2} - x, -\frac{1}{2} + y, \frac{3}{2} - z$
O(20)···O(21)			2.717(5)		x, y, z
O(18)···O(22)			2.674(5)		$\frac{3}{2} - x, -\frac{1}{2} + y, \frac{3}{2} - z$
O(20)···O(22)			2.728(5)		$1 + x, y, z$
O(23)···O(18)			2.892(5)		$-1 + x, y, z$
O(23)···O(24)			2.672(6)		x, y, z
4					
N(7)–H(7)···O(35)	0.86	2.38	3.156(9)	150.9	$-x + 2, -y + 1, -z + 1$
N(7)–H(7)···O(35)	0.86	2.53	3.268(9)	143.8	$x, -y + 1, z + \frac{1}{2}$
N(10)–H(10)···O(35)	0.86	1.99	2.844(9)	170.1	$-x + 2, -y + 1, -z + 1$
N(23)–H(23)···O(34)	0.86	2.21	3.060(9)	170.2	$-x + \frac{3}{2}, -y + \frac{3}{2}, -z + 1$
N(26)–H(26)···O(35)	0.86	2.07	2.860(9)	152.6	$-x + \frac{3}{2}, -y + \frac{3}{2}, -z + 1$
O(33)···O(36)			2.667(8)		$\frac{1}{2} + x, \frac{1}{2} + y, z$
O(33)···O(37)			2.781(10)		$\frac{1}{2} + x, \frac{1}{2} + y, z$
O(34)···O(39)			2.978(10)		$1 + x, y, z$
O(38)···O(39)			2.772(15)		$\frac{1}{2} + x, \frac{3}{2} - y, \frac{1}{2} + z$
O(37)···O(39)			2.942(11)		$\frac{1}{2} - x, \frac{3}{2} - y, 1 - z$
O(37)···O(33)			2.781(10)		$-\frac{1}{2} + x, -\frac{1}{2} + y, z$
O(37)···O(38)			2.732(12)		$x, 1 - y, -\frac{1}{2} + z$
O(37)···O(25)			2.872(10)		$-\frac{1}{2} + x, \frac{3}{2} - y, -\frac{1}{2} + z$
O(37)···N(14)			2.708(12)		$\frac{3}{2} - x, \frac{1}{2} - y, 2 - z$
O(36)···O(36)			2.884(14)		$1 - x, y, \frac{3}{2} - z$
O(38)···N(30)			2.808(10)		$-\frac{1}{2} + x, \frac{3}{2} - y, -\frac{1}{2} + z$
5					
N(9)–H(9)···O(17)	0.86	2.43	3.245(4)	158.6	x, y, z
N(9)–H(9)···O(18)	0.86	2.47	3.201(4)	143.8	x, y, z
O(20)–H(20A)···O(21)	0.877(10)	1.955(12)	2.830(4)	175(5)	$x - \frac{1}{2}, -y + \frac{1}{2}, z - \frac{1}{2}$
O(20)–H(20B)···O(21)	0.879(10)	1.99(2)	2.838(4)	163(6)	$-x + \frac{1}{2}, y - \frac{1}{2}, -z + \frac{1}{2}$
O(21)–H(21A)···O(19)	0.878(10)	1.91(3)	2.720(4)	154(5)	x, y, z
O(21)–H(21B)···O(22)	0.878(10)	1.892(17)	2.745(5)	164(5)	$-x + 1, -y + 1, -z + 1$
O(22)–H(22A)···O(19)	0.875(10)	1.889(17)	2.743(4)	165(5)	$x, y + 1, z$
O(22)–H(22B)···O(8)	0.870(10)	1.980(15)	2.838(4)	168(5)	$x + 1, y + 1, z$

[a] For molecular plots of compounds **1**–**5**, see Figures S1–S5.

in which the metal/ligand ratio is 1:1 (Figure 2c). The two crystallographically independent molecules of **L4** present in compound **4** display both a planar and non-planar confor-

mation (Figure 2b), as is evident from the corresponding dihedral angles of 8.1(7)–10.3(6) and 22.7(3)–23.5(5)°, respectively. Interestingly, complex **4** is an ML₄-type dis-

crete coordination complex in which the metal/ligand ratio is 1:4. The metal centres in both structures **3** and **4** display a distorted octahedral geometry (Table 2). The equatorial positions in compound **3** are occupied by three water molecules and one O atom from the SO_4^{2-} counter-anion, and the apical positions are coordinated by the N atoms of the pyridyl rings of ligand **L3**. However, in compound **4**, the equatorial positions are occupied by the pyridyl N atoms of the ligands **L4**, and the axial positions are occupied by two water molecules. In this structure the SO_4^{2-} counter-anion does not coordinate to the metal centre. The SO_4^{2-} counter-anion in both structures is extensively hydrogen-bonded. The non-coordinated O atoms of SO_4^{2-} in compound **3** are intermolecularly hydrogen-bonded to both the N atoms of the urea moiety of a neighbouring 1D zigzag chain and metal-bound waters of two other neighbouring chains and intramolecularly hydrogen bonded to metal-bound water of the same chain. The coordinated O atom of the counter-anion forms hydrogen-bonded contacts with the metal-bound water molecule of the neighbouring chain (Figure 2d). The SO_4^{2-} counter-anion in **4** is hydrogen-bonded to the urea moieties of four neighbouring discrete complexes and two lattice-included water molecules. The 1D zigzag coordination polymeric chains in **3** are packed in a parallel fashion, and the interstitial space within these

packed chains is occupied by lattice-included MeOH, which is found to be hydrogen-bonded to the O atoms of the urea moiety and metal-bound water (Figure 2e). A channel-type arrangement is observed in compound **4** in which the channels are occupied by both the SO_4^{2-} counter-anion and lattice-included water molecules (Figure 2f), three of which form an intriguing hexameric hydrogen-bonded water cluster with a chair conformation located around a centre of symmetry (Figure 2g).^[16]

The reaction of **L5** with CdSO_4 resulted in crystalline product **5**, which turned out to be an interesting coordination polymer that crystallized in the centrosymmetric monoclinic space group $P2_1/n$ (Table 1). In this structure the SO_4^{2-} counter-anion acts as a tridentate bridging ligand by extended coordination with adjacent Cd^{II} centres. The ligand **L5** displays an *anti* conformation (Figure 3a), which is significantly non-planar, as is evident from the dihedral angle of $29.4(1)^\circ$ involving the terminal pyridyl rings. Thus, the metal centre, which displays a slightly distorted octahedral geometry (Table 2), is coordinated by three O atoms from the SO_4^{2-} anion, one water molecule and the two pyridyl N atoms of ligand **L5**, which ultimately led to the formation of a 2D coordination polymer (Figure 3b). Guest water molecules were found to be occluded within the interstitial space generated by parallel packing of the 2D sheets. The SO_4^{2-} counter-anion was found to be involved in intermolecular hydrogen-bonding interactions with the guest water molecules. Unfortunately, the crystalline material obtained in the reaction between **L6** and CdSO_4 could not be characterized by single-crystal X-ray diffraction. However, the presence of a band at 1145 cm^{-1} in the FTIR spectrum presumably indicates the formation of a coordination compound of unknown composition with SO_4^{2-} as a counter-anion. Note that the TGA data of **1–5** also correspond well with the structures revealed by single-crystal X-ray diffraction (Figures S6–S10).

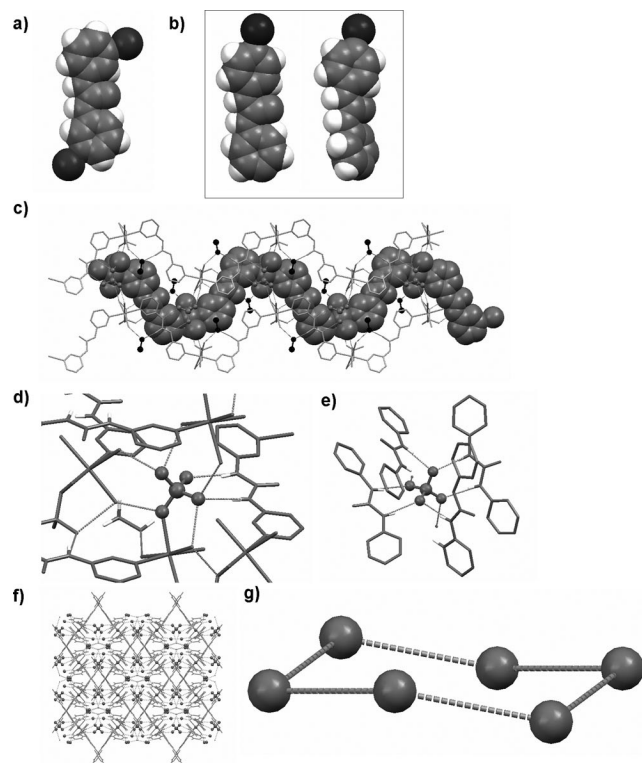


Figure 2. Crystal structures of **3** and **4**. (a) Non-planar “*anti*” conformation of **L3** in **3**. (b) Planar and non-planar conformations of **L4** in **4**. (c) Parallel packing of the 1D zigzag CP displaying the entrapment of MeOH within the interstitial space in **3**. Various hydrogen-bonding interactions involving the counter-anion SO_4^{2-} in (d) **3** and (e) **4**. (f) Channel-type packing in **4** displaying the inclusion of a hexameric water cluster within the channel. (g) Chair conformation of the hexameric water cluster.

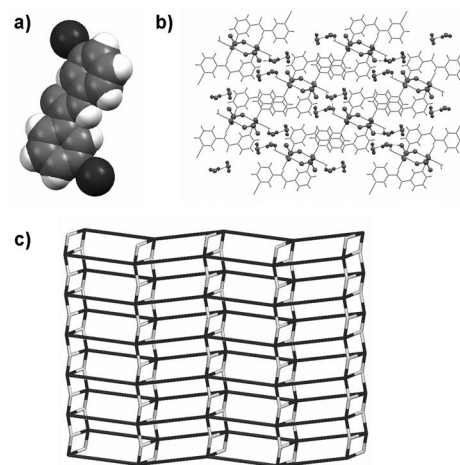
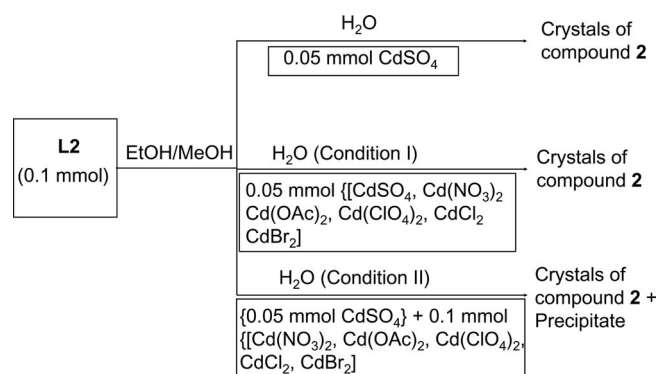


Figure 3. Crystal structure of **5**. (a) Non-planar *anti* conformation of **L5** in **5**. (b) 2D corrugated-sheet architecture displaying the sulfate anion as the bridging ligand and the entrapment of guest water molecules within the sheet through various hydrogen-bonding interactions. (c) Topological diagram (TOPOS)^[19] of the 2D corrugated sheet in **5**.

Anion Separation

To see how the coordination compounds **1–5** can be exploited to separate SO_4^{2-} anions from a mixture of other competing anions, we performed experiments under two different conditions. Under condition I, the corresponding ligand was treated with CdSO_4 , $\text{Cd}(\text{NO}_3)_2$, $\text{Cd}(\text{ClO}_4)_2$, $\text{Cd}(\text{OAc})_2$, CdCl_2 and CdBr_2 in a metal/ligand ratio of 1:2 under crystallization conditions identical to those used to generate the corresponding coordination compounds. Under condition II, the only change made was in the concentration of the other competing Cd^{II} salts, with twice the amount of CdSO_4 used (see the Supporting Information for experimental details). In the cases of **L1** and **L4**, crystalline precipitates were obtained within 3–4 d, whereas in the case of **L3**, a crystalline precipitate was mainly obtained with the occasional formation of block-shaped crystals. In these cases, FTIR and XRPD data clearly indicate the formation of a mixture of coordination compounds (see the Supporting Information). In the case of **L2**, aggregates of block-shaped crystals were obtained after 2 weeks as an exclusive product. FTIR, XRPD and elemental analysis suggested that the SO_4^{2-} anion could be exclusively separated from an aqueous solution containing other competing anions (Scheme 3, Figure 4). Figure 4 indicates that the SO_4^{2-} anion was separated as compound **2** under competitive condition I, as is evident from the near-identical FTIR spectra and XRPD patterns of the products isolated under both competitive and non-competitive conditions. However, under condition II, neither the IR spectra nor the XRPD patterns match those of the compound isolated under non-competitive conditions, which indicates the isolation of a mixture of coordination products. The stretching frequencies of S–O are observed at 1134 cm^{-1} under both non-competitive conditions and competitive condition I, which indicates the presence of SO_4^{2-} . However, under condition II, the presence of both SO_4^{2-} (1114 cm^{-1}) and NO_3^- (1386 cm^{-1}) is evident (Table S1), which indicates the failure

to selectively separate SO_4^{2-} . Elemental analyses also support the selective separation of SO_4^{2-} under condition I and the failure of the same under condition II (Table S2).



Scheme 3. Schematic representation of the anion-separation experiment carried out under various conditions by the in situ crystallization technique.

Many factors like the hard/soft acid/base (HSAB) nature of the metal ion and anions, the dimensionality of the framework of the resultant coordination compounds, the packing efficiency, interligand interactions, anion coordination to the metal centre and its hydrogen-bonding environment, solubility, nucleation and crystal growth are important in anion selectivity. The total exclusion of anions such as NO_3^- , AcO^- , ClO_4^- , Cl^- and Br^- and the isolation of the corresponding sulfate coordination compounds **1–5** in the individual experiments involving ligands **L1–L5** with the corresponding Cd^{II} salts may be rationalized on the basis of the Lewis acid/base nature of the Cd^{II} metal centre and the anions under study and their ability to form hydrogen bonds with the urea/amide backbone of the corresponding ligands. It may be noted that both AcO^- and ClO_4^- are hard bases, whereas the other anions studied herein decrease in softness in the order $\text{Br}^- > \text{Cl}^- > \text{NO}_3^- > \text{SO}_4^{2-}$ in the context of Cd^{II} as a soft acid complexes.^[17] It is reasonable

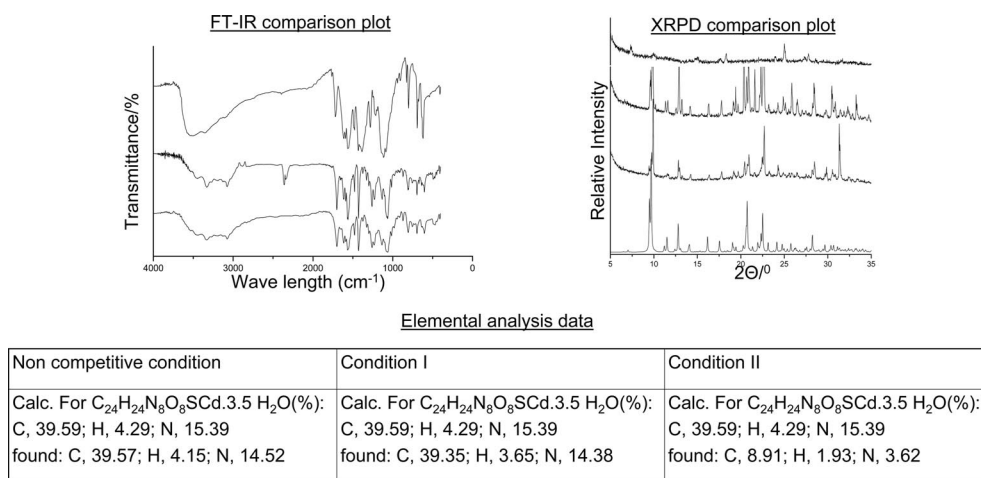


Figure 4. FTIR spectra, XRPD patterns and elemental analysis data under various conditions showing the selective separation of the sulfate anion with compound **2** under competitive conditions. FTIR: (i) non-competitive, (ii) competitive condition I and (iii) competitive condition II. XRPD: (i) simulated, (ii) non-competitive, (iii) competitive condition I and (iv) competitive condition II.

to argue that there is a greater possibility of both SO_4^{2-} and NO_3^- being isolated as the corresponding coordination compounds under competitive conditions as these oxo anions can interact with the urea moiety through complementary hydrogen bonds^[7b] that might supersede the softness of the other competing anions such as Cl^- and Br^- . In fact, SO_4^{2-} was found to be bidentate-, unidentate- and tridentate-bridging in **1**, **2–3** and **5**, respectively, whereas in **4**, the SO_4^{2-} anion is not coordinated to the metal centre. The presence of both SO_4^{2-} and NO_3^- in the isolated products obtained under competitive condition II with ligand **L2** and various Cd^{II} salts (Table S1) testifies to the possibility of the formation of the coordination compound with NO_3^- as the counter-anion. For the coordination compounds **1** and **2**, which were generated from the positional isomers **L1** and **L2**, respectively, selective SO_4^{2-} separation was observed only in the case of **2**. It is interesting to note that the dimensionality of these networks, ligating behaviour and hydrogen-bonding environment of SO_4^{2-} are drastically different in these two cases. Whereas **1** is a 3D network in which the anion acts as a bridging ligand, **2** shows a 1D looped-chain topology with SO_4^{2-} as a unidentate ligand. The SO_4^{2-} anion seems to be more efficiently hydrogen-bonded to the urea moieties in **2** compared with in **1**; in **2**, the SO_4^{2-} anion is involved in intermolecular hydrogen bonding with two urea moieties and lattice-included and metal-bound water molecules from neighbouring 1D chains, whereas the SO_4^{2-} anion in **1** is involved in hydrogen-bonding interactions with one urea moiety and with metal-bound water molecules in an intramolecular fashion. Thus, intermolecular hydrogen bonding with a greater number of urea moieties and the unidentate nature of the SO_4^{2-} anion in **2** as compared with in **1** may play a crucial role in SO_4^{2-} anion selectivity in **2**.

On the other hand, the environment of the SO_4^{2-} anion in **3** and **4** is significantly different. Whereas SO_4^{2-} acts as a bridging ligand in **3**, it remains uncoordinated in **4**. Both Lewis acid/base interactions as well as intermolecular hydrogen bonding with the urea moiety and metal-bound water molecules are the main driving forces for the incorporation of SO_4^{2-} within **3**, whereas in **4** the SO_4^{2-} anion is included in the crystal structure only through intermolecular hydrogen bonding with urea and lattice-included water molecules. Therefore, it can be expected that the incorporation of SO_4^{2-} is relatively easy in **3** compared with in **4**. Indeed, this is reflected in the competitive crystallization condition I in which both block-shaped crystals and a precipitate were obtained with **3**, whereas only a precipitate was obtained with **4**. FTIR analysis of the crystals and precipitates formed with **L3** and **L4** indicated the presence of SO_4^{2-} (1118 cm^{-1}) and both SO_4^{2-} (ca. 1118 cm^{-1}) and NO_3^- (ca. 1383 cm^{-1}), respectively.

Interestingly, in the case of **5**, the isolated precipitate obtained in the experiment under competitive condition I indicates the formation of compound **5**, as revealed by a comparison of the FTIR spectra of compound **5** and the precipitate (Figure S18). Elemental analysis of the precipitate also match quite well that of compound **5**, which indicates

that SO_4^{2-} is separated in this case as well. However, the XRPD patterns recorded for various samples of the isolated precipitate are found to be inconsistent. This could be because of the loss of lattice-included water in **5** during sample preparation and/or the formation of other crystalline phases under competitive crystallization conditions (Figure S14).

It should be mentioned here that because **L2** is a new ligand, there is no structure involving **L2** in the literature for comparison. However, the divalent nature of the SO_4^{2-} anion might be one of the driving forces for the selectivity in sulfate separation from a mixture containing mostly monovalent anions; the higher charge of the sulfate anion may provide relatively higher stabilization due to greater electrostatic interactions allowing the corresponding coordination compound **2** to crystallize. On the other hand, seven structures involving **L5** have been reported.^[7a,20] In these structures, Co^{II} , Zn^{II} and Cd^{II} were the metal centres, and the anions were NCS^- , NO_3^- , Cl^- , Br^- , OAc^- and BF_4^- . Most of the structures display a 2D grid architecture and the anions remain unidentate except OAc^- ^[7a] in which one of the acetate anions remains unidentate and the other one chelated to the adjacent Zn^{II} centre resulting in a 1D ladder-type architecture. Interestingly, in **5** the SO_4^{2-} anion is found to be coordinated with three adjacent Cd^{II} centres leading to the formation of a 2D corrugated-sheet architecture. Thus, the tri-coordinated SO_4^{2-} ion might contribute significantly towards the stabilization of **5** and observed sulfate selectivity.

Conclusions

Because the structural environment around an anion is argued to be important in the selective separation of anions,^[4a] we have undertaken a systematic study in which three pairs of positional isomers, namely **L1**, **L2**, **L3**, **L4** and **L5**, **L6**, with a hydrogen-bonding backbone (urea/amide) were used as organic linkers in the separation of SO_4^{2-} by in situ crystallization of the corresponding coordination compound of Cd^{II} . It has been revealed from the crystal structures of **1–5** that the positional isomers indeed play a crucial role in the resultant structures of the coordination compounds. Selective separation of SO_4^{2-} was exclusively established in the case of **2**, as revealed by FTIR spectroscopy, XRPD and elemental analysis data, whereas a mismatch of XRPD data indicated the formation of desolvated and/or a different crystalline morph of **5** under competitive conditions, with both FTIR and elemental analysis data in this case clearly indicating the formation of compound **5**. We believe that this work contributes to the development of selective anion separation by in situ crystallization of coordination compounds.

Experimental Section

Materials and Method: All chemicals were commercially available (Aldrich) and used without further purification. Ligands **L1** and

L2 were synthesized according to a reported procedure.^[18a] Ligands **L3** and **L4**^[18b] and **L5** and **L6**^[18c] have previously been reported by our group. Elemental analysis was carried out with a Perkin–Elmer 2400 Series-II CHN analyzer, FTIR spectra were recorded with a Perkin–Elmer Spectrum GX spectrometer, and TGA analyses were performed with an SDT Q Series 600 Universal VA.2E TA instrument. Powder X-ray patterns were recorded with a Bruker AXS D8 Advance Powder diffractometer (Cu- $K_{\alpha 1}$ radiation, $\lambda = 1.5406 \text{ \AA}$). The mass spectrum was recorded with a QTOF Micro YA263 spectrometer. ^1H and ^{13}C NMR spectra were recorded with a Bruker Avance DPX300 spectrometer.

Characterization Data

L1: Yield: 660 mg, 35.7%; m.p. 199 °C. ^1H NMR (300 MHz, $[\text{D}_6]$ -dmso, 25 °C): $\delta = 8.97$ (s, 1 H, urea NH), 8.59 (s, 1 H, NH), 8.51–6.81 (m, 8 H, aromatic), 4.32–4.30 (d, CH_2) ppm. FTIR (KBr pellet): $\tilde{\nu} = 3284$ (s, N–H stretch), 3091 (w, aromatic C–H stretch), 3026 (m, aliphatic C–H stretch), 2943 (w), 1662 (s, urea C=O stretch), 1602 (s, urea N–H bend), 1587 (m), 1556 (m), 1533 (m), 1508 (m), 1473 (s), 1419 (s), 1359 (m), 1329 (s), 1280 (s), 1101 (w), 1047 (s), 1024 (s), 812 (s), 794 (w), 719 (w), 704 (w), 669 (w), 680 (w), 503 (w) cm^{-1} . HRMS (ESI, CH_3OH): m/z (%) = 229 $[(\text{PyNHCONHCH}_2\text{Py})] [\text{M} + \text{H}]^+$. $\text{C}_{12}\text{H}_{12}\text{N}_4\text{O}$ (228.25): calcd. C 63.15, H 5.30, N 24.55; found C 62.96, H 5.08, N 24.22.

L2: Yield: 550 mg, 29.7%; m.p. 218 °C. ^1H NMR (300 MHz, $[\text{D}_6]$ -dmso, 25 °C): $\delta = 8.91$ (s, 1 H, urea NH), 8.55 (s, 1 H, urea NH), 8.49–6.89 (m, 8 H, aromatic), 4.32–4.34 (d, 2 H, CH_2) ppm. FTIR (KBr pellet): $\tilde{\nu} = 3286$ (s, N–H stretch), 3178 (m, aromatic C–H stretch), 2993 (s, aliphatic C–H stretch), 2929, 1662 (m, urea C=O stretch), 1600 (s, urea N–H bend), 1585 (m), 1525 (s), 1473 (s), 1363 (w), 1327 (s), 1284 (s), 1051 (s), 709 (s) cm^{-1} . HRMS (ESI, CH_3OH): m/z = 229 $[(\text{PyNHCONHCH}_2\text{Py})] [\text{M} + \text{H}]^+$. $\text{C}_{12}\text{H}_{12}\text{N}_4\text{O}$ (228.25): calcd. C 63.15, H 5.30, N 25.17; found C 62.96, H 4.99, N 24.31.

$[\{\text{Cd}(\mu\text{-L1})(\mu\text{-SO}_4)(\text{H}_2\text{O})_2\} \cdot \text{MeOH}]_\infty$ (1): Complex **1** was synthesized by adding an aqueous solution of CdSO_4 hydrate (769.51; 38 mg, 0.05 mmol) to a methanol/ethanol solution of **L1** (22.8 mg, 0.0973 mmol). After 2 weeks, X-ray quality crystals were obtained. Yield: 16 mg, 0.028 mmol, 64%. FTIR (KBr pellet): $\tilde{\nu} = 3433$ (w), 2925, 2922 (w), 1706 (s, urea C=O stretch), 1616 (s, N–H bend), 1558 (s), 1483 (m), 1429 (s), 1334 (w), 1284 (s), 1118 (vs, SO_4^{2-} ν_{asym} S–O), 808 (w), 692 (s), 622 (m) cm^{-1} . $\text{C}_{13}\text{H}_{20}\text{CdN}_4\text{O}_8\text{S}$ (504.79): C 30.9, H 3.99, N 11.10; found C 28.89, H 3.54, N 10.50.

$[\{\text{Cd}(\mu\text{-L2})_2(\text{SO}_4)(\text{H}_2\text{O})\} \cdot 3.5\text{H}_2\text{O}]_\infty$ (2): Complex **2** was synthesized by adding an aqueous solution of CdSO_4 hydrate (769.51; 38 mg, 0.05 mmol) to a methanol/ethanol solution of **L2** (22 mg, 0.0973 mmol). After 2 weeks, X-ray quality crystals were obtained. Yield: 22 mg, 0.03 mmol, 61%. FTIR (KBr pellet): $\tilde{\nu} = 3535$ (w), 3333 (m, water ν O–H), 3074 (m, aliphatic C–H stretch) 2922 (w), 1699 (s, urea C=O stretch), 1614 (m, urea N–H bend), 1564 (s), 1479 (m), 1427 (s), 1325 (w), 1134 (s, SO_4^{2-} ν_{asym} S–O), 1298 (s), 1259 (w), 1232 (m), 1062 (s), 1016 (w), 981 (m), 871 (m), 752 (w), 696 (s), 601 (m) cm^{-1} . $\text{C}_{24}\text{H}_{24}\text{CdN}_8\text{O}_8\text{S} \cdot 3.5\text{H}_2\text{O}$ (701.00): calcd. C 39.29, H 4.26, N 15.27; found C 39.35, H 3.65, N 14.38.

$[\{\text{Cd}(\mu\text{-L3})(\text{SO}_4)(\text{H}_2\text{O})_3\} \cdot \text{MeOH}]_\infty$ (3): Complex **3** was synthesized by adding an aqueous solution of CdSO_4 hydrate (769.51; 38 mg, 0.05 mmol) to a methanol/ethanol solution of **L3** (21.5 mg, 0.0973 mmol). After 1 week, X-ray quality crystals were obtained. Yield: 20 mg, 0.039 mmol, 80%. FTIR (KBr pellet): $\tilde{\nu} = 3323$ (m, aromatic C–H stretch), 3142 (w), 3091 (m), 3028 (w), 1703 (s, C=O stretch), 1614 (s, N–H bending), 1593 (s), 1558 (s), 1479 (s), 1433 (s), 1284 (s), 1226 (m), 1143 (m), 1118 (s, SO_4^{2-} ν_{asym} S–O), 1055

(w), 977 (w), 802 (w), 694 (m), 617 (s) cm^{-1} . $\text{C}_{12}\text{H}_{20}\text{CdN}_4\text{O}_9\text{S}$ (508.77): calcd. C 28.33, H 3.96, N 11.01; found C 27.97, H 3.76, N 10.81.

$[\{\text{Cd}(\text{L4})_4(\text{H}_2\text{O})_2\} \cdot \text{SO}_4 \cdot 8\text{H}_2\text{O}]$ (4): Complex **4** was synthesized by adding an aqueous solution of CdSO_4 hydrate (769.51; 38 mg, 0.05 mmol) to a methanol/ethanol solution of **L4** (21.5 mg, 0.05 mmol). After 5 d, X-ray quality crystals were obtained. Yield: 20 mg, 0.018 mmol, 32%. FTIR (KBr pellet): $\tilde{\nu} = 3493$ (w, N–H stretch), 3355 (w), 3181 (w, aliphatic C–H stretch), 2995 (m), 1722 (s, urea C=O stretch), 1595 (s, N–H bending), 1527 (s), 1506 (s), 1521 (w), 1334 (m), 1288 (s), 1207 (s), 1117 (m), 1085 (s, SO_4^{2-} ν_{asym} S–O), 1035 (w), 827 (s), 798 (m), 740 (s), 528 (m) cm^{-1} . $\text{C}_{44}\text{H}_{60}\text{CdN}_{16}\text{O}_{18}\text{S}$ (1245.54): C 42.43, H 4.86, N 17.99; found C 42.69, H 4.08, N 17.76.

$[\{\text{Cd}(\mu\text{-L5})(\mu_3\text{-SO}_4)(\text{H}_2\text{O})\} \cdot 2\text{H}_2\text{O}]_\infty$ (5): Complex **5** was synthesized by adding an aqueous solution of CdSO_4 hydrate (769.51; 38 mg, 0.05 mmol) to a methanol/ethanol solution of **L5** (20 mg, 0.0973 mmol). After 2 weeks, X-ray quality crystals were obtained. Yield: 20 mg, 0.043 mmol, 86%. FTIR (KBr pellet): $\tilde{\nu} = 3512$ (m, amide N–H stretch), 3379 (w), 3263 (s, aromatic C–H stretch), 3061 (w), 2923 (w), 1668 (s, amide C=O stretch), 1585 (s, amide N–H bend), 1431 (s), 1340 (s), 1307 (s), 1120 (s, SO_4^{2-} ν_{asym} S–O), 817 (m), 744 (w), 698 (s), 646 (m), 596 (m) cm^{-1} . $\text{C}_{11}\text{H}_{15}\text{CdN}_3\text{O}_8\text{S}$ (461.72): calcd. C 28.61, H 3.27, N 9.10; found C 28.96, H 3.18, N 9.08.

X-ray Crystallography: Single-crystal X-ray data were collected by using Mo- K_{α} ($\lambda = 0.7107 \text{ \AA}$) radiation with a Bruker APEX II diffractometer equipped with a CCD area detector. Data collection, data reduction and structure solution/refinement were carried out by using the APEX II software package. The structures of **1–4** and **5** were solved by direct and Patterson methods, respectively, and refined in a routine manner. In all cases, non-hydrogen atoms were treated anisotropically. Whenever possible, the hydrogen atoms were located on a difference Fourier map and refined. In other cases, the hydrogen atoms were geometrically fixed. CCDC-771621–771625 contain the supplementary crystallographic data for this paper. These data can be obtained free of charge from The Cambridge Crystallographic Data Centre via www.ccdc.cam.ac.uk/data_request/cif.

Supporting Information (see footnote on the first page of this article): ORTEP plots of compounds **1–5** (Figures S1–S5), TGA of compounds **1–5** (Figures S6–S10), XRPD plots (Figures S11–S14), FT-IR spectra (Figures S15–S18), experimental details of anion separation studies, selected bond lengths and angles (Table S3).

Acknowledgments

We thank the Department of Science & Technology (DST), New Delhi, India for financial support. S. B. and N. N. A. thank the Indian Association for the Cultivation of Science (IACS) for research fellowships. Single-crystal X-ray diffraction was performed at the DST-funded National Single Crystal Diffractometer Facility at the Department of Inorganic Chemistry, IACS.

- [1] a) B. Kesanli, W. Lin, *Coord. Chem. Rev.* **2003**, *252*, 305–326; b) S. Kitagawa, R. Matsuda, *Coord. Chem. Rev.* **2007**, *251*, 2490–2509; c) M. Dinca, J. R. Long, *Angew. Chem. Int. Ed.* **2008**, *47*, 6766–6779; d) L. R. Macgillivray, G. S. Papaefstathiou, T. Friscic, T. D. Hamilton, D.-K. Bucar, Q. Chu, D. B.

- Varshney, I. G. Georgiev, *Acc. Chem. Res.* **2008**, *41*, 280–291; e) G. Férey, *Chem. Soc. Rev.* **2008**, *37*, 191–214; f) M. H. Filby, J. W. Steed, *Coord. Chem. Rev.* **2006**, *250*, 3200–3218; g) C. N. R. Rao, S. Natarajan, R. Vaidhyanathan, *Angew. Chem. Int. Ed.* **2004**, *43*, 1466–1496; h) V. Chandrasekhar, P. Thilagar, B. M. Pandian, *Coord. Chem. Rev.* **2007**, *251*, 1045–1074.
- [2] a) G. J. Lumetta, “The Problem with Anions in the DOE Complex” in *Fundamental and Applications of Anion Separations* (Eds.: B. A. Moyer, R. P. Singh), Kluwer, New York, **2004**; b) B. A. Moyer, L. H. Delmau, C. J. Fowler, A. Ruas, D. A. Bostick, J. L. Sessler, E. Katayev, G. D. Pantos, J. M. Llinares, M. A. Hossain, S. O. Kang, K. Bowman-James, “Supramolecular Chemistry of Environmentally Relevant Anions” in *Advances in Inorganic Chemistry, Vol. 59: Template Effects and Molecular Organization* (Eds.: R. van Eldik, K. Bowman-James), Elsevier, Oxford, **2007**, p. 175; c) J. L. Sessler, E. Katayev, G. D. Pantos, Y. A. Ustynyuk, *Chem. Commun.* **2004**, 1276–1277.
- [3] B. F. Hoskins, R. Robson, *J. Am. Chem. Soc.* **1990**, *112*, 1546–1554.
- [4] a) R. Custelcean, B. A. Moyer, *Eur. J. Inorg. Chem.* **2007**, 1321–1340; b) R. Custelcean, *Curr. Opin. Solid State Mater. Sci.* **2009**, *13*, 68–75.
- [5] a) C. Thompson, N. R. Champness, A. N. Khlobystov, C. J. Roberts, M. Schröder, S. J. B. Tendler, M. J. Wilkinson, *J. Microsc.* **2004**, *214*, 261–271; b) A. N. Khlobystov, N. R. Champness, C. J. Roberts, S. J. B. Tendler, C. Thompson, M. Schröder, *CrystEngComm* **2002**, *4*, 426–431.
- [6] a) R. Custelcean, B. A. Moyer, V. S. Bryantsev, B. P. Hay, *Cryst. Growth Des.* **2006**, *6*, 555–563; b) R. Custelcean, T. J. Haverlock, B. A. Moyer, *Inorg. Chem.* **2006**, *45*, 6446–6452; c) R. Custelcean, D. Jiang, B. P. Hay, W. Luo, B. Gu, *Cryst. Growth Des.* **2008**, *8*, 1909–1915; d) R. Custelcean, V. Sellin, B. A. Moyer, *Chem. Commun.* **2007**, 1541–1543; e) R. Custelcean, P. Remy, P. V. Bonnesen, D. E. Jiang, B. A. Moyer, *Angew. Chem. Int. Ed.* **2008**, *47*, 1866–1870.
- [7] a) D. K. Kumar, A. Das, P. Dastidar, *CrystEngComm* **2007**, *9*, 548–555; b) D. K. Kumar, A. Das, P. Dastidar, *New J. Chem.* **2006**, *30*, 1267–1275; c) D. K. Kumar, A. Das, P. Dastidar, *Cryst. Growth Des.* **2006**, *6*, 1903–1909; d) D. K. Kumar, A. Das, P. Dastidar, *CrystEngComm* **2007**, *9*, 895–901; e) D. K. Kumar, A. Das, P. Dastidar, *Inorg. Chem.* **2007**, *46*, 7351–7361; f) A. D. Shukla, P. C. Dave, E. Suresh, A. Das, P. Dastidar, *J. Chem. Soc., Dalton Trans.* **2000**, 4459–4463; g) S. Banerjee, N. N. Adarsh, P. Dastidar, *CrystEngComm* **2009**, *11*, 746–749; h) D. K. Kumar, A. Das, P. Dastidar, *CrystEngComm* **2006**, *8*, 805–814; i) D. K. Kumar, A. Ballabh, D. A. Jose, P. Dastidar, A. Das, *Cryst. Growth Des.* **2005**, *5*, 651–660; j) N. N. Adarsh, D. K. Kumar, P. Dastidar, *Cryst. Growth Des.* **2009**, *9*, 2979–2983.
- [8] a) N. N. Adarsh, D. K. Kumar, P. Dastidar, *CrystEngComm* **2008**, *10*, 1565–1573; b) N. N. Adarsh, D. K. Kumar, P. Dastidar, *CrystEngComm* **2009**, *11*, 796–802.
- [9] F. Hofmesiter, *Arch. Exp. Pathol. Pharmacol.* **1888**, *24*, 247–260.
- [10] N. N. Adarsh, P. Dastidar, *Cryst. Growth Des.* **2010**, *10*, 483–487.
- [11] a) B. P. Hay, T. K. Firman, B. A. Moyer, *J. Am. Chem. Soc.* **2005**, *127*, 1810–1819; b) V. Amendola, M. Bonizzoni, D. Esteban-Gómez, L. Fabbri, M. Licchelli, F. Sancenón, A. Taglietti, *Coord. Chem. Rev.* **2006**, *250*, 1451–1470.
- [12] L. Carlucci, G. Ciani, D. M. Proserpio, *CrystEngComm* **2003**, *5*, 269–279.
- [13] P. Van der Sluis, A. L. Spek, *Acta Crystallogr., Sect. A* **1990**, *46*, 194–201.
- [14] a) D. K. Kumar, A. Das, P. Dastidar, *Cryst. Growth Des.* **2007**, *7*, 205–207; b) D. K. Kumar, A. Das, P. Dastidar, *Cryst. Growth Des.* **2007**, *7*, 2096–2105; c) D. K. Kumar, A. Das, P. Dastidar, *CrystEngComm* **2006**, *8*, 805–814; d) D. K. Kumar, D. Amilan Jose, A. Das, P. Dastidar, *Inorg. Chem.* **2005**, *44*, 6933–6935.
- [15] L. S. Reddy, S. Basavoju, V. R. Vangala, A. Nangia, *Cryst. Growth Des.* **2006**, *6*, 161–173.
- [16] a) K. A. Siddiqui, G. K. Mehrotra, J. Mrozinski, R. J. Butcher, *Eur. J. Inorg. Chem.* **2008**, 4166–4172; b) U. Mukhopadhyay, I. Bernal, *Cryst. Growth Des.* **2005**, *5*, 1687–1689; c) P. S. Lakshminarayanan, E. Suresh, P. Ghosh, *J. Am. Chem. Soc.* **2005**, *127*, 13132–13133; d) S. K. Ghosh, P. K. Bharadwaj, *Angew. Chem. Int. Ed.* **2004**, *43*, 3577–3580; e) J. N. Moorthy, R. Natarajan, P. Venugopalan, *Angew. Chem. Int. Ed.* **2002**, *41*, 3417–3420.
- [17] C. G. S. Philips, R. J. P. Williams, *Inorganic Chemistry*, Oxford University, Oxford, **1966**, vol. II, chapter 31.
- [18] a) P. Byrne, D. R. Turner, G. O. Lloyd, N. Clarke, J. W. Steed, *Cryst. Growth Des.* **2008**, *8*, 3335–3344; b) D. K. Kumar, D. A. Jose, A. Das, P. Dastidar, *Chem. Commun.* **2005**, 4059–4061; c) D. K. Kumar, D. Amilan Jose, A. Das, P. Dastidar, *Langmuir* **2004**, *20*, 10413–10418.
- [19] V. A. Blatov, D. M. Proserpio, *TOPOS 4.0, A program package for multipurpose crystallochemical analysis*.
- [20] a) K. Uemura, S. Kitagawa, K. Fukui, K. Saito, *J. Am. Chem. Soc.* **2004**, *126*, 3817–3828; b) K. Uemura, S. Kitagawa, M. Kondo, K. Fukui, R. Kitaura, H.-C. Chang, T. Mizutani, *Chem. Eur. J.* **2002**, *8*, 3586–3600.

Received: March 31, 2010
Published Online: July 14, 2010

Construction of Three-Dimensional Uranyl–Organic Frameworks with Benzenetricarboxylate Ligands

Zuo-Lei Liao,^[a,b] Guo-Dong Li,^[b] Xiao Wei,^[a] Yang Yu,^[b] and Jie-Sheng Chen^{*[a]}

Keywords: Uranium / Metal-organic frameworks / Microporous materials / Photovoltaics

Three new uranyl–organic coordination frameworks $(\text{UO}_2)_3(\nu\text{-BTC})_2(\text{H}_2\text{O})_4$ (**1**), $(\text{UO}_2)_6\text{O}(\text{OH})(m\text{-BTC})_2(m\text{-HBTC})_2(\text{H}_2\text{O})_2(\text{H}_3\text{O})\cdot 6\text{H}_2\text{O}$ (**2**), and $(\text{UO}_2)_2\text{O}(m\text{-BTC})[\text{NH}_2(\text{CH}_3)_2]_2\cdot \text{H}_2\text{O}$ (**3**), where $\nu\text{-BTC}$ = 1,2,3-benzenetricarboxylate and $m\text{-BTC}$ = 1,2,4-benzenetricarboxylate, have been prepared under hydrothermal conditions. All three compounds possess three-dimensional (3D) architectures. The adjacent carboxylate groups attached to the aromatic ring in the ligands result in strong steric hindrance, and, therefore, they are forced to ori-

ent themselves vertically to the aromatic ring. This conformation contributes to the formation of the 3D structures to a great extent. Among these three compounds, **1** has a dense structure, whereas compounds **2** and **3** possess channels that can accommodate water and/or protonated dimethylamine species. Further investigations reveal a microporous adsorption property of compound **2** and a photovoltaic response of compound **3**.

Introduction

Considerable research efforts have been directed towards the construction of metal–organic hybrid compounds because of their rich structural features and potential applications as functional materials.^[1] Besides the extensively studied d block metals and 4f lanthanides, 5f actinides are recently gaining continuing interest as construction nodes for the formation of coordination polymers.^[2] In particular, the coordination chemistry of uranium has been explored by a number of research groups, which has led to a variety of novel structures with attractive functions and diverse topologies.^[2b–2f,3] Among these actinide coordination compounds, the three-dimensional (3D) uranyl–organic architectures are of significance, as the 3D materials are considered to be superior in stability to 1D or 2D structures and may exhibit properties such as porous adsorption, ion exchange, and catalysis. However, unlike the Ln analogues, 3D monometallic uranium–organic frameworks have hardly been reported, with the exception of a few examples of aliphatic and alicyclic dicarboxylates.^[2e,4] This is mainly because of the easy formation of the linear uranyl unit with strong U=O bonds.^[5] As a result, the accessibility of the uranium center in the uranyl units is limited to a great ex-

tent, and the incoming ligands can only bond to the center at the equatorial positions. Despite the high coordination number for U^{VI} , the uranyl unit is most likely to adopt a planar coordination environment. As a result of the lack of bonding from axial directions, uranyl–organic coordination compounds usually prefer chain/sheet arrangements to 3D structures, especially when planar aromatic ligands are employed.^[2d,6] Obviously, the crosslinking ability of construction units is of great importance for the design and synthesis of 3D uranyl–organic compounds. To increase the dimensionality of uranium–organic coordination compounds, two strategies have been developed. Firstly, d block metal ions with high crosslinking ability, such as Ni^{2+} or Zn^{2+} , are introduced into the uranyl–organic reaction systems to act as additional connecting nodes.^[2c,7] Secondly, aliphatic and alicyclic dicarboxylic acids with flexible backbones are used as the ligands, which fold to “kinked” arrangements, and therefore increase the possibility of crosslinking the inorganic chains/sheets to form 3D structures.^[2e,4] In fact, for construction of 3D uranyl–organic coordination compounds, the search for proper ligands is one of the central challenges.

On the other hand, uranyl compounds feature rich photochemical and photophysical properties, such as photoluminescence, photocatalysis, and photocurrent and photovoltaic responses.^[3a–3c,7a,8] The photoluminescence of uranyl compounds has been elucidated extensively,^[3a–3c,7b–7e,8a] while the photocatalytic properties of solid uranyl materials has been investigated to a lesser extent.^[7a,7b] Although the photoelectric conversion of uranyl compounds was reported previously, the origin of this photoelectric behavior needs to be further clarified as the involved compounds contain not only uranyl units but also Zn^{2+} cations.^[7a,8b]

[a] School of Chemistry and Chemical Engineering, Shanghai Jiao Tong University, Shanghai 200240, P. R. China
Fax: +86-21-5474-1297
E-mail: chemcj@sjtu.edu.cn

[b] State Key Laboratory of Inorganic Synthesis and Preparative Chemistry, Jilin University, Changchun 130012, P. R. China

Supporting information for this article is available on the WWW under <http://dx.doi.org/10.1002/ejic.201000298>.

Zinc species are well known to be photoactive and are widely employed in photovoltaic materials,^[9] and, therefore, the presence of Zn^{2+} in the structures causes additional difficulties for the elucidation of the photoelectric properties of the compounds. To rule out the possibility that the photoelectric properties arise as a result of the Zn^{2+} ions and not the uranyl species in the previously reported uranyl compounds, it is necessary to obtain monometallic uranyl coordination compounds with photoelectric behavior. In this context, we tried to prepare uranyl–organic compounds by using benzenetricarboxylic acids as the ligands under hydrothermal conditions, and three new uranyl benzene-carboxylate coordination polymers, $(\text{UO}_2)_3(\nu\text{-BTC})_2(\text{H}_2\text{O})_4$ (**1**), $(\text{UO}_2)_6\text{O}(\text{OH})(m\text{-BTC})_2(m\text{-HBTC})_2(\text{H}_2\text{O})_2(\text{H}_3\text{O})\cdot 6\text{H}_2\text{O}$ (**2**), and $(\text{UO}_2)_4\text{O}_2(m\text{-BTC})_2[\text{NH}_2(\text{CH}_3)_2]_2\cdot \text{H}_2\text{O}$ (**3**), were successfully crystallized from the reaction systems. Although the ligands we used are aromatic (not aliphatic or alicyclic), the carboxylate groups on the aromatic ring are able to rotate and consequently the ligands are flexible, in a sense. These three compounds provide ideal models for revealing the relationship between the ligands and the dimensionality of the coordination compound, and because the compounds are monometallic, it is possible to concentrate on the uranyl centers alone for investigating the photoelectric behavior.

Results and Discussion

Compound **1** (Figure 1), $(\text{UO}_2)_3(\text{C}_9\text{H}_3\text{O}_6)_2(\text{H}_2\text{O})_4$, crystallizes in the space group $P2_1/c$. It consists of both seven-coordinate and eight-coordinate U^{VI} centers bound by $\nu\text{-BTC}$ ligands. Two crystallographically independent uranium atoms and one $\nu\text{-BTC}$ ligand are found within **1**. The eight-coordinate U1 atom lies on the inversion center and is chelated by two carboxylate groups from two BTC ligands in the equatorial plane. The remaining two equatorial positions are occupied by coordination water molecules. Therefore, with two axial uranyl oxygen atoms, the hexagonal-bipyramid coordination sphere of U1 is complete. The average U–O bond length is 2.49 Å, whereas the U=O uranyl bond length is 1.77 Å. U2 adopts a pentagonal-bipyramid geometry, and this metal center is coordinated by three BTC ligands and one water molecule. Four carboxylate groups are involved in the coordination to U2, with two from two different BTC ligands in a monodentate mode and another two from the third BTC molecule in a bidentate mode. The BTC ligand gives up all its carboxylate protons to provide six O donors for coordination to the four uranyl centers, which include one eight-coordinate and three seven-coordinate uranyl acceptors. The overall structure of **1** (Figure 2) can be regarded as being constructed from uranyl–organic layers, which are further linked into a three-dimensional framework. The layers are composed of seven-coordinate uranyl polyhedral and BTC linkers, and they extend in the bc plane. In the individual layer, each uranyl polyhedron is connected to four neighbors through three BTC ligands. The connection of the uranyl sites is

accomplished by the bridging of carboxylate groups. Each BTC ligand donates two adjacent carboxylate groups to connect three uranyl sites in the same layer together, which leaves the third carboxylate group above or below the layer to chelate the eight-coordinate uranyl site. In this manner, the eight-coordinate uranyl sites crosslink adjacent layers to form a 3D framework. Although there are voids in the framework structure of **1**, the voids are occupied by coordinating water molecules, and, therefore, the structure is considered to be nonporous. The removal of the coordinating water molecules leads to the collapse of the structure.

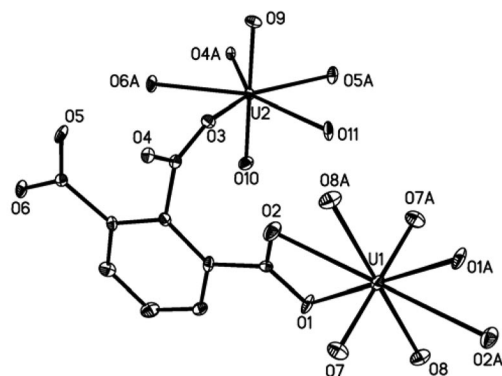


Figure 1. ORTEP drawing of the asymmetric unit of compound **1**. Thermal ellipsoids are drawn at the 30% probability level, and the hydrogen atoms are omitted for clarity.

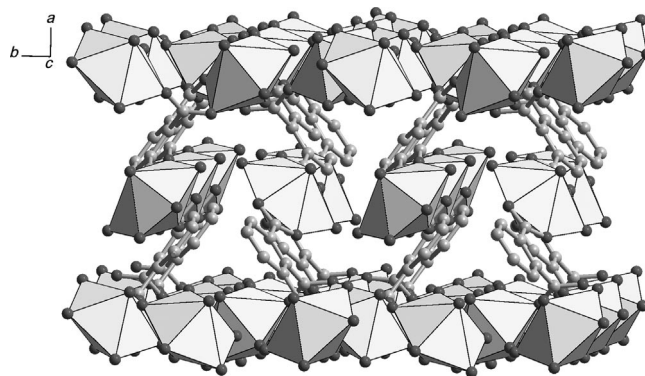
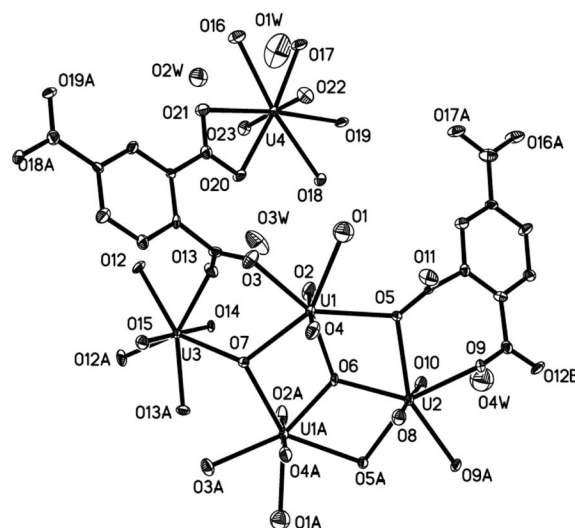


Figure 2. The structure of **1** viewed from the c axis. The hydrogen atoms are omitted for clarity.

Compound **2** (Figure 3) also consists of seven-coordinate and eight-coordinate U^{VI} centers. The seven-coordinate uranium atoms polymerize into tetranuclear clusters (Figure 4). Unlike the known planar tetranuclear cluster with C_2 symmetry in many uranyl–organic coordination compounds, the tetramer in **2** adopts an unusual “3+1” polymerization fashion that has never been reported before in uranyl compounds;^[3c,3d,6b,8b] that is, three of the four uranyl units polymerize into a trimer in a planar conformation, sharing three common edges and one corner that is occupied by a $\mu\text{-3}$ oxo site (average U–O separation of 2.22 Å), and then attach to the fourth unit through a $\mu\text{-3}$ hydroxy group (average U–O separation of 2.47 Å), which serves as a common corner. The fourth uranyl unit is distorted out of the mean plane defined by the other three centers, which

results in a bent tetranuclear cluster. Instead of a C_2 symmetry, this tetramer possesses a symmetry plane. However, despite the unusual arrangement of the cluster, the uranium atoms themselves are in a typical coordination environment. The terminal oxygen atoms occupy the axial positions, with U–O separations that range from 1.75 to 1.79 Å, all of which are typical for U=O contacts. Equatorially, each uranyl unit is coordinated to 5 O donors with an average bond length of 2.40 Å. Of the fourteen equatorial oxygen donors within every tetranuclear cluster, there is a bridging hydroxy group and an oxo site that serve as common corners, two coordinating water molecules, and ten O-donors from the carboxylate groups. Furthermore, the tetranuclear clusters are bridged by carboxylate groups into 1D chains along the [0 1 0] direction. In each chain, the clusters are oriented in the same direction, and the bent uranyl corner connects to the planar part of another cluster through two bridging carboxylate groups. All the chains are oriented in a parallel fashion to each other, but the adjacent chains run in opposite directions. The eight-coordinate uranyl units are in the same coordination environment, with two uranyl oxygen atoms at the axial positions and three carboxylate groups in the equatorial plane. In this manner, U–O hexagonal bipyramids are formed, with average U–O separations of 2.48 Å and 1.77 Å for equatorial U–O bonds and uranyl U=O bonds, respectively. There are two types of chelating BTC molecules in the pentagonal bipyramids. One BTC ligand donates two of the *meta*-carboxylate groups (in the 2- and 4-positions) to bridge adjacent monomers into zig-zag chains along the *c* axis, and the third functional group binds to one of the tetranuclear clusters. The other BTC ligand chelates to one hexagonal bipyramid through the carboxylate group in the 4-position, while the two *ortho* groups (in the 1- and 2-positions) bind to the tetranuclear cluster. In this way, the two different uranyl-organic chains are crosslinked together by the BTC ligands. Every tetranuclear chain connects a number of monomer-organic chains, and vice versa. As a result, the 3D framework structure of **2** (Figure 5) is constructed, and 1D channels are formed within the structure. The largest dimension of the channels is about 2.5×5.0 Å (shortest O–O contact), and these channels accommodate neutral and protonized water. Upon removal of the water molecules, compound **2** exhibits a considerable adsorption capacity. Only water can be adsorbed into the structure of **2**, while larger molecules such as methanol and ethanol are not able to penetrate into the channels of the dehydrated **2** (Figure 6).

In compound **3** (Figure 7), all the uranyl units polymerize into the same type of tetranuclear clusters. This tetranuclear cluster, however, is different from that in compound **2** and possesses the well-known planar conformation.^[3c,3d,6b,8b] All the uranyl units are in a pentagonal bipyramid environment. The average U–O separation for the uranyl U=O bonds is 1.77 Å, while the distances for the equatorial U–O bonds range from 2.22 to 2.59 Å. The uranyl-oxygen bipyramids polymerize into clusters sharing three common edges. In addition, two hydroxy groups and two oxygen donors from the carboxylate groups serve as



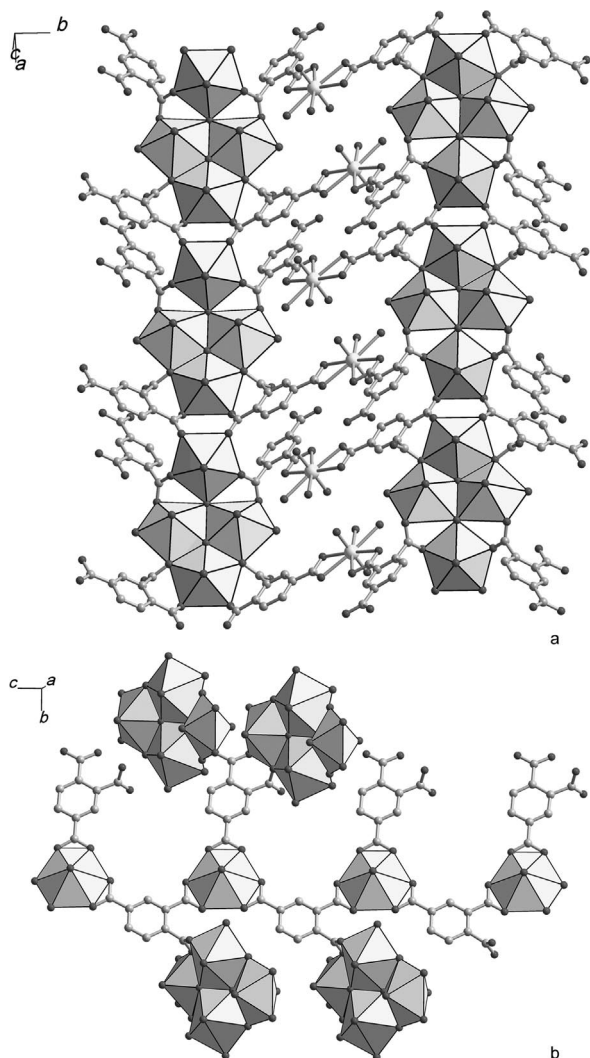


Figure 5. (a) The tetramer-organic-tetramer ribbons and (b) the monomer-organic-monomer chain within compound **2**. The hydrogen atoms are omitted for clarity.

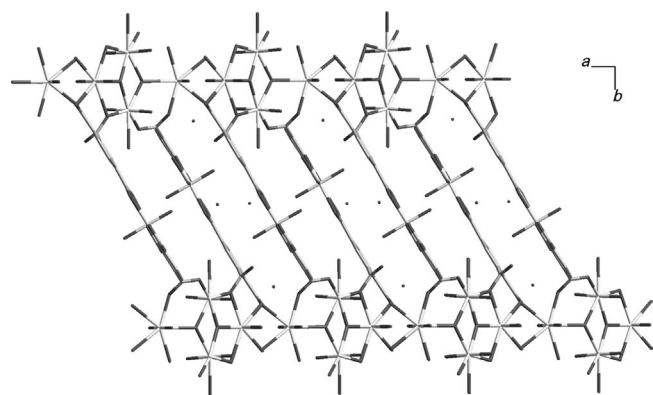


Figure 6. View of the structure of compound **2** along the *c* axis. All hydrogen atoms are omitted for clarity.

from both sides. Each ribbon connects to two adjacent ribbons from its edges and two more from its faces, and as a result, all the ribbons are crosslinked together to form the

walls of the channels within **3** (Figure 8). The channels run along the *a* axis, with an aperture size of 3.4×6.8 Å (shortest O–O and C–C contacts). Inside the channels, there exist dimethylamine and water molecules, and the former is protonated to balance the negative charges of the framework. In addition to electrostatic interactions, the amine species interact with the water molecules and the framework oxygen atoms through hydrogen bonding. Although the positions of the hydrogen atoms could not be calculated because of vibrations of the O atoms, the separations of the N and O atoms and the arrangements of the guest species definitely indicate the formation of hydrogen bonds.

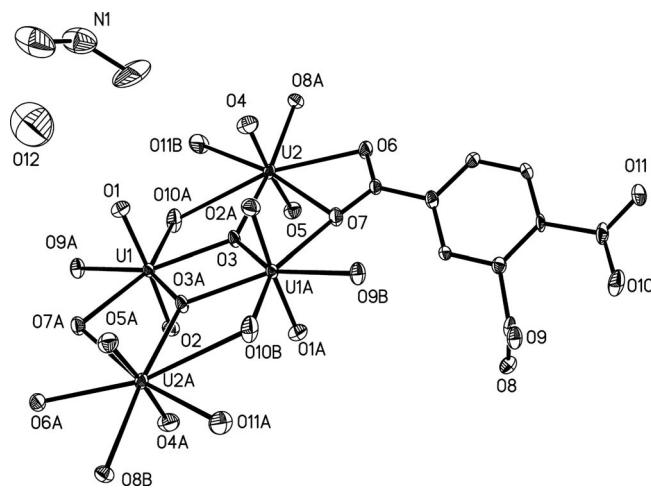
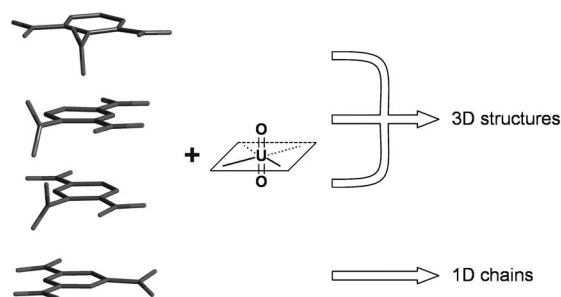


Figure 7. ORTEP drawing of the asymmetric unit of compound **3**. Thermal ellipsoids are drawn at the 30% probability level, and the hydrogen atoms are omitted for clarity.



Scheme 1. Schematic diagram of the relationship between ligand conformation and product structures.

All three compounds possess a 3D framework constructed from uranyl cations and arylcarboxylic acid ligands. It is rather unusual to construct 3D uranyl–organic materials by using arylcarboxylate ligands because chains or layer structures of the uranyl units are favored in the absence of other crosslinking species such as transition-metal ions and bipyridine ligands. The successful construction of the 3D compounds **1–3** is attributed to the conformation of the BTC ligands. In the previously used 1,4-naphthalenedicarboxylate and 1,3,5-benzenetricarboxylate ligands,^[6b,10] the carboxylate groups are equally linked to the

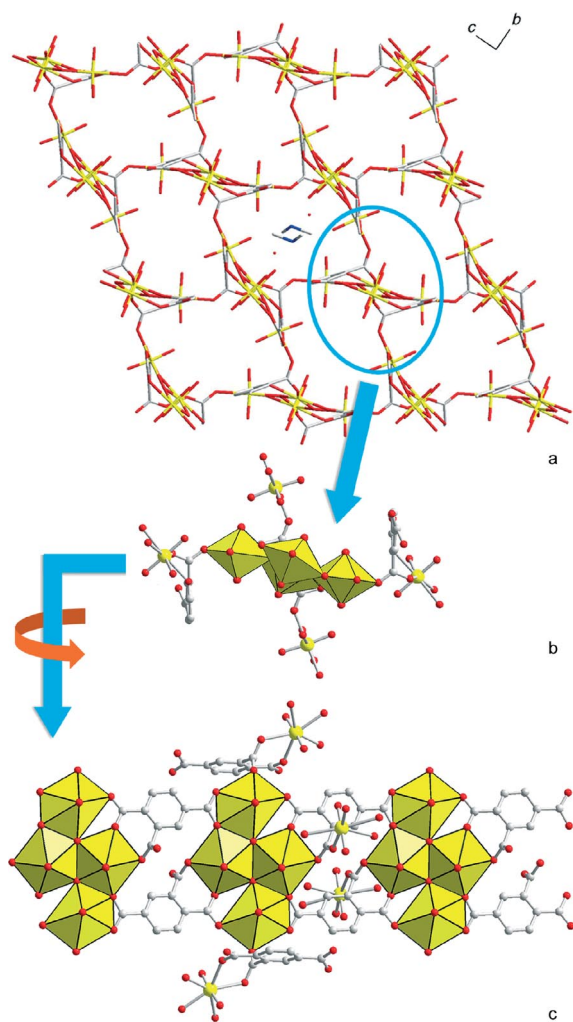


Figure 8. (a) Structure of compound **3** viewed along the *a* axis. The guest species are shown in only one channel for clarity; (b) Projection of the tetramer-organic ribbon along the *a* axis; (c) Arrangement of the tetranuclear uranyl clusters and the *m*-BTC linkers. Only one uranyl site of each neighbouring ribbon is illustrated for clarity. Hydrogen atoms in all figures are omitted.

aromatic rings and are well separated from one another. Because of the ease of delocalizing the electrons through conjugated π orbitals, the carboxylate groups in these ligands have a strong tendency to orient within the ring plane, which leads to a planar conformation. As a result, when coordinating to uranyl ions, which also prefer planar coordination geometries, these molecules form 1D or 2D structures rather than 3D coordination architectures. In contrast, in the *v*-BTC and *m*-BTC ligands used in this work, there are at least two carboxylate groups in the *ortho* positions. Because of steric hindrance, at least one of the adjacent carboxylate groups in these molecules is forced out of the ring plane and adopts a vertical conformation to avoid short contact of the O donors. This is critical for construction of 3D uranyl-organic coordination structures. The vertically oriented carboxylate groups increase the connectivity of the coordination structures from planar to three-dimensional, as is clearly demonstrated by the forma-

tion of compounds **1** and **2**. For compound **3**, the three carboxylate groups in the ligand function at three different levels for the construction of the framework. Firstly, the carboxylate groups in the 1- and 4-positions facilitate the polymerization of the uranyl units into tetranuclear clusters. Secondly, through the two carboxylate groups, the BTC ligands connect the tetranuclear clusters into 1D ribbons. Finally, the third carboxylate group in the 2-position orients almost vertically to the aromatic ring and connects two uranyl sites in different clusters and bridges them together to form a 3D architecture. In previous studies, high-symmetry ligands with low steric hindrance have been employed to obtain metal-organic frameworks (MOFs) with large pore sizes by using d block metals.^[11] However, the formation of **1–3** reveals the possibility of using ligands with strong steric hindrance for the construction of MOFs by taking advantage of their additional connectivity.

Comparison of compounds **2** and **3** also demonstrates the importance of structure-directing agents (SDAs) in the construction of uranyl-organic MOFs. For compound **2**, the only guest species are water molecules, and, therefore, a framework with relatively small pores is formed. Whereas for compound **3**, because of the presence of dimethylamine species, which are larger than water molecules in volume, the pores in the framework structure are significantly expanded to 3.4×6.8 Å. The use of structure-directing agents (sometimes termed as templates) is one of the key factors in the design and construction of inorganic zeolite materials.^[12] Although the details are still not very clear, the spatial structures of the SDAs and the interaction between the SDAs and the host frameworks are considered to play important roles in the stabilization of the porous structures. By comparing the structures of **2** and **3**, it can be concluded that the presence of dimethylamine exerts an influence on the structures and pore dimensions of the uranyl-organic MOFs.

Thermogravimetric and differential thermal analysis were conducted to elucidate the thermal behavior of the three compounds, and the results are illustrated in Figures 9, 10, and 11. For compound **1**, the TG curve shows a small weight loss below 200 °C (less than 0.5%), which suggests that the compound is stable up to this temperature. The corresponding DTA curve shows no sign of phase transition below 200 °C. Further heating gradually leads to weight loss, and at temperatures above 400 °C, the weight loss becomes distinct, with a sharp exothermic effect at around 500 °C attributable to the decomposition of the compound. The total weight loss reaches 35.6% (calcd.: 35.1%), and the residue is U_3O_8 based on powder X-ray diffraction characterization. The thermal analysis results also indicate that the water molecules in **1** are not reversibly removable without collapse of the framework, and, therefore, porous adsorption for this compound is not available.

For compound **2**, the TG curve shows a small weight loss below 130 °C (less than 0.8%). From 130 to 285 °C, a weight loss of about 3.8% is observed. The total weight loss below 285 °C is thus 4.6%, attributable to the removal of adsorbed water molecules (calcd.: 4.8%) in the compound.

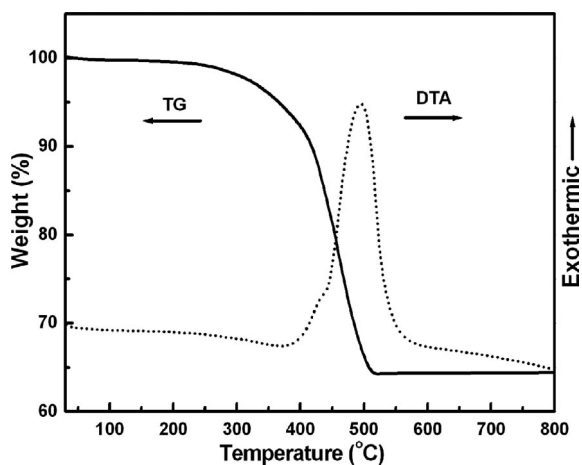


Figure 9. The TG (solid) and DTA (dot) curves for compound 1.

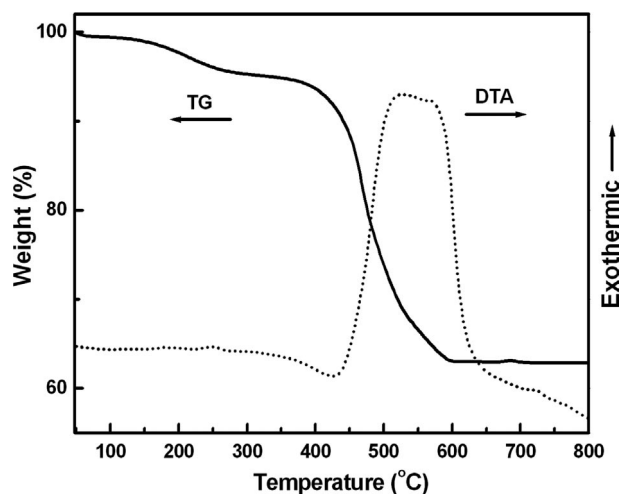


Figure 10. The TG (solid) and DTA (dot) curves for compound 2.

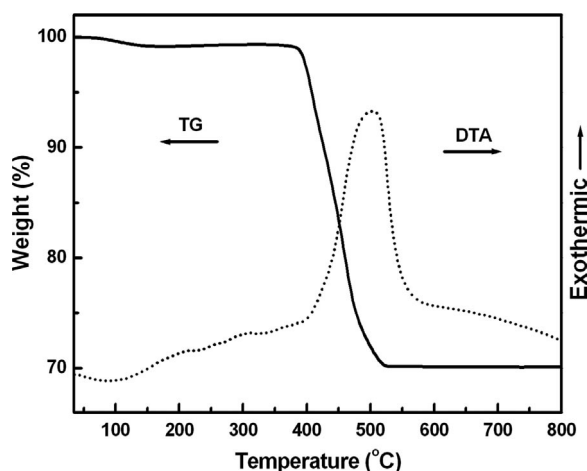


Figure 11. The TG (solid) and DTA (dot) curves of compound 3.

At higher temperatures, the compound remains stable up to 360 °C, followed by a sharp weight loss from about 400 °C with a corresponding exothermic effect between 500 to 600 °C. This thermal effect is attributed to the oxidative de-

composition of the compound. At above 600 °C, the compound decomposes completely to form a residue of U_3O_8 , and the corresponding total weight loss is 38.0%, which is in good agreement with the calculated value (38.0%) based on the single-crystal structure of the compound.

The weight loss for compound 3 at below 140 °C is about 0.8%. This value is in accordance with the crystal structure of the compound, which contains a small amount of water (1.1 wt.-%). The dimethylamine species in 3 are protonated and, therefore, cannot be removed through sample heating. At higher temperatures, the TG curve of 3 remains flat until 380 °C, followed by a sharp drop, which corresponds to a distinct weight loss. An apparent exothermic effect is observed in the DTA curve at around 500 °C, attributable to the oxidative decomposition of the compound. The final weight loss reaches 29.9% at 530 °C, in agreement with the calculated value (31.4%) based on the single-crystal structure.

Further experiments have been conducted to investigate the adsorption properties of the compounds obtained. Prior to adsorption measurements, crystals of 1–3 were heated in vacuo at 200 °C for 1 h. No significant adsorption capacity has been observed for 1 and 3, but compound 2 adsorbs a considerable amount of water molecules after evacuation treatment. The adsorption isotherms for water and methanol for 2 are illustrated in Figure 12. The water adsorption isotherm is a typical type-I curve, characteristic of microporous materials. On the other hand, the methanol adsorption capacity for 2 is negligible, which suggests that this compound may be used to selectively abstract water from organic solvents.

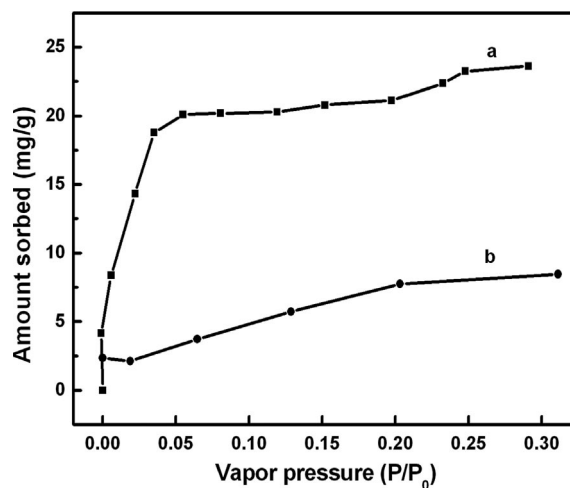


Figure 12. The water (a) and methanol (b) adsorption isotherms of compound 2 at 298 K.

Photophysical and photochemical properties are key features of uranyl compounds, which may find applications as photoluminescent, photocatalytic, and photovoltaic materials.^[3a–3c,7a,8] The three compounds we prepared exhibit typical uranyl photoluminescent properties, as presented in Figure 13. Upon excitation at around 360 nm, intense pho-

toluminescent emission peaks in the range from 480 to 580 nm are observed. The excitation spectra correlate very well with the UV/Vis spectra (in Figure S4, Supporting Information). As previously documented, the luminescence of uranyl compounds relies on photoexcitation and relaxation of the U=O double bonds, and, in some cases, the ligand molecules may also be involved in the luminescence.^[2c,13]

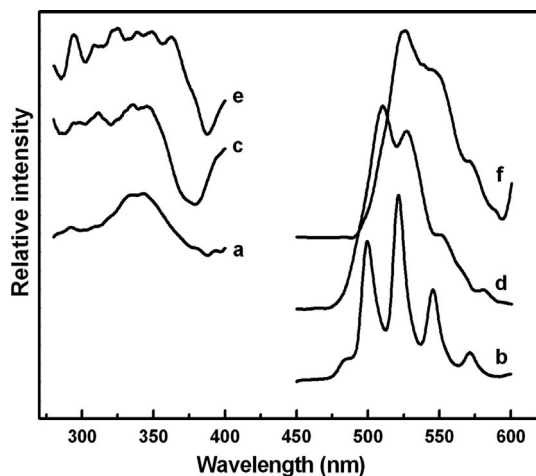


Figure 13. The excitation and emission spectra for compounds 1 (a, b), 2 (c, d), and 3 (e, f).

Photoelectric properties have also been investigated for compounds 1–3 by surface photovoltage spectroscopy (SPS) and field-induced photovoltage spectroscopy (FISPS). Compound 3 exhibits a significant photovoltaic response, whereas no positive results are recorded for compounds 1 and 2 (Figure 14). The response signal in the SPS spectrum for 3 is in agreement with the results from the UV/Vis and the excitation spectra, which indicates that the same photoenergy adsorption process of the uranyl center is responsible for the photovoltaic response.^[8b] Since only a single peak is observed in the 200–600 nm wavelength range, it is obvious that the uranyl center leads to the photoelectric property in this case. Furthermore, the absence of Zn^{2+} or other transition-metal ions in the compound clearly demonstrates that the uranyl species alone is photoelectrically active. Upon application of a positive field, the photovoltaic response is significantly enhanced with increasing biases, while when the negative field is applied, the response completely disappears. This indicates that the photogenerated field of the compound accords with the bias. In addition, it can be noticed that in the framework of compound 3, the alternative aromatic rings and the planar tetranuclear uranyl clusters are connected side by side. This configuration favors long-range overlap between the uranium orbitals and the delocalized π orbitals of neighboring ligand molecules, and, consequently, the transfer of charge carriers along the framework structure is facilitated. This might be the reason behind the fact that the photovoltaic response is observed only for compound 3 but not for 1 and 2.

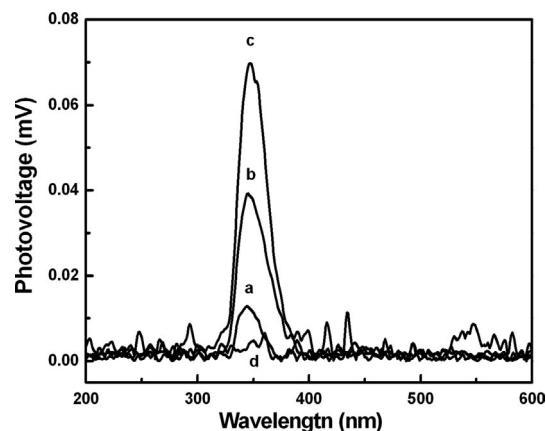


Figure 14. The SPS and FISPS spectra of compound 3 under the biases of 0 (a), +0.5 (b), +1.0 V (c), and −0.5 V (d).

Conclusions

The use of benzenetricarboxylic acids with *ortho*-carboxylate groups as ligands leads to successful formation of three new 3D uranyl–organic coordination assemblies. The key in the crystallization of the compounds is to take advantage of the steric hindrance of the carboxylate groups to create a nonplanar conformation of ligands, which increases its crosslinking ability when the ligand coordinates to planar uranyl ions. With increased connectivity, the structures of the coordination compounds extend to three-dimensional topologies. A unique “3+1” tetranuclear uranyl cluster is observed in one of the obtained crystalline materials (compound 2). Among the three compounds, 1 possesses a nonporous framework, whereas 2 and 3 contain channels in their framework structures. The channel dimension of 2 is $2.5 \times 5.0 \text{ \AA}$, and within the channels, reversibly removable water molecules are accommodated. For compound 3, the protonated dimethylamine species in the channels are not reversibly removable through heating of the sample. All three compounds exhibit typical uranyl luminescent emissions upon photoexcitation. Surface photovoltaic spectroscopy reveals that compound 3 exhibits a photoelectric conversion property. Inspection of the surface photovoltaic spectra in combination with the UV/Vis and the photoexcitation spectra indicates that the photoelectric conversion property for 3 arises from the uranyl centers, whereas the framework structure of the compound also exerts an influence on the photoelectric behavior.

Experimental Section

All chemicals were commercially available. Uranyl acetate was recrystallized from hot water, whereas the other reagents were used as received without further purification.

Synthesis of 1: A mixture of $\nu\text{-H}_3\text{BTC}$ (0.104 g, 0.50 mmol) and uranyl acetate (0.210 g, 0.50 mmol) was dispersed in water (11 mL) and stirred for 3 h in air. The final reaction mixture was transferred to a 15-mL Teflon-lined autoclave, which was subsequently sealed and heated at 160°C for 3 d, followed by cooling to room temperature at 10°C/h . Yellow block crystals of 1 (0.033 g) were obtained

after washing with distilled water and drying in air, and the yield of the product was about 16% based on U. $C_{18}H_{14}O_{22}U_3$ (1296.38): calcd. C 16.32, H 1.28; found C 16.64, H 1.26.

Synthesis of 2 and 3: The synthesis procedures for compounds **2** and **3** were similar to that for **1**. For **2**, the reaction system was a mixture of *m*-H₃BTC (0.106 g, 0.50 mmol), uranyl acetate (0.104 g, 0.25 mmol), ammonia solution (25 wt.-%, 0.04 mL, 0.54 mmol), and water (11 mL). The final product was obtained in a yield of about 50% (0.095 g) based on U. $C_{36}H_{34}O_{47}U_6$ (2646.81): calcd. C 16.32, H 1.28; found C 16.22, H 1.07. For **3**, the reaction mixture consisted of *m*-H₃BTC (0.05 g, 0.24 mmol), uranyl acetate (0.105 g, 0.25 mmol), dimethylamine (40 wt.-%, 0.024 mL, 0.20 mmol), water (6 mL), and ethanol (6 mL). Compound **3** was obtained in a yield of about 37% (0.038 g) based on U. $C_{11}H_{13}NO_{12}U_2$ (827.28): calcd. C 15.95, H 1.45, N 1.69; found C 15.94, H 1.55, N 1.61.

Characterization and Physical Measurements: The C, H and N elemental analysis was conducted on a Flash EA 1112 elemental analyzer. The powder XRD data were collected on a Siemens D5005 diffractometer with Cu- K_{α} radiation ($\lambda = 1.5418 \text{ \AA}$) over the 2θ range of $4\text{--}40^\circ$ at room temperature. The solid diffuse reflectance UV/Vis spectra were recorded on a Shimadzu UV 3600 spectrometer, whereas the IR spectra were recorded on a Bruker IFS 66v/S FTIR spectrometer. The photoluminescent spectra were obtained on a Perkin-Elmer LS 55 spectrometer, and the thermogravimetric (TG) and differential thermal analysis (DTA) curves were recorded in air on a Netzsch STA 449C TG/DTA thermal analyzer at a heating rate of $20^\circ\text{C}/\text{min}$. The adsorption measurements were performed on a CAHN 2000 electrogravimetric balance. The surface photovoltaic spectra (SPS) and field-induced surface photovoltaic spectra (FISPS) were obtained from an assembled apparatus including a 500 W xenon lamp (CHF XQ500 W), a monochromator (Omni-I 500, Zolix Instruments Co.), a 1 mm wide slit, a lock-in amplifier (SR830-DSP), and a light chopper (SR540).

X-ray Crystallography: Crystallographic data of compounds **1** and **2** (Table 1) were collected on a Rigaku RAXIS-RAPID single-crystal diffractometer equipped with a narrow-focus, 5.4-kW sealed-tube X-ray source (graphite-monochromated Mo- K_{α} radiation with $\lambda = 0.71073 \text{ \AA}$) at room temperature. Data processing was accomplished with the PROCESS-AUTO processing program. Crystallographic data for **3** were recorded at room temperature on a Bruker-AXS Smart CCD diffractometer equipped with a normal-focus, 2.4-kW X-ray source (graphite-monochromated Mo- K_{α} radiation with $\lambda = 0.71073 \text{ \AA}$) operating at 50 kV and 40 mA with increasing ω . All of the structures were solved by direct methods by using the program SHELXS-97^[14] and refined by full-matrix least-squares techniques against F^2 by using the SHELXTL-97 crystallographic software package.^[15] All non-H atoms were easily found from the difference Fourier maps and refined anisotropically, whereas the H atoms of the organic molecules were placed by geometrical considerations and were added to the structure factor calculation. The H atoms attached to N and O atoms were unable to be located because of high thermal vibration levels. Crystal data: **1**, monoclinic, space group $P2_1/c$, $a = 11.050(2) \text{ \AA}$, $b = 10.994(2) \text{ \AA}$, $c = 10.593(2) \text{ \AA}$, $\beta = 97.93(3)^\circ$, and $Z = 2$; **2**, monoclinic, space group $P2_1/m$, $a = 8.6591(17) \text{ \AA}$, $b = 32.508(7) \text{ \AA}$, $c = 9.979(2) \text{ \AA}$, $\beta = 97.77(3)^\circ$, and $Z = 2$; **3**, monoclinic, space group $P2_1/n$, $a = 11.750(2) \text{ \AA}$, $b = 9.832(2) \text{ \AA}$, $c = 14.630(3) \text{ \AA}$, $\beta = 97.73(3)^\circ$, and $Z = 4$. CCDC-769205 (for **1**), -769206 (for **2**) and -769207 (for **3**) contain the supplementary crystallographic data. These data can be obtained free of charge from the Cambridge Crystallographic Data Centre via www.ccdc.cam.ac.uk/data_request/cif.

Table 1. Crystallographic data and structure refinement for compounds **1**, **2**, and **3**.

Compound	1	2	3
Empirical formula	$C_{18}H_{14}O_{22}U_3$	$C_{36}H_{34}O_{47}U_6$	$C_{11}NH_{13}O_{12}U_2$
Formula weight	1296.38	2644.8	827.28
T (K)	293(2)	293(2)	293(2)
Space group	$P2_1/c$	$P2_1/m$	$P2_1/n$
a (Å)	11.050(2)	8.6591(17)	11.750(2)
b (Å)	10.994(2)	32.508(7)	9.832(2)
c (Å)	10.593(2)	9.979(2)	14.630(3)
α (°)	90	90	90
β (°)	97.93(3)	97.77(3)	97.73(3)
γ (°)	90	90	90
V (Å ³)	1274.6(4)	2783.2(10)	1674.8(6)
Z	2	2	4
ρ (g cm ^{−3})	3.378	3.156	3.281
$F(000)$	1148	2352	1464
μ (mm ^{−1})	19.117	17.516	19.380
θ range (°)	3.11–27.39	2.99–27.47	3.16–27.47
Limiting indices	$-14 \leq h \leq 14$ $-13 \leq k \leq 14$ $-13 \leq l \leq 13$	$-11 \leq h \leq 11$ $-42 \leq k \leq 42$ $-12 \leq l \leq 12$	$-14 \leq h \leq 14$ $-12 \leq k \leq 12$ $-18 \leq l \leq 18$
Reflections collected/unique	11693/2888, [$R(\text{int}) = 0.0485$]	27532/6459, [$R(\text{int}) = 0.0841$]	15733/3802, [$R(\text{int}) = 0.0505$]
GOF on F^2	0.827	1.042	1.023
R	$R_1 = 0.0237$	$R_1 = 0.0427$	$R_1 = 0.0395$
$[I > 2\sigma(I)]^{[a]}$	$wR_2 = 0.0393$	$wR_2 = 0.0814$	$wR_2 = 0.0539$

$$[a] \quad R_1 = \sum |F_o| - |F_c| / \sum |F_o|, \quad wR_2 = \sum w[(F_o^2 - F_c^2)^2 / \sum w(F_o^2)^2]^{1/2}.$$

Supporting Information (see footnote on the first page of this article): Selected bond length and angles, XRD patterns, solid diffuse reflectance UV/Vis spectra, and IR spectra are presented.

Acknowledgments

This work was financially supported by the National Basic Research Program (2007CB613303) and the National Natural Science Foundation of China (20731003).

- a) B. Moulton, M. J. Zaworotko, *Chem. Rev.* **2001**, *101*, 1629–1658; b) A. N. Khlobystov, A. J. Blake, N. R. Champness, D. A. Lemenovskii, A. G. Majouga, N. V. Zyk, M. Schröder, *Coord. Chem. Rev.* **2001**, *222*, 155–192; c) O. R. Evans, W. B. Lin, *Acc. Chem. Res.* **2002**, *35*, 511–522; d) X. B. Zhao, B. Xiao, A. J. Fletcher, K. M. Thomas, D. Bradshaw, M. J. Rosseinsky, *Science* **2004**, *306*, 1012–1015; e) S. Kitagawa, R. Kitaura, S.-I. Noro, *Angew. Chem. Int. Ed.* **2004**, *43*, 2334–2375; f) G. Férey, *Chem. Mater.* **2001**, *13*, 3084–3098; g) P. J. Hagrman, D. Hagrman, J. Zubietta, *Angew. Chem. Int. Ed.* **1999**, *38*, 2638–2684; h) C. N. R. Rao, S. Natarajan, R. Vaidhyanathan, *Angew. Chem. Int. Ed.* **2004**, *43*, 1466–1496; i) A. Phan, C. J. Doonan, F. J. Uribe-Romo, C. B. Knobler, M. O’Keeffe, O. M. Yaghi, *Acc. Chem. Res.* **2010**, *43*, 58–67.
- a) M. Frisch, C. L. Cahill, *Dalton Trans.* **2005**, 1518–1523; b) K. M. Ok, M. B. Doran, D. O’Hare, *J. Mater. Chem.* **2006**, *16*, 3366–3368; c) P. Thuéry, *CrystEngComm* **2007**, *9*, 358–360; d) Y. R. Xie, H. Zhao, X. S. Wang, Z. R. Qu, R. G. Xiong, X. Xue, Z. L. Xue, X. Z. You, *Eur. J. Inorg. Chem.* **2003**, 3712–3715; e) L. A. Borkowski, C. L. Cahill, *Inorg. Chem.* **2003**, *42*, 7041–7045; f) C. M. Wang, C. H. Liao, P. L. Chen, K. H. Lii, *Inorg. Chem.* **2006**, *45*, 1436–1438; g) K. M. Ok, J. Sung, G. Hu, R. M. J. Jacobs, D. O’Hare, *J. Am. Chem. Soc.* **2008**, *12*, 3762–3763.
- a) D. Grohol, A. Clearfield, *J. Am. Chem. Soc.* **1997**, *119*, 4662–4668; b) L. A. Borkowski, C. L. Cahill, *Cryst. Growth Des.* **2006**, *6*, 2241–2247; c) L. A. Borkowski, C. L. Cahill,

- Cryst. Growth Des.* **2006**, *6*, 2248–2259; d) P. C. Burns, *Can. Mineral.* **2005**, *43*, 1839–1894.
- [4] a) P. Thuéry, *Chem. Commun.* **2006**, 853–855; b) P. Thuéry, *Polyhedron* **2006**, *27*, 101–106.
- [5] P. Thuéry, *Cryst. Growth Des.* **2009**, *9*, 4592–4594.
- [6] a) Y. Z. Zheng, M. L. Tong, X. M. Chen, *Eur. J. Inorg. Chem.* **2005**, 4109–4117; b) Z. L. Liao, G. D. Li, M. H. Bi, J. S. Chen, *Inorg. Chem.* **2008**, *47*, 4844–4853.
- [7] a) W. Chen, H. M. Yuan, J. Y. Wang, Z. Y. Liu, J. J. Xu, M. Yang, J. S. Chen, *J. Am. Chem. Soc.* **2003**, *125*, 9266–9267; b) Z. T. Yu, Z. L. Liao, Y. S. Jiang, G. H. Li, G. D. Li, J. S. Chen, *Chem. Commun.* **2004**, 1814–1815; c) M. Frisch, C. L. Cahill, *Dalton Trans.* **2006**, 4679–4690; d) C. L. Cahill, D. T. de Lill, M. Frisch, *CrystEngComm* **2007**, *9*, 15–26; e) K. E. Konpe, C. L. Cahill, *Eur. J. Inorg. Chem.* **2010**, 1177–1185.
- [8] a) L. R. Morss, N. M. Edelstein, J. Fuger, *The Chemistry of Actinide and Transactinide Elements*, 3rd. ed., Springer, Dordrecht, **2006**, vol. 1, chap. 5, pp. 624–630; b) Z. T. Yu, G. D. Li, Y. S. Jiang, J. J. Xu, J. S. Chen, *Dalton Trans.* **2003**, 4219–4220.
- [9] a) H. Imahori, T. Umeyama, S. Ito, *Acc. Chem. Res.* **2009**, *42*, 1809–1818; b) V. Balzani, A. Credi, M. Venturi, *ChemSusChem* **2008**, *1*, 26–58; c) T. Pauporte, D. Lincot, *Electrochim. Acta* **2000**, *45*, 3345–3353; d) L. Q. Jing, B. F. Xin, F. L. Yuan, L. P. Xue, B. Q. Wang, H. G. Fu, *J. Phys. Chem. B* **2006**, *36*, 17860–17865.
- [10] L. A. Borkowski, C. L. Cahill, *Acta Crystallogr., Sect. E* **2004**, *60*, m198–m120.
- [11] a) M. Eddaoudi, J. Kim, N. Rosi, D. Vodak, J. Wachter, M. O’Keeffe, O. M. Yaghi, *Science* **2002**, *295*, 469–472; b) G. Férey, *Chem. Soc. Rev.* **2008**, *37*, 191–214.
- [12] M. E. Davis, R. F. Lobo, *Chem. Mater.* **1992**, *4*, 756–768.
- [13] a) E. Colacio, R. Kivekäs, F. Lloret, M. Sunberg, J. Suarez-Varela, M. Bardaji, A. Laguna, *Inorg. Chem.* **2002**, *41*, 5141–5149; b) Y. B. Go, X. Q. Wang, A. J. Jacobson, *Inorg. Chem.* **2007**, *46*, 6594–6600; c) D. L. Clark, S. D. Conradson, R. J. Donohoe, D. W. Keogh, D. E. Morris, P. D. Palmer, R. D. Rogers, C. D. Tait, *Inorg. Chem.* **1999**, *38*, 1456–1466.
- [14] G. M. Sheldrick, *SHELXS-97, Programs for X-ray Crystal Structure Solution* University of Göttingen, Göttingen, Germany, **1997**.
- [15] G. M. Sheldrick, *SHELXL-97, Programs for X-ray Crystal Structure Refinement* University of Göttingen, Göttingen, Germany, **1997**.

Received: March 16, 2010

Published Online: May 20, 2010

Synthesis, Structure, Characterization, and Redox Properties of the Porous MIL-68(Fe) Solid

Alexandra Fateeva,^[a] Patricia Horcajada,^[a] Thomas Devic,^{*,[a]} Christian Serre,^{*,[a]} Jérôme Marrot,^[a] Jean-Marc Grenèche,^[b] Mathieu Morcrette,^[c] Jean-Marie Tarascon,^[c] Guillaume Maurin,^[d] and Gérard Férey^[a]

Keywords: Metal–organic frameworks / Iron / Microporous materials / Redox activity / Polymorphism

A new porous Fe^{III}-based MOF, formulated Fe(OH)(BDC)·(dmf)_x with $x \approx 1.1$ and presenting the MIL-68 topology, was prepared by reaction of an iron(III) salt and terephthalic acid (H₂BDC) in *N,N'*-dimethylformamide (dmf) under acidic con-

ditions. The structure and properties of this solid were studied by means of X-ray diffraction, thermogravimetric analysis, nitrogen sorption, ⁵⁷Fe Mössbauer spectrometry, and electrochemical lithium insertion.

Introduction

Porous coordination polymers (PCPs) or metal–organic frameworks (MOFs) are porous materials with potential applications in gas storage and capture, gas or liquid purification, catalysis, sensor devices, or controlled drug release.^[1,2] The design of MOFs is possible, under specific reaction conditions, by using a linker with a given symmetry and a predetermined inorganic secondary building unit (SBU).^[3–5] Nevertheless, polymorphism or pseudopolymorphism can also occur in such compounds. For the 1,4-benzenedicarboxylic acid (H₂BDC)/M³⁺ system (M = Al, Cr, Fe, Ga, In, Sc, V), a large number of 3D porous solids have been reported, exhibiting either a rigid or a flexible framework. MIL-101 [M₃O(OH)(BDC)₃·(solv)_x, M = Cr,^[6] MIL-68 [M(OH)(BDC)·(solv)_x, M = V,^[7] Al,^[8] In,^[9] Ga,^[9] MIL-71 [M₂F₂(OH)₂(BDC)·(solv)_x, M = V^[10]], M(BDC) (M = Sc^[11]), and QMOF-2 [MH(BDC)₂, M = In^[12]] exhibit rigid MOFs, whereas MIL-53 [M(OH)(BDC)·(solv)_x, M = Al,^[13] Cr,^[14] Fe,^[15] Ga,^[16] V,^[17] In^[18]], MIL-85 [M₂O(O₂CCH₃)₂(BDC)·(solv)_x, M = Fe^[19]], or MIL-88B/MOF-235 [M₃O(OH)(BDC)₃·(solv)_x, M = Cr, Fe^[20,21]] are examples of flexible MOFs (MIL stands for Materials from Institut Lavoisier). Among the aforementioned cations,

iron(III) is of particular interest due to its low toxicity, redox activity, and low cost. Fe-based MOFs were shown to be suitable for pharmaceutical and biomedical applications (drug release, imaging)^[22] and as a positive electrode material for lithium ion batteries.^[23,24] When considering the H₂BDC/Fe³⁺ pair, only the porous MIL-53, MIL-88B, and MIL-101-NH₂ with H₂BDC-NH₂^[25,26] phases have been reported to date. In this paper, we report the synthesis, ⁵⁷Fe Mössbauer spectrometry, structural and thermal characterization of the MIL-68(Fe) solid, as well as its behavior as a positive electrode for a lithium ion battery.

Results and Discussion

MIL-68(Fe) was synthesized in the presence of hydrofluoric (HF) and hydrochloric acid (HCl) under subsolvothermal conditions (100 °C) in *N,N'*-dimethylformamide (dmf) and yielded crystals suitable for single-crystal X-ray diffraction. MIL-68(Fe), formulated M(OH)(BDC)·(dmf)_x ($x \approx 1.1$, see below), crystallizes in the orthorhombic *Cmcm* (n°63) space group and is isostructural with the V,^[7] Ga, and In^[9] analogs (see Table S1 for details). The bond valence calculations are in agreement with the presence of Fe^{III} (see Table S2). The structure consists of chains of corner-sharing Fe(OH)₂(O_{car})₄ octahedra connected through a BDC linker, defining two types of one-dimensional pores, either triangular or hexagonal (Figure 1). The structure thus presents a pseudohexagonal symmetry, which is broken by the μ_2 -hydroxy groups connecting the metallic cations. The pores are filled with solvent molecules, which cannot be located because of both their intrinsic disorder and the poor quality of the diffraction data. IR spectroscopy indicates that the pores contain both dmf molecules [$\nu(\text{C}=\text{O}) \approx 1660 \text{ cm}^{-1}$] and minor amounts of free terephthalic acid [$\nu(\text{C}=\text{O}) \approx 1700 \text{ cm}^{-1}$] (Figure S2).

[a] Institut Lavoisier, UMR CNRS 8180, Université de Versailles Saint Quentin en Yvelines, 45 Avenue des Etats-Unis, 78035 Versailles, France
Fax: +33-1-39254452
E-mail: devic@chimie.uvsq.fr
serre@chimie.uvsq.fr

[b] LPEC, UMR CNRS 6087, Université du Maine, Avenue Olivier Messiaen, 72085 Le Mans, France

[c] LRCS UMR CNRS 6007, Université de Picardie Jules Verne, 33 Rue Saint-Leu, 80039 Amiens, France

[d] Institut Charles Gerhardt Montpellier, UMR 5253 CNRS, Université Montpellier 2, Place Eugène Bataillon, 34095 Montpellier, France

Supporting information for this article is available on the WWW under <http://dx.doi.org/10.1002/ejic.201000486>.

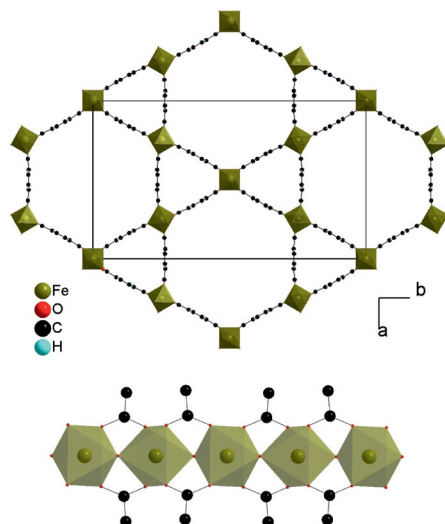


Figure 1. The crystal structure of MIL-68(Fe). Top: view along the channel axis; bottom: chain of corner-sharing FeO_6 octahedra.

In its solvent-free form, MIL-68(Fe) is a polymorph of MIL-53(Fe) [both are formulated $\text{Fe}(\text{OH})(\text{BDC})$]. A few trends can be observed even though the reason that one forms in preference to the other is not fully understood. The experimental conditions are similar to those used for the preparation of MIL-53(Fe). MIL-53(Fe), however, required a higher temperature (150 °C) and could be produced either with^[24] or without^[27] HF. MIL-88B(Fe) and MIL-101(Fe), on the other hand, were produced more quickly at a lower temperature (100 °C) and in the absence of HF. MIL-88B(Fe) eventually required the presence of a base. In summary, the molecular trimeric (MIL-88 and MIL-101) SBUs formed at lower temperatures, higher pH and required shorter reaction times than the one-dimensional (MIL-53 and MIL-68) SBUs that formed in more acidic media and/or at higher temperatures. These results are consistent with experiments performed on the Cr/ H_2BDC ^[28,29] and Fe/ H_2BDC systems,^[30] which showed that the trimer-based solids (MIL-101 and MOF-235) are formed prior to the chain-based ones (MIL-53) and in less acidic media. This is also in agreement with our previous findings for the Fe/ $\text{H}_2\text{BDC-NH}_2$ system.^[25] It can also be noted that syntheses reported for MIL-68, regardless of the cation (V,^[7] Al,^[8] In,^[9,31] Ga,^[9] Fe), used dmf as the solvent, whereas MIL-53 could be prepared in various media (water, dmf, or alcohol).^[24,25,27,32] For the MIL-68(In) solid, it was possible to locate the dmf molecules in the triangular pores.^[9]

A template effect could be proposed to favor the formation of these triangular-shaped pores, and ultimately MIL-68. The μ_2 -OH bridge for MIL-53 points towards the cage from an obtuse linker–metal–linker angle (regardless of the cation or pore content and pore opening considered), whereas this is an acute angle for MIL-68 (see Figure S3).

This geometry, which is less favorable from a steric point of view, could arise from the formation of various $\text{dmf}\cdots\text{framework}$ interactions that compensate for this re-

pulsion. The formation of $\text{dmf}\cdots\text{framework C=O}\cdots\text{H-O}$ hydrogen bonds, causing the dmf molecules to point towards the bridging hydroxy groups, has been previously established.^[9] Extra interactions, possibly involving the lone pair on the nitrogen atoms, could lead to a tight entrapment of the dmf molecules between the two BDC moieties, leading to the formation of triangular-shaped pores. Alternatively, better packing of the dmf molecules in the triangular- (MIL-68) than the hexagonal-shaped (MIL-53) pores might explain the geometry. Further evidence for the correct explanation might be deduced from the structure of MIL-53(Fe) loaded with dmf, for which only the unit cell has been reported to date.^[33]

The purity of MIL-68(Fe) was checked by X-ray powder diffraction. The experimental pattern agrees well with the theoretical one, although traces of MIL-53(Fe) were sometimes detected (see Figure S1 and Figure 3b).

The Mössbauer spectra of the as-synthesized powder were first recorded at 300 K at room pressure and then under vacuum (Figure 2). In addition to some preferential orientation that originated from the layered powder, the quadrupolar hyperfine structures are dependent on the sample atmosphere: quadrupolar doublets corresponding to three types of Fe sites are observed at room pressure, while only two quadrupolar doublets are unambiguously estimated in a 2:1 ratio when the powder is under vacuum. These signals could indicate a distribution of the local Fe^{III} environment in the as-synthesized solid related to the presence of the solvent molecules in the pores, as already observed for the MIL-53(Fe) solids.^[32,34] Placing the powder under vacuum provided the structure of the ideal MIL-68(Fe) phase in agreement with the two crystallographic sites of Fe identified in the single-crystal structure. Further Mössbauer experiments on the activated solid under different atmospheres should confirm this hypothesis. The isomer shift values (0.35 and 0.39 mm s^{-1} at 300 K relative to α -Fe) are fairly consistent with the presence of only octahedral high-spin Fe^{III} sites and with the absence of any Fe^{II} . The quadrupolar splitting values (0.64 and 1.17 mm s^{-1}) suggest two types of distorted octahedral units. Taking into account the charge balance, this confirms that no partial or complete replacement of the μ_2 -hydroxy group by a μ_2 -dmf bridge occurs, as reported for MIL-53(Fe^{II}).^[15]

The thermal behavior of MIL-68(Fe) was studied concomitantly by X-ray thermogravimetry (in air) and thermogravimetric analysis (under O_2), as shown in Figure 3. Both techniques indicated that the solid is stable up to 300–320 °C and collapses at higher temperatures to afford Fe_2O_3 . As observed from the previous studies on the V, In, and Ga analogs, the structure remains rigid upon removal of the guest molecules. The mass losses are in agreement with the proposed formula $\text{Fe}(\text{OH})(\text{BDC})\cdot(\text{dmf})_x$ with $x \approx 1.1$ [a value similar to the one obtained for MIL-68(Ga, In)]. The first mass loss at low temperature is associated with the departure of the solvent (experimental and theoretical mass losses are 26 and 25%, respectively) and the second one with the calcination of the framework (experimental and theoretical mass losses are 75 and 75%, respec-

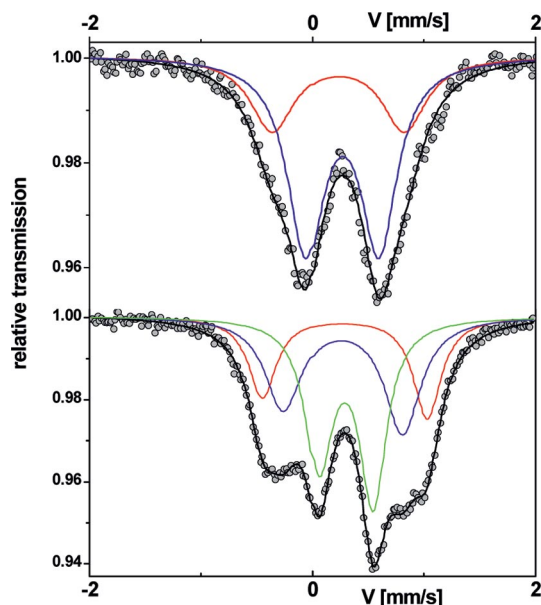


Figure 2. The Mössbauer spectra of MIL-68(Fe) recorded at 300 K at room pressure (bottom) and under vacuum (top).

tively). During the first loss of mass, most of the dmf is released below 110 °C, but a total removal of the solvent is achieved only at 250 °C. The dmf/ μ_2 -OH ratio (about 1:1) is in agreement with the presence of $\text{C}=\text{O}(\text{dmf})\cdots\text{H}-\text{O}(\text{MIL-68})$ interactions. As one third of the hydroxy groups point towards the triangular tunnels and two thirds point towards the hexagonal ones, it is expected that most of the dmf molecules lie in the large tunnels and are released before 110 °C, while the rest are located in the small tunnels and leave at higher temperatures due to steric constraints. This hypothesis is in accordance with the results obtained from the nitrogen sorption experiments (see below).

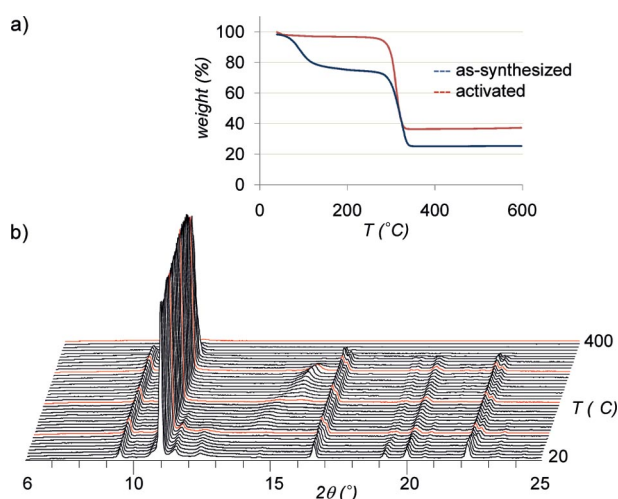


Figure 3. Thermal analysis of MIL-68(Fe) ($\lambda_{\text{Co}} \approx 1.7906 \text{ \AA}$): (a) thermogravimetric analysis of the as-synthesized and activated forms; (b) X-ray thermodiffraction of the as-synthesized form (red patterns: 100, 200, 300, and 400 °C). The peaks at 12–13 (low temperature) and 14–16 (high temperature) are associated with the flexible MIL-53(Fe) solid.

The MIL-68(V) structure was predicted to present a very high surface area (above $3000 \text{ m}^2 \text{ g}^{-1}$).^[35] However, the experimental BET surface areas derived from nitrogen sorption experiments performed at 77 K were estimated to be about 600, 750, and $1120 \text{ m}^2 \text{ g}^{-1}$ for the V,^[7] In,^[9] and Ga^[9] analogs, respectively. It was thought that this discrepancy was related to a partial activation procedure; however, for MIL-68(Ga), solid-state NMR spectroscopy confirmed the almost complete departure of the solvent molecules from the pores. As an overestimation of the theoretical surface cannot be ruled out, the theoretical surface of MIL-68(Fe) was calculated by using the same procedure as the one previously established for MIL-68(V).^[35] This calculation indicated that the theoretical surface areas are 1450 and $1200 \text{ m}^2 \text{ g}^{-1}$ including and excluding the triangular pores, respectively. In the case of MIL-68(Fe) a low BET surface area ($355 \text{ m}^2 \text{ g}^{-1}$) was obtained after the solid was degassed at 250 °C. The temperature of activation was optimized by using the results of nitrogen sorption experiments and powder X-ray diffraction data (see Figure 4 and Figure S4, respectively).

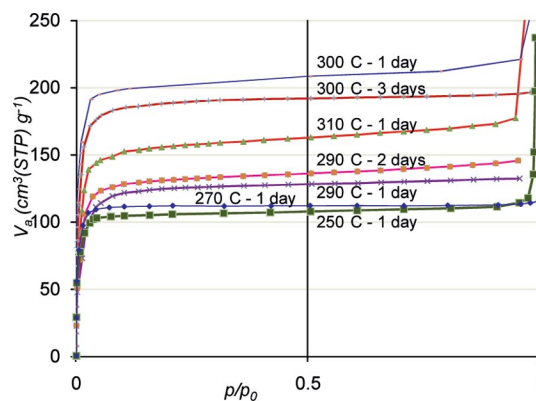


Figure 4. Nitrogen sorption isotherms of MIL-68(Fe) measured at various temperatures and activation times ($P_0 = 1 \text{ atm.}$).

A slight increase in the surface area was obtained upon heating to 290 °C, but doubling the activation time did not further improve it. The best-fit value, corresponding to a BET surface area of $665(10) \text{ m}^2 \text{ g}^{-1}$, was achieved upon activation at 300 °C under secondary vacuum for one day. A higher temperature or a longer activation time leads to a decrease in the accessible pore volume in agreement with the degradation of the structure [a phenomenon already observed, for example, for $\text{V}^{\text{IV}}\text{O}(\text{BDC})$ or MIL-47]^[36]. This result is significantly lower than the optimal value experimentally observed for Ga as well as the simulated values. The presence of a dense inorganic impurity cannot be totally ruled out, but was not observed in Mössbauer spectrometry or X-ray diffraction experiments. Short distances between the BDC linkers along the pore axis prevent the formation of an interpenetrated form of MIL-68(Fe) that would lead to a restricted pore volume. Two other reasons could be suggested: (1) Partial activation of the solid. IR spectroscopy showed that trace amounts of dmf remain in the activated solid (see Supporting Information), although

thermogravimetric analysis of the sample indicated that this corresponds to a very low amount (Figure 3a). (2) The small size of the triangular channels, which may have limited the diffusion of the molecular species with the following consequences: (i) dmf could not be totally evacuated (see above); (ii) nitrogen could not easily enter into the triangular pores. In particular, the diffusion of the N_2 species may require the rotation of the phenyl rings, which could be considerably slowed down at low temperature (77 K). This seems to be confirmed by the fact that the surface area measured for MIL-68(Ga), which was shown to possess empty channels by NMR spectroscopy,^[9] is close to the simulated one when the triangular channels are not taken into account ($1200 \text{ m}^2 \text{ g}^{-1}$).

In the case of MIL-68(Fe), both reasons could explain the low surface area. Other synthesis conditions or different activation methods (such as the use of supercritical CO_2 ^[37] or ultrasonic treatment^[38]) may lead to an improvement in the total pore volume.

Finally, the redox activity of the MIL-68(Fe) was tested. The propensity of Fe^{III} to be reversibly reduced to Fe^{II} was previously exploited for the flexible MIL-53(Fe) solid. It was shown that MIL-53(Fe) acted as a good positive electrode for a lithium ion battery, but with a limited capacity (ca. 70 mA h g^{-1}).^[24] Only 0.6 e^- per Fe could be reversibly accepted by the framework. This limitation could be related to either an electronic effect (such as a gap opening when half of the Fe is reduced) or a steric effect (limitation by the steric hindrance of the Li^+ ion with its solvation shell).^[24,39] MIL-68(Fe) appears to be a potential candidate for lithium insertion as it possesses the same inorganic SBU as MIL-53(Fe) but has larger and more rigid pores. It was thus investigated as a positive electrode material in a classical two-electrode SwagelokTM-type cell using LiPF_6 -containing ethylene carbonate/dimethyl carbonate (EC/DMC) electrolyte in which metallic lithium foil was used as the negative and reference electrode. In Figure 5, MIL68(Fe) has been evaluated as the positive electrode in lithium ion batteries. At a regime of $C/10$ in galvanostatic mode, around 0.35 Li per Fe atom can be inserted into the MIL-68(Fe)

structure, which is slightly lower than the corresponding value for MIL-53(Fe). According to the molecular weight of MIL-68(Fe), this corresponds to 30 mA h g^{-1} . Note that this capacity can be increased to 40 mA h g^{-1} if the current density is decreased to $C/50$ (inset Figure 5). It is difficult to explain these differences between MIL-53(Fe) and MIL68(Fe). The main difference between these two structures is based on the presence of triangular-shaped pores. It is probable that no electrolyte can enter these pores unlike the hexagonal pores of MIL-68(Fe) or the uniform porous structure of MIL-53(Fe). This difference could limit the diffusion of lithium into the structure and may be the cause of the lower capacity observed with MIL-68(Fe).

Conclusions

A porous Fe^{III} -based MOF belonging to the MIL-68 series was synthesized and characterized. This solid, which can easily be produced on the gram scale, is found to be stable up to 300°C under aerobic conditions and has a maximum BET surface area of $665(10) \text{ m}^2 \text{ g}^{-1}$, which is lower than expected. Mössbauer analysis of the metallic sites was found to be in good agreement with the structural data. MIL-68(Fe) presents a lower lithium battery capacity compared with the one previously reported for MIL-53(Fe).^[24] This indicates that the pore size and the flexible or rigid nature of the framework can play a significant role when looking at such properties.

Experimental Section

Synthesis: MIL-68(Fe) or $\text{Fe}(\text{OH})(\text{BDC})\cdot(\text{solv})_x$ was synthesized from a mixture of iron (III) perchlorate hexahydrate (30 mmol), aqueous hydrofluoric acid (5 M , 15 mmol), and aqueous hydrochloric acid (1 M , 3 mmol) in N,N' -dimethylformamide (300 mL) by using a 500 mL Teflon Liner and a metallic autoclave. After being stirred for a few minutes, the mixture was heated at 100°C for 120 h . The yellow-brown product was recovered by filtration and washed with water and acetone (yield 67%). In order to get rid of minor amounts of entrapped free terephthalic acid, the solid was dispersed in N,N' -dimethylformamide (300 mL) and heated at 100°C for 18 h . The solid was recovered by filtration as crystalline needles having approximate dimensions of $200 \times 20 \times 20 \mu\text{m}$. Final activation was performed by heating (see the main text) under secondary vacuum.

Characterization

The IR spectra were recorded with a Fourier Transform Nicolet Magna-IR 550 spectrometer in KBr pellets in the $350\text{--}4000 \text{ cm}^{-1}$ region. Thermogravimetric analyses were performed with a TA-instrument 2050 under an O_2 atmosphere between room temperature and 600°C in an aluminum crucible (heating speed 1°C min^{-1}) using $5\text{--}10 \text{ mg}$ of solid. The X-ray powder diffraction pattern was collected at 293 K with a Siemens D5000 Diffractometer working in the $(\theta\text{--}2\theta)$ mode by using $\text{Cu-K}\alpha$ radiation. X-ray thermodiffraction was performed with a Siemens D-5000 diffractometer ($\theta\text{--}2\theta$ mode, $\text{Co-K}\alpha$ radiation) equipped with an M Braun linear position-sensitive detector (PSD), under static air in the Anton Parr HTK16 high-temperature device. The thermal behavior was studied in the $20\text{--}400^\circ\text{C}$ range with 10°C intervals. A single crystal of

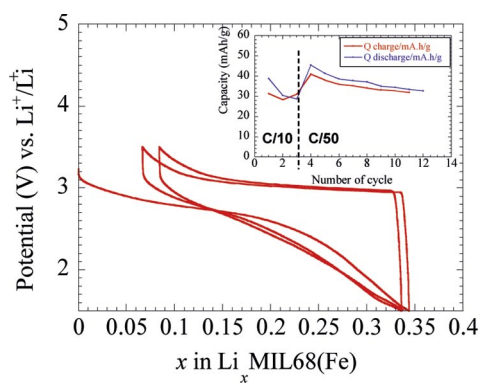


Figure 5. Redox potential (Li/Li^+) vs. Li composition of an MIL-68(Fe) electrode cycled in a galvanostatic mode at $C/10$ between 1.5 and 3.5 V . The inset displays the capacity retention of the electrode at regimes of $C/10$ and $C/50$.

MIL-68(Fe), mounted with Paratone oil on a nylon CryoLoop™, was measured at 293 K with a Bruker X8-APEX 2 diffractometer equipped with a Mo anode, a graphite monochromator, and a CCD camera detector. The data reduction and absorption correction were performed with the SAINT and SADABS software, respectively. The structure was solved and refined by full-matrix least-squares techniques, based on F^2 , using the SHELX software package.^[40] All non-hydrogen atoms were refined anisotropically, whereas hydrogen atoms were introduced geometrically and not refined. The pore content was not refined and was discarded using the SQUEEZE routine. Crystallographic data are summarized in Table S1. CCDC-778931 contains the supplementary crystallographic data for this paper. These data can be obtained free of charge from The Cambridge Crystallographic Data Centre via www.ccdc.cam.ac.uk/data_request/cif.

Sorption experiments were performed at 77 K with a Belsorb Max apparatus using nitrogen as the probing gas. MIL-68(Fe) samples (25–40 mg) were degassed at various temperatures (see main text) under secondary vacuum prior to the measurement. The measurement was performed according to the equilibrium criterion, which consists of 0.5% differential pressure within 400 s. The pressure range for BET surface calculations was $0 \leq p/p_0 \leq 0.13$. The ^{57}Fe Mössbauer spectra were recorded at 300 K using a constant acceleration spectrometer and a ^{57}Co source diffused into a rhodium matrix. The powdered sample was placed either under helium gas in a cryostat bath or under vacuum in a homemade cryofurnace. Velocity calibrations were performed by using an α -Fe foil at 300 K. The hyperfine parameters were refined by using a least-squares fitting with the unpublished MOSFIT program. In addition to the number and the relative proportions of Fe species, the hyperfine quadrupolar parameters are the isomer shift and the quadrupolar splitting, which provide relevant information on the valency state, the spin state, the coordination, and the chemical nature of ligands of ^{57}Fe nuclei. Galvanostatic charge–discharge experiments were carried out by using two-electrode Swagelok™-type cells assembled inside an argon-filled glove box and a VMP potentiostat. The working electrodes were prepared by mixing 70 wt.-% of the MIL-68(Fe) solid and 30 wt.-% of Ketjen black carbon (as conductor) in an agate mortar. The glass fiber (GF/D) from Whatman® was used as a separator, and pure lithium foil (Aldrich) was used as counterelectrode. The electrolyte consisted of a solution of 1 M LiPF_6 in ethylene carbonate (EC)/dimethyl carbonate (DMC) (1:1 by volume). The accessible surface area of the MIL-68(Fe) solid was estimated by using a Monte Carlo algorithm and following the same strategy as those previously reported by Dören et al.^[35] starting from the single-crystal MIL-68 structure. This surface area was calculated from the center of a nitrogen probe molecule rolling across the surface. The following diameters for each atom constituting the MIL-68 framework were taken from the UFF force field:^[41] C (3.43 Å), O (3.12 Å), H (2.57 Å), Fe (2.59 Å), while the diameter of the nitrogen probe molecule was considered to be 3.60 Å.

Supporting Information (see footnote on the first page of this article): IR spectra, powder XRD patterns, and crystallographic data.

Acknowledgments

The authors acknowledge the Ministère de l'Éducation Nationale, de la Recherche et de la Technologie [MENRT], the Centre National de la Recherche Scientifique [CNRS], and the Agence Nationale de la Recherche [ANR] (project “CONDMOFs”) for financial support.

- [1] G. Férey, *Chem. Soc. Rev.* **2008**, 37, 191.
- [2] See the special issue: *Chem. Soc. Rev.* **2009**, 38, 1201–1507 and references cited therein.
- [3] X. Lin, J. Jia, X. Zhao, K. M. Thomas, A. J. Blake, G. S. Walker, N. R. Champness, P. Hubberstey, M. Schröder, *Angew. Chem. Int. Ed.* **2006**, 45, 7358.
- [4] S. Surblé, C. Serre, C. Mellot-Draznieks, F. Millange, G. Férey, *Chem. Commun.* **2006**, 284.
- [5] O. M. Yaghi, M. O'Keeffe, N. W. Ockwig, H. K. Chae, M. Eddaoudi, J. Kim, *Nature* **2003**, 423, 705.
- [6] G. Férey, C. Mellot-Draznieks, C. Serre, F. Millange, J. Dutour, S. Surblé, I. Margiolaki, *Science* **2005**, 309, 2040.
- [7] K. Barthelet, J. Marrot, G. Férey, D. Riou, *Chem. Commun.* **2004**, 520.
- [8] BASF, Vol. WO200812 9051, **2008**.
- [9] C. Volkringer, M. Meddouri, T. Loiseau, N. Guillou, J. Marrot, G. Férey, M. Haeuvas, F. Taulelle, N. Audebrand, M. Latroche, *Inorg. Chem.* **2008**, 47, 11892.
- [10] K. Barthelet, K. Adil, F. Millange, C. Serre, D. Riou, G. Férey, *J. Mater. Chem.* **2003**, 2208.
- [11] S. R. Miller, P. A. Wright, C. Serre, T. Loiseau, J. Marrot, G. Férey, *Chem. Commun.* **2005**, 3850–3852.
- [12] J. Sun, L. Weng, Y. Zhou, J. Chen, Z. Chen, Z. Liu, D. Zhao, *Angew. Chem. Int. Ed.* **2002**, 41, 4471.
- [13] T. Loiseau, C. Serre, C. Huguenard, G. Fink, F. Taulelle, M. Henry, T. Bataille, G. Férey, *Chem. Eur. J.* **2004**, 10, 1373.
- [14] C. Serre, F. Millange, C. Thouvenot, M. Nogues, G. Marsolier, D. Louër, G. Férey, *J. Am. Chem. Soc.* **2002**, 124, 13519.
- [15] T. R. Whitfield, X. Wang, L. Liu, A. J. Jacobson, *Solid State Sci.* **2005**, 7, 1096.
- [16] C. Volkringer, T. Loiseau, N. Guillou, G. Férey, E. Elkaïm, A. Vimont, *Dalton Trans.* **2009**, 2241.
- [17] K. Barthelet, J. Marrot, D. Riou, G. Férey, *Angew. Chem. Int. Ed.* **2002**, 41, 281.
- [18] E. V. Anokhina, M. Vougo-Zanda, X. Wang, A. J. Jacobson, *J. Am. Chem. Soc.* **2005**, 127, 15000.
- [19] C. Serre, F. Millange, S. Surblé, J.-M. Grenèche, G. Férey, *Chem. Mater.* **2004**, 16, 2706.
- [20] C. Serre, F. Millange, S. Surblé, G. Férey, *Angew. Chem. Int. Ed.* **2004**, 43, 6285.
- [21] A. C. Sudik, A. P. Cote, O. M. Yaghi, *Inorg. Chem.* **2005**, 44, 2998.
- [22] P. Horcajada, T. Chalati, C. Serre, B. Gillet, C. Sebrie, T. Baati, J. F. Eubank, D. Heurtaux, P. Clayette, C. Kreuz, J.-S. Chang, Y. K. Hwang, V. Marsaud, P. N. Bories, L. Cynober, S. Gil, G. Férey, P. Couvreur, R. Gref, *Nat. Mater.* **2010**, 9, 172.
- [23] G. de Combarieu, M. Morcrette, F. Millange, N. Guillou, J. Cabana, C. P. Grey, I. Margiolaki, G. Férey, J. M. Tarascon, *Chem. Mater.* **2009**, 21, 1602.
- [24] G. Férey, F. Millange, M. Morcrette, C. Serre, M.-L. Doublet, J. M. Grenèche, J.-M. Tarascon, *Angew. Chem. Int. Ed.* **2007**, 46, 3259.
- [25] S. Bauer, C. Serre, T. Devic, P. Horcajada, J. Marrot, G. Férey, N. Stock, *Inorg. Chem.* **2008**, 47, 7568.
- [26] K. M. L. Taylor-Pashow, J. D. Rocca, Z. Xie, S. Tran, W. Lin, *J. Am. Chem. Soc.* **2009**, 131, 14261.
- [27] P. Horcajada, C. Serre, G. Maurin, N. A. Ramsahye, F. Balas, M. Vallet-Regi, M. Sebban, F. Taulelle, G. Férey, *J. Am. Chem. Soc.* **2008**, 130, 6774.
- [28] N. A. Khan, S. H. Jhung, *Cryst. Growth Des.* **2010**, 10, 1860.
- [29] N. A. Khan, J. W. Jun, S. H. Jhung, *Eur. J. Inorg. Chem.* **2010**, 7, 1043.
- [30] F. Millange, M. I. Medina, N. Guillou, G. Férey, K. M. Golden, R. I. Walton, *Angew. Chem. Int. Ed.* **2010**, 49, 763.
- [31] M. Savonnet, D. Bazer-Bachi, N. Bats, J. Perez-Pellitero, E. Jeannean, V. Lecocq, C. Pinel, D. Farrusseng, *J. Am. Chem. Soc.* **2010**, 132, 4518.
- [32] T. Devic, P. Horcajada, C. Serre, F. Salles, G. Maurin, B. Moulin, D. Heurtaux, G. Clet, A. Vimont, J. M. Grenèche, B. L.

- Ouay, F. Moreau, E. Magnier, Y. Filinchuk, J. Marrot, J.-C. Lavalley, M. Daturi, G. Férey, *J. Am. Chem. Soc.* **2010**, *132*, 1127.
- [33] F. Millange, C. Serre, N. Guillou, G. Férey, R. I. Walton, *Angew. Chem. Int. Ed.* **2008**, *47*, 4100.
- [34] F. Millange, N. Guillou, R. I. Walton, J. M. Grenèche, I. Margiolaki, G. Férey, *Chem. Commun.* **2008**, 4732.
- [35] T. Düren, F. Millange, G. Férey, K. S. Walton, R. Q. Snurr, *J. Phys. Chem. C* **2007**, *111*, 15350.
- [36] L. Alaerts, M. Maes, P. A. Jacobs, J. F. M. Denayer, D. E. De Vos, *Phys. Chem. Chem. Phys.* **2008**, *10*, 2979.
- [37] A. P. Nelson, O. K. Farha, K. L. Mulfort, J. T. Hupp, *J. Am. Chem. Soc.* **2008**, *131*, 458.
- [38] E. Haque, N. A. Khan, J. E. Lee, S. H. Jhung, *Chem. Eur. J.* **2009**, *15*, 11730.
- [39] C. Combelles, M.-L. Doublet, *Ionics* **2008**, *14*, 279.
- [40] G. M. Sheldrick, *Acta Crystallogr., Sect. A* **2008**, *64*, 112.
- [41] K. Rappé, C. J. Casewit, K. S. Colwell, W. A. Goddard III, W. M. Skiff, *J. Am. Chem. Soc.* **1992**, *114*, 10024.

Received: April 30, 2010
Published Online: July 7, 2010

Flexible and Redox-Active Coordination Polymer: Control of the Network Structure by Pendant Arms of a Macrocyclic Complex

Hoi Ri Moon^[a] and Myunghyun Paik Suh^{*[a]}

Keywords: Coordination polymers / Flexible networks / Macrocycles / Palladium / Nickel

The coordination polymer $\{[\text{Ni}(\text{C}_{20}\text{H}_{32}\text{N}_8)]_2[\text{TCM}]\} \cdot 5\text{DMF} \cdot 8\text{H}_2\text{O}$ (**1**) has been assembled from a Ni^{II} macrocyclic complex that contains two pyridyl pendant arms, $[\text{Ni}(\text{C}_{20}\text{H}_{32}\text{N}_8)](\text{ClO}_4)_2$, and sodium tetrakis[4-(carboxyphenyl)oxamethyl]methane (Na_4TCM) in DMF/water. The X-ray structure of **1** reveals that the pyridyl pendant arms in the macrocyclic complex play a crucial role in determining the network structure through the π - π interactions. Compound **1** forms doubly

catenated rhombic grids that generate 1D channels. It exhibits its flexible behavior upon desorption/resorption and exchange of organic guest molecules as well as temperature change. Solid **1** is redox active due to the incorporated Ni^{II} macrocyclic species, and reacts with $\text{Pd}(\text{NO}_3)_2$ dissolved in acetonitrile at room temperature to produce small Pd nanoparticles $[(2.9 \pm 0.4) \text{ nm}]$ in the channels in the absence of extra reducing or capping agents.

Introduction

Porous coordination polymers have attracted great attention because they can be applied in selective molecular recognition and separation,^[1,2] gas storage,^[3,4] ion exchange,^[5] sensors,^[6] and catalysis.^[7] In particular, flexible coordination polymers that transform their structures in response to external stimuli are interesting^[1,3b,8,9] due to their potential to be applied in the development of sensors and devices. Redox-active coordination polymers can be utilized as the matrices for the production of small and monodispersed metal nanoparticles.^[3a,10,11] Metal nanoparticles less than 10 nm in diameter exhibit a quantum-size effect,^[12] and can be utilized in optics, electronics, and catalysis.^[13] Porous solids including small palladium nanoparticles (Pd NPs) are promising candidates for heterogeneous catalysts^[14] as well as H_2 gas storage materials.^[3a,15]

For the preparation of Pd NPs@porous solid nanocomposites, various methods such as impregnation, sublimation, and infiltration methods have been utilized, but the methods are not very convenient as they require high reaction temperature and several synthetic steps. There have been a few reports of the fabrication of Pd NPs in porous coordination polymers. For example, Pd NPs in MOF-5 were prepared by introducing a precursor complex followed by reduction with H_2 gas.^[15,16] In particular, it has been reported that small Pd NPs are produced in the pores of SNU-3^[3a] as well as in the fourfold interpenetrating diamondoid network^[11] by the reaction of organic and inor-

ganic redox-active species, respectively, which are incorporated in the coordination polymers, with the Pd^{II} ions at room temperature in the absence of extra reducing or capping agents.

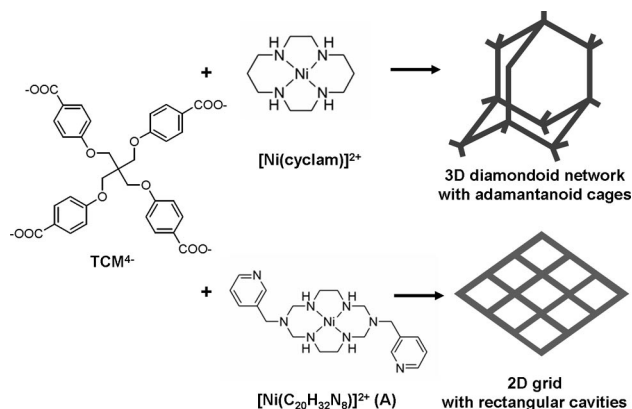
Square-planar macrocyclic complexes are useful metal building blocks for the construction of porous coordination polymers. They act as linear linkers for the organic ligands and allow the design of the network structures to be simple and easy.^[17] A straightforward design strategy for construction of a porous 3D structure is to interconnect a tetrahedral building block and a linear linker. Previously, we reported an eightfold interpenetrating diamondoid network, $\{[\text{Ni}(\text{cyclam})]_2[\text{TCM}]\} \cdot 2\text{DMF} \cdot 10\text{H}_2\text{O}$, which was prepared from tetrakis[4-(carboxyphenyl)oxamethyl]methane (TCM^{4-})^[18] as a tetrahedral organic building block and $[\text{Ni}^{\text{II}}(\text{cyclam})]^{2+}$ complex as a linear linker, in which cyclam is 1,4,8,11-tetraazacyclotetradecane.^[19] The network generated 1D channels of effective window size $(6.7 \times 4.7) \text{ \AA}$ despite the high degree of interpenetration.

In this work, to see how the substituent of the macrocycle affects the structure of the coordination polymer, we have utilized a Ni^{II} hexaazamacrocyclic complex that contains pyridyl pendant arms, $[\text{Ni}^{\text{II}}(\text{C}_{20}\text{H}_{32}\text{N}_8)](\text{ClO}_4)_2$ (**A**), as a metal building block in the self-assembly with TCM^{4-} . The results indicate that the pendant group of the macrocyclic complex greatly influences the network topology even if it is not involved in the coordination bonds that form the network. The resulting coordination polymer, $\{[\text{Ni}(\text{C}_{20}\text{H}_{32}\text{N}_8)]_2[\text{TCM}]\} \cdot 5\text{DMF} \cdot 8\text{H}_2\text{O}$ (**1**), is a doubly catenated 2D grid that generates 1D channels, completely different from the eightfold interpenetrating diamondoid network that we previously reported (Scheme 1).^[19] Network **1** exhibits flexible behavior upon desorption/resorption of guest molecules, guest exchange, and temperature change,

[a] Department of Chemistry, Seoul National University, Seoul 151-747, Republic of Korea
Fax: +82-2-886-8516
E-mail: mpsuh@snu.ac.kr

Supporting information for this article is available on the WWW under <http://dx.doi.org/10.1002/ejic.201000555>.

and alters its structure and cell parameters. Furthermore, coordination polymer **1** incorporating **A** is redox-active, and produces small $[(2.9 \pm 0.4) \text{ nm in diameter}]$ and mono-dispersed Pd NPs at room temperature, simply on immersion in a solution of $\text{Pd}(\text{NO}_3)_2$ in acetonitrile (MeCN) in the absence of extra reducing or capping agents.

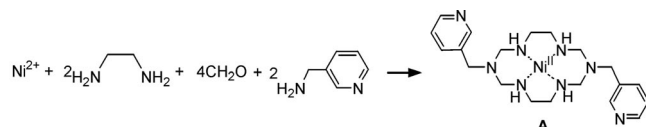


Scheme 1. Self-assembly of TCM^{4-} with two different Ni^{II} macrocyclic complexes; top: previous work;^[19] bottom: present work.

Results and Discussion

Preparation and X-ray Crystal Structure of **1**

The Ni^{II} macrocyclic complex that contains pyridyl pendant arms (**A**) was prepared from the Ni^{II} -directed template Schiff base reaction of ethylenediamine, formaldehyde, and 3-(aminomethyl)pyridine in methanol (MeOH) by modifying the one-pot condensation reactions that we previously developed.^[20] The self-assembly of **A** and Na_4TCM in N,N' -dimethylformamide (DMF)/ H_2O (12:5 v/v) resulted in $\{[\text{Ni}(\text{C}_{20}\text{H}_{32}\text{N}_8)]_2[\text{TCM}]\} \cdot 5\text{DMF} \cdot 8\text{H}_2\text{O}$ (**1**), which is a doubly catenated 2D (4,4)-net that generates 1D channels of rhombic aperture. The pale violet crystal of **1** is insoluble in water and common organic solvents.



In the X-ray structure of **1** (Figure 1), each Ni^{II} macrocyclic complex is coordinated with two TCM^{4-} ligands at the axial positions to display a distorted octahedral coordination geometry, and each TCM^{4-} ligand binds four Ni^{II} ions in a tetrakis-monodentate mode. The average $\text{Ni-N}(\text{macrocycle})$ and $\text{Ni-O}(\text{carboxylate})$ bond lengths are 2.054(2) and 2.092(2) Å, respectively. The uncoordinated carbonyl oxygen atoms of TCM^{4-} are involved in the hydrogen bonding with the secondary amines of the macrocycle to form six-membered rings $[\text{O}2 \cdots \text{N}4 \text{ } 2.887(4) \text{ Å}, \text{O}2 \cdots \text{H}4\text{A}-\text{N}1 \text{ } 146.8^\circ; \text{O}6 \cdots \text{N}3 \text{ } 2.917(4) \text{ Å}, \text{O}6 \cdots \text{H}3\text{A}-\text{N}3 \text{ } 149.0^\circ]$. The dihedral angles between the macrocyclic coordination plane and phenyl rings of TCM^{4-} that involve C22 and C34 atoms are 97.06 and 93.79°, respectively. The ge-

ometry of the central carbon of TCM^{4-} is tetrahedral; the angles around the central C atom ($\angle \text{C}-\text{C}29-\text{C}$) are 106.1–111.9°. However, four carboxylate arms of TCM^{4-} extend in a planar fashion instead of a tetrahedral manner due to the offset face-to-face $\pi-\pi$ interactions between the pyridine pendants of the macrocycles that form the same cavity: the shortest $\text{C} \cdots \text{C}$ distances, 3.100 and 3.353 Å; centroid–centroid distance, 4.028 and 4.742 Å; and dihedral angle, 163.3 and 155.0° (Figure 1, b). These intercentroid distances are comparable to those (4.741 and 4.847 Å) in the supramolecular compounds constructed by the offset face-to-face $\pi-\pi$ interactions between the pyridyl moieties.^[21] As a result, the self-assembly of **A** and TCM^{4-} gives rise to the 2D (4,4)-net that generates 1D channels of rhombic aperture. Each rhombic compartment is composed of four macrocyclic complexes and four TCM^{4-} ions, with the cen-

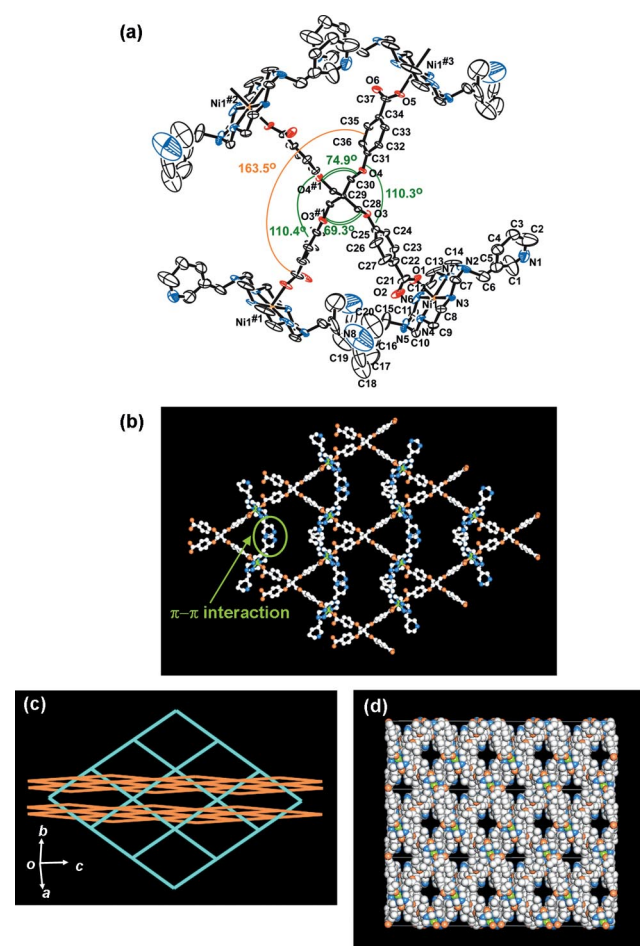


Figure 1. X-ray crystal structure of **1**. (a) An ORTEP drawing of **1**. Thermal ellipsoids are drawn with 30% probability. Symmetry transformations: #1, $-x + 1, -y + 3/2, z$; #2, $x - 1/2, y - 1/2, z + 1/2$; #3, $-x + 3/2, -y + 2, z + 1/2$. (b) A 2D network with rhombic cavities. The $\pi-\pi$ interactions between the pyridine pendants of **A** in the rhombic cavity are shown by a circle. The edge distance of a rhombic cavity is $(21 \times 21) \text{ Å}$. (c) A view from the (110) plane. Line drawing of a doubly catenated network in 2/2 mode: only C29 atoms of the central carbon in the TCM ligand are linked for simplicity. (d) A Corey–Pauling–Koltun (CPK) representation of **1** on the ab plane, showing 1D channels [effective window size $(4.5 \times 2.1) \text{ Å}$]. Color codes: green: Ni, white: C, orange: O, blue: N.

tral carbon atoms (C29) of TCM^{4-} located at the nodes of the compartment. The longest edge distance and the diagonal lengths of the rhombic cavity are (21×21) and (34.5×24.3) Å, respectively. The angle of Ni1-C29-Ni1 ($-x + 3/2, -y + 2, z + 1/2$) is 163.5° , and the angles of Ni-C29-Ni that involve two adjacent nickel ions forming a rhombic cavity are in the range of 69.3 – 110.4° . The 2D network is doubly catenated (Figure 1, c). A series of layers extend parallel to the (110) plane and the others run parallel to the (-110) plane. The dihedral angle between the two different series of planes is 112° . Between two catenated networks, there exist $\text{C-H}\cdots\pi$ interactions^[22] that involve C–H of the macrocycle and the phenyl rings of TCM^{4-} (C–H $\cdots\pi$ distance 3.529–3.585 Å) as well as π – π interactions between the pyridine rings of macrocycle and the phenyl rings of TCM^{4-} (shortest C \cdots C distance 2.999 Å; dihedral angle 143.3°). The doubly catenated network generates 1D channels of effective aperture size (4.5×2.1) Å (Figure 1, d). The channels are filled with eight H_2O and five DMF guest molecules per unit formula of the host, as evidenced by the elemental analysis and thermogravimetric analysis (TGA)/differential scanning calorimetry (DSC) data. The solvent-accessible volume estimated by PLATON^[23] is 35.2%. Contrary to the present network **1**, when the $[\text{Ni}(\text{cyclam})]^{2+}$ complex that possesses no pendant arms was employed as the metal building block, TCM^{4-} was linked with the Ni^{II} species in the tetrahedral manner, which resulted in an eightfold interpenetrating diamondoid network.^[19] The present doubly catenated 2D grid structure clearly indicates that introduction of pyridyl pendants in the macrocycle greatly affects the topology of the coordination polymer. TGA for **1** revealed 24.5% weight loss at 30–215 °C, which corresponds to the loss of eight H_2O and five DMF guest molecules per formula unit (calcd. total 25.4%). The guest-free network started to decompose at 215 °C.

Flexible and Dynamic Nature of **1** on Guest Removal, Guest Exchange, and Temperature Change

By heating the crystal of **1** at 120 °C under around 10^{-3} Torr for 12 h, desolvated solid $\{[\text{Ni}(\text{C}_{20}\text{H}_{32}\text{N}_8)]_2\text{-}[\text{TCM}]\}$ (**1_{des}**) was prepared. Compound **1_{des}** lost transparency and single crystallinity, and its X-ray crystal structure was not able to be determined, although it still possessed crystallinity as evidenced by the powder X-ray diffraction (PXRD) pattern (Figure 2). The PXRD pattern of **1_{des}** was different from that of **1**, thereby indicating that the network structure was altered on guest removal. The structure of **1_{des}** was retained up to 200 °C as evidenced by the temperature-dependent PXRD patterns (see the Supporting Information). When **1_{des}** was exposed to the vapor of DMF and H_2O mixture (9.5:0.5 v/v) at 38 °C for 4.5 d to result in **1_{res}**, the PXRD pattern same as that of **1** was obtained, indicating that the original structure was restored on resolution. Upon immersion of solid **1** in MeCN for 10 min, guest-exchanged solid $\{[\text{Ni}(\text{C}_{20}\text{H}_{32}\text{N}_8)]_2\text{-}[\text{TCM}]\}\cdot 12\text{MeCN}$ (**1_{MeCN}**) resulted, which showed a PXRD

pattern different from that of **1** or **1_{des}**. However, **1_{MeCN}** became the same as **1_{des}** when all guest molecules were removed by heating at 50 °C under vacuum for 12 h, even though the desolvating route was different. In particular, even after **1_{des}** was exposed to air for 24 h, its PXRD pattern remained intact, indicating that **1_{des}** is stable in air. The PXRD patterns of **1**, **1_{des}**, **1_{res}**, and **1_{MeCN}** in Figure 2 reveal the flexible and dynamic nature of the network on guest removal, reintroduction, and guest exchange. Furthermore, the PXRD pattern of **1** measured at room temperature is not exactly in agreement with the pattern simulated from the X-ray single-crystal data collected at 100 K (Figure 2). The peak at $2\theta = 7.38^\circ$ that corresponds to the (110) plane of the single-crystal structure of **1** shifts to 7.16° , indicating the expansion of the interlayer distance by 0.38 Å. This must be attributed to the different temperatures at which the X-ray diffraction data were collected. To scrutinize the structural changes induced by the temperature change, we performed the Rietveld refinement with the measured PXRD pattern of **1** at room temp. The result indicated that the unit-cell volume increased by 5% compared to that at 100 K, thus reflecting the expansion of the interlayer distances, although molecular components did not show significant rearrangement (Figure 3). Although the X-ray diffraction data collected at room temp. for single-crys-

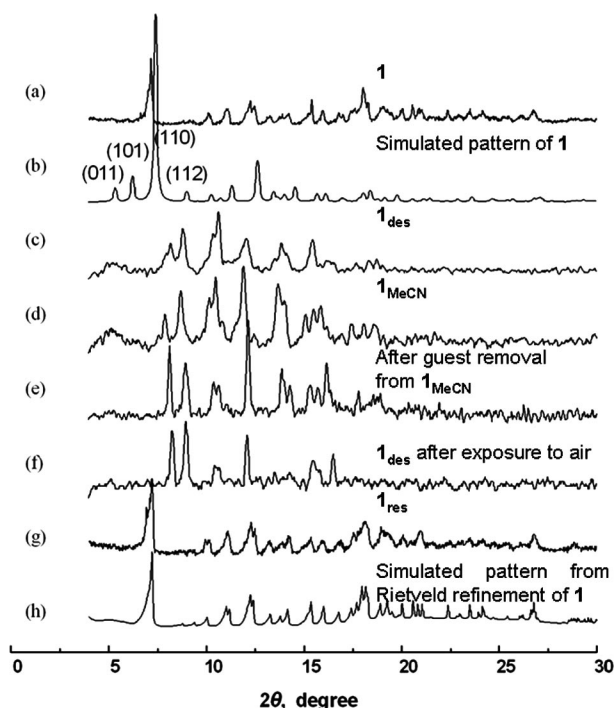


Figure 2. PXRD patterns for (a) as-synthesized **1** measured at room temperature, (b) simulated pattern based on X-ray single-crystal data of **1** collected at 100 K, (c) **1_{des}** prepared by drying **1** at 120 °C under vacuum for 12 h, (d) solid **1_{MeCN}** isolated after immersion of **1** in MeCN for 10 min, (e) **1_{des}** prepared by drying **1_{MeCN}** at 50 °C under vacuum for 12 h, (f) **1_{des}** after exposure to air for 24 h, (g) **1_{res}** isolated after **1_{des}** was exposed to the vapor of DMF and H_2O mixture (9.5:0.5 v/v) at 38 °C for 4.5 d, and (h) simulated pattern of (a) after Rietveld refinement, which affords the 3D structure in Figure 3.

tal **1** were not good enough for the refinement due to large thermal disorder, the cell parameters obtained were in good accordance with those extracted from Rietveld refinement of the PXRD pattern measured at room temp. This again indicates the flexible nature of network **1** being sensitive to temperature change. The cell parameters of **1** at 100 K and at room temp. are compared in Table 1.

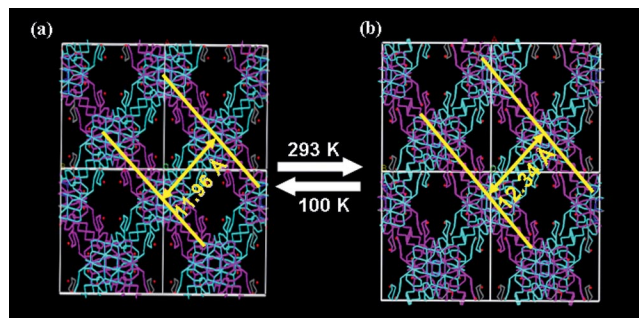


Figure 3. Comparison of the structure of **1** at 100 K versus 293 K. (a) Single-crystal X-ray structure of **1** collected at 100 K. (b) Simulated structure obtained from Rietveld refinement for the PXRD data of **1** measured at room temp. Interlayer distance between the (110) planes increases from 12.0 to 12.3 Å by changing the temperature from 100 to 293 K.

Table 1. Cell parameters for the X-ray structures of single-crystal **1** measured at 100 K and r.t. as well as those from Rietveld refinement of the PXRD measured at room temp.

Cell parameter	X-ray single-crystal structure of 1 100 K	X-ray single-crystal structure of 1 Room temp.	Rietveld refinement ^[a] Room temp.
<i>a</i> [Å]	15.525(3)	16.214(1)	16.085(10)
<i>b</i> [Å]	18.764(4)	18.970(1)	18.933(7)
<i>c</i> [Å]	34.496(7)	34.458(2)	34.638(10)
<i>V</i> [Å ³]	10049(3)	10540(1)	10549(8)

[a] Structure simulated from Rietveld refinement of PXRD of **1**.

Production of Small Palladium Nanoparticles in **1** by Redox Reaction between Solid **1** and Pd^{II} Ions

Solid **1** incorporates redox-active Ni^{II} macrocyclic species, which can be oxidized to Ni^{III} by the appropriate oxidizing agent.^[20a,24] Previously we reported on Ag, Au, and Pd nanoparticles embedded in the coordination polymer networks, which were produced from the reaction between the corresponding metal ions and the redox-active species incorporated in the networks at room temperature in the absence of reducing or capping agents.^[3a,10,11] In the present work, when solid **1** was immersed in the solution of Pd(NO₃)₂ in MeCN (1.0 × 10^{−2} M) at room temperature for 10 min, the color of **1** changed from pale purple to brown by forming Pd nanoparticles (Pd NPs) of diameter (2.9 ± 0.4) nm in **1** (Figure 4, a). The autoredox reaction between the included Pd^{II} ions and the Ni^{II} macrocyclic species incorporated in **1** yielded Pd⁰ and Ni^{III} species, and the Pd⁰ atoms must be aggregated into nanoparticles. The fast Fourier transform (FFT) analysis afforded a face-centered cubic (fcc) Pd NP with *d*(111) spacing of 0.23 nm (JCPDS

card no. 87-0641). The size of the Pd nanoparticles did not change even when solid **1** was immersed in the Pd(NO₃)₂ solution for 16 h.

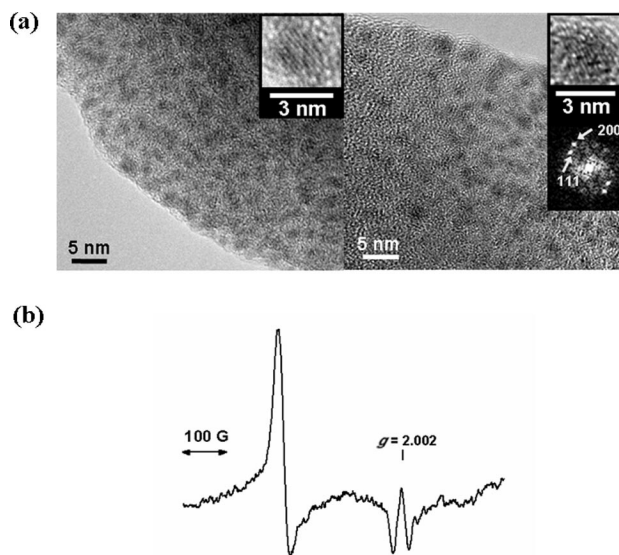


Figure 4. (a) Field-emission transmission electron microscopy (FETEM) images of Pd nanoparticles in **1** (powder sample), which were formed by immersion of **1** in the solution of Pd(NO₃)₂ in MeCN (1.0 × 10^{−2} M) at room temperature for 10 min (left) and for 16 h (right). Inset: fast Fourier transform (FFT) patterns for an approximately 3 nm Pd nanoparticle. (b) Electron paramagnetic resonance (EPR) spectrum measured at room temperature for Pd nanoparticles embedded in **1** (powder sample), which were formed by immersion of **1** in the solution of Pd(NO₃)₂ in MeCN (1.0 × 10^{−2} M) for 10 min. *g*_⊥ = 2.179 and *g*_{||} = 2.016 for Ni^{III}, *g* = 1.995.

The EPR spectrum (Figure 4, b) of the resulting solid shows anisotropic signals at *g*_⊥ = 2.179 and *g*_{||} = 2.016, which are indicative of the tetragonally distorted Ni^{III} species,^[1c,10,11,23] and a peak at *g* = 1.995 for metallic palladium. Although Pd⁰ with a 4d¹⁰ electronic configuration is not paramagnetic, a very small Pd⁰ cluster shows a broad conduction electron paramagnetic resonance (CEPR).^[25,26] When the metal particles are sufficiently small, the average electronic energy-level spacing becomes larger than the Zeeman energy *hν*_e and the spin-relaxation processes are quenched by quantum-size effects, thereby resulting in a narrow CEPR line.

In general, the size, shape, and crystallinity of nanoparticles depend on the concentration of metal ions, temperature, and the type of solvent.^[27] In this study, we carried out the experiments in various experimental conditions: metal-ion concentration range of 1.0 × 10^{−4} to 1.0 × 10^{−1} M, mole ratio (Ni²⁺/Pd²⁺) of 0.1–5, temperature 0–65 °C, and MeCN and acetone as solvent. The results indicated that the temperature, concentration of Pd^{II} salt, and the type of solvent did not significantly affect the size of the Pd NPs (see the Supporting Information). When a low mole ratio (0.1:1.0) of Pd²⁺/Ni²⁺ was employed, however, a broad size distribution [(3.6 ± 0.7) nm] of Pd NPs or sometimes no Pd NP formation resulted.

To see if Pd NPs were produced only by the Ni^{II} macrocyclic complex in the absence of a porous coordination polymer matrix, a Ni^{II} macrocyclic complex with similar octahedral coordination geometry to that of **1** was prepared, and then the thus-prepared complex, [Ni(C₂₀H₃₂N₈)-(2-naphthalenecarboxylate)₂] (0.030 g, 0.038 mmol), was immersed in the solution of Pd(NO₃)₂ in MeCN (1.0 × 10⁻² M, 2 mL, 0.02 mmol) for 10 min. The pale violet complex showed no color change and its EPR spectrum was inactive, thus indicating that a redox reaction between Ni^{II} macrocyclic species and Pd^{II} ions did not occur. This suggests that an open network structure as well as the incorporation of redox-active species is necessary to obtain monodispersed and small Pd nanoparticles.

The PXRD patterns indicate that **1** transforms into the same structure as the desolvated solid when Pd nanoparticles are formed in it (see the Supporting Information). This is contrary to our previous reports that demonstrated the retention of network structures even after the formation of Ag, Au, and Pd nanoparticles.^[3a,10,11] Interestingly, when solid **1** was immersed simply in MeCN for 10 min without Pd(NO₃)₂, its guests were exchanged with MeCN and the PXRD pattern became the same as that of the desolvated solid. This indicates that the network structure of **1** alters on formation of Pd NPs because of the simultaneous guest exchange. To understand why the guest-exchanged structure could be maintained even after the nanoparticles greater than channel size were formed, we calculated the volume ratio of Pd NPs formed (80% by stoichiometry) versus the network skeleton by assuming that all Pd NPs destroyed the network skeleton. According to the calculation, the Pd NPs destroy a maximum of 1.2% of the network skeleton by volume, which is too small to alter the PXRD pattern of the network. It has been reported that metal nanoparticles much greater than the cavity sizes have been embedded in coordination polymers by maintaining the network structure.^[3a,10,11,28] The PXRD peaks of crystalline Pd generally appear at 2θ = 39.9 and 46.4°^[29] but the present nanocomposite does not show these peaks because the size of the nanoparticles is too small.

According to our independent experiments, the amount of Pd nanoparticles formed in the porous solid depends on the concentration of Pd(NO₃)₂ as well as the immersion time, although particle size is independent of them (see the Supporting Information).^[3a] The elemental analysis data (see the Experimental Section) indicate that an almost stoichiometric amount (80%, 5 wt.-%) of Pd nanoparticles relative to Ni^{II} species incorporated in **1** was formed when the solid was immersed for 16 h in the Pd^{II} solution (1.0 × 10⁻² M), which excludes the possibility of formation of Pd NPs only on the surface of the host solid.

We suggest the mechanism for the formation of Pd NPs as follows, based on PXRD and elemental analysis (EA) data as well as EPR and TEM results: Pd(NO₃)₂ and MeCN are introduced to the channels and react with the Ni^{II} macrocyclic species incorporated in **1** to form Pd⁰ atoms, which aggregate into nanoparticles in the channels. Since we cannot directly prove the inclusion of Pd^{II} ions in

the channels at the initial stage because of the immediate redox reaction, we independently measured the inclusion of redox inactive [Cu(NO₃)₂]·2.5H₂O in **1** by the spectrophotometric method (see the Supporting Information). The [Cu(NO₃)₂]·2.5H₂O dissolved in MeCN was included in **1** to afford a Langmuir-type curve, which provided a binding constant of *K_f* = 1110 and a maximum inclusion capacity {[BS]₀/ω; BS = binding site, ω = amount of host solid per unit volume of solution (mg mL⁻¹)} of 2.7 mol of Cu^{II} complex per formula unit of the host at ambient temperature. This inclusion experiment suggests that Pd(NO₃)₂ should be included in the channels of the host for the formation of the Pd NPs.

To establish the location of Pd NPs as being inside the channels or on the surface of the solid, we performed the following experiment: Pd NPs (5 wt.-%)@**1** was stirred in a solution of trioctylphosphane (TOP) in toluene (Pd/TOP ratio = 1:70) at 80 °C for 1 h. The TEM and energy-dispersive X-ray spectra (EDS) data obtained for the isolated solid indicated that the host solid still contained Pd NPs by maintaining the small size of the Pd NPs (Figure 5, a and b). However, the TEM and EDS data of the supernatant showed that the Pd NPs trapped with TOP had a broad size distribution (3–8 nm in diameter; Figure 5, c and d). The results indicate that the Pd NPs mainly exist inside the channels of **1**, but some Pd NPs located on the surface of the host solid can be removed by capping with TOP in toluene.

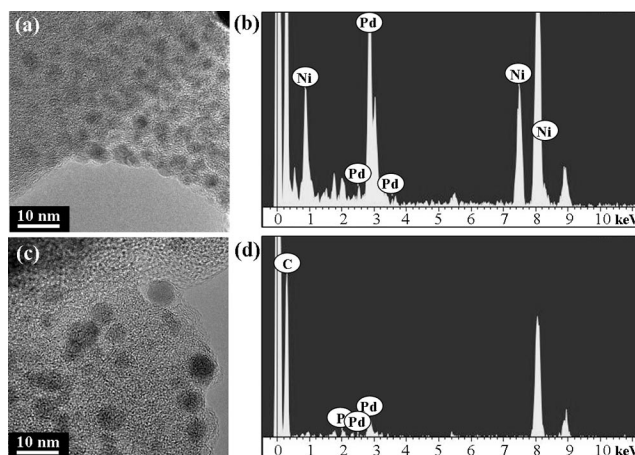


Figure 5. The results after Pd NPs (5 wt.-%)@**1** was stirred in the solution of trioctylphosphane in toluene at 80 °C for 1 h. (a) FETEM image and (b) EDS data for the isolated solid. (c) HRTEM image and (d) EDS data for the supernatant.

In general, Pd NPs have been prepared by reducing Pd^{II} ions in organic or aqueous solutions in the presence of capping agents as well as extra stimuli such as microwave, ultrasonic waves, UV light, flame spray, or chemical reducing agents.^[28] However, the capping agents that cover Pd NPs are often believed to exert a negative effect on catalytic reaction with the substrates. There have been some examples for the production of Pd NPs in porous solids,^[16,30] but several reaction steps and harsh reaction conditions were required. Therefore, production of metal nanoparticles in the present

work together with our previous reports^[3a,10,11] by using simple redox reactions between redox-active networks and metal ions is particularly important because the processes are simple and mild and the resulting Pd NPs are small and bare, thus making them ready to interact with the substrate directly.

Conclusion

We have demonstrated that the pendant arms of a macrocyclic ligand greatly affect the network structure as well as the degree of interpenetration, even though they do not directly involve in the metal–ligand bond formation. A doubly catenated grid network that generates 1D channels has been assembled from a Ni^{II} macrocyclic complex that contains pyridyl pendant arms and organic tetracarboxylate TCM⁴⁻. The network shows flexible behavior on desolvation/resolution, guest exchange, and temperature change. The present network is redox active and produces small [(2.9 ± 0.4) nm in diameter] and bare Pd nanoparticles inside the channels at room temperature simply on immersion in the solution of Pd(NO₃)₂ in MeCN. The present network might be applied in the development of sensors, and the Pd NPs@porous solid nanocomposite might be utilized as a model heterogeneous catalyst.

Experimental Section

General Methods: All chemicals and solvents used in the syntheses were of reagent grade and used without further purification, except for MeCN, which was dried by using molecular sieves before use. Na₄TCM was prepared according to the method previously reported.^[18,19] Infrared spectra were recorded with a Perkin–Elmer Spectrum One FTIR spectrophotometer. UV/Vis diffuse reflectance spectra were recorded with a Perkin–Elmer Lambda 35 UV/Vis spectrophotometer. Elemental analyses were performed by the analytical laboratory of Seoul National University. Thermogravimetric analysis (TGA) and differential scanning calorimetry (DSC) were performed under N₂(g) at a scan rate of 5 °C min⁻¹ with Q50 and Q10 model devices from TA Instruments, respectively. EPR spectra were recorded with a Bruker EPR EMX spectrometer. Field-emission transmission emission microscopy (FETEM) images and energy-dispersive X-ray spectra (EDS) were obtained with a JEOL JEM-2100F microscope, which was equipped with an Oxford INCA EDS unit.

Preparation of [Ni(C₂₀H₃₂N₈)](ClO₄)₂·1.5H₂O (A): Ethylenediamine (6.8 mL, 0.10 mol), paraformaldehyde (6.0 g, 0.20 mol), and 3-(aminomethyl)pyridine (10.8 g, 0.10 mol) were slowly added to a stirred solution of Ni(OAc)₂·4H₂O (12.4 g, 0.05 mol) in methanol (75 mL). The mixture was heated at reflux for 24 h. The solution was filtered while hot and the filtrate was concentrated to around 1/5 of the original volume. HClO₄ (60%, 20 mL) was added to the purple solution until the solution turned to yellow-brown. The solution was allowed to stand in a refrigerator until yellow crystals of [Ni(C₂₀H₃₂N₈)](ClO₄)₂·2H₂O formed, which were filtered off, washed with methanol, and dried in air; yield 35%. FTIR (KBr pellet): $\tilde{\nu}_{\text{NH}}$ = 3207 (s, br.), 3145 (s); $\tilde{\nu}_{\text{CH}_2}$ = 3090 (s); $\tilde{\nu}_{\text{ClO}_4^-}$ = 1097 (s) cm⁻¹. UV/Vis (MeNO₂): λ_{max} (ϵ , M⁻¹cm⁻¹) = 451 nm (75). C₄₀H₇₀Cl₆N₁₆Ni₂O₂₆ (1521.19): calcd. C

28.19, H 4.14, N 13.15; found C 28.10, H 4.23, N 13.23. An excess amount of triethylamine (2 mL) was added to a suspension of [Ni(C₂₀H₃₂N₈)](ClO₄)₂·2H₂O (2.5 g) in MeCN (40 mL). The complex dissolved into the solution and yellow crystals of [Ni(C₂₀H₃₂N₈)](ClO₄)₂·1.5H₂O (A) formed in a few minutes. The crystals were filtered off, washed with water, and dried in air; yield 90%. FTIR (KBr pellet): $\tilde{\nu}_{\text{OH}}$ = 3435 (s, br.); $\tilde{\nu}_{\text{NH}}$ = 3203 (s), 3033 (s); $\tilde{\nu}_{\text{CH}_2}$ = 2954 (s); $\tilde{\nu}_{\text{ClO}_4^-}$ = 1087 (s) cm⁻¹. UV/Vis (MeNO₂): λ_{max} (ϵ , M⁻¹cm⁻¹) = 448 nm (97). C₂₀H₃₅Cl₂N₈NiO_{9.5} (669.14): calcd. C 35.90, H 5.27, N 16.75; found C 35.87, H 5.28, N 16.44.

Preparation of [Ni(C₂₀H₃₂N₈)]₂[TCM]·5DMF·8H₂O (I): Metal building block A (48 mg, 7.2 × 10⁻⁵ mol) was dissolved in DMF (4 mL), and the solution was allowed to diffuse into the solution of Na₄TCM (24 mg, 3.4 × 10⁻⁵ mol) in DMF/H₂O (4.5 mL, 2:2.5 v/v) at room temperature for one week. Pale violet crystals formed, which were filtered off, washed with DMF/H₂O (3:1 v/v), and briefly dried in air; yield 0.061 g (89%). FTIR (KBr pellet): $\tilde{\nu}_{\text{OH}}$ = 3409 (m, br.); $\tilde{\nu}_{\text{NH}}$ = 3253 (m), 3166 (m); $\tilde{\nu}_{\text{CH}_2}$ = 2927 (m), 2867 (m); $\tilde{\nu}_{\text{C=O(DMF)}}$ = 1668 (s); $\tilde{\nu}_{\text{O-C=O}}$ = 1598 (s), 1557 (s) cm⁻¹. UV/Vis (diffuse reflectance spectrum): λ_{max} = 506 nm. C₈₈H₁₃₉N₂₁Ni₂O₂₅ (2008.58): calcd. C 52.62, H 6.98, N 14.64; found C 52.60, H 6.54, N 14.68.

Preparation of Desolvated Solid [Ni(C₂₀H₃₂N₈)]₂[TCM] (I_{des}): To remove all guest solvent molecules, **1** was heated at 120 °C under 10⁻³ Torr for 12 h, and then cooled to room temperature while maintaining the high vacuum conditions. Alternatively, solid **1** was heated at 50 °C under vacuum for 20 h. FTIR (Nujol mull): $\tilde{\nu}_{\text{NH}}$ = 3286 (m), 3140 (m); $\tilde{\nu}_{\text{O-C=O}}$ = 1597 (s), 1556 (s) cm⁻¹. C₇₃H₈₈N₁₆Ni₂O₁₂ (1498.99): calcd. C 58.49, H 5.92, N 14.95; found C 57.08, H 5.87, N 14.76.

Preparation of Resolvated Solid [Ni(C₂₀H₃₂N₈)]₂[TCM]·5DMF·4H₂O (I_{res}): The desolvated solid **1_{des}** was exposed to the vapor of DMF and H₂O mixture (9.5:0.5 v/v) at 38 °C for 4.5 d. FTIR (Nujol mull): $\tilde{\nu}_{\text{OH}}$ = 3405 (m, br.); $\tilde{\nu}_{\text{NH}}$ = 3270 (m), 3176 (m); $\tilde{\nu}_{\text{C=O(DMF)}}$ = 1673 (s); $\tilde{\nu}_{\text{O-C=O}}$ = 1596 (s), 1557 (s) cm⁻¹. C₈₃H₁₃₁N₂₁Ni₂O₂₁ (1876.47): calcd. C 54.58, H 6.82, N 15.19; found C 54.51, H 6.77, N 15.09.

Preparation of Guest-Exchanged Solid [Ni(C₂₀H₃₂N₈)]₂[TCM]·12MeCN (I_{MeCN}): To exchange DMF guest molecules in **1** with more volatile ones, guest exchange was performed with MeCN. Solid **1** was pulverized and then immersed in MeCN at room temperature for 10 min. The solid was filtered off, washed with MeCN, and dried briefly in air. FTIR (Nujol mull): $\tilde{\nu}_{\text{OH(water)}}$ = 3379 (m, br.); $\tilde{\nu}_{\text{NH}}$ = 3286 (m), 3140 (m); $\tilde{\nu}_{\text{C=N(acetonitrile)}}$ = 2250 (m); $\tilde{\nu}_{\text{O-C=O}}$ = 1598 (s), 1557 (s) cm⁻¹. C₉₇H₁₂₄N₂₈Ni₂O₁₂ (1991.62): calcd. C 58.50, H 6.28, N 19.69; found C 55.35, H 6.36, N 19.61.

Crystallography: The diffraction data of crystal **1** that was mounted on the loop with Paratone oil were collected at 100 K with an ADSC Quantum 210 CCD diffractometer with synchrotron radiation (λ = 0.75000 Å) at Macromolecular Crystallography Wiggler Beamline 4A, Pohang Accelerator Laboratory (PAL), Pohang, Korea. The crystal was rotated through a total of 360°. The raw data were processed and scaled using the program HKL2000. The structure was solved by the direct method^[31] and refined by full-matrix least-squares refinement with the SHELXL-97 computer program.^[32] The positions of all non-hydrogen atoms were refined with anisotropic displacement factors. The hydrogen atoms were positioned geometrically and refined using a riding model. As for the guest molecules of **1**, four residual electron densities per asymmetric unit were found with severe disorder. Therefore, the identity and number of the guest molecules (five DMF and eight H₂O) in **1** were

determined on the basis of IR, elemental analysis, and TGA data. The densities of the disordered guest molecules were flattened by using the SQUEEZE option^[33] of PLATON. The crystallographic data and selected bond lengths and angles of **1** are provided in Tables S1 and S2 of the Supporting Information.

CCDC-775784 (for **1**) contains the supplementary crystallographic data for this paper. These data can be obtained free of charge from The Cambridge Crystallographic Data Centre via www.ccdc.cam.ac.uk/data_request/cif.

Collection and Refinement of PXRD Pattern of 1: Powder X-ray diffraction (PXRD) data were recorded with a Bruker D5005 diffractometer at 40 kV and 40 mA with nickel-filtered Cu- K_{α} radiations including both $K_{\alpha 1}$ (1.5406 Å) and $K_{\alpha 2}$ (1.5444 Å) with a scan speed of 5 °min⁻¹ and a step size of 0.02° in 2 θ at room temperature. The fine-powder samples were prepared by careful grinding. The background of the experimental PXRD data was corrected and the pattern was smoothed for reliable peak picking. Using the X-CELL^[34] indexing program on the corrected PXRD data of **1**, an orthorhombic unit cell and the space group $I2_12_12_1$ were determined. With this unit-cell structure, Pawley refinement was performed repeatedly to optimize the lattice parameters, and the R_p and R_{wp} values of 0.10 and 0.11, respectively, were obtained. The peak shape was modeled with a pseudo-Voigt function. Final Rietveld refinement was converged to R_{wp} = 0.14. For this refinement, bond lengths and angle restraints were taken from the X-ray single-crystal structure of **1**. Unit-cell indexing, and Pawley and Rietveld refinements were carried out with Reflex^[35] a software module implemented in Materials Studio modeling v4.1 (Accelrys Inc.).

Binding of 1 with Cu^{II} Complex: The formation constant K_f for the complexes formed between a binding site (BS) of the insoluble host **1** and a guest molecule (G) can be defined as k_{ad}/k_{de} [Equation (1)] by analogy with the Langmuir isotherm for adsorption of gas molecules on solid surfaces.^[1,2,20] A plot of the concentration of G bound to BS ([BS•G]) against [G] at equilibrium was made and the K_f and [BS]₀ values were estimated by the analysis of the data according to Equation (2).

$$\text{BS} + \text{G} \xrightleftharpoons[k_{de}]{k_{ad}} \text{BS} \cdot \text{G}$$

$$K_f = \frac{k_{ad}}{k_{de}} = \frac{[\text{BS} \cdot \text{G}]}{[\text{BS}][\text{G}]} \quad (1)$$

If θ is defined as fractional coverage

$$\theta = \frac{[\text{BS} \cdot \text{G}]}{[\text{BS}]_0} = \frac{[\text{G}]}{([\text{G}] + 1/K_f)}$$

then $[\text{BS} \cdot \text{G}]/\omega = \frac{([\text{BS}]_0/\omega)[\text{G}]}{([\text{G}] + 1/K_f)} \quad (2)$

in which ω is the amount of host solid per unit volume of the solution (mgmL⁻¹).

Pale pink crystals of **1** were pulverized, and an exactly measured amount (9.8–10.4 mg) was immersed in the solutions of [Cu(NO₃)₂] \cdot 2.5H₂O in MeCN for 20 h at ambient temperature. The initial concentrations of the Cu^{II} complex were varied as 3.48×10^{-3} – 2.22×10^{-2} M to keep the saturation values in the range of 20–80%.

The time required to attain the equilibrium for the host–guest complex formation was estimated by monitoring the change of the guest concentration spectrophotometrically. A typical time dependency of Cu^{II} binding was measured (see the Supporting Information). According to this, we assumed that the equilibrium could be reached in 20 h. The concentration changes of the Cu^{II} complex were measured by UV/Vis spectra, and the data were fit to Equation (2).

Measurement of Cu^{II} Complex Inclusion in 1: When solid **1** was immersed in the solution of [Cu(NO₃)₂] \cdot 2.5H₂O in MeCN, the Cu^{II} complex was included in **1**, and the peak intensity of the Cu^{II} solution in UV/Vis was reduced and the pale pink color of solid **1** became yellowish green. The time required to attain the equilibrium was measured by monitoring the changes of the Cu^{II} concentration spectrophotometrically (Figure S4 in the Supporting Information). To obtain K_f and [BS]₀/ ω values for the host–guest complex formation according to Equation (2), the absorbance changes for the solutions of [Cu(NO₃)₂] \cdot 2.5H₂O in MeCN were measured at 755 nm by varying the initial concentration of the Cu^{II} complex ([G]₀) with the measured amount of the host solid. The plot of [BS•G] (the concentration of guest G bound to BS) against [G] is illustrated in Figure S5 in the Supporting Information. Analysis of the data provides K_f = 1110 and [BS]₀/ ω = 1.36 mmol g⁻¹ for **1** at ambient temperature. The values of [BS]₀/ ω indicate that the host solid **1** has 2.7 binding sites for the Cu^{II} guest molecule per formula unit of the host solid (Cu²⁺/Ni²⁺ = 1.36). The host including Cu^{II} ions was characterized by EA, IR, as well as PXRD patterns (Figure S6); elemental analysis calcd. for {[Ni(C₂₀H₃₂N₈)₂][TCM]} \cdot 3Cu(NO₃)₂ \cdot 14H₂O: C 37.89, H 5.05, N 13.32; found C 37.21, H 4.30, N 13.33. The infrared spectra and elemental analyses indicate that MeCN molecules are not included in the host, and the PXRD patterns indicate that **1** transforms into the same structure as that of the desolvated solid by inclusion of Cu^{II} complex. This result suggests that [Pd(NO₃)₂] must also be included in **1** at the initial stage, instead of simply adsorbed on the surface.

Preparation of Pd Nanocomposites: Solid **1** (0.040 g, 2.0×10^{-2} mmol) was pulverized and then immersed in the solution of Pd(NO₃)₂ (1.0×10^{-2} M, 2.0×10^{-2} mmol) in MeCN (2 mL) at room temperature for 10 min to 16 h. A brown solid resulted, the color of which became darker as the immersion time passed. The solid was filtered off, washed with MeCN, and dried in air. Solid isolated after 10 min of immersion: {[Ni(C₂₀H₃₂N₈)₂][TCM]} \cdot 0.5[Pd(NO₃)₂] \cdot 6H₂O (Ni₂C₇₃H₁₁₀N₁₇O₂₁Pd_{0.5}): calcd. C 50.91, H 5.85, N 13.83; found C 50.98, H 5.43, N 13.84. FTIR (KBr pellet): 3390 (m, br.), 2925 (m), 1599 (s), 1553 (m), 1460 (s), 1377 (s) cm⁻¹. The solid isolated after 16 h of immersion: {[Ni(C₂₀H₃₂N₈)₂][TCM]} \cdot 0.8[Pd(NO₃)₂] (Ni₂C₇₃H₈₈N_{17.6}O_{16.8}Pd_{0.8}): calcd. C 52.09, H 5.27, N 14.64; found C 52.06, H 5.24, N 14.79. FTIR (KBr pellet): 3410 (m, br.), 2925 (m), 1602 (s), 1552 (s), 1380 (s) cm⁻¹.

Reaction of Pd Nanocomposites with TOP: Pd NPs (5 wt.-%)@**1** (20 mg, 9.5×10^{-3} mmol based on Pd) was stirred in the solution of trioctylphosphane (TOP; 0.3 mL, 6.7×10^{-1} mmol) in toluene (2 mL) at 80 °C for 1 h. After the reaction mixture was cooled to room temperature, the solid was separated from the solution by using a centrifuge (5000 rpm, 10 min), and the isolated solid was washed with toluene. The isolated solid and the supernatant, respectively, were loaded on the carbon-coated copper grids for TEM analysis.

Supporting Information (see also the footnote on the first page of this article): TGA/DSC trace of **1**, temperature-dependent PXRD patterns of **1**, time and concentration dependencies of binding of

1 with Cu²⁺, PXRD patterns, EDS data for Pd NPs embedded in 1, FETEM images for Pd nanoparticles obtained at various experimental conditions, tables summarizing the various experimental conditions and the size of Pd nanoparticles formed, and tables of X-ray crystal data for 1.

Acknowledgments

This work was supported by a National Research Foundation of Korea (NRF) Grant funded by the Korean Government (MEST) (grant numbers 2009-0093842 and 2010-0001485). The authors acknowledge Pohang Accelerator Laboratory (PAL) for synchrotron beamline use.

- [1] a) E. Y. Lee, S. Y. Jang, M. P. Suh, *J. Am. Chem. Soc.* **2005**, *127*, 6374–6381; b) M. P. Suh, J. W. Ko, H. J. Choi, *J. Am. Chem. Soc.* **2002**, *124*, 10976–10977; c) H. J. Choi, M. P. Suh, *J. Am. Chem. Soc.* **2004**, *126*, 15844–15851.
- [2] a) J. W. Ko, K. S. Min, M. P. Suh, *Inorg. Chem.* **2002**, *41*, 2151–2157; b) K. S. Min, M. P. Suh, *Chem. Eur. J.* **2001**, *7*, 303–313; c) B. Chen, J. Liang, J. Yang, D. S. Contreras, Y. L. Clancy, E. B. Lobkovsky, O. M. Yaghi, S. Dai, *Angew. Chem.* **2006**, *118*, 1418–1421; *Angew. Chem. Int. Ed.* **2006**, *45*, 1390–1393; d) J. Y. Lee, D. H. Olson, L. Pan, T. J. Erng, J. Li, *Adv. Funct. Mater.* **2007**, *17*, 1255–1262.
- [3] a) Y. E. Cheon, M. P. Suh, *Angew. Chem.* **2009**, *121*, 2943–2947; *Angew. Chem. Int. Ed.* **2009**, *48*, 2899–2903; b) H. S. Choi, M. P. Suh, *Angew. Chem.* **2009**, *121*, 6997–7001; *Angew. Chem. Int. Ed.* **2009**, *48*, 6865–6869; c) Y.-G. Lee, H. R. Moon, Y. E. Cheon, M. P. Suh, *Angew. Chem.* **2008**, *120*, 7855–7859; *Angew. Chem. Int. Ed.* **2008**, *47*, 7741–7745; d) H. J. Park, M. P. Suh, *Chem. Eur. J.* **2008**, *14*, 8812–8821; e) M. P. Suh, Y. E. Cheon, E. Y. Lee, *Chem. Eur. J.* **2007**, *13*, 4208–4215; f) E. Y. Lee, M. P. Suh, *Angew. Chem.* **2004**, *116*, 2858–2861; *Angew. Chem. Int. Ed.* **2004**, *43*, 2798–2801.
- [4] a) L. J. Murray, M. Dincă, J. R. Long, *Chem. Soc. Rev.* **2009**, *38*, 1294–1314; b) S. S. Kaye, A. Dailly, O. M. Yaghi, J. R. Long, *J. Am. Chem. Soc.* **2007**, *129*, 14176–14177; c) S. Ma, D. Sun, J. M. Simmons, C. D. Collier, D. Yuan, H.-C. Zhou, *J. Am. Chem. Soc.* **2008**, *130*, 1012–1016; d) D. Britt, D. Tranchemontagne, O. M. Yaghi, *PNAS* **2008**, *105*, 11623–11627.
- [5] a) K. S. Min, M. P. Suh, *J. Am. Chem. Soc.* **2000**, *122*, 6834–6840; b) H. J. Choi, M. P. Suh, *Inorg. Chem.* **2003**, *42*, 1151–1157; c) M. J. Manos, R. Iyer, G. E. Quarez, J. H. Liao, M. G. Kanatzidis, *Angew. Chem.* **2005**, *117*, 3618–3621; *Angew. Chem. Int. Ed.* **2005**, *44*, 3552–3555; d) P. N. Trikalitis, K. K. Rangan, T. Bakas, M. G. Kanatzidis, *J. Am. Chem. Soc.* **2002**, *124*, 12255–12260; e) M. Dincă, J. R. Long, *J. Am. Chem. Soc.* **2007**, *129*, 11172–11176.
- [6] a) B. Chen, L. Wang, F. Zapata, G. Qian, E. B. Lobkovsky, *J. Am. Chem. Soc.* **2008**, *130*, 6718–6719; b) B. V. Harbuzaru, A. Corma, F. Rey, P. Atienzar, J. L. Jorda, H. Garcia, D. Ananias, L. D. Carlos, J. Rocha, *Angew. Chem.* **2008**, *120*, 1096–1099; *Angew. Chem. Int. Ed.* **2008**, *47*, 1080–1083; c) C. A. Bauer, T. V. Timofeeva, T. B. Settersten, B. D. Patterson, V. H. Liu, B. A. Simmons, M. D. Allendorf, *J. Am. Chem. Soc.* **2007**, *129*, 7136–7144; d) B. Chen, Y. Yang, F. Zapata, G. Lin, G. Qian, E. B. Lobkovsky, *Adv. Mater.* **2007**, *19*, 1693–1696; e) S. Shimomura, R. Matsuda, T. Tsujino, T. Kawamura, S. Kitagawa, *J. Am. Chem. Soc.* **2006**, *128*, 16416–16417; f) L. G. Beauvais, M. P. Shores, J. R. Long, *J. Am. Chem. Soc.* **2000**, *122*, 2763–2772.
- [7] a) S. Horike, M. Dincă, K. Tamaki, J. R. Long, *J. Am. Chem. Soc.* **2008**, *130*, 5854–5855; b) C.-D. Wu, W. Lin, *Angew. Chem.* **2007**, *119*, 1093–1096; *Angew. Chem. Int. Ed.* **2007**, *46*, 1075–1078; c) T. Uemura, R. Kitaura, Y. Ohta, N. Nagaoka, S. Kitagawa, *Angew. Chem.* **2006**, *118*, 4218–4222; *Angew. Chem. Int. Ed.* **2006**, *45*, 4112–4116; d) D. N. Dybtsev, A. L. Nuzhdin, H. Chun, K. P. Bryliakov, E. P. Talsi, V. P. Fedin, K. Kim, *Angew. Chem.* **2006**, *118*, 930–934; *Angew. Chem. Int. Ed.* **2006**, *45*, 916–920; e) R.-Q. Zou, H. Sakurai, Q. Xu, *Angew. Chem.* **2006**, *118*, 2604–2608; *Angew. Chem. Int. Ed.* **2006**, *45*, 2542–2546.
- [8] a) S. Kitagawa, K. Uemura, *Chem. Soc. Rev.* **2005**, *34*, 109–119; b) A. J. Fletcher, K. Thomas, M. Rosseinsky, *J. Solid State Chem.* **2005**, *178*, 2491–2510.
- [9] a) T. Devic, P. Horcajada, C. Serre, F. Salles, G. Maurin, B. Moulin, D. Heurtaux, G. Clet, A. Vimont, J.-M. Grenèche, B. Le Ouay, F. Moreau, E. Magnier, Y. Filinchuk, J. Marrot, J.-C. Lavalley, M. Daturi, G. Férey, *J. Am. Chem. Soc.* **2010**, *132*, 1127–1136; b) P. L. Llewellyn, S. Bourrelly, C. Serre, Y. Filinchuk, G. Férey, *Angew. Chem.* **2006**, *118*, 7915–7918; *Angew. Chem. Int. Ed.* **2006**, *45*, 7751–7754; c) C. Serre, C. Mellot-Draznicks, S. Surblé, N. Audebrand, Y. Filinchuk, G. Férey, *Science* **2007**, *315*, 1828–1831.
- [10] a) M. P. Suh, H. R. Moon, E. Y. Lee, S. Y. Jang, *J. Am. Chem. Soc.* **2006**, *128*, 4710–4718; b) H. R. Moon, J. H. Kim, M. P. Suh, *Angew. Chem.* **2005**, *117*, 1287–1291; *Angew. Chem. Int. Ed.* **2005**, *44*, 1261–1265.
- [11] Y. E. Cheon, M. P. Suh, *Chem. Eur. J.* **2008**, *14*, 3961–3967.
- [12] K. L. Kelly, E. Coronado, L. Zhao, G. C. Schatz, *J. Phys. Chem. B* **2003**, *107*, 668–677.
- [13] a) M. A. El-Sayed, *Acc. Chem. Res.* **2001**, *34*, 257–264; b) J. S. Bradley, in: *Clusters and Colloids* (Ed.: G. Schmid), VCH, Weinheim, **1994**, p. 459; c) W. R. Moser, in: *Advanced Catalysis and Nanostructured Materials*, Academic Press, San Diego, **1996**.
- [14] J. L. Malleron, J. C. Fiaud, J. Y. Legros (Eds.), in: *Handbook of Palladium-Catalysed Organic Reaction*, Academic Press, London, **1997**.
- [15] M. Sabo, A. Henschel, H. Fröde, E. Klemmb, S. Kaskel, *J. Mater. Chem.* **2007**, *17*, 3827–3832.
- [16] a) S. Hermes, M. K. Schröter, R. Schmid, L. Khodeir, M. Muhler, A. Tissler, R. W. Fischer, R. A. Fischer, *Angew. Chem.* **2005**, *117*, 6394–6397; *Angew. Chem. Int. Ed.* **2005**, *44*, 6237–6241; b) D. Esken, X. Zhang, O. I. Lebedev, F. Schröder, R. A. Fischer, *J. Mater. Chem.* **2009**, *19*, 1314–1319.
- [17] M. P. Suh, H. R. Moon, *Adv. Inorg. Chem.* **2007**, *59*, 39–79.
- [18] H. Oike, H. Imamura, H. Imaizumi, Y. Tezuka, *Macromolecules* **1999**, *32*, 4819–4825.
- [19] H. Kim, M. P. Suh, *Inorg. Chem.* **2005**, *44*, 810–812.
- [20] a) M. P. Suh, *Adv. Inorg. Chem.* **1997**, *44*, 93–146, Academic Press, Inc., New York, NY; b) S. K. Jung, S. G. Kang, M. P. Suh, *Bull. Korea Chem. Soc.* **1989**, *10*, 362–366.
- [21] K. S. Min, M. P. Suh, *Eur. J. Inorg. Chem.* **2001**, 449–455.
- [22] M. Nishio, M. Hirota, Y. Umezawa, in: *The CH–π Interactions: Evidence, Nature and Consequences*, Wiley, New York, **1998**, pp. 52–56.
- [23] A. L. Spek, *PLATON99, A Multipurpose Crystallographic Tool*; Utrecht University, Utrecht, The Netherlands, **1999**.
- [24] M. P. Suh, E. Y. Lee, B. Y. Shim, *Inorg. Chim. Acta* **1998**, *337*–341.
- [25] M. Narayana, J. Michalik, S. Contarini, L. Kevan, *J. Phys. Chem.* **1985**, *89*, 3895–3899.
- [26] a) J. Michalik, D. Brown, J.-S. Yu, M. Danilczuk, J. Y. Kim, L. Kevan, *Phys. Chem. Chem. Phys.* **2001**, *3*, 1705–1708; b) J. P. Candy, V. Perrichon, *J. Catal.* **1984**, *89*, 93–99.
- [27] a) R. He, X. Qian, J. Yin, Z. Zhu, *J. Mater. Chem.* **2002**, *12*, 3783–3786; b) H. H. Huang, X. P. Ni, G. L. Loy, C. H. Chew, K. L. Tan, F. C. Loh, J. F. Deng, G. Q. Xu, *Langmuir* **1996**, *12*, 909–912; c) M. Yamada, H. Nishihara, *Langmuir* **2003**, *19*, 8050–8056; d) L. Lu, H. Wang, Y. Zhou, S. Xi, H. Zhang, J. Hu, B. Zhao, *Chem. Commun.* **2002**, 144–145.
- [28] a) F. Schröder, D. Esken, M. Cokoja, M. W. E. van den Berg, O. Lebedev, G. V. Tendeloo, W. Walaszek, G. Buntkowsky, H.-H. Limbach, B. Chaudret, R. A. Fischer, *J. Am. Chem. Soc.* **2008**, *130*, 6119–6130; b) M. Müller, O. I. Lebedev, R. A. Fischer, *J. Mater. Chem.* **2008**, *18*, 5274–5281.

- [29] a) G. Glaspell, L. Fuoco, M. S. El-Shall, *J. Phys. Chem. B* **2005**, *109*, 17350–17355; b) A. Nemamcha, J.-L. Rehspringer, D. Khatmi, *J. Phys. Chem. B* **2006**, *110*, 383–387; c) H. Tan, T. Zhan, W. Y. Fan, *Chem. Phys. Lett.* **2006**, *428*, 352–355; d) R. Strobel, S. E. Pratsinis, A. Baiker, *J. Mater. Chem.* **2005**, *15*, 605–610; e) M. A. R. Meier, M. Filali, J.-F. Gohy, U. S. Schubert, *J. Mater. Chem.* **2006**, *16*, 3001–3006; f) Y. Piao, Y. Jang, M. Shokouhimehr, I. S. Lee, T. Hyeon, *Small* **2007**, *3*, 255–260.
- [30] a) A. Fukuoka, H. Araki, J.-I. Kimura, Y. Sakamoto, T. Higuchi, N. Sugimoto, S. Inagakic, M. Ichikawa, *J. Mater. Chem.* **2004**, *14*, 752–756; b) F. Cheng, S. M. Kelly, N. A. Young, C. N. Hope, K. Beverley, M. G. Francesconi, S. Clark, J. S. Bradley, F. Lefebvre, *Chem. Mater.* **2006**, *18*, 5996–6005; c) I. Yuranov, L. Kiwi-Minsker, P. Buffat, A. Renken, *Chem. Mater.* **2004**, *16*, 760–761; d) L.-C. Wang, C.-Y. Huang, C.-Y. Chang, W.-C. Lin, K.-J. Chao, *Microporous Mesoporous Mater.* **2008**, *110*, 451–460; e) P. Wang, Z. Wang, J. Li, Y. Bai, *Microporous Mesoporous Mater.* **2008**, *116*, 400–405.
- [31] G. M. Sheldrick, *Acta Crystallogr., Sect. A* **1990**, *46*, 467–473.
- [32] G. M. Sheldrick, *SHELXL97, Program for the Crystal Structure Refinement*, University of Göttingen, Göttingen, Germany, **1993**.
- [33] P. v. d. Sluis, A. L. Spek, *Acta Crystallogr., Sect. A* **1990**, *46*, 194–201.
- [34] M. A. Neumann, *J. Appl. Crystallogr.* **2003**, *36*, 356–365.
- [35] *Reflex*, Materials Studio Release Notes, release 4.1, Accelrys Software, Accelrys, San Diego, **2006**.

Received: May 19, 2010

Published Online: July 21, 2010

Manganese-Based Metal–Organic Frameworks as Heterogeneous Catalysts for the Cyanosilylation of Acetaldehyde

Tim Ladrak,^[a] Simon Smulders,^[a] Olivier Roubeau,^{*,[b]} Simon J. Teat,^[c] Patrick Gamez,^{*,[a]} and Jan Reedijk^[a]

Keywords: Metal–organic networks / Heterogeneous catalysis / Manganese / Lewis acids / Trigonal prisms

Two new metal–organic frameworks (MOFs), namely $[\text{Mn}_3(\text{atpa})_3(\text{dmf})_2]$ and $[\text{Mn}_2(\text{tpa})_2(\text{dmf})_2]$, were prepared in *N,N*-dimethylformamide (dmf) from manganese(II) nitrate and two dicarboxylic acid ligands, 2-aminoterephthalic acid (H_2atpa) and terephthalic acid (H_2tpa). The molecular structures of these MOFs are compared to two related coordination polymers, namely $[\text{Mn}_3(\text{atpa})_2(\text{Hatpa})_2]$ and $[\text{Mn}_3(\text{tpa})_3(\text{def})_2]$, which were obtained in *N,N*-diethylformamide (def), to examine the effect of slight ligand or solvent changes on the framework architecture. The four Mn-based MOFs were used as effective Lewis catalysts for the cyanosilylation of acetaldehyde. The four heterogeneous catalytic systems can be re-used without any apparent loss of activity.

Two new metal–organic frameworks (MOFs), namely $[\text{Mn}_3(\text{atpa})_3(\text{dmf})_2]$ and $[\text{Mn}_2(\text{tpa})_2(\text{dmf})_2]$, were prepared in *N,N*-dimethylformamide (dmf) from manganese(II) nitrate and two dicarboxylic acid ligands, 2-aminoterephthalic acid (H_2atpa) and terephthalic acid (H_2tpa). The molecular structures of these MOFs are compared to two related coordination polymers, namely $[\text{Mn}_3(\text{atpa})_2(\text{Hatpa})_2]$ and $[\text{Mn}_3(\text{tpa})_3(\text{def})_2]$, which were obtained in *N,N*-diethylformamide (def), to examine the effect of slight ligand or solvent changes on the framework architecture. The four Mn-based MOFs were used as effective Lewis catalysts for the cyanosilylation of acetaldehyde. The four heterogeneous catalytic systems can be re-used without any apparent loss of activity.

Introduction

Metal–organic frameworks (MOFs) are a remarkable class of crystalline porous materials, whose popularity is growing exponentially.^[1] MOFs are infinite hybrid organic–inorganic networks assembled by the coordination of metal ions to polyfunctional ligands with multidirectional bonding capabilities.^[2] MOFs have received a great deal of attention in recent years as the result of their diverse architectures and for their many potential applications in gas storage and separation,^[3] ion exchange,^[4] magnetism,^[5] luminescence,^[6] sensor technology^[7] and optoelectronics.^[8] In comparison with the above applications (and especially gas storage and separation), the use of MOFs in catalysis is less developed.^[9] The molecular structures of a number of MOFs are analogous to those of well-known zeolites. Recently, the third generation of these synthetic frameworks has revealed so far unseen levels of porosity, so called nanoporosity, as well as remarkable stabilities.^[10] These exceptional properties of many MOFs make them perfect candidates for use in catalysis; therefore, increasing examples of catalytic systems based on MOFs are to be expected in the near future.

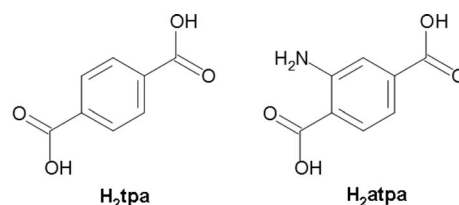
In the present study, two known and two new, closely related manganese(II)-based MOFs were prepared. The

molecular structures of $[\text{Mn}_3(\text{atpa})_2(\text{Hatpa})_2]$ (**1**), $[\text{Mn}_3(\text{atpa})_3(\text{dmf})_4]$ (**2**), $[\text{Mn}_3(\text{tpa})_3(\text{def})_2]$ (**3**) and $[\text{Mn}_2(\text{tpa})_2(\text{dmf})_2]$ (**4**) are compared to examine the effect of minor changes in experimental conditions, such as the solvent (dmf or def), or slight ligand modifications, on the resulting framework architectures. All four MOFs were used as Lewis catalysts for the cyanosilylation of acetaldehyde, and the results are reported.

Results and Discussion

Description of the Structures

Four related MOFs were prepared from manganese(II) nitrate and two readily available dicarboxylic ligands, namely terephthalic acid and 2-aminoterephthalic acid (H_2tpa and H_2atpa , Scheme 1). Two of these MOFs (compounds **1** and **3**, see below) have been separately reported;^[11–13] therefore, their structures were not compared to each other. H_2tpa is well known in the area of MOF chemistry^[14] and has been extensively used.^[12,15] However, outstanding new coordination networks involving this ligand are still regularly reported.^[16] H_2atpa is relatively less investigated in MOF chemistry than H_2tpa .^[17]



Scheme 1. Schematic representations of terephthalic acid (H_2tpa) and 2-aminoterephthalic acid (H_2atpa).

[a] Leiden Institute of Chemistry, Leiden University
P. O. Box 9502, 2300 RA Leiden, The Netherlands
E-mail: p.gamez@chem.leidenuniv.nl

[b] Instituto de Ciencia de Materiales de Aragón, CSIC and
Universidad de Zaragoza,
Plaza San Francisco, s/n 50009 Zaragoza, Spain
E-mail: roubeau@unizar.es

[c] Advanced Light Source, Lawrence Berkeley National
Laboratory,
Berkeley, California 94720, USA

Supporting information for this article is available on the
WWW under <http://dx.doi.org/10.1002/ejic.201000378>.

[Mn₃(atpa)₂(Hatpa)₂] (1)

The reaction of Mn(NO₃)₂·4H₂O with H₂atpa (2:3 molar ratio) in diethylformamide (def), at 120 °C under autogenous pressure, produces colourless block-shaped crystals, suitable for X-ray crystallography.

The identity of the product was established as [Mn₃(atpa)₂(Hatpa)₂] (1), and its structure is depicted in Figure 1. Selected bond lengths and angles of 1 are given in Table 1. Compound 1 crystallizes in the centred space group *C2/c*, as reported earlier in the literature.^[11] The structure reported here was determined at a lower temperature and is described again in detail for the purpose of comparison. Compound 1 consists of a chain-like arrangement of three manganese(II) ions held together by four deprotonated carboxylato groups (oxygen atoms O3c, O4b, O5, O6 and their symmetry-related counterparts) and two protonated carboxylic moieties (oxygen atoms O1 and O1e) belonging to six different bidirectional aminoterephthalic ligands. In addition, the external Mn^{II} ions, that is, Mn1 and Mn1a, are coordinated by one chelating carboxylato unit (oxygen atoms O7 and O8 for Mn1) from another aminoterephthalic ligand. Mn1 (and Mn1a) has a distorted trigonal-prismatic geometry (Figure S1), formed by six oxygen atoms from three atpa (O5, O6, O7, O8, and O3c) and one

Hatpa (O1e) ligands (Figure 1). The Mn1–O bond lengths ranging from 2.085(2) to 2.331(2) Å (Table 1) can be regarded as normal for this type of coordination environment.^[11,18] The strong distortion of the trigonal prism, reflected by angles varying from 84.85(9) to 100.20(8)° (Table 1), is most likely due to the coordination of both a chelating carboxylato group (oxygen atoms O7 and O8) and a μ -O,O',O' carboxylato ligand (oxygen atoms O5 and O6). Furthermore, for a regular trigonal prism, the angle α in Scheme 2 is 0°. Compound 1 displays α angles of 1.96, 23.5 and 59.28°. The last angle is clearly illustrative of the severe distortion of the trigonal-prismatic environment around Mn1, caused by steric constraints induced by the formation of the trimanganese core.



Scheme 2. Angle α characterizing the distortion of a trigonal prism.

Mn1 and Mn1a are bridged to the central Mn2 ion through six μ -OCO units. Mn2 is in an octahedral coordination environment, whose basal plane comprises four oxygen atoms (O2, O2e, O4b and O4c) belonging to four μ -O,O',O' ligands (Figure 1). The axial positions are occupied by the oxygen atoms (O6 and O6e) from two μ -O,O',O' ligands. The Mn–O_{equatorial} and Mn–O_{axial} bond lengths,

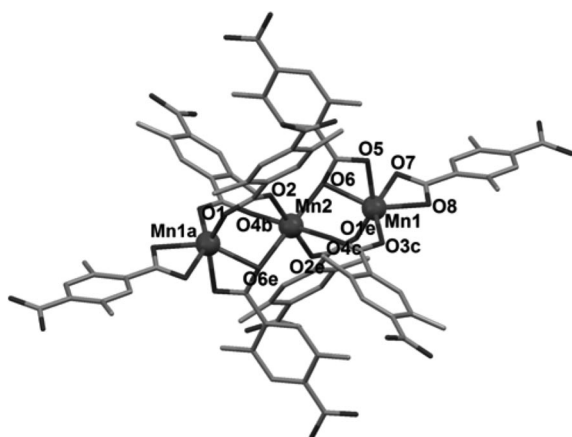


Figure 1. Representation of the crystal structure of [Mn₃(atpa)₂(Hatpa)₂] (1). The hydrogen atoms are omitted for clarity. Symmetry operations: a = $x, 2 - y, -1/2 + z$; b = $x, 2 - y, 1/2 + z$; c = $1/2 - x, -1/2 + y, 1/2 - z$; e = $1/2 - x, 3/2 - y, 1 - z$.

Table 1. Selected bond lengths [Å] and angles [°] for compound 1.^[a]

Bond length		Bond angle	
Mn1–O5	2.274(2)	O8–Mn1–O5	98.77(10)
Mn1–O6	2.256(2)	O8–Mn1–O3c	90.76(10)
Mn1–O7	2.331(2)	O3c–Mn1–O5	98.89(8)
Mn1–O8	2.200(3)	O6–Mn1–O7	100.20(8)
Mn1–O1e	2.093(2)	O1e–Mn1–O7	84.85(9)
Mn1–O3c	2.085(2)	O6–Mn1–O1e	92.07(8)
Mn1–Mn2	3.521(1)		
Mn2–O2	2.094(2)	O2–Mn2–O4b	92.37(9)
Mn2–O4b	2.139(2)	O2–Mn2–O4c	87.63(9)
Mn2–O6	2.244(2)	O6–Mn2–O6e	180

[a] Symmetry operations: b = $x, 2 - y, 1/2 + z$; c = $1/2 - x, -1/2 + y, 1/2 - z$; e = $1/2 - x, 3/2 - y, 1 - z$.

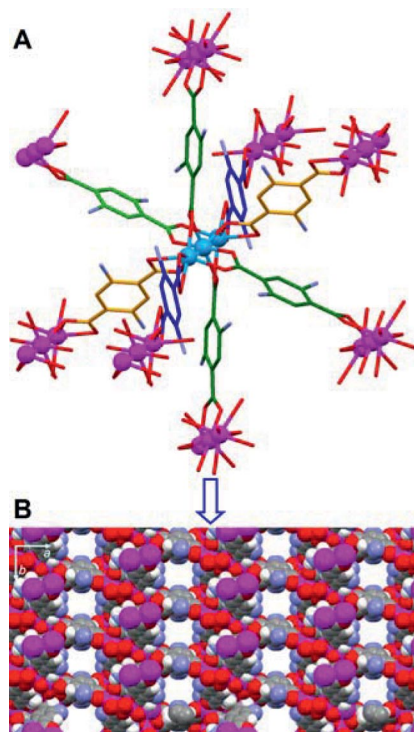


Figure 2. (A) Illustration of the building unit of the MOF observed for 1. (B) Representation (in space-filling mode) of the 3D MOF in 1, showing porous channels along the *c* axis.

varying from 2.094(2) to 2.244(2) Å (Table 1), are in normal ranges.^[18,20] The coordination angles, ranging from 87.63(9) to 92.37(9)°, are indicative of an almost perfect octahedral geometry (the ideal angle being 90°). The separation distance between the metal centres within the Mn^{II} triad is 3.521(1) Å.

The trinuclear cluster is surrounded by eight *O,O*-ligands. Thus, the trimanganese unit is connected to eight adjacent Mn^{II}₃ clusters (Figure 2A). Since each cluster is linked to eight Mn^{II}₃ neighbours in all directions, a remarkable three-dimensional MOF is generated (Figure 2B). This MOF exhibits channels along the crystallographic axis *c*, which may host guest molecules (such as substrate molecules).

[Mn₃(atpa)₃(dmf)₄] (2)

Next, the influence of the solvent on the coordination network architecture was examined. The same reaction was carried out in dmf (instead of def), at 120 °C under autogenous pressure. Yellow crystals (plates), suitable for X-ray crystallography studies, were obtained.

[Mn₃(atpa)₃(dmf)₄] (2) crystallizes in the triclinic space group *P* $\bar{1}$. A representation of the molecular structure of 2 is shown in Figure 3, and selected bond lengths and angles are listed in Table 2. Compound 2 exhibits four distinct hexacoordinate manganese(II) centres with octahedral geometries. The coordination sphere of Mn1 is formed by oxygen atoms belonging to four μ -*O,O'*-carboxylato groups (oxygen atoms O2, O2d, O5 and O5d) and two μ -*O,O',O'*-carboxylato ligands (oxygen atoms O9 and O9d). The Mn1–O bond lengths are in agreement with distances reported earlier for similar coordination environments.^[18] The coordination angles, ranging from 86.02(13) to 93.98(13)° (see Table 2), are close to 90°, the ideal value for a perfect octahedron. Mn1 is bridged to Mn2 and to its symmetry-related counterpart Mn2a [the distance Mn1–Mn2 is 3.6024(10) Å], generating a trinuclear cluster.

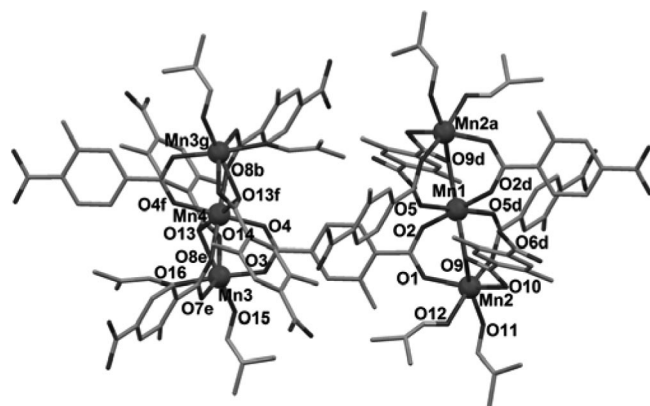


Figure 3. Representation of the crystal structure of [Mn₃(atpa)₃(dmf)₂] (2). The hydrogen atoms are omitted for clarity. Symmetry operations: a = $-1 + x, y, z$; b = $1 + x, y, z$; d = $1 - x, 1 - y, 2 - z$; e = $1 - x, 2 - y, 1 - z$; f = $2 - x, 2 - y, 1 - z$; g = $3 - x, 2 - y, 1 - z$.

Table 2. Selected bond lengths [Å] and angles [°] for compound 2.^[a]

Bond length		Bond angle	
Mn1–O2	2.127(3)	O2–Mn1–O5	86.02(13)
Mn1–O5	2.145(3)	O5–Mn1–O2d	93.98(13)
Mn1–O9	2.200(3)	O9–Mn1–O9d	180.00
Mn2–O1	2.096(4)	O1–Mn2–O6d	97.92(14)
Mn2–O9	2.260(3)	O6d–Mn2–O10	98.12(13)
Mn2–O10	2.296(4)	O10–Mn2–O12	83.98(15)
Mn2–O11	2.113(5)	O12–Mn2–O1	84.15(16)
Mn2–O12	2.245(5)	O9–Mn2–O11	159.31(16)
Mn1–Mn2	3.6024(10)		
Mn3–O3	2.108(3)	O3–Mn3–O7e	96.87(14)
Mn3–O13	2.260(3)	O7e–Mn3–O16	83.75(14)
Mn3–O14	2.285(4)	O16–Mn3–O14	84.19(13)
Mn3–O15	2.120(5)	O14–Mn3–O3	97.53(13)
Mn3–O16	2.246(4)	O13–Mn3–O15	155.21(18)
Mn3–O7e	2.115(4)	O4–Mn4–O13	89.93(13)
Mn4–O4	2.144(3)	O13–Mn4–O4f	90.07(13)
Mn4–O13	2.195(3)	O8b–Mn4–O8e	180.00
Mn4–O8b	2.133(3)		
Mn3–Mn4	3.6229(10)		

[a] Symmetry operations: b = $1 + x, y, z$; d = $1 - x, 1 - y, 2 - z$; e = $1 - x, 2 - y, 1 - z$; f = $2 - x, 2 - y, 1 - z$.

Mn2 has a highly distorted octahedral geometry, consisting of four carboxylato oxygen atoms (from two μ -*O,O'*- and one μ -*O,O',O'*-carboxylato ligands) and two *cis*-dmf oxygen atoms. The strong distortion is most likely due to the coordination of the μ -*O,O',O'*-carboxylato ligand with a very small bite angle O9–Mn2–O10 of 57.80(12)°. The Mn2–O bond lengths can be considered as normal, and the O–Mn2–O coordination angles reflect the octahedral distortion (Table 2). The distorted octahedral environment around Mn3 is comparable to that of Mn2, and the almost perfect octahedron characterizing the coordination geometry of Mn4 is very similar to that of Mn1. In the same way as for Mn1 and Mn2, Mn3 and Mn4 are bridged to each other and to the symmetry-related manganese(II) ion Mn3g, producing a linear trinuclear array of metal ions. The two trinuclear units are linked by an atpa ligand (oxygen atoms O1, O2, O3 and O4; Figure 3).

The trinuclear clusters {Mn2, Mn1, Mn2a} in 2 resemble those observed in the structure of compound 1 (see Figures 1 and 2). The main difference between these clusters is the coordination of dmf molecules in 2, whereas no def molecules are present in 1. This disparity may be explained by the bigger size of def, which apparently does not allow its coordination to the external metal ions Mn1 and Mn1a of the triad (Figure 1). As a result, the trinuclear units in 1 are further bridged to adjacent clusters, allowing the formation of a 3D framework (Figure 2B). This is obviously not the case for the clusters in 2 as the corresponding binding sites are occupied by nonbridging dmf molecules (oxygen atoms O11, O12, O15 and O16 in Figure 3); consequently, a 2D sheet is formed along the crystallographic *a* axis (Figure 4). These 2D sheets are packed in a parallel fashion, all coordinated dmf molecules filling the voids between them (see Figure 4B, C). In summary, the comparison of the X-ray structures of 1 and 2 clearly illustrates the drastic effect of the solvent on the structural topology.

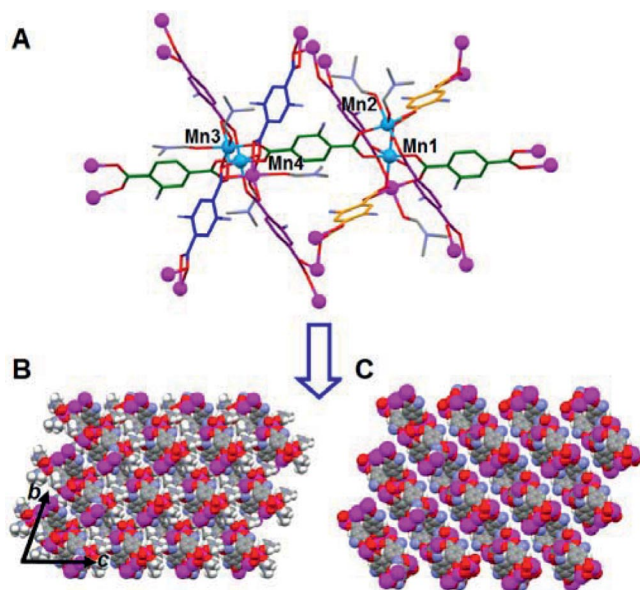


Figure 4. (A) Illustration of the building unit of the MOF observed for **2**. Representations (in space-filling mode) of the crystal packing of **2** with (B) the coordinated dmf molecules and (C) after removal of the dmf solvent molecules, showing the empty space between the 2D sheets.

$[Mn_3(tpa)_3(def)_2]$ (**3**)

Next, the effect of the amino substituent on the terephthalic ring on the 3D architecture of the MOF was investigated. The reaction of $Mn(NO_3)_2 \cdot 4H_2O$ with H_2tpa (2:3 molar ratio) in diethylformamide (def), at 120 °C under autogenous pressure, produces colourless single crystals (plates), suitable for X-ray crystallography.

$[Mn_3(tpa)_3(def)_2]$ (**3**), whose molecular structure has to be compared to that of **1**, crystallizes in the centred space group $C2/c$, as reported earlier in the literature.^[12] The structure reported here was determined at a lower temperature and is described again in detail for comparison. Selected bond lengths and angles for **3** are listed in Table 3, and a representation of its structure is shown in Figure 5. Compound **3** consists of infinite chains of manganese(II) ions bridged by two different types of deprotonated tpa ligands, exhibiting $\mu-O,O',O'$ -carboxylato (oxygen atoms O3e, O4e, O3 h and O4b in Figure 5) or $\mu-O,O'$ -carboxylato binding modes (oxygen atoms O1, O2, O5, O6, O2a and O6a in Figure 5). The crystal lattice of **3** displays two kinds of Mn^{II} ions, Mn1 and Mn2, characterized by distinct coordination environments. Mn1 is coordinated by five oxygen atoms from two $\mu-O,O',O'$ -tpa ligands (oxygen atoms O3e, O4e and O3h) and two $\mu-O,O'$ -tpa ligands (oxygen atoms O1 and O5). The last coordination site of the six-coordinate metal centre is occupied by oxygen atom O7 belonging to a def solvent molecule (Figure 5). Mn1 has a highly distorted trigonal-prismatic geometry (Figure S2), with α angles (Scheme 2) of 8.99, 35.86 and 77.85°. This last angle clearly reflects a very strong distortion of the trigonal-prismatic environment around Mn1, which is most likely due to the coordination of two $\mu-O,O',O'$ -carboxylato groups (see

Mn1 and Mn1d in Figure 6A). Actually, these steric constraints endow Mn1 with a geometry between an octahedron and a trigonal prism, but with a stronger trigonal-prismatic character.

Table 3. Selected bond lengths [Å] and angles [°] for compound **3**.^[a]

Bond length		Bond angle	
Mn1–O1	2.088(3)	O3e–Mn1–O4e	55.37(12)
Mn1–O5	2.185(3)	O4e–Mn1–O7	87.25(15)
Mn1–O6	2.552(3)	O7–Mn1–O3e	90.86(12)
Mn1–O7	2.148(3)	O1–Mn1–O3h	91.79(14)
Mn1–O3e	2.312(3)	O3 h–Mn1–O5	99.86(14)
Mn1–O4e	2.388(4)	O5–Mn1–O1	89.93(12)
Mn1–O3h	2.174(4)		
Mn1–Mn2	3.5332(9)		
Mn2–O2	2.122(4)	O2–Mn2–O6	89.24(14)
Mn2–O6	2.169(4)	O6–Mn2–O6a	82.91(15)
Mn2–O2a	2.122(4)	O6a–Mn2–O2a	89.24(14)
Mn2–O6a	2.169(4)	O2a–Mn2–O2	99.10(15)
Mn2–O4b	2.273(3)	O4b–Mn2–O4e	173.27(12)
Mn2–O4e	2.273(3)		

[a] Symmetry operations: $a = -x, y, 1/2 - z$; $b = -x, 1 - y, -z$; $c = x, 1 - y, 1/2 + z$; $h = 1/2 - x, 1/2 + y, 1/2 - z$.

The Mn1–O bond lengths ranging from 2.088(3) to 2.388(4) Å (Table 3) are comparable to those reported earlier for this compound.^[12,13] In addition, Mn1 is semi-coordinated by a bridging carboxylato group, with a Mn1–O6 contact distance of 2.552(3) Å. Mn2 exhibits an octahedral coordination geometry defined by six carboxylato oxygen atoms. Four O donors belong to four different $\mu-O,O'$ -tpa ligands (oxygen atoms O2, O6, O2a and O6a in Figure 5), while the remaining two are from two $\mu-O,O',O'$ -tpa ligands (oxygen atoms O4b and O4e in Figure 5). The Mn–O bond lengths are analogous to those reported earlier.^[12] The O–Mn2–O angles indicate a slight distortion of the octahedron, probably resulting from steric constraints due to the coordination of six tpa ligands to the metal centre (Figure 5).

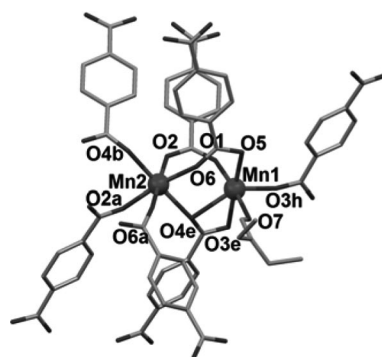


Figure 5. Representation of the coordination environments of the two types of Mn centres observed in the crystal structure of $[Mn_3(tpa)_3(def)_2]$ (**3**). The hydrogen atoms are omitted for clarity. Symmetry operations: $a = 2 - x, -1/2 + y, 3/2 - z$; $c = 1 - x, -y, 1 - z$; $d = 2 - x, -y, 1 - z$; $f = x, 1/2 - y, 1/2 + z$.

The Mn1 and Mn2 ions, generating infinite metallic chains, are held together by three different types of deprotonated tpa ligands (Figure 6A), with a Mn1–Mn2 separation distance of 3.5332(9) Å. These manganese(II) chains are connected, through three different types of tpa ligands (Figure 6A), to neighbouring chains, generating a 3D framework showing quadrangle channels along the crystallographic *a* axis (Figure 6B).

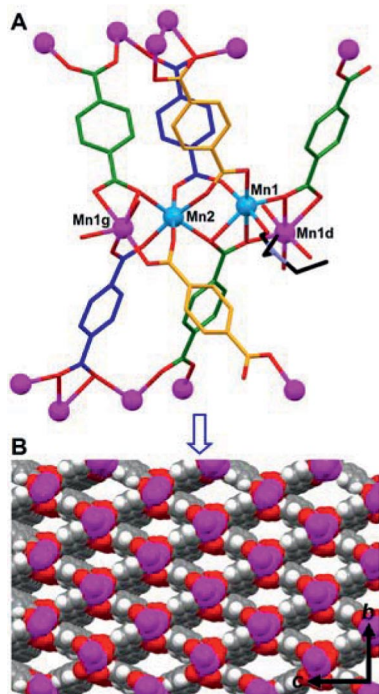


Figure 6. (A) Illustration of the building unit of the MOF observed for **3**. (B) Representation (in space-filling mode) of the 3D MOF in **3**, showing porous channels along the *a* axis (after removal of the def solvent molecules). Symmetry operations: d = *x*, 1 – *y*, –1/2 + *z*; g = 1/2 – *x*, –1/2 + *y*, 1/2 – *z* [Mn1–Mn2 3.533(1) Å; Mn1–Mn1d 3.490(1) Å; Mn2–Mn1g 3.533(1) Å].

The structures of **1** and **3** indicate that a slight modification of the bridging ligand (the presence or absence of a functional amino group) can lead to drastically distinct coordination frameworks (Figures 2 and 6). Indeed, **1** is formed by discrete trinuclear Mn^{II} clusters connected by atpa, whereas **3** is built up from metallic chains linked by tpa ligands. However, both materials possess channels that may allow substrates to reach the metal centres, and therefore they may be useful in MOF-catalyzed reactions.

[Mn₂(tpa)₂(dmf)₂] (**4**)

Similarly to compounds **1** and **2**, the solvent effect on the network architecture was subsequently investigated by replacing the def solvent, used to prepare **3**, with dmf. Hence, the reaction of Mn(NO₃)₂·4H₂O with H₂tpa (2:3 molar ratio) in dimethylformamide (dmf), at 120 °C under autogenous pressure, produces colourless block-shaped single crystals suitable for X-ray crystallography.

[Mn₂(tpa)₂(dmf)₂] (**4**), whose molecular structure was determined by single-crystal X-ray diffraction, is depicted in

Figure 7. It crystallizes in the monoclinic *P*2₁/*c* space group. Selected bond lengths and angles are given in Table 4. Compound **4** consists of two different manganese(II) centres that are triply bridged by two μ-*O*,*O'*-carboxylato and one μ-*O*,*O'*,*O'*-carboxylato groups. Mn1 is in a highly distorted octahedral coordination environment formed by five carboxylato oxygen donors (oxygen atoms O1, O2, O2c, O3f and O4f in Figure 7) and one dmf molecule (oxygen atom O9 in Figure 7). The Mn1–O bond lengths are comparable to those of the closely related compound [Mn₃(tpa)₃(dmf)₄].^[21] The strong distortion of the octahedron, most likely due to steric constraints induced by the coordination of two μ-*O*,*O'*,*O'*-tpa ligands, is revealed by the angle O1–Mn1–O3f of 100.49(5)°, which is 10.49° away from the ideal angle of 90°. The manganese(II) ion Mn2 exhibits a very similar distorted octahedral coordination environment (Figure 7) with normal Mn2–O bond lengths (Table 4). The angle O7–Mn2–O8d of 110.91(5)° characterizes the octahedral distortion caused by the bridging carboxylato ligands.

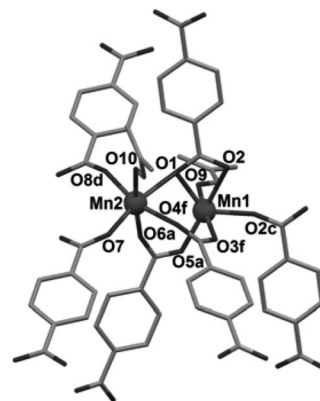


Figure 7. Representation of the crystal structure of [Mn₂(tpa)₂(dmf)₂] (**4**). The hydrogen atoms are omitted for clarity. Symmetry operations: a = 2 – *x*, –1/2 + *y*, 3/2 – *z*; c = 1 – *x*, –*y*, 1 – *z*; d = 2 – *x*, –*y*, 1 – *z*; f = *x*, 1/2 – *y*, 1/2 + *z*.

Table 4. Selected bond lengths [Å] and angles [°] for compound **4**.^[a]

Bond length		Bond angle	
Mn1–O1	2.2124(12)	O1–Mn1–O3f	100.49(5)
Mn1–O2	2.4578(13)	O3f–Mn1–O2c	86.07(5)
Mn1–O9	2.1635(13)	O2c–Mn1–O9	87.04(5)
Mn1–O5a	2.1078(13)	O9–Mn1–O1	87.09(5)
Mn1–O2c	2.1411(12)	O2–Mn1–O5a	170.11(5)
Mn1–O3f	2.0918(13)		
Mn1–Mn2	3.5512(9)		
Mn2–O1	2.3758(12)	O1–Mn2–O4f	82.85(5)
Mn2–O7	2.1249(13)	O4f–Mn2–O7	83.84(5)
Mn2–O10	2.1981(12)	O7–Mn2–O8d	110.91(5)
Mn2–O6a	2.1487(14)	O8d–Mn2–O1	82.18(5)
Mn2–O8d	2.0927(12)	O6a–Mn2–O10	174.06(6)
Mn2–O4f	2.1842(12)		

[a] Symmetry operations: a = 2 – *x*, –1/2 + *y*, 3/2 – *z*; c = 1 – *x*, –*y*, 1 – *z*; d = 2 – *x*, –*y*, 1 – *z*; f = *x*, 1/2 – *y*, 1/2 + *z*.

The crystal lattice of **4** is analogous to that of **3** (Figures 8 and 6). Indeed, the Mn1 and Mn2 ions, separated by a distance of 3.5512(9) Å, are bridged by two different types of deprotonated tpa ligands, producing infinite chains

(Figure 8A). These chains are linked by tpa ligands to neighbouring chains, thus generating a 3D framework with quadrangle channels along the crystallographic *a* axis (Figure 6B), closely related to the framework in **3**.

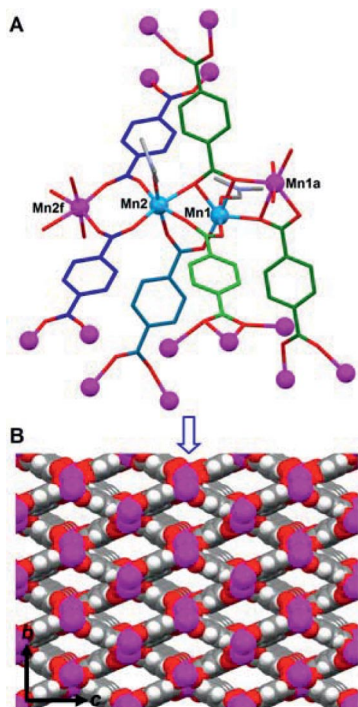
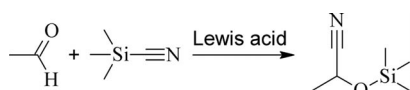


Figure 8. (A) Illustration of the building unit of the MOF observed for **4**. (B) Representation (in space-filling mode) of the 3D MOF in **4**, showing porous channels along the *a* axis (after removal of the dmf solvent molecules). Symmetry operations: $a = 2 - x, -1/2 + y, 3/2 - z$; $f = x, 1/2 - y, 1/2 + z$.

Therefore, the use of dmf instead of def does not lead to significant modifications of the coordination network. Actually, the sole difference between the Mn^{II} centres in **4**, relative to **3**, is that both Mn1 and Mn2 are coordinated by one dmf molecule. In contrast, only one of the two Mn^{II} ions in **3**, that is, Mn1, is coordinated by one def solvent molecule (Figures 5 and 7). This difference may be due to the larger size of def, which apparently does not allow the binding of two def molecules per dinuclear unit, contrary to dmf in **4**.

Catalytic Studies

The catalytic properties of MOFs **1–4** as Lewis catalysts for the cyanosilylation of acetaldehyde were investigated (Scheme 3). The reaction of an aldehyde with trimethylsilyl cyanide in the presence of a Lewis acid produces an *O*-silylated cyanohydrin.^[22]



Scheme 3. Cyanosilylation of acetaldehyde catalyzed by a Lewis acid.

Recently, Long and co-workers have used the compound $\text{Mn}_3[(\text{Mn}_4\text{Cl})_3(\text{btt})_8(\text{CH}_3\text{OH})_{10}]_2$ as catalyst for this reaction. It was assumed that the Mn²⁺ ions exposed on the surface of the framework act as Lewis acid sites.^[23] The SBUs (secondary building units) of copper(II)-,^[24] cadmium(II)-^[25] and samarium(III)-based^[26] MOFs have served as active centres for the cyanosilylation of aldehydes. To the best of our knowledge, the present utilization of MOFs **1–4** represents the first examples of Mn-based SBUs as Lewis catalysts for the preparation of a cyanohydrin from an aldehyde.

The room-temperature reaction of 0.9 mmol acetaldehyde with two equivalents of trimethylsilyl cyanide (TMSCN) in the presence of 0.0134 mmol freshly prepared MOF **1** (see Supporting Information for experimental details) produces 64% *O*-silylated lactonitrile (Scheme 3) after 24 hours of reaction (Table 5). Amazingly, no conversion is detected up to a reaction time of four hours (Table 5 and Figure S3A). This very long induction time may be explained by the presence of def solvent molecules in the channels of MOF **1** (which has not been dried prior to its use as cyanosilylation catalyst). Actually, def was detected by gas chromatography (GC), suggesting the release of this solvent from the MOF material during the catalysis process. This release is further confirmed by the re-use of MOF **1** after the first catalytic run. Indeed, the second catalytic run reveals a dramatically higher catalytic activity of MOF **1** (Table 5 and Figure S3A) and no induction time. In fact, 60% conversion is reached after one hour, whereas one day was required during the first run (Table 5). Moreover, 80% conversion is achieved after three hours, which is comparable with literature values obtained with homogeneous Lewis acids.^[27] This time, def could not be detected by GC. Next, the reaction was carried out with freshly prepared MOF **1** that was dried just before its use as catalyst. These experimental conditions led to 81% conversion after a reaction time of three hours, like the second catalytic run described earlier.

Table 5. Room-temperature cyanosilylation of acetaldehyde catalyzed by MOFs **1–4**.

MOF catalyst	Conversion [%]				
	1 h	2 h	3 h	4 h	24 h
MOF 1 1 st run ^[a]	0	0	0	1	64
MOF 1 2 nd run	60	77	80	80	80
MOF 2 1 st run	1	12	29	40	70
MOF 2 2 nd run	16	36	51	66	80
MOF 3 1 st run	27	66	74	77	79
MOF 3 2 nd run	68	74	74	76	80
MOF 4 1 st run	76	81	82	82	82
MOF 4 2 nd run	79	82	82	82	82

[a] With dried MOF **1**, 81% conversion is reached after 3 h reaction time.

All these results clearly indicate that the reaction is promoted by heterogeneous MOF **1**. In addition, no silylation reaction takes place with powdered $\text{Mn}(\text{NO}_3)_2 \cdot 4\text{H}_2\text{O}$ or with the supernatant liquid of a CH_2Cl_2 suspension of

MOF **1**, further corroborating the essential involvement of the coordination network as catalyst. The structural integrity of MOF **1** was established by X-ray powder diffraction (XRPD). The XRPD patterns of MOF **1** were recorded before and after a catalytic run (see Figure S4). These XRPD studies show that the XRPD patterns are fully conserved during the catalytic reaction. In addition, an attempt was made to convert benzaldehyde to the corresponding cyanosilylated product, with MOF **1** as catalyst. After 24 hours, only a conversion of 2% is observed, suggesting that the reaction principally occurs in the cavities of the material. It appears that benzaldehyde can not enter the pores of the MOF catalyst for steric reasons. Further investigations are currently carried out to study the mechanism of this reaction.

MOFs **2–4** were dried under reduced pressure, at 50 °C for 12 hours, prior to their use as catalysts, to remove lattice solvent molecules that may retard the cyanosilylation reaction. With MOF **2**, the reaction is slow with only about 1% conversion to O-silylated lactonitrile after one hour (Table 5 and Figure S3B). The cyanosilylation of acetaldehyde proceeds smoothly, reaching a conversion of 70% after 24 hours (Table 5). The heterogeneous catalyst was then filtered out and re-used in a second catalytic run. Surprisingly, a higher catalytic activity of MOF **2** is observed (see Table 5 and Figure S3B). This higher catalytic activity of re-used MOF **2** can be justified by a gradual release of coordinated dmf molecules, through their replacement by reactant molecules (acetaldehyde and/or trimethylsilyl cyanide). Actually, a GC peak corresponding to dmf was detected during the first catalytic run, while it is not observed with re-used MOF **2**. These results suggest that the coordinated dmf molecules in **2** are difficult to be taken out and exchanged (for instance by a substrate molecule), probably because they are not easily accessible. Indeed, as is clearly evidenced in Figure 4B, C, the coordinated dmf molecules are located in small chinks between 2D sheets that are tightly packed. The accessibility of the Lewis Mn sites is clearly inferior in **2** to that in **1** (see Figures 2B and 4C).

MOF **3** and MOF **4** exhibit comparable activities, which are significantly higher than that observed for MOF **1**, and better than that obtained with MOF **2** (Table 5 and Figure S3). As mentioned earlier, MOFs **3** and **4** have similar structural features (Figures 6B and 8B); therefore, it is not surprising that their catalytic behaviour is analogous. In addition, in contrast to MOFs **1** and **2**, there are almost no differences between the first and second runs for MOFs **3** and **4** (Table 5 and Figures S3C and S3D). This can be explained by an easier access of solvent/substrate molecules into the large channels. Accordingly, the removal of solvent molecules by drying MOFs **3** and **4** under reduced pressure, at 50 °C for 12 hours, appears to be more effective (relative to MOFs **1** and **2**), hence increasing the availability of the Lewis Mn sites for catalysis. In that context, the lower catalytic activity shown by MOF **1**, which possesses porous channels like MOFs **3** and **4**, most likely results from the presence of amino groups situated inside the cavities, which make the access to the Lewis acid sites more difficult.

Conclusions

In summary, the preparation of MOFs **1–4**, whose notable structural disparities result from the use of (i) different solvents during their synthesis, that is, dmf or def, or (ii) slightly distinct ligands, that is, terephthalic acid (H_2tpa) or 2-aminoterephthalic acid (H_2atpa), has clearly revealed the crucial influence of a priori unimportant experimental parameters on framework topologies. These MOFs, showing different molecular architectures, naturally exhibit distinct catalytic activities for the cyanosilylation of acetaldehyde. However, all four MOFs are effective heterogeneous catalysts for this reaction, and moreover they can be re-used without any loss of activity.

Experimental Section

General: All reagents were commercially available (Acros Organics) and used without any further purification. All reactions were carried out in aerobic conditions. IR spectra were recorded by using a Perkin–Elmer Paragon 1000 spectrophotometer equipped with a Golden Gate Diamond ATR as a sample support, and data are represented as the frequency of absorption (cm^{-1}). Powder X-ray diffraction patterns were obtained with a Philips X'pert diffractometer. The surface areas were measured with a Nova Surface Area Analyser. Thermogravimetric analyses were performed with a TAG 24 simultaneous a-symmetrical thermo analyzer. C, H, N analyses were carried out with an automatic Perkin–Elmer 2400 Series II CHNS/O analyzer. GC analysis was carried out by using a Hewlett–Packard 5890 Series GC (CP-Sil-5 CB WCOT Fused Silica capillary column, 50 m \times 0.25 mm inside diameter, 0.25 μm film thickness) with dihydrogen as the carrier gas. The oven temperature was programmed as follows: the temperature was held at 50 °C for 2 min and then raised to 250 °C at a rate of 10 °C/min, where it was held for 3 min.

[Mn₃(atpa)₂(Hatpa)₂] (1): Mn(NO₃)₂·4H₂O (92 mg, 0.365 mmol) and H₂atpa (99 mg, 0.5475 mmol) were dissolved in *N,N*-diethylformamide (def, 10 mL). The resulting reaction mixture was introduced into a pressure tube (Corning Pyrex culture tube, diameter 20 mm, height 220 mm), and the tube was sealed. It was placed in an oven at 120 °C overnight. Colourless block-shaped single crystals, suitable for X-ray diffraction analysis, were obtained. The single crystals were isolated, washed with dichloromethane and dried overnight at 50 °C, under reduced pressure. Yield: 66 mg (62% based on Mn). C₃₂H₂₂Mn₃N₄O₁₆ (883.35): calcd. C 43.52, H 2.52, N 6.34; found C 43.37, H 2.55, N 6.41. IR: $\tilde{\nu}$ = 1615, 1557, 1368, 1327, 769 cm^{-1} . The thermogravimetric analysis of **1** shows a first weight loss between 155 °C and 200 °C, corresponding to the release of solvent molecules. Above 205 °C, the framework starts to collapse, as an abrupt weight loss is observed (Figure S5). Surface area of MOF **1** after washing in dichloromethane for 2 d: 16 m² g⁻¹.

[Mn₃(atpa)₃(dmf)₄] (2): The reaction of Mn(NO₃)₂·4H₂O and H₂atpa in *N,N*-dimethylformamide (dmf) under the reaction conditions applied to obtain **1** (see above) yields yellow crystals of **2**. Yield: 86 mg (71% based on Mn). C₃₆H₄₃Mn₃N₇O₁₆ (994.59): calcd. C 43.47, H 4.36, N 9.86; found C 42.91, H 3.35, N 10.83. IR: $\tilde{\nu}$ = 2364, 1652, 1558, 1386, 1250, 1106, 769, 668 cm^{-1} . The thermogravimetric analysis of **2** reveals that the material loses solvent molecules between 150 °C and 200 °C. Above 205 °C, the framework is degraded (Figure S6).

Table 6. Crystal data and structure refinement for compounds 1–4.

	1	2	3	4
Empirical formula	C ₃₂ H ₂₂ Mn ₃ N ₄ O ₁₆	C ₃₆ H ₄₃ Mn ₃ N ₇ O ₁₆	C ₃₄ H ₃₄ Mn ₃ N ₂ O ₁₄	C ₂₂ H ₂₂ Mn ₂ N ₂ O ₁₀
Formula weight [g mol ⁻¹]	883.35	994.59	859.45	584.30
Temperature [K]	100(2)	150(2)	150(2)	150(2)
Wavelength [Å]	0.77490	0.75150	0.71073	0.75150
Crystal system	monoclinic	triclinic	monoclinic	monoclinic
Space group	C2/c	P1	C2/c	P2 ₁ /c
<i>a</i> [Å]	34.251(3)	9.816(2)	24.804(2)	13.414(3)
<i>b</i> [Å]	10.062(1)	15.329(3)	10.7115(4)	10.162(2)
<i>c</i> [Å]	17.911(2)	15.716(3)	17.332(2)	17.653(4)
<i>α</i> [°]	90	71.78(3)	90	90
<i>β</i> [°]	98.297(1)	84.48(3)	129.90(2)	90.21(3)
<i>γ</i> [°]	90	83.60(3)	90	90
Volume [Å ³]	6108.1(11)	2227.5(9)	3532.7(12)	2406.3(8)
<i>Z</i>	4	2	4	4
Calculated density [g cm ⁻³]	0.952	1.483	1.616	1.613
Absorption coefficient [mm ⁻¹]	0.828	1.055	1.128	1.283
<i>F</i> (000)	1750	1022	1756	1192
<i>θ</i> range for data collection [°]	3.0–26.9	1.5–28.0	3.04–26.36	1.60–30.06
Reflections collected	21065	34750	34047	10717
Reflections unique	5041	7974	3605	5885
<i>R</i> (int)	0.041	0.045	0.145	0.034
Parameters	309	632	242	329
Goodness-of-fit on <i>F</i> ²	0.991	1.694	1.017	1.074
<i>R</i> ₁ [<i>I</i> > 2σ(<i>I</i>)] ^[a]	0.0428	0.1124	0.0564	0.0444
<i>wR</i> ₂ [<i>I</i> > 2σ(<i>I</i>)] ^[b]	0.1332	0.3426	0.1168	0.1257

[a] $R_1 = \sum ||F_o| - |F_c|| / \sum |F_o|$. [b] $wR_2 = \{\sum [w(F_o^2 - F_c^2)^2] / \sum [w(F_o^2)^2]\}^{1/2}$.

[Mn₃(tpa)₃(def)₂] (3): The reaction of Mn(NO₃)₂·4H₂O and H₂tpa in def under the reaction conditions applied to obtain **1** (see above) yields colourless crystals of **3**. Yield: 60 mg (58% based on Mn). C₃₄H₃₄Mn₃N₂O₁₄ (859.45): calcd. C 47.52, H 3.99, N 3.26; found C 47.51, H 4.39, N 3.51. IR: $\tilde{\nu}$ = 1616, 1575, 1386, 1331, 771, 750, 524 cm⁻¹. The thermogravimetric analysis of **3** reveals that this compound is thermally stable up to about 230 °C, after which it collapses (Figure S7).

[Mn₂(tpa)₂(dmf)₂] (4): The reaction of Mn(NO₃)₂·4H₂O and H₂tpa in dmf under the reaction conditions applied to obtain **1** (see above) yields colourless crystals of **4**. Yield: 91 mg (85% based on Mn). C₂₂H₂₂Mn₂N₂O₁₀ (584.30): calcd. C 45.22, H 3.79, N 4.79; found C 45.12, H 3.74, N 4.56. IR: $\tilde{\nu}$ = 1652, 1622, 1575, 1386, 1104, 814, 752, 668 cm⁻¹. The thermogravimetric analysis of **4** shows that this compound is stable up to 100 °C and is dramatically degraded above 150 °C (Figure S8).

Typical MOF-catalyzed Cyanosilylation Reaction: MOF (0.134 mmol) was introduced into a round-bottomed flask containing CH₂Cl₂ (20 mL) freshly distilled over CaH₂. Next, acetaldehyde (0.900 mmol, 39.4 mg), followed by trimethylsilyl cyanide (TMSCN, 1.800 mmol, 186 mg), was added, and the reaction was carried out under an argon atmosphere. The progress of the reaction was monitored by gas chromatography (GC) at regular intervals (at 1, 2, 3, 4 and 24 h). The conversions were determined by GC with dodecane as internal standard.

Structural Determination: Crystal data and structure refinement for compounds **1–4** are listed in Table 6. Data for compound **1** were collected with a Bruker APEX II CCD diffractometer on the Advanced Light Source beamline 11.3.1 at Lawrence Berkeley National Laboratory, from a silicon 111 monochromator (*T* = 100 K, λ = 0.7749 Å). Data reduction and absorption corrections were performed with SAINT^[28] and SADABS^[29] respectively. For compounds **2** and **4**, data were collected by using a single-axis

HUBER diffractometer on station BM16 of the European Synchrotron Radiation Facility, Grenoble, France (*T* = 150 K, λ = 0.7515 Å). Cell refinement, data reduction and absorption corrections were performed with the HKL-2000 suite.^[30] For compound **3**, data were collected with an Oxford Diffraction Excalibur diffractometer with Enhanced Mo-*K*_α radiation (*T* = 150 K, λ = 0.71073 Å) at the X-ray diffraction service of the University of Zaragoza. Cell refinement and data reduction were performed with the CrysAlisPro suite. Absorption corrections were performed from directors *cosinus* with MULABS as implemented in PLATON.^[31] All structures were solved by direct methods and refined on *F*² with the SHELXTL suite.^[32] CCDC-771994, -771995, -771996 and -771997 contain the supplementary crystallographic data for compounds **1–4**, respectively. These data can be obtained free of charge from The Cambridge Crystallographic Data Centre via www.ccdc.cam.ac.uk/data_request/cif.

Supporting Information (see footnote on the first page of this article): Figures illustrating the trigonal-prismatic coordination environments around the Mn^{II} ions in **1** and **3**; catalytic curves for the cyanosilylation of acetaldehyde catalyzed by **1–4**; XRPD patterns for **1**; TGA curves for **1–4**.

Acknowledgments

Support from the Graduate Research School Combination “Catalysis” and the European Cooperation in the Field of Science and Technology (COST) program Action D35/0011, the Spanish Consejo Superior de Investigaciones Científicas (CSIC), as well as from the Spanish Ministerio de Ciencia y Innovación, for access to BM16 at the European synchrotron radiation facility (ESRF) through grant number 16-01-723, are acknowledged. The Advanced Light Source is supported by the Director, Office of Science, Office of Basic Energy Sciences, of the U.S. Department of Energy under Contract No. DE-AC02-05CH11231.

- [1] S. Natarajan, P. Mahata, *Chem. Soc. Rev.* **2009**, *38*, 2304–2318; J. Seo, H. Sakamoto, R. Matsuda, S. Kitagawa, *J. Nanosci. Nanotechnol.* **2010**, *10*, 3–20; G. Ferey, *Chem. Soc. Rev.* **2008**, *37*, 191–214; J. L. C. Rowsell, O. M. Yaghi, *Microporous Mesoporous Mater.* **2004**, *73*, 3–14.
- [2] D. J. Tranchemontagne, J. L. Mendoza-Cortes, M. O’Keeffe, O. M. Yaghi, *Chem. Soc. Rev.* **2009**, *38*, 1257–1283; J. J. Perry, J. A. Perman, M. J. Zaworotko, *Chem. Soc. Rev.* **2009**, *38*, 1400–1417.
- [3] L. J. Murray, M. Dinca, J. R. Long, *Chem. Soc. Rev.* **2009**, *38*, 1294–1314; J. R. Li, R. J. Kuppler, H. C. Zhou, *Chem. Soc. Rev.* **2009**, *38*, 1477–1504; S. Q. Ma, *Pure Appl. Chem.* **2009**, *81*, 2235–2251.
- [4] S. Kitagawa, R. Kitaura, S. Noro, *Angew. Chem. Int. Ed.* **2004**, *43*, 2334–2375; M. Plabst, L. B. McCusker, T. Bein, *J. Am. Chem. Soc.* **2009**, *131*, 18112–18118; J. J. Zhang, Y. Zhao, S. A. Gamboa, M. Munoz, A. Lachgar, *Eur. J. Inorg. Chem.* **2008**, 2982–2990.
- [5] M. Kurmoo, *Chem. Soc. Rev.* **2009**, *38*, 1353–1379; Y. J. Zhang, T. Liu, S. Kanegawa, O. Sato, *J. Am. Chem. Soc.* **2010**, *132*, 912–913; A. Demessence, A. Mesbah, M. Francois, G. Rogez, P. Rabu, *Eur. J. Inorg. Chem.* **2009**, 3713–3720.
- [6] M. D. Allendorf, C. A. Bauer, R. K. Bhakta, R. J. T. Houk, *Chem. Soc. Rev.* **2009**, *38*, 1330–1352; M. S. Wang, S. P. Guo, Y. Li, L. Z. Cai, J. P. Zou, G. Xu, W. W. Zhou, F. K. Zheng, G. C. Guo, *J. Am. Chem. Soc.* **2009**, *131*, 13572–13573; J. Rocha, F. A. A. Paz, F. N. Shi, R. A. S. Ferreira, T. Trindade, L. D. Carlos, *Eur. J. Inorg. Chem.* **2009**, 4931–4945.
- [7] Z. G. Xie, L. Q. Ma, K. E. de Krafft, A. Jin, W. B. Lin, *J. Am. Chem. Soc.* **2010**, *132*, 922–923; S. Achmann, G. Hagen, J. Kita, I. M. Malkowsky, C. Kiener, R. Moos, *Sensors* **2009**, *9*, 1574–1589; B. V. Harbuzaru, A. Corma, F. Rey, J. L. Jorda, D. Ananias, L. D. Carlos, J. Rocha, *Angew. Chem. Int. Ed.* **2009**, *48*, 6476–6479.
- [8] S. Bordiga, C. Lamberti, G. Ricchiardi, L. Regli, F. Bonino, A. Damin, K. P. Lillerud, M. Bjorgen, A. Zecchina, *Chem. Commun.* **2004**, 2300–2301.
- [9] L. Q. Ma, C. Abney, W. B. Lin, *Chem. Soc. Rev.* **2009**, *38*, 1248–1256; J. Lee, O. K. Farha, J. Roberts, K. A. Scheidt, S. T. Nguyen, J. T. Hupp, *Chem. Soc. Rev.* **2009**, *38*, 1450–1459; K. Ohara, M. Kawano, Y. Inokuma, M. Fujita, *J. Am. Chem. Soc.* **2010**, *132*, 30–31.
- [10] M. J. Zaworotko, *Angew. Chem. Int. Ed.* **2000**, *39*, 3052–3054.
- [11] K. O. Kongshaug, H. Fjellvag, *Polyhedron* **2007**, *26*, 5113–5119.
- [12] N. L. Rosi, J. Kim, M. Eddaoudi, B. L. Chen, M. O’Keeffe, O. M. Yaghi, *J. Am. Chem. Soc.* **2005**, *127*, 1504–1518.
- [13] R. D. Poulson, A. Bentien, M. Chevalier, B. B. Iversen, *J. Am. Chem. Soc.* **2005**, *127*, 9156–9166.
- [14] J. L. C. Rowsell, E. C. Spencer, J. Eckert, J. A. K. Howard, O. M. Yaghi, *Science* **2005**, *309*, 1350–1354; G. Ferey, C. Mellot-Draznieks, C. Serre, F. Millange, J. Dutour, S. Surble, I. Margiolaki, *Science* **2005**, *309*, 2040–2042.
- [15] K. Barthelet, K. Adil, F. Millange, C. Serre, D. Riou, G. Ferey, *J. Mater. Chem.* **2003**, *13*, 2208–2212; K. Barthelet, J. Marrot, G. Ferey, D. Riou, *Chem. Commun.* **2004**, 520–521; D. F. Sun, R. Cao, W. H. Bi, J. B. Weng, M. C. Hong, Y. C. Liang, *Inorg. Chim. Acta* **2004**, *357*, 991–1001; M. Kurmoo, H. Kumagai, M. A. Green, B. W. Lovett, S. J. Blundell, A. Ardavan, J. Singleton, *J. Solid State Chem.* **2001**, *159*, 343–351.
- [16] F. Millange, N. Guillou, R. I. Walton, J. M. Greneche, I. Margiolaki, G. Ferey, *Chem. Commun.* **2008**, 4732–4734; H. F. Clausen, J. Overgaard, Y. S. Chen, B. B. Lversen, *J. Am. Chem. Soc.* **2008**, *130*, 7988–7996; F. K. Wang, S. Y. Yang, R. B. Huang, L. S. Zheng, S. R. Batten, *Crystengcomm* **2008**, *10*, 1211–1215.
- [17] Y. G. Wu, N. W. Zheng, R. Y. Yang, H. T. Xu, E. Y. Ye, *J. Mol. Struct.* **2002**, *610*, 181–186; C. A. Black, J. S. Costa, W. T. Fu, C. Massera, O. Roubeau, S. J. Teat, G. Aromi, P. Gamez, J. Reedijk, *Inorg. Chem.* **2009**, *48*, 1062–1068; K. L. Zhang, H. Y. Gao, N. Qiao, F. Zhou, G. W. Diao, *Inorg. Chim. Acta* **2008**, *361*, 153–160; C. B. Liu, X. J. Zheng, Y. Y. Yang, L. P. Jin, *Inorg. Chem. Commun.* **2005**, *8*, 1045–1048; H. T. Xu, N. W. Zheng, X. L. Jin, R. Y. Yang, Z. Q. Li, *Chem. Lett.* **2002**, 350–351; M. E. Braun, C. D. Steffek, J. Kim, P. G. Rasmussen, O. M. Yaghi, *Chem. Commun.* **2001**, 2532–2533; J. S. Costa, P. Gamez, C. A. Black, O. Roubeau, S. J. Teat, J. Reedijk, *Eur. J. Inorg. Chem.* **2008**, 1551–1554.
- [18] R. A. Reynolds, W. R. Dunham, D. Coucouvanis, *Inorg. Chem.* **1998**, *37*, 1232–1241.
- [19] S. G. Sreerama, S. Pal, S. Pal, *Inorg. Chem. Commun.* **2001**, *4*, 656–660.
- [20] E. V. Amel’chenkova, T. O. Denisova, S. E. Nefedov, *Mendeleev Commun.* **2004**, 103–104.
- [21] Y. L. Fu, J. L. Ren, H. P. Qiao, S. W. Ng, *Acta Crystallogr., Sect. E* **2004**, *60*, M1510–M1512; F. Luo, Y. X. Che, J. M. Zheng, *Inorg. Chem. Commun.* **2008**, *11*, 358–362.
- [22] W. J. Greenlee, D. G. Hangauer, *Tetrahedron Lett.* **1983**, *24*, 4559–4560; M. Bandini, P. G. Cozzi, A. Garelli, P. Melchiorre, A. Umani-Ronchi, *Eur. J. Org. Chem.* **2002**, 3243–3249.
- [23] S. Horike, M. Dinca, K. Tamaki, J. R. Long, *J. Am. Chem. Soc.* **2008**, *130*, 5854–5855.
- [24] K. Schlichte, T. Kratzke, S. Kaskel, *Microporous Mesoporous Mater.* **2004**, *73*, 81–88.
- [25] M. Fujita, Y. J. Kwon, S. Washizu, K. Ogura, *J. Am. Chem. Soc.* **1994**, *116*, 1151–1152.
- [26] O. R. Evans, H. L. Ngo, W. B. Lin, *J. Am. Chem. Soc.* **2001**, *123*, 10395–10396.
- [27] G. Rajagopal, S. S. Kim, S. C. George, *Appl. Organomet. Chem.* **2007**, *21*, 198–202; H. C. Aspinall, N. Greeves, P. M. Smith, *Tetrahedron Lett.* **1999**, *40*, 1763–1766.
- [28] SAINT, version 7.36a Bruker AXS, Madison, Wisconsin.
- [29] SADABS, version 2.0 Bruker AXS, Madison, Wisconsin.
- [30] Z. Otwinowski, W. Minor, *Methods in Enzymology*, Academic Press Inc., San Diego, **1997**, p. 307–326.
- [31] A. L. Spek, PLATON, A Multipurpose Crystallographic Tool, Utrecht University, Utrecht, The Netherlands, **2008**; A. L. Spek, *J. Appl. Crystallogr.* **2003**, *36*, 7–13.
- [32] G. M. Sheldrick, *Acta Crystallogr., Sect. A* **2008**, *64*, 112–122.

Received: April 5, 2010

Published Online: June 25, 2010

Synthesis, Structure and Optical Studies of a Family of Three-Dimensional Rare-Earth Aminoisophthalates $[M(\mu_2\text{-OH})(\text{C}_8\text{H}_5\text{NO}_4)]$ ($M = \text{Y}^{3+}$, La^{3+} , Pr^{3+} , Nd^{3+} , Sm^{3+} , Eu^{3+} , Gd^{3+} , Dy^{3+} , and Er^{3+})

Debajit Sarma,^[a] Manikanda Prabu,^[a] Silvanose Biju,^[b] M. L. P. Reddy,^{*,[b]} and Srinivasan Natarajan^{*,[a]}

Keywords: Rare earths / Metal-organic frameworks / Luminescence / Doping

A hydrothermal reaction of the acetate salts of the rare-earths, 5-aminoisophthalic acid (H_2AIP), and NaOH at $150\text{ }^\circ\text{C}$ for 3 days gave rise to a new family of three-dimensional rare-earth aminoisophthalates, $[M(\mu_2\text{-OH})(\text{C}_8\text{H}_5\text{NO}_4)]$ [$M = \text{Y}^{3+}$ (I), La^{3+} (II), Pr^{3+} (III), Nd^{3+} (IV), Sm^{3+} (V), Eu^{3+} (VI), Gd^{3+} (VII), Dy^{3+} (VIII), and Er^{3+} (IX)]. The structures contain M-O(H)-M chains connected by AIP anions. The AIP ions are connected to five metal centers and each metal center is connected with five AIP anions giving rise to a unique (5,5) net. To the best of our knowledge, this is the first observation

of a (5,5) net in metal-organic frameworks that involve rare-earth elements. The doping of $\text{Eu}^{3+}/\text{Tb}^{3+}$ ions in place of $\text{Y}^{3+}/\text{La}^{3+}$ in the parent structures gave rise to characteristic metal-centered emission (red = Eu^{3+} , green = Tb^{3+}). Life-time studies indicated that the excited emission states in the case of Eu^{3+} (4 mol-% doped) are in the range 0.287–0.490 ms and for Tb^{3+} (4 mol-% doped) are in the range of 1.265–1.702 ms. The Nd^{3+} -containing compound exhibits up-conversion behavior based on two-photon absorption when excited using $\lambda = 580\text{ nm}$.

Introduction

Metal-organic framework (MOF) compounds exhibiting open structures, which often mimic classic inorganic analogues,^[1] continue to provide opportunities for synthetic chemists as they are considered as promising materials for many applications.^[2] In many MOF compounds, a fine balance between the coordination requirements of the metal and the organic linkers is achieved to form a given structure.^[3] From the available literature on MOFs, it is clear that transition-metal-based compounds dominate over the other elements of the periodic table in this type of structure. However, the lanthanide elements, in spite of their higher coordination preferences, form interesting framework structures.^[4]

The impetus for research on lanthanide elements is due to their interesting emission properties. The f electrons remain localized in all the compounds, giving rise to narrow f→f transitions. The earliest study of f→f transitions was of Eu^{3+} complexes in the early 40s.^[5] The narrow f→f tran-

sitions are attractive for the study of many optical properties and for exploring light-emitting device (LED) applications.^[6] The f→f transitions, however, are spin- and parity-forbidden and suitable sensitizers are required^[7] to understand and exploit the luminescence behavior of the rare-earth ions. It has been shown that the incorporation of $\text{Eu}^{3+}/\text{Sm}^{3+}$ (red: $\lambda \approx 590\text{--}700\text{ nm}$), $\text{Tb}^{3+}/\text{Er}^{3+}$ (green: $\lambda \approx 490\text{--}560\text{ nm}$), and $\text{Tm}^{3+}/\text{Ce}^{3+}$ (blue: $\lambda \approx 450\text{--}490\text{ nm}$) into host lattices gives rise to sharp characteristic emissions.^[8] There is also a growing interest in the study of the emission behavior of Nd^{3+} compounds as Nd^{3+} emissions can be observed in the near-IR region ($\lambda = 800\text{--}1700\text{ nm}$). In addition, Nd^{3+} compounds have been shown to exhibit up-conversion behavior by converting IR radiation into the visible region through a two-photon absorption process.^[9]

We were interested in studying MOF structures based on lanthanides to explore their reactivity and to understand the various photophysical properties. In this connection, the isolation of a CdCl_2 -related pillared layer structure is important and interesting.^[10] As a continuation of this theme, we have now isolated a new family of rare-earth compounds of the general formula $[M(\mu_2\text{-OH})(\text{C}_8\text{H}_5\text{NO}_4)]$ [$M = \text{Y}^{3+}$ (I), La^{3+} (II), Pr^{3+} (III), Nd^{3+} (IV), Sm^{3+} (V), Eu^{3+} (VI), Gd^{3+} (VII), Dy^{3+} (VIII), and Er^{3+} (IX)] and characterized them by a variety of techniques. Doping of 4, 6, and 10 mol-% Eu and Tb in place of Y and La was carried out to investigate metal-centered emissions. In this paper we describe the synthesis, structure, and photophysical studies of the rare-earth MOF compounds.

[a] Framework Solids Laboratory, Solid State and Structural Chemistry Unit, Indian Institute of Science, Bangalore 560012, India

E-mail: snatarajan@sscu.iisc.ernet.in

[b] Chemical Sciences and Technology Division, National Institute for Interdisciplinary Science & Technology (NIIST), Thiruvananthapuram 695019, India

E-mail: mlpredy55@gmail.com

Supporting information for this article is available on the WWW under <http://dx.doi.org/10.1002/ejic.201000225>.

Results and Discussions

Structure

Of the nine compounds prepared in this study, we have been able to isolate suitable single crystals only in the cases of the La-, Pr-, and Nd-containing compounds. The other compounds were obtained as good quality, highly crystalline, powdered samples. We determined the structures of the La-, Pr-, and Nd-containing compounds by employing single-crystal methods. The other compounds were identified and characterized by powder XRD studies. The powder XRD patterns of these compounds matched exactly the simulated XRD patterns generated from the single-crystal structures of the La, Pr, and Nd compounds. In all cases there was a good match between the experimental and simulated PXRD patterns, which suggests that pure single-phasic materials were obtained (see the Supporting Information, Figures S1–S5). Thus, compounds with Y^{3+} (I), Sm^{3+} (V), Eu^{3+} (VI), Gd^{3+} (VII), Dy^{3+} (VIII), and Er^{3+} (IX), were isolated and characterized.

All the compounds are isostructural and the asymmetric unit consists of 10 non-hydrogen atoms of which only one M^{3+} ion ($M = La, Pr, \text{ and } Nd$) is crystallographically independent. The M^{3+} ion occupies a special position (4c) with a site multiplicity of 0.5. The asymmetric unit also contains one μ_2 -hydroxy group and half an aminoisophthalate (AIP) unit (Figure S6). The M^{3+} ions are surrounded by one nitrogen, two μ_2 -hydroxy oxygens, and six carboxylate oxygens forming an MO_8N polyhedra (Figure S7) with a distorted tricapped trigonal prismatic coordination environment around the central M^{3+} ions (Figure 1, a). The M–O bond lengths are in the range of 2.318(4)–2.654(3) Å (av. 2.556 Å for La, 2.511 Å for Pr, and 2.554 Å for Nd) and the M–N bond length is 2.851(5) Å for La, 2.769(5) Å for Pr, and 2.838(5) Å for Nd. The O/N–M–O/N bond angles are in the range 49.21(9)–146.09(7)°. Selected bond lengths are given in Table 1.

The structure consists of a linkage between the M^{3+} ions and the AIP anions. Thus, each AIP anion is bonded to five different metal centers (Figure S8). The two carboxylate groups exhibit similar connectivity bonding with two M^{3+} ions through one μ_2 -connectivity and one μ_1 -connectivity. The amino group binds with the fifth metal center.

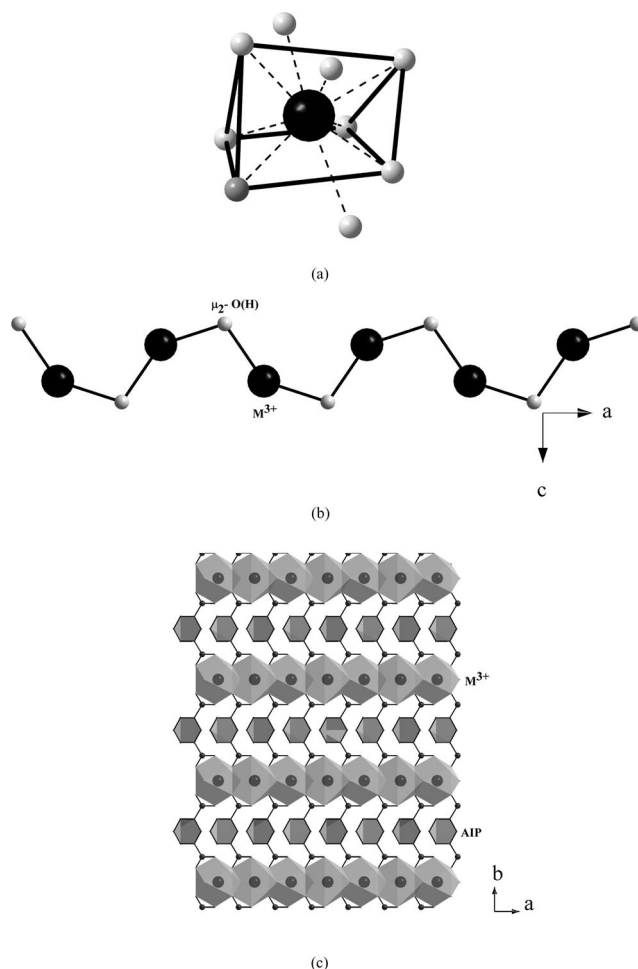


Figure 1. (a) The distorted tricapped trigonal prismatic geometry of the central lanthanide ion. (b) View of the one-dimensional M–O(H)–M chain along the “ b ” axis. (c) The two-dimensional layer formed by the connectivity between the one-dimensional chains and the carboxylate groups of the aminoisophthalate in the “ ab ” plane.

The metal center is also bonded to five different aminoisophthalate anions (Figure S9).

The structure can be simplified by considering the connectivity between the metal centers. Thus, the M^{3+} ions are connected by a μ_2 -hydroxy oxygen [O(1)] to form one-di-

Table 1. Selected observed bond lengths in compounds II, III, and IV.^[a]

C ₈ H ₆ NO ₅ La (II)		C ₈ H ₆ NO ₅ Pr (III)		C ₈ H ₆ NO ₅ Nd (IV)	
Bond	Distance [Å]	Bond	Distance [Å]	Bond	Distance [Å]
La(1)–O(1)#1	2.370(4)	Pr(1)–O(1)#1	2.318(4)	Nd(1)–O(1)#1	2.376(4)
La(1)–O(1)	2.446(4)	Pr(1)–O(1)	2.391(4)	Nd(1)–O(1)	2.431(4)
La(1)–O(2)#1	2.548(3)	Pr(1)–O(2)#1	2.507(3)	Nd(1)–O(2)#1	2.548(3)
La(1)–O(2)#2	2.548(3)	Pr(1)–O(2)#2	2.507(3)	Nd(1)–O(2)#2	2.548(3)
La(1)–O(3)#3	2.612(3)	Pr(1)–O(3)#3	2.582(3)	Nd(1)–O(3)#3	2.614(3)
La(1)–O(3)	2.612(3)	Pr(1)–O(3)	2.582(3)	Nd(1)–O(3)	2.614(3)
La(1)–O(2)#3	2.654(3)	Pr(1)–O(2)#3	2.600(3)	Nd(1)–O(2)#3	2.652(3)
La(1)–O(2)	2.654(3)	Pr(1)–O(2)	2.600(3)	Nd(1)–O(2)	2.652(3)
La(1)–N(1)#4	2.851(5)	Pr(1)–N(1)#4	2.769(5)	Nd(1)–N(1)#4	2.838(5)

[a] Symmetry transformations used to generate equivalent atoms: #1: $x + \frac{1}{2}, y, -z + \frac{3}{2}$; #2: $x + \frac{1}{2}, -y + \frac{1}{2}, -z + \frac{3}{2}$; #3: $x, -y + \frac{1}{2}, z$; #4: $-x + 1, -y + 1, -z + 1$.

mensional M–O(H)–M chains (Figures 1, b and S10). The one-dimensional chains are connected by the carboxylate group of the aminoisophthalate in the *ab* plane thereby forming a two-dimensional layer structure (Figure 1, c). The amino group of the AIP anions bonds with the metal centers and connects the layers by acting as a pillar to complete the three-dimensional structure (Figures 2 and S11). It is unusual to have a structure in which the metal is connected to five anions and for each anion to be connected to five metal centers. One can carry out a uninodal analysis^[11] of the structure and the Schlafli symbol for the five-connected net is $4^6.6^4$ (Figures S12–S14). To the best of our knowledge this is the first observation of a (5,5) net involving rare-earth ions.

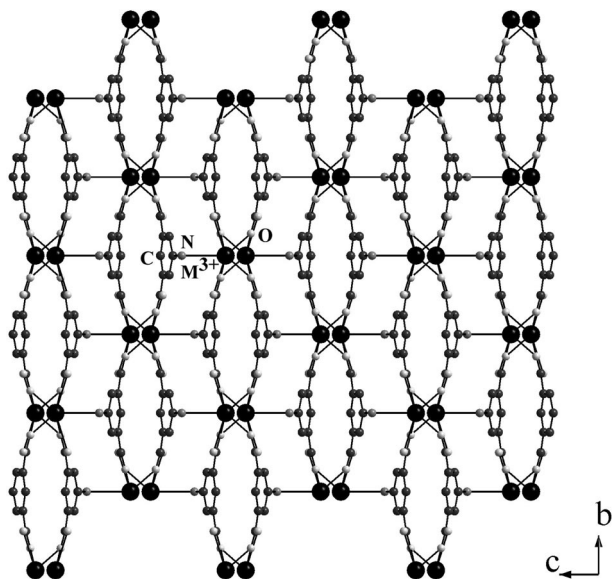


Figure 2. View of the 3D structure formed by the connectivity between the two-dimensional layers through the amino groups along the (100) direction.

The use of AIP along with lanthanides in the synthesis of metal-organic framework compounds has previously been reported.^[12,13] Thus, the compound $[\text{La}(\text{AIP})_{1.5}(\text{H}_2\text{O})_n]_n$ has a two-dimensional layered structure (Figure S15).^[12] Recently, two structures based on praseodymium and AIP ions, $[\text{Pr}_2(\text{AIP})_3(\text{H}_2\text{O})_2 \cdot 3\text{H}_2\text{O}]_n$ and $[\text{Pr}_2(\text{HAIP})_2(\text{AIP})(\text{NO}_3)_2 \cdot 8\text{H}_2\text{O}]_n$, were reported.^[13] In both of these compounds, the structures have praseodymium carboxylate layers cross-linked by another AIP unit, similar to the present structures, but the connectivity between the layers is different. In the praseodymium structures the amino group of the acid does not participate in the bonding, whereas in the present structures the amino groups bind to the rare-earth ions (Figure 3). We believe that this is the first observation of the bonding of the amino group in rare-earth compounds based on AIP anions.

Thermal Studies

Thermogravimetric analyses (TGA) of compounds **I–IX** were carried out in air (flow rate = 50 mL min^{-1}) in the

temperature range $30\text{--}850^\circ\text{C}$ (heating rate = 5°C min^{-1}) (Figure S16). All the compounds exhibited comparable behavior and have a single-step weight loss in the temperature range of around $360\text{--}400^\circ\text{C}$. The total observed weight loss, in all cases, corresponds well with the loss of the carboxylate and the hydroxy group: 53.6% (calcd. 50.4%) for **I**, 51.2% (calcd. 51.4%) for **II**, 54% (calcd. 49.5%) for **III**, 53.5% (calcd. 50.6%) for **IV**, 52.5% (calcd. 49.7%) for **V**, 53.5% (calcd. 49.5%) for **VI**, 53.8% (calcd. 48.7%) for **VII**, 53.4% (calcd. 48%) for **VIII**, and 50.8% (calcd. 47.3%) for **IX**. The final calcined products were found to be crystalline by powder XRD and corresponded to the respective oxides.

Luminescence Studies

One of the persistent issues with regard to the use of rare-earth elements is their low molar absorbance. This can be partially overcome by the use of a coordinated aromatic system as has been shown earlier.^[6b] The delocalized π system can be excited easily and can, in turn, transfer energy to the metal center to exhibit sensitized emission through an intramolecular pathway (Figure S17).^[6b,14] This process is known as the “antenna effect” and has been well studied in the literature.^[15] The efficiency of the energy-transfer process in such cases can be visualized by the reduction of the intensity of the intraligand emission. The aminoisophthalate units of the present compounds absorb strongly in the UV region, so we expected the present compounds to respond reasonably in optical studies.

The solid-state photoluminescence spectra of the compounds **I–IX** and the partially doped samples [4 (**Ia**), 6 (**Ib**), and 10 (**Ic**) mol-% Eu^{3+} and 4 (**Id**), 6 (**Ie**), and 10 (**If**) mol-% Tb^{3+} doped samples of yttrium (**I**), and the correspondingly doped samples (**IIa–IIf**) of lanthanum (**II**)] were recorded at room temperature. The photoluminescence spectrum of the Na salt of the aminoisophthalate (Figure S18) shows a broad emission peak centered at around 460 nm with a shoulder at around 490 nm ($\lambda_{\text{ex}} = 275 \text{ nm}$). Compounds **I–IX** also exhibit a main emission peak centered at around 400 nm ($\lambda_{\text{ex}} = 275 \text{ nm}$), which may be due to the intraligand transitions of the 5-aminoisophthalate units. The shift in the main intraligand peak may arise from the change in electronic distribution of the aminoisophthalate after coordination, which has been observed before for aminoisophthalate compounds.^[16] The broad peaks at around 490 and 535 nm may be due to singlet-to-triplet-state transitions of the ligand. Of all the compounds (Figure S19) prepared in the present study, only Eu^{3+} (**VI**) shows characteristic metal-centered emission. The 590 and 625 nm emission bands for compound **VI** correspond to the $^5\text{D}_0 \rightarrow ^7\text{F}_1$ and $^5\text{D}_0 \rightarrow ^7\text{F}_2$ transitions of Eu^{3+} (Figure S20). To appreciate the metal-centered emission, we doped the yttrium and lanthanum compounds (f^0 systems) with Eu^{3+} and Tb^{3+} ions and examined the effect of doping on the intraligand and other transitions (see Figures 4 and 5). As can be noted, the doped samples indeed exhibit a suppression of the main intraligand emission accompanied by the emergence of a

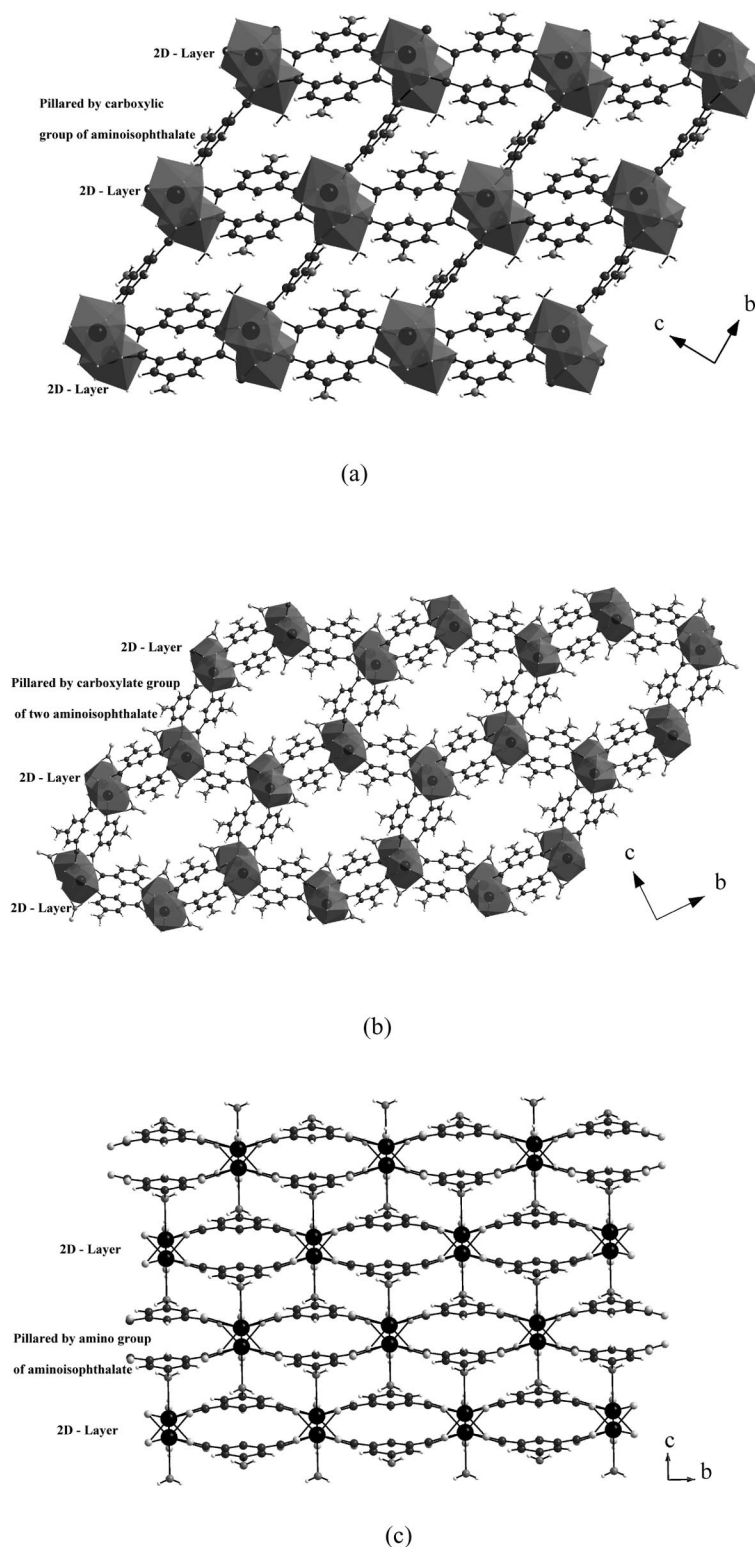
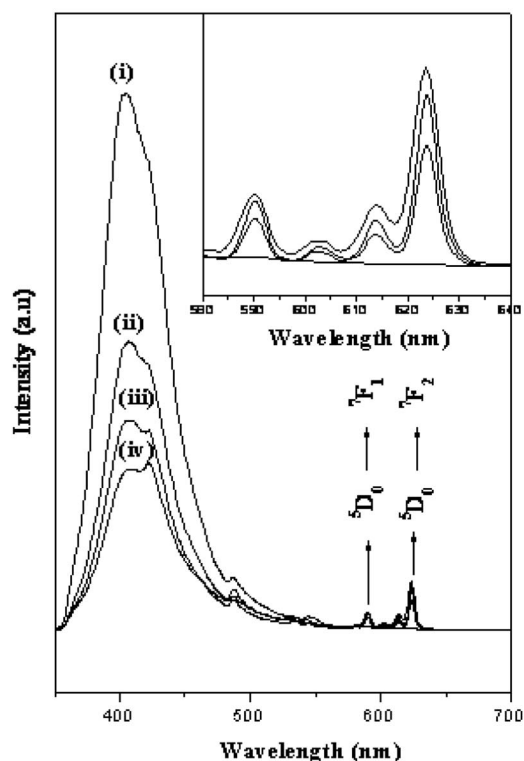


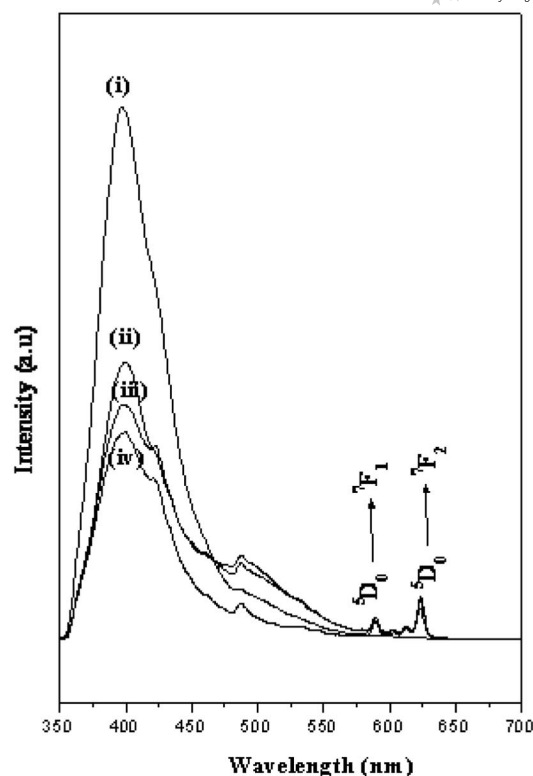
Figure 3. (a) The three-dimensional structure of $[\text{Pr}_2(\text{AIP})_3(\text{H}_2\text{O})_2 \cdot 3\text{H}_2\text{O}]_n$. (b) View of the three-dimensional structure of $[\text{Pr}_2(\text{HAIP})_2(\text{AIP})(\text{NO}_3)_2 \cdot 8\text{H}_2\text{O}]_n$. (c) The three-dimensional structure of the present structures formed by the pillaring of layers through the amino group.

strong luminescent emission characteristic of the doped metal. We observed an intense red color for Eu^{3+} -doped samples and a green color for the Tb^{3+} -doped samples (Figures S21 and S22) when exposed to UV light. The emission

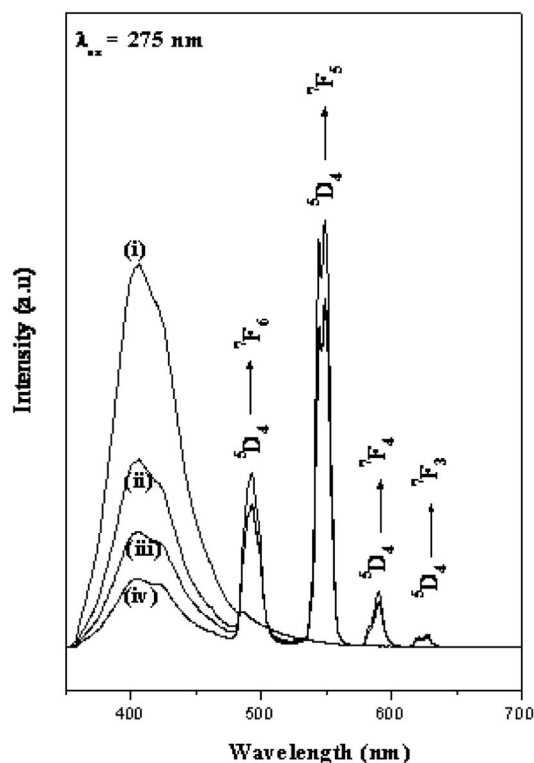
spectra shown in parts a,b of Figure 4 exhibit $^5\text{D}_0 \rightarrow ^7\text{F}_J$ ($J = 1, 2$) emission bands for Eu^{3+} and $^5\text{D}_4 \rightarrow ^7\text{F}_J$ ($J = 3-6$) emission bands for Tb^{3+} , respectively. The 590 and 623 nm emission bands correspond to the $^5\text{D}_0 \rightarrow ^7\text{F}_1$ and $^5\text{D}_0 \rightarrow ^7\text{F}_2$



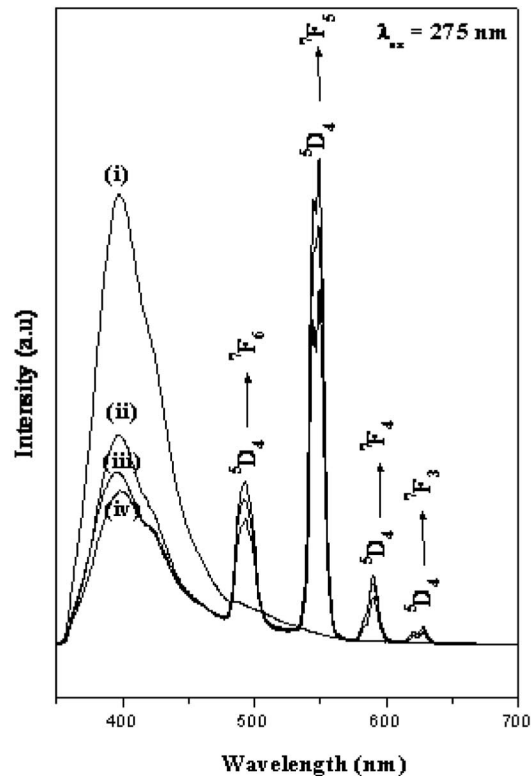
(a)



(a)



(b)



(b)

Figure 4. Room-temperature photoluminescence spectra of the Y compound. (a) (i) The parent Y compound and samples doped with (ii) 4, (iii) 6, and (iv) 10 mol-% Eu^{3+} . (b) (i) The parent Y compound and samples doped with (ii) 4, (iii) 6, and (iv) 10 mol-% Tb^{3+} .

Figure 5. Room-temperature photoluminescence spectra of the La compound. (a) (i) The parent La compound and samples doped with (ii) 4, (iii) 6, and (iv) 10 mol-% Eu^{3+} . (b) (i) The parent La compound and samples doped with (ii) 4, (iii) 6, and (iv) 10 mol-% Tb^{3+} .

transitions of Eu^{3+} . The other possible transitions $^5\text{D}_0 \rightarrow ^7\text{F}_3$ and $^5\text{D}_0 \rightarrow ^7\text{F}_4$ were not observed, which can be attributed to the low intensity of the metal-centered emissions. It may be noted that the $^5\text{D}_0 \rightarrow ^7\text{F}_2$ transition has a greater intensity than the $^5\text{D}_0 \rightarrow ^7\text{F}_1$ transition. The differences in the intensities of the emission peaks have been employed to understand the coordination and site symmetry around the Eu^{3+} ion because the $^5\text{D}_0 \rightarrow ^7\text{F}_1$ emission, due to the magnetic dipole, is independent of the environment of the central metal ion.^[17] The $^5\text{D}_0 \rightarrow ^7\text{F}_2$ emission, on the other hand, arises from the electric dipole and is sensitive to the crystal field symmetry. The observation of a larger intensity for the $^5\text{D}_0 \rightarrow ^7\text{F}_2$ transitions suggests the Eu^{3+} ion is not at the inversion center and the symmetry of the Eu^{3+} site is low. This is in agreement with the single-crystal structure, which shows that Eu^{3+} occupies the “4c” position with a mirror plane and not with an inversion center. The Tb^{3+} doping exhibits more pronounced metal-centered emissions with bands at 492, 548, 589, and 625 nm, which correspond to the $^5\text{D}_4 \rightarrow ^7\text{F}_J$ (for $J = 6, 5, 4$, and 3 , respectively) transitions of Tb^{3+} . The observation of these various transitions clearly indicates that the energy transfer from the AIP ligand to the metal center is quite efficient. We have also noted the suppression of the main intraligand emission band (ca. 400 nm) along with the observation of metal-centered emission, which also suggests that the energy transfer is reasonable. It may be noted that the intraligand transitions are more suppressed as the dopant concentration increases. This indicates that increased dopant levels lead to more quenching of the intraligand emissions and hence to the transfer of more energy to the dopants (Eu^{3+} and Tb^{3+}). However, a linear relationship is not expected at higher dopant levels due to self-quenching effects.^[6h]

The Eu^{3+} (**IIa**, **IIb**, and **IIc**) and Tb^{3+} (**IIId**, **IIe**, and **IIIf**) doped samples of lanthanum also exhibit similar characteristic transitions of the dopant elements (Figure 5a,b). The observed emission bands for the Eu^{3+} -doped samples are at 588 and 623 nm, which are due to the $^5\text{D}_0 \rightarrow ^7\text{F}_J$ ($J = 1$ and 2) transitions. The observed emission bands for the Tb^{3+} -doped samples are 493, 548, 589, and 625 nm, which may be due to the $^5\text{D}_4 \rightarrow ^7\text{F}_J$ (for $J = 6, 5, 4$, and 3 , respectively) transitions.

In both cases, we consistently observed much sharper transitions in the Tb^{3+} -doped samples than in the Eu^{3+} -doped samples. This behavior may be due to the environment around the metal ions. As described earlier, the metal centers are connected by hydroxide units forming one-dimensional $\text{M}-\text{O}(\text{H})-\text{M}$ chains. The presence of $-\text{OH}$ units next to the metal centers would lead to the suppression of the emission from the Eu^{3+} ions as the Tb^{3+} ions have a larger gap between the emitting level and the next lower one. Similar effects have been observed previously in Eu^{3+} -doped compounds.^[6h]

Life-Time Studies

The luminescence life-times of the excited states of the 4 mol-% doped samples of yttrium (**Ia** = Eu ; **Id** = Tb), lan-

thanum (**IIa** = Eu ; **IIId** = Tb), and pure europium (**VI**) compounds were studied. The $^5\text{D}_0 \rightarrow ^7\text{F}_1$ and $^5\text{D}_0 \rightarrow ^7\text{F}_2$ emission bands for the Eu^{3+} samples (**Ia**, **IIa**, and **VI**) and the $^5\text{D}_4 \rightarrow ^7\text{F}_6$ and $^5\text{D}_4 \rightarrow ^7\text{F}_5$ emission bands for the Tb^{3+} samples (**Id** and **IIId**) were monitored in the life-time studies

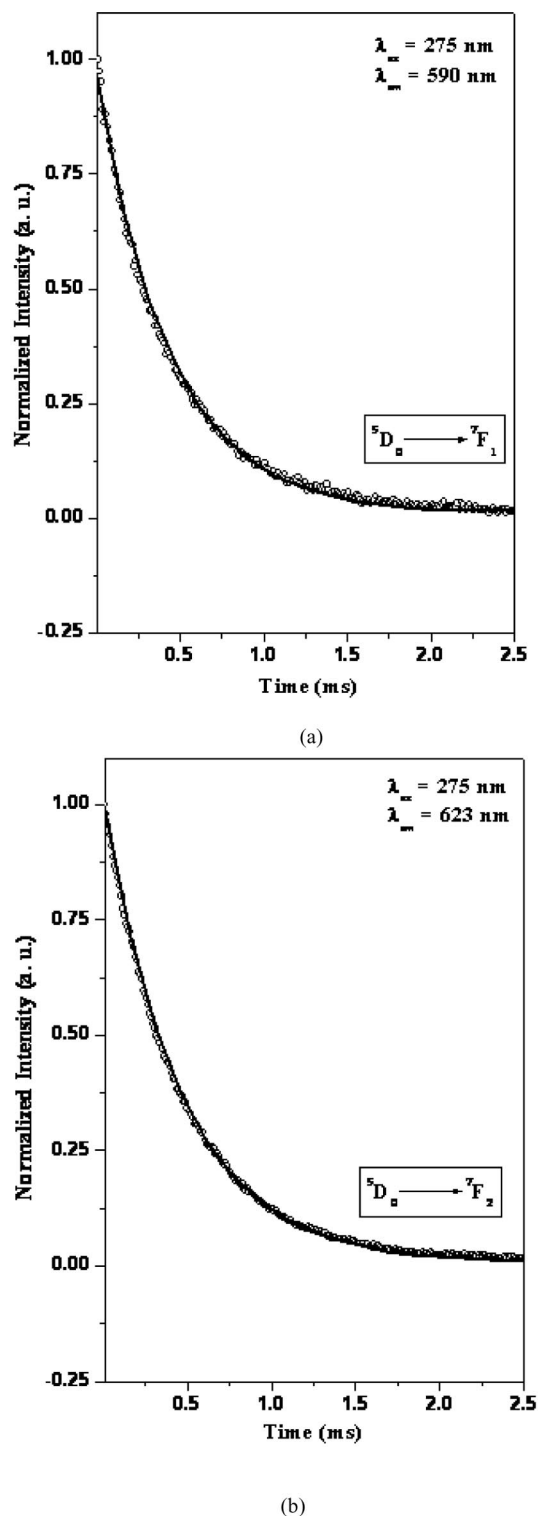


Figure 6. Room-temperature luminescence decay behavior for the compound **Ia** (4 mol-% Eu) for the $^5\text{D}_0 \rightarrow ^7\text{F}_1$ and $^5\text{D}_0 \rightarrow ^7\text{F}_2$ emission bands.

by employing 275 nm excitation at room temperature. The experimental luminescent decay curve fits well the single exponential decay function given by Equation (1) in which I and I_0 are the luminescent intensities at time t and 0 and τ is defined as the luminescent lifetime. The fit of the curve to the single exponential decay function indicates life-time values of 0.429 and 0.464 ms for **Ia** for the transitions $^5D_0 \rightarrow ^7F_1$ and $^5D_0 \rightarrow ^7F_2$, respectively (Figure 6, a and b). The luminescence life-times for the other samples are listed in Table 2 (see Figures S23–S30). The luminescence life-times for the doped and the pure Eu sample in the present study appear to be comparable to the life-times obtained generally for the pure Eu^{3+} and Tb^{3+} carboxylates reported in the literature.^[17]

$$I = I_0 \exp(-t/\tau) \quad (1)$$

Table 2. Life-times of the compounds **Ia**, **Id**, **IIa**, **IId**, and **VI**.

Compound		Life-time [ms]	
		$^5D_0 \rightarrow ^7F_1$	$^5D_0 \rightarrow ^7F_2$
1.	Ia (4 mol-% Eu)	0.429	0.464
2.	IIa (4 mol-% Eu)	0.464	0.490
3.	VI	0.306	0.287
		$^5D_4 \rightarrow ^7F_6$	$^5D_4 \rightarrow ^7F_5$
4.	Id (4 mol-% Tb)	1.297	1.493
5.	IId (4 mol-% Tb)	1.264	1.702

Up-Conversion Studies

There has been considerable interest in the study of compounds that can exhibit up-conversion behavior ever since the reviews of Auzel and Wright were published.^[18] The up-conversion is in fact anti-Stokes emission and could be utilized to detect infrared radiation visually. It is a two-stage electron-transfer process and involves a reasonably stable intermediate. There has been some interest in investigating the rare-earth carboxylates as possible up-conversion materials as such behavior has been observed in Nd^{3+} -containing compounds.^[9,19] Among the compounds **I–IX** prepared in this study, compound **IV**, $[\text{Nd}(\mu_2\text{-OH})][\text{C}_8\text{H}_3(\text{COO})_2(\text{NH}_2)]$, can be studied for up-conversion. The UV/Vis spectrum of **IV** shows that the absorption increases rapidly with decreasing wavelength due to intraligand absorption (Figure S31). At room temperature, the details of the Stark components at each level could not be fully resolved from the absorption spectrum as the thermally excited upper Stark levels of the ground state, which give rise to a complicated pattern with additional absorption peaks, are superimposed upon other zero-temperature peaks. The absorption bands of the Nd^{3+} ions indicate primary ground-state Stark splitting of the eigenstates due to crystal field effects.^[20] The UV/Vis spectra could be resolved to identify the $^4D_{5/2}$, $^4D_{3/2}$, $^4G_{5/2}$, and $^4F_{3/2}$ transitions.

Figure 7 shows a Jablonski diagram of the possible energy transfer processes during the up-conversion using the Nd^{3+} ion. The Nd^{3+} compound **IV** exhibits an intense absorption at around 580 nm, which corresponds to the tran-

sition $^4I_{9/2} \rightarrow ^4G_{5/2}$, a hypersensitive band that satisfies the selection rule $\Delta J = \pm 2$, $\Delta L = \pm 2$, and $\Delta S = 0$. The short-wavelength luminescence of **IV** could be from the $^4D_{3/2}$ level; the excitation of either the $^4D_{3/2}$ or the $^4D_{5/2}$ band may be employed, but the direct excitation of these levels is limited by the strong intraligand absorption (ca. 400 nm). The use of an excitation wavelength of around 580 nm may not give rise to such problems as the excitation wavelength is far removed from the intraligand absorption band (ca. 400 nm). During the excitation, the $^4G_{5/2}$ level could relax nonradiatively to the $^4F_{3/2}$ level where some populations could take part in the excited-state absorption (ESA) and others relax to lower energy levels. Thus, the excitation wavelength ($\lambda = 580$ nm) has an energy such that the populated $^4F_{3/2}$ level can be excited further from the $^4F_{3/2}$ to the $^4D_{5/2}$ levels. The $^4D_{5/2}$ and $^4D_{3/2}$ levels have comparable energies from which the luminescence is emitted. The up-converted luminescence spectra for this yellow pumping (580 nm excitation) from the $^4D_{3/2}$ level is shown in Figure 8.

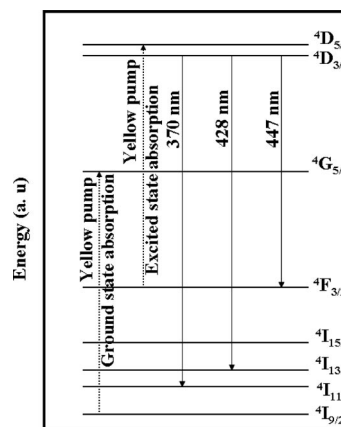


Figure 7. A Jablonski diagram showing the various transitions in a Nd^{3+} compound.

To understand the up-conversion process and to evaluate the number of photons involved in the up-conversion process, we sought to relate the excitation intensity to the luminescence intensity. To study the dependence of the excitation intensity on the up-converted luminescence intensity, we carried out a power-dependence experiment. Thus, we reduced the incident intensity by using a series of sterile glass plates sequentially in the pathway between the excitation source and the sample. The corresponding decrease in the excitation intensity per glass plate was calibrated separately using the UV/Vis spectrophotometer in the transmission mode and normalized with respect to the transmission obtained in the absence of any glass slides. The luminescence behavior and the dependence of the luminescence intensity as a function of the glass plates is shown in Figure 9. The log–log plots of luminescence intensity versus excitation intensity were plotted for the transitions $^4D_{3/2} \rightarrow ^4I_{11/2}$ (370 nm), $^4D_{3/2} \rightarrow ^4I_{13/2}$ (428 nm), and $^4D_{3/2} \rightarrow ^4I_{15/2}$ (448 nm), which were found to be linear with slopes of 2.51, 2.23, and 1.77, respectively (Figure 10). The

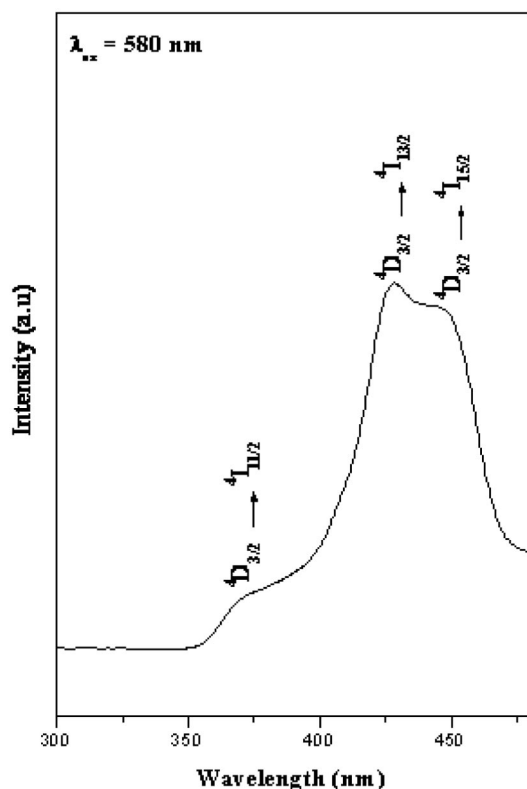


Figure 8. Room-temperature spectra for the Nd compound IV when excited using $\lambda = 580$ nm.

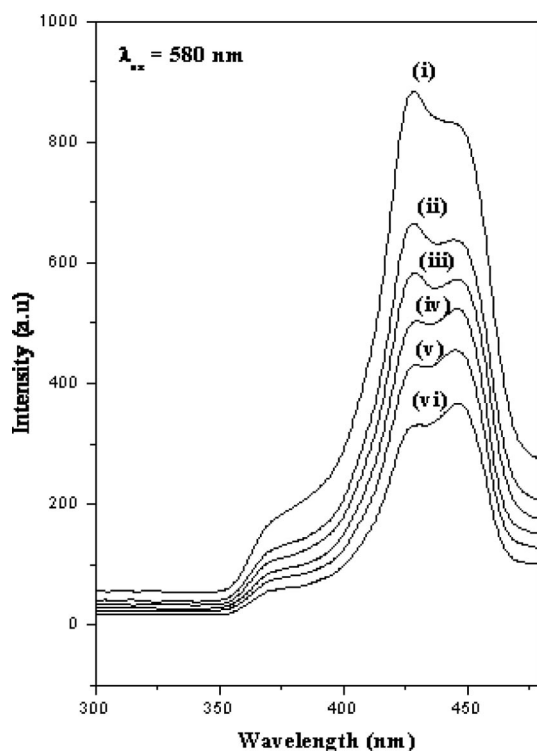


Figure 9. The emission dependence on the excitation intensity for the Nd compound $[\text{Nd}(\mu_2\text{-OH})(\text{C}_6\text{H}_5\text{NO}_4)]$ (IV). (i) 100, (ii) 91.68, (iii) 84.07, (iv) 77.62, (v) 71.76, and (vi) 66.3%.

good fits suggest that the up-conversion behavior exhibited in compound IV is due to the successive absorption of two photons.

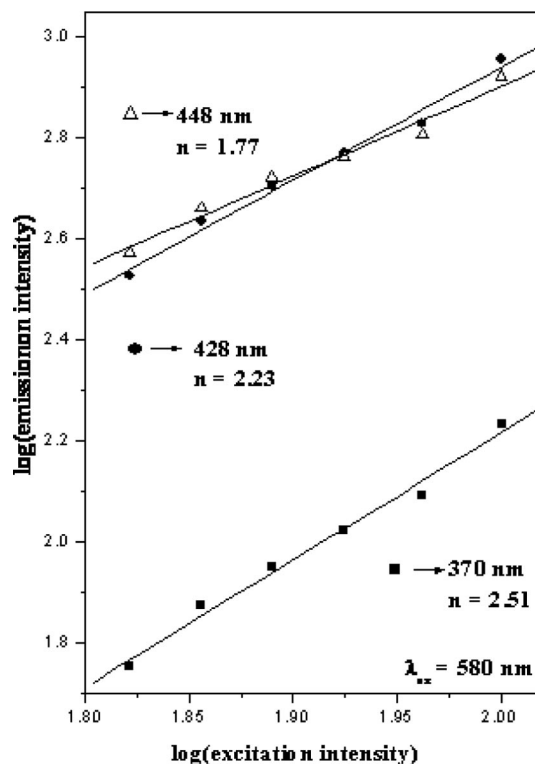


Figure 10. Log-log plots of the excitation intensity dependence of the luminescence intensity for the transitions $4\text{D}_{3/2} \rightarrow 4\text{I}_{11/2}$ (370 nm), $4\text{D}_{3/2} \rightarrow 4\text{I}_{13/2}$ (428 nm), and $4\text{D}_{3/2} \rightarrow 4\text{I}_{15/2}$ (448 nm).

Conclusions

The synthesis, characterization, and structural determination of a family of rare-earth aminoisophthalate phases have been accomplished. The observation of a (5,5) net, for the first time, is important and noteworthy. The doping of Eu^{3+} and Tb^{3+} ions in place of La^{3+} and Y^{3+} in the parent structures gives rise to red and green emissions, respectively, when excited using $\lambda = 275$ nm. The study of the life-times at room temperature suggests that the values are in the range of 0.287–0.490 ms for Eu^{3+} ions and 1.265–1.702 ms for Tb^{3+} ions. The observation of a two-photon absorption in the Nd^{3+} compound suggests that the rare-earth compounds can be utilized for their interesting optical properties, converting the IR radiation into the visible region.

Experimental Section

Synthesis and Initial Characterization: All the compounds were prepared by employing the hydrothermal method. In a typical synthesis, for I, $\text{Y}(\text{CH}_3\text{COO})_2 \cdot x\text{H}_2\text{O}$ (0.266 g, 1 mm) was dissolved in water (10 mL). To this, 5-aminoisophthalic acid (0.181 g, 1 mm) and NaOH (0.08 g, 2 mm) were added under continuous stirring. The mixture was homogenized for 30 min at room temperature. The final mixture was transferred to and sealed in a 23 mL PTFE-lined autoclave and heated at 150 °C for 3 d under autogenous pressure. The final product contained large quantities of colorless

block-type single crystals, which were filtered under vacuum, washed with deionized water, and dried under ambient conditions (yield: ca. 75% based on Y). For the preparation of the other isostructural compounds, the corresponding acetate salts were used in place of yttrium acetate, keeping the composition and other conditions the same. In the case of Pr (**III**) and Nd (**IV**) the final product contained large quantities of pale-green and pale-violet block-type single crystals. For the remaining rare earths, the final product contained only white powders with comparable yields. The Eu-doped (4 mol-% **Ia**, 6 mol-% **Ib**, 10 mol-% **Ic**, 4 mol-% **IIa**, 6 mol-% **IIb**, and 10 mol-% **IIc**) and Tb-doped (4 mol-% **Id**, 6 mol-% **Ie**, 10 mol-% **If**, 4 mol-% **IId**, 6 mol-% **IIe**, and 10 mol-% **IIIf**) samples of Y (**I**) and La (**II**) were prepared by employing a procedure similar to the one described above. In each case, the mole fraction ratios of the lanthanide ions were adjusted to give the nominal compositions given in the present work. We carried out C,H,N analysis for all the prepared compounds. Elemental analysis: **I**: calcd. C 28.68, H 1.81, N 4.18; found C 29.15, H 2.56, N 3.96; **II**: calcd. C 28.51, H 1.80, N 4.16; found C 28.94, H 2.68, N 4.22; **III**: calcd. C 28.23, H 1.78, N 4.12; found C 28.86, H 2.73, N 4.38.

Initial characterizations were carried out by elemental analysis, powder X-ray diffraction (XRD), thermogravimetric analysis, and IR spectroscopy. Powder X-ray diffraction (XRD) patterns were recorded in the 2θ range of 5–50° using Cu- K_α radiation (Philips X'pert; see the Supporting Information, Figures S1–S5). The IR spectra were recorded as KBr pellets (Perkin–Elmer, SPECTRUM 1000). The IR spectra exhibit typical peaks corresponding to the hydroxy, amino, and carboxylate groups of the compounds (see the Supporting Information, Figure S32). IR (KBr): $\tilde{\nu}$ = 3635–3670 [$\gamma_{\text{as}}(\text{O–H})$], 3264–3308 [$\gamma_{\text{s}}(\text{N–H})$], 2916–2942 [$\gamma_{\text{s}}(\text{C–H})_{\text{aromatic}}$], 1611–1614 [$\gamma_{\text{s}}(\text{C=O})$], 1541–1548 [$\delta(\text{H}_2\text{O})$], 1400–1412 [$\delta(\text{COO})$], 1015–1030 [$\gamma_{\text{s}}(\text{C–C})_{\text{skeletal}}$], 946–961 [$\delta(\text{CN})_{\text{skeletal}}$], and 777–782 [$\delta(\text{CH}_{\text{aromatic}})_{\text{out-of-plane}}$] cm^{-1} (see Table S1).

Single-Crystal Structure Determination: A suitable single crystal of the compound (La, Pr, and Nd) was carefully selected under a pola-

rizing microscope and glued to a thin glass fiber. The single-crystal data were collected with a Bruker AXS Smart Apex CCD diffractometer at 293(2) K. The X-ray generator was operated at 50 kV and 35 mA using Mo- K_α ($\lambda = 0.71073 \text{ \AA}$) radiation. Data were collected with an ω scan width of 0.3°. A total of 606 frames were collected in three different settings of ϕ (0, 90, and 180°) keeping the sample-to-detector distance fixed at 6.03 cm and the detector position (2θ) fixed at -25° . The data were reduced using SAINTPLUS,^[21] and an empirical absorption correction was applied using the SADABS program.^[22] The structure was solved and refined by using SHELXL-97^[23] in the WinGx suit of programs (v. 1.63.04a).^[24] All the hydrogen positions were initially located in the difference Fourier maps and for the final refinement, the hydrogen atoms were placed in geometrically ideal positions and refined in the riding mode. Final refinement included the atomic positions for all the atoms, anisotropic thermal parameters for all the non-hydrogen atoms, and isotropic thermal parameters for all the hydrogen atoms. Full-matrix least-squares refinement against $|F^2|$ was carried out by using the WinGx package of programs.^[23] Details of the structure solutions and final refinements for the compounds are given in Table 3. The unit cell parameters of the compounds (**I**, **V**, **VI**, **VII**, **VIII**, and **IX**) were obtained from the powder X-ray diffraction patterns by the Le Bail method.^[25] By using the atomic coordinates of **II** (La compound), the extraction of the structure factor amplitudes was achieved by using this method in which the structural refinement cycles included the scale factor, the zero-point shift, the lattice parameters, and the background parameters as variables. The parameters are presented in Table S2 (for Le Bail fit see the Supporting Information, Figures S33–S38).

CCDC-747717 (for **II**), -747718 (for **III**), and -747719 (for **IV**) contain the crystallographic data for this paper. These data can be obtained free of charge from The Cambridge Crystallographic Data Center (CCDC) via www.ccdc.cam.ac.uk/data_request/cif.

Supporting Information (see also the footnote on the first page of this article): Simulated and experimental powder XRD patterns of

Table 3. Crystal data and structure refinement parameters for compounds **II**, **III**, and **IV**.^[a]

	II	III	IV
Empirical formula	C ₈ H ₆ LaNO ₅	C ₈ H ₆ NO ₅ Pr	C ₈ H ₆ NNdO ₅
Formula mass	335.04	337.04	340.37
Crystal system	orthorhombic	orthorhombic	orthorhombic
Space group	<i>Pnma</i>	<i>Pnma</i>	<i>Pnma</i>
<i>a</i> [Å]	7.2267(6)	7.1000(6)	7.2256(3)
<i>b</i> [Å]	9.8928(6)	9.8557(8)	9.8972(4)
<i>c</i> [Å]	11.9367(9)	11.9012(10)	11.9301(6)
α [°]	90	90	90
β [°]	90	90	90
γ [°]	90	90	90
Volume [Å ³]	853.38(11)	832.79(12)	853.16(7)
<i>Z</i>	4	4	4
<i>T</i> [K]	293(2)	293(2)	293(2)
$\rho_{\text{calcd.}}$ [g cm ⁻³]	2.600	2.680	2.642
μ [mm ⁻¹]	5.005	5.849	6.084
θ range [°]	3.30–25.99	2.68–28.03	3.30–25.98
$\lambda(\text{Mo-}K_\alpha)$ [Å]	0.71073	0.71073	0.71073
<i>R</i> _{int}	0.0498	0.0385	0.0280
Reflections collected	4710	8980	4811
Unique reflections	885	1061	885
Number of parameters	76	76	76
<i>R</i> indices [$I > 2\sigma(I)$]	<i>R</i> ₁ = 0.0240, <i>wR</i> ₂ = 0.0530	<i>R</i> ₁ = 0.0281, <i>wR</i> ₂ = 0.0576	<i>R</i> ₁ = 0.0206, <i>wR</i> ₂ = 0.0563
<i>R</i> indices (all data)	<i>R</i> ₁ = 0.0323, <i>wR</i> ₂ = 0.0540	<i>R</i> ₁ = 0.0341, <i>wR</i> ₂ = 0.0591	<i>R</i> ₁ = 0.0239, <i>wR</i> ₂ = 0.0572

[a] $R_1 = \Sigma |F_o| - |F_c| / \Sigma |F_o|$; $wR_2 = \{\Sigma [w(F_o^2 - F_c^2)] / \Sigma [w(F_o^2)]\}^{1/2}$; $w = 1 / [\rho^2(F_o)^2 + (aP)^2 + bP]$; $P = [\max(F_o, O) + 2(F_c)^2] / 3$, where $a = 0.0252$ and $b = 0.0000$ for **II**, $a = 0.0244$ and $b = 1.7647$ for **III**, and $a = 0.0263$ and $b = 2.8022$ for **IV**.

I–IX and the doped samples, TGA curves of I–IX, IR spectra and bond angles of II, III and IV; UV/Vis spectra of I–IX, UV/Vis spectra of the Na salts of aminoisophthalates, the decay curves of the excited state of the doped samples and the Le Bail fit for the compounds I, V, VI, VII, VIII and IX.

Acknowledgments

S. N. thanks the Department of Science and Technology (DST), Government of India, for the award of a research grant and the authors thanks the Council of Scientific and Industrial Research (CSIR), Government of India, for the award of a fellowship (D. S.) and a research grant. S. N. also thanks the DST for the award of a RAMANNA fellowship.

- [1] a) P. Mahata, S. Natarajan, *Chem. Soc. Rev.* **2009**, 38, 2304–2318; b) M. O’Keeffe, M. A. Peskov, S. J. Ramsden, O. M. Yaghi, *Acc. Chem. Res.* **2008**, 41, 1782–1789; c) O. D. Friedrichs, M. O’Keeffe, O. M. Yaghi, *Phys. Chem. Chem. Phys.* **2007**, 9, 1035–1043; d) R. J. Hill, D. L. Long, N. R. Champness, P. Hubberstey, M. Schröder, *Acc. Chem. Res.* **2005**, 38, 335–348; e) S. R. Batten, R. Robson, *Angew. Chem. Int. Ed.* **1998**, 37, 1460–1494.
- [2] a) Special Issue on MOF: *Chem. Soc. Rev.* **2009**, 38, 1213–1504; b) C. J. Doonan, W. Morris, H. Furukawa, O. M. Yaghi, *J. Am. Chem. Soc.* **2009**, 131, 9492–9493; c) R. E. Morris, P. S. Wheatley, *Angew. Chem. Int. Ed.* **2008**, 47, 4966–4981; d) S. Horike, M. Dinca, K. Tamaki, J. R. Long, *J. Am. Chem. Soc.* **2008**, 130, 5854–5855; e) T. K. Maji, R. Matsuda, S. Kitawaga, *Nat. Mater.* **2007**, 6, 142–148; f) G. Ferey, C. Mellot-Draznieks, C. Serre, F. Millange, *Acc. Chem. Res.* **2005**, 38, 217–225; g) H. R. Moon, J. H. Kim, M. P. Suh, *Angew. Chem. Int. Ed.* **2005**, 44, 1261–1265; h) S. S. Kaye, J. R. Long, *J. Am. Chem. Soc.* **2005**, 127, 6506–6507; i) S. Kitagawa, R. Kitaura, S. Noro, *Angew. Chem. Int. Ed.* **2004**, 43, 2334–2375.
- [3] a) Z. Lu, C. B. Knobler, H. Furukawa, B. Wang, G. Liu, O. M. Yaghi, *J. Am. Chem. Soc.* **2009**, 131, 12532–12533; b) P. Mahata, D. Sen, S. Natarajan, *Chem. Commun.* **2008**, 1278–1280; c) L. Xie, S. Liu, B. Gao, C. Zhang, C. Sun, D. Li, Z. Su, *Chem. Commun.* **2005**, 2402–2404; d) H. Chun, D. Kim, D. N. Dybtsev, K. Kim, *Angew. Chem. Int. Ed.* **2004**, 43, 971–974; e) H. Li, M. Eddaoudi, M. O’Keeffe, O. M. Yaghi, *Nature* **1999**, 402, 276–279.
- [4] a) X.-J. Kong, Y. Wu, L.-S. Long, L.-S. Zheng, Z. Zheng, *J. Am. Chem. Soc.* **2009**, 131, 6918–6919; b) F. N. Shi, L. Cunha-Silva, R. A. Sa Ferreira, L. Mafra, T. Trindade, L. D. Carlos, F. A. Almeida Paz, J. Rocha, *J. Am. Chem. Soc.* **2008**, 130, 150–167; c) B. Chen, L. Wang, F. Zapata, G. Qian, B. Lobkovsky, *J. Am. Chem. Soc.* **2008**, 130, 6718–6719; d) M. B. Zhang, J. Zhang, S. T. Zheng, G. Y. Yang, *Angew. Chem. Int. Ed.* **2005**, 44, 1385–1388; e) D. L. Long, R. J. Hill, A. L. Blake, N. R. Champness, P. Hubberstey, D. M. Proserpio, C. Wilson, M. Schröder, *Angew. Chem. Int. Ed.* **2004**, 43, 1851–1854; f) T. M. Reineke, M. Eddaoudi, D. Moler, M. O’Keeffe, O. M. Yaghi, *J. Am. Chem. Soc.* **2000**, 122, 4843–4844.
- [5] S. I. Weissman, *J. Chem. Phys.* **1942**, 31, 214–217.
- [6] a) K. Binnemans, *Chem. Rev.* **2009**, 109, 4283–4374; b) L. Yan, Q. Yue, Q.-X. Jia, G. Lemercier, E.-Q. Gao, *Cryst. Growth Des.* **2009**, 9, 2984–2987; c) S. J. A. Pope, B. J. Coe, S. Faulkner, E. V. Bichenkova, X. Yu, K. Douglas, *J. Am. Chem. Soc.* **2004**, 126, 9490–9491; d) B. Zhao, X. Y. Chen, P. Cheng, D. Z. Liao, S. P. Yan, Z. H. Jiang, *J. Am. Chem. Soc.* **2004**, 126, 15394–16395; e) C. M. Rudzinski, A. M. Young, D. G. Nocera, *J. Am. Chem. Soc.* **2002**, 124, 1723–1727; f) T. Justel, H. Nikol, C. Ronda, *Angew. Chem. Int. Ed.* **1998**, 37, 3084–3103; g) G. Blasse, B. C. Grabmaier, *Luminescent Materials*, Springer, Berlin, **1994**; h) J. C. G. Bunzli, G. R. Choppin, *Lanthanide Probes in Life, Chemical and Earth Science Theory and Practice*, Elsevier, Amsterdam, **1989**.
- [7] a) X.-P. Yang, R. A. Jones, *J. Am. Chem. Soc.* **2005**, 127, 7686–7687; b) N. Sabbatini, M. Guardigli, F. Bolletta, I. Manet, R. Ziessel, *Angew. Chem. Int. Ed. Engl.* **1994**, 33, 1501–1503; c) N. Sabbatini, M. Guardigli, J. M. Lehn, *Coord. Chem. Rev.* **1993**, 123, 201–228.
- [8] a) C. A. Black, J. S. Costa, W. T. Fu, C. Massera, O. Roubeau, S. J. Teat, G. Aromi, P. Gamez, J. Reedijk, *Inorg. Chem.* **2009**, 48, 1062–1068; b) D. T. de Lill, A. de Bettencourt-Dias, C. L. Cahill, *Inorg. Chem.* **2007**, 46, 3960–3965; c) D. Sendor, M. Hilder, T. Juestel, P. C. Junk, U. H. Kynast, *New J. Chem.* **2003**, 27, 1070–1077.
- [9] a) C.-Y. Sun, X.-J. Zheng, X.-B. Chen, L.-C. Li, L.-P. Jin, *Inorg. Chim. Acta* **2009**, 362, 325–330; b) P. Mahata, K. V. Ramya, S. Natarajan, *Dalton Trans.* **2007**, 4017–4026; c) P. Mahata, S. Natarajan, *Inorg. Chem.* **2007**, 46, 1250–1258; d) X. Wang, X. Kong, G. Shan, Y. Yu, Y. Sun, L. Feng, K. Chao, S. Lu, Y. Li, *J. Phys. Chem. B* **2004**, 108, 18408–18413; e) A. Patra, C. S. Friend, R. Kapoor, P. N. Prasad, *Chem. Mater.* **2003**, 15, 3650–3655.
- [10] P. Mahata, K. V. Ramya, S. Natarajan, *Chem. Eur. J.* **2008**, 14, 5839–5850.
- [11] a) V. A. Blatov, <http://www.topos.ssu.samara.ru/>, **2006**; b) V. A. Blatov, A. P. Shevchenko, V. N. Serezhkin, *J. Appl. Crystallogr.* **2000**, 33, 1193–1193.
- [12] a) R. Adnan, H.-K. Fun, S. R. Jebas, *Acta Crystallogr., Sect. E* **2008**, 64, m971–m972; b) C.-B. Liu, H.-L. Wen, S.-S. Tan, X.-G. Yi, *J. Mol. Struct.* **2008**, 879, 25–29; c) Z. Rzacynska, M. Wozniak, W. Wolodkiewicz, A. Ostasz, S. Pikus, *J. Therm. Anal. Calorim.* **2007**, 88, 871–876; d) R. Yang, N. Zheng, H. Xu, Z. Li, *Huaxue Tongbao* **2003**, 66, 492–495; e) R. Yang, N. Zheng, H. Xu, Z. Li, X. Jin, *Chin. Sci. Bull.* **2003**, 48, 1111–1114; f) H. Xu, N. Zheng, X. Jin, R. Yang, Z. Li, *Chem. Lett.* **2002**, 11, 1144–1145.
- [13] Y. Qiu, H. Deng, S. Yang, J. Mou, C. Daiguebonne, N. Kerbellec, O. Guillou, S. R. Batten, *Inorg. Chem.* **2009**, 48, 3976–3981.
- [14] a) B. D. Chandler, D. T. Cramb, G. K. H. Shimizu, *J. Am. Chem. Soc.* **2006**, 128, 10403–10412; b) P. R. Selvin, *Nat. Struct. Biol.* **2000**, 7, 730–734.
- [15] R. E. Whan, G. A. Crosby, *J. Mol. Spectrosc.* **1962**, 8, 315–327.
- [16] a) Y. Huang, B. Yan, M. Shao, *Solid State Sci.* **2008**, 10, 90–98; b) R. Murugavel, P. Kumar, M. G. Walawalkar, R. Mathialagan, *Inorg. Chem.* **2007**, 46, 6828–6830; c) K. L. Zhang, N. Qiao, H. Y. Gao, F. Z. Ming Zhang, *Polyhedron* **2007**, 26, 2461–2469.
- [17] Z. H. Zhang, T. Okamura, Y. Hasuchika, H. Kawaguchi, L. Y. Kong, W. Y. Sun, N. Ueyam, *Inorg. Chem.* **2005**, 44, 6219–6227.
- [18] a) J. C. Wright, *Topics in Applied Physics: Radiationless Processes in Molecules and Condensed Phases* (Ed.: F. K. Fong), Springer, Berlin, **1976**; b) F. Auzel, *C. R. Acad. Sci. Paris* **1966**, 1016.
- [19] F. Auzel, *Chem. Rev.* **2004**, 104, 139–174.
- [20] J. J. Ju, T. Y. Kwon, H. K. Kim, J. H. Kim, S. C. Kim, M. Cha, S. I. Yun, *Mater. Lett.* **1996**, 29, 13–18.
- [21] SMART (v. 5.628), SAINT (v. 6.45a), XPREP, *SHELXTL*, Bruker AXS Inc., Madison, WI, **2004**.
- [22] G. M. Sheldrick, *Siemens area correction absorption correction program*, University of Göttingen, Göttingen, Germany, **1994**.
- [23] G. M. Sheldrick, *SHELXL-97, Program for crystal structure solution and refinement*, University of Göttingen, Göttingen, Germany, **1997**.
- [24] WinGx suite for small-molecule single-crystal crystallography: J. L. Farrugia, *J. Appl. Crystallogr.* **1999**, 32, 837–838.
- [25] A. Le Bail, H. Duroy, J. L. Fourquet, *Mater. Res. Bull.* **1988**, 23, 447–452.

Received: February 25, 2010
Published Online: June 15, 2010

Anionic Metal–Organic Frameworks of Bismuth Benzenedicarboxylates: Synthesis, Structure and Ligand-Sensitized Photoluminescence

A. Thirumurugan^[a] and Anthony K. Cheetham^{*[a]}

Keywords: Metal–organic frameworks / Bismuth / Luminescence / Lanthanides / Network topology

Four organic–inorganic bismuth benzenedicarboxylate (bdc) frameworks, $[\text{Bi}(1,4\text{-bdc})_2(\text{dmf})] \cdot (\text{dma})(\text{dmf})_2$ (**1**), $[\text{Bi}(1,4\text{-bdc})_2] \cdot (\text{dma})(\text{dmf})$ (**2**), $[\text{Bi}_4(1,4\text{-bdc})_7(\text{HIm})] \cdot (\text{dma})_2(\text{dmf})_2$ (**3**) and $[\text{Bi}(1,4\text{-bdc})_2] \cdot (\text{dma})$ (**4**) (where dma = dimethyl ammonium cation, HIm = imidazole and dmf = dimethylformamide) have been synthesized under solvothermal conditions, and their structures were determined by single-crystal X-ray diffraction. Compound **1** has a layer structure, whereas compounds **2–4** have three-dimensional structures. All four frameworks are anionic and contain dma cations within cavities in their structures. Compounds **1–3** also contain coordinated and/or

guest dmf molecules. The topologies of compounds **1–3** have 4-connecting nodes; the layer structure in **1** is a corrugated (4,4)-connected square lattice, but the three-dimensional structures of **2** and **3** adopt the (dia) net topology. Compound **4** has a 6-connecting node with a (pcu) net topology. The BiO_n polyhedra are hemidirected with a stereochemically active lone pair of electrons in **2**, but holodirected with a stereochemically inactive lone pair of electrons in **1**, **3** and **4**. Tb^{3+} - and Eu^{3+} -doped and co-doped **3** and **4** emit intense, ligand-sensitized green, red or orange luminescence, respectively.

Introduction

Hybrid organic–inorganic or metal–organic frameworks (MOFs) are an important class of compounds that have attracted much attention during the last decade due to their wide ranging properties and emerging applications.^[1–6] MOFs based on dicarboxylic acid ligands of various sizes and geometries have been extensively studied because of their chemical diversity and novel architectures, especially the MOFs based on transition-metal benzenedicarboxylates.^[7] Metal–organic coordination polymers based on lanthanide ions have also been studied for their catalytic, magnetic and optical properties.^[8–11] In common with the lanthanides, the Bi^{3+} cation, with its geometrically flexible coordination environments, can act as an interesting node in the construction of MOFs. The added advantage is that it can exist with or without an active lone pair of electrons, which can be used to fine tune the coordination geometry of the Bi^{3+} cation and the collective properties of the materials.^[12,13] Compounds containing Bi^{3+} cations are also used in oxidation catalysis and can act as lanthanide hosts for optical applications.^[14–16] Only a few frameworks based on bismuth carboxylates have been reported to date,^[17–20] so we have recently begun to explore the structures and properties of these interesting materials.^[21] In the present work,

we describe a new family of anionic metal–organic frameworks based on Bi benzenedicarboxylates (bdc). Compounds $[\text{Bi}(1,4\text{-bdc})_2(\text{dmf})] \cdot (\text{dma})(\text{dmf})_2$ (**1**), $[\text{Bi}(1,4\text{-bdc})_2] \cdot (\text{dma})(\text{dmf})$ (**2**), $[\text{Bi}_4(1,4\text{-bdc})_7(\text{HIm})] \cdot (\text{dma})_2(\text{dmf})_2$ (**3**) and $[\text{Bi}(1,4\text{-bdc})_2] \cdot (\text{dma})$ (**4**) have been synthesized and structurally characterized. We describe their novel structural features and discuss their ligand-sensitized rare-earth-centred photoluminescence.

Results and Discussion

Four bismuth 1,4-benzenedicarboxylates, **1–4**, have been synthesized solvothermally and characterized by X-ray diffraction and other techniques. Of these, compound **1** is a two-dimensional coordination polymer with T^0O^2 connectivity, and compounds **2–4** are three-dimensional coordination polymers with T^0O^3 connectivity.^[3] All four frameworks are anionic, having dma cations for charge compensation. Compounds **1–3** also contain coordinated and/or guest dmf molecules.

Structure of $[\text{Bi}(1,4\text{-bdc})_2(\text{dmf})] \cdot (\text{dma})(\text{dmf})_2$ (**1**)

Two-dimensional benzenedicarboxylate **1** has an asymmetric unit of 43 non-hydrogen atoms with one Bi^{3+} cation, one and two half 1,4-benzenedicarboxylate (1,4-bdc) dianions, one dma cation and three dmf molecules. The Bi^{3+} cation is ninefold coordinated by eight oxygen atoms from four different bdc anions and one from a terminal dmf molecule (Figure S1a). The BiO_9 polyhedron is holodirected

[a] Department of Materials Science and Metallurgy, University of Cambridge, Pembroke Street, Cambridge CB2 3QZ, UK
Fax: +44-1223-334567
E-mail: akc30@cam.ac.uk

Supporting information for this article is available on the WWW under <http://dx.doi.org/10.1002/ejic.201000535>.

with a stereochemically inactive lone pair of electrons. The Bi–O bond lengths are in the range 2.300(3)–2.865(4) Å. The bdc anions are of three crystallographically unique types, bdc-1, bdc-2 and bdc-3, all exhibiting similar coordination modes (1111)^[22] and each coordinating to two Bi³⁺ cations (Figure S1b). The carboxylate groups in the bdc anions chelate in a bidentate manner with the Bi³⁺ cation. The torsional angles between the two carboxylate groups are 20.00(1)° in bdc-1 and 0° in both bdc-2 and bdc-3. Each Bi³⁺ cation is connected to four other Bi³⁺ cations through the bdc anions, leading to the formation of an infinite two-dimensional layer structure (Figure 1a) with a (4,4)-connected square lattice (sql) net topology (Figure S1c). Coordination by the terminal dmf molecule results in an asymmetric coordination sphere with respect to bdc anion binding, effecting a corrugation in the layer (Figure 1b). The corrugated layers are stacked along the *a* axis with dma cations in between them, hydrogen-bonding to the carboxylate oxygen atoms. The dmf molecules are situated both within and between the layers, thus creating two types of square voids; while one contains coordinated dmf molecules, the other has extra-framework dmf molecules (Figure 1a). The Bi···Bi distances are in the range 10.096(1)–11.186(3) Å within the layer. The shortest Bi···Bi distance between the adjacent layers is 9.138(4) Å. The structure without the dmf molecules possesses 48.3% solvent-accessible void space based on a PLATON calculation.

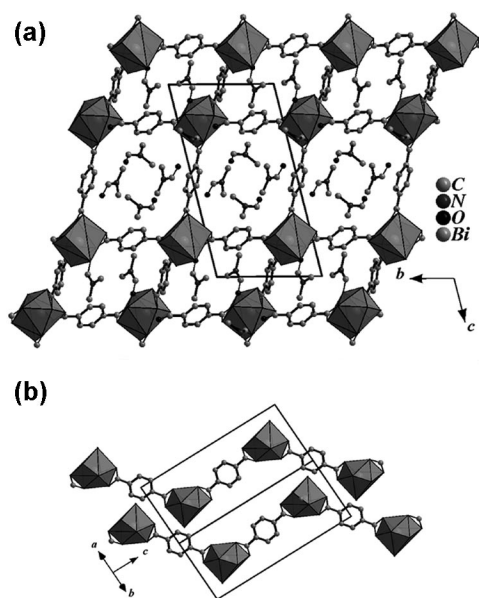


Figure 1. The view of the two-dimensional structure in **1** down (a) the *a* axis and (b) the corrugation in the layers.

Structure of [Bi(1,4-bdc)₂](dma)(dmf) (**2**)

Three-dimensional benzenedicarboxylate **2** has an asymmetric unit with 0.5 Bi³⁺ cation, one 1,4-benzenedicarboxylate (1,4-bdc) dianion, 0.5 dma cation and 0.5 dmf molecule. The Bi³⁺ cation is eightfold coordinated by oxygen atoms from four different bdc anions (Figure S2a). The BiO₈ poly-

hedron is hemidirected with a stereochemically active lone pair of electrons and Bi–O bond lengths in the range 2.282(2)–2.712(4) Å. The bdc anions are of two crystallographically unique types; bdc-1 and bdc-2 both exhibit similar coordination modes (1111) and each coordinate to two Bi³⁺ cations (Figure S2b). The carboxylate groups in the bdc anions chelate in a bidentate manner with the Bi³⁺ cation. The torsional angles between the two carboxylate groups are 0° in both bdc-1 and bdc-2, which are therefore planar. Each Bi³⁺ cation is connected to four other Bi³⁺ cations through four different bdc anions. These connectivities lead to the formation of an infinite three-dimensional structure (Figure 2) with a threefold interpenetrated diamond net (dia) topology (Figure S2c).^[23] The dma cations, which are disordered, occupy space between the bdc anions and appear to hydrogen-bond to the carboxylate oxygen atoms. The structure without the dmf molecules possesses 18.1% solvent-accessible void space based on a PLATON calculation. The Bi···Bi distances are in the range 11.334(2)–11.414(4) Å. H₂ and N₂ sorption measurements at 77 K were carried out to explore the porosity and hydrogen storage behaviour. At 77 K and 113 kPa, the hydrogen uptake capacity of activated **2** is 0.25 wt.-% with a Langmuir surface area of 110.15 m²/g. The type-1-like N₂ sorption isotherm indicates a Langmuir surface area of 57.86 m²/g.

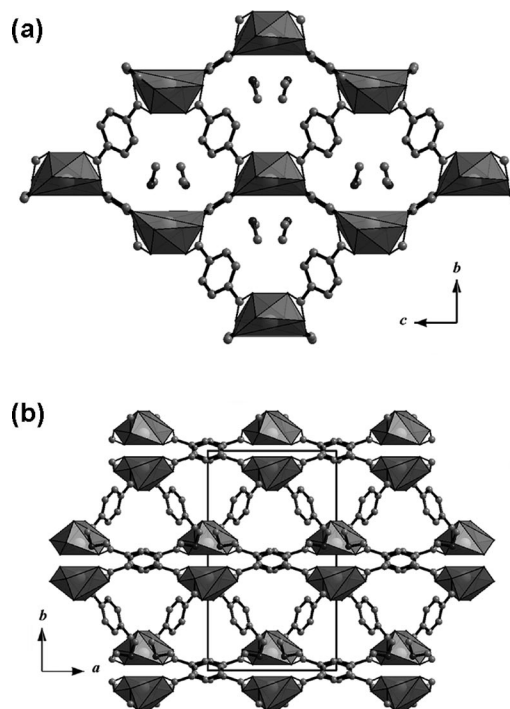


Figure 2. The view of the three-dimensional structure in **2** down (a) the *a* axis and (b) the *c* axis.

Structure of [Bi₄(1,4-bdc)₇(Him)]·(dma)₂(dmf)₂ (**3**)

Three-dimensional framework **3** has an asymmetric unit with two Bi³⁺ cations, 3.5 1,4-benzenedicarboxylate (1,4-bdc) dianions, 0.5 imidazole (Him) molecule, one dma cation and one dmf molecule. There are two types of Bi³⁺ cat-

ions, Bi1 and Bi2, both nine-coordinate and holodirected with stereochemically inactive lone pairs of electrons. The Bi(1)NO₈ polyhedron is coordinated by eight oxygen atoms from four different bdc anions and one nitrogen atom from a terminal imidazole molecule. The Bi–O bond lengths are in the range 2.381(4)–2.724(3) Å and the Bi–N bond length is 2.430(3) Å. The Bi(2)O₉ polyhedron is coordinated by nine oxygen atoms from six different bdc anions. The Bi–O bond lengths are in the range 2.254(2)–2.840(3) Å. The bdc anions are of four crystallographically unique types; bdc-1, bdc-2 and bdc-3 exhibit a (2111) mode (Figure S3a), each coordinating one Bi1 and two Bi2 cations, while bdc-4 exhibit a different mode (1111) (Figure S3b), coordinating with two Bi1 cations. The torsional angles between the two carboxylate groups are 10.002(3), 15.202(2), 22.203(2) and 0° in bdc-1, bdc-2, bdc-3 and bdc-4, respectively. Each Bi(1)NO₈ polyhedron shares a face with a Bi(2)O₉ polyhedron through three carboxylate oxygen atoms, resulting in the formation of a dimeric unit (Figure S3c). Each dimer is connected to four other dimers by seven bdc anions (Figure 3). These connectivities lead to the formation of an infinite three-dimensional structure (Figure 3) with a twofold interpenetrated diamond net (dia) topology (Figure S3d).^[23] The terminal imidazole molecules project out into the voids from the Bi(1) cations. The disordered dma cations and dmf molecules occupy space between the bdc anions and appear to hydrogen-bond with the carboxylate oxygen atoms. The Bi···Bi distances are in the range 11.380(2)–14.982(3) Å. The structure without the dmf molecules possesses 44.5% solvent-accessible void space based on a PLATON calculation.

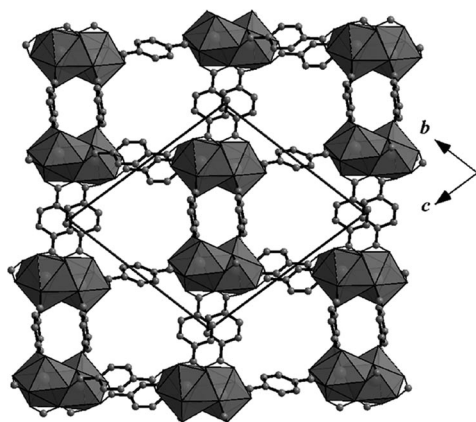


Figure 3. The view of the three-dimensional structure in **3** down the *a* axis. (HIm, dma and dmf molecules are not shown for clarity).

Structure of [Bi(1,4-bdc)₂](dma) (**4**)

Three-dimensional structure **4** has an asymmetric unit with two Bi³⁺ cations (occupancies 0.167 and 0.333), one 1,4-benzenedicarboxylate (1,4-bdc) dianion and one dma cation. There are two types of Bi³⁺ cations, Bi1 and Bi2, which are twelve- and nine-coordinate, respectively, both being holodirected with a stereochemically inactive lone

pair of electrons. The Bi(1)O₁₂ polyhedron is coordinated by twelve oxygen atoms from six bdc anions. The Bi–O bond lengths are in the range 2.488(3)–3.035(1) Å. The Bi(2)O₉ polyhedron is coordinated by nine oxygen atoms from six different bdc anions. The Bi–O bond lengths are in the range 2.309(4)–2.675(5) Å. The bdc anion exhibits the (2111) mode (Figure S4a) with each coordinating one Bi1 and two Bi2 cations. The torsional angle between the two carboxylate groups is 17.614(3)°. The Bi(1)O₁₂ polyhedron shares two of its faces with two different Bi(2)O₉ polyhedra through three carboxylate oxygen atoms, resulting in the formation of a trimeric unit (Figure S4b). Each trimer is connected to six similar trimers by twelve bdc anions (Figure 4). These connectivities lead to the formation of an infinite three-dimensional structure (Figure 4) with a two-fold interpenetrated (pcu) net topology (Figure S4c).^[23] The disordered dma cations occupy space between the bdc anions and appear to hydrogen-bond with the carboxylate oxygen atoms. The distance between the neighbouring trimers is 11.354(4) Å. Unlike **1–3**, **4** is a dense structure without any solvent-accessible void space.

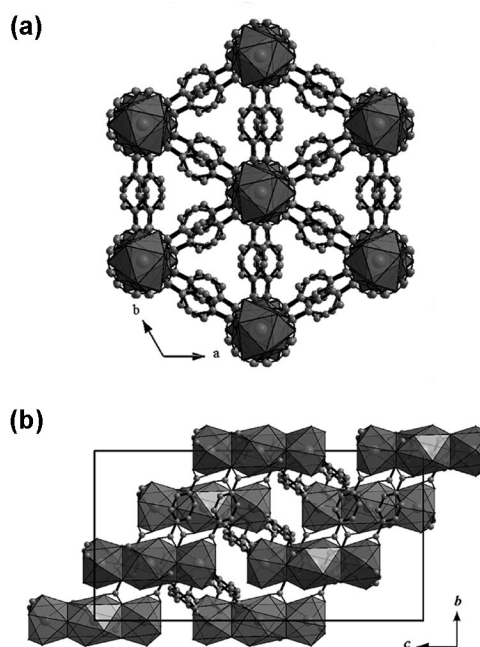


Figure 4. The view of the three-dimensional structure down (a) the *c* axis and (b) the *a* axis in [Bi(1,4-bdc)₂](dma) (**4**). (dma cations are not shown for clarity).

Comparison of Structures

The bismuth benzene dicarboxylates **1–4** are an interesting family of coordination polymers with anionic host frameworks, cationic amines and (in **1–3**) dmf guest molecules. Though anionic framework structures are abundant in zeolites and zeolitic analogues, such as metal phosphates and sulfates, they are relatively rare in metal–organic frameworks.^[24–27] Compounds **1–3** have four-connecting nodes,

whereas **4** has a six-connecting node. These different structures arise as a consequence of quite subtle differences in the synthetic reactions. The dma cations are generated in situ by the partial decomposition of dmf solvent molecules; similar in situ reactions are quite common in the MOF literature.^[28,29] It is interesting to note that the six-connected net of framework **4** is significantly more stable than the four-connected nets of phases **2** and **3** (see TGA results, Figures S7a–S7c).

Optical Properties

Due to the similar charges and ionic radii, bismuth-containing compounds are known to act as good hosts for rare-earth-doped optical materials.^[15,16,21] In order to evaluate the performance of the different structures as hosts, we have investigated the luminescence properties of the Tb³⁺- and Eu³⁺-doped frameworks **3** and **4** (compound **1** could not be obtained as a pure phase and doping into compound **2** was not successful, perhaps due to the effect of the stereochemically active lone pair in the Bi environment). We have partially doped Tb³⁺ and Eu³⁺ (2 mol-%) at the Bi site in **3** and **4**. The room-temperature photoluminescence properties of these compounds were studied by using an excitation wavelength of 295 or 305 nm. The emission spectra of the undoped compounds have a broad peak centred at approximately 420 nm, which may be attributed to intraligand luminescence ($n\leftarrow\pi^*/(\pi\leftarrow\pi^*)$ or charge-transfer transitions (Figures 5a and 6a). An optical emission study of the doped

compounds **3a** (2 mol-% Tb), **3b** (2 mol-% Eu), **3c** (2 mol-% Tb and 2 mol-% Eu), **4a** (2 mol-% Tb), **4b** (2 mol-% Eu) and **4c** (2 mol-% Tb and 2 mol-% Eu) revealed excitation spectra with a band maximum at around 295 nm for **3a–c** (Figure 5b–d) and 335 nm for **4a–c** (Figure 6b–d). The process probably involves intersystem crossing (ISC) from the singlet to the triplet excited state of the 1,4-bdc anion, followed by energy transfer to the ⁵D₄ state of Tb³⁺ ions and to the ⁵D_J, $J = 3, 2, 1, 0$ state of Eu³⁺ ions.^[10,11,30] In the Tb³⁺-doped compounds **3a**, **3c**, **4a**, and **4c**, the emission from the ⁵D₄→⁷F_J states is responsible for the green luminescence. In the Eu³⁺-doped compounds **3b**, **3c**, **4b** and **4c**, the emission from the ⁵D₀→⁷F_J states is responsible for the red luminescence. Co-doping with both rare-earth elements gives rise to orange luminescence. The main emission band of the intraligand luminescence is almost completely suppressed in all systems, confirming that efficient energy transfer takes place from the ligand to the rare-earth ions. Strong green, red or orange emissions visible to the naked eye were observed for all the doped samples. A qualitative comparison reveals that the emission intensities are higher in **4a–c** than in those **3a–c**, which may be attributed to the smaller Stokes shift for **4** or to the differences in the structures.

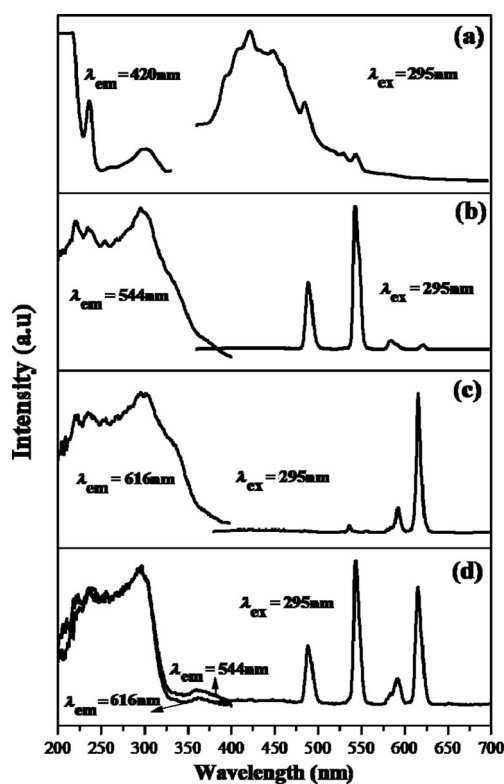


Figure 5. Photoluminescence spectra of (a) **3**, (b) **3a** (2 mol-% Tb), (c) **3b** (2 mol-% Eu) and (d) **3c** (2 mol-% Tb + 2 mol-% Eu).

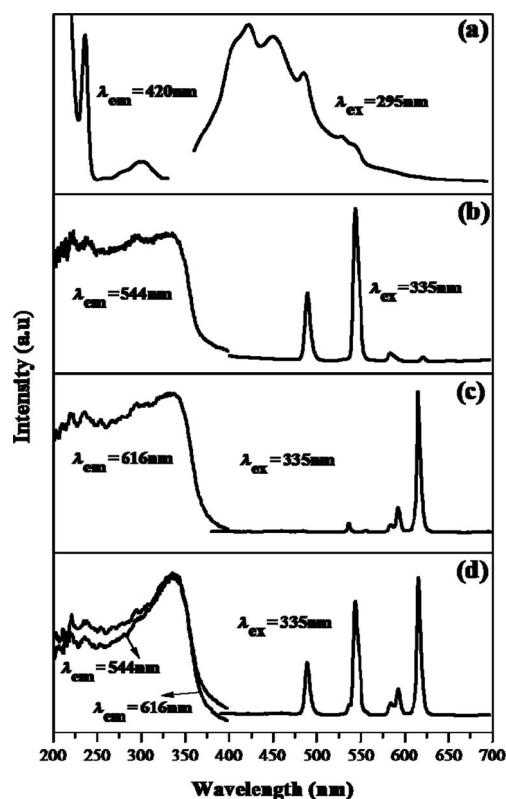


Figure 6. Photoluminescence spectra of (a) **4**, (b) **4a** (2 mol-% Tb), (c) **4b** (2 mol-% Eu) and (d) **4c** (2 mol-% Tb + 2 mol-% Eu).

Conclusions

Four anionic frameworks of bismuth benzenedicarboxylates with two- and three-dimensional structures have been

synthesized and structurally characterized. Variation in the topology is achieved by varying the Bi salts, amines and the composition of reactants in the synthesis. The in situ generation of dma cations is utilized as a useful method in the assembly of bdc as anionic frameworks. Strong ligand-sensitized lanthanide luminescence is achieved in Tb³⁺- and Eu³⁺-doped and co-doped derivatives of **3** and **4**.

Experimental Section

Synthesis and Characterization

Materials: Triphenylbismuth carbonate (TPBC) (C₁₃H₁₅BiO₃), Bi(NO₃)₃·5H₂O (Aldrich, 98%), Tb(NO₃)₃·5H₂O (Acros, 99.9%), Eu(NO₃)₃·5H₂O (Aldrich, 99.9%), LiOH·H₂O (Fisher, 99%), 1,4-benzenedicarboxylic acid (1,4-H₂bdc) (C₈H₆O₄) (Acros, 98%), piperazine (pip) (C₄H₁₀N₂) (Acros, 99%), imidazole (HIm) (C₃H₄N₂) (Acros, 99%) and dimethyl formamide (dmf) (Fisher, 99%) were used for the syntheses, as purchased.

Synthesis of 1–4: In a typical synthesis of **1**, a homogeneous mixture of TPBC (0.3 mmol), 1,4-H₂bdc (1.5 mmol), pip (0.3 mmol) and dmf (5 mL), was sealed in a 23 mL stainless steel reactor with a PTFE liner and heated at 100 °C for 3 d, then cooled to room temperature. The reaction gave a mixture of crystals of **1** and 1,4-H₂bdc-dmf co-crystals admixed with another unidentified powder phase. Changing the bismuth salt from TPBC to Bi(NO₃)₃·5H₂O (0.3 mmol) and pip by LiOH·H₂O (0.6 mmol) in the synthesis of **1** gave crystals of **2** [yield 70% based on Bi(NO₃)₃·5H₂O]. Replacing the pip with HIm (0.3 mmol) in the synthesis of **1** gave crystals of **3** admixed with another unidentified powder phase, but replacing the LiOH·H₂O with HIm (1.2 mmol) in the synthesis of **2** gave crystals of **4** [yield 63% based on Bi(NO₃)₃·5H₂O]. The impure products obtained with **1** limited the number of characterizations that we were able to make on this compound. In the case of **3**, crystals were manually separated from the reaction products and

used for further characterization. 2% Eu³⁺- and Tb³⁺-doped **3** and **4** were prepared by using the stoichiometric amounts of Eu/Bi and Tb/Bi nitrates. Rare-earth doping of the bismuth phases is possible for concentrations up to ca. 20%. Concentrations beyond this limit gave an unidentified powder phase along with the parent compound.

Elemental analyses of **2–4** were in good agreement with our expectations. For **2**: C₂₁H₂₃N₂O₉Bi (656.59): calcd. C 38.41, H 3.51, N 4.27; found C 38.21, H 3.24, N 4.05. For **3**: C₃₆H₃₃N₄O₁₅Bi₂ (1179.62): calcd C 36.64, H 2.80, N 4.75; found C 36.80, H 2.97, N 4.43. For **4**: C₁₈H₁₆NO₈Bi (583.30): calcd C 37.05, H 2.74, N 2.40; found C 36.56, H 2.32, N 2.78. It was not possible to obtain phase-pure samples of **1** for chemical analysis and other measurements. Powder X-ray diffraction (PXRD) patterns were collected by using Cu-K_α radiation with a Bruker D8 powder X-ray diffractometer having a position-sensitive detector (LynxEye) and graphite monochromator. The program PowderCell 2.4 was used for simulation of powder patterns based upon our crystal structures. The patterns agreed well with those calculated for single-crystal structure determination. Experimental and simulated powder patterns of **2–4** are given in the Supporting Information (Figures S5a–S5c). Infrared spectroscopy was performed at room temperature in the mid-IR range with a Bruker Tensor 27 infrared spectrometer equipped with an ATR diamond cell. Compounds **2–4** showed characteristic bands for the functional groups. The bands around 1550 and 1350 cm^{−1} can be assigned to carboxylate ν_{as} C=O and ν_s C=O stretching, and the absence of a band at 1700 cm^{−1} confirms the binding of deprotonated carboxylate groups to the cations. The band at 3150 (ν_s N–H) indicates the presence of protonated amine in **2**. Infrared spectra are given in the Supporting Information (Figures S6a–S6c). Thermogravimetric analyses data were obtained with a TA Instruments Q500 with a heating rate of 10 °C min^{−1} in air for **2**, **3** and **4**. For **2**, the first weight loss of 12.5% occurred around 180 °C, and the second weight loss of 39% was in the 350–450 °C range. For **3**, the first weight loss of 16.3% occurred around 200 °C, and the second weight loss was around 415 °C. For

Table 1. Crystal data and structure refinement parameters for **1–4**.

Structure parameter	1	2	3	4
Empirical formula	C ₂₇ H ₃₇ N ₄ O ₁₁ Bi	C ₂₁ H ₂₃ N ₂ O ₉ Bi	C ₃₆ H ₃₃ N ₄ O ₁₅ Bi ₂	C ₁₈ H ₁₆ NO ₈ Bi
Formula weight	802.59	656.59	1179.62	583.30
Crystal system	Triclinic	Monoclinic	Triclinic	Trigonal
Space group	<i>P</i> 1̄ (no. 2)	<i>C</i> 2/c (no. 15)	<i>P</i> 1̄ (no. 2)	<i>R</i> 3̄c (no. 167)
<i>a</i> (Å)	9.1381(1)	10.7068(2)	13.6855(3)	17.6932(7)
<i>b</i> (Å)	10.0961(2)	17.7294(4)	13.7530(3)	17.6932(7)
<i>c</i> (Å)	18.7143(3)	13.2435(2)	15.3046(3)	29.7350(9)
<i>α</i> (°)	99.5467(11)	90	73.0350(14)	90
<i>β</i> (°)	101.9611(10)	104.446(1)	75.0470(13)	90
<i>γ</i> (°)	105.9549(11)	90	82.0480(14)	120
<i>V</i> (Å ³)	1577.79(05)	2434.47(8)	2655.73(10)	8061.4(5)
<i>Z</i>	2	4	2	18
<i>D</i> _{calc} (g cm ^{−3})	1.689	1.791	1.475	2.163
<i>μ</i> (mm ^{−1})	5.650	7.293	6.672	9.91
Total data collected	32736	18832	62588	29128
Unique data	7216	4227	12184	2064
Observed data [<i>I</i> > 2σ (<i>I</i>)]	6661	3956	9538	1381
<i>R</i> _{merg}	0.0402	0.0363	0.0510	0.0344
<i>R</i> indexes [<i>I</i> > 2σ (<i>I</i>)]	<i>R</i> ₁ = 0.0314 ^[a] ; <i>wR</i> ₂ = 0.0628 ^[b]	<i>R</i> ₁ = 0.0405 ^[a] ; <i>wR</i> ₂ = 0.1207 ^[b]	<i>R</i> ₁ = 0.0481 ^[a] ; <i>wR</i> ₂ = 0.1282 ^[b]	<i>R</i> ₁ = 0.0701 ^[a] ; <i>wR</i> ₂ = 0.1247 ^[b]
<i>R</i> indexes [all data]	<i>R</i> ₁ = 0.0367 ^[a] ; <i>wR</i> ₂ = 0.0351 ^[b]	<i>R</i> ₁ = 0.0444 ^[a] ; <i>wR</i> ₂ = 0.1229 ^[b]	<i>R</i> ₁ = 0.0668 ^[a] ; <i>wR</i> ₂ = 0.1377 ^[b]	<i>R</i> ₁ = 0.1059 ^[a] ; <i>wR</i> ₂ = 0.1410 ^[b]
Goodness of fit (GOF)	1.100	1.184	1.037	1.166

[a] *R*₁ = Σ ||*F*_o| − |*F*_c||/Σ |*F*_o|. [b] *wR*₂ = {Σ[w(*F*_o² − *F*_c²)²]/Σ[w(*F*_o²)²]}^{1/2}; *w* = 1/[σ²(*F*_o)² + (*aP*)² + *bP*], *P* = [max(*F*_o², 0) + 2(*F*_c)²]/3, where *a* = 0 and *b* = 6.668 for **1**, *a* = 0.0772 and *b* = 7.7213 for **2**, *a* = 0.0643 and *b* = 26.7687 for **3** and *a* = 0.0120 and *b* = 916.4543 for **4**.

4, the weight losses occurred in two steps, one around 300 °C and another around 400 °C. In **2** and **4** the first weight loss corresponds to the loss of dmf molecules. TGA plots are given in the Supporting Information (Figures S7a–S7c). Photoluminescence spectra on solid samples were recorded by using a Perkin–Elmer LS55 fluorescence (Xenon lamp) spectrometer.

Single-Crystal Structure Determination: Single-crystal structure determination by X-ray diffraction was performed in the Kappa geometry with a Bruker-Nonius diffractometer having a Roper CCD detector, graphite monochromator and a Bruker-Nonius FR591 rotating-anode X-ray source (Mo- K_{α} radiation, $\lambda = 0.71073$ Å) for **1**, **3** and **4** at 120 K. For **2**, the data were collected at 180 K with a fine-focus sealed tube X-ray source (Mo- K_{α} radiation, $\lambda = 0.71073$ Å). An empirical absorption correction based on symmetry-equivalent reflections was applied by using the SADABS program.^[31] The structures were solved and refined with the SHELXTL PLUS suite of programs.^[32] For the final refinements, the hydrogen atoms were placed geometrically and held in the riding mode. The final refinements included atomic positions for all the atoms, anisotropic thermal parameters for all the non-hydrogen atoms (except in **3** and **4** where the guest entities are refined isotropically and include only non-hydrogen atoms) and isotropic thermal parameters for the hydrogen atoms. The attempts made to model the dmf molecules in **2** did not lead to the identification of guest entities in the structure because of the disordered solvent molecules in the crystals. The amount of dmf molecules in the structure per unit cell was obtained by the electron count within the pore (calculated using the SQUEEZE algorithm within PLATON)^[33] and the final formula was assigned accordingly. Details of the structure solution and final refinements for the compounds are given in Table 1. CCDC-776712, -776713, -776714, -776715 contain the supplementary crystallographic data for this paper. These data can be obtained free of charge from The Cambridge Crystallographic Data Centre via www.ccdc.cam.ac.uk/data_request/cif.

Supporting Information (see footnote on the first page of this article): Additional plots of coordination geometries, PXRD patterns, IR spectra and TGA plots.

Acknowledgments

We gratefully acknowledge the Isaac Newton Trust, Cambridge for the financial support for A. T, the Engineering and Physical Sciences Research Council (EPSRC) UK National Crystallography Service and Dr. John Davies (Department of Chemistry, University of Cambridge) for the single-crystal X-ray diffraction data collection. A. K. C thanks the European Research Council for an Advanced Investigator Award.

- [1] S. Kitagawa, R. Kitaura, S.-i. Noro, *Angew. Chem. Int. Ed.* **2004**, *43*, 2334–2375.
- [2] D. Bradshaw, J. B. Claridge, E. J. Cussen, T. J. Prior, M. J. Rosseinsky, *Acc. Chem. Res.* **2005**, *38*, 273–282.
- [3] A. K. Cheetham, C. N. R. Rao, R. K. Feller, *Chem. Commun.* **2006**, 4780–4795.

- [4] G. Férey, *Chem. Soc. Rev.* **2008**, *37*, 191–214.
- [5] C. N. R. Rao, A. K. Cheetham, A. Thirumurugan, *J. Phys.: Cond. Matt.* **2008**, 083202.
- [6] Themed issue: “Metal–Organic Frameworks”, *Chem. Soc. Rev.* **2009**, *38*, 1201–1508.
- [7] C. N. R. Rao, S. Natarajan, R. Vaidyanathan, *Angew. Chem. Int. Ed.* **2004**, *43*, 1466–1496.
- [8] J. W. Han, C. L. Hill, *J. Am. Chem. Soc.* **2007**, *129*, 15094–15095.
- [9] A. Thirumurugan, S. K. Pati, M. A. Green, S. Natarajan, *J. Mater. Chem.* **2003**, *13*, 2937–2941.
- [10] F. Serpaggi, T. Luxbacher, A. K. Cheetham, G. Férey, *J. Solid State Chem.* **1999**, *145*, 580–586.
- [11] A. Thirumurugan, S. Natarajan, *J. Mater. Chem.* **2005**, *15*, 4588–4594.
- [12] R. E. Cohen, *Nature* **1992**, *358*, 136–138.
- [13] W. Bi, N. Leblanc, N. Mercier, P. Auban-Senzier, C. Pasquier, *Chem. Mater.* **2009**, *21*, 4099–4101.
- [14] M. Postel, E. Duñach, *Coord. Chem. Rev.* **1996**, *155*, 127–144.
- [15] S. Neeraj, N. Kijima, A. K. Cheetham, *Chem. Phys. Lett.* **2004**, *387*, 2–6.
- [16] S. Neeraj, N. Kijima, A. K. Cheetham, *Solid State Commun.* **2004**, *131*, 65–69.
- [17] U. Kolitsch, *Acta Crystallogr., Sect. C* **2003**, *59*, m501–m504.
- [18] W. Li, L. Jin, N. Zhu, X. Hou, F. Deng, H. Sun, *J. Am. Chem. Soc.* **2003**, *125*, 12408–12409.
- [19] X. Chen, Y. Cao, H. Zhang, Y. Chen, X. Chen, X. Chai, *J. Solid State Chem.* **2008**, *181*, 1133–1140.
- [20] M. Rivenet, P. Roussel, F. Abraham, *J. Solid State Chem.* **2008**, *181*, 2586–2590.
- [21] A. Thirumurugan, J. C. Tan, A. K. Cheetham, *Cryst. Growth Des.* **2010**, *10*, 1736–1741.
- [22] For description of connectivity see: D. Massiot, S. Drumel, P. Janvier, M. Bujoli-Doeuff, B. Bujoli, *Chem. Mater.* **1997**, *9*, 6–7.
- [23] TOPOS website: <http://www.topos.ssu.samara.ru/>, Ac. Pavlov St. 1, 443011 Samara, Russia, January **2009**.
- [24] S. Natarajan, A. Thirumurugan, *Inorg. Chim. Acta* **2005**, *358*, 4051–4056.
- [25] Z. Lin, D. S. Wragg, R. E. Morris, *Chem. Commun.* **2006**, 2021.
- [26] F. Nouar, J. Eckert, J. F. Eubank, P. M. Forster, M. Eddaoudi, *J. Am. Chem. Soc.* **2009**, *131*, 2864–2870.
- [27] X. Wang, L. Liu, T. Makarenko, A. J. Jacobson, *Cryst. Growth Des.* **2010**, *10*, 1960–1965.
- [28] X. Y. Wang, L. Gan, S. W. Zhang, S. Gao, *Inorg. Chem.* **2004**, *43*, 4615–4625.
- [29] P. Jain, V. Ramachandran, R. J. Clark, H. D. Zhou, B. H. Toby, N. S. Dalal, H. W. Kroto, A. K. Cheetham, *J. Am. Chem. Soc.* **2009**, *131*, 13625–13627.
- [30] G. Blasse, B. C. Grabmaier, *Luminescent Materials*, Springer, Berlin, **1994**.
- [31] G. M. Sheldrick, *SADABS*, Version 2007/2, Bruker AXS Inc., Madison, Wisconsin, USA., **2007**.
- [32] G. M. Sheldrick, *SHELXTLPLUS Program for Crystal Structure Solution and Refinement*, University of Göttingen, Göttingen, Germany, **1997**.
- [33] A. L. Spek, *PLATON, A Multipurpose Crystallographic Tool*, Utrecht University, Utrecht, The Netherlands, **2004**.

Received: May 14, 2010

Published Online: July 16, 2010

A Dynamically Entangled Coordination Polymer: Synthesis, Structure, Luminescence, Single-Crystal-to-Single-Crystal Reversible Guest Inclusion and Structural Transformation

Arshad Aijaz,^[a] Prem Lama,^[a] and Parimal K. Bharadwaj*^[a]

Keywords: Coordination polymers / Dynamic frameworks / Inclusion compounds / SC-SC transformation / Photoluminescence / Zinc

A Zn^{II} coordination polymer $\{[\text{Zn}_2(\text{cpa})_2(\text{bpy})]\cdot 3\text{H}_2\text{O}\}_n$ (**1**) ($\text{cpa}^{2-} = 4$ -(methoxycarbonyl)benzoate and $\text{bpy} = 4,4'$ -bipyridine) has been synthesized under solvothermal condition and structurally characterized. This coordination polymer has nanotubular threefold entangled (2D \rightarrow 3D) structure with embedded water molecules; the water molecules can be partially exchanged in reversible single-crystal-to-single-crystal (SC-SC) fashion by different solvent molecules like methanol, ethanol and acetone giving rise to $\{[\text{Zn}_2(\text{cpa})_2(\text{bpy})]\cdot (0.5\text{MeOH})\cdot (2.5\text{H}_2\text{O})\}_n$ (**2**), $\{[\text{Zn}_2(\text{cpa})_2(\text{bpy})]\cdot (0.5\text{EtOH})\cdot (0.5\text{H}_2\text{O})\}_n$ (**3**) and $\{[\text{Zn}_2(\text{cpa})_2(\text{bpy})]\cdot (0.5\text{Me}_2\text{CO})\cdot (\text{H}_2\text{O})\}_n$ (**4**). Inclusion of EtOH or MeOH leaves the size of the voids in the framework unaltered. Inclusion of acetone, however, is

accompanied by shrinking of the voids in the framework. Heating of **1** at 100 °C under vacuum for 4 h affords the desolvated compound, $\{[\text{Zn}_2(\text{cpa})_2(\text{bpy})]\}_n$ (**1'**). Single-crystal X-ray structure of **1'** shows sliding of the individual nanotubular components expanding the overall framework. Thus, the coordination polymer exhibits dynamic motion of the molecular components in SC-SC fashion. All compounds were further characterized via IR spectroscopy, PXRD, elemental and TGA analysis. When **1** is placed in benzene at 100 °C for 2 days, compound $\{[\text{Zn}_2(\text{cpa})_2(\text{bpy})]\cdot (2.5\text{H}_2\text{O})\}_n$ (**5**) is formed in a SC-SC fashion where coordination number of Zn^{II} ion increases from four to five. Compound **1** also exhibits reversible guest-dependent photoluminescence properties.

Introduction

Microporous coordination polymers having open channels, are of considerable interest because of their potential applications.^[1] Success in producing such structures depend on understanding and controlling the topological and geometric relationships between molecular modules, along with the coordination tendencies of the metal ions.^[2] When two or more ligands are used, the design and choice of these components must fulfil criteria for spontaneously generating well-defined architectures.^[3] As the number of such framework materials are increasingly made available, it is observed that they exhibit a tendency to form entangled structures where two or more independent infinite networks interpenetrate each other.^[4] It is also possible that interpenetration may be able to sustain a framework showing dynamic porosity.^[5] For instance, the cavity inside an interpenetrated coordination polymer can change via sliding of the individual networks. This sliding can be triggered by guest exchange/inclusion leading to changes in the dimension of channels.^[6] There are few reports showing interpenetrated networks can shrink or swell when guest molecules

are removed and then re-adsorbed.^[7,5c] The flexible nature of entangled frameworks makes it uncommon in comparison to conventional coordination polymers.

Synthetic nanotubular architectures, which represent a unique class of open framework material, have attracted intensive attention due to their uniform and fixed internal diameters that could be potentially useful in ion or molecular transport. Their hydrophobic or hydrophilic pockets make them specific for understanding the mechanism of the assembly process leading to their formation and host-guest chemistry. Since the discovery of carbon nanotube in 1991,^[8] significant progress has been made in the realm of organic nanotubular architectures from cyclic peptides, oligo-cyclodextrins, lipids, etc and also inorganic nanotubes containing elements other than carbon and different metal ions.^[9] However, only few nanotubular metal-organic polymers have been reported in the literature.^[10] Synthetic strategy for coordination framework-based tubular structures could be obtained by coiling linear coordination chains into hollow, helical conformations, while the interweaving of two independent undulating networks can lead to the serendipitous formation of nanotubes. But the effective strategy is first to construct a square as a subunit by connecting the metal ions with organic linkers and secondly these squares are linked by another organic ligands from the four vertexes to generate a 1D nanotubular framework.^[11]

[a] Department of Chemistry, Indian Institute of Technology Kanpur, 208016 Kanpur, Uttar Pradesh, India
E-mail: pkb@iitk.ac.in

Supporting information for this article is available on the WWW under <http://dx.doi.org/10.1002/ejic.201000436>.

Aromatic polycarboxylates are chosen as rigid tectons, to bind metal centers for constructing supramolecular coordination polymer structures. Herein, we have synthesized an entangled coordination polymer $\{[\text{Zn}_2(\text{cpa})_2(\text{bpy})]\cdot 3\text{H}_2\text{O}\}_n$ (**1**) with a semi-flexible dicarboxylate linker cpa^{2-} . The reason to select this semi-flexible ligand is associated with the conformational freedom that imparts a large variety of structures, topologies and also flexibility. The co-ligand 4,4'-bipyridine is chosen as an appropriate spacer for generating a predetermined network structure. This highly crystalline stable framework (**1**) is showing reversible adsorption-desorption of solvent molecules like water, methanol, ethanol and acetone in the channels keeping the crystallinity intact. The dynamic processes are manifested through sliding of the entangled layers triggered by guest exchange.

Results and Discussion

Compound **1** was synthesized by solvothermal reaction of $\text{Zn}(\text{NO}_3)_2\cdot 6\text{H}_2\text{O}$, cpaH_2 and 4,4'-bipyridine in a mixture of ethanol and water at 130 °C for 3 days as colorless block-shaped crystals. It is formulated as $\{[\text{Zn}_2(\text{cpa})_2(\text{bpy})]\cdot 3\text{H}_2\text{O}\}_n$ by TGA, elemental analysis and single-crystal X-ray diffraction studies while the phase purity of the bulk material is confirmed by powder X-ray diffraction (PXRD). The complex once isolated is air-stable and insoluble in common organic solvents as well as water. A broad peak at 3457 cm^{-1} and strong absorption bands between 1420 and 1606 cm^{-1} in the IR spectrum of **1** are indicative of the presence of water molecules and of coordinated carboxylates respectively.^[12]

Single-crystal X-ray structural studies reveal two crystallographically independent Zn^{II} ions, two cpa^{2-} , one 4,4'-bipyridine and four free water molecules (two have half occupancy out of four water molecules) in the asymmetric unit. The two crystallographically different Zn^{II} centers (one octahedral and other tetrahedral) form a bimetallic secondary building unit (SBU) ($\text{Zn}\cdots\text{Zn}$ separation, 3.175 \AA). Two types of cpa^{2-} ligands exist in **1**; one cpa^{2-} ligand shows the aliphatic carboxylate to be chelating while the aromatic carboxylate is mono-dentate, whereas other cpa^{2-} ligand acts as bridging carboxylate at either end. The distorted octahedral Zn^{II} is coordinated to five O atoms from four cpa^{2-} ligands and one N of 4,4'-bipyridine ($\text{Zn}-\text{O}$ 2.019 – 2.324 \AA , $\text{Zn}-\text{N}$ 2.102 \AA). On the other hand, the distorted tetrahedral Zn^{II} is coordinated to three O atoms from three cpa^{2-} ligands (Figure 1) besides one N of 4,4'-bipyridine ($\text{Zn}-\text{O}$ 1.961 – 1.986 \AA , $\text{Zn}-\text{N}$ 2.004 \AA).

All the $\text{Zn}-\text{O}$ and $\text{Zn}-\text{N}$ distances are similar to normal $\text{Zn}-\text{O}$ and $\text{Zn}-\text{N}$ distances found in other octahedral and tetrahedral complexes.^[13] This bimetallic unit forms a $\{[\text{Zn}_2(\text{cpa})(0.5\text{bpy})]_4\}^{8+}$ ladder-like molecular rectangle with $\text{Zn}\cdots\text{Zn}$ separations of 12.78 and 11.07 \AA (Figure 2, a). Both the carboxylate groups, aromatic and aliphatic of ligand cpaH_2 , acts as a bridging linker to connect two SBUs in a *syn*-bridging mode. Thus, the $\{[\text{Zn}_2(\text{cpa})(0.5\text{bpy})]_4\}^{8+}$ rectangles are infinitely connected by anionic cpa^{2-} ligands

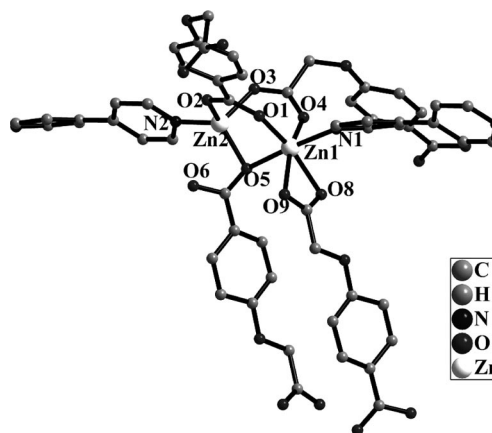


Figure 1. Coordination environment of Zn^{II} atoms with atomic labeling Scheme in **1**.

along the *b* axis to give rise to a 2D-metal-organic sheet framework having large cube-like boxes of dimension $12.78 \times 11.07 \times 10.56\text{ \AA}^3$ spreading in the crystallographic *bc* plane. Thus, the 2D sheet network is composed of 1D nanotubes joined together by covalent bonds (Figure 3).

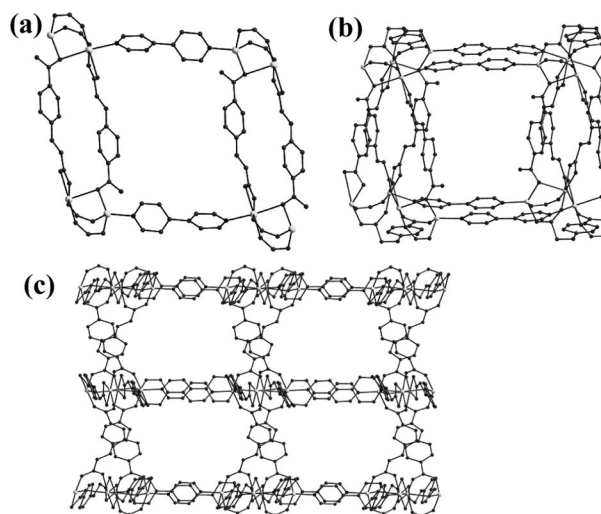


Figure 2. (a) View of the rectangular subunit $\{[\text{Zn}_2(\text{cpa})(0.5\text{bpy})]_4\}^{8+}$ in **1**. (b) distorted cube-like box. (c) View of the 2D sheet.

The fascinating structural feature of **1** is that each nanotube in 2D-framework, which is aligned parallel to the *b* axis, is interlocked in parallel fashion with the two similarly constructed neighboring tubular networks to form a 3D polycatenated framework (Figure 4). This kind of entanglement is still quite rare in the literature.

Complex **1** still possesses significant void space that is occupied by water molecules in which OW1 form H-bonds with OW2 and OW4 ($\text{OW1}\cdots\text{OW2}$ 2.971 \AA , $\text{OW1}\cdots\text{OW4}$ 2.996 \AA) while distorted OW3 is far from these water clusters ($\text{OW2}\cdots\text{OW3}$ 3.727 \AA). Also, OW2 forms a moderately strong H-bond with the aliphatic carboxylate of the framework ($\text{O3}\cdots\text{OW2}$ 2.883 \AA). The total potential solvent accessible void volume of **1** calculated by PLATON^[14] is found to be 20.2% of the crystal volume.

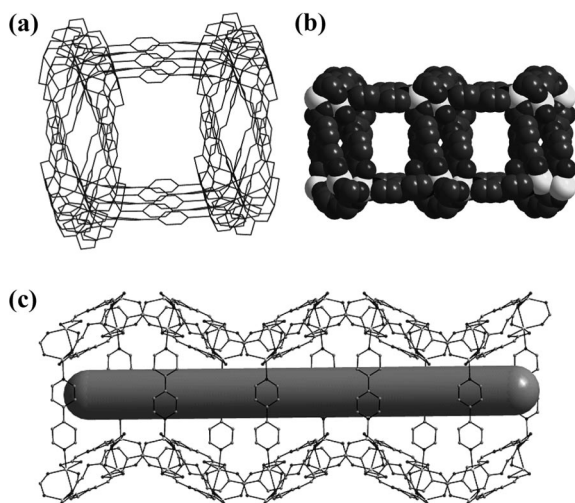


Figure 3. (a) Perspective view of the 1D channels of **1** showing single nanotube, (b) a portion of **1** having two joined nanotubes and (c) nanotubular structure showing the tube interior.

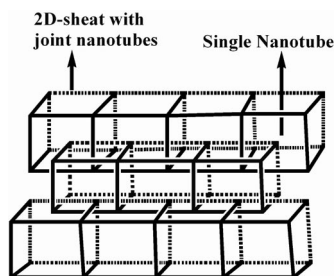


Figure 4. Schematic view of the threefold entanglement among the nanotubular sheets of framework **1**.

Thermal stability of **1** examined by TGA shows a weight loss of 7.5% from 80 to 150 °C, corresponding to loss of three water molecules (calcd. 7.4%). No further weight loss is shown till ≈ 310 °C.^[13] The PXRD pattern of the as-synthesized sample is very similar to that of the simulated pattern obtained from the single-crystal structural parameters showing the phase purity of the bulk samples.^[13] When crystals of **1** are heated at 100 °C under vacuum for 4 h, desolvated crystals of $\{[\text{Zn}_2(\text{cpa})_2(\text{bpy})]\}_n$ (**1'**) is formed. The X-ray crystal structure of **1'** reveals the same connectivity as in **1**. The space group (*C2/c*) also remains unaltered. Thermogram^[13] of **1'** shows no weight loss up to about 310 °C signifying absence of solvent water molecules. An examination of the PXRD pattern^[13] of **1** and that of **1'** shows small differences in the two, indicative of slight structural changes in the two cases. Careful examination of the crystal structure of **1'** shows some sliding of the entangled 2D frameworks. The total solvent accessible void volume in **1'** calculated by PLATON is found to be 21.0% of the crystal volume, which is somewhat larger than **1**. This suggests the interpenetrating networks undergo stress relaxation upon solvent removal with concomitant increase of the void volume.^[5c] When **1'** is exposed to open air having humidity (ca. 80%) for 12 h, water molecules are re-intro-

duced to obtain **1** as confirmed by PXRD pattern and single-crystal data.

In order to investigate replacement of water molecules in the channels by other solvent molecules, crystals of **1** are immersed in organic solvents like MeCN, MeOH, EtOH, CHCl_3 , benzene, acetone and hexane. In case of MeOH, EtOH and acetone, a few water molecules in the channels are partially replaced by organic solvent molecules in 2 days at room temperature, to afford the products $\{[\text{Zn}_2(\text{cpa})_2(\text{bpy})]\cdot(0.5\text{MeOH})\cdot(2.5\text{H}_2\text{O})\}_n$ (**2**), $\{[\text{Zn}_2(\text{cpa})_2(\text{bpy})]\cdot(0.5\text{EtOH})\cdot(0.5\text{H}_2\text{O})\}_n$ (**3**) and $\{[\text{Zn}_2(\text{cpa})_2(\text{bpy})]\cdot(0.5\text{Me}_2\text{CO})\cdot(\text{H}_2\text{O})\}_n$ (**4**) with maintaining crystallinity. In other cases, however, no solvents exchange can be observed even after 7 days at room temperature. X-ray structural analyses demonstrate that **2**, **3** and **4** have the same overall structure as **1** although, some of the lattice water molecules are replaced by the distorted organic solvent molecules with sufficient movement of their original positions. MeOH replaces half of the water molecule in **2** while EtOH and acetone replace 2.5 water molecules in their asymmetric unit. MeOH is H-bonded with carboxylate of cpa^{2-} ($\text{O2}\cdots\text{O11}$ 2.946 Å) and OW1 ($\text{OW1}\cdots\text{O11}$ 2.449 Å) in case of **2**, while remaining distorted water molecules show no H-bond with framework or other lattice solvent molecules. In case of **3** and **4** no substantial H-bonding interactions exist among the host framework and guest solvent molecules, although weak C–H \cdots O interaction (ca. 3.5 Å) is present to hold the guest molecules. Interestingly, the entangled 2D networks do not move in **2** and **3**, a slight movement is, however, observed in **4**. Here, the void volume shrinks to 19.4% from the value of 20.2% in **1**. When crystals of **2**, **3** and **4** are kept in water at room temperature for 2 days, compound **1** is regenerated in each case again maintaining crystallinity. Thus, expulsion and introduction of the lattice solvents molecules are reversible. Also, the size of H_2O , MeOH, EtOH and Me_2CO are calculated to be approximately 2.8, 4.0, 4.8 and 6.2 Å, respectively, and thus it would seem that the guest exchange is closely related to the size of the cavities in **1** (ca. 6.4×6.3 Å² by considering the van der Waals radii) compared to the sizes of the various guest molecules. When crystals of **1** are dipped in a mixture of acetone/DMF or acetone/benzene, only acetone molecules enter the voids forming **4**. The reason of non-exchange with CH_3CN (4.3 Å), benzene (5.8 Å) like molecules could be associated with their nature, geometry and comparable size to the channel aperture of **1**.

As benzene cannot replace water molecules in **1** at room temperature due to their hydrophilic pocket, **1** was heated solvothermally at 100 °C for two days in presence of benzene. Compound $\{[\text{Zn}_2(\text{cpa})_2(\text{bpy})]\cdot(2.5\text{H}_2\text{O})\}_n$ (**5**) was obtained as block-shaped colorless crystals. X-ray structural analysis reveals the overall structure of **5** to be similar to that of **1** except coordination geometry of the tetrahedral Zn^{II} is changed to trigonal bipyramidal. The monodentate carboxylate group is now bonded as a chelating ligand ($\text{Zn2}\cdots\text{O6}$ 2.55 Å) (Figure 5). Instead of three water molecules as in **1**, only 2.5 water molecules exist in the asymmetric unit of **5** (Figure 6). Also, there is a H-bond between

OW2 and OW3 (OW2...OW3 2.905 Å). The solvent accessible volume of **5** calculated using PLATON affords 21.8% which is larger than in **1** (20.3%). Keeping crystals of **5** dipped in water or exposed to air does not change it to **1**. So, this is a non-reversible structural transformation. In all transformed compounds it is not certain, which water molecules of **1** were substituted by organic solvent molecules, as position of exchanged solvents is quite different in comparison to **1**.

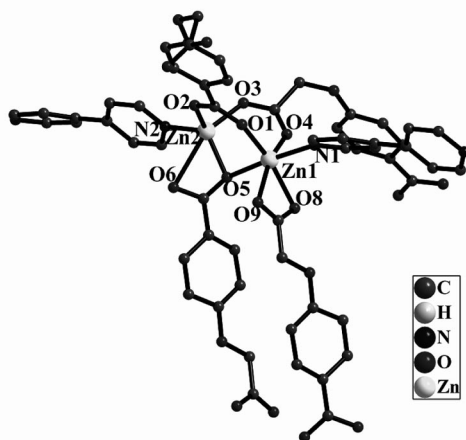


Figure 5. Coordination environment of Zn^{II} atoms with coordinated atomic labeling Scheme in **5**.

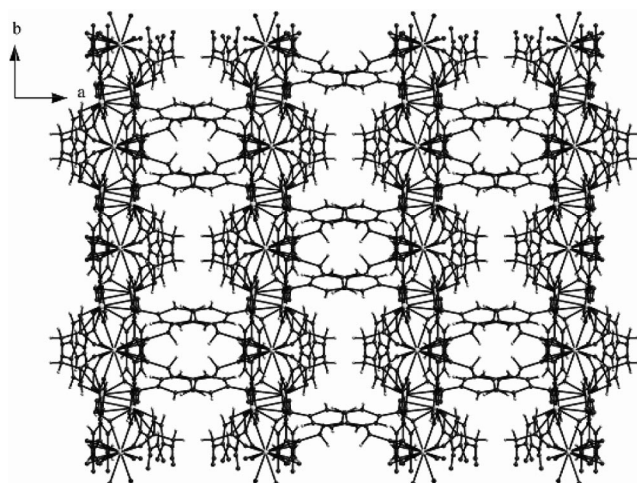


Figure 6. Crystal packing structure of **5** along the *c* axis.

Luminescent Properties

Luminescent compounds are of great current interest because of their various applications in chemical sensors, photochemistry, and electroluminescent display.^[15] Recently, the luminescent properties of d¹⁰ metal with carboxylate donors have been investigated.^[16] The solid-state luminescence of compounds **1** and **1'** and different solvent exchanged products are investigated at room temperature and the results are shown in Figure 7. Upon excitation at 270 nm, **1** exhibits strong luminescence centered at $\lambda_{\text{max}} =$

440 nm. Compared with the ligands, which has no luminescence, the greatly enhanced photoluminescence intensities may be attributed to the charge-transfer transition between ligands and metal centers,^[17] as ligand coordination to the metal center effectively increases rigidity of the ligand and reduces the loss of energy by radiation-less decay.^[18] An interesting feature in these systems is the fact that they show guest dependent photoluminescence. This may cause by the elastic nature of the frameworks. There are some reported guest dependent photoluminescence of polymeric compounds in literature.^[19]

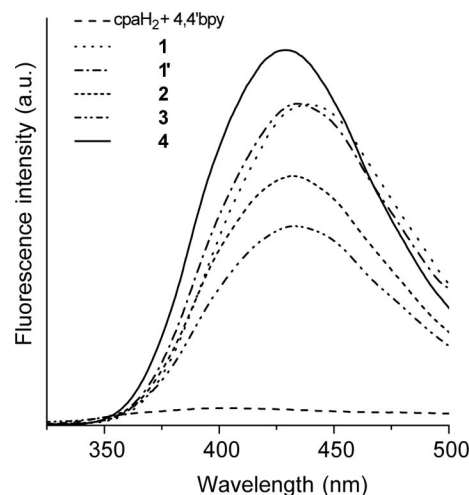


Figure 7. Solid-state emissions at room temperature.

Observation of guest-dependent luminescence property in the present studies can be the starting point to design photoactive materials as sensors for organic molecules.

Conclusions

In conclusion, we describe here an entangled tubular 3D framework structure built from Zn^{II} with semi-flexible 4-(methoxycarbonyl)benzoic acid and 4,4'-bipyridine. This interpenetrated coordination polymer exhibit movement of the entangled independent networks triggered by guest inclusion/removal. The robustness of the framework (**1**) is shown by reversible inclusion and expulsion of water, methanol, ethanol and acetone molecules in its cavity in SC-SC manner. We are presently studying similar systems for potential applications as sensors, storage of organic molecules and also as heterogeneous catalysts.

Experimental Section

Materials: The metal salt, 4,4'-bipyridine, and chloroethyl acetate were obtained from Aldrich and used as received. All other chemicals were procured from S. D. Fine Chemicals, India. All solvents were purified prior to use.

Physical Measurements: Infrared spectra were measured on a Perkin-Elmer Model 1320 (KBr disk, 400–4000 cm⁻¹), while X-ray powder pattern on Phillips PW 100 X-ray generator (Cu-K_α radiation at a scan rate of 3 °/min, 293 K). Thermogravimetric analyses

(TGA) were recorded on a Mettler–Toledo thermal analyzer (heating rate of 5 °C/min). Microanalyses for the compounds were obtained using a CE-440 elemental analyzer (Exeter Analytical Inc.). Solid-state photo-excitation and emission spectra were performed on double UV/Vis/NIR spectrophotometer (Varian Cary 5000) and Jobin Yvon Horiba Fluorolog-3 spectrophotometer respectively at room temperature.

Synthesis of cpaH₂: The ligand cpaH₂ was prepared by the reported literature procedure.^[20]

Synthesis of 1: A mixture of Zn(NO₃)₂·6H₂O (450 mg, 1.51 mmol), cpaH₂ (50 mg, 0.25 mmol) and 4,4′-bipyridine (40 mg, 0.25), in ethanol (2 mL) and H₂O (2 mL) were placed in a Teflon[®]-lined stainless steel autoclave and heated to 130 °C for 72 h. After the mixture was cooled to room temperature at the rate of 0.1 °C/min, colorless crystals of **1** were collected, washed with water and ethanol, and dried at room temperature to give 32% yield based on Zn(NO₃)₂·6H₂O. Anal. calcd. for **1**: C 46.11, H 3.59, N 3.84%; found C 46.06, H 3.48, N 3.99%. IR: $\tilde{\nu}$ = 3457 (w, br.), 3108 (s), 2926 (s), 1606 (m), 1536 (s), 1420 (m), 1339 (s), 1263 (m), 1225 (m), 1144 (m), 1088 (m), 852 (s), 823 (m), 781 (m), 643 (m) cm⁻¹.

Synthesis of 1′: Single crystal of desolvated framework of **1** was obtained by drying at 100 °C under vacuum for 4 h. The crystals were subsequently used for single-crystal X-ray diffraction studies. Anal. calcd. for **1′**: C 49.80, H 2.98, N 4.14%; found C 49.79, H 2.79, N 4.01%. IR: $\tilde{\nu}$ = 3107 (s), 2925 (s), 1607 (m), 1536 (s), 1421 (m), 1336 (s), 1263 (m), 1225 (m), 1144 (m), 1087 (m), 852 (m), 823 (m), 781 (m), 731 (s), 698 (m), 643 (m) cm⁻¹.

Synthesis of 2, 3, 4: Suitably sized single crystals of **1** were immersed in methanol, ethanol and acetone solvents at room temperature in small sealed tubes, and then keeping still for two days. The crystals retain their primary well-defined external form throughout the solvent exchange process. Anal. calcd. for **2**: C 46.45, H 3.76, N 3.80%; found C 46.23, H 3.98, N 3.57%. IR: $\tilde{\nu}$ = 3455 (w, br.), 3107 (s), 2937 (s), 2556 (s), 1607 (m), 1537 (s), 1420 (m), 1340 (s), 1264 (m), 1226 (m), 1172 (m), 1070 (m), 1017 (w), 852 (m), 823 (m), 781 (m), 731 (m), 699 (m), 643 (m) cm⁻¹. Anal. calcd. for **3**: C 49.24, H 3.42, N 3.96%; found C 48.80, H 3.32, N 3.96%. IR: $\tilde{\nu}$ = 3444 (w, br.), 3109 (s), 2987 (s), 1607 (m), 1538 (s), 1421 (m), 1308 (s), 1263 (m), 1226 (m), 1171 (m), 1105 (m), 1068 (s), 1040 (w), 852 (m), 823 (m), 781 (m), 730 (s), 697 (s), 643 (m) cm⁻¹. Anal. calcd. for **4**: C 48.62, H 3.51, N 3.91%; found C 48.63,

H 3.26, N 3.97%. IR: $\tilde{\nu}$ = 3415 (w, br.), 3109 (s), 2943 (s), 1716 (s), 1606 (m), 1537 (s), 1420 (m), 1343 (s), 1264 (m), 1223 (m), 1171 (m), 1066 (m), 853 (s), 822 (m), 781 (m), 732 (m), 698 (m), 644 (m) cm⁻¹.

Synthesis of 5: Compound {[Zn₂(cpa)₂(bpy)]·(3H₂O)}_n (**1**) (50 mg) and benzene (3 mL) were placed in a Teflon[®]-lined stainless steel autoclave and heated to 100 °C for 48 h. After the mixture was cooled to room temperature at the rate of 0.1 °C/min, colorless crystals of **5** similar to **1**, were filtered, washed with water and ethanol, and dried at room temperature to give quantitative yield. Anal. calcd. for **5**: C 46.69, H 3.49, N 3.88%; found C 46.49, H 3.57, N 3.76%. IR: $\tilde{\nu}$ = 3429 (w, br.), 3036 (s), 2936 (s), 1606 (m), 1538 (s), 1419 (m), 1307 (s), 1265 (m), 1227 (m), 1145 (m), 1070 (m), 851 (s), 823 (m), 780 (m), 643 (m) cm⁻¹.

X-ray Structural Studies: Single-crystal X-ray data of **1–4** were collected at 100 K on a Bruker SMART APEX CCD diffractometer using graphite-monochromated Mo-*K*_α radiation (λ = 0.71069 Å) while temperature for **1′** and **5** was 293 K. For each case, a crystal of suitable size was selected from the mother liquor and immersed in paraffin oil, and then it was mounted on the tip of a glass fiber and cemented using epoxy resin. The linear absorption coefficients, scattering factors for the atoms, and the anomalous dispersion corrections were taken from the International Tables for X-ray Crystallography. The data integration and reduction were processed with SAINT^[21] software. An empirical absorption correction was applied to the collected reflections with SADABS^[22] using XPREP^[23]. The structure was solved by the direct method using SHELXTL and was refined on *F*² by full-matrix least-squares technique using the SHELXL-97^[24] program package. All non-hydrogen atoms were refined anisotropically except O11, C29 in **2**, C30 in **3** and OW1 in **4** are refined isotropically. All hydrogen atoms were geometrically fixed and treated as riding atoms using SHELXL default parameters. However, hydrogen atoms on water and ethanol solvent molecules could not be located even in successive difference Fourier maps due to their distorted nature. The crystal and refinement data for **1–5**, **1′** are collected in Table 1 while selective bond lengths and angles are given in Table S1 (Supporting Information).

CCDC numbers CCDC-773570 (for **1**), -773571 (for **1′**), -773572 (for **5**), -773573 (for **2**), -773574 (for **3**), -773575 (for **4**) contain the supplementary crystallographic data for this paper. These data can

Table 1. Crystal and structure refinement data for **1′** and **1–5**.

	1	1′	2	3	4	5
Formula	C ₂₈ H ₂₀ N ₂ O ₁₃ Zn ₂	C ₂₈ H ₂₀ N ₂ O ₁₀ Zn ₂	C ₅₇ H ₄₅ N ₄ O ₂₆ Zn ₄	C ₂₉ H ₂₀ N ₂ O ₁₁ Zn ₂	C ₅₈ H ₄₆ N ₄ O ₂₃ Zn ₄	C ₅₆ H ₄₀ N ₄ O ₂₅ Zn ₄
fw	723.24	675.24	1463.53	703.25	1428.55	1430.48
<i>T</i> [K]	100(2)	293(2)	100(2)	100(2)	100(2)	293(2)
System	monoclinic	monoclinic	monoclinic	monoclinic	monoclinic	monoclinic
Space group	<i>C2/c</i>	<i>C2/c</i>	<i>C2/c</i>	<i>C2/c</i>	<i>C2/c</i>	<i>C2/c</i>
<i>a</i> [Å]	21.153(2)	21.483(5)	21.181(4)	21.170(4)	21.193(6)	21.588(5)
<i>b</i> [Å]	14.080(4)	14.139(3)	14.080(4)	14.081(4)	14.047(5)	14.151(4)
<i>c</i> [Å]	20.595(4)	20.803(5)	20.584(3)	20.577(5)	20.725(5)	20.933(2)
β [°]	98.143(5)	99.816(6)	98.298(5)	98.230(3)	100.205(4)	100.129(5)
<i>U</i> [Å ³]	6072(2)	6226(2)	6075(2)	6071(3)	6072(3)	6295(2)
<i>Z</i>	8	8	4	8	4	4
ρ_{calc} [g/cm ³]	1.582	1.441	1.600	1.539	1.563	1.509
μ [mm ⁻¹]	1.649	1.596	1.649	1.642	1.644	1.589
GOF	0.976	1.022	1.036	1.031	1.074	1.051
Final <i>R</i> _{int} , [<i>I</i> > 2σ(<i>I</i>)]	<i>R</i> ₁ = 0.065, <i>wR</i> ₂ = 0.156	<i>R</i> ₁ = 0.078, <i>wR</i> ₂ = 0.218	<i>R</i> ₁ = 0.069, <i>wR</i> ₂ = 0.181	<i>R</i> ₁ = 0.066, <i>wR</i> ₂ = 0.175	<i>R</i> ₁ = 0.058, <i>wR</i> ₂ = 0.168	<i>R</i> ₁ = 0.077, <i>wR</i> ₂ = 0.218
<i>R</i> _{in} all data, <i>F</i> ² refin.	<i>R</i> ₁ = 0.100, <i>wR</i> ₂ = 0.181	<i>R</i> ₁ = 0.121, <i>wR</i> ₂ = 0.262	<i>R</i> ₁ = 0.092, <i>wR</i> ₂ = 0.205	<i>R</i> ₁ = 0.085, <i>wR</i> ₂ = 0.175	<i>R</i> ₁ = 0.079, <i>wR</i> ₂ = 0.199,	<i>R</i> ₁ = 0.115, <i>wR</i> ₂ = 0.259

be obtained free of charge from The Cambridge Crystallographic Data Centre via www.ccdc.cam.ac.uk/data_request/cif.

Supporting Information (see also the footnote on the first page of this article): Selected bond lengths and bond angles, additional figures IR spectra, TG curve, PXRD patterns and solid-state UV spectra.

Acknowledgments

We gratefully acknowledge the financial support received from the Department of Science and Technology, New Delhi, India (to P. K. B.) and a SRF from the Council of Scientific and Industrial Research (CSIR) to A. A. and P. L.

- [1] a) H. Li, M. Eddaoudi, M. O'Keeffe, M. Yaghi, *Nature* **1999**, *402*, 276–279; b) H. K. Chae, D. Y. Siberio-Perez, J. Kim, Y. B. Go, M. Eddaoudi, A. J. Matzger, M. O'Keeffe, O. M. Yaghi, *Nature* **2004**, *427*, 523–527; c) C. Janiak, *Dalton Trans.* **2003**, 2781–2804; d) M. C. Das, P. K. Bharadwaj, *J. Am. Chem. Soc.* **2009**, *131*, 10942–10949; e) D. N. Dybtsev, H. Chun, K. Kim, *Angew. Chem. Int. Ed.* **2004**, *43*, 5033–5036.
- [2] a) J. R. Li, R. J. Kuppler, H. C. Zhou, *Chem. Soc. Rev.* **2009**, *38*, 1477–1504; b) S. R. Batten, R. Robson, *Angew. Chem. Int. Ed.* **1998**, *37*, 1460–1494; c) A. Aijaz, E. Barea, P. K. Bharadwaj, *Cryst. Growth Des.* **2009**, *9*, 4480–4486; d) J. J. Perry IV, J. A. Perman, M. J. Zaworotko, *Chem. Soc. Rev.* **2009**, *38*, 1400–1417; e) G. J. McManus, J. J. Perry IV, M. Perry, B. D. Wagner, M. J. Zaworotko, *J. Am. Chem. Soc.* **2007**, *129*, 9094–9101.
- [3] a) S. K. Ghosh, J. Ribas, P. K. Bharadwaj, *Cryst. Eng. Commun.* **2004**, *6*, 250–256; b) P. Lama, A. Aijaz, E. C. Sañudo, P. K. Bharadwaj, *Cryst. Growth Des.* **2010**, *10*, 283–290; c) L. Carlucci, G. Ciani, D. M. Proserpio, *Coord. Chem. Rev.* **2003**, *246*, 247–289; d) A. L. Cheng, N. Liu, Y. F. Yue, Y. W. Jiang, E. Q. Gao, C. H. Yan, M. Y. He, *Chem. Commun.* **2007**, 407–409; e) R. L. La Duca, *Coord. Chem. Rev.* **2009**, *253*, 1759–1792; f) J.-J. Zhang, L. Wojtas, R. W. Larsen, M. Eddaoudi, M. J. Zaworotko, *J. Am. Chem. Soc.* **2009**, *131*, 17040–17041.
- [4] S. R. Batten, R. Robson, *Angew. Chem.* **1998**, *110*, 1558–1595.
- [5] a) S. Ma, D. Sun, P. M. Forster, D. Yuan, W. Zhuang, Y. S. Chen, J. B. Parise, H. C. Zhou, *Inorg. Chem.* **2009**, *48*, 4616–4618; b) B. Chen, S. Ma, F. Zapata, E. B. Lobkovsky, J. Yang, *Inorg. Chem.* **2006**, *45*, 5718–5720; c) T. K. Maji, R. Matsuda, S. Kitagawa, *Nat. Mater.* **2007**, *6*, 142–148.
- [6] a) J. J. Vittal, *Coord. Chem. Rev.* **2007**, *251*, 1781–1795; b) K. Biradha, Y. Hongo, M. Fujita, *Angew. Chem. Int. Ed.* **2002**, *41*, 3395–3398; c) A. B. Gaspar, M. C. Munoz, J. A. Real, *Inorg. Chem. Commun.* **2004**, *7*, 815–817; d) S. Takamizawa, E.-I. Nakata, H. Yokoyama, K. Mochizuki, W. Mori, *Angew. Chem. Int. Ed.* **2003**, *42*, 4331–4334; e) M. P. Suh, J. W. Ko, H. J. Choi, *J. Am. Chem. Soc.* **2002**, *124*, 10976–10977.
- [7] a) K. Biradha, M. Fujita, *Angew. Chem. Int. Ed.* **2002**, *41*, 3392–3395; b) P. K. Thallapally, J. Tian, M. R. Kishan, C. A. Fernandez, S. J. Dalgarno, P. B. McGrail, J. E. Warren, J. L. Atwood, *J. Am. Chem. Soc.* **2008**, *130*, 16842–16843; c) R. Kitaura, K. Seki, G. Akiyama, S. Kitagawa, *Angew. Chem. Int. Ed.* **2003**, *42*, 428–431.
- [8] S. Iijima, *Nature* **1991**, *354*, 56–58.
- [9] a) T. Kraus, M. Budesinsky, I. Cisarova, J. Zavada, *Angew. Chem. Int. Ed.* **2002**, *41*, 1715–1717; b) M. Karlsson, K. Sott, M. Davidson, A. S. Cans, P. Linderholm, D. Chiu, O. Orwar, *Proc. Natl. Acad. Sci. USA* **2002**, *99*, 11573–11578; c) B. H. Hong, J. Y. Lee, C. W. Lee, J. C. Kim, S. C. Bae, K. S. Kim, *J. Am. Chem. Soc.* **2001**, *123*, 10748–10749; d) M. Terrones, W. K. Shu, H. W. Kroto, D. R. M. Walton, *Fullerenes and Related Structures*; Springer-Verlag, Berlin, **1999**; vol. 199.
- [10] a) T. Kaczorowski, I. Justyniak, T. Lipinska, J. Lipkowski, J. Lewinski, *J. Am. Chem. Soc.* **2009**, *131*, 5393–5395; b) B. Zhao, P. Cheng, X. Chen, C. Cheng, W. Shi, D. Liao, S. Yan, Z. Jiang, *J. Am. Chem. Soc.* **2004**, *126*, 3012–3013; c) Y. B. Dong, Y. Y. Jiang, J. Li, J. P. Ma, F. L. Liu, B. Tang, R. Q. Huang, S. R. Batten, *J. Am. Chem. Soc.* **2007**, *129*, 4520–4521; d) C. Yang, X. Wang, M. A. Omary, *J. Am. Chem. Soc.* **2007**, *129*, 15454–15455; e) M. Hong, Y. Zhao, W. Su, R. Cao, M. Fujita, Z. Zhou, A. S. C. Chan, *Angew. Chem. Int. Ed.* **2000**, *39*, 2468–2470; f) S. K. Ghosh, P. K. Bharadwaj, *Inorg. Chem.* **2005**, *44*, 3156–3161.
- [11] F. Dai, H. He, D. Sun, *J. Am. Chem. Soc.* **2008**, *130*, 14064–14065.
- [12] a) K. Nakamoto, *Infrared and Raman Spectra of Inorganic and Coordination Compounds*, 5th ed., John Wiley & Sons, New York, **1997**; b) L. Lisnard, P. Mialane, A. Dolbecq, J. Marrot, J. M. Clemente-Juan, E. Coronado, B. Keita, P. de Oliveira, L. Nadjio, F. Secheresse, *Chem. Eur. J.* **2007**, *13*, 3525–3536.
- [13] See Supporting Information.
- [14] A. L. Spek, *Appl. Crystallogr.* **2003**, *36*, 7–13.
- [15] a) J. E. McGarrah, Y. J. Kim, M. Hissler, R. Eisenberg, *Inorg. Chem.* **2001**, *40*, 4510–4511; b) Q. Wu, M. Esteghamatian, N. X. Hu, Z. Popovic, G. Enright, Y. Tao, M. D'Iorio, S. Wang, *Chem. Mater.* **2000**, *12*, 79–83; c) G. D. Santis, L. Fabbrizzi, M. Licchelli, A. Poggi, A. Taglietti, *Angew. Chem. Int. Ed. Engl.* **1996**, *35*, 202–204.
- [16] E. Y. Lee, S. Y. Jang, M. P. Suh, *J. Am. Chem. Soc.* **2005**, *127*, 6374–6381.
- [17] a) S. L. Li, Y. Q. Lan, J. F. Ma, J. Yang, G. H. Wei, L. P. Zhang, Z. M. Su, *Cryst. Growth Des.* **2008**, *8*, 675–684; b) S. L. Li, Y. Q. Lan, J. F. Ma, Y. M. Fu, J. Yang, G. J. Ping, J. Liu, Z. M. Su, *Cryst. Growth Des.* **2008**, *8*, 1610–1616.
- [18] a) S. L. Zheng, J. H. Yang, X. L. Yu, X. M. Chen, W. T. Wong, *Inorg. Chem.* **2004**, *43*, 830–838; b) B. Valeur, *Molecular Fluorescence: Principles and Applications*, Wiley-VCH, Weinheim, Germany, **2002**.
- [19] a) B. Xi, S. Xiong, D. Xu, J. Li, H. Zhou, J. Pan, J. Li, Y. Qian, *Chem. Eur. J.* **2008**, *14*, 9786–9791; b) S. L. Zheng, P. Coppens, *Chem. Eur. J.* **2005**, *11*, 3583–3590.
- [20] X. Wang, Z. Li, D. Yuxia, J. Chen, T. Wei, *Synth. Commun.* **1999**, *29*, 4153–4161.
- [21] *SAINT+*, 6.02 ed., Bruker AXS, Madison, WI, **1999**.
- [22] G. M. Sheldrick, *SADABS*, Empirical Absorption Correction Program, University of Göttingen, Germany, **1997**.
- [23] *XPRED*, 5.1 ed., Siemens Industrial Automation Inc., Madison, WI (USA), **1995**.
- [24] G. M. Sheldrick, *SHELXL-97*, Program for Crystal Structure Refinement, University of Göttingen, Germany, **1997**.

Received: April 20, 2010

Published Online: July 21, 2010

Topological Diversity, Adsorption and Fluorescence Properties of MOFs Based on a Tetracarboxylate Ligand

Ronny Grünker,^[a] Irena Senkowska,^[a] Ralf Biedermann,^[a] Nicole Klein,^[a] Andrea Klausch,^[a] Igor A. Baburin,^[b] Uwe Mueller,^[c] and Stefan Kaskel^{*[a]}

Keywords: Metal–organic frameworks / Carboxylate ligands / Physisorption / Gas separation / Topology

The combination of a tetradentate ligand, *N,N,N',N'*-benzidinetetrabenzoate (BenzTB), with paddle-wheel SBUs based on Zn, Co or Cu has led to a series of new metal–organic frameworks (MOFs) with different structural motifs, depending on the additional acid present and the reaction temperature. Isomorphous compounds $M_2(H_2O)_2(BenzTB)$ [DUT-10(M), M = Zn, Cu, Co] crystallize in the *Imma* space group

(sp. gr.) and adopt the **lvt** topology, whereas the use of Zn and Cu under modified crystallization conditions gives rise to new phases $Zn_2(H_2O)_2(BenzTB)$ (sp. gr. *Cccm*, DUT-11) and $Cu_2(H_2O)_2(BenzTB)$ (sp. gr. *P4/mnc*, DUT-12) with **pts** and **ssb** framework topologies, respectively. DUT-10(Zn) exhibits selective gas sorption properties for H_2 and CO_2 over N_2 and solvent-induced change in fluorescence.

Introduction

Over the last decades, the development of novel porous materials, particularly metal–organic frameworks (MOFs), and investigation of their properties regarding gas storage^[1] or gas separation,^[2] catalysis,^[3] sensor properties^[4] and functionality,^[5] has been one of the most active research fields. In comparison to traditional porous materials such as zeolites, MOF chemistry offers a greater variety of structures, since the restriction to only tetrahedral frameworks no longer holds. An unlimited number of organic ligands combined with different metals/clusters leads to a large number of materials with sometimes unexpected and fascinating structures, topologies and properties. On the other hand, the *isorecticular* design and existence of preferred secondary building units (SBUs) allow certain control over the resulting crystalline architectures and tuning of pore sizes (e.g. the linker length is monitored to adjust the pore diameter).^[6]

Recently, tetracarboxylate-based molecules have successfully been used for the construction of MOFs.^[7] For example, Schröder et al. synthesized a series of highly porous

MOFs utilizing tetracarboxylate linkers of different sizes such as biphenyl-3,3',5,5'-tetracarboxylate, terphenyl-3,3'',5,5'''-tetracarboxylate and quaterphenyl-3,3''',5,5''''-tetracarboxylate, all showing high hydrogen storage capacities.^[8] Chen and co-workers used an acetylene-elongated version of biphenyl-3,3',5,5'-tetracarboxylate to form a MOF-505 analogue with new adsorption properties.^[9] Zhou et al. reported two temperature-controlled supramolecular stereoisomers (having either **lvt**^[10] or **pts** topology depending on the conformation of the ligand) based on copper-containing paddle-wheel units and the organic linker *N,N,N',N'*-tetrakis(4-carboxyphenyl)-1,4-phenylenediamine (TCPPDA).^[11] Quite recently an elongated version of TCPPDA, *N,N,N',N'*-benzidinetetrabenzoic acid ($H_4BenzTB$) (**2**) was found to form a doubly interpenetrated framework $Mg(BenzTB)(H_2O)_2$ (SNU-25) with **lvt** topology.^[12]

In our study, we systematically used the $H_4BenzTB$ ligand together with paddle-wheel SBUs based on Zn, Co or Cu for the construction of coordination polymers. As a result, a series of non-interpenetrated MOFs with the same chemical composition, $[M_2(H_2O)_2(BenzTB)]$, but different network topologies was obtained. Isomorphous compounds $M_2(H_2O)_2(BenzTB)$ [DUT-10(M), DUT = Dresden University of Technology, M = Zn, Cu, Co] crystallize in the *Imma* space group (sp. gr.) and adopt the **lvt** topology. However, utilizing Zn and Cu under modified crystallization conditions gives rise to new phases $Zn_2(H_2O)_2(BenzTB)$ (sp. gr. *Cccm*, DUT-11) and $Cu_2(H_2O)_2(BenzTB)$ (sp. gr. *P4/mnc*, DUT-12), with **pts** and **ssb** framework topologies, respectively. Furthermore, DUT-10(Zn) exhibits selective gas sorption properties for H_2 and CO_2 over N_2 and solvent-induced change in fluorescence.

[a] Department of Inorganic Chemistry, Dresden University of Technology, Mommsenstrasse 6, 01069 Dresden, Germany
Fax: +49-035-146337287
E-mail: Stefan.Kaskel@chemie.tu-dresden.de

[b] Max Planck Institute for Chemical Physics of Solids, Nöthnitzer Strasse 40, 01187 Dresden, Germany

[c] Helmholtz-Zentrum Berlin für Materialien und Energie, BESSY-MX Group, Albert-Einstein-Strasse 15, 12489 Berlin, Germany

Supporting information for this article is available on the WWW under <http://dx.doi.org/10.1002/ejic.201000415>.

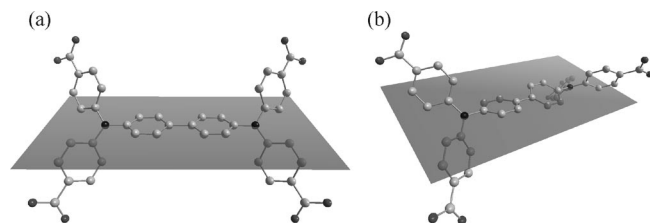
Results and Discussion

Structure and Topology

The *N,N,N',N'*-benzidinetetrazobenzoic acid (**2**) was synthesized according to modified literature procedures (Figure S1, Supporting Information).^[13] The single crystals of isomorphous compounds $M_2(H_2O)_2(\text{BenzTB})$ were obtained by conversion of **2** with zinc, cobalt or copper nitrate in *N,N*-dimethylformamide (DMF) as solvent under elevated temperature in the presence of additives (acids). Interestingly, the reactions are highly sensitive to the choice of pH, reaction temperature, as well as to the reactant concentrations.

For DUT-10(M) compounds (M = Zn, Cu, Co), X-ray crystallographic analysis revealed isotopic structures with *Imma* symmetry, differing only in the substitution of metal ion in the paddle-wheel cluster core. This causes an increase in the metal–metal distance from 2.81 Å for the Co to 2.94 Å for the Zn cluster.

The axial positions of the clusters are occupied by water molecules. The ligands in DUT-10 have C_{2h} symmetry (Scheme 1a) and connect four paddle-wheels into a 3D framework. Projections along the crystallographic *a*, *b* or *c* axis show channels of different sizes running through the structure in all directions (Figure 1). The calculation of the void volume with PLATON^[14] reveals a free volume of about 11700 Å³, which represents 82% of the unit cell volume.



Scheme 1. (a) The eclipsed (C_{2h} symmetry) and (b) staggered (D_2 symmetry) conformations of the BenzTB ligand found in DUT-10/-12 and DUT-11, respectively.

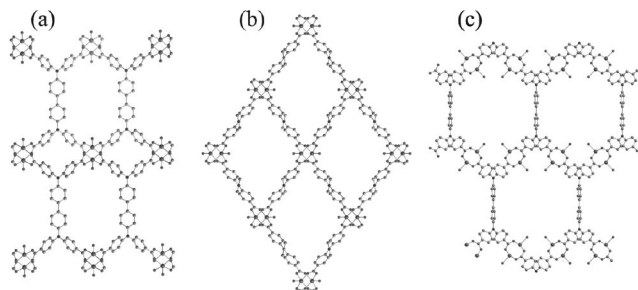


Figure 1. View of the structure of DUT-10 along the (a) *a*, (b) *b* and (c) *c* axes.

A further Zn-based compound (DUT-11) with the same chemical composition as DUT-10(Zn) was prepared. It crystallizes in the *Cccm* space group and contains a racemic mixture of a second diastereomer of the linker (the

staggered conformation with D_2 symmetry, Scheme 1b). Because of this conformational change, the size of the channels along the crystallographic [010] direction becomes approximately four times smaller whereas the size of the channels along [100] and [001] remains constant (Figure 2). In this case the Zn–Zn distance is 2.95 Å. The total potential solvent accessible volume for DUT-11 is 82%.

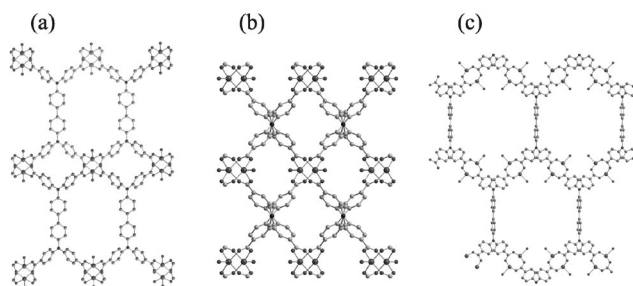


Figure 2. View of the structure of DUT-11 along the (a) *a*, (b) *b* and (c) *c* axes.

By the reaction of copper nitrate with BenzTB in the presence of HNO_3 as additional acid, DUT-12 (sp. gr. *P4/mmc*) is formed preferentially. The paddle-wheel units act as connectors in this structure as well. The $\text{Cu}_2(\text{O}_2\text{C})_4$ clusters are interlinked via BenzTB (with C_{2h} symmetry) to form a 3D network in a manner very similar to DUT-10 (cf. below). The structure has open channels along all three crystallographic directions (Figure 3). The accessible pore volume in this case amounts to 84% of the unit cell volume.

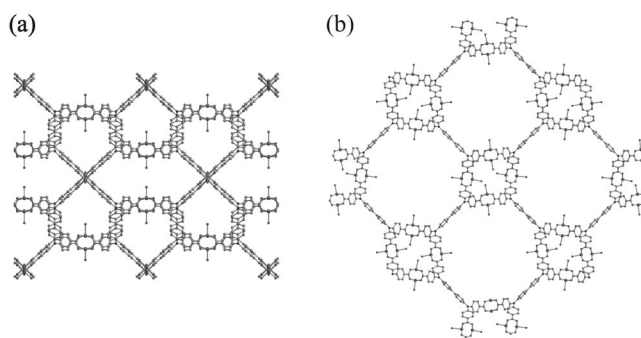


Figure 3. View of the structure of DUT-12 along the (a) *a* and (b) *c* axes.

DUT-10(Co) adopts the topology of the *lvt* net, Cu-containing isomers show the topology of *lvt* [DUT-10(Cu)] and *ssb* (DUT-12) nets, while for Zn-containing MOFs two different polymorphs with *lvt* [DUT-10(Zn)] and *pts* (DUT-11) underlying networks were obtained (Figure 4). In the latter case the “choice” of the networks is dictated mainly by the conformation of the ligand as was previously observed in the case of MOFs with TCPPDA as linker molecule.^[11a] In an eclipsed conformation with the C_{2h} symmetry, the ligand acts as a square-like connector just as the paddle-wheel unit does, whereas in the case of the conformation with D_2 symmetry, it plays the role of a tetrahedral SBU, and, together with the paddle-wheel SBU, forms a

network having alternating square-like and tetrahedral nodes, for which **pts** topology is considered to be the default structure.^[15]

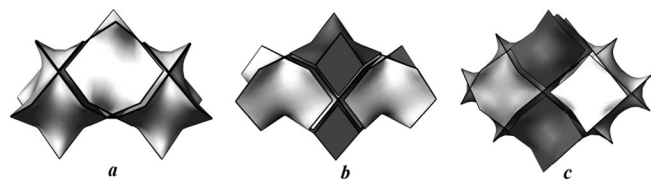


Figure 4. (a) Tiling of the **lvt** net (DUT-10): $[4^2.8^4]$; (b) tiling of the **pts** net (DUT-11): $[4^2.8^2] + [8^4]$ ($[4^2.8^2]$ and $[8^4]$ tiles are shown in dark grey and light grey, respectively); (c) tiling of the **ssb** net (DUT-12): $[4^4.8^2] + [4^4.8^6] + 2[8^4]$ ($[4^4.8^2]$, $[4^4.8^6]$ and $[8^4]$ tiles are shown in white, light grey and dark grey, respectively).

Furthermore, occurrence of two distinct topologies in Cu-containing MOFs (where the same eclipsed conformation of a ligand is realized) deserves a closer look. Note that the **lvt** net is *uninodal*, whereas **ssb** is *binodal*.

This means that, in the structure with the **lvt** topology [DUT-10(Cu)], both ligands and paddle-wheel SBUs play the same topological role, whereas in the **ssb** net (DUT-12) each species is topologically unique. At the same time, a graph-theoretical analysis using a recently proposed algorithm^[16] shows that these nets (**lvt** and **ssb**) are strictly equal to each other (as well as to the **pts** net of DUT-11) within the first three coordination spheres. However, the difference between the nets becomes obvious if one considers the arrangement of the pores (*tiles*): the **lvt** net is carried by tile-transitive tiling $[4^2.8^4]$, in the **ssb** net there are three different kinds of tiles, namely, $[4^4.8^2]$, $[4^4.8^6]$ and $[8^4]$, and in the **pts** net there are two kinds of tiles, $[4^2.8^2]$ and $[8^4]$ (Figure 4).

The topological equivalence of nets within n coordination spheres (in our case $n = 3$) physically means that, during crystallization the system at that moment has not yet established the law of its growth, and hence, this is a prerequisite for a polymorphism. For example, if one starts modelling the growth from the paddle-wheel unit, the first three coordination spheres are represented by an aggregate containing 2160 atoms with a diameter of approximately 8 nm (Figure S5). Similarly, the first three coordination spheres around the ligand give rise to an aggregate of 1038 atoms with approximately the same diameter. As a result, the difference between the two alternative structures – based either on the **lvt** or the **ssb** net (in the case of an eclipsed conformation of the ligand) – starts appearing only at the nano level and is a subtle compromise between reaction conditions and stereochemical preferences.

Adsorption and Fluorescence Properties

Phase purity of the bulk material used for the experiments was proven by powder X-ray diffraction (PXRD) analysis. The compounds show very similar thermal stability up to 573 K for DUT-10(Zn) and 513 K for DUT-12, as determined by thermogravimetric analysis (Figure S6).

The gas adsorption properties were studied for compounds DUT-10(Zn) and DUT-12. For this purpose, the samples were dried in vacuo at 393 K for 24 h to give a fully desolvated sample. X-ray powder diffraction data indicate that evacuation of the compounds results in the loss of the initial framework structures and formation of new phases due to the flexibility of the linker (Figures 5 and 6).^[17]

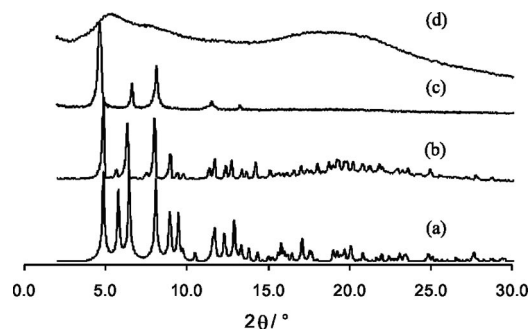


Figure 5. Powder X-ray diffraction patterns of DUT-10(Zn): (a) simulated from single-crystal structure, (b) as synthesized, (c) dried in vacuo, (d) after H₂O adsorption.

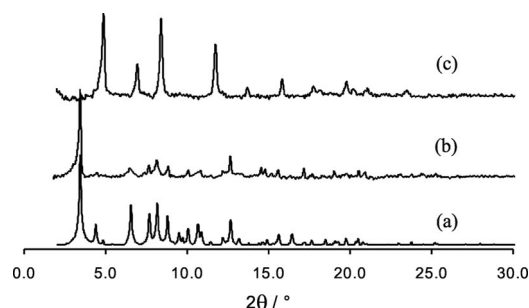


Figure 6. Powder X-ray diffraction patterns of DUT-12: (a) simulated from single-crystal structure, (b) as synthesized, (c) dried in vacuo.

As shown in Figure 7, DUT-10(Zn) adsorbs no significant amount of nitrogen at 77 K up to 1 bar. Apart from that, 160 cm³ g^{−1} of carbon dioxide can be adsorbed at 195 K and 0.95 bar, featuring a specific surface area of 423 m² g^{−1}.

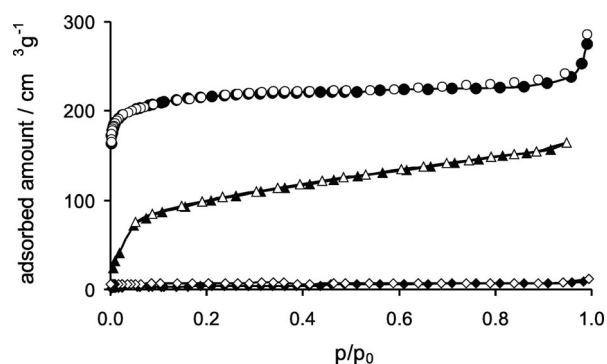


Figure 7. N₂ (◆/◇) and CO₂ (▲/Δ) adsorption/desorption isotherms for DUT-10(Zn) measured at 77 and 195 K, respectively. N₂ physisorption isotherm for DUT-12 (●/○) measured at 77 K.

Hydrogen adsorption at 77 K reveals an uptake of $74 \text{ cm}^3 \text{ g}^{-1}$ (0.7 wt.-%) hydrogen at 1 bar (Figure 8). The similar selective adsorption behaviour was observed for the Mg-based doubly interpenetrated compound with *lvt* topology containing the BenzTB linker reported by Cheon et al.^[12]

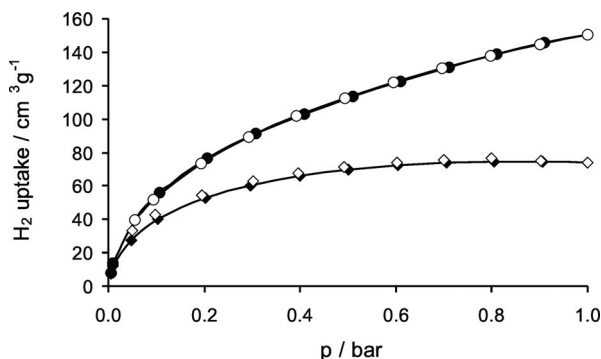


Figure 8. H_2 adsorption/desorption isotherm of DUT-10(Zn) (\blacklozenge/\diamond) and DUT-12 (\bullet/\circ) measured at 77 K.

The nitrogen physisorption experiment on the DUT-12 sample performed at 77 K displays a typical type I isotherm (Figure 7). The nitrogen uptake corresponds to a BET specific surface area of $824 \text{ m}^2 \text{ g}^{-1}$ and a total pore volume of $0.36 \text{ cm}^3 \text{ g}^{-1}$. DUT-12 adsorbs up to $150 \text{ cm}^3 \text{ g}^{-1}$ (equal to 1.33 wt.-%) hydrogen at 77 K and 1 bar (Figure 8).

Because of water-sensitive fluorescence properties of DUT-10(Zn), the water vapour adsorption isotherm was measured at 298 K. As depicted in Figure 9, the compound shows a type V isotherm with no significant initial water uptake below $p/p_0 = 0.4$ and a dominant adsorption from $p/p_0 = 0.8$. The shape of the isotherm points at a rather hydrophobic character of the adsorbent. The similar behaviour is typical for the adsorption of moisture on porous carbons, where the width of hysteresis loop depends on the pore structure.^[18,19]

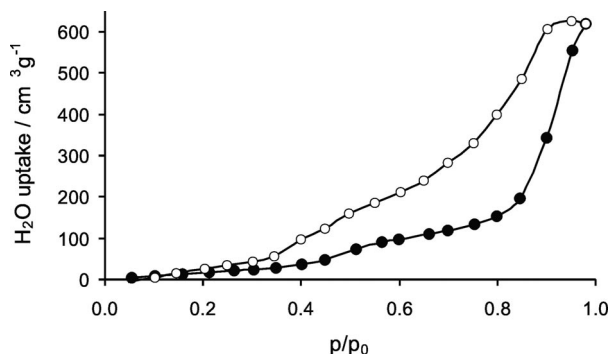


Figure 9. H_2O adsorption/desorption (\bullet/\circ) isotherm of DUT-10(Zn) measured at 298 K.

Even though the water adsorption isotherms were reproducible over two adsorption/desorption cycles, the PXRD analysis shows the distortion of the network (Figure 5), probably due to the hydrolysis process, which occurs often in MOFs.

The fluorescence properties of DUT-10(Zn) in the solid state were studied. The as-synthesized compound appears transparent and, as shown in Figure 10, exhibits blue fluorescent emission bands at 431 nm under 333 nm irradiation. For comparison the spectrum of the free solid linker **2** was also recorded. The ligand exhibits an emission maximum at 471 nm. Fluorescence measurements of **1** in different organic solvents showed a shift of the emission maximum depending on the polarity of the solvent (Figure S8).^[20]

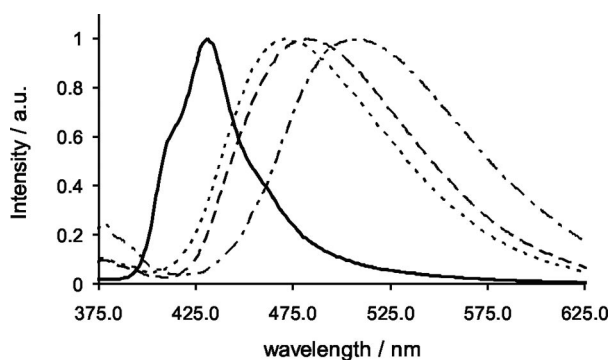


Figure 10. Fluorescent emission spectra of H_4BenzTB (**2**) (dotted line), as-synthesized DUT-10(Zn) (solid line), activated DUT-10(Zn) (dashed line) and $\text{H}_2\text{O}@$ DUT-10(Zn) (dashed-dotted line).

DUT-10 undergoes a fluorescence change from blue to light green upon thermal activation, and a 29 nm redshift in the fluorescence was observed. The reason for this phenomena is obviously the change in the polarity of the linker environment on the one hand, and the structural change during activation, where π - π interactions between contiguous linker molecules may occur, on the other hand.^[21] The structural and fluorescence changes are irreversible, and the activated compound cannot be returned to its as-synthesized state by resolvatization in DMF.

After the activated crystals were soaked in water [$\text{H}_2\text{O}@$ -DUT-10(Zn)], the emission changed from green to yellow (Figure S7), and the band in the fluorescence spectrum of the hydrated compound was shifted to 522 nm. Interestingly, the green emission reappeared when the crystals were dried again. Due to the fact that the as-made material and the $\text{H}_2\text{O}@$ DUT-10(Zn) both have axial water molecules at the paddle-wheel unit, the main emission mechanism seems to be linker-based, as already proposed by Suh et al. for a MOF containing the aminobenzoate linker.^[21,22] Considering these attributes, the compound can be potentially used as moisture sensor.

Conclusions

Four supramolecular, isomeric, non-interpenetrated MOFs based on a tetradentate ligand were synthesized and structurally characterized. Conformational effects of the ligand were observed in the case of Zn-containing MOFs DUT-10(Zn) and DUT-11, which possess an *lvt* and *pts* net, respectively. Two Cu-based supramolecular isomeric MOFs [DUT-10(Cu) and DUT-12] having *lvt* and *ssb* net topolog-

ies were obtained with the same linker conformation. The DUT-10 structure (**1vt**) for Zn is more preferable at the employed reaction conditions and can be obtained as a pure phase. In case of Cu, the **ssb** topology seems to be more attractive. DUT-10(Zn) shows a solvent-dependent change in fluorescence and selective gas adsorption properties. Because of its flexibility, the linker shows the potential to isolate and characterize diverse structures by simple variation of the crystallization conditions.

Experimental Section

General Information

$\text{Cu}(\text{NO}_3)_2 \cdot 3\text{H}_2\text{O}$ (Fluka), $\text{Co}(\text{NO}_3)_2 \cdot 6\text{H}_2\text{O}$ (Fluka) and $\text{Zn}(\text{NO}_3)_2 \cdot 4\text{H}_2\text{O}$ (Fluka) were used as received. *N,N*-dimethylformamide (DMF) was distilled from phosphorus pentoxide and stored under argon.

Powder X-ray diffraction (PXRD) patterns were collected in transmission geometry with a STOE STADI P diffractometer operated at 40 kV and 30 mA with monochromated $\text{Cu-K}\alpha_1$ ($\lambda = 0.15405$ nm) radiation and with a scan speed of 30 s/step and a step size of 0.1° .

N_2 , CO_2 and H_2 physisorption isotherms were measured up to 1 bar with a Quantachrome Autosorb 1C apparatus. The water adsorption isotherm was measured with a Quantachrome Hydrosorb 1000 apparatus.

Thermogravimetric analyses (TGA) were carried out under air with a Netzsch STA 409 thermal analyzer. Infrared spectra (IR) were recorded in diffuse reflection geometry using a BIORAD Excalibur FTS3000 (Varian Inc.) infrared spectrometer. For the examination of fluorescence, a Cary Eclipse (Varian) instrument was used. The powder samples were filled into a solid sample holder. The excitation wavelength for all samples was 333 nm. Elemental analysis (C, H, N) was performed with a CHNS 932 analyzer from LECO. The oxygen content was determined by coupling of the CHNS 932 analyzer with the pyrolysis furnace VTF-900. The respective metal content was determined with an ICP-OES Vista RL apparatus from Varian Inc.

Synthesis of the Ligand

***N,N,N',N'*-Tetrakis-(4-ethoxycarbonylphenyl)-biphenyl-4,4'-diamine (1):** A mixture of ethyl 4-bromobenzoate (0.89 mL, 1.243 g, 5.428 mmol), $\text{Pd}(\text{OAc})_2$ (10 mg, 0.043 mmol), Cs_2CO_3 (2.123 g, 6.516 mol) and *rac*-2,2'-bis(diphenylphosphanyl)-1,1'-binaphthyl (*rac*-BINAP) (54 mg, 0.086 mmol) were solved in 1,4-dioxane (6 mL) and stirred for 20 min at 373 K. Subsequently, a solution of benzidine (200 mg, 1.086 mmol) in 1,4-dioxane (15 mL) was added. After 90 h at 373 K, the orange suspension was cooled to room temperature, and the inorganic salts were removed by filtration through a pad of Celite®. After removal of the solvent in vacuo, the product was purified by column chromatography [diethyl ether/pentane (1:1)]. Yield: 842 mg (100%). The crystal structure of **1** was determined by single-crystal X-ray analysis (see Supporting Information). ^1H NMR (500 MHz, CDCl_3): $\delta = 1.38$ (t, $J_{1,10} = 7.3$ Hz, 12 H, 11- H_3), 4.35 (q, $J_{10,11} = 7.3$ Hz, 8 H, 10- H_2), 7.13 (d, $J_{6,7} = 8.8$ Hz, 8 H, 6-H), 7.19 (d, $J_{3,2} = 8.5$ Hz, 4 H, 3-H), 7.54 (d, $J_{2,3} = 8.5$ Hz, 4 H, 2-H), 7.93 (d, $J_{7,6} = 8.8$ Hz, 8 H, 7-H) ppm. ^{13}C NMR (125 MHz, CDCl_3): $\delta = 14.38$ (CH_3 , C-11), 60.79 (CH_2 , C-10), 122.66 (CH, C-6), 124.72 (C_q , C-8), 126.38 (CH, C-3), 128.06 (CH, C-2), 130.99 (CH, C-7), 136.81 (C_q , C-1), 145.38 (C_q , C-4),

150.76 (C_q , C-5), 166.12 (C_q , C-9) ppm. IR: $\tilde{\nu} = 3068, 3037, 2985, 2904, 1720, 1605, 1500, 1367, 1325, 1182, 1111, 1028, 845, 768$ cm^{-1} . HRMS (EI): calcd. for $[\text{M}]^+$ 776.3098; found 776.3093. $\text{C}_{48}\text{H}_{44}\text{N}_2\text{O}_8$ (776.31): calcd. C 74.21, H 5.71, N 3.61; found C 73.43, H 5.53, N 3.52.

***N,N,N',N'*-Benzidinetetrazobenzoic Acid (H_4BenzTB) (2):** In a round-bottomed flask *N,N,N',N'*-tetrakis(4-ethoxycarbonylphenyl)biphenyl-4,4'-diamine (**1**) (300 mg, 0.386 mmol) was dissolved in tetrahydrofuran (THF) (15 mL), and a solution of KOH (433 mg, 7.72 mmol) in H_2O (2.5 mL) was added. This mixture was heated at reflux for 24 h. After cooling the mixture down to room temperature, the THF was evaporated and the resulting water phase was acidified with conc. HCl until no further precipitate was detected. The slightly yellow solid was collected by filtration, washed with water, a small amount of acetone and diethyl ether and dried in vacuo. Yield: 218 mg (100%). ^1H NMR (500 MHz, $[\text{D}_6]\text{DMSO}$): $\delta = 7.11$ (d, $J_{6,7} = 8.8$ Hz, 8 H, 6-H), 7.20 (d, $J_{3,2} = 8.8$ Hz, 4 H, 3-H), 7.71 (d, $J_{2,3} = 8.8$ Hz, 4 H, 2-H), 7.88 (d, $J_{7,6} = 8.8$ Hz, 8 H, 7-H), 12.76 (br., 4 H, CO_2 H) ppm. ^{13}C NMR (125 MHz, $[\text{D}_6]\text{DMSO}$): $\delta = 122.49$ (CH, C-6), 124.90 (C_q , C-8), 126.40 (CH, C-3), 128.07 (CH, C-2), 131.09 (CH, C-7), 136.00 (C_q , C-1), 144.97 (C_q , C-4), 150.24 (C_q , C-5), 166.82 (C_q , C-9) ppm. IR: $\tilde{\nu} = 3070, 3035, 2958, 2873, 2663, 2559, 1699, 1603, 1510, 1435, 1331, 1304, 1184, 852, 775$ cm^{-1} . HRMS (EI): calcd. for $[\text{M}]^+$ 664.1846, found 664.1827; calcd. for $[\text{M} - \text{CO}_2]^+$ 620.6494, found 620.1959; calcd. for $[\text{M} - 2\text{CO}_2]^+$ 576.6399, found 576.2033; calcd. for $[\text{M} - 3\text{CO}_2]^+$ 532.6304, found 532.2159.

Synthesis of the MOFs

$\text{Zn}_2(\text{BenzTB})(\text{H}_2\text{O})_2$ [DUT-10(Zn)]: $\text{Zn}(\text{NO}_3)_2 \cdot 4\text{H}_2\text{O}$ (15.7 mg, 0.061 mmol) and H_4BenzTB (**2**) (4 mg, 0.006 mmol) were dissolved in DMF (2 mL) by sonication for 1 min. The mixture was spiked with one drop of glacial acetic acid (ca. 4.3 μL) and heated to 353 K in a Pyrex® tube. After 48 h, the hot mother liquor was exchanged by fresh DMF (2 mL) and heated to 353 K for further 24 h to remove excess metal salt. The resulting colourless needles were filtered under argon, washed with DMF (3×2 mL) and dried in vacuo. Yield: 3 mg (62%). $\text{C}_{40}\text{H}_{24}\text{N}_2\text{O}_8\text{Zn}_2$ (788.01): calcd. C 60.71, H 3.06, N 3.54, O 16.17, Zn 16.52; found C 60.5, H 3.4, N 3.75, O 17.6, Zn 16.3.

$\text{Co}_2(\text{BenzTB})(\text{H}_2\text{O})_2$ [DUT-10(Co)]: $\text{Co}(\text{NO}_3)_2 \cdot 6\text{H}_2\text{O}$ (17.5 mg, 0.060 mmol), H_4BenzTB (**2**) (4 mg, 0.006 mmol) and one drop of glacial acetic acid (ca. 4.3 μL) were dissolved in DMF (2 mL) by sonication for 1 min. The mixture was heated to 335.5 K in a Pyrex® tube and kept at this temperature for 48 h to obtain the compound as purple needles. The hot mother liquor was exchanged by fresh DMF (2 mL) and heated to 353 K for further 24 h. The hot mother liquor was decanted and replaced by fresh DMF. Yield: 1 mg (20%).

$\text{Cu}_2(\text{BenzTB})(\text{H}_2\text{O})_2$ [DUT-10(Cu)]: $\text{Cu}(\text{NO}_3)_2 \cdot 3\text{H}_2\text{O}$ (36.5 mg, 0.151 mmol), H_4BenzTB (**2**) (10 mg, 0.015 mmol) and one drop of conc. HNO_3 (ca. 5.6 μL) were dissolved in DMF (10 mL) by sonication for 1 min. The mixture was heated to 353 K in a Pyrex® tube and kept at this temperature for 48 h. The hot mother liquor was exchanged by fresh DMF (10 mL) and heated to 353 K for further 24 h. The resulting product was a mixture of DUT-10(Cu) and DUT-12 crystals. One of the resulting green block-shaped crystals of DUT-10(Cu) was sealed in a capillary for single-crystal X-ray structure analysis. The yield could not be determined because of phase impurity.

$\text{Zn}_2(\text{BenzTB})(\text{H}_2\text{O})_2$ (DUT-11): $\text{Zn}(\text{NO}_3)_2 \cdot 4\text{H}_2\text{O}$ (28.3 mg, 0.108 mmol) and H_4BenzTB (**2**) (16 mg, 0.024 mmol) were dis-

solved in DMF (2 mL) by sonication for 1 min. The mixture was spiked with one drop of trifluoroacetic acid and heated to 373 K in a Pyrex® tube. After 24 h the mixture was allowed to cool at room temperature, and the resulting colourless needles were washed with fresh DMF (3 × 2 mL). Yield: 8 mg (41%).

Cu₂(BenzTB)(H₂O)₂ (DUT-12): Cu(NO₃)₂·3H₂O (36.5 mg, 0.151 mmol), H₄BenzTB (**2**) (10 mg, 0.015 mmol) and one drop of conc. HNO₃ (ca. 5.6 µL) were dissolved in DMF (5 mL) by sonication for 1 min. The mixture was heated to 358 K in a Pyrex® tube and kept at this temperature for 48 h. The hot mother liquor was decanted, and the crystals were washed with fresh DMF (5 mL). The resulting green to brown block-shaped crystals were filtered under argon, washed with DMF (3 × 5 mL) and dried in vacuo. Yield: 5 mg (40%). Cu₂C₄₀H₂₄N₂O₈ (786.03): calcd. C 60.99, H 3.07, Cu 16.13, N 3.56, O 16.25; found C 60.1, H 3.4, Cu 15.4, N 4.21, O 17.8.

Single-Crystal X-ray Structure Analysis and Crystallographic Data: The crystals of all compounds were sealed in glass capillaries with a small amount of solvent. For the MOFs, the data were collected by using synchrotron radiation at beamline BL14.2 of the Joint Berlin-MX Laboratory at BESSY-II (Berlin, Germany) with a MX-225 CCD detector (Rayonics, Illinois) at 263 K with an exposure time of 1 s/frame. These data were integrated and scaled with XDS Software.^[23] For compound **1**, the intensity data set was collected with a Bruker X8 ApexII 4 K Kappa CCD diffractometer by using Mo-K_α radiation. The structures were solved by using a charge-flipping algorithm with the help of SUPERFLIP^[24] and refined by full-matrix least-squares techniques with SHELXL-97.^[25] Non-hydrogen atoms of the networks were refined with anisotropic temperature parameters. The hydrogen atoms of the linker molecules were geometrically constrained. Hydrogen atoms of the metal-coordinating water molecules were not taken into account during refinement, to avoid misinterpretation. Due to the high symmetry of the space group and the low residual electron density, it was impossible to locate the guest molecules in the crystal structures. Application of the SQUEEZE^[26] routine in the PLATON software package produced a new intensity data set excluding the intensity contribution from disordered solvent molecules. CCDC-772845 [DUT-10(Zn)], CCDC-772847 [DUT-10(Co)], CCDC-772848 [DUT-10(Cu)], CCDC-772846 (DUT-11), CCDC-772849 (DUT-12) and CCDC-772850 (**1**) contain the supplementary crystallographic data for this paper. These data can be obtained free of charge from the Cambridge Crystallographic Data Centre via www.ccdc.cam.ac.uk/data_request/cif. The topology of the networks has been examined with the program package TOPOS^[27] and *Gavrog Sysre*.^[28]

Crystal Data for Zn₂(BenzTB)(H₂O)₂ [DUT-10(Zn)]: *M* = 824.03 g mol⁻¹, orthorhombic, *Imma*, *a* = 23.353(5) Å, *b* = 35.883(7) Å, *c* = 17.178(3) Å, *V* = 14395(5) Å³, *Z* = 8, *T* = 293(2) K, *ρ* = 0.382 g cm⁻³, *μ* = 0.349 cm⁻¹ (solvent-free), *λ* = 0.88561 Å, 1.44° < *θ* < 32.00°, 40987 measured reflections, 6589 independent, *R*_{int} = 0.0559, *R*₁ (observed reflections) = 0.0622, *wR*₂ (all reflections) = 0.1271, max./min. residual electron density: 0.268/−0.351.

Crystal Data for Co₂(BenzTB)(H₂O)₂ [DUT-10(Co)]: *M* = 814.04 g mol⁻¹, orthorhombic, *Imma*, *a* = 23.415(5) Å, *b* = 35.948(7) Å, *c* = 17.141(3) Å, *V* = 14428(5) Å³, *Z* = 8, *T* = 293(2) K, *ρ* = 0.375 g cm⁻³, *μ* = 0.246 cm⁻¹ (solvent-free), *λ* = 0.88561 Å, 1.83° < *θ* < 32.00°, 47357 measured reflections, 6216 independent, *R*_{int} = 0.1612, *R*₁ (observed reflections) = 0.0617, *wR*₂ (all reflections) = 0.1336, max./min. residual electron density: 0.575/−0.299.

Crystal Data for Cu₂(BenzTB)(H₂O)₂ [DUT-10(Cu)]: *M* = 822.06 g mol⁻¹, orthorhombic, *Imma*, *a* = 23.264(1) Å, *b* = 35.595(4) Å, *c* = 17.217(4) Å, *V* = 14257(4) Å³, *Z* = 8, *T* = 293(2) K, *ρ* = 0.384 g cm⁻³, *μ* = 0.314 cm⁻¹ (solvent-free), *λ* = 0.88561 Å, 2.18° < *θ* < 33.14°, 22742 measured reflections, 7199 independent, *R*_{int} = 0.0455, *R*₁ (observed reflections) = 0.0590, *wR*₂ (all reflections) = 0.1708, max./min. residual electron density: 0.516/−0.722.

Crystal Data for Zn₂(BenzTB)(H₂O)₂ (DUT-11): *M* = 824.03 g mol⁻¹, orthorhombic, *Cccm*, *a* = 17.953(4) Å, *b* = 35.340(7) Å, *c* = 23.023(5) Å, *V* = 14607(5) Å³, *Z* = 8, *T* = 293(2) K, *ρ* = 0.376 g cm⁻³, *μ* = 0.344 cm⁻¹ (solvent-free), *λ* = 0.88561 Å, 1.44° < *θ* < 32.00°, 28926 measured reflections, 6461 independent, *R*_{int} = 0.0691, *R*₁ (observed reflections) = 0.0539, *wR*₂ (all reflections) = 0.1327, max./min. residual electron density: 0.222/−0.421.

Crystal Data for Cu₂(BenzTB)(H₂O)₂ (DUT-12): *M* = 822.06 g mol⁻¹, tetragonal, *P4/mnc*, *a* = 36.3295(5) Å, *b* = 36.3295(5) Å, *c* = 24.0870(3) Å, *V* = 31790.8(7) Å³, *Z* = 16, *T* = 293(2) K, *ρ* = 0.344 g cm⁻³, *μ* = 0.282 cm⁻¹ (solvent-free), *λ* = 0.88561 Å, 0.99° < *θ* < 28.77°, 211893 measured reflections, 14589 independent, *R*_{int} = 0.0776, *R*₁ (observed reflections) = 0.0623, *wR*₂ (all reflections) = 0.1942, max./min. residual electron density: 0.527/−0.435.

Supporting Information (see footnote on the first page of this article): Synthesis of **2**; crystal structure of **1**, further TGA curves, IR and fluorescence spectra.

Acknowledgments

This work was financially supported by the German Research Foundation (SPP 1362) and the Helmholtz Zentrum Berlin (HZB). The authors thank Dr. G. Auffermann (Max Planck Institute for Chemical Physics of Solids) for the performance of elemental analyses and P. Wollmann for measurement of IR spectra.

- [1] a) K. M. Thomas, *Dalton Trans.* **2009**, 1487–1505; b) H. Furukawa, M. A. Miller, O. M. Yaghi, *J. Mater. Chem.* **2007**, *17*, 3197–3204; c) I. Senkovska, S. Kaskel, *Microporous Mesoporous Mater.* **2008**, *112*, 108–115.
- [2] a) J.-R. Li, R. J. Kuppler, H.-C. Zhou, *Chem. Soc. Rev.* **2009**, *38*, 1477–1504; b) B. Chen, C. Liang, J. Yang, D. S. Contreras, Y. L. Clancy, E. B. Lobkovsky, O. M. Yaghi, S. Dai, *Angew. Chem. Int. Ed.* **2006**, *45*, 1390–1393.
- [3] L. Ma, C. Abney, W. Lin, *Chem. Soc. Rev.* **2009**, *38*, 1248–1256.
- [4] a) M. D. Allendorf, R. J. T. Houk, L. Andruszkiewicz, A. A. Talin, J. Pikarsky, A. Choudhury, K. A. Gall, P. J. Hesketh, *J. Am. Chem. Soc.* **2008**, *130*, 14404–14405; b) A. Lan, K. Li, H. Wu, D. H. Olson, T. J. Emge, W. Ki, M. Hong, J. Li, *Angew. Chem. Int. Ed.* **2009**, *48*, 2334–2338.
- [5] Z. Wang, S. M. Cohen, *Chem. Soc. Rev.* **2009**, *38*, 1315–1329.
- [6] M. Eddaoudi, J. Kim, N. Rosi, D. Vodak, J. Wachter, M. O'Keefe, O. M. Yaghi, *Science* **2002**, *295*, 469–472.
- [7] a) B. Chen, N. W. Ockwig, A. R. Millward, D. S. Contreras, O. M. Yaghi, *Angew. Chem. Int. Ed.* **2005**, *44*, 4745–4749; b) S. Yang, X. Lin, A. Dailly, A. J. Blake, P. Hubberstey, N. R. Champness, M. Schröder, *Chem. Eur. J.* **2009**, *15*, 4829–4835; c) X. Lin, I. Telepeni, A. J. Blake, A. Dailly, C. M. Brown, J. M. Simmons, M. Zoppi, G. S. Walker, K. M. Thomas, T. J. Mays, P. Hubberstey, N. R. Champness, M. Schröder, *J. Am. Chem. Soc.* **2009**, *131*, 2159–2171; d) S. Ma, D. Sun, J. M. Simmons, C. D. Collier, D. Yuan, H.-C. Zhou, *J. Am. Chem. Soc.* **2008**, *130*, 1012–1016; e) X.-S. Wang, S. Ma, P. M. Forster, D. Yuan, J. Eckert, J. J. Lopez, B. J. Murphy, J. B. Parise, H.-C. Zhou,

- Angew. Chem. Int. Ed.* **2008**, *47*, 7263–7266; f) K. C. Stylianou, R. Heck, S. Y. Chong, J. Bacsá, J. T. A. Jones, Y. Z. Khimyak, D. Bradshaw, M. J. Rosseinsky, *J. Am. Chem. Soc.* **2010**, *132*, 4119–4130.
- [8] X. Lin, J. Jia, X. Zhao, K. M. Thomas, A. J. Blake, G. S. Walker, N. R. Champness, P. Hubberstey, M. Schröder, *Angew. Chem. Int. Ed.* **2006**, *45*, 7358–7364.
- [9] Y. Hu, S. Xiang, W. Zhang, Z. Zhang, L. Wang, J. Bai, B. Chen, *Chem. Commun.* **2009**, 7551–7553.
- [10] In the original paper **nbo** topology (instead of **lvt**) was erroneously assigned to the stereoisomer with *Imma* symmetry. Note that the **nbo** net with two symmetrically independent vertices (representing paddle-wheel SBUs and ligands, respectively) cannot be realized in the *Imma* space group for symmetry reasons.
- [11] a) D. Sun, Y. Ke, T. M. Mattox, B. A. Ooro, H.-C. Zhou, *Chem. Commun.* **2005**, 5447–5449; b) D. Sun, D. J. Collins, Y. Ke, J.-L. Zuo, H.-C. Zhou, *Chem. Eur. J.* **2006**, *12*, 3768–3776.
- [12] Y. E. Cheon, J. Park, M. P. Suh, *Chem. Commun.* **2009**, 5436–5438.
- [13] J. P. Wolfe, S. L. Buchwald, *Org. Synth.* **2002**, *78*, 23–30.
- [14] a) P. Van der Sluis, A. L. Spek, *Acta Crystallogr., Sect. A* **1990**, *46*, 194–201; b) A. L. Spek, *PLATON*, A Multipurpose Crystallographic Tool, Utrecht University, Utrecht, The Netherlands, **2008**.
- [15] a) M. O’Keeffe, M. Eddaoudi, H. Li, T. Reineke, O. M. Yaghi, *J. Solid State Chem.* **2000**, *152*, 3–20; b) O. Delgado-Friedrichs, M. O’Keeffe, O. M. Yaghi, *Solid State Sci.* **2003**, *5*, 73–78.
- [16] V. A. Blatov, D. M. Proserpio, *Acta Crystallogr., Sect. A* **2009**, *65*, 202–212.
- [17] L. Ma, A. Jin, Z. Xie, W. Lin, *Angew. Chem.* **2009**, *121*, 10089–10092; *Angew. Chem. Int. Ed.* **2009**, *48*, 9905–9908.
- [18] L. R. Radovic, R. Radovic, *Chemistry & Physics of Carbon: Volume 28: A Series of Advances*, Marcel Dekker Inc., New York, **2003**.
- [19] E. Kockrick, C. Schrage, L. Borchardt, N. Klein, M. Rose, I. Senkowska, S. Kaskel, *Carbon* **2010**, *48*, 1707–1717.
- [20] Fluorescence measurements were performed by using ester **1** instead of acid **2**, because **2** is insoluble in most of the common solvents.
- [21] E. Y. Lee, S. Y. Jang, M. P. Suh, *J. Am. Chem. Soc.* **2005**, *127*, 6374–6381.
- [22] M. D. Allendorf, C. A. Bauer, R. K. Bhakta, R. J. T. Houk, *Chem. Soc. Rev.* **2009**, *38*, 1330–1352.
- [23] W. Kabsch, *J. Appl. Crystallogr.* **1993**, *26*, 795–800.
- [24] L. Palatinus, G. Chapuis, *J. Appl. Crystallogr.* **2007**, *40*, 786–790.
- [25] G. M. Sheldrick, 97–2 ed., *University of Göttingen*, Germany, **1997**.
- [26] P. Van der Sluis, A. L. Spek, *Acta Crystallogr., Sect. A* **1990**, *46*, 194–201.
- [27] V. A. Blatov, *IUCr Compcomm Newsletter* **2006**, *7*, 4–38.
- [28] <http://gavrog.sourceforge.net>.

Received: April 15, 2010
Published Online: July 15, 2010

A Series of Lanthanide Metal–Organic Frameworks Based on Biphenyl-3,4',5-tricarboxylate: Syntheses, Structures, Luminescence and Magnetic Properties

Zu-Jin Lin,^[a] Bo Xu,^[a] Tian-Fu Liu,^[a] Min-Na Cao,^[a] Jian Lü,^[a] and Rong Cao*^[a]

Keywords: Metal–organic frameworks / Luminescence / Magnetic properties / Lanthanides / Carboxylate ligands

A series of isostructural lanthanide metal–organic frameworks (MOFs) formulated as $[\text{Ln}_4(\text{BPT})_4(\text{DMF})_2(\text{H}_2\text{O})_8] \cdot (\text{DMF})_5 \cdot (\text{H}_2\text{O})_3$ {BPT = biphenyl-3,4',5-tricarboxylate, Ln = Eu(1), Gd(2), Tb (3), Dy (4), Ho (5), or Er (6)} have been hydrothermally synthesized and structurally characterized. X-ray diffraction analysis reveals that these complexes are isomorphous and isostructural, and each forms a three-dimensional structure possessing one-dimensional channels filled with lattice and coordinated water and DMF molecules. They show framework dynamics upon dehydration and rehydration. When heated above 220 °C for four hours, the crys-

tallinity of the as-prepared hydrated materials degrades completely to the amorphous dehydrated phases, but the structure is restored upon rehydration. Photoluminescence measurements show that complexes 1 and 3 are highly emissive at room temperature with quantum yields of 14.4 % and 60.9 %, respectively, but the yields unexpectedly fall to 5.2 % and 32.6 % after thermal treatment. The recovery of the quantum yields upon rehydration indicates that guest molecules enhance the luminescence rather than quench it. Results of magnetic measurements indicate that all complexes display antiferromagnetic behavior.

Introduction

Metal–organic framework (MOF) materials have attracted much attention in recent years due to their potential applications in a wide variety of fields such as catalysis,^[1] magnetism,^[2] gas storage,^[3] ion exchange,^[4] and molecular separation.^[5] As transition-metal chemistry offers some readily exploitable secondary building units (SBUs), which are essential to the rational design of MOFs and to the achievement of robust frameworks, many researches have prepared materials containing first-row transition metals.^[3b,6] Compared to first-row transition metals, lanthanides have larger coordination spheres and more flexible coordination geometries.^[7] These characteristics make it difficult to control the preparation of lanthanide complexes or even to predict the final topology of a lanthanide MOF.^[8] However, the flexibility of the coordination sphere, coupled with the tendency of lanthanides to adopt high coordination numbers, makes the f-block metal ions attractive for the discovery of new and unusual networks.^[8a,9]

Most importantly, lanthanide metal–organic frameworks are attractive because of their unique luminescence and magnetic properties.^[10] Lanthanide complexes usually exhibit

intense luminescence and are potentially applicable for sensors, lighting devices, and optical storage.^[11] Different from other metal ions and molecular species, the lanthanide ions have a narrow absorbance and emission band with high quantum yields when excited via the antenna effect.^[12] In addition, they emit in the visible and IR regions of the spectrum. Among the lanthanide ions, Eu^{III} and Tb^{III} are two of the most important luminescent centers, and their complexes have been regarded as attractive candidates for use as visible luminescent materials because of their strong red and green emissions, respectively.^[13] The magnetic properties of rare-earth ions are also characteristic due to the strong unquenched orbital angular momentum originating from f electrons, which are shielded by s and p electrons. The different emission and magnetic properties of Ln ions ensure that, through judicious choice, it is possible to precisely tailor individual MOFs according to specific requirements.^[14]

In this paper, we chose the robust ligand H_3BPT , for the following reasons: (1) It absorbs strongly in the ultraviolet range and may efficiently sensitize lanthanide ions. In lanthanide complexes, the f electron remains highly localized, and the emission behavior of the rare-earth ions based on f–f transitions have narrow wavelength ranges. However, Ln electronic transitions are forbidden by parity (Laporte) selection rules, leading to weak absorbance and low quantum yields. Lanthanides need to be sensitized by a suitable chromophoric moiety, since the weak absorbance of free lanthanide cations limits their luminescence intensity. Acting as a strongly absorbing linker, H_3BPT may circumvent this

[a] State Key Laboratory of Structural Chemistry, Fujian Institute of Research on the Structure of Matter, Chinese Academy of Sciences, Fuzhou 350002, P. R. China
Fax: +86-591-83796710
E-mail: rcao@fjirsm.ac.cn

Supporting information for this article is available on the WWW under <http://dx.doi.org/10.1002/ejic.201000353>.

problem by sensitization (called the “antenna effect”) to produce coordination polymers with high quantum yields.^[12] (2) It could promote the formation of extended MOF structures. As known, lanthanide ions have a high affinity for hard donor atoms and ligands containing oxygen or hybrid oxygen/nitrogen atoms, especially multicarboxylate ligands, which are usually employed in the architectures of lanthanide coordination polymers.^[14b] The H₃BPT ligand is able to act as bridging ligand in various ligating modes to construct high-dimensional porous lanthanide MOFs. Herein, we present a family of lanthanide–organic frameworks containing the tricarboxylate ligand H₃BPT. These frameworks are porous 3D structures with rectangular channels occupied by DMF/H₂O molecules. Interestingly, the materials exhibit reversible de-/rehydration processes, and the as-prepared, dehydrated, and rehydrated samples show variations in their luminescence properties. The magnetic properties have also been investigated.

Results and Discussion

Complexes **1–6** have been successfully synthesized under solvothermal conditions. Single-crystal X-ray diffraction, elemental analysis, IR spectroscopic, and TGA studies performed on complexes **1–6** indicate that they are isostructural and have the formula [Ln₄(BPT)₄(DMF)₂(H₂O)₈]·(DMF)₅·(H₂O)₃ {Ln = Eu (**1**), Gd (**2**), Tb (**3**), Dy (**4**), Ho (**5**), Er (**6**)}. Herein, only the structure of **3** will be described in detail as a representative of the series.

Crystal Structure of Complex 3

The single-crystal X-ray diffraction study performed on complex **3** reveals that it is a three-dimensional framework, crystallizing in the triclinic space group *P* $\bar{1}$. Each asymmetric unit contains four crystallographically independent terbium ions, four BPT ligands, two coordinated DMF molecules, eight coordinated water molecules, five free DMF molecules, and three free water molecules (Figure 1).

As shown in Figure 2, Tb1 is coordinated by eight oxygen atoms from one chelating carboxyl group (O17 and O18), four bis(monodentate) bridging carboxylate groups (O33, O11#2, O3#1, and O4#3), one terminal DMF molecule (O34), and one coordinated water molecule (O32) (Figure 2a). The nine oxygen atoms coordinated to Tb2 are from one chelating carboxyl group (O7 and O8), two bis(monodentate) bridging carboxyl groups (O19 and O20#4), two chelating/bridging carboxyl groups (O13, O13#4, and O14#4), and two terminal water molecules (O28 and O29) (Figure 2b). Tb3 is coordinated by two oxygen atoms from one chelating bidentate carboxyl group (O21#7 and O22#7), two oxygen atoms from two different bis(monodentate) carboxyl groups (O15#6 and O16#5), one monodentate carboxyl group (O1), one terminal water molecule (O30), and one terminal DMF molecule (O36) (Figure 2c).

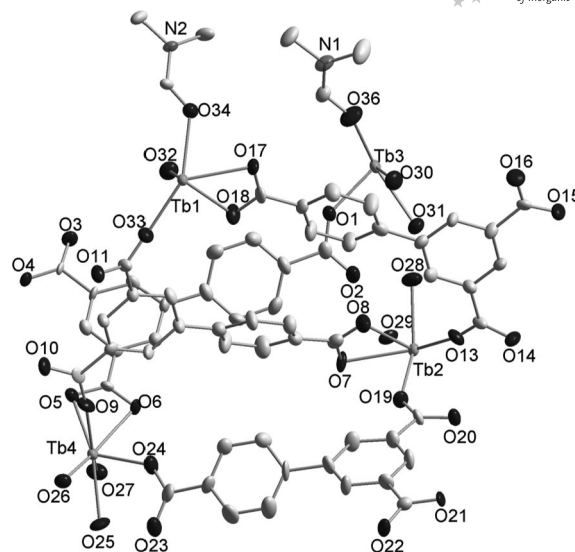


Figure 1. The asymmetric unit of complex **3** with non-hydrogen atoms represented by thermal ellipsoids drawn at the 50% probability level (all H atoms and noncoordinated guest molecules are omitted for clarity).

Tb4 is coordinated by a total of eight oxygen atoms, two from one chelating bidentate carboxyl group (O5 and O6), two from two different bis(monodentate) carboxyl groups (O9 and O10#8), one from a monodentate carboxyl group (O24), and three from terminal water molecules (O25, O26, and O27) (Figure 2d). Four crystallographically different terbium atoms (Tb1, Tb2, Tb3, and Tb4) and their corresponding centrosymmetric atoms are linked through bridging/bridging-bidentate carboxylate groups to form four different Tb dimers (Tb1, Tb2, Tb3, and Tb4 dimers, respectively), which are shown in Figure 2. The distances between the Tb1 (Tb2, Tb3, and Tb4) ions in the Tb1 (Tb2, Tb3, and Tb4) dimers are 4.3490 Å (3.9835, 4.8439, and 4.9758 Å). The coordination environments of the four crystallographically independent terbium ions, represented by coordination polyhedra (Figure S2), are best described as distorted bicapped for Tb1, tricapped for Tb2, bicapped for Tb3, and bicapped trigonal-pyramidal for Tb4. The carboxylic Tb–O, Tb–O_w, and Tb–O_{DMF} bonds are in the ranges 2.276(4)–2.486(4), 2.393(4)–2.466(4), and 2.338(4)–2.402(4) Å, respectively, all of which are comparable to those reported for other terbium–oxygen donor complexes.^[14b,15] Selected bond lengths and angles for complex **3** are listed in Table S2 in the Supporting Information.

The four different dinuclear Tb^{III} units in compound **3** are further connected through BPT ligands, resulting in a unique 3D metal–organic framework. First, the BPT ligands alternately link the Tb2 and Tb4 dimer units to form 1D infinite A chains, which alternately link the Tb1 and Tb3 dimer units to form another 1D infinite B chain in the same direction as shown in Figure 3. Second, the A and B chains alternately link to each other through phenyl groups of the BPT ligands in two different ways (Figure 4) to gen-

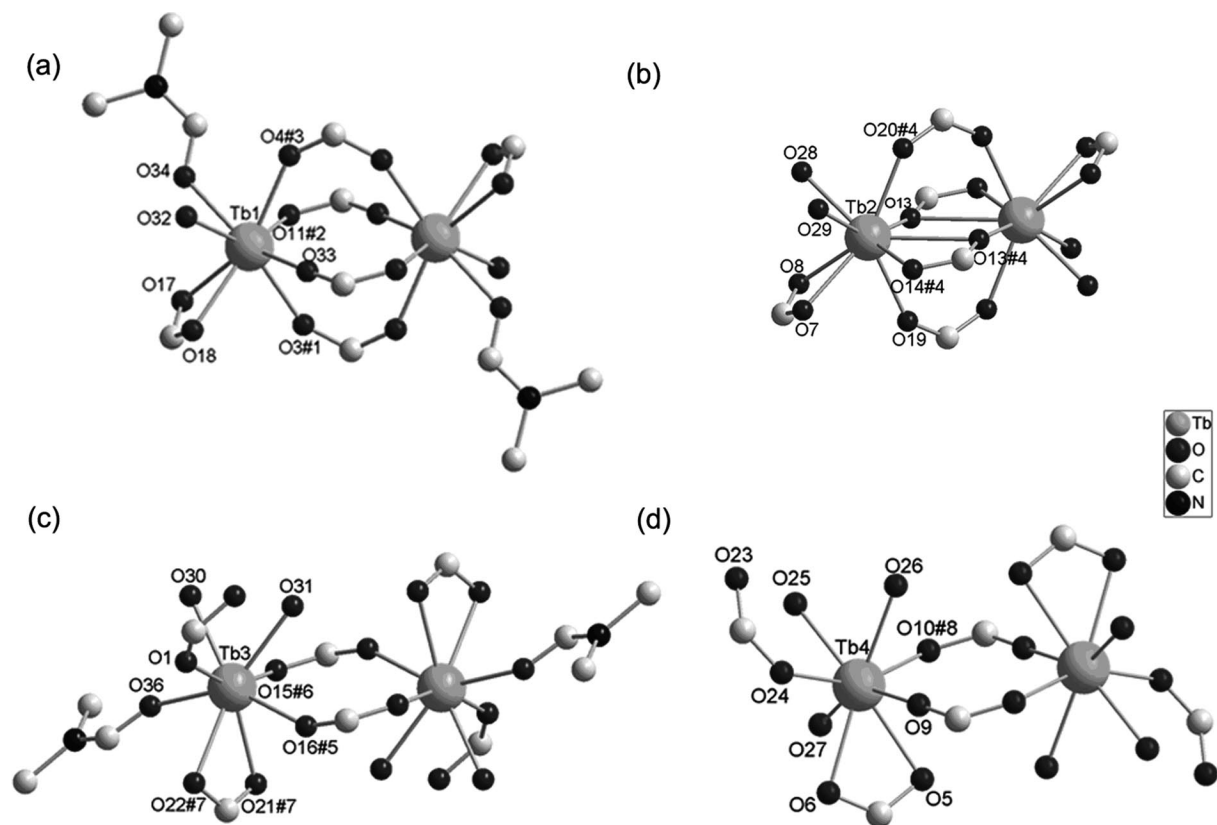


Figure 2. Ball-and-stick representation of coordination environments of the four crystallographically independent Tb ions, (a) Tb1, (b) Tb2, (c) Tb3, and (d) Tb4, in complex **3**. Symmetry transformations used to generate equivalent atoms: #1 $x + 1, y, z$; #2 $-x + 4, -y + 1, -z$; #3 $-x + 3, -y + 1, -z$; #4 $-x + 4, -y + 2, -z + 1$; #5 $x - 1, y, z$; #6 $-x + 4, -y + 1, -z + 1$; #7 $x - 1, y - 1, z$; #8 $-x + 3, -y + 2, -z$; #9 $x + 1, y + 1, z$.

erate two different 2D planes in two different directions. Moreover, the planes acting as impenetrable organic walls are cross-linked by BPT ligands to form a 3D framework (Figure 5). PLATON calculation yields a solvent-accessible area of 1651.5 \AA^3 per unit cell (4672.2 \AA^3), amounting to 35.3% of the crystal lattice (free guest removal). Guest molecules fill in the channels as a result of extensive hydrogen interactions with the host skeleton. Better insight into this framework can be achieved by topology analysis. With regard to connectivity, Tb dimers and BPT ligands are considered to be six-connected and three-connected nodes,

respectively. According to the topology definition of Wells, the present new topos is a (3,6)-connected net with a Schläfli point symbol of $(4.6^2)_2(4^2.6^6.8^5.10^2)(4^2.6)_2(4^4.6^5.8^5.10)$ (Figure 6).



Figure 3. Ball-and-stick depiction of infinite chains A and B. (Tb1, Tb2, Tb3, and Tb4 ions are represented as: gray, black, transparent, and white polyhedra, respectively.)

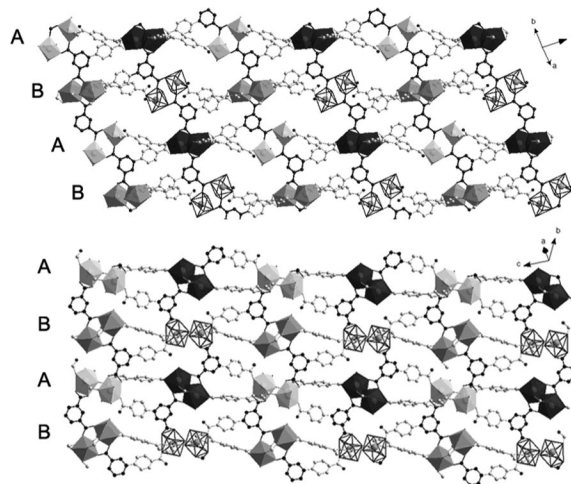


Figure 4. A and B chains alternately linked by BPT ligands to generate two different 2D planes. (Tb ions are represented as polyhedra.)

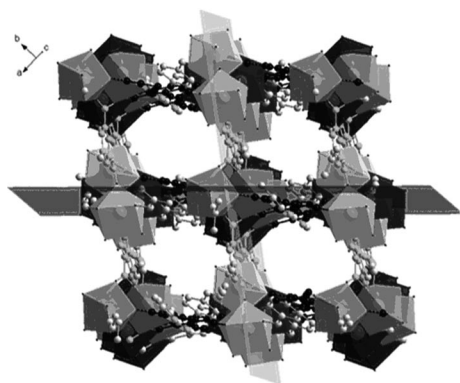


Figure 5. A three-dimensional network with approximately $9.25 \times 8.26 \text{ \AA}^2$ rectangular channels. (Tb ions are represented as polyhedra.)



Figure 6. View of the (3,6)-connected net.

Thermal Properties and De-/Rehydration Behavior

The infrared spectra of complexes **1–6** were recorded between 400 cm^{-1} and 4000 cm^{-1} in KBr pellets (Figure S3). Their peak positions are the same, indicating that the six complexes are isostructural. The experimental and simulated XPRD patterns of complexes **1–6** are also displayed in Figure S4. Their peak positions are in good agreement with each other, further indicating the same structure for the six complexes and the phase purity of the products.

To investigate their thermal stabilities, thermal gravimetric analysis (TGA) for complexes **1–6** was performed from $30 \text{ }^\circ\text{C}$ to $800 \text{ }^\circ\text{C}$ under N_2 gas flow. As shown in Figure 7 and Figure S5, because these six complexes are isomorphous and isostructural, the six as-prepared compounds exhibited similar thermal stability. For complex **3**, the continuous weight losses from $30 \text{ }^\circ\text{C}$ to $450 \text{ }^\circ\text{C}$ correspond to the loss of all guest solvent molecules, containing seven DMF and eleven H_2O molecules (calculated: 28.97%). Their frameworks start to burn off with the loss of H_3BPT ligands at approximately $500 \text{ }^\circ\text{C}$.

To investigate if the materials are robust to guest removal or exchange, their dehydration and rehydration were studied, and X-ray powder diffraction (PXRD) was used to check the phases. PXRD studies were performed for the as-synthesized sample and for the samples heated at 120, 150, 180, 210, and $240 \text{ }^\circ\text{C}$ for 4 h. The PXRD pattern for complex **3** heated at $150 \text{ }^\circ\text{C}$ is similar to that of the as-synthesized sample, which indicates that such temperatures do not lead to an obvious phase transformation. When the sample is heated at $180 \text{ }^\circ\text{C}$, the long-range order of the structure is lost and an amorphous phase is formed. So, the departure

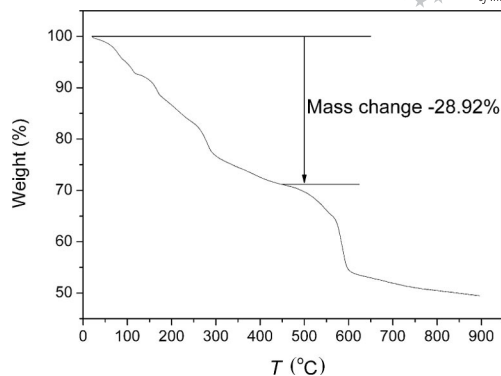


Figure 7. TGA analysis for complex **3**.

of the guest molecule leads to the loss of the structure and a phase transformation, as shown in Figure 8.

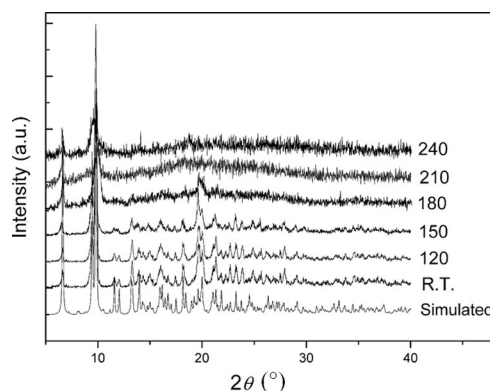


Figure 8. PXRD patterns for complex **3** after being heated at different temperatures for 4 h.

After annealing at $220 \text{ }^\circ\text{C}$ in air for 4 h, both complexes **1** and **3** were fully transformed to amorphous phases (named **1A** and **3A**, respectively, for convenience). However, when the dehydrated phases **1A** and **3A** were immersed in $\text{H}_2\text{O}/\text{DMF}$ ($v/v = 1:1$) solution at room temperature for one day, the two samples recovered their original structures, as indicated by comparing their PXRD patterns to those of the as-prepared samples (Figure 9). Consequently, dehydration and rehydration are reversible for these materials,

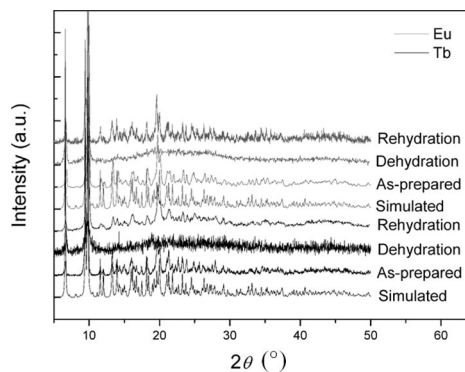


Figure 9. Powder X-ray diffraction patterns of complexes **1** and **3**, their dehydrated and rehydrated phases, and the simulated patterns based on the single-crystal structure of the as-prepared complexes.

and the frameworks show dynamics upon de-/rehydration. This is similar to the behavior of other previously reported Ln MOFs.^[15–16]

Photoluminescence Properties

Lanthanide complexes are known for their photoluminescence properties. Solid-state photoluminescence spectra were recorded at room temperature. No apparent fluorescent emission has been observed for complex **4** under UV light. In contrast, complexes **1** and **3** emit intense red and turquoise fluorescence, respectively. The photoluminescence spectra of complexes **1**, **3**, **4**, and free H₃BPT are shown in Figures 10, 11, 12, and 13. When excited at 300 nm at room temperature, H₃BPT exhibits a broad emission band at 370 nm (Figure 10), which can be ascribed to the ligand π – π^* transitions.^[17] Complex **1** displays intense red luminescence and shows the characteristic emission bands for f–f transitions of the Eu^{III} ion when excited at 320 nm (Figure 11). The strong emission at 617 nm in the red region is attributed to $^5D_0 \rightarrow ^7F_2$ transitions. The medium emission at 592 nm corresponds to the $^5D_0 \rightarrow ^7F_1$ transition, and the other medium emission at 700 nm is ascribed to $^5D_0 \rightarrow ^7F_4$ transitions. The weak emission bands at 580 and 650 nm arise from the $^5D_0 \rightarrow ^7F_0$ and $^5D_0 \rightarrow ^7F_3$ transitions, respectively. The spectrum is dominated by the intense band of the $^5D_0 \rightarrow ^7F_2$ electron dipole transition, which is the so-called hypersensitive transition and is responsible for the brilliant red emission of these complexes. The intensity of $^5D_0 \rightarrow ^7F_2$ is much stronger than the intensity of $^5D_0 \rightarrow ^7F_1$, indicating that the Eu^{III} ion adopts a noncentrosymmetric coordination environment without an inversion center,^[18] in agreement with the crystal structural analysis. This is also supported by the appearance of the $^5D_0 \rightarrow ^7F_0$ transition, which is forbidden in a symmetry field. The emission peaks of 650 nm and 700 nm correspond to the magnetic dipole transitions.^[19] The quantum yield of complex **1** was determined by means of an integrating sphere and was found to be 14.42% under excitation at 320 nm.

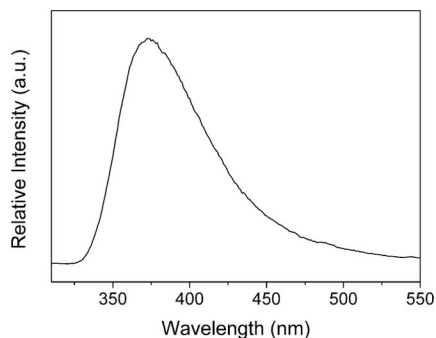


Figure 10. The solid-state photoluminescence spectrum of H₃BPT.

The excitation spectrum of complex **3** monitored around the peak of the intense $^5D_4 \rightarrow ^7F_5$ transition of the Tb^{III} ion exhibits a broadband between 250 nm and 350 nm with a maximum at approximately 320 nm, which can be assigned

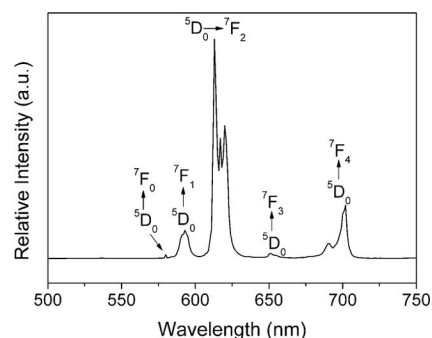


Figure 11. The solid-state photoluminescence spectrum of complex **1**.

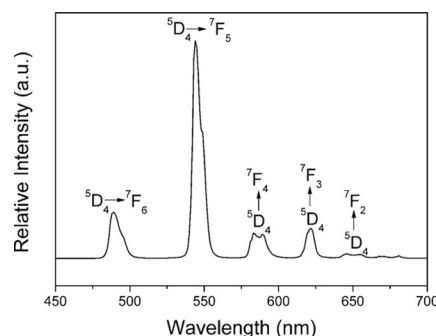


Figure 12. The solid-state photoluminescence spectrum of complex **3**.

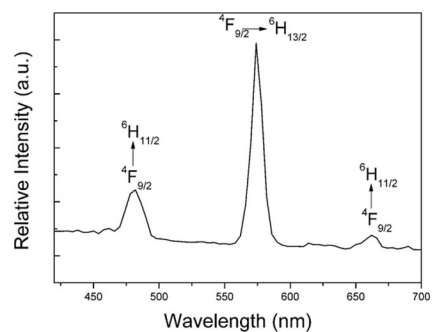


Figure 13. The solid-state photoluminescence spectrum of complex **4**.

to the π – π^* electronic transition of the H₃BPT ligands (Figure S6b). This broadband has also been observed in the excitation spectrum of other complexes (Figure S6). As can be seen, under excitation of 320 nm, complex **3** exhibits characteristic Tb^{III} emissions, resulting from the $^5D_4 \rightarrow ^7F_J$ ($J = 6, 5, 4, 3$, and 2) transitions (Figure 12). The emission band at 490 nm arises from the $^5D_4 \rightarrow ^7F_6$ transition; the strong band at 544 nm is attributed to the $^5D_4 \rightarrow ^7F_5$ transition; the band at 587 nm corresponds to the $^5D_4 \rightarrow ^7F_4$ transition; the band at 621 nm is attributed to the $^5D_4 \rightarrow ^7F_3$ transition; the weak band at 650 nm is attributed to the $^5D_4 \rightarrow ^7F_2$ transition. Surprisingly, the quantum yield is up to 60.87%, albeit there are nine coordinated water molecules and two coordinated DMF molecules in each asymmetric unit, which is usually believed and observed to

quench the lanthanide luminescence in other lanthanide porous metal–organic frameworks (PMOFs).^[12] In some cases, relatively high quantum yields ($\Phi > 40\%$) have been obtained.^[20] However, to the best of our knowledge, only a few best results ($\Phi > 60\%$) appeared in microporous metal–organic frameworks up to now.^[21]

As shown in Figure 13, the profiles of the emission bands in the range 475 to 675 nm for complex **4** are in agreement with previously reported spectra of Dy^{III} complexes.^[17c] Under an excitation of 320 nm, complex **4** displays a strong emission band at 573 nm ($^4F_{9/2} \rightarrow ^6H_{13/2}$), an emission band at 480 nm ($^4F_{9/2} \rightarrow ^6H_{15/2}$) with a much lower intensity, and a very weak band at 662 nm ($^4F_{9/2} \rightarrow ^6H_{11/2}$).

The photoluminescence properties of complexes **1** and **3** after being annealed at 220 °C in air for 4 h (**1A** and **3A**) and those of their rehydrated phases are also measured at room temperature. The quantum yields unexpectedly change to 5.2% and 32.6% for complex **1** and **3**, respectively, after thermal treatment, while both quantum yields recover upon rehydration (Table 1). It is interesting to observe that the dehydration process is accompanied by the weakening of the luminescence of the Tb^{III} ion, and the luminescence is recovered upon rehydration. The result indicates that guest molecules enhance the luminescence but do not quench it in these complexes, as is usually believed and observed in other lanthanide MOFs. This is probably due to the modification of the lanthanide–lanthanide distance or of the local symmetry in the compound during the de-/rehydration process or may be due to the softened environment of the lanthanide ion in the dehydrated amorphous phases and the recovery of the stiffness after rehydration.^[15]

Table 1. Quantum yield (q) measurements of complexes **1**, **3**, their dehydrated phases, and rehydrated phases.

Sample	1	1A ^[a]	1 ^[b]
q (%)	14.4	5.2	12.0
Sample	3	3A ^[a]	3 ^[b]
q (%)	60.9	32.6	58.2

[a] Synthesized samples annealed at 220 °C in air for 4 h. [b] Dehydrated samples immersed in H₂O/DMF (v/v = 1:1) solution at room temperature for one day.

The photoluminescence spectra of complexes **1**, **3**, and **4** exhibit emission bands characteristic of the corresponding luminescent lanthanide ions, whereas the emissions arising from the free ligand are not observable for the three complexes. The absence of ligand-based emission suggests efficient energy transfer from the ligands to the lanthanide centers during photoluminescence.^[21] The efficient energy transfer is further confirmed by the remarkably high quantum yield for complex **3** (60.9%). The results indicate that the BPT ligands are capable of converting energy efficiently to the lanthanide centers in complexes **1**, **3**, and **4**, acting as efficient sensitizers of MOFs luminescence. The results are quite promising and indicate that, by careful selection of ligand, lanthanide emission can be enhanced to produce superior quantum yields.

Magnetic Properties

The variable-temperature susceptibility measurements for complexes **1–6** have been performed in the range 2–300 K at a magnetic field of 1000 Oe. For compound **1**, the observed $\chi_M T$ at room temperature is 5.27 cm³ K mol^{−1}, which is slightly less than the value of 6 cm³ K mol^{−1} calculated for four uncoupled Eu^{III} ions. As the temperature is lowered from room temperature, the $\chi_M T$ value decreases, owing to the depopulation of the Stark levels with nonzero J values for a single Eu^{III} ion (Figure 14). At the lowest temperature, $\chi_M T$ is close to zero, which is indicative of a $J = 0$ ground state of the Eu^{III} ion (7F_0).^[22] The magnetic susceptibility above 170 K follows the Curie–Weiss law because of the presence of thermally populated excited states.

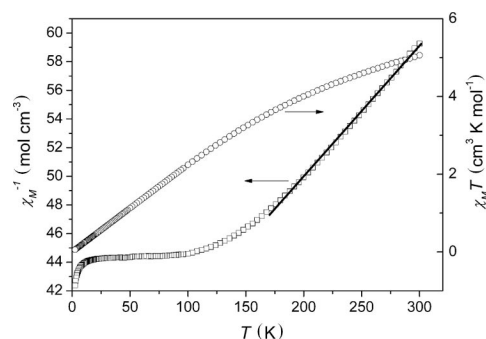


Figure 14. Temperature dependence of $\chi_M T$ and χ_M^{-1} for complex **1**.

The temperature dependence of the magnetic susceptibilities in the form of $\chi_M T$ and χ_M vs. T for the complex **3** is given in Figure 15. The value of χ_M continuously increases from 0.16 cm³ mol^{−1} at 300 K to 9.90 cm³ mol^{−1} at 2 K. The observed value of $\chi_M T$ is 46.66 cm³ K mol^{−1} at room temperature, which is slightly smaller than the calculated value of 47.28 cm³ K mol^{−1} for four uncoupled Tb^{III} ions in the 7F_6 state.^[23] Also, with a decrease in the temperature, $\chi_M T$ decreases smoothly to a minimum of 19.75 cm³ K mol^{−1} at 2 K.

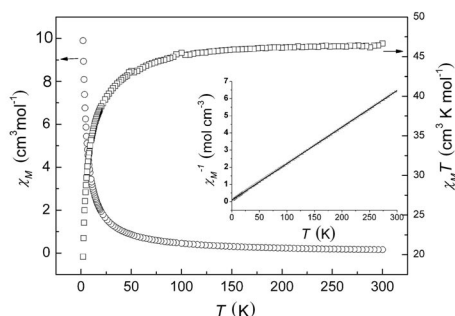


Figure 15. Thermal evolution of the magnetic susceptibility and $\chi_M T$ for complex **3**. The inset shows a plot of χ_M^{-1} vs. T .

The plot of χ_M^{-1} vs. T over the whole temperature range obeys the Curie–Weiss equation with a Curie constant of $C = 47.04$ cm³ mol^{−1} K and Weiss constant of $\theta = -4.01$ K. The decrease in $\chi_M T$ and the negative value of θ indicate

that the antiferromagnetic interaction between the terbium ions dominates the magnetic properties of complex **3**. Complexes **2–5** all have $\chi_M T$ and χ_M vs. T plots similar to that of complex **3** and negative values of θ , so the series of complexes exhibit similar antiferromagnetic interactions between Ln^{III} ions (Figure S7).

Conclusions

A series of isostructural lanthanide metal–organic frameworks (MOFs) based on the tricarboxylate ligand H_3BPT have been synthesized and characterized. Complexes **1** and **3** exhibit framework dynamics upon dehydration and rehydration, and a change in their luminescence intensities upon de/rehydration, where guest ($\text{DMF}/\text{H}_2\text{O}$) molecules enhance the luminescence rather than quench it. The significant luminescence changes upon de/rehydration render complex **3** a potential candidate for use as a sensor. Magnetic studies on complexes **2–6** show that antiferromagnetic interactions dominate between the Ln^{III} centers. Thus, these compounds could be anticipated as potential antiferromagnetic and fluorescent materials. The work may provide helpful information for the design and construction of highly luminescent Ln-based metal–organic frameworks (MOFs).

Experimental Section

Materials and Measurements: All chemicals purchased were of reagent grade and used without further purification. Ligand H_3BPT was synthesized according to the literature.^[24] The hydrothermal reactions were carried out in 23 mL stainless steel autoclaves lined with Teflon under autogenous pressure. Fluorescence spectroscopy data were recorded with a FLS920 fluorescence spectrophotometer. Thermogravimetric analyses (TGA) were performed under nitrogen with a heating rate of 10 °C/min using a NETZSCH STA 449F3 thermogravimetric analyzer. Elemental analyses (C, H, and N) were carried out with an Elementar Vario EL III analyzer. The infrared (IR) spectra were recorded (400–4000 cm^{-1} region) with a Perkin–Elmer Spectrum One FTIR spectrometer using KBr pellets. Powder X-ray diffraction (PXRD) data were collected with a Rigaku Mini-Flex2 diffractometer working with Cu-K_α radiation, and the recording speed was 8°min^{−1} over the 2θ range of 5–50° at room temperature. Temperature-dependent magnetic susceptibility data for complexes **2–6** were obtained with a PPMS60000 magnetometer under an applied field of 1000 Oe over the temperature range 2–300 K. The simulated and experimental powder XRD patterns of complexes **1–6** are shown in the Supporting Information (Figure S4).

[Eu₄(BPT)₄(DMF)₂(H₂O)₈](DMF)₅·(H₂O)₃ (1**):** Eu(NO₃)₃·6H₂O (0.20 mmol, 89 mg), H_3BPT (0.075 mmol, 20 mg), DMF (2 mL), and distilled water (2 mL) were mixed in a 23 mL stainless steel vessel lined with Teflon. The mixture was heated under autogenous pressure at 363 K for 48 h and then cooled to room temperature at a constant rate of 0.1 °C/min. Colorless block crystals suitable for X-ray crystal analysis were obtained by filtration and washed for several times with $\text{DMF}/\text{H}_2\text{O}$ ($v/v = 1:1$), and dried in air at ambient temperature. The complex is stable in air and is insoluble in common organic solvents such as methanol, ethanol, acetonitrile, acetone, DMSO, and DMF. Yield: 80% (based on H_3BPT).

$\text{C}_{81}\text{H}_{99}\text{Eu}_4\text{N}_7\text{O}_{42}$ (2453.27): calcd. C 39.70, H 4.07, N 4.00; found C 40.10, H 3.99, N 4.11. IR (KBr): $\tilde{\nu} = 3395$ (br), 3077 (s), 2936 (w), 1649 (s), 1585 (s), 1538 (s), 1400 (s), 1448 (s), 770 (s), 718 (m) cm^{-1} .

[Gd₄(BPT)₄(DMF)₂(H₂O)₈](DMF)₅·(H₂O)₃ (2**):** The procedure was the same as that for complex **1** except that $\text{Eu}(\text{NO}_3)_3 \cdot 6\text{H}_2\text{O}$ (0.20 mmol, 89 mg) was replaced by $\text{Gd}(\text{NO}_3)_3 \cdot 6\text{H}_2\text{O}$ (0.20 mmol, 90 mg). Yield: 75% (based on H_3BPT). $\text{C}_{81}\text{H}_{99}\text{Gd}_4\text{N}_7\text{O}_{42}$ (2471.67): calcd. C 39.36, H 4.04, N 3.97; found C 39.32, H 4.02, N 3.97. $\tilde{\nu} = 33–97$ (br), 3078 (s), 2936(w), 1648 (s), 1587 (s), 1539 (s), 1400 (s), 1400 (s), 1448 (s), 770 (s), 718 (m) cm^{-1} .

[Tb₄(BPT)₄(DMF)₂(H₂O)₈](DMF)₅·(H₂O)₃ (3**):** The procedure was the same as that for complex **1** except that $\text{Eu}(\text{NO}_3)_3 \cdot 6\text{H}_2\text{O}$ (0.20 mmol, 89 mg) was replaced by $\text{Tb}(\text{NO}_3)_3 \cdot 6\text{H}_2\text{O}$ (0.20 mmol, 90 mg). Yield: 76% (based on H_3BPT). $\text{C}_{81}\text{H}_{99}\text{Tb}_4\text{N}_7\text{O}_{42}$ (2478.38): calcd. C 38.25, H 4.03, N 3.96; found C 38.65, H 3.97, N 3.99. $\tilde{\nu} = 33–99$ (br), 3076 (s), 2936(w), 1649 (s), 1585 (s), 1537 (s), 1400 (s), 1448 (s), 770 (s), 718 (m) cm^{-1} .

[Dy₄(BPT)₄(DMF)₂(H₂O)₈](DMF)₅·(H₂O)₃ (4**):** The procedure was the same as that for complex **1** except that $\text{Eu}(\text{NO}_3)_3 \cdot 6\text{H}_2\text{O}$ (0.20 mmol, 89 mg) was replaced by $\text{Dy}(\text{NO}_3)_3 \cdot 6\text{H}_2\text{O}$ (0.20 mmol, 91 mg). Yield: 76% (based on H_3BPT). $\text{C}_{81}\text{H}_{99}\text{Dy}_4\text{N}_7\text{O}_{42}$ (2492.67): calcd. C 39.03, H 4.00, N 3.93; found C 39.21, H 3.98, N 3.96. $\tilde{\nu} = 33–90$ (br), 3074 (s), 2935(w), 1649 (s), 1585 (s), 1538 (s), 1400 (s), 1445 (s), 770 (s), 718 (m) cm^{-1} .

[Ho₄(BPT)₄(DMF)₂(H₂O)₈](DMF)₅·(H₂O)₃ (5**):** The procedure was the same as that for complex **1** except that $\text{Eu}(\text{NO}_3)_3 \cdot 6\text{H}_2\text{O}$ (0.20 mmol, 89 mg) was replaced by $\text{Ho}(\text{NO}_3)_3 \cdot 6\text{H}_2\text{O}$ (0.20 mmol, 91 mg). Yield: 78% (based on H_3BPT). $\text{C}_{81}\text{H}_{99}\text{Ho}_4\text{N}_7\text{O}_{42}$ (2502.40): calcd. C 38.88, H 3.99, N 3.92; found C 38.94, H 3.87, N 4.02. $\tilde{\nu} = 33–99$ (br), 3078 (s), 2937(w), 1649 (s), 1586 (s), 1538 (s), 1400 (s), 1448 (s), 770 (s), 718 (m) cm^{-1} .

[Er₄(BPT)₄(DMF)₂(H₂O)₈](DMF)₅·(H₂O)₃ (6**):** The procedure was the same as that for complex **1** except that $\text{Eu}(\text{NO}_3)_3 \cdot 6\text{H}_2\text{O}$ (0.20 mmol, 89 mg) was replaced by $\text{Er}(\text{NO}_3)_3 \cdot 6\text{H}_2\text{O}$ (0.20 mmol, 91 mg). Yield: 75% (based on H_3BPT). $\text{C}_{81}\text{H}_{99}\text{Er}_4\text{N}_7\text{O}_{42}$ (2511.71): calcd. C 38.73, H 3.97, N 3.90; found C 38.82, H 3.87, N 3.95. $\tilde{\nu} = 34–00$ (br), 3077 (s), 2938(w), 1649 (s), 1587 (s), 1538 (s), 1400 (s), 1448 (s), 770 (s), 718 (m) cm^{-1} .

X-ray Crystallography: Crystallographic data for complex **3** was collected with a Saturn 70 single-crystal diffractometer with graphite-monochromated Mo- K_α radiation ($\lambda = 0.71073$ Å) at 142 K. An empirical absorption correction was applied to the data using the SADABS program.^[25] The structure was solved by direct methods and refined by the full-matrix least-squares method on F^2 with the SHELXTL-97 program.^[26] All non-hydrogen atoms were refined with anisotropic displacement parameters.^[27] The positions of hydrogen atoms attached to carbon atoms were generated geometrically. A summary of crystallographic data and structure determination are listed in Table S1. CCDC-771609 contains the supplementary crystallographic data for this paper. These data can be obtained free of charge from The Cambridge Crystallographic Data Centre via www.ccdc.cam.ac.uk/data_request/cif.

Supporting Information (see footnote on the first page of this article): Ball-and-stick representations of Tb dimers, coordination polyhedra, IR spectra, XRD patterns, TGA curves, excitation spectra, magnetic susceptibility plots, and tables of X-ray crystallographic data.

Acknowledgments

This work was financially supported by the 973 Program (2006CB932903, 2007CB815303), the National Natural Science Foundation of China (20731005, 20921061, 20873151), the Natural Science Foundation of Fujian Province (2006F3134), the Fujian Key Laboratory of Nanomaterials (2006L2005), and a key project from the Chinese Academy of Sciences.

- [1] a) J. S. Seo, D. Whang, H. Lee, S. I. Jun, J. Oh, Y. J. Jeon, K. Kim, *Nature* **2000**, *404*, 982–986; b) D. N. Dybtsev, A. L. Nuzhdin, H. Chun, K. P. Bryliakov, E. P. Talsi, V. P. Fedin, K. Kim, *Angew. Chem. Int. Ed.* **2006**, *45*, 916–920; c) S. Horike, M. Dinca, K. Tamaki, J. R. Long, *J. Am. Chem. Soc.* **2008**, *130*, 5854–5855; d) J.-Y. Lee, O. K. Farha, J. Roberts, K. A. Scheidt, S. T. Nguyen, J. T. Hupp, *Chem. Soc. Rev.* **2009**, *38*, 1450–1459.
- [2] G. J. Halder, C. J. Kepert, B. Moubaraki, K. S. Murray, J. D. Cashion, *Science* **2002**, *298*, 1762–1765.
- [3] a) T. M. Reineke, M. Eddaoudi, M. O’Keeffe, O. M. Yaghi, *Angew. Chem. Int. Ed.* **1999**, *38*, 2590–2594; b) J. P. Zhang, X. M. Chen, *J. Am. Chem. Soc.* **2008**, *130*, 6010–6017; c) Y. K. Park, S. B. Choi, H. Kim, K. Kim, B. H. Won, K. Choi, J. S. Choi, W. S. Ahn, N. Won, S. Kim, D. H. Jung, S. H. Choi, G. H. Kim, S. S. Cha, Y. H. Jhon, J. K. Yang, J. Kim, *Angew. Chem. Int. Ed.* **2007**, *46*, 8230–8233; d) S. Hong, M. Oh, M. Park, J. W. Yoon, J. S. Chang, M. S. Lah, *Chem. Commun.* **2009**, 5397–5399; e) Y. X. Hu, S. C. Xiang, W. W. Zhang, Z. X. Zhang, L. Wang, J. F. Bai, B. L. Chen, *Chem. Commun.* **2009**, 7551–7553; f) X. F. Liu, M. Park, S. Hong, M. Oh, J. W. Yoon, J. S. Chang, M. S. Lah, *Inorg. Chem.* **2009**, *48*, 11507–11509; g) D. Zhao, D. Q. Yuan, D. F. Sun, H. C. Zhou, *J. Am. Chem. Soc.* **2009**, *131*, 9186–9188.
- [4] K. S. Min, M. P. Suh, *J. Am. Chem. Soc.* **2000**, *122*, 6834–6840.
- [5] a) Y. S. Bae, O. K. Farha, A. M. Spokoyny, C. A. Mirkin, J. T. Hupp, R. Q. Snurr, *Chem. Commun.* **2008**, 4135–4137; b) J. R. Li, R. J. Kuppler, H. C. Zhou, *Chem. Soc. Rev.* **2009**, *38*, 1477–1504.
- [6] a) M. Eddaoudi, J. Kim, N. Rosi, D. Vodak, J. Wachter, M. O’Keeffe, O. M. Yaghi, *Science* **2002**, *295*, 469–472; b) Z. G. Guo, R. Cao, X. Wang, H. F. Li, W. B. Yuan, G. J. Wang, H. H. Wu, J. Li, *J. Am. Chem. Soc.* **2009**, *131*, 6894–6895.
- [7] D. J. Tranchemontagne, J. L. Mendoza-Cortes, M. O’Keeffe, O. M. Yaghi, *Chem. Soc. Rev.* **2009**, *38*, 1257–1283.
- [8] a) D. L. Long, A. J. Blake, N. R. Champness, C. Wilson, M. Schroder, *J. Am. Chem. Soc.* **2001**, *123*, 3401–3402; b) S. K. Ghosh, P. K. Bharadwaj, *Inorg. Chem.* **2004**, *43*, 2293–2298.
- [9] a) D. L. Long, A. J. Blake, N. R. Champness, M. Schroder, *Chem. Commun.* **2000**, 1369–1370; b) Z. Wang, C. M. Jin, T. Shao, Y. Z. Li, K. L. Zhang, H. T. Zhang, X. Z. You, *Inorg. Chem. Commun.* **2002**, *5*, 642–648.
- [10] T. K. Maji, G. Mostafa, H. C. Chang, S. Kitagawa, *Chem. Commun.* **2005**, 2436–2438.
- [11] a) J. C. G. Bünzli, C. Piguet, *Chem. Soc. Rev.* **2005**, *34*, 1048–1077; b) R. J. Hill, D. L. Long, P. Hubberstey, M. Schroder, N. R. Champness, *J. Solid State Chem.* **2005**, *178*, 2414–2419; c) K.-L. Wong, G.-L. Law, Y.-Y. Yang, W.-T. Wong, *Adv. Mater.* **2006**, *18*, 1051–1054; d) C. L. Cahill, D. T. de Lill, M. Frisch, *CrystEngcomm* **2007**, *9*, 15–26; e) C. Marchal, Y. Filinchuk, D. Imbert, J. C. G. Bünzli, M. Mazzanti, *Inorg. Chem.* **2007**, *46*, 6242–6244.
- [12] M. D. Allendorf, C. A. Bauer, R. K. Bhakta, R. J. T. Houk, *Chem. Soc. Rev.* **2009**, *38*, 1330–1352.
- [13] K. Binnemans, *Chem. Rev.* **2009**, *109*, 4283–4374.
- [14] a) T. M. Reineke, M. Eddaoudi, M. Fehr, D. Kelley, O. M. Yaghi, *J. Am. Chem. Soc.* **1999**, *121*, 1651–1657; b) X. D. Guo, G. S. Zhu, F. X. Sun, Z. Y. Li, X. J. Zhao, X. T. Li, H. C. Wang, S. L. Qiu, *Inorg. Chem.* **2006**, *45*, 2581–2587; c) B. L. Chen, Y. Yang, F. Zapata, G. N. Lin, G. D. Qian, E. B. Lobkovsky, *Adv. Mater.* **2007**, *19*, 1693–1696; d) B. L. Chen, L. B. Wang, F. Zapata, G. D. Qian, E. B. Lobkovsky, *J. Am. Chem. Soc.* **2008**, *130*, 6718–6719.
- [15] W. H. Zhu, Z. M. Wang, S. Gao, *Inorg. Chem.* **2007**, *46*, 1337–1342.
- [16] A. Michaelides, S. Skoulika, *Cryst. Growth Des.* **2005**, *5*, 529–533.
- [17] a) D. F. Sun, S. Q. Ma, Y. X. Ke, T. M. Petersen, H. C. Zhou, *Chem. Commun.* **2005**, 2663–2665; b) D. F. Sun, S. Q. Ma, Y. X. Ke, D. J. Collins, H. C. Zhou, *J. Am. Chem. Soc.* **2006**, *128*, 3896–3897; c) S. Q. Ma, D. Q. Yuan, X. S. Wang, H. C. Zhou, *Inorg. Chem.* **2009**, *48*, 2072–2077.
- [18] J. Yang, Q. Yue, G. D. Li, J. J. Cao, G. H. Li, J. S. Chen, *Inorg. Chem.* **2006**, *45*, 2857–2865.
- [19] S. N. Wang, R. Sun, X. S. Wang, Y. Z. Li, Y. Pan, J. f. Bai, M. Scheer, X. Z. You, *CrystEngcomm* **2007**, *9*, 1051–1061.
- [20] a) L. Ma, O. R. Evans, B. M. Foxman, W. B. Lin, *Inorg. Chem.* **1999**, *38*, 5837–5840; b) T. Fiedler, M. Hilder, P. C. Junk, U. H. Kynast, M. M. Lezhnina, M. Warzala, *Eur. J. Inorg. Chem.* **2007**, 291–301.
- [21] Q. L. Zhu, T. L. Sheng, R. B. Fu, S. M. Hu, J. S. Chen, S. C. Xiang, C. J. Shen, X. T. Wu, *Cryst. Growth Des.* **2009**, *9*, 5128–5134.
- [22] Y. H. Wan, L. P. Zhang, L. P. Jin, S. Gao, S. Z. Lu, *Inorg. Chem.* **2003**, *42*, 4985–4994.
- [23] a) C. Benelli, D. Gatteschi, *Chem. Rev.* **2002**, *102*, 2369–2388; b) X. J. Zheng, Z. M. Wang, S. Gao, F. H. Liao, C. H. Yan, L. P. Jin, *Eur. J. Inorg. Chem.* **2004**, 2968–2973; c) Z. Y. Li, G. S. Zhu, X. D. Guo, X. J. Zhao, Z. Jin, S. L. Qiu, *Inorg. Chem.* **2007**, *46*, 5174–5178.
- [24] A. G. Wong-Foy, O. Lebel, A. J. Matzger, *J. Am. Chem. Soc.* **2007**, *129*, 15740–15741.
- [25] G. M. Sheldrick, *SADABS, Program for Empirical Absorption Correction of Area Detector Data*, University of Göttingen, Germany, **1996**.
- [26] G. M. Sheldrick, *SHELXTL Version 5.1*, Bruker Analytical X-ray Instruments Inc., Madison, Wisconsin, USA, **1998**.
- [27] D. Lee, P.-L. Hung, B. Spingler, S. J. Lippard, *Inorg. Chem.* **2002**, *41*, 521–531.

Received: March 30, 2010
Published Online: July 23, 2010

Synthesis, Structures, and Magnetic Properties of Two Cobalt(II) Isophthalate Coordination Polymers

Xiao-Ning Cheng,^{*,[a,b]} Wei Xue,^[a] and Xiao-Ming Chen^{*,[a]}

Keywords: Cobalt / Carboxylate ligands / Magnetic properties / Cluster compounds / Chain structures

Two new 3D coordination polymers, $[\text{Co}_6(\mu_3\text{-OH})_2(\text{ipa})_5(\text{H}_2\text{O})_5] \cdot 8\text{H}_2\text{O}$ (**1**) and $[\text{Co}_2(\text{ipa})_2(\text{iPrOH})_{0.5}(\text{H}_2\text{O})_{0.5}] \cdot (\text{iPrOH})_{0.5}(\text{H}_2\text{O})$ (**2**) (H_2ipa = isophthalic acid, iPrOH = 2-propanol), were synthesized by solvothermal reactions of $\text{Co}(\text{OAc})_2$ and H_2ipa in methanol and iPrOH , respectively. Compound **1** is a cluster-based 3D porous framework with Co_6 nodes and ipa^{2-} link-

ers. Compound **2** is a chain-based framework composed of Co^{II} 4_1 helical Δ chains cross-linked by ipa^{2-} ligands with one-dimensional channels in the c direction. Both **1** and **2** show spin-canting behavior for the antiferromagnetic triangular geometry and weak long-range ordering for the existence of guest molecules.

Introduction

Metal clusters and chains are useful secondary building blocks for the construction of metal-organic frameworks with extraordinary redox, magnetic, and spectroscopic properties.^[1–3] Multifarious magnetic characters emerge when the clusters or chains are composed of paramagnetic metal ions.^[2] The research interest in these compounds has been renewed in recent years after the discovery of single-molecule magnets (SMMs) and single-chain magnets (SCMs).^[4] Nice examples include a series of 1D, 2D, and 3D compounds based on double-cuboidal Mn_4 SMMs, which were obtained by a bottom-up approach through connecting Mn_4 SMMs by N_3^- and $\text{N}(\text{CN})_2^-$. They show properties ranging from those of SMMs to classical magnets and dynamic behavior.^[5] More cluster-based high-dimensional compounds having SMM behavior, such as $\{\text{Mn}_{19}\}$ and $\{\text{Fe}_{13}\}$, were obtained by direct synthesis.^[6] A few chain-based magnets showing SCM behavior were also reported.^[7] Moreover, clusters and chains acting as multiconnectors could be easily linked by organic ligands into high-dimensional porous structures.^[8] For instance, Williams et al. created a 3D porous network by connecting the typical paddle-wheel copper dimers with trimesate; the compound shows interesting guest-modulated magnetic properties.^[9] Zaworotko et al. obtained Kagomé and

square-grid type molecular nanoporous frameworks by linking copper dimers with isophthalate ligands.^[10] A few fascinating porous magnets built up from other types of clusters and chains have also been reported.^[11–13]

Phenyldicarboxylates are frequently used in the design of porous magnets as efficient linkers/spacers.^[13–15] The carboxylate groups of phenyldicarboxylates, which adopt various coordination modes, can provide strong magnetic exchange within the clusters/chains, and the phenyl fragment, which offers weak magnetic interactions, separates the clusters/chains to enable these complexes to possess the magnetic behavior of low-dimensional magnets.^[13–14] Férey and co-workers reported a series of porous magnets based on clusters/chains with terephthalate.^[1a] We have recently used V-shaped isophthalate (ipa) to construct a porous magnet based Co_7 units, which exhibits a reversible single-crystal-to-single-crystal transformation, concomitant with a reversible change in magnetic properties upon the absorption/desorption of guest molecules.^[15] Here we report two porous magnets also constructed by ipa^{2-} ligands, $[\text{Co}_6(\mu_3\text{-OH})_2(\text{ipa})_5(\text{H}_2\text{O})_5] \cdot 8\text{H}_2\text{O}$ (**1**) and $[\text{Co}_2(\text{ipa})_2(\text{iPrOH})_{0.5}(\text{H}_2\text{O})_{0.5}] \cdot (\text{iPrOH})_{0.5}(\text{H}_2\text{O})$ (**2**), which feature Co_6 clusters and 4_1 helical chains, respectively, and were synthesized by changing the solvents under similar conditions.

Results and Discussion

Synthesis and Structures

Solvent, metal/ligand ratio, pH value, reaction temperature, and noncovalent interactions such as π - π interactions, are all important factors to determine the final network structure.^[16] Rigid, V-shaped isophthalic acid was used to construct zigzag and helical chains, and Kagomé layers, while the various coordination modes of the carboxylate groups may also furnish other complicated and unexpected

[a] MOE Key Laboratory of Bioinorganic and Synthetic Chemistry, State Key Laboratory of Optoelectronic Materials, School of Chemistry & Chemical Engineering, Sun Yat-Sen University, Guangzhou 510275, P. R. China
Fax: +86-20-8411-2245
E-mail: chengxn7@mail.sysu.edu.cn
cxm@mail.sysu.edu.cn

[b] Instrumental Analysis and Research Center, Sun Yat-Sen University, Guangzhou 510275, P. R. China

Supporting information for this article is available on the WWW under <http://dx.doi.org/10.1002/ejic.201000146>.

metal complexes. For example, by use of different alkali metals, some porous magnets, based on $\{\text{Co}_6\text{Na}\}$, $\{\text{Co}_7\text{K}\}$ clusters, and other connectors, were generated.^[15,17] Here, two different porous coordination polymers, **1** and **2**, were obtained by only changing the solvent in the reaction between $\text{Co}(\text{OAc})_2 \cdot 5\text{H}_2\text{O}$ and H_2ipa . We also found that the same products can also be obtained by adding LiOH .

Single-crystal X-ray diffraction analysis reveals that the asymmetric unit of **1** contains six independent Co^{II} atoms, two $\mu_3\text{-OH}^-$ groups, five ipa^{2-} ligands, as well as coordinated and guest H_2O molecules (Figure 1a). Both Co1 and Co2 are coordinated by one μ_3 -hydroxy group and five carboxylate O atoms from five ipa^{2-} ligands, furnishing distorted octahedral geometries [Co1-O 2.043(6)–2.298(5) Å, O-Co1-O 77.6(2)–173.2(2)°; Co2-O 2.007(6)–2.215(5) Å, O-Co2-O 79.9(2)–174.9(3)°]. Both Co3 and Co4 are also in distorted octahedral geometries: each of them is composed of one μ_3 -hydroxy oxygen atom, three carboxylate O atoms from different ipa^{2-} ligands, and two water molecules [Co3-O 2.037(6)–2.12(1) Å, O-Co3-O 85.5(4)–178.1(3)°; Co4-O 2.049(6)–2.159(8) Å, O-Co4-O 83.9(3)–178.8(4)°]. Co5 is in a distorted tetrahedral geometry with one μ_3 -hydroxy oxygen atom and three carboxylate O atoms from different ipa^{2-} ligands [Co5-O 1.942(6)–1.974(7) Å, O-Co5-O 97.9(3)–119.0(3)°], while Co6 is ligated with one μ_3 -hydroxy oxygen atom, three carboxylate O atoms, and one water molecule, giving a triangular bipyramid [Co6-O 1.971(6)–2.34(1) Å, O-Co6-O 80.5(3)–173.2(3)°]. The different coordination geometries induced by the water molecules ligating Co5 and Co6 should be an important reason for the crystallization of **1** in a chiral space group. The two $\mu_3\text{-OH}^-$ groups connect three Co^{II} atoms into two scalene [$\text{Co}_3(\mu_3\text{-OH})$] triangles [Co1-O1-Co4 109.0(3)°, $\text{Co1}\cdots\text{Co4}$ 3.375(2) Å; Co1-O1-Co6 117.9(3)°, $\text{Co1}\cdots\text{Co6}$ 3.514(2) Å; Co6-O1-Co4 119.6(2)°, $\text{Co4}\cdots\text{Co6}$ 3.552(2) Å; Co2-O2-Co3 111.8(3)°, $\text{Co2}\cdots\text{Co3}$ 3.466(2) Å; Co2-O2-Co5 109.5(3)°, $\text{Co2}\cdots\text{Co5}$ 3.307(2) Å; Co3-O2-Co5 115.1(2)°, $\text{Co3}\cdots\text{Co5}$ 3.395(2) Å]. Co1 and Co2 in the two different triangles are further bridged by carboxylate oxygen atoms O13 and O15 [Co1-O13-Co2 102.1(2)°, Co2-O15-Co1 100.3(2)°, $\text{Co1}\cdots\text{Co2}$ 3.402(1) Å] connecting the two triangles to a Co_6 cluster. Co2 and Co6 , and Co1 and Co5 are further connected by *syn-anti* carboxylate bridges. The ipa^{2-} ligands in **1** adopt two kinds of coordination modes, $\mu_4\text{-}\eta^1\text{:}\eta^1\text{:}\eta^1\text{:}\eta^1$ and $\mu_5\text{-}\eta^2\text{:}\eta^1\text{:}\eta^1\text{:}\eta^1$, which envelope the Co_6 clusters and connect them to the adjacent four equivalent units in pairs to afford a 3D porous distorted NaCl network based on Co_6 clusters with the shortest intercluster $\text{Co}\cdots\text{Co}$ distance of 7.11 Å (Figure 1). The solvent-accessible volume of the framework has 39.3% of the total crystal volume, which is occupied by disordered water molecules.

Complex **2** crystallizes in the space group $I4_1/a$ with two Co^{II} atoms, two ipa^{2-} ligands, two halves of *i*PrOH molecules, and disordered water molecules in an asymmetric unit (Figure 2a). Both Co1 and Co2 are in distorted octahedral geometries. Co1 is surrounded by five carboxylate oxygen atoms from four different ipa^{2-} ligands, while its sixth coordination site is occupied by a half *i*PrOH molecule and a

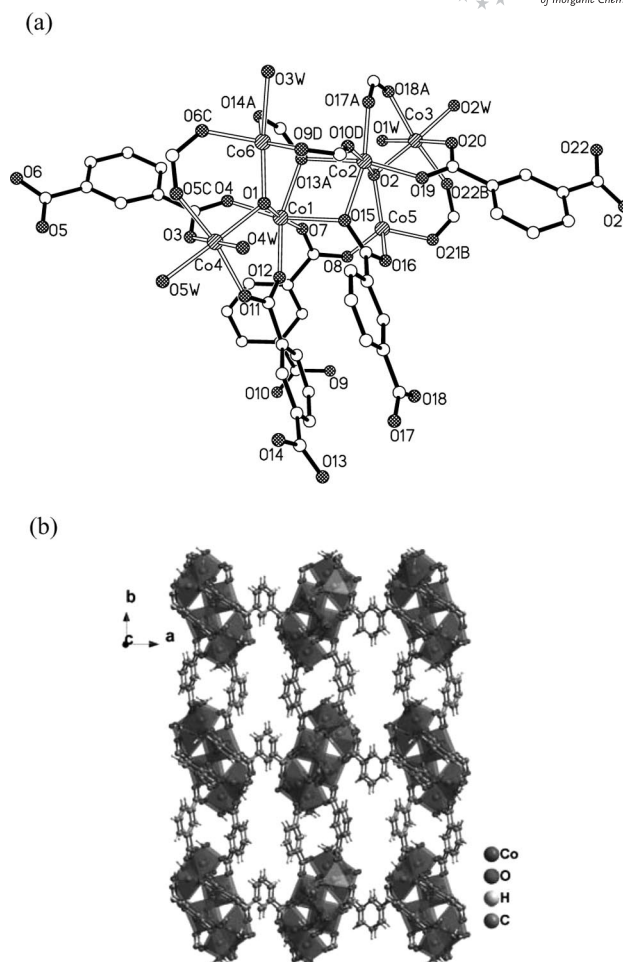


Figure 1. Coordination environments of the Co^{II} atoms (a) and the 3D framework (b) of **1**. Symmetry codes: A) $+x, +y, 1+z$; B) $1-x, -y, +z$; C) $1-x, 1-y, +z$; D) $-1/2+x, 1/2-y, -z$.

half water molecule [Co1-O 1.983(2)–2.259(2) Å, O-Co1-O 59.51(8)–173.4(1)°]. However, Co2 is coordinated to six carboxylate O atoms of six different ipa^{2-} ligands [Co2-O 1.999(2)–2.322(2) Å, O-Co2-O 75.13(8)–169.6(1)°]. The ipa^{2-} ligands adopt $\mu_6\text{-}\eta^2\text{:}\eta^2\text{:}\eta^2\text{:}\eta^1$ and $\mu^4\text{-}\eta^1\text{:}\eta^1\text{:}\eta^1\text{:}\eta^1$ coordination modes (Figure 2a). Co1 joins two adjacent Co2 atoms through two kinds of triple bridges, one is through a pair of single carboxylate O atoms and a *syn-syn* carboxylate bridge [Co1-O5-Co2 93.41(8)°, Co1-O7-Co2 87.51(8)°, $\text{Co1}\cdots\text{Co2}$ 3.167(1) Å], and the other is through one single carboxylate O atom and a pair of *syn-syn* carboxylate bridges [Co1-O8-Co2 105.8(1)°, $\text{Co1}\cdots\text{Co2}$ 3.416(1) Å]. Two Co2 atoms are further connected together through one *syn-anti* and one *anti-anti* carboxylate bridge to form a triangular lattice [$\text{Co2}\cdots\text{Co2}$ 5.367(1) Å]. These triangles are corner-shared via the Co2 atom to form a helical chain along the crystallographic 4_1 axis with a pitch of 11.21 Å (Figure 2b). This is an important feature for the magnetic properties and is not observed in other magnetic compounds.^[18] Moreover, the Co^{II} helix is enlaced by a reverse chiral 4_1 helical chain comprising the $\mu^4\text{-}\eta^1\text{:}\eta^1\text{:}\eta^1\text{:}\eta^1$ ipa^{2-} ligands, showing a double-stranded helical structure. Finally, these

helices are further associated with the same four adjacent helices with different chiralities by pairs of $\mu^4\text{-}\eta^1\text{:}\eta^1\text{:}\eta^1\text{:}\eta^1$ ipa²⁻ ligands, to form the centrosymmetric 3D porous network with 1D channels along the *c* direction, in which the shortest interchain Co...Co distance is 7.26 Å (Figure 2c). The channels occupy 34.9% of the total volume of **2** and are filled with guest *i*PrOH and water molecules.

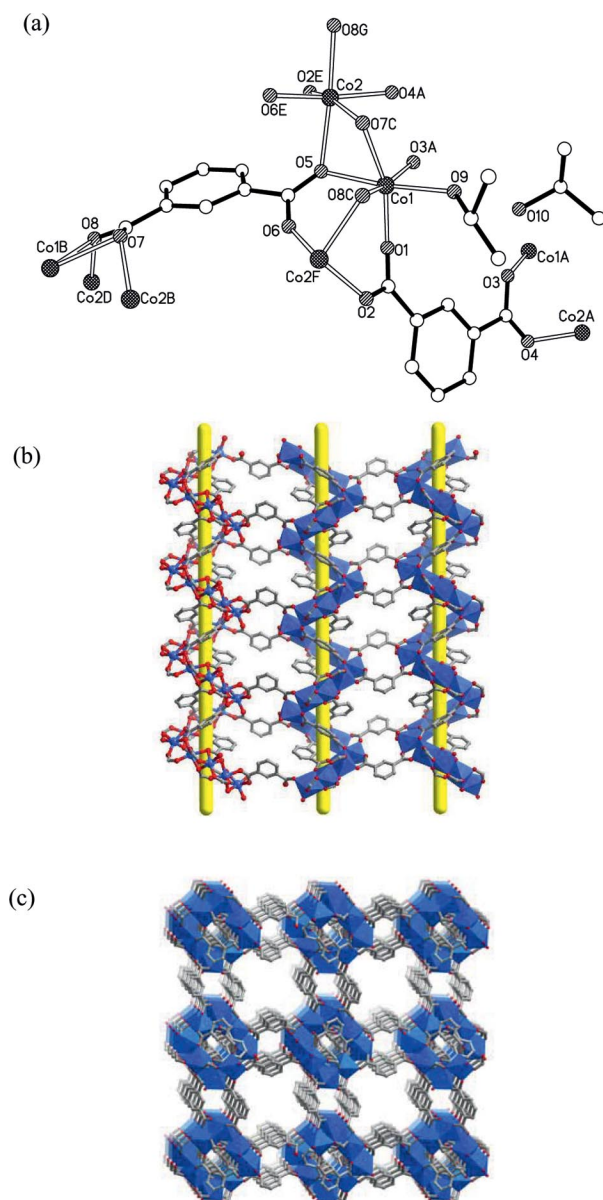


Figure 2. Coordination environments of the Co^{II} atoms and the coordination modes of the ipa²⁻ ligands (a), the 4_1 helical chains viewed down the *b* axis (b), and the 3D network viewed along the *c* axis (c) of **2**. Symmetry codes: A) $3/2 - x, 3/2 - y, -1/2 - z$; B) $3/2 - x, 2 - y, -1/2 + z$; C) $3/2 - x, 2 - y, 1/2 + z$; D) $7/4 - y, 1/4 + x, -3/4 + z$; E) $7/4 - y, 1/4 + x, 1/4 + z$; F) $-1/4 + y, 7/4 - x, -1/4 + z$; G) $-1/4 + y, 7/4 - x, 3/4 + z$.

Thermal Stability

Thermogravimetric analysis of **1** (Figure S1) shows a complete loss of water molecules and almost no further

weight loss between 100 and 410 °C, which indicates that the framework is stable in this region. Then there is an abrupt decrease indicating the collapse of the framework. However, powder X-ray diffraction (PXRD) analysis of **1** reveals that the framework was not intact after removal of the guest molecules, and the single crystals became amorphous after being crushed, even at room temperature (Figure S2). After five hours under vacuum at room temperature to remove the guest molecules, gas sorption studies on **1** showed that it had no distinct N₂ sorption. Compound **2** turns amorphous soon after abrasion, and no peak was observed in its PXRD pattern. Therefore, the PXRD data were obtained with crushed crystals in the solvents (Figures S3 and S4).

Magnetic Properties of **1**

The dc susceptibility data of a polycrystalline sample of **1** was measured with a Quantum Design MPMS-XL7 SQUID magnetometer (Figure 3). The value of $\chi_M T$ per Co₆ unit at 300 K is 17.0 cm³ mol⁻¹ K for **1**, and the effective magnetic moment μ_{eff} is 11.66 μ_B , being slightly higher than the spin-only value, which results from the orbital contribution and the different coordination numbers of Co^{II} ions. As the temperature decreases, the $\chi_M T$ of **1** decreases smoothly with a small lift at about 6 K and finally drops rapidly up to 2 K. Between 100 and 300 K, the magnetic susceptibility data of **1** obey the Curie–Weiss law with Curie constant $C = 18.5 \text{ cm}^3 \text{ K mol}^{-1}$ and Weiss constant $\theta = -58.1 \text{ K}$ for one Co₆ unit. The C value corresponds to $g = 2.56$ for $S = 3/2$, which is normal for an octahedral Co^{II}, and the large negative value of the Weiss constant confirms that the dominant exchange between Co^{II} ions in **1** is anti-ferromagnetic. This behavior is consistent with the larger angle of Co–O–Co in the Co₆ unit (Table S1).

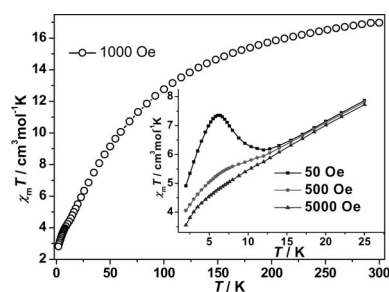


Figure 3. The temperature-dependent magnetic susceptibility of **1**. Inset: field-cooled magnetizations.

Field-cooled (FC) magnetizations of **1** were measured under different applied fields to further investigate the magnetic behavior at low temperature. The magnetic behavior is quite field-dependent, in which the rises of the $\chi_M T$ values at low temperature become less pronounced at higher fields [Figure 3 (inset)]. This is an important feature of spin-canting behavior, which is in accord with the triangular geometry.^[19] Moreover, the FC and zero-field-cooled (ZFC) magnetization measurements were also performed for **1** at 20 Oe in the 2–25 K range (Figure S5 inset). The FC curve of **1**

shows an abrupt increase with decreasing temperature, while the ZFC curve exhibits a rounded maximum at approximately 6 K and then also increases fast upon cooling below $T = 4$ K. The FC and ZFC data are divergent below the critical temperature $T_c = 10$ K, which indicates a possible transition from a paramagnetic state to a long-range ordered state. To confirm this phase transition, the temperature dependence of real (χ') and imaginary (χ'') parts of the ac susceptibility of **1** was then measured in an ac driving field of 3 Oe at different frequencies (Figure S5). The peaks are both observed in the real part (χ') and the imaginary part (χ'') at about 6 K, which confirms that the phase transition occurred at low temperature. The intensity of the peak in χ' is slightly changed with different frequencies, while no change is observed in either the intensity or the position of the peak in χ'' . It must be noted that the signals of ac data are all very weak, indicating that the appearance of long-range order in **1**, to a certain extent, should be attributed to guest molecules with weak magnetic exchange. Finally, the field-dependence of magnetization of **1** was studied at 2 K (Figure S6). The magnetization value at the highest field investigated (7 T) is $4.45 N\beta$, which is far below the saturation value for antiferromagnetic exchange. No hysteresis loop was observed, which also shows the counterfeit long-range order induced by guest molecules. There are two similar Co_6 clusters composed of two $\{\text{Co}_3(\mu_3\text{-OH})\}$ triangles, which were reported to show similar magnetic behavior.^[20]

Magnetic Properties of **2**

The temperature dependence of $\chi_M T$ for **2** at an applied field of 1 kOe is shown in Figure 4. At room temperature, the χT value of **2** is $6.89 \text{ cm}^3 \text{ mol}^{-1} \text{ K}$ per Co^{II}_2 unit, which is much higher than the spin-only value, similar to **1**, which results from the orbital contribution of the octahedral Co^{II} ions. Between 100 and 300 K, **2** obeys the Curie–Weiss law with a θ value of -32 K, which confirms the dominant exchange to be antiferromagnetic. By ignoring the magnetic exchange of phenyl ring, the magnetic topology of **2** can be simplified to a Δ chain with triangular geometry (Figure 4, left). In this triangular geometry, J1 represents two single O bridges and one *syn-syn* carboxylate bridge from three ipa²⁻ ligands, J2 stands for one single oxygen atom of carboxylate group and two *syn-syn* carboxylate bridges, while J3 represents one *syn-anti* and one *anti-anti* carboxylate bridge. The antiferromagnetic interactions and triangular geometry in the Δ chain leads to a complicated magnetic behavior for the competitive effect in **2**.^[21]

The χT value decreases slowly upon cooling down, then abruptly increases at about 10 K to a maximum at about 3 K before decreasing again. This ferrimagnetic-like behavior is consistent with reported compounds having similar Δ -chain magnetic topology.^[21] Moreover, the χT value is also quite field-dependent at low temperatures, it is larger at smaller field and almost does not increase at 10 kOe at low temperature (Figure 4 inset).

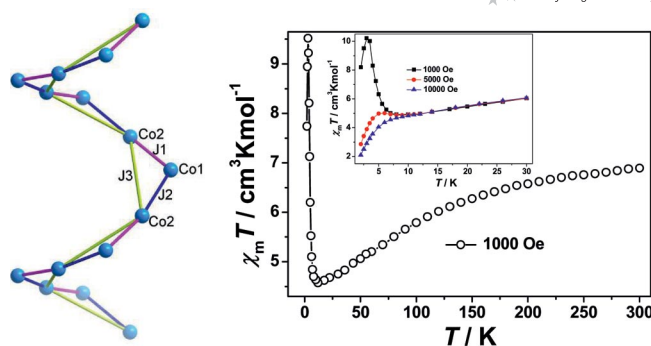


Figure 4. The magnetic topology (left) and temperature-dependent magnetic susceptibility (right) of **2**. Inset: field-cooled magnetization.

For **2**, a confined hysteresis loop is observed at 2 K (Figure S7), giving a coercive field of approximately 30 Oe and a remnant magnetization of $0.04 N\beta$. The magnetization at 70 kOe is $3.29 N\beta$ for the formula Co_2 unit, suggesting a complicated ground-state spin configuration. In the ac susceptibility data of **2**, the obvious frequency-dependent behavior is observed (Figure S8). The shift of peak temperature (T_p) of χ' was measured by a parameter f ($f = \Delta T_p / [T_p \Delta(\log f)] = 0.07$), which is in the range of the spin glass.^[22] The slow magnetic relaxation in high-dimensional compounds comprising ferro- or ferrimagnetic chains has attracted much attention in recent years for SCM behavior. However, the Arrhenius law is not appropriate for this slow magnetic relaxation of **2**, which excludes the possibility of SCM behavior. The confined hysteresis loop and spin glass behavior confirm the weak ordering phenomenon and should be attributed to the interactions of guest molecules.^[22]

Conclusions

By changing the solvents, two new 3D compounds featuring carboxylate-bridged Co^{II} clusters/chains have been synthesized by solvothermal reactions from the same starting materials. With absolute methanol as solvent, a cluster-based compound with Co_6 units as connectors and ipa²⁻ ligands as linkers was obtained, which shows a 3D porous NaCl topology and spin-canting magnetic behavior. With *i*PrOH instead of methanol as solvent, a new and completely different compound is obtained, which comprises Co^{II} 4₁-helical chains with Δ -chain magnetic topology as connectors and shows ferrimagnetic-like behavior. These two compounds are successful attempts for modulating structures by changing the reaction conditions and are good examples for magnetic studies on clusters/chains in higher dimensional systems. Moreover, the 4₁ helix and Δ -chain topology are both scarce in molecular magnets.

Experimental Section

Materials and Physical Measurements: All solvents and starting materials for synthesis were purchased commercially and were used

as received. X-ray powder diffraction (XRPD) patterns were recorded with a Bruker D8 Advance diffractometer. FTIR (KBr) spectra were recorded from KBr pellets in the range 400–4000 cm^{-1} with a Bruker TENSOR 27 FTIR spectrometer. Elemental analysis (C, H, N) was performed with a Perkin–Elmer 240 elemental analyzer. Both ac and dc magnetic data were collected by using a Quantum Design MPMS XL-7-SQUID magnetometer on phase-pure samples from slightly crushed single crystals in the solvents. The polycrystalline samples of these compounds were embedded in grease to avoid any field-induced crystal reorientation. The magnetic data were corrected for the diamagnetic contribution calculated from Pascal constants.

[Co₆(μ₃-OH)₂(ipa)₅(H₂O)₅·8H₂O (1): Solvothermal reaction of a mixture of Co(OAc)₂·5H₂O (0.060 g, 0.25 mmol), H₂ipa (0.066 g, 0.40 mmol), and methanol (5 mL) in a 10 mL Teflon-lined bomb at 160 °C for 3 d afforded red block crystals of **1** (yield ca. 65%). Compound **1** can be also obtained with adding LiOH (0.023 g, 1.0 mmol) in the above reaction system. C₄₀H₄₈Co₆O₃₅ (1442.36): C 33.31, H 3.35; found C 33.36, H 3.38. FTIR (KBr): $\tilde{\nu}$ = 3410 (m), 1610 (s), 1546 (m), 1481 (m), 1386 (s), 1078 (w), 747 (m), 715 (m) cm^{-1} .

[Co₂(ipa)₂(iPrOH)_{0.5}(H₂O)_{0.5}·(iPrOH)_{0.5}(H₂O) (2): Solvothermal reaction of a mixture of Co(OAc)₂·5H₂O (0.060 g, 0.25 mmol), H₂ipa (0.066 g, 0.40 mmol), and 2-propanol (5 mL) in a 10 mL Teflon-lined bomb at 160 °C for 3 d afforded red prismatic crystals of **2** (yield ca. 61%). Compound **2** can be also obtained with adding LiOH (0.023 g, 1.0 mmol) in the above reaction system. C₁₉H₁₉Co₂O_{10.5} (533.21): C 42.80, H 3.59; found C 42.92, H 3.64. FTIR (KBr): $\tilde{\nu}$ = 3392 (m), 1611 (s), 1551 (s), 1482 (m), 1387 (vs), 1163 (w), 1078 (w), 742 (s), 715 (m), 445 (w) cm^{-1} .

Crystallographic Data Collection and Refinement: Single-crystal X-ray diffraction measurements of **1** and **2** were carried out with a Bruker Smart APEX CCD area-detector diffractometer (Mo- K_{α} , 0.71073 Å) at 293(2) K. Absorption corrections were applied by using the multiscan program SADABS^[23]. The structures were solved with direct methods and refined with the full-matrix least-squares technique with the SHELXTL program package.^[24] All non-hydrogen atoms, except those of the highly disordered guest water molecules, were refined with anisotropic displacement parameters. The organic hydrogen atoms were generated geometrically (C–H 0.96 Å), and the hydrogen atoms of coordinated water

molecules were located from the difference Fourier map. Because the lattice water molecules are highly disordered, only part of them were located and included in the final stage of refinement without their hydrogen atoms. Crystal data and details of data collection and refinement for **1** and **2** are summarized in Table 1. The selected bond lengths and bond angles of **1** and **2** are listed in Table S1. CCDC-764887 and -764888 contain the supplementary crystallographic data for this paper. These data can be obtained free of charge from the Cambridge Crystallographic Data Centre via www.ccdc.cam.ac.uk/datarequest/cif.

Supporting Information (see footnote on the first page of this article): TGA, simulated and experimental PXRD patterns, selected bond lengths and bond angles, and additional magnetic data.

Acknowledgments

We gratefully acknowledge financial support from the National Natural Science Foundation of China (NSFC) (Grant Nos. 20821001, 90922031, and 50902151), the “973 Project” (Grant No. 2007CB815302), and Sun Yat-Sen University (Grant 2008050401131085).

Table 1. Crystal data and details of data collections and refinement for **1** and **2**.

	1	2
Formula	C ₄₀ H ₄₈ Co ₆ O ₃₅	C ₁₉ H ₁₉ Co ₂ O _{10.5}
F.w.	1442.36	533.21
T / K	293(2)	293(2)
Space group	P2 ₁ /2 ₁ 2 (No. 18)	I4 ₁ /a (No. 88)
a / Å	21.024(2)	30.530(2)
b / Å	28.741(3)	30.530(2)
c / Å	10.8969(12)	11.2072(9)
V / Å ³	6584.3(12)	10446.3(14)
Z	4	16
D _c / g cm ⁻³	1.455	1.356
μ / mm ⁻¹	1.561	1.316
Data collected/unique	33954/12721	5105/4446
R ₁ (>2σ/all data) ^[a]	0.0751/0.0926	0.0439/0.0503
wR ₂ (>2σ/all data)	0.2174/0.2338	0.1268/0.1317
GOF	1.061	1.040
Residues / e Å ⁻³	−0.613/1.339	−0.419/0.703

[a] $R_1 = \sum |F_o| - |F_c| / \sum |F_o|$, $wR_2 = [\sum w(F_o^2 - F_c^2)^2 / \sum w(F_o^2)^2]^{1/2}$.

- a) M. Eddaoudi, J. Kim, J. B. Wachter, H. K. Chae, M. O’Keeffe, O. M. Yaghi, *J. Am. Chem. Soc.* **2001**, *123*, 4368–4369; b) M. Eddaoudi, J. Kim, M. O’Keeffe, O. M. Yaghi, *J. Am. Chem. Soc.* **2002**, *124*, 376–377; c) A. Thirumurugan, S. Natarajan, *Cryst. Growth Des.* **2006**, *6*, 983–988.
- a) R. Murugavel, M. G. Walawalkar, M. Dan, H. W. Roesky, C. N. R. Rao, *Acc. Chem. Res.* **2004**, *37*, 763–774; b) M. Kurmoo, *Chem. Soc. Rev.* **2009**, *38*, 1353–1379.
- a) S. K. Ghosh, S. Bureekaew, S. Kitagawa, *Angew. Chem. Int. Ed.* **2008**, *47*, 3403–3406; b) J. S. Seo, D. Whang, H. Lee, S. I. Jun, J. Oh, Y. J. Jeon, K. Kim, *Nature* **2000**, *404*, 982–986; c) Q.-R. Fang, G.-S. Zhu, Z. Jin, M. Xue, X. Wei, D.-J. Wang, S.-L. Qiu, *Angew. Chem. Int. Ed.* **2006**, *45*, 6126–6130.
- a) R. Sessoli, H. L. Tsai, A. R. Schake, S. Y. Wang, J. B. Vincent, K. Folting, D. Gatteschi, G. Christou, D. N. Hendrickson, *J. Am. Chem. Soc.* **1993**, *115*, 1804–1816; b) R. Sessoli, D. Gatteschi, A. Caneschi, M. A. Novak, *Nature* **1993**, *365*, 141–143; c) A. Caneschi, D. Gatteschi, N. Laloti, C. Sangregorio, R. Sessoli, G. Venturi, A. Vindigni, A. Rettori, M. G. Pini, M. A. Novak, *Angew. Chem. Int. Ed.* **2001**, *40*, 1760–1763; d) T.-F. Liu, D. Fu, S. Gao, Y.-Z. Zhang, H.-L. Sun, G. Su, Y.-J. Liu, *J. Am. Chem. Soc.* **2003**, *125*, 13976–13977; e) S. Wang, J.-L. Zuo, S. Gao, H.-C. Zhou, Y.-Z. Zhang, X.-Z. You, *J. Am. Chem. Soc.* **2004**, *126*, 8900–8901.
- a) R. Clérac, H. Miyasaka, M. Yamashita, C. Coulon, *J. Am. Chem. Soc.* **2002**, *124*, 12837–12844; b) H. Miyasaka, K. Nakata, K.-i. Sugiura, M. Yamashita, R. Clérac, *Angew. Chem. Int. Ed.* **2004**, *43*, 707–711; c) H. Miyasaka, K. Nakata, L. Lecren, C. Coulon, Y. Nakazawa, T. Fujisaki, K.-i. Sugiura, M. Yamashita, R. Clérac, *J. Am. Chem. Soc.* **2006**, *128*, 3770–3783; d) H. Miyasaka, M. Yamashita, *Dalton Trans.* **2007**, 399–406; e) O. Roubeau, R. Clérac, *Eur. J. Inorg. Chem.* **2008**, 4325–4342.
- a) M. Murugesu, R. Clérac, W. Wernsdorfer, C. E. Anson, A. K. Powell, *Angew. Chem. Int. Ed.* **2005**, *44*, 6678–6682; b) E. E. Moushi, T. C. Stamatatos, W. Wernsdorfer, V. Nastopoulos, G. Christou, A. J. Tasiopoulos, *Angew. Chem. Int. Ed.* **2006**, *45*, 7722–7725.
- a) Y.-Z. Zheng, M.-L. Tong, W.-X. Zhang, X.-M. Chen, *Angew. Chem. Int. Ed.* **2006**, *45*, 6310–6314; b) Y.-Z. Zheng, W. Xue, M.-L. Tong, X.-M. Chen, F. Grandjean, G. J. Long, *Inorg. Chem.* **2008**, *47*, 4077–4087.
- a) D. Maspoch, D. Ruiz-Molina, J. Veciana, *J. Mater. Chem.* **2004**, *14*, 2713–2723, and references cited therein; b) D. Maspoch, D. Ruiz-Molina, K. Wurst, N. Domingo, M. Cavallini,

- F. Biscarini, J. Tejada, C. Rovira, J. Veciana, *Nat. Mater.* **2003**, 2, 190–195; c) C. J. Kepert, *Chem. Commun.* **2006**, 695–700.
- [9] a) S. S.-Y. Chui, S. M.-F. Lo, J. P. H. Charmant, A. G. Orpen, I. D. Williams, *Science* **1999**, 283, 1148–1150; b) X. X. Zhang, S. S.-Y. Chui, I. D. Williams, *J. Appl. Phys.* **2000**, 87, 6007.
- [10] a) B. Moulton, J. Lu, R. Hajndl, S. Hariharan, M. J. Zaworotko, *Angew. Chem. Int. Ed.* **2002**, 41, 2821–2824; b) S. A. Bourne, J. Lu, A. Mondal, B. Moulton, M. J. Zaworotko, *Angew. Chem. Int. Ed.* **2001**, 40, 2111–2113.
- [11] a) G. J. Halder, C. J. Kepert, B. Moubaraki, K. S. Murray, J. D. Cashion, *Science* **2002**, 298, 1762–1765; b) M. Kurmoo, H. Kumagai, K. W. Chapman, C. J. Kepert, *Chem. Commun.* **2005**, 3012–3014; c) A. Rujiwatra, C. J. Kepert, J. B. Claridge, M. J. Rosseinsky, H. Kumagai, M. Kurmoo, *J. Am. Chem. Soc.* **2001**, 123, 10584–10594; d) M. Kurmoo, H. Kumagai, M. Akita-Tanaka, K. Inoue, S. Takagi, *Inorg. Chem.* **2006**, 45, 1627–1637; e) Z.-M. Wang, B. Zhang, H. Fujiwara, H. Kobayashi, M. Kurmoo, *Chem. Commun.* **2004**, 416–417.
- [12] a) C. Serre, F. Millage, C. Thouvenot, M. Noguès, G. Marsolier, D. Louër, G. Férey, *J. Am. Chem. Soc.* **2002**, 124, 13519–13526; b) K. Barthelet, J. Marrot, D. Riou, G. Férey, *Angew. Chem. Int. Ed.* **2002**, 41, 281–284.
- [13] a) X.-L. Wang, C. Qin, E.-B. Wang, Z.-M. Su, *Chem. Eur. J.* **2006**, 12, 2680–2691; b) D.-X. Hu, F. Luo, Y.-X. Che, J.-M. Zheng, *Cryst. Growth Des.* **2007**, 7, 1733–1737; c) Y.-F. Han, X.-H. Zhou, Y.-X. Zheng, Z. Shen, Y. Song, X.-Z. You, *CrystEngComm* **2008**, 10, 1237–1242; d) Q. Sun, Q. Yue, J.-Y. Zhang, L. Wang, X. Li, E.-Q. Gao, *Cryst. Growth Des.* **2009**, 9, 2310–2317; e) F. Luo, Y.-X. Che, J.-M. Zheng, *Cryst. Growth Des.* **2009**, 9, 1066–1071.
- [14] a) C.-B. Ma, C.-N. Chen, Q.-T. Liu, D.-Z. Liao, L.-C. Li, *Eur. J. Inorg. Chem.* **2008**, 1865–1870; b) F. Luo, S. R. Batten, Y.-X. Che, J.-M. Zheng, *Chem. Eur. J.* **2007**, 13, 4948–4955; c) P. Mahata, K. V. Ramya, S. Natarajan, *Dalton Trans.* **2007**, 4017–4026; d) X. Shi, G.-S. Zhu, X.-H. Wang, G.-H. Li, Q.-R. Fang, X.-J. Zhao, G. Wu, G. Tian, M. Xue, R.-W. Wang, S.-L. Qiu, *Cryst. Growth Des.* **2005**, 5, 341–346; e) X.-M. Chen, G.-F. Liu, *Chem. Eur. J.* **2002**, 8, 4811–4817.
- [15] X.-N. Cheng, W.-X. Zhang, Y.-Y. Lin, Y.-Z. Zheng, X.-M. Chen, *Adv. Mater.* **2007**, 19, 1494–1498.
- [16] a) Z.-G. Guo, R. Cao, X.-J. Li, D.-Q. Yuan, W.-H. Bi, X.-D. Zhu, Y.-F. Li, *Eur. J. Inorg. Chem.* **2007**, 742–748; b) X.-H. Bu, Y.-B. Xie, J.-R. Li, R.-H. Zhang, *Inorg. Chem.* **2003**, 42, 7422–7430; c) X.-R. Meng, Y.-L. Song, H.-W. Hou, H.-Y. Han, B. Xiao, Y.-T. Fan, Y. Zhu, *Inorg. Chem.* **2004**, 43, 3528–3536; d) M. Du, X.-H. Bu, Y.-M. Guo, H. Liu, *Inorg. Chem.* **2002**, 41, 4904–4908; e) L.-F. Ma, L.-Y. Wang, Y.-Y. Wang, M. Du, J.-G. Wang, *CrystEngComm* **2009**, 11, 109–117.
- [17] a) C. Livage, N. Guillo, J. Chaigneau, P. Rabu, M. Drillon, G. Férey, *Angew. Chem. Int. Ed.* **2005**, 44, 6488–6491; b) J.-P. Zhang, S. K. Ghosh, J.-B. Lin, S. Kitagawa, *Inorg. Chem.* **2009**, 48, 7970–7976.
- [18] L. Han, M.-C. Hong, *Inorg. Chem. Commun.* **2005**, 8, 406–419.
- [19] a) X.-Y. Wang, H.-Y. Wei, Z.-M. Wang, Z.-D. Chen, S. Gao, *Inorg. Chem.* **2005**, 44, 572–583; b) J. L. Manson, C. R. Kmetz, F. Palacio, A. J. Epstein, J. S. Miller, *Chem. Mater.* **2001**, 13, 1068–1073; c) A. Escuer, J. Cano, M. A. S. Goher, Y. Journaux, F. Lloret, F. A. Mautner, R. Vicente, *Inorg. Chem.* **2000**, 39, 4688–4695; d) L. Cheng, W.-X. Zhang, B.-H. Ye, J.-B. Lin, X.-M. Chen, *Eur. J. Inorg. Chem.* **2007**, 2668–2676.
- [20] a) H. Kumagai, Y. Oka, S. Kawata, M. Ohba, K. Inoue, M. Kurmoo, H. Okawa, *Polyhedron* **2003**, 22, 1917–1920; b) X.-Y. Wang, S. C. Sevov, *Inorg. Chem.* **2008**, 47, 1037–1043.
- [21] a) X.-N. Cheng, W.-X. Zhang, Y.-Z. Zheng, X.-M. Chen, *Chem. Commun.* **2006**, 3603–3609; b) S. O. H. Gutschke, D. J. Price, A. K. Powell, P. T. Wood, *Angew. Chem. Int. Ed.* **2001**, 40, 1920–1923; c) X.-J. Li, X.-Y. Wang, S. Gao, R. Cao, *Inorg. Chem.* **2006**, 45, 1508–1516.
- [22] J. A. Mydosh, *Spin Glasses: An Experimental Introduction*, Taylor & Francis, London, **1993**.
- [23] G. M. Sheldrick, *SADABS v.2.01*, Bruker/Siemens Area Detector Absorption Correction Program, Bruker AXS, Madison, WI, USA, **1998**.
- [24] *SHELXTL 6.0*, Bruker Analytical Instrumentation, Madison, Wisconsin, USA, **2000**.

Received: February 6, 2010
Published Online: June 24, 2010

Cobalt(II) Coordination Polymers Containing *trans*-1,2-Bis(4-pyridyl)ethene and Their Magnetic Properties

Abdul Malik Puthan Peedikakkal,^[a] Yu-Mei Song,^[b] Ren-Gen Xiong,^[b] Song Gao,^[c] and Jagadese J. Vittal^{*[a]}

Keywords: Cobalt / Metal–organic frameworks / Bridging ligands / Magnetic properties / Anions

Reaction of the Co^{II} ion and the bpe [*trans*-1,2-bis(4-pyridyl)ethene] ligand in the presence of the CH₃CO₂[−], CF₃CO₂[−], C₆H₅CO₂[−] and NO₃[−] anions affords six coordination polymers, namely [Co₂(μ-bpe)₂(μ-O₂CCH₃)₂(O₂CCH₃)₂]·H₂O (**1**), [Co₂(μ-bpe)₂(μ-O₂CCF₃)₂(O₂CCH₃)₂] (**2**), [Co(μ-bpe)₂(O₂CCF₃)₂] (**3**), [Co(μ-bpe)(O₂CC₆H₅)₂(HO{O}CC₆H₅)₂] (**4**), [Co(μ-bpe)(O₂CC₆H₅)₂(CH₃OH)₂] (**5**) and [Co₂(μ-bpe)₃(NO₃)₃·(CH₃OH)](NO₃) (**6**). All the compounds have been characterized by X-ray crystallography, IR spectroscopy and thermogravimetry. Variable-temperature magnetic measurements were also performed on **3** and **6**. Compounds **1** and **2** form 1D molecular ladder coordination polymers bridged by acetate ligands. Replacing the acetate ligands completely by

trifluoroacetate ligands produced interpenetrated square-grid sheets in **3**. Replacing acetate and trifluoroacetate ligands by benzoate ligands resulted in two 1D coordination polymers, **4** and **5**, having zigzag and linear structures, respectively. When the nitrate anion was used, a 3D network, **6**, was afforded with inclined interpenetration of a 1D molecular ladder structure with threefold polycatenation. The variation of anions, reaction conditions and the ratio of reactants profoundly affect the final topological structure of the coordination polymers synthesized. The trifluoroacetate and nitrate anions influence the topology and the degree of interpenetration in the coordination polymers **3** and **6**, respectively.

Introduction

Coordination polymers are rapidly emerging solid-state materials that provide boundless opportunity for designed chemical and physical properties.^[1] The physical properties of these materials mostly depend on the topology of the overall structure of the frameworks.^[1–2] The topology of these highly crystalline materials is constructed from self-assembly of metal ions or metal clusters with organic ligands through coordination bonds to form one-, two- and three-dimensional structures. Depending on the properties of metal cations, the binding strength and directionality of ligands, and the reaction conditions, coordination polymers exhibit a wide variety of topologies.^[1a,2a] The connectivity of the ligands, various intermolecular interactions and anions also play a major role on the topology of the frameworks.^[1–3] Because of their diverse coordination modes and bridging ability, polycarboxylates have been widely used in the construction of coordination polymers.^[1c] Two-connect-

ing linear bifunctional spacers are the most commonly used nitrogen-based ligands for the construction of cationic frameworks. The stability of the coordination polymers containing nitrogen-based ligands can be improved by introducing carboxylate ligands. For example, ligands containing both pyridyl and carboxyl functional groups have been successfully used for the construction of various coordination polymers.^[1a,1b,4] Furthermore, several coordination polymers have been designed and synthesized from more than one bridging ligand.^[1a,1b,5,6] In these cases, controlling the reaction may be more challenging, since the spacers can interfere with the reaction that affords various topologies and obviate the desired network. Monocarboxylate ligands with pyridyl donors can be used to vary the topology of the frameworks. Owing to their bridging ability, acetate and trifluoroacetate have been efficiently utilized to orient the C=C bonds of *trans*-1,2-bis(4-pyridyl)ethene (bpe) ligands in ladder coordination polymers for photodimerization reactions.^[7]

In this report, we describe the formation of six coordination polymers, of which two are molecular ladders: [Co₂(μ-bpe)₂(μ-O₂CCH₃)₂(O₂CCH₃)₂]·H₂O (**1**), [Co₂(μ-bpe)₂(μ-O₂CCH₃)₂(O₂CCF₃)₂] (**2**). Replacing all the acetate ligands by trifluoroacetate ligands produced interpenetrated square-grid sheets [Co(μ-bpe)₂(O₂CCF₃)₂] (**3**). Replacing acetate and trifluoroacetate by benzoate ligands resulted in two 1D coordination polymers, [Co(μ-bpe)(O₂CC₆H₅)₂(HO{O}CC₆H₅)₂] (**4**), having zigzag structure, and [Co(μ-

[a] Department of Chemistry, National University of Singapore, 3 Science Drive 3, Singapore 117543, Singapore
Fax: +65-6779-1691
E-mail: chmjv@nus.edu.sg

[b] Ordered Matter Science Research Center, Southeast University, Nanjing, Jiangsu 211189, P. R. China

[c] Beijing National Laboratory for Molecular Sciences, College of Chemistry and Molecular Engineering, Peking University, Beijing 100871, P. R. China

Supporting information for this article is available on the WWW under <http://dx.doi.org/10.1002/ejic.201000375>.

bpe)(O₂CC₆H₅)₂(CH₃OH)₂] (**5**), having linear conformation. Changing the anion to nitrate resulted in [Co₂(μ-bpe)₃-(NO₃)₃(CH₃OH)](NO₃) (**6**), having inclined interpenetration of 1D molecular ladder structures with threefold polycatenation. The above-mentioned solid-state structures indicate that the anions have a profound effect in forming the different topological networks. The magnetic properties of interpenetrated networks of **3** and **6** have been investigated.

Results and Discussion

Reactivity of the Co^{II} Metal Ion towards the bpe Spacer Ligand

Coordination polymers **1** to **6** were prepared either under different reaction conditions or by using different molar ratios. Such influence of the experimental conditions and stoichiometric ratios on the formation of products has been very well explored in the literature.^[1a,2a,3] Previously, a number of zinc(II) coordination polymers were synthesized in our lab in this way.^[7] The composition and the solid-state structures of these reported compounds indicate the influence of crystallization conditions and molar ratios of the reactants in their formation. In this work, we tried to prepare similar coordination polymers of the cobalt(II) ion but observed different types of products.

Rodlike pink crystals of **1** were formed in two days by layering a methanol solution of bpe over an aqueous solution of Co(OAc)₂·4H₂O in 1:1 molar ratio. Solvothermal reaction of bpe, HTFA and Co(OAc)₂·4H₂O in 1:1:1 ratio in MeOH/H₂O (1:4 v/v) at 90 °C afforded dark pinkish rodlike crystals of **2** after three days. On the other hand, solvothermal reaction of Co(OAc)₂·4H₂O, bpe and HTFA in 1:2:2 ratio in MeOH at 90 °C yielded golden yellow blocklike crystals of **3** in two days. The XRPD patterns (Figure S1 in the Supporting Information) of the crystalline solids suggest that formation of **3** is more prominent than that of **2** from the reaction of Co(OAc)₂·4H₂O, bpe and HTFA under various crystallization conditions and at various molar ratios. Solvothermal reaction (MeOH, 90 °C) and slow evaporation (DMF) with a 1:2:2 molar ratio of the reactants have been found to be the best method for synthesizing **3**. However, a single phase of **2** was obtained from the solvothermal (MeOH/H₂O, 90 °C) reaction with 1:1:1 ratio. A solvothermal reaction of Co(OAc)₂·4H₂O, bpe and benzoic acid in a ratio of 1:1:2 in methanol produced rodlike yellowish-orange crystals of **4**. However, orange-red blocklike crystals of **5** were obtained by layering a methanol solution of bpe over a mixture of Co(OAc)₂·4H₂O and benzoic acid in MeOH/H₂O (1:2, v/v) in the same ratio.

The nature of the anions greatly influences the crystal growth and the resultant coordination polymers.^[8–9] To distinguish the effect of monocarboxylates in the above reaction from that of other anions, a reaction of Co(NO₃)₆·6H₂O with bpe was conducted. The solvothermal reaction of Co(NO₃)₆·6H₂O and bpe in a ratio range of 1:1–2 in MeOH at 90 °C produced tetragonal pink crystals of **6**. [Co₂-

(bpethy)₃(NO₃)₄]·MeOH, which has a similar topological structure, was prepared by zur Loye and co-workers by using bpethy [bpethy = 1,2-bis(4-pyridyl)ethyne].^[10] They found that this compound could also be formed irrespective of the ratios of the starting materials in MeOH/CH₃CN. Carlucci et al. reported two compounds, [M₂(bpethy)₃-(NO₃)₄] (M = Zn^{II} and Co^{II}) with similar topology^[11a] by diffusion of an acetone/ethanol solvent system. The cobalt(II) compound reported by these authors is the pseudomorph of the compound reported by zur Loye and co-workers. In both compounds, the nitrate ions are coordinated to the metal centre. However in **6**, one of the nitrate ions is noncoordinated, and a methanol is coordinated instead.

Molecular Ladder Structures of [Co₂(μ-bpe)₂(μ-O₂CCH₃)₂-(O₂CCH₃)₂]·H₂O (**1**) and [Co₂(μ-bpe)₂(μ-O₂CCF₃)₂-(O₂CCH₃)₂] (**2**)

A perspective view of a portion of the 1D polymer **1** is given in Figure 1a. A 1D molecular ladder polymer formed from two infinite linear polymers of [Co(μ-bpe)]_n are bridged by two acetate ligands. The bond angles around highly distorted octahedral geometry vary between approximately 87 and 95°. Two N pyridyl atoms occupy the axial positions [Co1–N1 2.161(2) Å and Co1–N2^a 2.150(3) Å], and four O atoms from acetate equatorially. Two acetate ligands bridged (η²) symmetrically between two Co^{II} ions act as the rungs [Co1–O3 2.005(3) Å and Co1–O4 2.022(3) Å] and generate an eight-membered ring (Co···Co distance: 4.003 Å). A crystallographic twofold axis exists at the centre of this ring. 1D ladder coordination polymers run along the [101] axis. This causes the C=C bonds in the

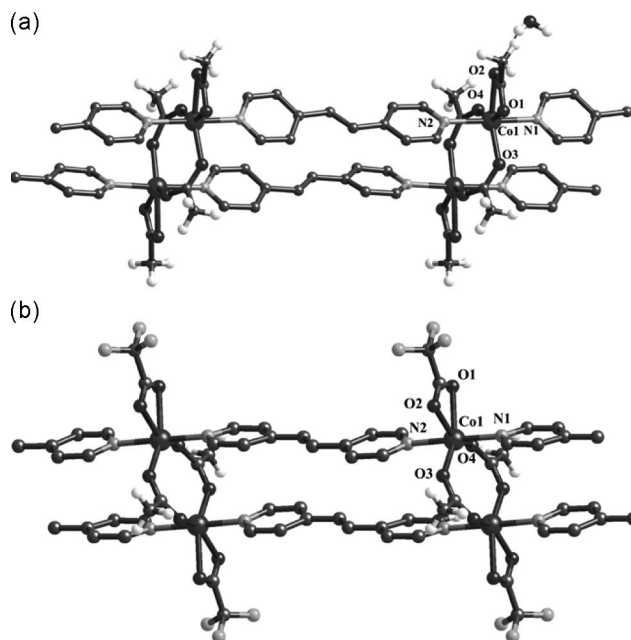


Figure 1. Perspective views of the 1D molecular ladder polymeric structures of (a) **1** and (b) **2**.

bpe pairs to be aligned in antiparallel fashion, but the closest nonbonded distance between the centre of C=C bonds is 3.865 Å. Although the pyridyl pairs are tilted by 18.9°, strong $\pi\cdots\pi$ interactions between the pyridyl pairs are indicated by distances of 3.916 Å. There is a water molecule present in the lattice, which is strongly hydrogen-bonded to O2 [O–H \cdots O, 2.193(3) Å].

The structure of **2** (Figure 1b) is very similar to that of **1**, except that the C=C bonds in the bpe pairs of the ladder structure are aligned in a parallel fashion with a gap of 3.765 Å. The pyridyl ligands are also aligned parallel with tilt angle of 7°, a nonbonding distance of 3.838 Å indicating strong $\pi\cdots\pi$ interaction. In this structure, the crystallographic inversion centres pass through the centres of the Co₂(OAc)₂ ring and bpe pairs. The 1D chains are propagated along the [01 $\bar{1}$] direction.

Although the C=C bonds are likely to undergo [2+2] cycloaddition reactions, redox properties of the transition metal ions are known to suppress such photochemical reactions, and hence such a reaction was not attempted. It is worth noting that, in most of the ladder structures studied so far, the bpe pairs have been aligned in a parallel fashion.^[12] However, **1** exhibits an unusual structure.

Twofold Interpenetrated (4,4) Sheet Structure of [Co(μ -bpe)₂(O₂CCF₃)₂] (**3**)

The crystal structure of **3** reveals that the octahedral Co^{II} metal centre is strongly coordinated to four N atoms of the bpe molecules, forming a square plane [Co1–N1 2.128(2) Å and Co1–N2 2.155(2) Å]. The oxygen atoms of two trifluoroacetate anions complete the octahedral geometry by occupying the axial positions [Co1–O1 2.089(2) Å]. Figure 2a shows the coordination environment of Co^{II} in **3**, which possesses twofold crystallographic symmetry. The crystallographic inversion present in the middle of the C=C bond of the bpe ligand in **3** generates a square-grid network.

The extended structure shows that each Co^{II} octahedral centre is further connected to form a 2D square-grid structure, as shown in Figure 2b, with cavity dimensions measured by Co \cdots Co distances of approximately 13.66 Å \times 13.66 Å. The shape is approximately a square, as inferred from the diagonal Co \cdots Co distances, 18.65–19.79 Å and Co–Co–Co angles, 86.6–92.9°. These (4,4) square-grid sheets are further interpenetrated in an inclined fashion at a dihedral angle of 40° to form diagonal/diagonal inclined interpenetrated 3D networks. The schematic diagram in Figure 2c represents the diagonal/diagonal twofold inclined interpenetration of square-grid 2D sheets in **3**. The metal centres of each interpenetrating square occupy the centre of the other inclined square. Diagonal/diagonal interpenetration of (4,4) networks are well known in coordination polymers.^[2,13] The effect of the anion on the topology of square-grid sheets has been previously investigated.^[8] Large CF₃CO₂[–] anions placed in *trans* positions to the Co^{II} centre restrict further interpenetration of the square-grid network in **3**. The type of interpenetration observed in **3** is

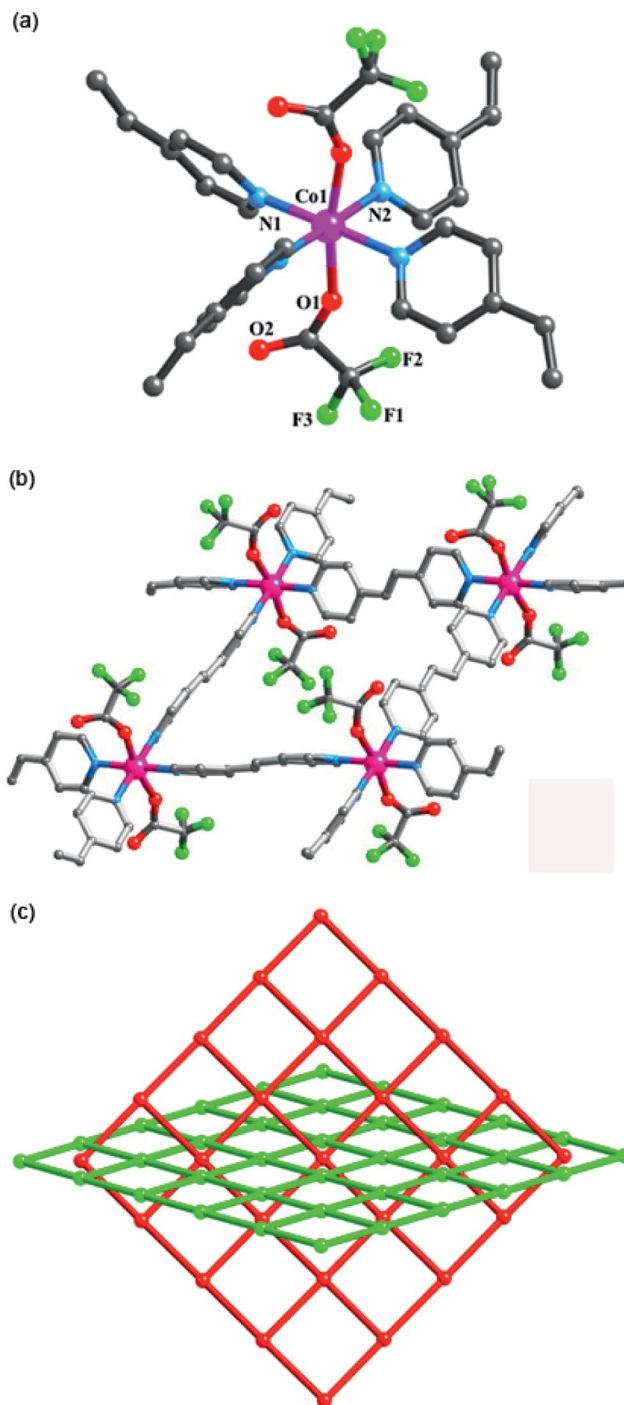


Figure 2. (a) A view showing the coordination geometry of the metal centre in **3**. (b) A portion of square grid formed in **3**. (c) A schematic diagram showing the interpenetration of two diagonal square-grid sheets generated by connecting the Co^{II} metal atoms in **3**.

very similar to that reported by Robson in [Zn(bipy)₂(H₂O)₂](SF₆) (bipy = 4,4'-bipyridine), which is interlocked, perpendicular (4,4) square-grid [Zn(H₂O)₂(bipy)₂]²ⁿ⁺ sheets in a diagonal/diagonal mode.^[13b] A topologically identical structure was also observed in [Fe(bpe)₂(NCS)₂]·CH₃OH.^[13c]

The diversity of networks depends not only on the properties of metal ion or ligands but also on the metal-to-ligand ratio. For example, bpy (4,4'-bipyridine), by coordinating to metals in 1:1 metal/ligand ratios can afford 1D zigzag, linear or helical chains, but a 1:2 stoichiometry can give a 2D square grid. Due to their predictable pore size and selective inclusion of guest molecules, square-grid networks with (4,4) topology have gained special attention.^[1a–1c,2a–2c] Zaworotko et al. described topologically different modes of interpenetration for (4,4) networks such as parallel/parallel, diagonal/diagonal and parallel/diagonal inclined interpenetrations.^[2a–2b] The diagonal/diagonal interpenetration contains windows of sheets with the nodes of their interpenetrating partners.^[2a–2b,2d,13] Although diagonal/diagonal interpenetration is commonly encountered in inclined interpenetration, exact diagonal/diagonal inclined sheets with connection at the midpoint of the square-grid sheets are very rare.^[2d]

1D Zigzag Chain Structure of [Co(μ -bpe)(O₂CC₆H₅)₂-(HO{O}CC₆H₅)₂] (4)

A portion of the polymeric segment showing the coordination environment of the octahedral Co^{II} centre in **4** is displayed in Figure 3.

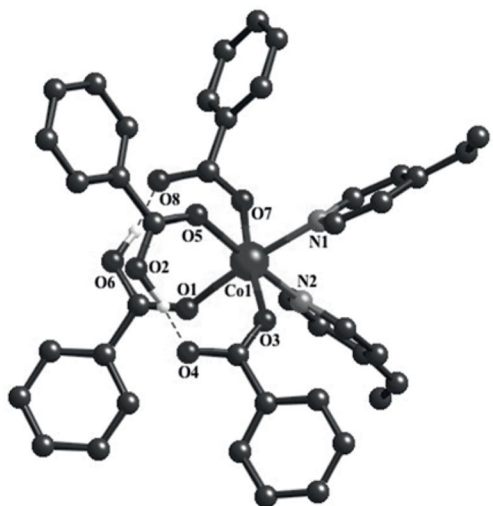


Figure 3. Asymmetric unit of **4** showing the coordination geometry of the Co^{II} ion and the O–H \cdots O hydrogen bonding interactions between the benzoic acid and benzoate ligands.

The crystal structure reveals that each Co^{II} metal centre adopts a six-coordinate octahedral geometry by coordinating to two N atoms [Co1–N1 2.153(2) Å and Co1–N2 2.156(2) Å] of the bpe molecules in *cis* fashion [N–Co–N 87.4°]. The Co^{II} centre is further coordinated to oxygen atoms, two from two benzoate anions [Co1–O3 2.075(2) Å and Co1–O7 2.056(2) Å] and two from two neutral benzoic acid ligands [Co1–O1 2.110(2) Å and Co1–O5 2.108(2) Å]. The two acidic protons from the benzoic acid ligand are strongly hydrogen-bonded to oxygen atoms of the benzoate ligands [O(2)–H(2) \cdots O(8) 2.441 Å and O(6)–H(1) \cdots O(4)

2.449 Å], as shown in Figure 3. These interactions lead to a *cis* geometry of the bpe ligands at the metal centre. The bpe ligands bridge two different Co^{II} centres, thus generating a 1D coordination polymer, [Co(μ -bpe)(O₂CC₆H₅)₂(HO{O}CC₆H₅)₂], as shown in Figure 4, and the *cis* geometry at the metal centre dictates the zigzag conformation of the polymer.

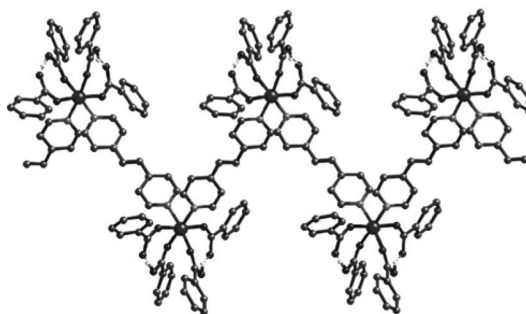


Figure 4. A portion of 1D zigzag polymeric strand formed by **4**. Benzoic acid and benzoate form O–H \cdots O hydrogen-bonding interactions along the 1D polymer.

The packing structure of **4** shows that the 1D polymeric strands propagate along the [011] and [01 $\bar{1}$] directions and lie parallel to each other, forming a layer in the *bc* plane. In other words, the direction of propagation of the 1D polymers is different in adjacent layers along the *a* axis with a twisting angle of 64.6°. Compound **4** also possesses weak intermolecular hydrogen-bonding interactions between the chains. A very weak intermolecular C–H \cdots O hydrogen-bonding interaction [C(12)–H(12) \cdots O(4) 3.474 Å] was observed between the double bond hydrogen atom of the coordinated bpe spacer from one chain and the oxygen atom of PhCO₂[–] of the next chain.

The packing is in such a way that the coordinated PhCO₂[–] and PhCO₂H occupy either side of the V-shaped N–Co–N of the next chain, and the chains interact via C–H \cdots O hydrogen-bonding in perpendicular fashion. The closest Co \cdots Co distances are 9.833 Å between the chains and 13.645 Å along the 1D chain.

1D Linear Chain Structure of [Co(μ -bpe)(O₂CC₆H₅)₂-(CH₃OH)₂] (5)

The crystal structure of **5** reveals that the asymmetric unit contains one and one half of the molecular formula. There are two crystallographically independent metal atoms, Co1 and Co2: while Co1 occupies the general position, Co2 sits on the centre of crystallographic inversion. Both Co^{II} centres adopt an octahedral geometry by coordinating two N atoms of the bpe ligand [Co1–N1 2.158(1); Co1–N2 2.131(1); Co2–N3 2.133(1) and Co2–N4 2.133(1) Å], oxygen atoms of two benzoate ligands [Co1–O1 2.082(1); Co1–O3, 2.063(1) and Co2–O7 2.098(1) Å] and two oxygen atoms [Co1–O5 2.134(1); Co1–O6, 2.129(1) and Co2–O9 2.122(1) Å] of methanol in *trans*-fashion

as shown in Figure 5. The *trans* disposition of the bpe ligands lead to the formation of a linear 1D coordination polymer.



Figure 5. Two independent 1D polymeric strands in **5**. The benzoate anion interacts with the coordinated methanol through O–H···O hydrogen bonding.

In **5**, the 1D coordination polymers propagate alternatively along the [110] and $\bar{[110]}$ directions. These 1D polymers form layers as noted in **4**. The angle between the propagation of these polymers is 41.8° . Strong intermolecular O–H···O hydrogen bonding [O(6)–H(3S)···O(4) 2.610(1); O(5)–H(5S)···O(2) 2.577(1) and O(9)–H(9S)···O(8) 2.593(2) Å] was observed between the coordinated MeOH and the PhCO_2^- ligand in the single chain. A weak intermolecular C–H···O hydrogen-bonding interaction [C(8)–H(8)···O(5) 3.222 Å] is present between the oxygen atom of MeOH and the *meta* hydrogen atom of neighbouring benzoate anion, as shown in Figure 6. Another weak hydrogen-bonding interaction [C(16)–H(16)···O(8) 3.305 Å] is present between the ring hydrogen atom and the oxygen atom of the benzoate anions between the chains of two layers in which they are assembled in perpendicular fashion. The 1D coordination polymers in the adjacent layers display $\pi\cdots\pi$ interactions between the centres of the pyridyl rings with a plane-to-plane distance of 3.557–3.618 Å. Here, weak intermolecular hydrogen bonding facilitates the formation of 3D hydrogen-bonded networks of the 1D coordination polymer. The Co···Co distance is 13.642 Å along the 1D chain and 6.740 Å between the nearest 1D chains.

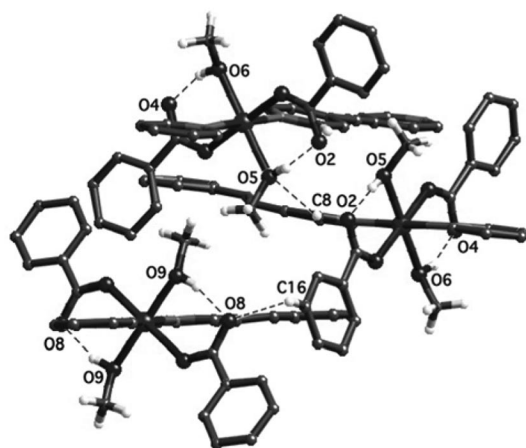


Figure 6. The 1D coordination polymers are stabilized by weak O–H···O hydrogen-bonding interactions in the linear chain and weak C–H···O hydrogen-bonding interactions between the adjacent linear chains in **5**.

Twofold Interpenetrated Ladder Structure of $[\text{Co}_2(\mu\text{-bpe})_3(\text{NO}_3)_3(\text{CH}_3\text{OH})](\text{NO}_3)_3$ (**6**)

The asymmetric unit of **6** is given in Figure 7. In **6**, there are two crystallographically independent Co^{II} metal centres, of which Co1 has distorted octahedral geometry and Co2 has distorted pentagonal-bipyramidal heptacoordinate geometry.

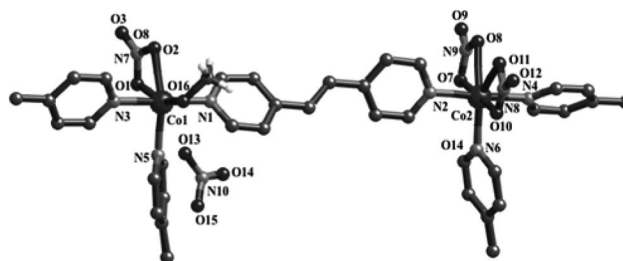


Figure 7. A perspective view of the asymmetric unit of **6**. The Co^{II} metal centre represents a T-shaped geometry.

Each metal centre is strongly coordinated to N atoms of the three bpe spacer ligands [Co1–N1 2.132(5); Co1–N3 2.146(5); Co1–N5 2.124(6); Co2–N2 2.130(5); Co2–N6 2.136(6) and Co2–N4 2.161(5) Å]. Co1 is coordinated to a nitrate anion in bidentate manner [Co1–O1 2.101(5) Å and Co1–O2 2.212(5) Å] and an oxygen atom of the methanol ligand [Co1–O16 2.059(5) Å]. On the other hand, two nitrate ions are chelated to the Co2 metal centre [Co2–O7 2.150(5); Co2–O10 2.151(7); Co2–O8 2.274(7) and Co2–O11A 2.310(1) Å]. The N donors of the pyridyl bpe spacer ligands are bonded to the Co^{II} centres to provide T-shaped geometry^[14] for the CoN_3 core. The T-shaped building blocks are further connected to each other to form an infinite 1D molecular ladder with (4,3) square-grid ladder networks. Four Co atoms in the ladder occupy roughly the corners of a square as shown in Figure 8 with a Co···Co distance of 13.52 Å in the rung and 13.59 Å along the pole. The diagonal Co···Co distances of the squares are 17.99 Å and 20.39 Å. Each square in the ladder is filled by two squares from two different ladders. This interpenetration occurs in an inclined fashion with a dihedral angle of 75° . Hence, the overall structural motif results in threefold interpenetration of 1D molecular ladders to a 3D network structure, as shown in the schematic diagram in Figure 9.

The ladders are stacked in off-set arrangement to provide the 3D network structure in **6**. The closest distance between the pyridyl rings of different ladders are C10···C10, 5.78 Å and C=C···C10, 3.82 Å. Such threefold catenation has also been observed in $\{[\text{Cd}_2(4,4'\text{-pytz})_3(\mu\text{-NO}_3)(\text{NO}_3)_3(\text{MeOH})]\}_n$ [4,4'-pytz = 3,6-bis(pyridine-4-yl)-1,2,4,5-tetrazine],^[11a] in $[\text{Cu}_2(\text{ip})(\text{bipy})]\cdot 3.5\text{H}_2\text{O}$ (ip = isophthalate)^[11b] and in $[\text{M}_2(\text{bpethy})_3(\text{NO}_3)_4]_n$ {M = Zn or Co; bpethy = *trans*-1,2-bis(4-pyridyl)ethyne}.^[11c]

The structural motif observed with T-shaped connecting nodes is particularly of interest in constructing ladders, brick walls, bilayers and 3D frameworks.^[6,10,11,14–18] Long linear spacer ligands favour the formation of square-grid networks or tend to favour higher-folded interpenetrated

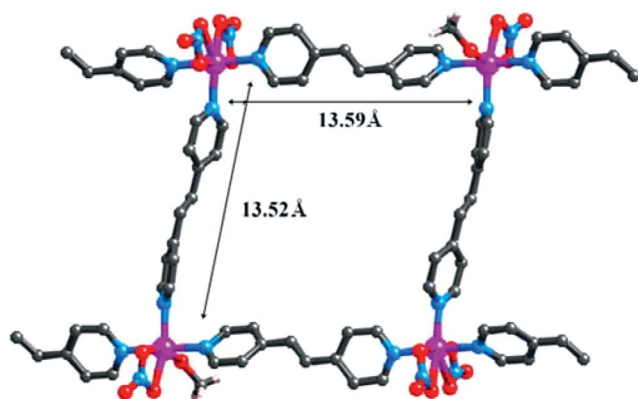


Figure 8. A portion of the square-grid formed of the 1D ladder in **6**. The Co \cdots Co distance along the rung is 13.52 Å and along the rails is 13.59 Å in the ladder.

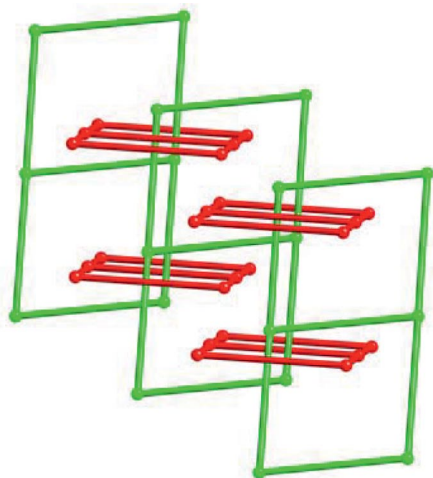
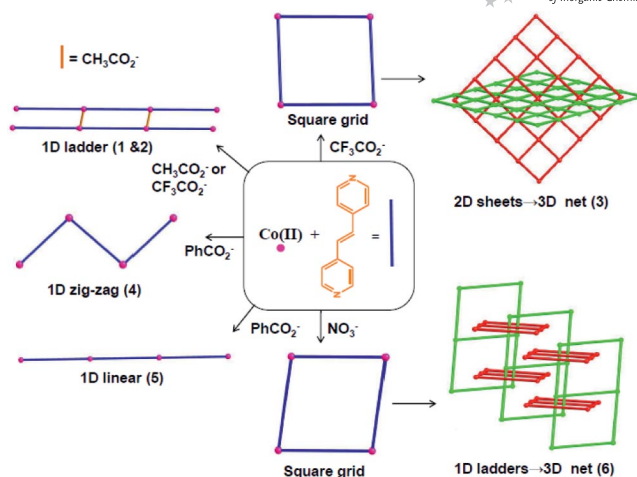


Figure 9. A schematic diagram showing the topology generated by connecting Co II metal atoms in **6**. Three-fold interpenetration of ladders result in 1D \rightarrow 3D nets.

3D nets.^[11,16] Despite the few threefold interpenetrated ladder structures that have been reported, molecular ladders formed by the bpe spacer ligand with a rigid backbone are not fully understood.^[2d] Metal ions bridged by conjugated or spacer ligands attract enormous interest, because of their fascinating magnetic properties, especially those with the Co II ion.^[13a,13c,17–19] There are good examples of compounds that have interpenetrated (4,4) sheets, which show excellent magnetic properties, reported by Chen, Kepert and others.^[13a,13c,18]

Influence of the Various Factors on the Structures

The topologies formed from the Co II ion and the bpe ligand in this study are given in Scheme 1. Carboxylate anions show a variety of bonding modes in forming coordination polymers with different topologies. Of these, acetate ligands show symmetrical *syn-syn* (η^2) bridging in forming 1D ladders **1** and **2**. Acetate and trifluoroacetate ligands symmetrically chelate in **1** and **2**, respectively.



Scheme 1. Distinct topological networks formed from the Co II ion and the bpe ligand in the presence of the CH $_3$ CO $_2^-$, CF $_3$ CO $_2^-$, C $_6$ H $_5$ CO $_2^-$ and NO $_3^-$ anions.

The acetate anion has profound influence in forming the ladder topology, by bridging the metal cations. However, replacing the acetate anions completely by trifluoroacetate results in **3**, which has square-grid sheets with octahedral geometry at the metal centre, and the less basic trifluoroacetate ligand is situated at the axial position in monodentate fashion. The square grid generates large cavities with dimensions of 13.66 Å \times 13.66 Å without the inclusion of the guest molecules or counteranions. As a result, the square-grid sheets interpenetrate each other in an inclined fashion at the midpoint to furnish twofold interpenetration of (4,4) square-grid sheets and 2D \rightarrow 3D nets. In addition, weak C–H \cdots F interaction between the pyridyl rings of one sheet with fluorine atoms of coordinated F $_3$ C–CO $_2^-$ in the inclined sheet is found to stabilize the interpenetration. In this case, the formation of **3** is independent of temperature, concentration and solvent system. From these observations, it appears that the trifluoroacetate anion favours the formation of interpenetrated networks.

Although the coordination modes of carboxylates are unpredictable, it was expected that the aromatic monocarboxylates would form similar interpenetrated networks. However, the large size of the benzoate anion appears to hinder the formation of higher-dimensional networks. This is consistent with the monodentate coordination mode commonly found in complexes containing benzoate ligands. On the contrary, benzoic di- or tricarboxylates have shown bridging and chelation in most of the complexes. Interestingly, in **4**, benzoic acid acts as a neutral ligand by coordinating to the Co II ion in monodentate fashion, which is not common in coordination polymers.^[20] The benzoic acid ligand participates in intramolecular hydrogen bonding with the coordinated benzoate anion. The spatial distribution of the benzoate anion and the neutral benzoic acid ligand at the metal centre is greatly affected by the small bite angle of N–Co–N, 87.4°, in *cis* fashion, which promotes the zigzag conformation. However, the bite angle N–Co–N 180.0° (i.e. *trans* fashion) is maintained in **5**, because

the donor atoms of benzoate anions and coordinated methanol occupy a plane to facilitate the metal geometry. Such *cisoid* and *transoid* conformation in 1D coordination polymers are well studied in Ag^I compounds.^[2c] Intrachain hydrogen-bonding interactions between two neutral and two anionic ligands appear to dictate the ligand environments around the metal ions, in particular the distribution, and hence the bite angle of the two bpe ligands. This, in turn, causes the conformation of the 1D chain to be zigzag and linear in **4** and **5** respectively.

The coordination sphere of the metal ion can be influenced by the coordinating ability of the anion, which, in turn, controls the framework connectivity.^[21] Replacing the carboxylates by nitrate anions resulted in the change of Co^{II} metal geometry from an octahedron to a pentagonal bipyramid and highly distorted octahedron. Due to this preferred influence of the NO₃[−] anion, the metal-to-ligand ratio in **6** remains at 1:1.5 irrespective of the ratio used in the synthesis. The ability of the NO₃[−] anion to chelate the Co^{II} metal centre in **6** provides T-shaped geometry. Interpenetration of molecular ladders, such as 1D→2D or 1D→3D nets, is common if the cavities are not occupied by guest solvent molecules.^[2a–2c,22] The square-grid network in **6** generates similarly sized cavities as those in **3** in dimensions of approximately 13.52 Å × 13.59 Å without any guest molecules. This results in threefold interpenetration in **6**. It is known that adjacent interpenetrated ladders can be stabilized by strong $\pi \cdots \pi$ interaction in 1D→2D nets.^[23] However, we believe that the interpenetrated 1D ladders in **6** are stabilized by weak C–H \cdots O hydrogen-bonding interactions between the pyridyl rings and the oxygen atoms of the coordinated nitrate ligands.

Furthermore, it appears that the shape and size of the anion are responsible for the degree of interpenetration.^[8a,9] The CF₃CO₂[−] anion is larger than the NO₃[−] anion and that certainly restricts further catenation of the network by occupying the void space. Increasing degree of interpenetration from threefold to fivefold has been observed by using longer spacer ligands.^[16] For example, [Cd₂(L¹)₃](NO₃)₂ [L¹ = 1,4-bis(4-pyridylmethyl) benzene] shows nearly orthogonal interpenetration of ladders by fivefold polycatenation.^[16a–16b] A similar polycatenated structure observed in [Cd₂(nbpy4)₃(NO₃)₄] {nbpy4 = *N,N'*-bis(4-pyridinylmethylene)-1,5-naphthalenediamine} may be due to the large, long and rigid *exo*-bidentate ligand.^[10] Two different degrees of interpenetration and topologies in **3** and **6** have been attributed to the influence of the nature and size of anions present in those complexes.

To summarize, acetate prefers to form a ladder structure, whereas the structure between ladder and interpenetrated sheets can be controlled by the use of CF₃CO₂H. When the ratio Co^{II}/bpe/CF₃CO₂H is 1:2:2, it yields 2D sheets exclusively. On the other hand, experimental conditions influence the formation of two different products when the benzoate anion is used for the given ratio of the reactants used. Interestingly, the Co^{II}/bpe ratio has no effect on the topology of the product. Although a combination of the experimental conditions, the ratio of the reactants em-

ployed and the nature of the anions, is generally responsible for the formation of the final products, the anions do play a significant role on the conformation and packing of the coordination through supramolecular interactions. This has also been highlighted in the structures of **1–6**.

Magnetic Studies

The magnetic properties of the interpenetrated cobalt(II) three-dimensional network compounds of **3** and **6** have been investigated. The magnetic behaviour of **3** is shown in Figure 10. The $\chi_M T$ value of 3.52 cm³ mol^{−1} K at 300 K under 1 kOe field is typical for high-spin Co^{II} ions with significant orbital contribution. $\chi_M T$ values decrease gradually upon lowering the temperature and reach 2.10 cm³ mol^{−1} K at 4 K, then drop sharply upon further cooling to 1.9 cm³ mol^{−1} K at 2 K. The susceptibility data above 210 K obeys the Curie–Weiss law, with a Curie constant of $C = 3.72$ cm³ mol^{−1} K and a Weiss constant of $\theta = -19.7$ K. The negative value of θ may be due to the spin-orbit coupling, which is remarkable for the ⁴T_{1g} state of Co²⁺ in an octahedral ligand field. Since the separation between the Co²⁺ ions are so long (13.66 Å), the magnetic interaction between the Co^{II} ions within a 2D net should be very weak, an anti-ferromagnetic interaction between the nets could be possible.

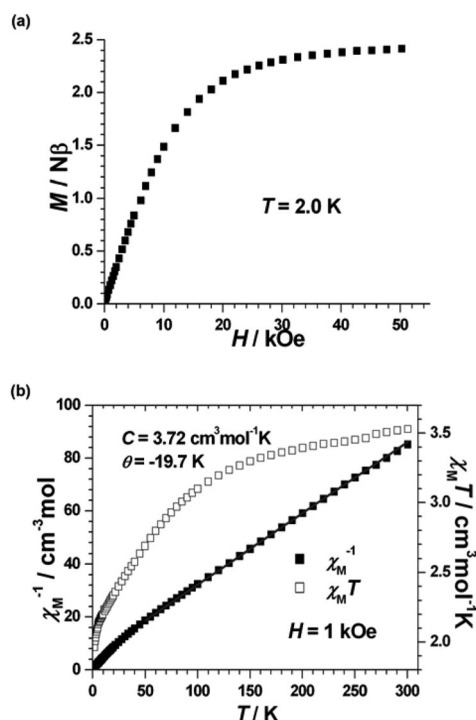


Figure 10. (a) Field dependence of magnetization of **3** at $T = 2$ K. (b) Temperature dependence of $\chi_M T$ and χ_M^{-1} of **3** at $H = 1$ kOe from 2 to 300 K. The line represents the best fit to the Curie–Weiss law.

The magnetic behaviour of **6** is shown in Figure 11. $\chi_M T$ values decrease gradually upon lowering the temperature and reach a minimum of 1.97 cm³ mol^{−1} K at 13 K, and then

increase quickly to a maximum of $2.23 \text{ cm}^3 \text{ mol}^{-1} \text{ K}$ at 6 K. $\chi_M T$ drops sharply on further cooling. This behaviour suggests the possible occurrence of weak ferromagnetism (WF) below 6 K. The susceptibility data above 180 K obeys the Curie–Weiss law, with a Curie constant of $C = 3.11 \text{ cm}^3 \text{ mol}^{-1} \text{ K}$ and a Weiss constant of $\theta = -14.4 \text{ K}$. Since there exist large separations of 13.66 \AA between Co^{II} ions within one net, and 9.325 \AA between different nets, **3** shows a single-ion-like behaviour without long-range order. However, in **6**, although the distance between Co^{II} ions within one net is 13.52 \AA , the nearest inter-net distance of 6.32 \AA is shorter than that found in **3**. This might be one of the reasons for the possible canted weak ferromagnetic state of **6** at low temperature.

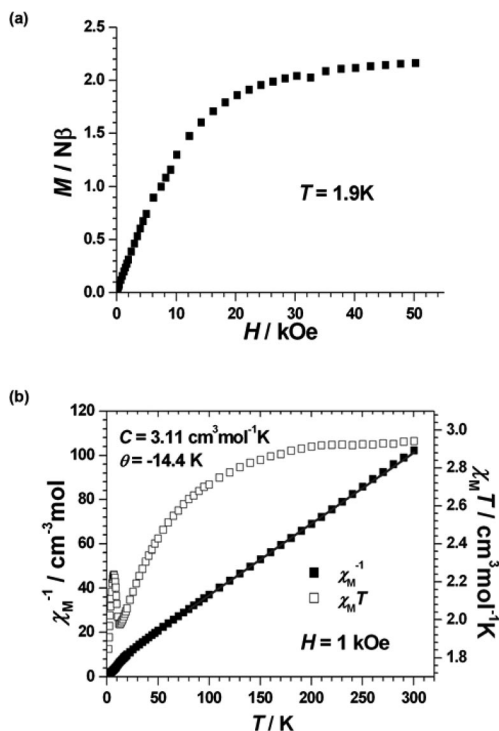


Figure 11. (a) Field dependence of magnetization of **6** at $T = 2 \text{ K}$. (b) Temperature dependence of $\chi_M T$ and χ_M^{-1} of **6** at $H = 1 \text{ kOe}$ from 2 to 300 K.

Conclusions

Six coordination polymers were isolated from the Co^{II} ion and the bpe ligand by varying the anions. Complexes **1** and **2** exhibit 1D molecular ladder structures with criss-cross and parallel aligned $\text{C}=\text{C}$ bonds at a distance less than 4.2 \AA . However, **3** forms square-grid 2D sheets when all the acetate ligands are replaced by trifluoroacetate ligands. Compound **3** features diagonally inclined twofold interpenetration of (4,4) square-grid sheets to form a $2\text{D} \rightarrow 3\text{D}$ net transformation. Replacing the aliphatic monocarboxylate by the aromatic monocarboxylate ligand results in 1D coordination polymers having zigzag (in **4**) and linear (in **5**) conformation. Assemblies of the six-coordinate metal ion with four carboxylate ligands with the bpe spacer ligand in *cis*

geometry produce the zigzag coordination polymer **4** from solvothermal synthesis. However, assemblies of the *trans*-six-coordinate metal ion with two carboxylate groups as bridging ligands, two methanol and two bpe spacer ligands produce the linear 1D chain **5** by the layering method with different composition. The size and coordination mode of the benzoate anion influence the formation of the 1D strand in **4** and **5**. The adjacent 1D chains in the subsequent layers are aligned perpendicularly in **4** and **5**, in a one-over and one-under fashion, with weak $\text{C}-\text{H} \cdots \text{O}$ hydrogen bonding between the chains resulting in a 3D hydrogen-bonded network structure. Replacing the carboxylate ligands by nitrate anions result in infinite molecular ladders in **6** with T-shaped geometry. These infinite 1D ladders have threefold interpenetration that leads to $1\text{D} \rightarrow 3\text{D}$ nets. The influence of the size and nature of anions on the degree of interpenetration and topology of the networks is highlighted in these structures. Variable-temperature magnetic measurements were also performed on two compounds (**3** and **6**). An unexpected weak ferromagnetism below 6 K in **6** was noted, which is probably due to interactions between Co^{II} ions from different nets.

Experimental Section

Materials and Methods: All the chemicals were purchased from commercial sources and used as received. All the solvents used were of reagent grade. The yield is reported with respect to the metal salts. Infrared spectra (KBr pellets) were recorded by using a FTS 165 Bio-Rad FTIR spectrometer in the range $4000\text{--}400 \text{ cm}^{-1}$. Elemental analyses were performed in the Micro Analytical Laboratory, Department of Chemistry, and National University of Singapore. Thermal analysis of the compounds was determined by using a SDT 2960 TGA Thermal Analyzer with a heating rate of $10 \text{ }^\circ\text{C min}^{-1}$ with a sample size of 15–20 mg per sample run.

[Co₂(μ-bpe)₂(μ-O₂CCH₃)₂(O₂CCH₃)₂·H₂O (1): A methanol solution (0.6 mL) of bpe (0.027 g, 0.15 mmol) was layered over an aqueous solution of $\text{Co}(\text{OAc})_2 \cdot 4\text{H}_2\text{O}$ (0.6 mL, 0.037 g, 0.15 mmol) and methanol (1 mL) used as buffer. Pink rodlike crystals formed after 4 d. Yield: 0.076 g (68%). $\text{C}_{32}\text{H}_{34}\text{Co}_2\text{N}_4\text{O}_9$ (736.49): calcd. C 53.49, H 4.49, N 7.8; found C 51.56, H 4.65, N 7.50. Selected IR (KBr): $\tilde{\nu} = 3042 \text{ (m)}, 3010 \text{ (w)}, 1607 \text{ (s)}, 1570 \text{ (s)}, 1504 \text{ (s)}, 1437 \text{ (s)}, 1385 \text{ (w)}, 1352 \text{ (m)}, 1305 \text{ (w)}, 1251 \text{ (m)}, 1220 \text{ (w)}, 1207 \text{ (w)}, 1071 \text{ (m)}, 1049 \text{ (w)}, 1016 \text{ (s)}, 983 \text{ (w)}, 974 \text{ (w)}, 832 \text{ (s)}, 671 \text{ (m)}, 646 \text{ (w)}, 622 \text{ (w)}, 554 \text{ (s)} \text{ cm}^{-1}$.

[Co₂(μ-bpe)₂(μ-O₂CCH₃)₂(O₂CCF₃)₂] (2): A methanol solution (0.5 mL) of bpe (0.018 g, 0.1 mmol) was mixed with an aqueous solution (2 mL) of $\text{Co}(\text{OAc})_2 \cdot 4\text{H}_2\text{O}$ (0.024 g, 0.1 mmol) and trifluoroacetic acid (HTFA) (0.011 g, 0.1 mmol), and the mixture was heated in a vial at $90 \text{ }^\circ\text{C}$. Pink rodlike crystals formed after 2 d, they were decanted and dried under vacuo. Yield: 0.024 g (58%). $\text{C}_{16}\text{H}_{13}\text{CoF}_3\text{N}_2\text{O}_4$ (413.21): calcd. C 46.51, H 3.17, N 6.78; found C 47.22, H 3.10, N 6.97. Selected IR (KBr): $\tilde{\nu} = 3077 \text{ (w)}, 3016 \text{ (w)}, 1703 \text{ (s)}, 1611 \text{ (s)}, 1584 \text{ (s)}, 1561 \text{ (s)}, 1504 \text{ (m)}, 1448 \text{ (s)}, 1428 \text{ (s)}, 1350 \text{ (w)}, 1301 \text{ (w)}, 1207 \text{ (w)}, 1193 \text{ (s)}, 1134 \text{ (s)}, 1072 \text{ (w)}, 1049 \text{ (w)}, 1018 \text{ (m)}, 969 \text{ (w)}, 952 \text{ (w)}, 827 \text{ (m)}, 794 \text{ (w)}, 718 \text{ (m)}, 678 \text{ (w)}, 647 \text{ (w)}, 614 \text{ (w)}, 554 \text{ (s)} \text{ cm}^{-1}$. The lattice water molecule appeared to have been lost while drying.

[Co(μ-bpe)₂(O₂CCF₃)₂] (3): A methanol solution (2 mL) of bpe (0.036 g, 0.2 mmol) was mixed with a solution of $\text{Co}(\text{OAc})_2 \cdot 4\text{H}_2\text{O}$

Table 1. Selected crystal data and refinement details for 1–6.

Compounds	1	2	3	4	5	6
Empirical formula	C ₃₂ H ₃₄ Co ₂ N ₄ O ₉	C ₁₆ H ₁₃ CoF ₃ N ₂ O ₄	C ₁₄ H ₁₀ N ₂ O ₂ F ₃ Co _{0.5}	C ₄₀ H ₃₂ N ₂ O ₈ Co	C ₈₄ H ₈₄ N ₆ O ₁₈ Co ₃	C _{18.5} H _{16.5} N ₅ O _{6.5} Co
F.w.	736.49	413.21	324.70	727.61	1642.36	471.8
<i>T</i> /K	223(2)	223(2)	223(2)	243(2)	293(2)	273(2)
Crystal system	Monoclinic	Triclinic	Orthorhombic	Orthorhombic	Monoclinic	Monoclinic
Space group	<i>C</i> 2 ₁ ^[a]	<i>P</i> $\bar{1}$	<i>Pccn</i>	<i>Pna</i> 2 ₁	<i>C</i> 2 ₁ / <i>c</i>	<i>P</i> 2 ₁ / <i>c</i>
<i>a</i> /Å	14.713(1)	8.107(5)	9.089(5)	19.652(2)	18.8858(7)	16.264(2)
<i>b</i> /Å	10.978(8)	9.392(5)	17.577(1)	16.797(1)	19.6906(8)	15.064(2)
<i>c</i> /Å	11.971(9)	11.514(7)	18.649(1)	10.6280(9)	22.5103(9)	16.882(2)
α /°	90	98.90(1)	90	90	90	90
β /°	119.256(1)	97.88(1)	90	90	108.93 (1)	93.476(3)
γ /°	90	102.79(1)	90	90	90	90
Volume/Å ³	1687.2(2)	831.27(8)	2979.3(3)	3508.3(5)	7918.2(5)	4128.8(9)
<i>Z</i>	2	2	8	4	4	8
ρ /Mgcm ^{−3}	1.450	1.651	1.448	1.378	1.378	1.518
μ /mm ^{−1}	1.041	1.089	0.653	0.546	0.695	0.880
Reflns. col.	6010	10805	23063	20666	28045	23091
Ind. Reflns/ <i>R</i> _{int} / <i>GooF</i>	3324/0.0251/1.074	3813/0.0248/1.051	4311/0.0457/1.127	6136/0.0417/1.034	9111/0.0325/1.073	7248/0.0665/1.060
Final ^[b] <i>R</i> [<i>I</i> >2 σ], <i>R</i> ₁ / <i>wR</i> ₂	0.0416/0.1034	0.0387/0.1047	0.0656/0.1535	0.0392/0.0799	0.0380/0.0972	0.0868/0.2253

[a] The absolute structural parameter for **1** was refined to 0.53(2), indicating a racemic twin. [b] $R_1 = (\Sigma||F_o| - |F_c||)/\Sigma|F_o|$; $wR_2 = [\Sigma w(F_o^2 - F_c^2)/\Sigma wF_o^4]^{1/2}$.

(0.024 g, 0.1 mmol) and HTFA (0.022 g, 0.2 mmol) in methanol (1 mL), and the mixture was heated in a sealed glass tube at 90 °C. Golden yellow rodlike crystals formed after 2 d, they were decanted and dried under vacuo. Yield: 0.048 g (75%). C₂₈H₂₀CoF₆N₄O₄ (649.4): calcd. C 51.79, H 3.1, N 8.63; found C 51.01, H 2.66, N 8.43. Selected IR (KBr): $\tilde{\nu}$ = 3065 (w), 3041 (w), 1681 (s), 1612 (s), 1561 (m), 1507 (m), 1429 (m), 1350 (w), 1303 (w), 1250 (m), 1198 (s), 1181 (s), 1132 (s), 1069 (m), 1019 (m), 992 (m), 952 (m), 828 (s), 716 (s), 554 (s) cm^{−1}.

[Co(μ -bpe)(O₂CC₆H₅)₂(HO₂CC₆H₅)₂] (4): A methanol solution (2 mL) of bpe (0.018 g, 0.1 mmol) was mixed with a solution mixture of Co(OAc)₂·4H₂O (0.024 g, 0.1 mmol) and benzoic acid (0.024 g, 0.2 mmol) in methanol (1 mL), and the final mixture was heated in a sealed glass tube at 90 °C. Rodlike yellowish-orange crystals formed after 1 d, they were decanted and dried under vacuo. Yield: 0.042 g (58%). C₄₀H₃₂CoN₂O₈ (727.61): calcd. C 66.03, H 4.43, N 3.85; found C 62.56, H 4.62, N 3.45. Selected IR (KBr): $\tilde{\nu}$ = 3422 (w), 3054 (w), 3024 (w), 2361 (w), 2342 (w), 1951 (w), 1935 (w), 1606 (s), 1569 (s), 1541 (s), 1502 (m), 1495 (m), 1426 (s), 1309 (w), 1247 (w), 1217 (w), 1175 (w), 1070 (w), 1025 (w), 1013 (m), 986 (w), 854 (m), 842 (m), 831 (s), 719 (m), 702 (s), 683 (m), 553 (s), 434 (w) cm^{−1}.

[Co(μ -bpe)(O₂CC₆H₅)₂(CH₃OH)₂] (5): A methanol solution (2 mL) of bpe (0.018 g, 0.1 mmol) was layered over a solution of Co(OAc)₂·4H₂O (0.024 g, 0.1 mmol) and benzoic acid (0.024 g, 0.2 mmol) in H₂O (1 mL) and methanol (0.5 mL). Orange-red block crystals formed after 2 d, they were decanted and dried under vacuo. Yield: 0.126 g (76%). C₈₄H₈₄Co₃N₆O₁₈ (1642.36): calcd. C 61.43, H 5.16, N 5.12; found C 60.30, H 5.01, N 5.26. Selected IR (KBr): $\tilde{\nu}$ = 3405 (w), 3058 (w), 3024 (w), 2457 (w), 2361 (w), 2342 (w), 1950 (w), 1706 (w), 1608 (s), 1569 (s), 1545 (s), 1503 (m), 1426 (s), 1414 (s), 1312 (w), 1248 (w), 1218 (w), 1174 (w), 1069 (w), 1015 (m), 985 (m), 973 (m), 969 (m), 842 (m), 830 (s), 718 (s), 702 (s), 683 (m), 617 (w), 553 (s), 433 (m) cm^{−1}.

[Co₂(μ -bpe)₃(NO₃)₃(CH₃OH)](NO₃) (6): A mixture of Co(NO₃)₂·6H₂O (0.058 g, 0.2 mmol) and bpe (0.072 g, 0.4 mmol) in methanol (3 mL) was heated in a sealed glass tube at 90 °C. Cubic pink crystals formed after 2 d, they were decanted and dried under vacuo. Yield: 0.03 g (65%). C₃₇H₃₁Co₂N₁₀O₁₃ (943.6): calcd. C 47.10, H 3.53, N 14.84; found C 46.71, H 3.93, N 14.15. Selected IR (KBr):

$\tilde{\nu}$ = 1609 (s), 1553 (w), 1504 (m), 1471 (m), 1384 (s), 1304 (m), 1219 (m), 1067 (m), 1017 (s), 974 (m), 826 (s), 549 (s) cm^{−1}.

X-ray Crystallographic Analysis: Intensity data for 1–6 were collected with a Bruker APEX diffractometer equipped with a CCD detector and graphite-monochromated Mo-K α (λ = 0.71073 Å) radiation by using a sealed tube (2.4 kW). Absorption corrections were made with the program SADABS,^[24] and the crystallographic package SHELXTL^[25] was used for all calculations. Selected crystal data and refinement details are given in Table 1. CCDC-772102 (for **1**), -772103 (for **2**), -772104 (for **3**), -772105 (for **4**), -772106 (for **5**), and -772107 (for **6**) contain the supplementary crystallographic data for this paper. These data can be obtained free of charge from The Cambridge Crystallographic Data Centre via www.ccdc.cam.ac.uk/data_request/cif.

Supporting Information (see footnote on the first page of this article): Experimental details, XRPD patterns, crystallographic details, IR spectra and TGA analysis.

Acknowledgments

We thank the Ministry of Education of Singapore for funding this project through National University of Singapore Faculty Research Committee Grant no. R-143-000-371-112. We thank Prof. Lip Lin Koh and Ms. Geok Kheng Tan of the X-ray diffraction laboratory for their help in X-ray crystallography.

- [1] a) S. Kitagawa, R. Kitaura, S. Noro, *Angew. Chem. Int. Ed.* **2004**, *43*, 2334–2375; b) S. R. Batten, S. M. Neville, D. R. Turner in *Coordination Polymers: Design, Analysis and Application*, Royal Society of Chemistry, Cambridge, **2009**; c) M. Edaoudi, D. B. Moler, H. Li, B. Chen, T. M. Reineke, M. O’Keeffe, O. M. Yaghi, *Acc. Chem. Res.* **2001**, *34*, 319–330; d) S. R. Batten, R. Robson, *Angew. Chem. Int. Ed.* **1998**, *37*, 1460–1494.
- [2] a) B. Moulton, M. J. Zaworotko, *Chem. Rev.* **2001**, *101*, 1629–1658; b) M. J. Zaworotko, *Chem. Commun.* **2001**, 1–9; c) A. J. Blake, N. R. Champness, P. Hubberstey, W. S. Li, M. A. Withersby, M. Schröder, *Coord. Chem. Rev.* **1999**, *183*, 117–138; d) S. R. Batten, *CrystEngComm* **2001**, *3*, 67–73.
- [3] G. Ferey, *Chem. Soc. Rev.* **2008**, *37*, 191–214.

- [4] J. M. Ellsworth, H. C. zur Loye, *Dalton Trans.* **2008**, 5823–5835.
- [5] S. Kitagawa, S. Kawata, *Coord. Chem. Rev.* **2002**, 224, 11–34.
- [6] S. A. Barnett, N. R. Champness, *Coord. Chem. Rev.* **2003**, 246, 145–168.
- [7] N. L. Toh, M. Nagarathinam, J. J. Vittal, *Angew. Chem. Int. Ed.* **2005**, 44, 2237–2241.
- [8] a) D. Long, R. B. Hill, A. J. Blake, N. R. Champness, P. Hubberstey, C. Wilson, M. Schröder, *Chem. Eur. J.* **2005**, 11, 1384–1391; b) N. R. Brooks, A. J. Blake, N. R. Champness, J. W. Cunningham, P. Hubberstey, S. J. Teat, M. Schröder, *J. Chem. Soc., Dalton Trans.* **2001**, 2530–2538; c) A. Jouaiti, V. Jullien, M. W. Hosseini, J.-M. Planeix, A. De Cian, *Chem. Commun.* **2001**, 1114–1115.
- [9] a) K. A. Hirsch, S. R. Wilson, J. S. Moore, *Inorg. Chem.* **1997**, 36, 2960–2968; b) M. Du, X.-H. Bu, Y.-M. Guo, H. Liu, *Inorg. Chem.* **2002**, 41, 4904–4908; c) R. Wang, D. Yuan, F. Jiang, L. Han, Y. Gong, M. Hong, *Cryst. Growth Des.* **2006**, 6, 1351–1360; d) L. J. May, G. K. H. Shimizu, *Chem. Commun.* **2005**, 1270–1272; e) J. Suárez-Varela, A. J. Mota, H. Aouryaghal, J. Cano, A. Rodríguez-Diéguez, D. Luneau, E. Colacio, *Inorg. Chem.* **2008**, 47, 8143–8158; f) C. Biswas, P. Mukherjee, M. G. B. Drew, C. J. Gmez-García, J. M. Clemente-Juan, A. Ghosh, *Inorg. Chem.* **2007**, 46, 10771–10780; g) K. Lyczko, W. Starosta, I. Persson, *Inorg. Chem.* **2007**, 46, 4402–4410; h) P. Diaz, J. Benet-Buchholz, R. Vilar, A. J. P. White, *Inorg. Chem.* **2006**, 45, 1617–1626; i) M. O. Awaleh, A. Badia, F. Brisse, *Cryst. Growth Des.* **2006**, 6, 2674–2685.
- [10] C.-Y. Su, A. M. Goforth, M. D. Smith, H. C. zur Loye, *Chem. Commun.* **2004**, 2158–2159.
- [11] For 1D ladders to 3D nets, threefold, see, for example: a) L. Carlucci, G. Ciani, D. M. Preserpio, *Chem. Commun.* **1999**, 1799–1804; b) M. A. Withersby, A. J. Blake, N. R. Champness, P. A. Cooke, P. Hubberstey, M. Schröder, *J. Am. Chem. Soc.* **2000**, 122, 4044–4046; c) J. Tao, X. Yin, R. B. Huang, L. S. Zheng, *Inorg. Chem. Commun.* **2002**, 5, 1000–1002.
- [12] M. Nagarathinam, A. M. P. Peedikakkal, J. J. Vittal, *Chem. Commun.* **2008**, 5277–5288.
- [13] For diagonal/diagonal interpenetration of (4,4) networks, see, for example: a) S. M. Neville, G. J. Halder, K. W. Chapman, M. B. Duriska, P. D. Southon, J. D. Cashion, J.-F. Le'tard, B. Moubaraki, K. S. Murray, C. J. Kepert, *J. Am. Chem. Soc.* **2008**, 130, 2869–2876; b) R. W. Gable, B. F. Hoskins, R. Robson, *J. Chem. Soc., Chem. Commun.* **1990**, 1677–1678; c) J. A. Real, E. Andres, M. C. Munoz, M. Julve, T. Grainer, A. Boussekou, F. Varret, *Science* **1995**, 268, 265–267; d) L. Carlucci, G. Ciani, D. M. Preserpio, S. Rizzato, *CrystEngComm* **2002**, 4, 413–425.
- [14] a) S. A. Barnett, N. R. Champness, *Coord. Chem. Rev.* **2003**, 246, 145–168; b) K. Biradha, M. Sarkar, L. Rajput, *Chem. Commun.* **2006**, 4169–4179.
- [15] For T-Shape geometry, see, for example: a) H. Gudbjartson, K. Biradha, K. M. Poirier, M. J. Zaworotko, *J. Am. Chem. Soc.* **1999**, 121, 2599–2600; b) T. L. Hennigar, D. C. MacQuarrie, P. Losier, R. D. Rogers, M. J. Zaworotko, *Angew. Chem. Int. Ed. Engl.* **1997**, 36, 972–973; c) M. J. Zaworotko, *Angew. Chem. Int. Ed. Engl.* **1996**, 35, 2779–2782.
- [16] For 1D ladders to 3D nets, fivefold, see, for example: a) M. Fujita, O. Sasaki, K.-Y. Watanabe, K. Ogura, K. Yamaguchi, *New J. Chem.* **1998**, 22, 189–191; b) M. Fujita, Y. J. Kwon, O. Sasaki, K. Yamaguchi, K. Ogura, *J. Am. Chem. Soc.* **1995**, 117, 7287–7288; c) H.-P. Wu, C. Janiak, L. Uehlin, P. Klüfers, P. Mayer, *Chem. Commun.* **1998**, 2637–2638.
- [17] a) R. Sessoli, D. Gatteschi, A. Caneschi, M. A. Novak, *Nature* **1993**, 365, 141–143; b) D. Gatteschi, A. Caneschi, L. Pardi, R. Sessoli, *Science* **1994**, 265, 1054–1058; c) W. Wernsdorfer, N. Aliaga-Alcalde, D. N. Hendrickson, G. Christou, *Nature* **2002**, 416, 406–409.
- [18] a) M.-H. Zeng, W.-X. Zhang, X.-Z. Sun, X.-M. Chen, *Angew. Chem. Int. Ed.* **2005**, 44, 3079–3082; b) A. N. Părvulescu, G. Marin, K. Suwinska, V. C. Kravtsov, M. Andruh, V. Părvulescu, V. I. Părvulescu, *J. Mater. Chem.* **2005**, 15, 4234–4240; c) Y.-Z. Zhang, H.-Y. Wei, F. Pan, Z.-M. Wang, Z.-D. Chen, S. Gao, *Angew. Chem. Int. Ed.* **2005**, 44, 5841–5846; d) G. J. Halder, C. J. Kepert, B. Moubaraki, K. S. Murray, J. D. Cashion, *Science* **2002**, 298, 1762–1765; e) A. N. Părvulescu, G. Marin, K. Suwinska, V. C. Kravtsov, M. Andruh, V. Părvulescu, V. I. Părvulescu, *J. Mater. Chem.* **2005**, 15, 4234–4240.
- [19] a) X.-T. Wang, Z.-M. Wang, S. Gao, *Chem. Commun.* **2008**, 281–294; b) X.-T. Wang, Z.-M. Wang, S. Gao, *Inorg. Chem.* **2007**, 46, 10452–10454; c) M. Yuan, F. Zao, W. Zhang, Z.-M. Wang, S. Gao, *Inorg. Chem.* **2007**, 46, 11235–11242; d) A. M. Kirillov, Y. Y. Karabach, M. Haukka, M. F. C. Guedes da Silva, J. Sanchiz, M. N. Kopylovich, A. J. L. Pombeiro, *Inorg. Chem.* **2008**, 47, 162–175.
- [20] a) L. Pan, M. B. Sander, X. Huang, J. Li, M. Smith, E. Bittner, B. Bockrath, J. K. Johnson, *J. Am. Chem. Soc.* **2004**, 126, 1308–1309; b) K. S. Gavrilenko, S. V. Punin, O. Cador, S. Golhen, L. Ouahab, V. V. Pavlishchuk, *J. Am. Chem. Soc.* **2005**, 127, 12246–12253.
- [21] A. N. Khlobystov, A. J. Blake, N. R. Champness, D. A. Le-menovskii, A. G. Majouga, N. V. Zyk, M. Schröder, *Coord. Chem. Rev.* **2001**, 222, 155–192.
- [22] P. Losier, M. J. Zaworotko, *Angew. Chem. Int. Ed. Engl.* **1996**, 35, 2779–2782.
- [23] M.-L. Tong, H.-J. Chen, X.-M. Chen, *Inorg. Chem.* **2000**, 39, 2235–2238.
- [24] G. M. Sheldrick, *SADABS*, version 2.05, University of Göttingen, Göttingen, Germany.
- [25] G. M. Sheldrick, *SHELXS-97, Program for X-ray Crystal Structure Determination*, University of Göttingen, Germany, **1997**; G. M. Sheldrick, *SHELXL-97, Program for X-ray Crystal Structure Refinement*, University of Göttingen, Germany, **1997**.

Received: April 4, 2010
Published Online: June 28, 2010

Systematic Hydrothermal Investigation of Metal Phosphonatobenzenesulfonates by High-Throughput Methods

Palanikumar Maniam,^[a] Christian Näther,^[a] and Norbert Stock*^[a]

Keywords: Organic-inorganic hybrid compounds / High-throughput screening / Hydrothermal synthesis / Metal phosphonatosulfonates

A high-throughput (HT) investigation using the rigid bifunctional ligand 4-phosphonobenzenesulfonic acid, $\text{H}_2\text{O}_3\text{P}-\text{C}_6\text{H}_4-\text{SO}_3\text{H}$ (H_3L), generated five new phosphonatobenzenesulfonates with copper(II) or lead(II) ions. A comprehensive HT study comprising the screenings of different metal ions, metal salt types and the synthesis optimization were conducted whereby the influence of pH and molar ratios $\text{M}^{2+}/\text{H}_3\text{L}$ were investigated. The HT-study led to five new compounds $\text{Pb}_2[(\text{O}_3\text{P}-\text{C}_6\text{H}_4-\text{SO}_3)(\text{OH})]$ (**1**), $\text{Cu}_{1.5}[(\text{O}_3\text{P}-\text{C}_6\text{H}_4-\text{SO}_3)(\text{H}_2\text{O})]$ (**2**), $\text{NaCu}(\text{O}_3\text{P}-\text{C}_6\text{H}_4-\text{SO}_3)(\text{H}_2\text{O})_3$ (**3**), $\text{Cu}_2[(\text{O}_3\text{P}-\text{C}_6\text{H}_4-\text{SO}_3)(\text{OH})(\text{H}_2\text{O})]$ (**4**) and $\text{Cu}_3[(\text{O}_3\text{P}-\text{C}_6\text{H}_4-\text{SO}_3)_2(\text{H}_2\text{O})_2]$ (**5**).

Metal ion screening showed lead(II) and copper(II) to be suitable metal ions. The utilization of discovery and focused arrays allowed to determine the optimal formation fields of the respective compounds. The crystal structures were determined from single-crystal X-ray diffraction and revealed the presence of various MO_x polyhedra that form clusters, chains or layers which are connected through the organic linker. IR spectra, thermogravimetric studies, magnetic susceptibility measurements and elemental analyses were conducted to further characterize the compounds **1**, **3**, **4** and **5**.

Introduction

The classes of inorganic-organic hybrid compounds range from amorphous nanocomposites such as self-assembled mesoporous materials to crystalline products.^[1] One intensively studied class of these compounds is the one of metal-organic frameworks (MOFs). These possess porous 3D networks and are therefore investigated for potential applications in gas storage, gas separation, catalysis and drug delivery.^[2,3] The organic building units that are mostly deployed in these materials are based on carboxylates ($\text{R}-\text{CO}_2^-$),^[4,5] and amines.^[6,7] On the other hand, sulfonate ($\text{R}-\text{SO}_3^-$) and phosphonate ($\text{R}-\text{PO}_3^{2-}$) based compounds have been less intensively investigated.^[8–14] This could be due to the more flexible coordination modes as well as the larger number of coordinating atoms which restricts structural diversity compared to the $-\text{CO}_2^-$ counterpart. Thus, for phosphonate-based compounds mostly more dense layered materials are formed.^[15,16] Only a few porous phosphonate based materials are known to date, for example Ni-STA-12 ,^[17] $\text{Al}_2(\text{CH}_3-\text{PO}_3)_3 \cdot \text{H}_2\text{O}$ ^[18] and $\text{Zr}(\text{O}_3\text{P}-\text{C}_6\text{H}_4-\text{PO}_3\text{H})$ ^[19] and there are even less examples described for sulfonate-based porous compounds.^[20] Our research focuses on the use of organic linker molecules containing two or more dif-

ferent functional groups for the synthesis of inorganic-organic hybrid compounds. In addition to the number of functional groups their geometry, coordination modes, as well as charge and acidity have a strong influence on the formation of the final crystal structures.

Examples from our previous work encompass the use of linkers containing phosphonate and carboxylate groups,^[21,22] phosphonate and amine groups such as iminobis(methylphosphonate) units^[23] or iminobis(methylphosphonate) and carboxylate units.^[24,25] Linkers containing a phosphonic and a sulfonic acid group have only been recently investigated. By using the flexible linker molecules 2-phosphonoethane- and 4-phosphonobutanesulfonic acid, our group has explored the synthesis of several hybrid compounds with different Cu^{2+} ,^[26] Sr^{2+} ,^[27] Ba^{2+} ,^[28] and lanthanide ions.^[29,30] Rigid phosphonoarylsulfonic acids, i.e. 3-phosphonobenzenesulfonic were employed by Mao et al.,^[31–35] 5-phosphono-1,3-disulfonic acid and 4-fluoro-3-sulfobenzylphosphonic acid by Montoneri et al.,^[36,37] mostly in combination with amine linkers. The synthesis of most metal phosphonates is accomplished under hydrothermal conditions. Such reactions are often known to be strongly dependent on the process parameters, e.g. reaction time, temperature, heating rate, and the compositional parameters, e.g. molar composition of the starting materials, pH of the reaction mixture or concentration. An elegant way for the exploration of these complex systems can be accomplished using high-throughput (HT) methods.^[38–41] These allow a systematic and efficient investigation of large parameter spaces giving rise to the accelerated discovery of

[a] Institut für Anorganische Chemie,
Christian-Albrechts-Universität,
Max-Eyth-Strasse 2, 24118 Kiel, Germany
Fax: +49-431-880-1775
E-mail: stock@ac.uni-kiel.de

Supporting information for this article is available on the WWW under <http://dx.doi.org/10.1002/ejic.201000393>.

new compounds and optimization of synthesis parameters. Due to the large amounts of data, reaction and structural trends can be obtained. Investigations using new organic linker molecules are typically conducted using a two step approach. In order to get an overview about suitable metal/organic linker combinations that lead to crystalline hybrid compounds, discovery arrays are set up. In these reactions a wide variety of metal ions as well as compositional parameters, especially the influence of pH is studied. Once new phases have been discovered, focused arrays are used, in which the synthesis parameters are only slightly varied in order to find the optimum synthesis conditions. Here we report, the synthesis and structural characterization of new copper(II)- and lead(II)-based compounds containing 4-phosphonobenzenesulfonic acid (H_3L) using our HT-methodology. Starting with metal screening discovery arrays Pb^{2+} as well as Cu^{2+} ions were identified to form new crystalline hybrid compounds. The in-depth HT study of the systems $M^{2+}/H_3L/NaOH/H_2O$ ($M = Pb^{2+}, Cu^{2+}$) using discovery and focused arrays allowed to establish the fields of formation of the title compounds.

Results and Discussion

Metal Screening Investigation

A high-throughput screening of different divalent metal ions was initiated. For this discovery array a set of twelve M^{2+} ions was tested in a 48 HT-reactor system (V_{max} per reaction of 200 μL).^[38,42] To determine the influence of ionic radii,^[43] Ni^{2+} , Mg^{2+} , Cu^{2+} , Zn^{2+} , Co^{2+} , Fe^{2+} , Mn^{2+} , Sn^{2+} , Cd^{2+} , Sr^{2+} , Pb^{2+} and Ba^{2+} ions were chosen and were varied in the molar ratio range $M^{2+}/H_3L/NaOH/H_2O = 1.5\text{--}4:1:3:556$ (see Table S1). Molar ratios $M^{2+}/H_3L > 1$ were used since the reported metal phosphonosulfonate compounds have always high metal-to-linker ratios.^[26,35] All products were analyzed via high-throughput X-ray powder diffraction (XRPD). In this discovery array, only reactions with Ni^{2+} , Mg^{2+} , Cu^{2+} , Zn^{2+} , Mn^{2+} , Sn^{2+} , Cd^{2+} and Pb^{2+} resulted in the formation of crystalline products, while Co^{2+} , Fe^{2+} , Sr^{2+} and Ba^{2+} ions produced only X-ray amorphous substances (see Figure S1). By focusing the study only on the crystalline substances, a second metal ion screening test was conducted and the amount of added base was varied. In this second discovery array molar ratios $M^{2+}/H_3L/NaOH/H_2O = 3:1:0\text{--}5:556$ for $M^{2+} = Ni^{2+}$, Mg^{2+} , Cu^{2+} , Zn^{2+} , Mn^{2+} , Sn^{2+} were used. For Cd^{2+} and Pb^{2+} molar ratios $M^{2+}/H_3L/NaOH/H_2O = 1.5:1:0\text{--}5:556$ and $4:1:0\text{--}5:556$, respectively, were chosen based on the results from the previous metal-screening investigations (see Table S2). The second discovery library yielded single crystalline compounds containing Pb^{2+} and Cu^{2+} ions. The other metal ions led to solids that were either X-ray amorphous or microcrystalline. Through comparison with literature data most of the crystalline compounds were identified as metal or metal hydroxides/oxides. Further investigations were fo-

cused on the use of Pb^{2+} and Cu^{2+} ions. Focused arrays were set-up in order to investigate these systems in more detail to establish their fields of formation.

High-Throughput Investigation of 1

To find the optimal precursor and to investigate the role of the counterion, various lead salts were screened. In addition to $Pb(NO_3)_2$, $PbCl_2$, $Pb(NO_3)_2$, $PbSO_4$ and $Pb(CH_3COO)_2$ were also tested as starting materials. $Pb(NO_3)_2$ was established as the best metal salt as the other salts produce mixed phases comprised of $Pb_2[(O_3P-C_6H_4-SO_3)(OH)]$ (**1**), PbO and unreacted starting materials. To establish the optimal formation field of **1**, the molar ratio $Pb(NO_3)_2/H_3L/NaOH/H_2O$ was varied in a broad range. In this focused array, the molar ratio $Pb(NO_3)_2/H_3L$ was kept fixed at 1:2, 1:1, 2:1, 3:1 and 4:1 and the amount of NaOH was varied (see Table S3). The ternary diagram in Figure 1 shows the result of that HT set-up which reveals the best molar ratios to be $Pb(NO_3)_2/H_3L/NaOH = 4:1:4\text{--}5$. At these compositions **1** is obtained as a pure phase product. Based on these results scale-up of **1** was accomplished in a Teflon lined reactor with a volume of 2 mL and the product was used for IR, TG and elemental analysis.

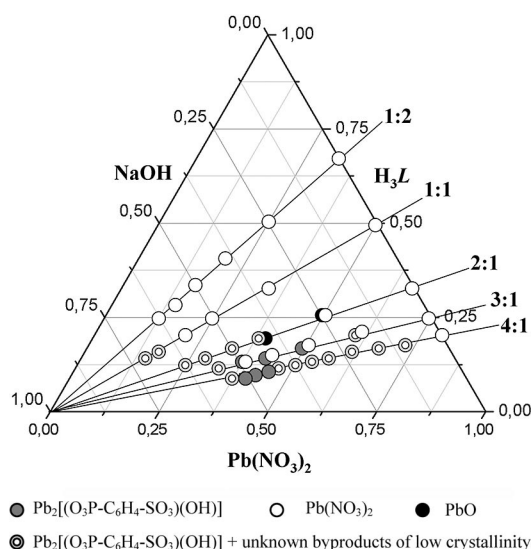


Figure 1. Crystallization diagram of the system $Pb(NO_3)_2/H_3L/NaOH/H_2O$ (**1**). Results are based on powder XRD measurements. Phase mixtures are indicated by overlapping symbols with two or more colors. Each diagonal line represents the fixed molar ratios of $Pb(NO_3)_2:H_3L$.

High-Throughput Investigation of 2, 3, 4 and 5

A comprehensive HT study was conducted to establish the formation fields of the copper compounds **2**, **3**, **4** and **5**. For that reason, the optimal starting copper(II) salt had to be determined and all possible areas in the ternary diagram had to be checked. HT-screening of various copper(II) salts comprising $Cu(NO_3)_2 \cdot 3H_2O$, $CuCl_2 \cdot 2H_2O$, $CuSO_4 \cdot 5H_2O$ and $Cu(CH_3COO)_2 \cdot H_2O$ was conducted with

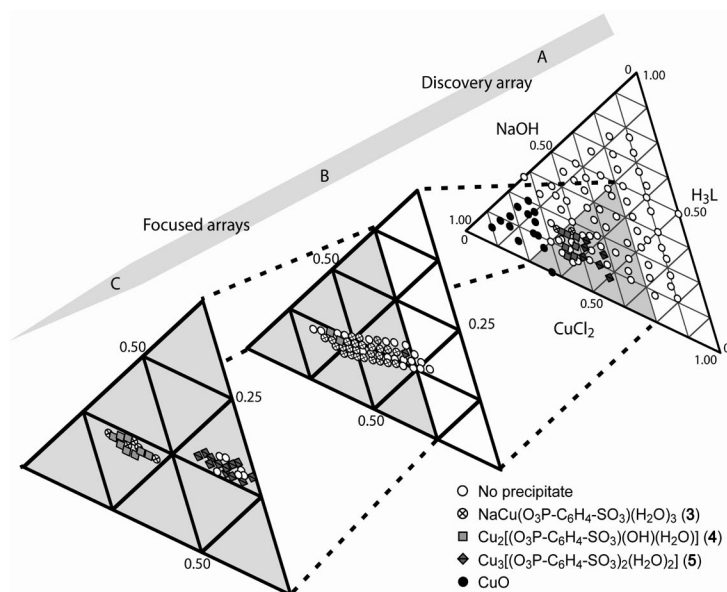


Figure 2. HT investigation of copper(II) compounds starting with the two discovery arrays A (96 individual reactions). Middle: focused array B with 48 reactions indicates the approximate formation fields of compounds 3, 4 and 5. Focused array C with 48 reactions reveals the specific formation field of compounds 4 and 5. Results are based on powder XRD patterns. Molar ratio values are normalized to 1.

the molar ratios $\text{Cu}^{2+}/\text{H}_3\text{L}/\text{NaOH} = 1\text{--}4:1\text{--}4:1\text{--}4$. $\text{Cu}(\text{CH}_3\text{COO})_2 \cdot \text{H}_2\text{O}$ salt tends to produce copper(I) oxide and $\text{CuSO}_4 \cdot 5\text{H}_2\text{O}$ exclusively led to X-ray amorphous substances. The results from the XRPD measurements showed that only $\text{Cu}(\text{NO}_3)_2 \cdot 3\text{H}_2\text{O}$ and $\text{CuCl}_2 \cdot 2\text{H}_2\text{O}$ produced the desired compounds. Since $\text{Cu}(\text{NO}_3)_2 \cdot 3\text{H}_2\text{O}$ produces mixed phase products, $\text{CuCl}_2 \cdot 2\text{H}_2\text{O}$ was established as the optimal starting material for further HT-studies. For the systematic investigation of the system $\text{CuCl}_2 \cdot 2\text{H}_2\text{O}/\text{H}_3\text{L}/\text{NaOH}$ two discovery arrays comprising 96 reactions were set up (see Figure 2). The ternary diagram showing the molar ratios employed as well as the results of the XRPD measurements is shown in part A of Figure 2. At molar ratios $\text{H}_3\text{L}/\text{NaOH} < 0.4$, CuO is formed (see black circles in Figure 2, A). Small amounts of NaOH, in combination with large amounts of H_3L and CuCl_2 led to clear solutions (see white circles in Figure 2, A). The three title compounds 3, 4 and 5 only form at well defined molar ratio ranges, each in a small field of formation. Compound 2, which was previously observed in the metal screening experiments, could not be reproduced in any following reaction. These results were used to set up focused arrays (Figure 2, B and C). The compound $\text{NaCu}(\text{O}_3\text{P-C}_6\text{H}_4\text{-SO}_3)(\text{H}_2\text{O})_3$ (3) was discovered in the focused arrays but could only be obtained as a microcrystalline product. Phase purity was demonstrated by elemental analysis as well as indexing of the X-ray powder pattern. The first focused array (Figure 2, B) indicated the preferred formation fields of compounds 3, 4, and 5. Compound 3 is obtained in a wide molar ratio ranges $\text{CuCl}_2 \cdot 2\text{H}_2\text{O}/\text{H}_3\text{L}/\text{NaOH} = 3\text{--}3.5:1:3\text{--}5.3$. The second focused array (Figure 2, C) was set up to get more precise information about the formation of 4 and 5. Title compound 4 is formed in the molar ratio ranges $\text{CuCl}_2 \cdot 2\text{H}_2\text{O}/\text{H}_3\text{L}/\text{NaOH} = 2.8\text{--}3:1:4.8\text{--}4.9$ ($\text{pH} \approx 5$) and compound 5 at

$2.9\text{--}3.2:1:2.6\text{--}2.9$ ($\text{pH} \approx 4$) respectively. To produce larger amounts of the substances, the HT reactors were used and the optimized reaction conditions were employed.

Crystal Structure Determination

The X-ray scattering factors of phosphorus and sulfur are very similar. Nevertheless, the distinction can be made by comparison of the P–O and S–O bond lengths. In $[\text{Pb}_3(\text{Z}_2)(\text{H}_2\text{O})_2] \cdot 4\text{H}_2\text{O}$ and $[\text{Pb}(\text{HZ})(\text{phen})]\text{H}_2\text{O}$ [$\text{Z} = (\text{O}_3\text{P-C}_6\text{H}_4\text{-SO}_3)^{3-}$, phen = 1,10-phenanthroline] P–O and S–O bond lengths in the range of 149.6(5)–157.8(5) pm and 144.3(9)–147.2(6) pm, respectively, were reported.^[35] The copper(II) phosphonatosulfonates, $\text{Cu}_2[(\text{O}_3\text{P-C}_2\text{H}_4\text{-SO}_3)(\text{OH})(\text{H}_2\text{O})](\text{H}_2\text{O})$ and $\text{Cu}_{2.5}(\text{O}_3\text{P-C}_2\text{H}_4\text{-SO}_3)(\text{OH})_2$ ranges from 151.9(3)–155.9(3) pm for P–O and 146.0(4)–147.2(3) pm for S–O.^[26] These values clearly show, that the S–O bond lengths are shorter than the P–O distances and thus, facilitate the identification of S and P atoms.

Crystal Structure of $\text{Pb}_2[(\text{O}_3\text{P-C}_6\text{H}_4\text{-SO}_3)(\text{OH})]$ (1)

The asymmetric unit of 1 is shown in Figure 3. The crystal structure was solved and refined in the triclinic space group $P\bar{1}$. The asymmetric unit contains two Pb^{2+} ions, one hydroxide ion O7–H7 and one $[\text{O}_3\text{P-C}_6\text{H}_4\text{-SO}_3]^{3-}$ ion with a positional disorder. Pb1 and Pb2 are seven- and fivefold coordinated, respectively, and form a distorted pentagonal bipyramidal (PbO_7) and a distorted square-pyramidal geometry (PbO_5 polyhedra). The Pb–O bond lengths are in the range of 225.3(12)–286.8(12) pm which are in agreement with literature data.^[35,44] Edge-sharing of the PbO_7 and PbO_5 polyhedra is observed which results in the formation of infinite zig-zag chains along the *b* axis. These chains are connected to each other by the sulfonate and phosphonate

groups along the *a* axis. These layers are interconnected via the phenyl groups of the ligand to form a three-dimensional framework (see Figure 4).

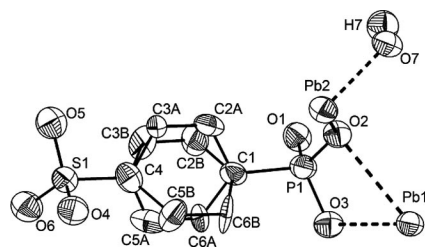


Figure 3. Asymmetric unit of **1**. Hydrogen atoms attached to C-atoms are not shown for clarity. Thermal ellipsoids are drawn at 50% probability.

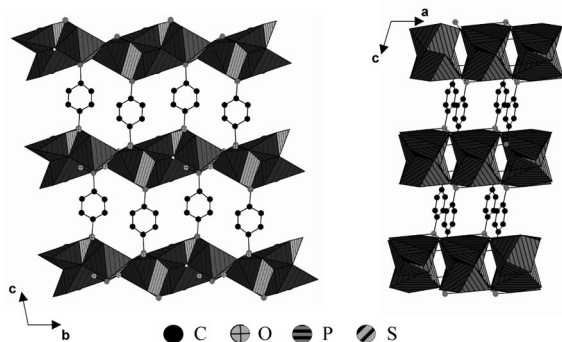


Figure 4. Left: infinite chains of edge-sharing (PbO₇/PbO₅) polyhedra along the *b* axis in (**1**). Right: chains of PbO_x polyhedra are connected to each other via $-(\text{PO}_3)^{2-}$ and $-(\text{SO}_3)^{-}$ groups along the *a* axis. Left and right: the layers are interconnected by the phenyl groups of the ligand molecules. The disordered phenyl rings and H-atoms were omitted for visual clarity.

Crystal Structure of $\text{Cu}_{1.5}[(\text{O}_3\text{P}-\text{C}_6\text{H}_4-\text{SO}_3)(\text{H}_2\text{O})]$ (**2**)

The Cu^{2+} ions in this structure have two types of coordination. One Cu^{2+} ion resides on a special position and is

coordinated by four oxygen atoms from the ligand and two oxygen atoms from water molecules to form Jahn–Teller distorted CuO_6 polyhedra. The other Cu^{2+} ion is surrounded by five oxygen atoms with a square-pyramidal geometry CuO_5 . These edge-sharing polyhedra form Cu_2O_8 clusters which are connected to the CuO_6 polyhedra through the phosphonate and sulfonate groups to form layers in the *a,c* plane (Figure 5, compound **2**, 2-D). The final three-dimensional assembly is achieved by the phenyl groups between the layers. Similar to compound **1**, the phenyl groups are disordered along the C1/C4 axis.

Crystal Structure of $\text{Cu}_2[(\text{O}_3\text{P}-\text{C}_6\text{H}_4-\text{SO}_3)(\text{OH})(\text{H}_2\text{O})]$ (**4**)

The asymmetric unit is composed of two Cu^{2+} ions (Cu1, Cu2) and one 4-phosphonatobenzenesulfonate ion, as well as one water molecule and one hydroxide ion. Cu1 is surrounded by three oxygen atoms from the ligands and two hydroxide $\mu_3\text{-O7}$ ions, thus forming a square-pyramidal CuO_5 unit. Cu2 is coordinated to four oxygen atoms from the ligand, one hydroxide oxygen atom and one water molecule which results in Jahn–Teller distorted CuO_6 polyhedra. Alternating edge-sharing CuO_5 and CuO_6 polyhedra form zig-zag chains along the *b* axis (Figure 5, compound **4**, 1-D). Phosphonate groups from the ligand link the chains along the *c* axis to create a layered structure in the *b,c* plane (Figure 5, compound **4**, 2-D). The final dense three-dimensional framework is then completed by the phenyl groups of the ligand which link the layers along the *a* axis (Figure 5, compound **4**, 3-D).

Crystal Structure of $\text{Cu}_3[(\text{O}_3\text{P}-\text{C}_6\text{H}_4-\text{SO}_3)_2(\text{H}_2\text{O})_2]$ (**5**)

The asymmetric unit of **5** is comprised of three Cu^{2+} ions, two 4-phosphonatobenzenesulfonate ions and two water molecules. Cu1 is exclusively coordinated by four oxygen atoms from phosphonate groups and forms a square

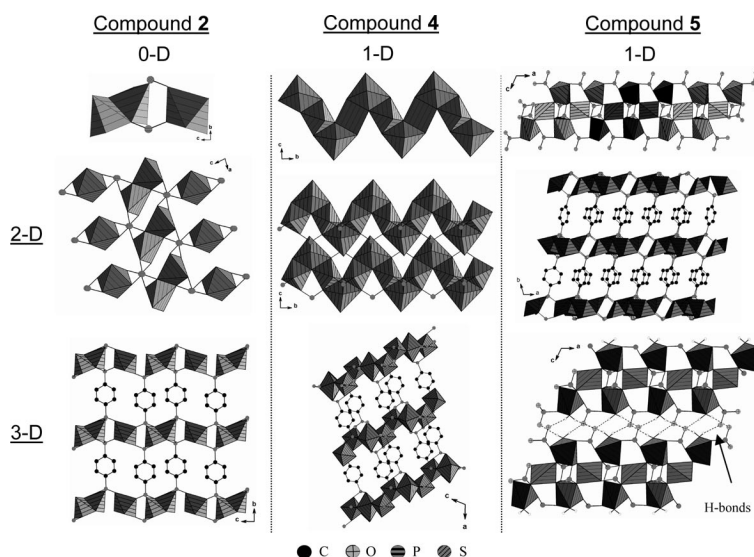


Figure 5. Crystal structure of compounds $\text{Cu}_{1.5}[(\text{O}_3\text{P}-\text{C}_6\text{H}_4-\text{SO}_3)(\text{H}_2\text{O})]$ (**2**), $\text{Cu}_2[(\text{O}_3\text{P}-\text{C}_6\text{H}_4-\text{SO}_3)(\text{OH})(\text{H}_2\text{O})]$ (**4**) and $\text{Cu}_3[(\text{O}_3\text{P}-\text{C}_6\text{H}_4-\text{SO}_3)_2(\text{H}_2\text{O})_2]$ (**5**) starting from the Cu–O building units as well as their connection by the phosphonate/sulfonate groups and the phenyl rings. For the sake of clarity, disordered phenyl rings and H-atoms from phenyl groups are omitted.

planar CuO_4 unit. Cu3 is connected to two sulfonate and phosphonate oxygen atoms each and one water molecule, thereby creating a square-pyramidal geometry (CuO_5 polyhedra). For Cu2 , Jahn–Teller distorted CuO_6 polyhedra are observed with three oxygen atoms from phosphonate groups, two from sulfonate groups and one from a water molecule. Corner-sharing, CuO_4 , CuO_5 and CuO_6 polyhedra build hexanuclear Cu_6O_{24} clusters (Figure 5, compound **5**, 1-D) which are connected through sulfonate and phosphonate groups along the a axis to form a chain-like structure. These chains are connected to each other by the phenyl rings to form layers (Figure 5, compound **5**, 2-D) which are held together exclusively by hydrogen bonding (Figure 5, compound **5**, 3-D, hydrogen bond lengths are given in Table S5 in the Supporting Information).

Characterization of Compound **3**

Up to now, **3** could only be isolated as a microcrystalline powder. The indexing and refinement of the powder XRD pattern using the Louer's algorithm implemented in the STOE WinXPOW^[45] program results in a monoclinic unit cell with the lattice parameters $a = 2162.35(14)$ pm, $b = 875.27(7)$ pm, $c = 1282.68(7)$ pm, $\beta = 113.445(5)^\circ$ (the results of the refinement in Table S7). The composition of **3** was determined with the combined interpretation of thermogravimetric (TG), CHNS and Energy Dispersive X-ray (EDX) analyses data. Composition of **3** was then determined to be $\text{NaCu}(\text{O}_3\text{P-C}_6\text{H}_4\text{-SO}_3)(\text{H}_2\text{O})_3$. Atomic ratio via EDX measurement: $\text{Na/Cu/P/S} = 1:1:1:1$. Experimental amount of water in % (theoretical) = 11.6 (12.3) (Figure S5).

IR-Spectroscopy

Compounds **1**, **3**, **4** and **5** were studied by IR spectroscopy (Figure S2). Their IR spectra exhibit broad bands in the region between 3600 and 3100 cm^{-1} , which are due to OH stretching vibrations of the water molecules involved in weak hydrogen bonding. The weak band at $1630 \pm 20\text{ cm}^{-1}$ is assigned to the deformation vibrations of water molecules. A sharp band seen at 3540 cm^{-1} for $\text{Cu}_2[(\text{O}_3\text{P-C}_6\text{H}_4\text{-SO}_3)(\text{OH})(\text{H}_2\text{O})]$ (**4**) is attributed to the hydroxy group, however, a similar band was not seen for $\text{Pb}_2[(\text{O}_3\text{P-C}_6\text{H}_4\text{-SO}_3)(\text{OH})]$ (**1**) due to overlapping by intensive water bands. $\text{NaCu}(\text{O}_3\text{P-C}_6\text{H}_4\text{-SO}_3)(\text{H}_2\text{O})_3$ (**3**) shows in addition a broad band at 3031 cm^{-1} and comparison with literature values indicates that this could be due to OH-stretching vibrations forming strong hydrogen bonds.^[46–48] For all compounds the C–H stretching bands could not be seen due to overlap with the broad O–H bands, but all compounds exhibit a band in the region of $830 \pm 10\text{ cm}^{-1}$ corresponding to the aromatic C–H out-of-plane deformation vibration. This band is typical for *para*-substituted phenyl rings.^[49] The weak narrow band at $1386 \pm 5\text{ cm}^{-1}$ which is found in all IR spectra can be assigned to the P–C stretching vibration. Strong sharp bands in the fingerprint region

of $1250\text{--}900\text{ cm}^{-1}$ are assigned to symmetric and asymmetric stretching vibrations of CPO_3 and CSO_3 groups.^[50]

Thermal Properties

Thermogravimetric measurements confirmed the number of water molecules in the structures and provide insight in the decomposition temperatures of the compounds (Figure S5). The solid substances after the TGA analyses were characterized by powder XRD measurements. Compounds **3–5** exhibit the presence of water molecules. $\text{Pb}_2[(\text{O}_3\text{P-C}_6\text{H}_4\text{-SO}_3)(\text{OH})]$ (**1**) decomposes at about 500°C to the final product, which is a mixture of $\text{Pb}_3(\text{PO}_4)_2$, PbO and PbSO_4 . The dehydration of compound **3** occurred in the temperature range of $30\text{--}150^\circ\text{C}$. The water molecules are released in two steps (weight loss [%] calcd./obsd.: $14.4/13.0$). Decomposition of the dehydrated phase is observed between 330 and 420°C and as the final product crystalline $\text{Na}_3\text{Cu}_9(\text{PO}_4)_7$ was identified.^[51] The TGA curve of **4** is rather elaborate. The dehydration occurs up to 250°C (weight loss [%] calcd./obsd.: $4.5/4.5$, one water molecule per formula unit). The decomposition of the dehydrated phase is a multistep process and was not completed at the final temperature of 650°C . These steps can not be assigned to defined decomposition products. CuO was identified as the only crystalline product by XRPD. The two coordinated water molecules in compound **5** are released from room temperature up to 150°C . The resulting dehydrated structure is thermally stable up to 450°C and decomposes into light blue coloured $\text{Cu}_3(\text{PO}_4)_2$ (weight loss [%] calcd./obsd.: $45.4/42.5$).

Magnetic Properties

Based on EDX measurements, compound **3** was always contaminated with minor impurities of CuO , which were not detectable in the XRPD investigation. Only **4** and **5** were obtained as pure compounds and therefore investigated by magnetic susceptibility measurements. Figure S7 shows the results of the magnetic investigation in the temperature from $2\text{--}300\text{ K}$. For compound **4** the following plots are shown: $\chi \cdot T$ plotted as a function of temperature (dc field) and frequency dependent ac-susceptibility (ac frequencies: 40 , 400 and 4000 Hz , $T = 2\text{--}7\text{ K}$). For compound **5** the susceptibility χ , inverse susceptibility χ^{-1} and $\chi \cdot T$ plotted as a function of temperature are shown. Compound **5** displays Curie–Weiss behaviour in the range between and $40\text{--}300\text{ K}$. The Curie–Weiss equation $\chi = C/(T - \theta)$ was applied to fit the data (**5**: $C = 1.03\text{ K cm}^3\text{ mol}^{-1}$, $\theta_{\text{W}} = 1.52\text{ K}$). The effective magnetic moment calculated from the fitted data is $1.7\mu_{\text{B}}$ for **5**. This value compares well with the spin-only theoretical value for Cu^{2+} ($1.73\mu_{\text{B}}$). Looking at the structure of **5** it appears that the primary magnetic motive is a trimer consisting of a square planar CuO_4 polyhedron $\mu\text{-O}$ connected to two square-pyramidal CuO_5 polyhedra. Only weak coupling through the phosphonate groups takes place. Antiferromagnetic interactions are

dominating at lower temperatures. For compound **4** at temperatures between 7 and 300 K, antiferromagnetic interactions were observed which switch to ferro/ferromagnetic interactions between 2.2 and 7 K in two steps and finally at 2.2 K antiferromagnetic interactions are found (inset Figure S7, top left). The ac measurements show an increase of the out-of-phase component at higher frequencies (Figure S7, top right). For **4** the spin-topology is more complex. Taking only the short Cu–O bond lengths into account a one-dimensional chain of square planar CuO₄ polyhedra is observed. Strong coupling takes place through the equal sided μ_3 -OH centred Cu₃ triangles which leads to spin frustration. Weaker coupling is only present through the phosphonate groups connecting neighbouring chains to layers and the organic part of the ligand connecting adjacent layers. The complex magnetic behaviour is probably further complicated by structural changes upon cooling. Thus, further studies need to be performed to fully characterize this phenomenon.^[52]

Discussion

High-throughput metal ion and counterion screening enabled the efficient search for optimal starting materials. From these results, Pb(NO₃)₂ and CuCl₂·2H₂O were selected for the discovery and focused arrays. Subsequent HT experiments led to the optimal synthesis conditions of the newly discovered compounds. These studies exemplify the multifaceted application of HT investigation and shows that the methodology can also be used in the discovery of new metal phosphonatosulfonates containing rigid organic linker molecules. The earliest report of the incorporation of 4-phosphonobenzenesulfonic acid was given by Clearfield et al., who obtained a zirconium sulfonophenylphosphonate by sulfonation of Zr(O₃P-C₆H₅)₂ with fuming sulfuric acid. However, no detailed structural characterization of the compound was mentioned.^[19] The first structural analysis of this class of compounds by single-crystal X-ray diffraction was done by Mao et al. by using 3-phosphonobenzenesulfonic acid in combination with co-ligands such as bipyridine or phenanthroline.^[31–35] These studies showed that 3-phosphonobenzenesulfonic acid is a versatile ligand that can adopt various coordination modes. Its use in combination with co-ligands lead mostly to structures containing isolated M–O clusters and the nature of the formed clusters is strongly affected by the amount and coordination nature of the co-ligand. The present study demonstrates that 4-phosphonobenzenesulfonic acid is also a versatile linker for the synthesis of metal phosphonatosulfonates. This can already be seen in the absence of co-ligands. Thus, the compounds in this work contain isolated mono-, di-, hexanuclear M–O clusters or infinite M–O chains which are, with the exception of **5**, connected by the 4-phosphonobenzenesulfonate ions to form pillared layered structures. In comparison to our previous results using the flexible phosphonoalkylsulfonic acids some structural similarities of the Cu²⁺ containing compounds are observed. Cu₂[(O₃P-

C₆H₄-SO₃)(OH)(H₂O)] (**4**), synthesized under similar reaction conditions as Cu₂[(O₃P-C₂H₄-SO₃)(OH)(H₂O)]-(H₂O)^[26] exhibits also infinite M–O–M zigzag chains of CuO₆ polyhedra which are further connected to a pillared layered structure. While the use of the alkyl linker leads to small pores that are filled with non-coordinating water molecules, the more bulky and rigid phenyl groups do not allow the incorporation of water molecules. These structural similarities are also reflected in the magnetic behaviour where switching from antiferromagnetic to ferro/ferromagnetic and again to antiferromagnetic interactions at very low temperatures are observed. Compound **5**, Cu₃[(O₃P-C₆H₄-SO₃)₂(H₂O)₂], is structurally related to the copper compounds with the –C₂H₄– and the –C₄H₈– containing linker molecules, i.e. Cu_{1.5}[(O₃P-C₂H₄-SO₃)(H₂O)] and Cu_{1.5}[(O₃P-C₄H₈-SO₃)(H₂O)]·1.15H₂O, respectively. Although the clusters in these compounds are slightly different, Cu₆O₂₄ cluster in **5** and Cu₃O₁₂ cluster in the other two compounds, they are interconnected to layers by the phosphonatosulfonate ions. These layers are only held together by hydrogen bonding interactions. Compound **1** is only the second example of co-ligand-free lead phosphonatosulfonate. [Pb₃(*m*-O₃P-C₆H₄-SO₃)₂(H₂O)₂]·4H₂O contains 1D chains of Pb₃O₄ clusters which are further bridged by the phosphonatosulfonate ligands.^[35] An open structure is formed with water molecules occupying the pores. The change of the position of the functional group from *meta* to *para* leads to drastic changes in the structure of **1**, although both compound were synthesized under very similar conditions. Thus we observe the formation of Pb–O zigzag chains that are connected to pillared layered structure without any pores.

Conclusions

High-throughput investigation of M²⁺/H₃L/NaOH/H₂O yielded five new compounds Pb₂[(O₃P-C₆H₄-SO₃)(OH)] (**1**), Cu_{1.5}[(O₃P-C₆H₄-SO₃)(H₂O)] (**2**), NaCu(O₃P-C₆H₄-SO₃)(H₂O)₃ (**3**), Cu₂[(O₃P-C₆H₄-SO₃)(OH)(H₂O)] (**4**) and Cu₃[(O₃P-C₆H₄-SO₃)₂(H₂O)₂] (**5**) in the phosphonatoaryl-sulfonate family. Metal screening provided the information about suitable metal ions for the linker 4-phosphonobenzenesulfonic acid. Discovery and focused arrays were employed to find and exactly determine the formation field of the respective compounds. All compounds are observed in a small formation field within well defined molar ratio ranges. Each of the title compounds, with the exception of **2**, can be synthesized with high reproducibility and phase purity. In the structures of **2**, **4** and **5** different coordination modes of the ligand are observed and thereby multiple types of Cu–O connectivities are observed. These range from isolated CuO₆ polyhedra and Cu₂O₈/Cu₆O₂₄ cluster to zig-zag chains of edge sharing CuO₅ and CuO₆ polyhedra. These are connected by the phosphonate and sulfonate groups to form layers or a chain-like structure, which are further connected by the phenyl rings of the linker molecules. We have demonstrated that our high-throughput methodology

can be employed with high efficiency for the detailed investigation of hydrothermal reaction systems ranging from metal screening experiments to the discovery of new compounds using discovery array as well as the optimization of synthesis conditions by employing focused arrays. Further experiments with the rigid ligand 4-phosphonobenzenesulfonic acid are underway to investigate the influence of the rigid aryl group on the structural chemistry.

Experimental Section

Materials and Methods: 4-Phosphonobenzenesulfonic acid (H_3L) was synthesized as described previously in three steps, starting from 4-bromobenzenesulfonyl chloride, sodium ethoxide and triethyl phosphite.^[53] All other reagents were of analytical grade (Aldrich and ABCR) and used without further purification. High-throughput XRPD experiments were carried out in transmission mode using a STOE high-throughput powder diffractometer equipped with an image-plate position-sensitive detector (IPPSD). MIR spectra were recorded with an ATI Matheson Genesis spectrometer in the spectral range 4000–400 cm^{-1} using the KBr disc method. Thermogravimetric analyses were carried out in a nitrogen atmosphere (75 mL min^{-1} , 30–650 $^{\circ}\text{C}$, 4 $^{\circ}\text{C min}^{-1}$) using a NETZSCH STA 409 CD analyzer. CHNS analyses were performed with a Eurovektor EuroEA Elemental Analyzer. The semiquantitative elemental analyses were performed with a Phillips ESEM XL 30 hot-cathode scanning electron microscope equipped with an energy-dispersive X-ray (EDX) EDAX analyzer for elemental analysis. Magnetic measurements for compounds **4** and **5** were performed with a Physical Property Measuring System (PPMS) from Quantum Design (9 T magnet), at 1 kOe and 10 kOe (DC field), respectively, in the temperature range of 2 to 300 K (ZFC).

High-Throughput Experiments: The reaction system $\text{M}^{2+}/\text{H}_3\text{L}/\text{NaOH}/\text{H}_2\text{O}$ was investigated using various molar ratios $\text{M}^{2+}/\text{H}_3\text{L}/\text{NaOH}$ (discovery and focused arrays) employing high-throughput methods (process and compositional parameters are listed in Tab. S1–S4 in the Supporting Information). Each HT experiment was performed under hydrothermal conditions in a custom-made stainless steel high-throughput reactor system containing 48 PTFE inserts each with a maximum volume of 300 μL .^[29] All reagents were manually dosed using aqueous solutions of the reactants (0.4 M to 1.2 M), with the exception of insoluble $\text{Pb}(\text{NO}_3)_2$ which was weighed in directly. The exact amounts of starting materials are given in the Table S1–S4. The evaluations of the HT experiments are based on XRPD measurements.

$\text{Pb}_2[(\text{O}_3\text{P}-\text{C}_6\text{H}_4-\text{SO}_3)(\text{OH})]$ (1**):** In a typical HT experiment **1** was obtained by the following procedure ($\text{Pb}^{2+}/\text{H}_3\text{L}/\text{NaOH} = 4:1:4$). $\text{Pb}(\text{NO}_3)_2$ (26.5 mg, 0.08 mmol) was weighed in the PTFE insert and was mixed with aqueous solutions of H_3L (20 μL , 0.02 mmol), 1 M NaOH (80 μL , 0.08 mmol) and 100 μL of deionized water. The mixture was heated at 150 $^{\circ}\text{C}$ for 48 h. The scale-up of **1** was accomplished using larger PTFE inserts with $V_{\text{max}} = 2500 \mu\text{L}$ employing $\text{Pb}(\text{NO}_3)_2$ (198.7 mg, 0.60 mmol), H_3L (200 μL , 0.15 mmol), 1 M NaOH (600 μL , 0.60 mmol) and 700 μL of deionized water. The product (74 mg, 75% based on H_3L) contained fine white needles (SEM micrograph Figure S6) and was identified by PXRD diffraction (Figure S3) and elemental analysis. $\text{Pb}_2[(\text{O}_3\text{P}-\text{C}_6\text{H}_4-\text{SO}_3)(\text{OH})]$ (**1**), $M = 666.51 \text{ g mol}^{-1}$; EDX measurement: atomic ratio P/S/Pb = 1:1:2; elemental analysis [%]: found C 10.5, H 0.5, S 4.6; calcd. C 10.8, H 0.8, S 4.8.

$\text{NaCu}(\text{O}_3\text{P}-\text{C}_6\text{H}_4-\text{SO}_3)(\text{H}_2\text{O})_3$ (3**):** In a typical HT experiment **3** was obtained by the following procedure ($\text{Cu}^{2+}/\text{H}_3\text{L}/\text{NaOH} =$

2.80:1:4.75). Aqueous solutions of CuCl_2 (0.056 mmol, 56 μL), H_3L (0.02 mmol, 20 μL), NaOH (0.095 mmol, 95 μL) and H_2O (1.61 mmol, 29 μL) were mixed in a 300 μL reactor. The mixture was heated at 150 $^{\circ}\text{C}$ for 48 h. The synthesis of compound **3** could not be scaled-up in glass or Teflon[®] reactors. Therefore, a larger amount of the pure phase product was collected from Teflon[®] reactors of a separate high-throughput experiment. The HT experiment contained 24 identical reaction mixtures with the same molar ratio $\text{Cu}^{2+}/\text{H}_3\text{L}/\text{NaOH} = 2.80:1:4.75$. The total product (72 mg, 40% based on H_3L) contained microcrystalline light blue powder and was identified by PXRD diffraction (Figure S3) and elemental analysis. $\text{NaCu}(\text{O}_3\text{P}-\text{C}_6\text{H}_4-\text{SO}_3)(\text{H}_2\text{O})_3$ (**3**), $M = 375.72 \text{ g mol}^{-1}$; EDX measurement: atomic ratio P/S/Cu/Na = 1:1:1:1; elemental analysis [%]: found C 19.2, H 1.7, S 8.3; calcd. C 19.7, H 2.4, S 8.7.

$\text{Cu}_2[(\text{O}_3\text{P}-\text{C}_6\text{H}_4-\text{SO}_3)(\text{OH})(\text{H}_2\text{O})]$ (4**):** In a typical HT experiment **4** was obtained by the following procedure ($\text{Cu}^{2+}/\text{H}_3\text{L}/\text{NaOH} = 3.00:1:4.85$). Aqueous solutions of CuCl_2 (0.06 mmol, 60 μL), H_3L (0.02 mmol, 20 μL), NaOH (0.097 mmol, 97 μL) and H_2O (1.28 mmol, 23 μL) were mixed in a 300 μL reactor. The mixture was heated at 150 $^{\circ}\text{C}$ for 48 h. The synthesis of compound **4** could not be scaled-up in glass or Teflon[®] reactors. Therefore, a larger amount of the pure phase product was collected from Teflon[®] reactors of a separate high-throughput experiment. The HT experiment contained 24 identical reaction mixtures with the molar ratio $\text{Cu}^{2+}/\text{H}_3\text{L}/\text{NaOH} = 3.00:1:4.85$. The product (64 mg, 34% based on H_3L) contained thin green plates (SEM micrograph Figure S6) and was identified by PXRD diffraction (Figure S3) and elemental analysis. $\text{Cu}_2[(\text{O}_3\text{P}-\text{C}_6\text{H}_4-\text{SO}_3)(\text{OH})(\text{H}_2\text{O})]$ (**4**), $M = 397.25 \text{ g mol}^{-1}$; EDX measurement: atomic ratio P/S/Cu = 1:1:2; found C 16.6, H 1.6, S 7.7; calcd. C 18.1, H 1.8, S 8.1.

$\text{Cu}_3[(\text{O}_3\text{P}-\text{C}_6\text{H}_4-\text{SO}_3)_2(\text{H}_2\text{O})_2]$ (5**):** In a typical HT experiment **5** was obtained by the following procedure ($\text{Cu}^{2+}/\text{H}_3\text{L}/\text{NaOH} = 3.20:1:2.75$). Aqueous solutions of CuCl_2 (0.064 mmol, 64 μL), H_3L (0.02 mmol, 20 μL), NaOH (0.055 mmol, 55 μL) and H_2O (3.39 mmol, 61 μL) were mixed in a 300 μL reactor and heated for 48 h at 150 $^{\circ}\text{C}$. The synthesis of compound **5** could not be scaled-up in glass or Teflon[®] reactors. Therefore, a larger amount of the pure phase product was collected from Teflon[®] reactors of a separate high-throughput experiment. The HT experiment contained 24 identical reaction mixtures with the same molar ratio $\text{Cu}^{2+}/\text{H}_3\text{L}/\text{NaOH} = 3.20:1:2.75$. The product (60 mg, 27% based on H_3L) contained thin blue needles (SEM micrograph Figure S6) and was identified by PXRD diffraction (Figure S3) and elemental analysis. $\text{Cu}_3[(\text{O}_3\text{P}-\text{C}_6\text{H}_4-\text{SO}_3)_2(\text{H}_2\text{O})_2]$ (**5**), $M = 696.90 \text{ g mol}^{-1}$; EDX measurement: atomic ratio P/S/Cu = 1:1:1.5; elemental analysis [%]: found C 19.8, H 1.6, S 8.5; calcd. C 20.7, H 1.7, S 9.2.

X-ray Crystallography: Suitable crystals of the compounds were carefully selected from the HT experiments using a polarizing microscope. Single-crystal X-ray diffraction for **1**, **2** and **4** were performed with a STOE IPDS-1 diffractometer equipped with a fine-focus sealed tube (Mo- K_α radiation, $\lambda = 71.073 \text{ pm}$). For data reduction and absorption correction the programs XRED and XSHAPE were used.^[54] Single crystal of **5** was measured with a Bruker–Nonius APEX II CCD equipped with a Bruker–Nonius FR591 rotating anode Mo- K_α radiation source. Absorption correction was done using SADABS software.^[55] The single crystal structures were solved by direct methods and refined using the program package SHELXTL.^[56] Crystals of compound **4** are nonmerohedrally twinned. The reflections of both individuals were indexed separately using RECIPE and integration of the intensities was performed using TWIN.^[54] By this procedure, overlapping re-

Table 1. Single crystal data for compounds $\text{Pb}_2[(\text{O}_3\text{P-C}_6\text{H}_4\text{-SO}_3)(\text{OH})]$ (**1**), $\text{Cu}_{1.5}[(\text{O}_3\text{P-C}_6\text{H}_4\text{-SO}_3)(\text{H}_2\text{O})]$ (**2**), $\text{Cu}_2[(\text{O}_3\text{P-C}_6\text{H}_4\text{-SO}_3)(\text{OH})(\text{H}_2\text{O})]$ (**4**) and $\text{Cu}_3[(\text{O}_3\text{P-C}_6\text{H}_4\text{-SO}_3)_2(\text{H}_2\text{O})_2]$ (**5**).

Parameter	1	2	4 ^[a]	5
Chemical formula	$\text{C}_6\text{H}_5\text{Pb}_2\text{O}_7\text{PS}$	$\text{C}_6\text{H}_6\text{Cu}_{1.5}\text{O}_7\text{PS}$	$\text{C}_6\text{H}_7\text{Cu}_2\text{O}_8\text{PS}$	$\text{C}_{12}\text{H}_{12}\text{Cu}_3\text{O}_{14}\text{P}_2\text{S}_2$
Crystal system	triclinic	triclinic	monoclinic	triclinic
Space group	$P\bar{1}$	$P\bar{1}$	$P2_1/n$	$P\bar{1}$
<i>a</i> /pm	515.75(7)	484.70(5)	1160.33(9)	998.0(2)
<i>b</i> /pm	1048.05(15)	994.49(11)	706.33(4)	1006.6(2)
<i>c</i> /pm	1085.83(17)	995.76(11)	1397.17(10)	1137.7(2)
α /°	96.502(12)	88.438(14)	90.00	96.63(3)
β /°	95.217(12)	78.152(13)	110.630(8)	113.63(3)
γ /°	94.515(11)	83.756(13)	90.00	101.82(3)
<i>V</i> [10 ⁶ pm ³]	578.38(15)	466.97(9)	1071.66(13)	999.7(3)
<i>Z</i>	2	2	4	2
Formula weight	666.51	348.45	397.25	696.90
Total number of data collected	8182	4645	7484	20336
Unique/obsd. data [<i>I</i> > 2σ(<i>I</i>)]	2458/1990	2233/1706	1861/1521	5794/3947
<i>R</i> (int.)	0.0748	0.0412	0.0479	0.0746
<i>R</i> 1, <i>wR</i> 2 [<i>I</i> > 2σ(<i>I</i>)]	0.0572/0.1057	0.0410/0.1008	0.0462/0.1212	0.0677/0.1227
<i>R</i> 1, <i>wR</i> 2 (all data)	0.0754/0.1122	0.0600/0.1097	0.0547/0.1310	0.1108/0.1375
GOF	1.144	1.040	1.024	1.065
Δ <i>e</i> min./max. /e Å ^{−3}	−2.322/1.769	−0.798/0.794	−0.998/1.188	−0.850/0.973

[a] Compound **4** is non-merohedrally twinned.

flections are omitted. Experimental data and results of the structure determination of **1–5** are given in Table 1. Selected bond lengths are summarized in the Table S1.

CCDC entries 772438–772441 (for compounds **1**, **2**, **4** and **5**) contain the supplementary crystallographic data for this paper. These data can be obtained free of charge from The Cambridge Crystallographic Data Centre via www.ccdc.cam.ac.uk/data_request/cif.

Supporting Information (see also the footnote on the first page of this article): Experimental powder patterns for **1**, **3**, **4** and **5** and simulated patterns for compounds **1**, **2**, **4** and **5**, IR spectra, magnetic measurement plots for **4** and **5**, SEM images and TGA measurements are attached.

Acknowledgments

We gratefully appreciate the help of Professor Paul Kögerler (RWTH Aachen) and Professor Wolfgang Bensch (Univ. of Kiel) for the discussions regarding the magnetic investigations. The authors thank Inke Jess and Alexandra Lieb for the acquisition of the single-crystal data, Adam Wutkowski for TG measurements, Henning Lühmann and Maren Rassmussen for magnetic measurements.

- [1] C. Sanchez, B. Julian, P. Belleville, M. Popall, *J. Mater. Chem.* **2005**, *15*, 3559–3592.
- [2] U. Müller, M. Schubert, F. Teich, H. Pütter, K. Schierle-Arndt, J. Pastré, *J. Mater. Chem.* **2006**, *16*, 626–636.
- [3] P. Horcajada, C. Serre, M. Vallet-Regí, M. Sebban, F. Taulelle, G. Férey, *Angew. Chem. Int. Ed.* **2006**, *45*, 5974–5978.
- [4] A. Sonnauer, F. Hoffmann, M. Froba, L. Kienle, V. Duppel, M. Thommes, C. Serre, G. Férey, N. Stock, *Angew. Chem. Int. Ed.* **2009**, *48*, 3791–3794.
- [5] H. Li, M. Eddaoudi, M. O’Keefe, O. M. Yaghi, *Nature* **1999**, *402*, 276–279.
- [6] D. N. Dybtsev, H. Chun, K. Kim, *Angew. Chem.* **2004**, *116*, 5143–5146.
- [7] K. S. Park, Z. Ni, A. P. Cote, J. Y. Choi, R. Huang, F. J. Uribe-Romo, H. K. Chae, M. O’Keefe, O. M. Yaghi, *Proc. Natl. Acad. Sci. USA* **2006**, *103*, 10186–10191.
- [8] A. Clearfield, *Curr. Opin. Solid State Mater. Sci.* **2002**, *6*, 495–506.
- [9] D. M. Poojary, B. Zhang, P. Bellinghausen, A. Clearfield, *Inorg. Chem.* **1996**, *35*, 5254–5263.
- [10] D. M. Poojary, B. Zhang, P. Bellinghausen, A. Clearfield, *Inorg. Chem.* **1996**, *35*, 4942–4949.
- [11] D. K. Cao, S. Gao, L.-M. Zheng, *J. Solid State Chem.* **2004**, *177*, 2311–2315.
- [12] K. Maeda, *Microporous Mesoporous Mater.* **2004**, *73*, 47–55.
- [13] R.-G. Xiong, J. Zhang, Z.-F. Chen, X.-Z. You, C.-M. Che, H.-K. Fun, *J. Chem. Soc., Dalton Trans.* **2001**, 780–782.
- [14] G. B. Deacon, R. Harika, P. C. Junk, B. W. Skelton, A. H. White, *New J. Chem.* **2007**, *31*, 634–645.
- [15] G. K. H. Shimizu, R. Vaidhyanathan, J. M. Taylor, *Chem. Soc. Rev.* **2009**, *38*, 1430–1449.
- [16] S. Natarajan, P. Mahata, *Curr. Opin. Solid State Mater. Sci.* **2009**, *13*, 46–53.
- [17] S. Miller, G. M. Pearce, P. A. Wright, F. Bonino, S. Chavan, S. Bordiga, I. Margiolaki, N. Guillou, G. Férey, S. Bourrelly, P. L. Llewellyn, *J. Am. Chem. Soc.* **2008**, *130*, 15967–15981.
- [18] K. Maeda, Y. Kiyozumi, F. Mizukami, *Angew. Chem. Int. Ed. Engl.* **1994**, *33*, 2335–2337.
- [19] A. Clearfield, Z. Wang, P. Bellinghausen, *J. Solid State Chem.* **2002**, *167*, 376–385.
- [20] B. D. Chandler, D. T. Cramb, G. K. H. Shimizu, *J. Am. Chem. Soc.* **2006**, *128*, 10403–10412.
- [21] N. Stock, T. Bein, *J. Mater. Chem.* **2005**, *15*, 1384–1391.
- [22] C. Serre, N. Stock, T. Bein, G. Férey, *Inorg. Chem.* **2004**, *43*, 3159.
- [23] N. Stock, A. Stoll, T. Bein, *Microporous Mesoporous Mater.* **2004**, *69*, 65–69.
- [24] S. Bauer, T. Bein, N. Stock, *J. Solid State Chem.* **2006**, *179*, 145–155.
- [25] S. Bauer, T. Bein, *Inorg. Chem.* **2005**, *44*, 5882–5899.
- [26] A. Sonnauer, N. Stock, *Eur. J. Inorg. Chem.* **2008**, 5038–5045.
- [27] A. Sonnauer, N. Stock, *Solid State Sci.* **2009**, *11*, 358–363.
- [28] A. Sonnauer, N. Stock, *J. Solid State Chem.* **2008**, *181*, 473–479.
- [29] A. Sonnauer, C. Näther, H. A. Hoppe, J. Senker, N. Stock, *Inorg. Chem.* **2007**, *46*, 9968–9974.
- [30] A. Sonnauer, N. Stock, *J. Solid State Chem.* **2008**, *181*, 3065–3070.
- [31] Z.-Y. Du, H.-B. Xu, J.-G. Mao, *Inorg. Chem.* **2006**, *45*, 9780–9788.

- [32] Z.-Y. Du, H.-B. Xu, J.-G. Mao, *Inorg. Chem.* **2006**, *45*, 6424–6430.
- [33] Z.-Y. Du, V. A. Prosvirin, J.-G. Mao, *Inorg. Chem.* **2007**, *46*, 9884–9894.
- [34] Z.-Y. Du, X.-L. Li, Q.-Y. Liu, J.-G. Mao, *Cryst. Growth Des.* **2007**, *7*, 1501–1507.
- [35] Z.-Y. Du, H.-B. Xu, X.-L. Li, J.-G. Mao, *Eur. J. Inorg. Chem.* **2007**, 4520–4529.
- [36] F. Adani, M. Casciola, D. J. Jones, L. Massinelli, E. Montoneri, J. Rozière, R. Viviani, *J. Mater. Chem.* **1998**, *8*, 961–964.
- [37] A. F. Benedetto, P. J. Squattrito, F. Adani, E. Montoneri, *Inorg. Chim. Acta* **1997**, *260*, 207–216.
- [38] N. Stock, T. Bein, *Angew. Chem.* **2004**, *116*, 767–770.
- [39] N. Stock, *Microporous Mesoporous Mater.* **2010**, *129*, 287–295.
- [40] S. Bauer, N. Stock, *Angew. Chem. Int. Ed.* **2007**, *46*, 6857–6860.
- [41] S. Bauer, T. Bein, N. Stock, *Solid State Sci.* **2008**, *10*, 837–846.
- [42] P. Forster, N. Stock, A. K. Cheetham, *Angew. Chem. Int. Ed.* **2005**, *44*, 7608–7611.
- [43] R. D. Shannon, *Acta Crystallogr., Sect. A* **1976**, *32*, 751–767.
- [44] N. Stock, *Solid State Sci.* **2002**, *4*, 1089–1094.
- [45] *STOE WinXPOW version 2.11*, Stoe & Cie GmbH, Darmstadt, Germany, **2005**.
- [46] D. Hadzi, *J. Chem. Phys.* **1961**, *34*, 1445.
- [47] K. Okaniwa, H. Okamoto, T. Mitani, K. Toriumi, M. Yamashita, *J. Phys. Soc. Jap.* **1991**, *60*, 997–1004.
- [48] E. Libowitzky, *Monatsh. Chem.* **1999**, *130*, 1047–1059.
- [49] A. Stojiljkovic, D. H. Whiffen, *Spectrochim. Acta* **1958**, *12*, 47–56.
- [50] G. Socrates, in: *Infrared and Raman Characteristic Group Frequencies*, John Wiley & Sons, Chichester, **2004**, 3rd. edition.
- [51] A. Kolsi, C. R. Seances, *C. R. Seances Acad. Sci., Ser. C* **1977**, *284*, 483–486.
- [52] S. Hatscher, H. Schilder, H. Lueken, W. Urland, *Pure Appl. Chem.* **2005**, *77*, 497–511.
- [53] E. Montoneri, G. Viscardi, S. Bottigliengo, R. Gobetto, M. R. Chierotti, R. Buscaino, P. Quagliotto, *Chem. Mater.* **2007**, *19*, 2671–2678.
- [54] *XRED version 1.19, XSHAPE version 1.06, RECIPE, TWIN*, Stoe & Cie GmbH, Darmstadt, Germany, **1999**.
- [55] G. M. Sheldrick, *SADABS version 2007/2*, Bruker AXS Inc., Madison, Wisconsin, USA.
- [56] G. M. Sheldrick, *SHELXTL-PLUS* Crystallographic System, Siemens Analytical X-ray Instruments Inc., Madison, Wisconsin, **1992**.

Received: April 9, 2010

Published Online: July 26, 2010